

**Impact Resistance and Damage Tolerance of
Composite Sandwich Panels**

by

Pui Ho Wilson Tsang

B. Eng., Imperial College of Science and Technology (1987)

S. M., Massachusetts Institute of Technology (1989)

Submitted to the Department of Aeronautics and Astronautics in partial
fulfillment of the requirements for the degree of

Doctor of Philosophy in
Aeronautics and Astronautics

at the

Massachusetts Institute of Technology
June 1994

© Massachusetts Institute of Technology 1994

Signature of Author _____
Department of Aeronautics and Astronautics

Certified by _____
Professor Paul A. Lagace
Chairman, Thesis Committee

Certified by _____
Professor John Dugundji
Thesis Committee

Certified by _____
Professor Hugh L. McManus
Thesis Committee

Accepted by _____
Professor Harold Y. Wachman
Chairman, Departmental Graduate Committee

ARCHIVES

JUN 09 1994

Impact Resistance and Damage Tolerance of Composite Sandwich Panels

by

Pui Ho Wilson Tsang

Submitted to the Department of Aeronautics and Astronautics on March 16, 1994 in partial fulfillment of the requirements for the Degree of Doctor of Philosophy

Abstract

Work was conducted to better understand the damage created in sandwich panels subjected to indentation/impact loading and the subsequent failure process under compressive loads. Three different damage states were created by indenting sandwich panels to a 3 mm indentation depth with indentors of three different diameters: 12.7 mm, 25.4 mm, and 38.1 mm. The sandwich panels were 89 mm wide and 356 mm long with (0/90) and (± 45) facesheets made from AW193/3501-6 graphite/epoxy plain weave fabric. The Nomex honeycomb core has a density of 48 kg/m^3 , a thickness of 25.4 mm, and a cell size of 3.2 mm. The damage states were characterized by various techniques in terms of geometric facesheet damage (shape of permanent dimple as a result of indentation), material facesheet damage (fiber damage, delaminations, and matrix cracks), and core damage (buckled/crushed cell walls). Damage inspection shows that the permanent dimple is deeper, more localized, and contains more extensive material facesheet damage for the smaller indenter diameter. Based on the damage characterization results, specimens with simulated damage types were designed and manufactured to separately model the core damage and geometric facesheet damage (simulated core damage) and the material facesheet damage (simulated facesheet damage) observed in the indented specimens. Uniaxial compression tests were conducted to failure and monitored with the shadow moiré method to obtain quantitative measurements of the out-of-plane deformation of the dimple. Existing analytical models were adapted to predict the damage propagation and the residual strengths of the specimens tested. The failure mechanism of specimens with simulated core damage and those with static indentation damage is via dimple propagation primarily perpendicular to the loading direction, followed by catastrophic failure in the form of facesheet fracture across the width of the specimens. The dimple propagation is driven by load redistribution in the presence of out-of-plane eccentricity (i.e. the dimple), a combination which causes local bending of the facesheet and progressive core crushing perpendicular to the loading direction. The dimple propagation model successfully predicts the evolving dimple profiles for specimens with (0/90) facesheets and simulated core damage. Material facesheet damage and nonlinear stress-strain behavior of the (± 45) facesheets cause a local reduction in facesheet stiffness which induces more severe load redistribution and, hence, greater rates of dimple propagation. Such local reduction in facesheet stiffness needs to be included in the dimple propagation model to improve the predictions for specimens with material facesheet damage and/or (± 45) facesheets. The final failure in specimens with static indentation damage and simulated core damage is caused by high longitudinal stress due to load redistribution in the facesheet within the dimple. The applied stress levels at which the calculated peak longitudinal membrane stress along the centerline through the dimple and perpendicular to the loading direction reaches the compressive strength of the corresponding undamaged specimens correlates well with the residual strengths of specimens with (0/90) facesheets and simulated core damage. Failure predictions for specimens with (0/90) facesheets and static indentation damage is not as good because the model does not account for the interaction between the geometric facesheet damage, core damage, and material facesheet damage. Visibility of the dimple and dimple depth alone are not good metrics for damage because barely visible damage can cause equally significant or greater reduction in compressive strength as easily visible damage. Proper three-dimensional damage characterization of all damage types is necessary to facilitate better assessment of damage tolerance.

Advisor: Paul A. Lagace

Title: Associate Professor, Department of Aeronautics and Astronautics,
Massachusetts Institute of Technology

Acknowledgements

I would like to thank my thesis advisor, Prof. Paul A. Lagace, for the opportunity to work in TELAC for the past six and a half years. His endless effort to keep the lab running is very much appreciated. In order to compensate for my mediocre writing skills, Paul has spent countless evenings and weekends to help me hammer this thesis into shape. I also owe my gratitude to Prof. John Dugundji and Prof. Hugh L. McManus for their valuable advice and encouragement through the years. Thanks also goes to Prof. James W. Mar and Prof. Michael J. Graves for their advice during their presence in TELAC. Thanks to Ping Lee and Al Supple for taking care of the administrative and technical aspects of the day-to-day operation of the lab.

My thesis would not have been possible without the help of my dedicated UROPers: John Van Houton, Mary Beth Richards, Nate Crosswhite, and Dan Dunn. Equally important is the friendly support I receive from many "generations" of graduate students in TELAC. Thanks also goes to Elaine Lee for being such a wonderful companion for the past four years. Finally, I would like to thank my family for their long-distance support through all these years I spent at MIT.

Foreword

This work was performed in the Technology Laboratory for Advanced Composites (TELAC) in the Department of Aeronautics and Astronautics at the Massachusetts Institute of Technology. This work was sponsored by Boeing Helicopters under Boeing Purchase Order Numbers ABQ042, ACP850, ADM652. Additional support was also provided through the Leaders for Manufacturing Program at M. I. T.

Table of Contents

List of Figures	8
List of Tables	25
Nomenclature	26
1. Introduction	28
2. Previous Work	33
2.1 Impact Damage Resistance	33
2.2 Damage Tolerance	44
2.3 Summary	49
3. Approach	51
3.1 Overview	51
3.2 Damage States and Characterization	54
3.3 Failure Mechanisms	57
3.4 Analyses	58
4. Analytical Methods	60
4.1 Dimple Propagation Model	60
4.1.1 Governing equations	61
4.1.2 Discretization of stress function and displacement function	64
4.1.3 Two-parameter foundation model	71
4.1.4 Core damage model	72
4.1.5 Solution procedure	79
4.1.6 Failure prediction	80
4.1.7 Computer program	81
4.1.8 Convergence studies	83
4.2 Mar-Lin Correlation	91
5. Experimental Procedures	97

5.1	Specimen Description	97
5.2	Test Matrices	98
5.3	Manufacturing Procedures	103
5.3.1	General procedures	104
5.3.2	Specimens with Static Indentation Damage (SID)	113
5.3.3	Specimens with Simulated Core Damage (SCD)	115
5.3.4	Specimens with Simulated Facesheet Damage (SFD)	125
5.4	Instrumentation and Surface Preparation	125
5.5	Test Procedures	129
5.5.1	Static Indentation Tests	129
5.5.2	Uniaxial Compression Tests	134
5.5.3	Shadow moiré method	135
5.5.4	Data reduction	142
5.6	Damage characterization	142
5.6.1	X-radiography	145
5.6.2	Microscopic inspection	146
5.6.3	Thermal depley	148
5.6.4	Dial gage measurements	151
6.	Results	153
6.1	Impact Resistance	155
6.1.1	Load-indentation data	155
6.1.2	Characterization of static indentation damage	159
6.1.3	Simulated Damage Types	182
6.2	Damage Tolerance	201
6.2.1	Input parameters for the dimple propagation model	205
6.2.2	Far-field stress-strain data	220
6.2.3	Dimple propagation	228
6.2.4	Post-mortem inspection of failed specimens	284
6.2.5	Compressive strength results	305

6.2.6 Predicted stress distributions and prediction of failure stress	309
7. Discussion	354
7.1 Impact Resistance	354
7.2 Damage Tolerance	360
7.2.1 Assessment of the dimple propagation model	360
7.2.2 Dimple propagation	362
7.2.3 Final failure	370
8. Conclusions and Recommendations	381
8.1 Conclusions	381
8.2 Recommendations	385
References	387
Appendix A	397
Appendix B	418
Appendix C	419
Appendix D	422

List of Figures

Figure 2.1	Sketch of permanent dent/dimple in sandwich panel with tape facesheets (taken from [27]).	37
Figure 2.2	Sketch of permanent dent/dimple in sandwich panel with fabric facesheets (taken from [33]).	38
Figure 3.1	Specimen configuration	52
Figure 4.1	Coordinate system used for dimple propagation model.	62
Figure 4.2	Sketch of stress-strain curve of flatwise compression test of bare Nomex honeycomb core (actual data can be found in [58]).	74
Figure 4.3	Flowchart for program GROWTH.	82
Figure 4.4	Predicted dimple profile, for various numbers of modes, along centerline perpendicular to loading in a (0/90) sandwich panel loaded to -250 MPa for an initial crushed core radius of 5 mm.	87
Figure 4.5	Predicted dimple profile, for various numbers of modes, along centerline perpendicular to loading in a (0/90) sandwich panel loaded to -250 MPa for an initial crushed core radius of 10 mm..	88
Figure 4.6	Predicted through-thickness stress (σ_{zz}) distribution, for various numbers of modes, at interface between core and facesheet along centerline perpendicular to loading in a (0/90) sandwich panel loaded to -250 MPa for an initial crushed core radius of 5 mm.	89
Figure 4.7	Predicted through-thickness stress (σ_{zz}) distribution, for various numbers of modes, at interface between core and facesheet along centerline perpendicular to loading in a (0/90) sandwich panel loaded to -250 MPa for an initial crushed core radius of 10 mm.	90
Figure 4.8	Predicted longitudinal stress (σ_{xx}) distribution, for various numbers of modes, at top surface of facesheet along centerline perpendicular to loading in an (0/90) sandwich panel loaded to -250 MPa for an initial crushed core radius of 5 mm.	92

Figure 4.9	Predicted longitudinal stress (σ_{xx}) distribution, for various numbers of modes, at top surface of facesheet along centerline perpendicular to loading in an (0/90) sandwich panel loaded to -250 MPa for an initial crushed core radius of 10 mm.	93
Figure 4.10	Predicted longitudinal stress (σ_{xx}) distribution, for various numbers of modes, at bottom surface of facesheet along centerline perpendicular to loading in an (0/90) sandwich panel loaded to -250 MPa for an initial crushed core radius of 10 mm.	94
Figure 4.11	Predicted longitudinal stress (σ_{xx}) distribution, for various numbers of modes, at bottom surface of facesheet along centerline perpendicular to loading in an (0/90) sandwich panel loaded to -250 MPa for an initial crushed core radius of 10 mm.	95
Figure 5.1	Illustration of specimen configuration.	100
Figure 5.2	Illustration of cure assembly for laminate (facesheet) cure of specimens with no damage, static indentation damage, and simulated facesheet damage.	105
Figure 5.3	Nominal temperature and pressure histories for laminate cure.	107
Figure 5.4	Locations for thickness measurements of undamaged facesheets.	108
Figure 5.5	Location of aluminum dams used for secondary bond cure and loading tab cure.	110
Figure 5.6	Illustration of cure assembly for secondary bond cure.	111
Figure 5.7	Nominal temperature and pressure histories for secondary bond cure and loading tab cure.	112
Figure 5.8	Illustration of assembly for loading tab cure.	114
Figure 5.9	Illustration of cure assembly for facesheets used in specimens with simulated core damage.	116
Figure 5.10	Illustration of detachable tups for manufacturing SCD1 and SCD2 specimens.	118
Figure 5.11	Illustration of special aluminum cure plate for manufacturing SCD1 and SCD2 specimens.	119
Figure 5.12	Illustration of mold for manufacturing special cure plates used in manufacture of SCD3 specimens.	121

Figure 5.13	Locations for thickness measurements for dimpled facesheets used in specimens with simulated core damage.	123
Figure 5.14	Cure assembly for secondary bond cure of panels with simulated core damage.	124
Figure 5.15	Slit locations for specimens with simulated facesheet damage.	126
Figure 5.16	Illustration of jig used to cut slits in specimens with simulated facesheet damage.	127
Figure 5.17	Strain gage locations for undamaged panels used to evaluate material properties.	128
Figure 5.18	Strain gage locations for specimens with static indentation damage, simulated core damage, and simulated facesheet damage.	130
Figure 5.19	Illustration of experimental setup for static indentation tests.	132
Figure 5.20	Illustration of indentors used for static indentation tests.	133
Figure 5.21	Photograph of moiré fringes of a hemispherical dimple, 16 mm in radius and 2 mm deep, machined in an aluminum plate with a ball-end mill.	137
Figure 5.22	Illustration of grating holder for the shadow moiré setup.	139
Figure 5.23	Illustration of angle finder used for measuring angle of incidence of light source for shadow moiré method.	141
Figure 5.24	Schematic of the moiré setup.	143
Figure 5.25	Moiré measurements of a hemispherical dimple, 16 mm in radius and 2 mm deep, machined in an aluminum plate with a ball-end mill (fringe pattern shown in Figure 5.21).	144
Figure 5.26	Typical X-radiographs of the specimens with (0/90) facesheets indented with the three different indentors.	147
Figure 5.27	Typical sketch of fiber damage due to indentation as observed in individual plies of the facesheets after thermal deply.	149
Figure 5.28	Photograph of typical cross-section of a specimen with (0/90) facesheets indented with the 12.7 mm-diameter indenter.	150

Figure 5.29	Locations for dial gage measurements of the dimple profiles.	152
Figure 6.1	Typical load-indentation curves of specimens with (0/90) facesheets for different indenter diameters.	156
Figure 6.2	Typical load-indentation curves of specimens with (± 45) facesheets for different indenter diameters.	158
Figure 6.3	Load-indentation curves of specimens with (0/90) facesheets and with (± 45) facesheets indented with the 12.7 mm-diameter indenter.	160
Figure 6.4	Load-indentation curves of specimens with (0/90) facesheets and with (± 45) facesheets indented with the 25.4 mm-diameter indenter.	161
Figure 6.5	Load-indentation curves of specimens with (0/90) facesheets and with (± 45) facesheets indented with the 38.1 mm-diameter indenter.	162
Figure 6.6	Permanent dent/dimple due to indentation with the 12.7 mm-diameter indenter in a specimen with (0/90) facesheets.	164
Figure 6.7	Permanent dent/dimple due to indentation with the 25.4 mm-diameter indenter in a specimen with (0/90) facesheets.	165
Figure 6.8	Permanent dent/dimple due to indentation with the 38.1 mm-diameter indenter in a specimen with (0/90) facesheets.	166
Figure 6.9	Sketch of facesheet damage due to indentation in specimens with (0/90) facesheets.	167
Figure 6.10	Photograph of facesheet damage due to indentation with the 12.7 mm-diameter indenter in a specimen with (0/90) facesheets.	168
Figure 6.11	Typical X-radiographs of the specimens with (0/90) facesheets indented with the three different indentors.	169
Figure 6.12	Photograph of cross-section of a specimen with (0/90) facesheets indented with the 12.7 mm-diameter indenter.	171
Figure 6.13	Photograph of cross-section of a specimen with (0/90) facesheets indented with the 25.4 mm-diameter indenter.	172

Figure 6.14	Photograph of cross-section of a specimen with (0/90) facesheets indented with the 38.1 mm-diameter indenter.	173
Figure 6.15	Photograph of facesheet damage due to indentation with the 12.7 mm-diameter indenter in a specimen with (± 45) facesheets.	176
Figure 6.16	Typical X-radiographs of specimens with (± 45) facesheets indented with the three different indentors.	177
Figure 6.17	Photograph of cross-section of a specimen with (± 45) facesheets indented with the 12.7 mm-diameter indenter.	179
Figure 6.18	Photograph of cross-section of a specimen with (± 45) facesheets indented with the 25.4 mm-diameter indenter.	180
Figure 6.19	Photograph of cross-section of a specimen with (± 45) facesheets indented with the 38.1 mm-diameter indenter.	181
Figure 6.20	Photograph of cross-section of a specimen with level 1 simulated core damage and (0/90) facesheets.	184
Figure 6.21	Photograph of cross-section of a specimen with level 2 simulated core damage and (0/90) facesheets.	185
Figure 6.22	Photograph of cross-section of a specimen with level 3 simulated core damage and (0/90) facesheets.	186
Figure 6.23	Sketch illustrating relative in-plane extent and through-thickness distribution of core damage in specimens with simulated core damage versus those with static indentation damage.	187
Figure 6.24	Dimple profiles along the warp direction of specimens with (0/90) facesheets and level 1 static indentation damage and level 1 simulated core damage.	189
Figure 6.25	Dimple profiles along the fill direction of specimens with (0/90) facesheets and level 1 static indentation damage and level 1 simulated core damage.	190
Figure 6.26	Dimple profiles along the warp direction of specimens with (0/90) facesheets and level 2 static indentation damage and level 2 simulated core damage.	191

Figure 6.27	Dimple profiles along the fill direction of specimens with (0/90) facesheets and level 2 static indentation damage and level 2 simulated core damage.	192
Figure 6.28	Dimple profiles along the warp direction of specimens with (0/90) facesheets and level 3 static indentation damage and level 3 simulated core damage.	193
Figure 6.29	Dimple profiles along the fill direction of specimens with (0/90) facesheets and level 3 static indentation damage and level 3 simulated core damage.	194
Figure 6.30	Dimple profiles along the warp direction of specimens with (± 45) facesheets and level 1 static indentation damage and level 1 simulated core damage.	195
Figure 6.31	Dimple profiles along the fill direction of specimens with (± 45) facesheets and level 1 static indentation damage and level 1 simulated core damage.	196
Figure 6.32	Dimple profiles along the warp direction of specimens with (± 45) facesheets and level 2 static indentation damage and level 2 simulated core damage.	197
Figure 6.33	Dimple profiles along the fill direction of specimens with (± 45) facesheets and level 2 static indentation damage and level 2 simulated core damage.	198
Figure 6.34	Dimple profiles along the warp direction of specimens with (± 45) facesheets and level 3 static indentation damage and level 3 simulated core damage.	199
Figure 6.35	Dimple profiles along the fill direction of specimens with (± 45) facesheets and level 3 static indentation damage and level 3 simulated core damage.	200
Figure 6.36	Photograph of simulated facesheet damage in (0/90) facesheet.	203
Figure 6.37	Photograph of simulated facesheet damage in (± 45) facesheet.	204
Figure 6.38	Assumed and measured shapes of the dimple in specimens with (0/90) facesheets and level 1 simulated core damage.	208

Figure 6.39	Assumed and measured shapes of the dimple in specimens with (0/90) facesheets and level 2 simulated core damage.	209
Figure 6.40	Assumed and measured shapes of the dimple in specimens with (0/90) facesheets and level 3 simulated core damage.	210
Figure 6.41	Assumed and measured shapes of the dimple in specimens with (± 45) facesheets and level 1 simulated core damage.	211
Figure 6.42	Assumed and measured shapes of the dimple in specimens with (± 45) facesheets and level 2 simulated core damage.	212
Figure 6.43	Assumed and measured shapes of the dimple in specimens with (± 45) facesheets and level 3 simulated core damage.	213
Figure 6.44	Predicted dimple profiles of a specimen with (0/90) facesheets and level 3 simulated core damage at an applied stress of -310 MPa for three values of splat.	216
Figure 6.45	Predicted through-thickness stress distribution of a specimen with (0/90) facesheets and level 3 simulated core damage at an applied stress of -310 MPa for three values of splat.	217
Figure 6.46	Predicted membrane stress distribution of a specimen with (0/90) facesheets and level 3 simulated core damage at an applied stress of -310 MPa for three values of splat.	218
Figure 6.47	Predicted bending stress distribution of a specimen with (0/90) facesheets and level 3 simulated core damage at an applied stress of -310 MPa for three values of splat.	219
Figure 6.48	Typical stress-strain results of an undamaged specimen with (0/90) facesheets.	223
Figure 6.49	Typical stress-strain results of a specimen with (0/90) facesheets and static indentation damage.	224
Figure 6.50	Typical stress-strain results of a specimen with (0/90) facesheets and simulated core damage.	225
Figure 6.51	Typical stress-strain results of a specimen with (0/90) facesheets and simulated facesheet damage.	226

Figure 6.52	Typical stress-strain results of an undamaged specimen with (± 45) facesheets.	229
Figure 6.53	Typical stress-strain results of a specimen with (± 45) facesheets and static indentation damage.	230
Figure 6.54	Typical stress-strain results of a specimen with (± 45) facesheets and simulated core damage.	231
Figure 6.55	Typical stress-strain results of a specimen with (± 45) facesheets and simulated facesheet damage.	232
Figure 6.56	Digitized moiré fringe patterns at various applied stress levels for a specimen with (0/90) facesheets and indentation damage inflicted with a 12.7 mm-diameter indenter.	235
Figure 6.57	Digitized moiré fringe patterns at various applied stress levels for a specimen with (0/90) facesheets and level 1 simulated core damage.	236
Figure 6.58	Measured dimple profiles along centerline in loading direction at various loads for a specimen with (0/90) facesheets and level 1 static indentation damage (corresponding moiré fringe patterns shown in Figure 6.56).	237
Figure 6.59	Measured dimple profiles along centerline perpendicular to loading direction at various loads for a specimen with (0/90) facesheets and level 1 static indentation damage (corresponding moiré fringe patterns shown in Figure 6.56).	238
Figure 6.60	Experimental and predicted dimple profiles along centerline perpendicular to loading direction at various loads for a specimen with (0/90) facesheets and with level 1 static indentation damage.	239
Figure 6.61	Experimental and predicted dimple profiles along centerline in loading direction at various loads for a specimen with (0/90) facesheets and with level 1 static indentation damage.	240
Figure 6.62	Experimental and predicted dimple profiles along centerline perpendicular to loading direction at various loads for a specimen with (0/90) facesheets and with level 2 static indentation damage.	241
Figure 6.63	Experimental and predicted dimple profiles along centerline in loading direction at various loads for a specimen with (0/90) facesheets and with level 2 static indentation damage.	242

Figure 6.64	Experimental and predicted dimple profiles along centerline perpendicular to loading direction at various loads for a specimen with (0/90) facesheets and with level 3 static indentation damage.	243
Figure 6.65	Experimental and predicted dimple profiles along centerline in loading direction at various loads for a specimen with (0/90) facesheets and with level 3 static indentation damage.	244
Figure 6.66	Experimental and predicted dimple profiles along centerline perpendicular to loading direction at various loads for a specimen with (0/90) facesheets and with level 1 simulated core damage.	246
Figure 6.67	Experimental and predicted dimple profiles along centerline in loading direction at various loads for a specimen with (0/90) facesheets and with level 1 simulated core damage.	247
Figure 6.68	Experimental and predicted dimple profiles along centerline perpendicular to loading direction at various loads for a specimen with (0/90) facesheets and with level 2 simulated core damage.	248
Figure 6.69	Experimental and predicted dimple profiles along centerline in loading direction at various loads for a specimen with (0/90) facesheets and with level 2 simulated core damage.	249
Figure 6.70	Experimental and predicted dimple profiles along centerline perpendicular to loading direction at various loads for a specimen with (0/90) facesheets and with level 3 simulated core damage.	250
Figure 6.71	Experimental and predicted dimple profiles along centerline in loading direction at various loads for a specimen with (0/90) facesheets and with level 3 simulated core damage.	251
Figure 6.72	Predicted and measured dimension of dimple along centerline perpendicular to loading at various applied stress levels for specimens with (0/90) facesheets and level 1 damage.	253
Figure 6.73	Predicted and measured dimension of dimple along centerline perpendicular to loading at various applied stress levels for specimens with (0/90) facesheets and level 2 damage.	254

Figure 6.74	Predicted and measured dimension of dimple along centerline perpendicular to loading at various applied stress levels for specimens with (0/90) facesheets and level 3 damage.	255
Figure 6.75	Dimension of dimple along centerline perpendicular to loading at various applied stress levels for specimens with (0/90) facesheets and static indentation damage.	256
Figure 6.76	Dimension of dimple along centerline perpendicular to loading at various applied stress levels for specimens with (0/90) facesheets and simulated core damage.	257
Figure 6.77	Digitized moiré fringe patterns at various applied stress levels for a specimen with (± 45) facesheets and indentation damage inflicted with a 12.7 mm-diameter indenter.	258
Figure 6.78	Digitized moiré fringe patterns at various applied stress levels for a specimen with (± 45) facesheets and level 1 simulated core damage.	259
Figure 6.79	Experimental and predicted dimple profiles along centerline perpendicular to loading direction at various loads for a specimen with (± 45) facesheets and with level 1 static indentation damage.	260
Figure 6.80	Experimental and predicted dimple profiles along centerline in loading direction at various loads for a specimen with (± 45) facesheets and with level 1 static indentation damage.	261
Figure 6.81	Experimental and predicted dimple profiles along centerline perpendicular to loading direction at various loads for a specimen with (± 45) facesheets and with level 2 static indentation damage.	262
Figure 6.82	Experimental and predicted dimple profiles along centerline in loading direction at various loads for a specimen with (± 45) facesheets and with level 2 static indentation damage.	263
Figure 6.83	Experimental and predicted dimple profiles along centerline perpendicular to loading direction at various loads for a specimen with (± 45) facesheets and with level 3 static indentation damage.	264

Figure 6.84	Experimental and predicted dimple profiles along centerline in loading direction at various loads for a specimen with (± 45) facesheets and with level 3 static indentation damage.	265
Figure 6.85	Experimental and predicted dimple profiles along centerline perpendicular to loading direction at various loads for a specimen with (± 45) facesheets and with level 1 simulated core damage.	267
Figure 6.86	Experimental and predicted dimple profiles along centerline in loading direction at various loads for a specimen with (± 45) facesheets and with level 1 simulated core damage.	268
Figure 6.87	Experimental and predicted dimple profiles along centerline perpendicular to loading direction at various loads for a specimen with (± 45) facesheets and with level 2 simulated core damage.	269
Figure 6.88	Experimental and predicted dimple profiles along centerline in loading direction at various loads for a specimen with (± 45) facesheets and with level 2 simulated core damage.	270
Figure 6.89	Experimental and predicted dimple profiles along centerline perpendicular to loading direction at various loads for a specimen with (± 45) facesheets and with level 3 simulated core damage.	271
Figure 6.90	Experimental and predicted dimple profiles along centerline in loading direction at various loads for a specimen with (± 45) facesheets and with level 3 simulated core damage.	272
Figure 6.91	Dimension of dimple along centerline perpendicular to loading at various applied stress levels for specimens with (± 45) facesheets and level 1 damage.	273
Figure 6.92	Dimension of dimple along centerline perpendicular to loading at various applied stress levels for specimens with (± 45) facesheets and level 2 damage.	274
Figure 6.93	Dimension of dimple along centerline perpendicular to loading at various applied stress levels for specimens with (± 45) facesheets and level 3 damage.	275
Figure 6.94	Dimension of dimple along centerline perpendicular to loading at various applied stress levels for specimens with (± 45) facesheets and static indentation damage.	277

Figure 6.95	Dimension of dimple along centerline perpendicular to loading at various applied stress levels for specimens with (± 45) facesheets and simulated core damage.	278
Figure 6.96	Dimension of dimple perpendicular to loading direction just before catastrophic failure, y_{crit} , for specimens with (0/90) facesheets versus simulated/actual indenter diameter.	279
Figure 6.97	Dimension of dimple perpendicular to loading direction just before catastrophic failure, y_{crit} , for specimens with (± 45) facesheets versus simulated/actual indenter diameter.	280
Figure 6.98	Depth of dimple just before catastrophic failure, z_{crit} , for specimens with (0/90) facesheets versus simulated/actual indenter diameter.	282
Figure 6.99	Depth of dimple just before catastrophic failure, z_{crit} , for specimens with (± 45) facesheets versus simulated/actual indenter diameter.	283
Figure 6.100	Photograph of failure mode of an undamaged specimen with (0/90) facesheets	285
Figure 6.101	Sketch of core tearing observed in failed sandwich panels.	286
Figure 6.102	Sketch of failure modes in specimens with (0/90) facesheets and static indentation damage as well as specimens with simulated core damage.	288
Figure 6.103	Sketch of core tearing and core crushing observed at edges of some failed specimens with static indentation damage and specimens with simulated core damage when dimple propagated to the edges.	289
Figure 6.104	Photograph of a typical straight-line fracture perpendicular to the loading direction for a specimen with (0/90) facesheets and static indentation damage.	290
Figure 6.105	Photograph of a typical straight-line fracture perpendicular to the loading direction for a specimen with (0/90) facesheets and simulated core damage.	291
Figure 6.106	Photograph of a typical straight-line fracture perpendicular to the loading direction for a specimen with (0/90) facesheets and simulated facesheet damage.	293

Figure 6.107	Photograph of failure mode of an undamaged specimen with (± 45) facesheets showing a straight-line fracture along one of the tow directions.	294
Figure 6.108	Photograph of failure mode of an undamaged specimen with (± 45) facesheets showing a "zig-zag" fracture along one of the tow directions.	295
Figure 6.109	Sketch of failure mode in specimens with (± 45) facesheets and static indentation damage or simulated core damage.	296
Figure 6.110	Photograph of failure mode of a specimen with static indentation damage and (± 45) facesheets showing a straight-line fracture perpendicular to the loading direction.	298
Figure 6.111	Photograph of failure mode of a specimen with (± 45) facesheets and simulated core damage showing a straight-line fracture perpendicular to the loading direction.	299
Figure 6.112	Photograph of failure mode of a specimen with (± 45) facesheets and static indentation damage showing a straight-line fracture at center and "branched" fracture beyond the extent of the dimple propagation.	300
Figure 6.113	Photograph of failure mode of a specimen with (± 45) facesheets and simulated core damage showing a straight-line fracture at center and "branched" fracture beyond the extent of the dimple propagation.	301
Figure 6.114	Photograph of fracture pattern of a specimen with (± 45) facesheets and simulated facesheet damage.	302
Figure 6.115	Sketch of the propagation of the slits in specimens with (± 45) facesheets and simulated facesheet damage.	303
Figure 6.116	Sketch of failure modes of specimens with (± 45) facesheets and simulated facesheet damage and specimens with simulated core damage.	304
Figure 6.117	Compressive strength of specimens with (0/90) facesheets versus simulated/actual indenter diameter.	307
Figure 6.118	Digitized video image of the specimen with (0/90) facesheets and level 1 static indentation damage that failed by developing a fracture on one side of the dimple.	308

Figure 6.119	Compressive strength of specimens with (± 45) facesheets versus simulated/actual indenter diameter.	311
Figure 6.120	Membrane stress distribution at two applied stress levels in a specimen with (0/90) facesheets and level 1 simulated core damage.	314
Figure 6.121	Bending stress distribution at top surface for two applied stress levels in a specimen with (0/90) facesheets and level 1 simulated core damage.	315
Figure 6.122	Total longitudinal stress distribution at top and bottom surfaces for two applied stress levels in a specimen with (0/90) facesheets and level 1 simulated core damage.	316
Figure 6.123	Membrane stress distribution at two applied stress levels in a specimen with (0/90) facesheets and level 2 simulated core damage.	317
Figure 6.124	Bending stress distribution at top surface for two applied stress levels in a specimen with (0/90) facesheets and level 2 simulated core damage.	318
Figure 6.125	Total longitudinal stress distribution at top and bottom surfaces for two applied stress levels in a specimen with (0/90) facesheets and level 2 simulated core damage.	319
Figure 6.126	Membrane stress distribution at two applied stress levels in a specimen with (0/90) facesheets and level 3 simulated core damage.	320
Figure 6.127	Bending stress distribution at top surface for two applied stress levels in a specimen with (0/90) facesheets and level 3 simulated core damage.	321
Figure 6.128	Total longitudinal stress distribution at top and bottom surfaces for two applied stress levels in a specimen with (0/90) facesheets and level 3 simulated core damage.	322
Figure 6.129	Membrane stress distribution at two applied stress levels in a specimen with (0/90) facesheets and level 1 static indentation damage.	324
Figure 6.130	Bending stress distribution at top surface for two applied stress levels in a specimen with (0/90) facesheets and level 1 static indentation damage.	325

Figure 6.131	Total longitudinal stress distribution at top and bottom surfaces for two applied stress levels in a specimen with (0/90) facesheets and level 1 static indentation damage.	326
Figure 6.132	Membrane stress distribution at two applied stress levels in a specimen with (0/90) facesheets and level 2 static indentation damage.	327
Figure 6.133	Bending stress distribution at top surface for two applied stress levels in a specimen with (0/90) facesheets and level 2 static indentation damage.	328
Figure 6.134	Total longitudinal stress distribution at top and bottom surfaces for two applied stress levels in a specimen with (0/90) facesheets and level 2 static indentation damage.	329
Figure 6.135	Membrane stress distribution at two applied stress levels in a specimen with (0/90) facesheets and level 3 static indentation damage.	330
Figure 6.136	Bending stress distribution at top surface for two applied stress levels in a specimen with (0/90) facesheets and level 3 static indentation damage.	331
Figure 6.137	Total longitudinal stress distribution at top and bottom surfaces for two applied stress levels in a specimen with (0/90) facesheets and level 3 static indentation damage.	332
Figure 6.138	Membrane stress distribution at two applied stress levels in a specimen with (± 45) facesheets and level 1 simulated core damage.	334
Figure 6.139	Bending stress distribution at top surface for two applied stress levels in a specimen with (± 45) facesheets and level 1 simulated core damage.	335
Figure 6.140	Total longitudinal stress distribution at top and bottom surfaces for two applied stress levels in a specimen with (± 45) facesheets and level 1 simulated core damage.	336
Figure 6.141	Membrane stress distribution at two applied stress levels in a specimen with (± 45) facesheets and level 2 simulated core damage.	337
Figure 6.142	Bending stress distribution at top surface for two applied stress levels in a specimen with (± 45) facesheets and level 2 simulated core damage.	338

Figure 6.143	Total longitudinal stress distribution at top and bottom surfaces for two applied stress levels in a specimen with (± 45) facesheets and level 2 simulated core damage.	339
Figure 6.144	Membrane stress distribution at two applied stress levels in a specimen with (± 45) facesheets and level 3 simulated core damage.	340
Figure 6.145	Bending stress distribution at top surface for two applied stress levels in a specimen with (± 45) facesheets and level 3 simulated core damage.	341
Figure 6.146	Total longitudinal stress distribution at top and bottom surfaces for two applied stress levels in a specimen with (± 45) facesheets and level 3 simulated core damage.	342
Figure 6.147	Membrane stress distribution at two applied stress levels in a specimen with (± 45) facesheets and level 1 static indentation damage.	344
Figure 6.148	Bending stress distribution at top surface for two applied stress levels in a specimen with (± 45) facesheets and level 1 static indentation damage.	345
Figure 6.149	Total longitudinal stress distribution at top and bottom surfaces for two applied stress levels in a specimen with (± 45) facesheets and level 1 static indentation damage.	346
Figure 6.150	Membrane stress distribution at two applied stress levels in a specimen with (± 45) facesheets and level 2 static indentation damage.	347
Figure 6.151	Bending stress distribution at top surface for two applied stress levels in a specimen with (± 45) facesheets and level 2 static indentation damage.	348
Figure 6.152	Total longitudinal stress distribution at top and bottom surfaces for two applied stress levels in a specimen with (± 45) facesheets and level 2 static indentation damage.	349
Figure 6.153	Membrane stress distribution at two applied stress levels in a specimen with (± 45) facesheets and level 3 static indentation damage.	350
Figure 6.154	Bending stress distribution at top surface for two applied stress levels in a specimen with (± 45) facesheets and level 3 static indentation damage.	351

Figure 6.155	Total longitudinal stress distribution at top and bottom surfaces for two applied stress levels in a specimen with (± 45) facesheets and level 3 static indentation damage.	352
Figure 7.1	Initial dimension of the dimple perpendicular to loading direction versus indenter diameter for specimens with (0/90) facesheets and static indentation damage.	357
Figure 7.2	Shear stress versus shear strain in an undamaged specimen with (± 45) facesheets loaded under uniaxial compression.	365
Figure 7.3	Experimental and predicted dimple profiles along centerline perpendicular to loading direction at an applied stress level of -240 MPa for a specimen with (± 45) and level 3 simulated core damage	369
Figure 7.4	Calculated maximum membrane stress versus applied stress for specimens with (0/90) facesheets and various levels of simulated core damage.	376
Figure 7.5	Calculated maximum membrane stress versus applied stress for specimens with (0/90) facesheets and various levels of static indentation damage.	377
Figures D.1 - D.12	Measured dimension of dimple along centerline perpendicular to loading at various applied stress levels for specimens with simulated core damage and those with static indentation damage	423-434

List of Tables

Table 4.1	Numbering system of the assumed modes for an N by N analysis (for $N > 3$)	69
Table 4.2	Input parameters for sample problem	85
Table 5.1	Test matrix for material property evaluation	101
Table 5.2	Test matrixa for damage tolerance investigation	102
Table 6.1	Measured material properties of AW193/3501-6	154
Table 6.2	Measured slit lengths of specimens with simulated facesheet damage	202
Table 6.3	Values of initial dimple parameters (R_x , R_y , and ξ_0) ^a which best match the experimentally measured dimple profiles in specimens with (0/90) facesheets	206
Table 6.4	Values of initial dimple parameters (R_x , R_y , and ξ_0) ^a which best match the experimentally measured dimple profiles in specimens with (± 45) facesheets	207
Table 6.5	Valuesa of the radius of the initial region of crushed core, R_0 , used in the dimple propagation model for specimens with (0/90) facesheets and those with (± 45) facesheets	214
Table 6.6	Input parameters for the dimple propagation model used for specimens with (0/90) facesheets	221
Tables 6.7	Input parameters for the dimple propagation model used for specimens with (± 45) facesheets	222
Table 6.8	Compressive moduli of specimens with (0/90) facesheets	227
Table 6.9	Compressive moduli of specimens with (± 45) facesheets	233
Table 6.10	Compressive strengths of specimens with (0/90) facesheets	306
Table 6.11	Compressive strength of specimens with (± 45) facesheets	310
Table 7.1	Elements of D-matrix of a (± 45) facesheet with a reduced shear modulus of 1.0 GPa	367
Table 7.2	Elements of A-matrix of a (± 45) facesheet with a reduced shear modulus of 1.0 GPa	368
Tables C.1 - C.2	Experimental data for specimens with (0/90) and (± 45) facesheets	420-421

Nomenclature

a	dimension of the dimple propagation model along the loading direction
A_{ij}	elements of the A-matrix in Classical Laminated Plate Theory
A_{ij}^*	elements of the inverse A-matrix in Classical Laminated Plate Theory
b	dimension of the dimple propagation model perpendicular to the loading direction
C_{ij}	parameter used to simplify derivation of governing equations
d	thickness of aluminum tups for manufacturing simulated core damage
D_{ij}	elements of the D-matrix in Classical Laminated Plate Theory
$F(x,y)$	Airy stress function
F_{ij}	modal amplitudes of the stress function $F(x,y)$
G_{ijmn}	parameter used to simplify derivation of governing equations
h	thickness of facesheets
H_c	composite fracture parameter in the Mar-Lin correlation
H_{ijmn}	parameter used to simplify derivation of governing equations
I_{ij}	parameter used to simplify derivation of governing equations
k_1	parameter used to characterize the two-parameter foundation
k_2	parameter used to characterize the two-parameter foundation
M_{kk}^F	diagonal elements of matrix in the compatibility equation
M_{kk}^W	diagonal elements of matrix in the equilibrium equation
M_{xx}	moment resultant in Classical Laminated Plate Theory
N_{xx}	stress resultant in Classical Laminated Plate Theory
N_{yy}	stress resultant in Classical Laminated Plate Theory
N_{xy}	stress resultant in Classical Laminated Plate Theory
R_c	base radius of aluminum tups for manufacturing simulated core damage
R_i	nose radius of aluminum tups for manufacturing simulated core damage
R_o	radius of initial region of crushed core

R_x	parameter defining in-plane dimension of initial deformation function $\xi(x,y)$ along the x-axis
R_y	parameter defining in-plane dimension of initial deformation function $\xi(x,y)$ along the y-axis
R_k^F	nonlinear force vector on the right hand side of the compatibility equation
R_k^W	nonlinear force vector on the right hand side of the equilibrium equation
SID	static indentation damage
SCD	simulated core damage
SFD	simulated facesheet damage
$w(x,y)$	transverse displacement function of the facesheet
w_{ij}	modal amplitudes of the transverse displacement function of the facesheet
x	axis along the loading direction
y	axis perpendicular to the loading direction
y_{crit}	dimension of the dimple at zeroth order fringe perpendicular to loading direction just before catastrophic failure
δF_{ij}	difference between modal amplitudes of the stress function at two consecutive iteration steps
δw_{ij}	difference between modal amplitudes of the transverse displacement function at two consecutive iteration steps
z_{crit}	maximum depth of the dimple just before catastrophic failure
$\bar{\sigma}_{xx}$	applied stress level
$\sigma_{plateau}$	support reaction provided by a crushed core
σ_{ult}	flatwise compressive strength of the honeycomb core
$\sigma_{xx}^{bending}$	longitudinal bending stress
$\sigma_{xx}^{membrane}$	longitudinal membrane stress
$\xi(x,y)$	initial deformation function
ξ_{ij}	modal amplitudes of $\xi(x,y)$
ξ_0	initial depth at the center of the dimple

Chapter 1

Introduction

Sandwich construction has gained increasing acceptance in structural applications since its introduction in the 1940's [1, 2]. Sandwich construction offers several advantages over conventional metallic structures and monolithic laminated structures. Sandwich structures have high bending-stiffness-to-weight ratios. They have good stability under in-plane compressive loading. Due to adhesive bonding used to bond the core and the facesheets, sandwich construction reduces production part count compared to conventional skin-stiffener construction. Since both facesheets can carry loads, sandwich construction inherently provides multiple load paths which can make them more "damage tolerant" in certain applications. The presence of the core, usually made of lightweight foams or honeycombs, provides good energy absorption capability for impact events. These properties have made sandwich construction an attractive candidate for many structural applications.

Not long after the introduction of composite laminated structures, structural designers started to use composite laminates as the facesheets in sandwich construction. The tailorability of the facesheets can be utilized to achieve optimum mechanical properties for the sandwich construction as a whole. The increasing popularity of composite sandwich constructions can best be seen in the aircraft industry. Examples of applications of composite sandwich structures are plentiful. In the Starship, the first all-composite aircraft certified by the FAA, extensive composite sandwich construction is utilized [3, 4]. Joy et al [5] describe several applications of sandwich

construction including helicopter rotor blades, floor boards, and drop tanks. The Fokker 100 aircraft has composite sandwich parts as secondary structures [6]. The helicopter industry has successfully incorporated sandwich constructions in many of its products [7-9]. Sandwich construction has also become a prime candidate in some space structures [10] and marine structures [11]. The increasing usage of composite sandwich construction means that such construction needs to be carefully evaluated within the appropriate design philosophy to ensure safety.

Aircraft must satisfy stringent safety regulations [12, 13] dictated by various governing authorities before they are certified. The need to satisfy these stringent safety regulations makes aircraft design one of the most demanding engineering endeavors. Design philosophies have evolved in order to assure safe design. The term "damage tolerance" was introduced in the 1970's when a major change in design philosophy occurred in the aircraft industry. The change was from the safe-life design philosophy to the damage-tolerant design philosophy. A brief description of the historical development and the bases of the damage-tolerant design philosophy are given by Lincoln [14, 15].

Damage tolerance can be defined as a measure of the ability of a material/structure to "perform" (given particular requirements) with damage present. The damage tolerance philosophy, when implemented in the structural design and assessment processes, is more realistic than the safe-life philosophy and has become the dominant design philosophy in the aircraft industry [16, 17]. However, in order to design a damage tolerant structure or component, designers first need to define and characterize the damage type(s) which are likely to occur. Given the material system and structural configuration, the damage inflicted in a structural component due

to a particular event is evaluated by a "damage resistance" study. Damage resistance can be defined as a measure of damage incurred by a material/structure due to a particular event. Such delineation between damage resistance and damage tolerance was formalized by Cairns & Lagace [18] in their presentation of a consistent methodology for impact studies of composite laminates. Earlier researchers have also recognized such delineation [e.g. 19, 20], although slightly different terminology was used. It should be noted that such delineation between damage resistance and damage tolerance is not universal. As indicated by de Jonge [21], historically researchers from European countries often refer to damage resistance, as defined above, as damage tolerance. Even today one can easily be misled by the titles of publications [22] because of the different interpretations of the terms.

In the aircraft industry, one of the toughest issues designers of composite structures must address is designing for the issue of impact. This is, in part, due to the complicated nature of the damage state which often results in a composite structure due to an impact event. Yet, impact damage is often the most detrimental damage type [23], and can threaten the integrity of aircraft structures. The study of impact damage resistance and damage tolerance of composite structures has, therefore, become one of the most researched topics in the last twenty years.

In contrast to monolithic laminated structures, however, composite sandwich construction has received relatively little attention with regard to the issues of impact damage resistance and damage tolerance. This is despite the fact that composite sandwich construction, with its ever increasing structural applications, has attracted researchers' attention since the late 1970's. The level of structural complexity of composite sandwich

structures is greater than that of metallic structures and monolithic laminated structures due to the presence of the core and the adhesive layer. The limited amount of research effort to date has, thus, left many questions unanswered. Therefore, much more needs to be done in order to help structural engineers design safer and more efficient composite sandwich structures.

In the present work, the impact damage resistance and damage tolerance of thin-faced composite sandwich panels are investigated via static indentation tests and uniaxial compression tests. There are four main objectives of the current research: one, to characterize the damage in the sandwich panels due to indentation/impact loading; two, to characterize the failure mechanisms of such damaged panels under uniaxial compression; three, to investigate the separate contributions of the facesheet damage and core damage to the failure mechanism and final failure of the panels; and four, to predict the failure mechanism and failure load of such damaged panels.

The overall work is organized in the remaining chapters as follows. Relevant work in the literature on the subject of damage resistance and damage tolerance of composite sandwich structures is reviewed in Chapter 2 in order to set up the background and need for the current research. The approach taken to achieve the aforementioned research goals is described in Chapter 3. The analytical models used for the damage tolerance part of the investigation are presented in Chapter 4 and preliminary results of the analyses are also included. The experimental procedures utilized in the current work including manufacturing procedures of the test specimens, experimental setups, test procedures, and procedures of data reduction are described in Chapter 5. All the experimental results along with the

analytical predictions, where available, are presented in Chapter 6 while the implications of these results are highlighted and discussed in Chapter 7. Finally, in Chapter 8, conclusions are drawn from the investigation and the research is evaluated with recommendations for further work.

Chapter 2

Previous Work

As noted in Chapter 1, "damage resistance" is a measure of the damage inflicted in a material/structure due to a particular event while "damage tolerance" is a measure of the ability of a material/structure to "perform" (given specific requirements) with damage present. In the present work, the "particular event" is low speed impact or static indentation and the "performance requirement" is to sustain uniaxial compressive load. In the following sections, relevant work on the subject of impact damage resistance and damage tolerance of composite sandwich panels is reviewed with regard to these particular facets. However, it is important to note that a much more extensive body of literature on impact damage resistance and damage tolerance studies of monolithic laminated structures exists. Some of the lessons learned from monolithic laminates have provided valuable guidelines for researchers studying the impact damage resistance and damage tolerance of composite sandwich structures. The review papers by Cantwell & Morton [24] and Abrate [25] are excellent starting points in researching what has been done with monolithic composite laminates in these areas. In the sections to follow, the behavior of composite sandwich panels is compared with that of monolithic laminates where appropriate.

2.1 Impact Damage Resistance

The work on impact damage resistance of composite sandwich panels is reviewed in this section. In particular, the following issues are examined through the work done in the open literature: the use of static indentation

tests to simulate impact damage, the damage types which occur in impacted/indented sandwich panels and the sequence in which these damage types occur, the effects of constituent (fibers, matrix, and core) properties and impactor size on the impact damage resistance of sandwich panels, and existing analyses relevant to the impact damage resistance of sandwich panels.

A number of researchers have compared damage in sandwich panels due to impact and damage due to static indentation [26-29]. They have concluded that the damage states resulting from these two types of tests are very similar provided that certain conditions are met. One of these conditions is that the dynamic effects in the impact event are not important. It is difficult to quantify this condition in terms of impact velocity or impact energy because other parameters, such as mass of the impactor, affect the dynamic response of the panel as well. However, two parameters can usually provide qualitative assessment of the importance of these dynamic effects: the mass ratio of the impactor to the impacted panel and the ratio of the contact stiffness to the bending stiffness of the impacted panel. In general, the higher the mass ratio or the lower the stiffness ratio, the less significant are the dynamic effects. Such rules of thumb explain why the use of static indentation tests to simulate impact damage in relatively thin monolithic laminates is less satisfactory [29] as laminates have significantly higher stiffness ratios than sandwich panels because the core of the sandwich panels reduces the contact stiffness and increases the bending stiffness. Another necessary condition is that the indentation test and the impact test are conducted up to the same force [29] or the same energy represented by the area under the load-displacement curve [26]. Indentation tests have the advantage over impact tests of being able to

produce more controllable and repeatable damage states than impact tests since impact velocity is very difficult to control either with high pressure gas passing through orifices or with mechanical compression of springs. On the other hand, indentation force and indentation depth can be controlled very accurately and easily via hydraulic testing machines. Since repeatable and controllable damage states are essential in damage tolerance studies, static indentation tests are often used as a means of simulating impact damage.

The damage which occurs in composite sandwich panels when they are subjected to impact/indentation loading is manifested in its components: the facesheets, the core, and the bonding agent. In general, core damage appears first, prior to any facesheet damage [30, 31]. In cellular/foam cores, the first sign of core damage is compressed cells underneath the point of impact/indentation [32] while in honeycomb cores, cell walls underneath the point of impact/indentation are buckled and crushed [31-33]. As impact velocity or indentation force increases, cracks start to develop in cellular/foam cores [32] and brittle honeycomb cores, e.g. phenolic glass [34], parallel to the surface of the panel near the skin/core bondline. In more ductile honeycomb cores, e.g. Nomex and aluminum, cell walls may split along the thickness direction near the point of impact/indentation. Facesheet damage then starts to appear. In tape facesheets with adjacent plies having different orientations, delaminations are first to occur [32]. The sizes of the delaminations usually increase from the impacted side of the facesheet to the interface between the impacted facesheet and the core [35]. The delamination is usually elliptical with the major axis aligned with the fiber direction of the bottom ply [32, 36]. Some researchers [32] have documented debonding of the adhesive layer from the facesheets of sandwich panels with aluminum honeycombs. As the impact velocity or

indentation force increases even further, fiber damage starts to occur. A permanent dent visible on the surface of the panel is generally an indicator of significant facesheet damage. In the case of relatively thin tape layups, a square plug with two sides parallel to the fiber direction of the surface ply tows of the fabric, as shown in Figure 2.1, was observed by some researchers [27, 37]. In the case of similarly thin plain weave fabric facesheets, a diamond-shaped dent with diagonals parallel to the tows of the fabric, as shown in Figure 2.2, has been observed [38, 39]. In the center of the dent, a cross-shaped crack divides the dent into four approximately equal triangular flaps.

A number of researchers have experimentally compared the impact damage resistance of composite sandwich panels made of different material systems. However, it is difficult to generalize these test results because a universal metric by which to measure the impact damage resistance of sandwich panels does not exist. While some authors define impact damage resistance as the amount of damage inflicted in the structure due to impact [27], others define it as the amount of energy absorbed during the impact event [36, 38]. A material/structure may absorb a lot of impact energy by promoting damage. Such a material/structure is very impact resistant by the second definition, but not so by the first definition. Even when damage is used as the metric to measure impact damage resistance, ambiguity can still arise because there are a number of damage types which can occur in the facesheet and the core. For a given impact event, Material System A can have more facesheet damage but less core damage than Material System B. Depending on which damage type is used to measure impact damage resistance, different conclusions can be drawn for Material Systems A and B. In the present review, explicit reference to the criterion(ia) used

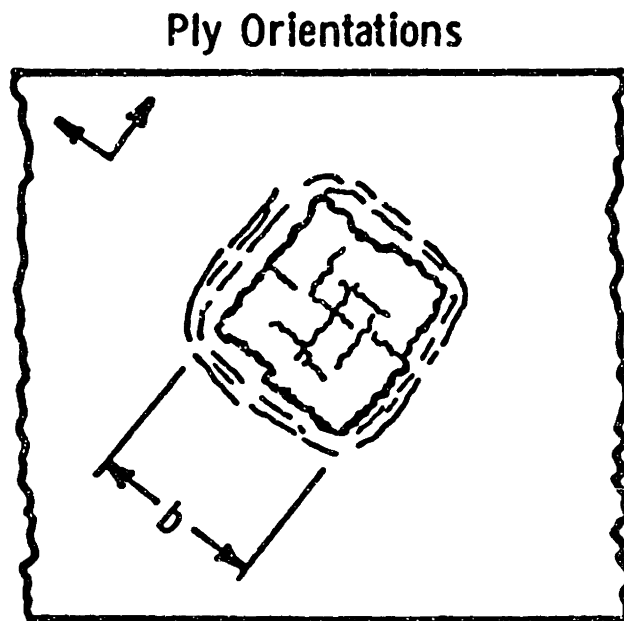


Figure 2.1 Sketch of permanent dent/dimple in sandwich panel with tape facesheets (taken from [27]).

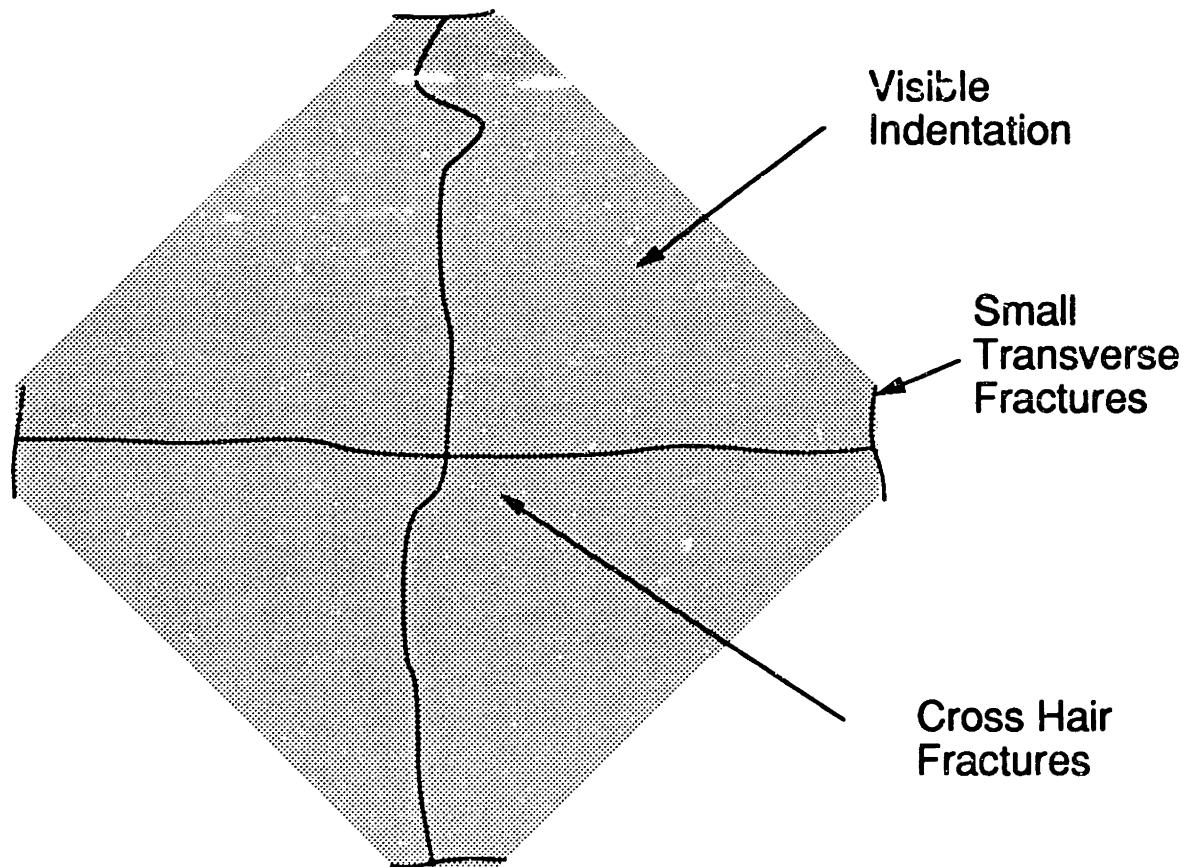


Figure 2.2 Sketch of permanent dent/dimple in sandwich panel with fabric facesheets (taken from [33]).

by the various authors to compare impact damage resistance is given.

Both facesheet constituents, fibers and matrix, can influence the impact damage resistance of composite sandwich panels. It has been observed [40] that a high failure strain of the fibers improves the impact damage resistance of the sandwich panel by providing high energy absorbing capability. Graphite/epoxy facesheets incur more damage than glass/epoxy facesheets under similar impact conditions [27] while Kevlar/epoxy facesheets require higher impact energy to obtain barely visible damage [39]. Boron/epoxy facesheets were found to require lower energy for facesheet penetration as compared to graphite/epoxy facesheets [30]. Using energy absorption as a measure of impact damage resistance some researchers [38] found that polyethylene fibers and polyester fibers are more impact resistant than graphite fibers and aramid fibers. The matrix of the facesheets also affects the impact damage resistance of sandwich panels. The use of toughened thermosets or thermoplastics for the facesheets has been shown to improve impact damage resistance [41] by raising the energy threshold for barely visible damage. High failure strain of fibers and toughened matrix have also been shown to be beneficial to the impact damage resistance of monolithic laminates [24, 25].

Fabric facesheets were found to better contain facesheet damage to an area approximately equal to the cross-section of the impactor than tape facesheets [30]. "Hybrid" configurations, either with different fibers woven in the same ply or by replacing individual plies with a different material, have been used with different degrees of success in improving the impact damage resistance of sandwich panels [37, 41, 42] by either raising the energy threshold for barely visible damage or by containing the facesheet

damage to a smaller area. Similar benefits were achieved in monolithic laminates [30, 43].

Core properties also influence the impact damage resistance of sandwich panels. For a given type of core, denser core was found to raise the energy threshold for facesheet penetration [30], to reduce the amount of facesheet damage and core damage [35], to improve the energy absorption per unit delamination [36], and to raise the energy threshold for barely visible damage [39]. Palm [31], on the other hand, reported that sandwich panels with denser core sustained more facesheet delaminations. Although Palm himself noted the contradiction between his findings and those of earlier researchers, he did not offer any explanation. The extent of debonding was found to be greater in sandwich configurations with aluminum honeycomb than in those with Nomex honeycomb [32]. Such observation was attributed to the different stiffnesses of the cores. Honeycomb core materials like Nomex are usually impregnated with resin to improve resistance against environmental degradation. Such core matrices were found to affect the impact damage resistance of sandwich panel as well. For example, nylon-modified phenolic resin with final dips in polyester and thermoplastic matrices were more impact resistant than phenolic resin because they result in reduced amounts of delaminations in the facesheet [34]. The effects of core geometric properties have also been investigated. Structural designers often increase the thickness of the core to achieve higher bending stiffness for the sandwich panel as a whole. However, care must be exercised in doing so because it has been shown that the impact/indentation damage in the facesheet and the core increases with core thickness because the panel cannot efficiently absorb the impact energy by global bending [44, 45] thus resulting in higher contact force. Steinmann

[26] investigated the effect of honeycomb core size on the impact damage resistance of sandwich panels and found no effect of the three core sizes he used (3.18 mm, 6.35 mm, and 9.53 mm). However, the three cores also had different densities and, hence, Steinmann's observations are combined effects of core size and core density.

A number of researchers have investigated the effects of impactor size on the impact damage resistance of sandwich panels [33, 46]. It was found that for a given material system, smaller tups have a reduced load-indentation slope and a lower facesheet penetration load [33]. For the same impact velocity, damage area (as determined by ultrasonic C-scan) increases with impactor diameter until the latter reaches such a large value that the loading becomes too "diffused" to cause any facesheet damage [46]. To put it more quantitatively, a larger indenter distributes the load over a larger area, and hence causes less stress concentration.

Some analytical work on the impact damage resistance of sandwich panels can be found in the open literature although it is not as abundant as that on monolithic laminates [24, 25]. Most analyses on the impact damage resistance of sandwich panels follow the same approach as the analyses of the impact damage resistance of monolithic laminates [18]. In that approach, a "global analysis" is used to model the dynamics and to obtain the force-time history of the impact event. Once the force-time history is obtained, the peak force is modelled as some kind of pressure loading in a "local analysis" to calculate the stresses and strains near the point of impact for damage prediction.

Dynamic modelling of the impact of a sandwich panel has been done by several researchers [28, 45, 47-50]. Typically the sandwich panel and the impactor are modelled as two dynamic systems coupled together through a

nonlinear contact spring. In such schemes, the sandwich panel can be modelled in a number of ways. The whole panel can be modelled as a shear deformable plate [45, 47]. Alternatively, the two facesheet can be modelled as two membranes [28] connected by the core. Finite element methods have also been used to model sandwich panels [48, 49, 51]. The constitutive properties of the contact spring is found either analytically [28, 47] or experimentally [45, 48, 49]. Some global analyses managed to predict the experimental force-time history fairly well [45, 48, 49] while others obtained only fair agreement with experiments[28].

In the local analysis, the goal is to predict the stress/strain fields near the point of impact or indentation for damage prediction. A popular approach is to model the sandwich panel as a plate resting on an elastic foundation [27, 28]. Other approaches include an axisymmetric elasticity model [52] and finite element analyses [48, 51]. With these analyses, researchers have identified the facesheet thickness and the radius of the indenter as key parameters in predicting facesheet failure under static indentation [27]. It was also found, in agreement with experimental observation, that core crushing could occur at very low load [27, 52]. Hence, core damage needs to be accounted for in the local analysis. Some researchers took into account of geometric nonlinearity of the indented facesheet and obtained fairly accurate analytical prediction of the load-indentation behavior [28]. Some of the analyses reviewed have achieved limited success in predicting the load-indentation curve of sandwich panels [28] while others have obtained qualitative agreement with experimental data for damage prediction [28, 48].

At an even higher level of complexity, the impact event has been analyzed as a dynamic contact problem with a nonlinear constitutive model

for the core [50]. This analysis is based on a three-dimensional finite element model and is very computationally intensive. Unfortunately, the results from the analysis, while qualitatively correct, overpredict the displacement of the sandwich panel by about 30% compared to the experimental data. The authors attribute the limitation of the analysis to the lack of accurate rate-dependent data of the facesheet and core materials.

Based on the literature reviewed, the following observations are made. The damage types and the damage sequence in sandwich panels under impact/indentation loading are fairly well documented although most researchers have characterized facesheet damage in much more detail than core damage. In particular, the geometric profile of the permanent dent has not been sufficiently characterized although a few authors have measured the dent depth. As shown later in the review on damage tolerance, such information may be important in understanding the failure mechanisms of the damaged panels under uniaxial compression. The lack of a universal metric for measuring impact damage resistance has been pointed out. A standardized set of metrics would allow better comparison among test results of different researchers. The effects of constituent properties (facesheets and core) on the impact damage resistance of sandwich panels have been investigated over a fair number of different material systems. However, the effects of impactor geometry and impactor size have attracted relatively little attention. This is reflected by the fact that most researchers used impactors or indentors with a hemispherical nose of a single radius. The analytical models reviewed have had limited success in predicting the load-indentation curve of a sandwich panel. However, some models provide a direction for future research by showing that core crushing and large deflection of the facesheet are important in modelling the deformation of

sandwich panels under impact/indentation loading. The damage predictions provided by existing impact damage resistance models are not very satisfactory and only match experimental results qualitatively. In addition, all the reviewed analyses on the impact damage resistance of sandwich panels predict only facesheet damage. No attempt to predict core damage or the shape of the resulting dent in the sandwich panel can be found in the literature.

2.2 Damage Tolerance

Once the damage state of an impacted/indented structure has been characterized, the means by which such damage was inflicted on the structure is not important [18, 53]. Only the damage state is important in the issue of damage tolerance. The relevant question in a damage tolerance study is how much strength is retained by the damaged structure. In the current work, the residual strength of indented sandwich panels under uniaxial compression is investigated. Relevant work reported to date in the literature is thus reviewed.

Researchers have used different test methods to assess the damage tolerance of composite sandwich panels. Among these test methods are bending tests [31, 35, 37, 38, 42, 53-57], uniaxial compression tests [28, 41, 44, 46, 58, 59], in-plane shear tests [27, 39, 46], and fatigue tests [35, 60]. Since damage tolerance is specific to the type of loading, the findings presented in this section on the damage tolerance of sandwich panels are specific to the given test methods. However, different residual strength tests sometimes produce similar failure modes (i.e. the damage state at failure). For example, bending tests with the damaged facesheet on the compression side usually induce line fracture through the damage site, a

failure mode also observed in uniaxial compression tests and in-plane shear tests.

In this section, the effects of constituent properties on the damage tolerance of composite sandwich panels is discussed first, followed by the effects of preloads. The use of simulated damage in damage tolerance studies is also examined. A failure mechanism of damaged panels with thin fabric facesheets under uniaxial compression is then described. A few delamination buckling models are presented because they have been used to predict compressive residual strength of impact-damaged panels. Other semi-empirical models for residual strength prediction are also mentioned.

Among the constituent properties of sandwich panels discussed here are fiber failure strain, core density, and core matrix. Although Kevlar/epoxy facesheets usually have a higher failure strain than graphite/epoxy facesheets, both material systems show approximately the same proportional reduction in failure strength [37, 39]. The compressive strength of undamaged and damaged sandwich panels was found to increase with core density [34, 41]. Such observation has been attributed to the wrinkling effect (a local instability phenomenon of the facesheet) [41] which is affected by core density. Residual strength in bending was found to increase when the core was impregnated with a tougher matrix [56]. Some researchers have discussed the effects of impactor size on the damage tolerance of sandwich panels, e.g. [46]. It should be noted, however, that in such a discussion [46] the issues of impact damage resistance and damage tolerance are inherently combined because different indenter sizes cause different damage states.

Some researchers have investigated the effect of preloads on the damage tolerance of sandwich panels [37, 55]. The effects of preloads are

important because sandwich structures may be loaded when impacts occur. It was found that impact energy below the level that causes visible damage in unloaded panels can induce catastrophic failure in panels loaded in tension or in compression [37, 42]. A "failure threshold" has been defined to assess the behavior of these loaded sandwich panels subjected to impact [37, 55]. The term "failure threshold" refers to the lowest static load at which catastrophic failure is precipitated in the facesheet of a sandwich panel at a given impact velocity. Experimental evidence shows that the failure threshold in tension approaches an asymptotic value as impact energy increases while the failure threshold in compression decreases monotonically [55]. However, such observations were based on limited experimental data (two facesheet layups) and further testing is necessary in order to generalize it to other facesheet layups.

Researchers have compared residual strength of sandwich panels with an open hole in one of the facesheets and that of sandwich panels with damage due to impact/indentation. Good correlation between the residual tensile strength of sandwich panels with an open hole and that of sandwich panels with impact damage was found [37, 61]. Experimental data also show that (± 45) fabric facesheets result in a lower proportional reduction in compressive strength than (0/90) fabric facesheets [59] in sandwich panels with an open hole in one of the facesheets. Other researchers used simulated damage types, e.g. teflon implants and core cut-outs, as a means to introduce controlled damage in the study of damage tolerance [62]. It was found that these simulated damage types had a secondary effect on the failure of the sandwich panel as final failure did not occur at the site of the implants. They reduce the stiffness of the panels and, hence, cause a reduction in buckling loads.

Most damage tolerance studies in the open literature provide two types of information: residual strength and postmortem damage inspection. Very little discussion on failure mechanisms (i.e. the process leading to final failure) of these damaged panels can be found in the literature, with one exception. For thin (2-ply) fabric-faced sandwich panels under uniaxial compression, a special failure mechanism has been identified by some researchers [28, 41]. The initial dent from impact/indentation damage propagates perpendicular to the direction of the loading in a stable manner, followed by catastrophic failure in the form of a line fracture across the dimension perpendicular to the loading. A similar pattern was observed in panels under in-plane shear [39]. Since this failure mechanism has only been reported with thin-faced sandwich panels, it is unclear whether sandwich panels of different configurations (e.g. with thicker facesheets) also exhibit such a failure mechanism.

The analytical models used to predict compressive residual strength are mostly borrowed from damage tolerance studies of monolithic laminates. One such example is a family of models on delamination buckling [53, 63-65]. The simplest members of this family of analytical models are the beam models with a through-width delamination [53, 66]. These beam models work well for sandwich panels with artificial implants but they have little use in predicting compressive residual strength of impacted/indented sandwich panels because impact/indentation rarely causes simple through-width delaminations. More sophisticated delamination buckling models simulate circular or elliptical delaminations within a laminated plate [64, 67]. The validity of these models was usually verified by applying them to laminates or sandwich panels with artificial implants. When applying these delamination buckling models to sandwich panels, some researchers

completely ignore the core [53, 66] while others account for the presence of the core through some kind of contact reaction [65, 67] between the core and the facesheet. In general, models that account for reaction between the core and the facesheet give better agreement with experimental results. In order to use a delamination buckling model to predict the residual compressive strength of impacted/indented sandwich panel, some researchers empirically determined an equivalent delamination size to account for the reduction in strength due to the complex damage state resulting from impact/indentation [68, 69].

Another set of analytical models used to predict the compressive residual strength of damaged panels only account for in-plane mechanisms. Among these models are the net-area model [28, 59], the Mar-Lin correlation [28, 59], and linear-fracture-mechanic-based models [37].

A recent model by Minguet [70] has included out-of-plane deformation of the sandwich panel. It was developed to capture the dimple propagation observed experimentally when damaged thin-faced sandwich panels were compressed uniaxially. In Minguet's model, an initially deformed plate is used to model the impacted/indented facesheet of the sandwich panel while the core is modelled as an orthotropic continuum. Since Minguet's model is adapted for the present investigation, it will be described in detail in Chapter 4.

Based on the literature reviewed in this section, the following observations are made. Very little attention has been given to the failure mechanisms of impact-damaged sandwich panel. The only experimentally documented failure mechanism is that which occurs in thin-faced fabric sandwich panel under uniaxial compression. In this failure mechanism, the dent/dimple grows in the direction perpendicular to that of the applied load,

stably at first, until a critical size where catastrophic failure follows. Without an understanding of the failure mechanism, matching the residual strength data usually becomes the only criterion to validate the corresponding analytical models. For example, a few researchers have shown that the delamination buckling models are useful in predicting failure mechanisms and failure loads of sandwich panels with artificial implants in one of the facesheets. The authors then went on to use these delamination buckling models to predict the compressive residual strength of sandwich panels without verifying that such impact-damaged sandwich panels do indeed fail by delamination buckling. A better approach is to verify the validity of the analytical model on the basis of both the failure mechanism and failure load.

2.3 Summary

After reviewing the literature on the subjects of impact damage resistance and damage tolerance of sandwich structures, several needs are identified as motivation for the current work.

First, although several researchers have used the dent depth as a parameter to characterize impact damage [35, 39, 57], the overall geometric profile of the dent has not been satisfactorily characterized. The profiles of the dent and the support from the core underneath may be controlling parameters in the failure mechanism under compressive loading. Such a conjecture is supported by the experimentally observed dimple propagation that leads to final failure of the damaged panel subjected to uniaxial compression. Thus, the profile of the dimple needs to be quantitatively characterized.

Second, there is a lack of understanding of the failure mechanisms of impact damaged sandwich panels under compressive loading. Most analytical models strive to predict the residual strength of sandwich panels without modelling the failure mechanism. The validity of such models is difficult to verify by the prediction of failure load alone because, oftentimes, these models contain empirical parameters which are adjusted to best correlate the experimental results. Minguet's model [70] is the only one that captures the failure mechanism of an impact-damaged sandwich panel under uniaxial compression. However, even in this case, the validity of the model was verified by matching the experimental failure stress alone. The evolving shape of the dimple as predicted by the model was not compared with experimental data because quantitative measurements of the shape of the evolving dimple do not exist. Hence, there is a need for such quantitative experimental data to verify the dimple propagation model in a more rigorous manner.

Lastly, all reviewed analyses on damage tolerance of sandwich panels ignore either facesheet damage [70] or core damage [28, 37, 64] in order to reduce the mathematical complexity of the model. It is important to investigate the relative importance of facesheet damage and core damage and when such assumptions cease to be valid

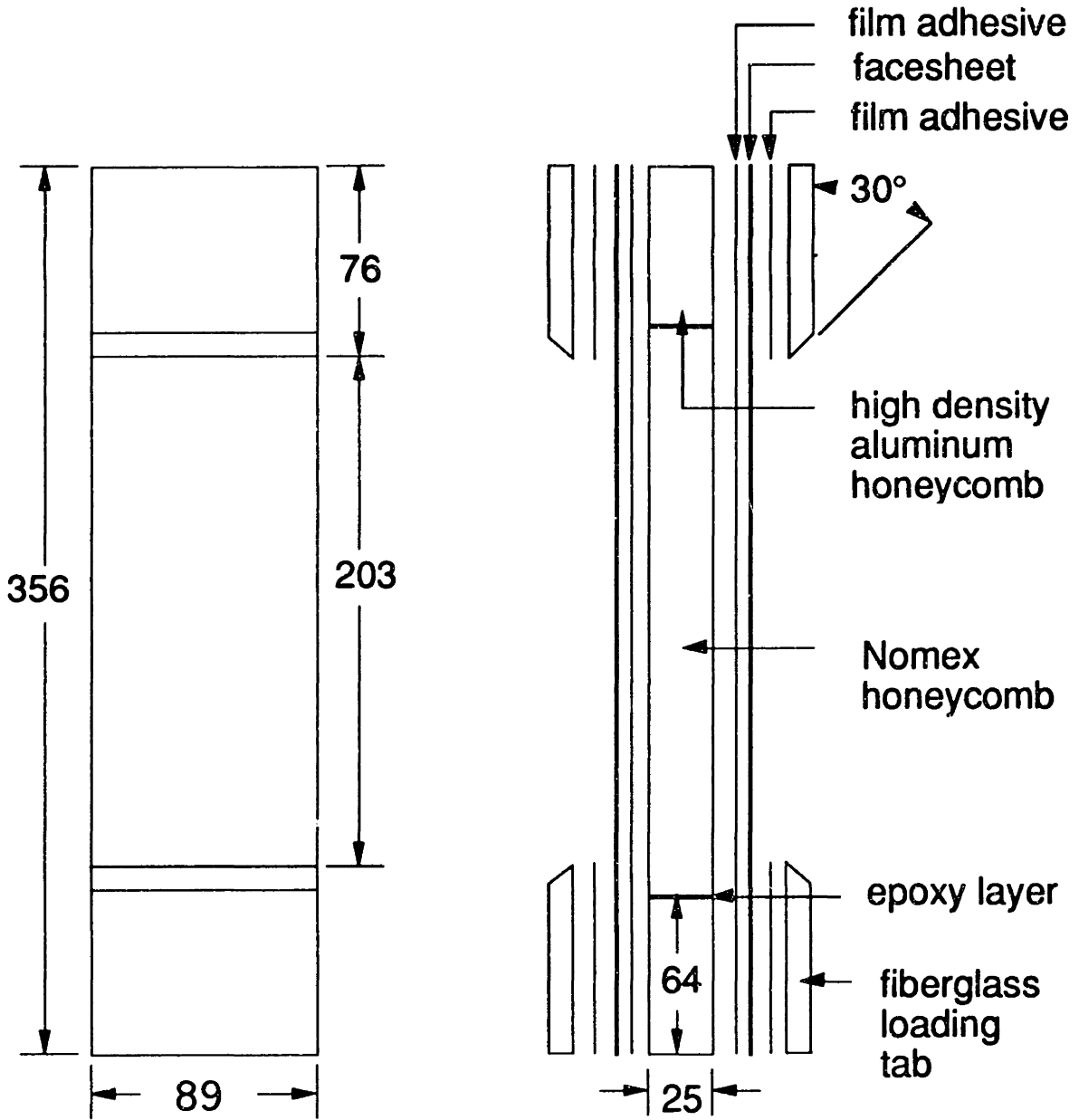
Chapter 3

Approach

As mentioned in Chapter 1, the present investigation has four main objectives: (i) to characterize the damage in the sandwich panels due to indentation/impact loading, (ii) to characterize failure mechanisms of such damaged panels under uniaxial compression, (iii) to investigate separately the contributions of facesheet damage and core damage to the failure mechanism and final failure, and (iv) to predict the failure mechanism and failure load of such damaged panels. The motivation for the present work is provided by the needs in the areas of impact damage resistance and damage tolerance of composite sandwich panels as identified in Chapter 2. A combination of experimental investigation and analytical modelling was used to achieve the aforementioned research goals. The overall approach for the present work is explained and outlined in this chapter while the specifics of the analytical models and experimental procedures are given in Chapters 4 and 5, respectively.

3.1 Overview

The plain weave graphite/epoxy fabric AW193/3501-6 was chosen as the facesheet material and the Nomex honeycomb core of 48.1 kg/m^3 (3 lb/ft^3) density and a cell size of 3.18 mm (0.125 inch) as the core material for the sandwich panels used in the present work. The specimen configuration is depicted in Figure 3.1. Two layups were used for the facesheets: (0/90) and (± 45). The above material system and the specimen configuration were chosen for two reasons. First, the failure mechanisms of such sandwich panels has been identified and qualitatively described (see Chapter 2); one



all dimensions in mm

Figure 3.1 Specimen configuration

of the objectives of the present work is to quantitatively characterize such failure mechanisms. The second reason for choosing the above material system and specimen configuration is that previous work in TELAC¹ has established a fairly good data base on the same material system and it is desirable to build upon that data base. The previous work includes: (i) extensive impact testing followed by uniaxial compression tests to evaluate residual strength [28], (ii) indentation tests on sandwich panels with different facesheet thicknesses, core thicknesses, and indenter sizes [58], and (iii) strength data of sandwich panels with open holes [59]. With the material system and specimen configuration decided, the experimental procedures are outlined next.

Static indentation tests were used to create three different damage states, corresponding to three different indenter sizes, in the sandwich panels. These statically indented panels were then examined carefully in order to characterize the amounts of different damage types present. Information from such a characterization process was used to design sandwich panels with "simulated damage types". These panels had either the core damage or the facesheet damage as observed in the indented panels.

All panels were eventually tested under uniaxial compression to failure. The uniaxial compression tests were monitored by the shadow moiré method which provides quantitative measurements of the out-of-plane deformation of the sandwich panels. By comparing the failure mechanisms and failure loads of panels with static indentation damage,

¹ Technology Laboratory for Advanced Composites, Massachusetts Institute of Technology, Cambridge, MA. — location of the present work.

simulated facesheet damage, and simulated core damage, the effects of facesheet damage and core damage were evaluated.

The experimental results are complemented by analytical modelling. Two existing analytical models were adapted to predict the failure loads of the sandwich panels. One of the models accounts for the facesheet damage only while the other accounts for core damage only. Comparing the experimental data with the predictions of the models should shed some light on the validity of the models and the relative importance of facesheet damage and core damage in reducing the compressive strength of the sandwich panels.

3.2 Damage States and Characterization

As discussed in Chapter 2, static indentation tests provide greater controllability and repeatability in creating damage than impact tests. It has also been shown that the amount, types, and location of damage in static indentation tests and impact tests correlate well for a given applied force. Therefore, static indentation tests were used in the present work to create different damage states in the sandwich specimens.

Since one of the objectives of the current work is to investigate the separate contributions of the facesheet damage and core damage, it is desirable to have damage states with different amounts of each damage type. A total of three damage states was created by three different hemispherical indentors of diameters 12.7 mm, 25.4 mm, and 38.1 mm. All indentors were driven to the same indentation depth. Based on previous work on the same material system [33], a depth of 3 mm was chosen. Such combinations of indenter diameters and indentation depth create damage states with three different proportions of facesheet damage and core damage

in these particular configurations. In particular, at a 3 mm indentation depth, the 12.7 mm indenter produces easily visible facesheet damage, the 25.4 mm indenter produces barely visible facesheet damage, and the 38.1 mm indenter yields no visible facesheet damage.

After the indentation tests, the amount, types and location of damage in the sandwich panels were carefully characterized. There are two generic types of damage in sandwich panels: facesheet damage and core damage. As illustrated in Chapter 2, researchers have spent more effort on characterizing facesheet damage than on core damage. In particular, to the author's best knowledge, the geometric profile of the permanent dent resulting from impact/indentation has never been characterized. Since the geometric profile of the dimple is believed to affect the failure mechanisms of the sandwich panels chosen for the present investigation, the profile of the dimple is carefully quantified. In particular, the depth of the dimple is measured along the two orthogonal tows that go through the center of the dimple. Measuring the profiles along two orthogonal directions is a practical compromise for a three-dimensional map of the profiles.

Besides measuring the profiles of the dimple, conventional damage inspection techniques are used to characterize other damage types. X-radiography and thermal depley techniques are used to quantify facesheet damage. A combination of sectioning and optical microscopy is used to examine core damage. The characterization procedures described above serve to quantify the damage types in the three damage states and to provide the information for designing sandwich panels with "simulated damage".

In addition to considering the effects of the actual damage which results from an impact/indentation event, the effects of facesheet damage

and core damage was to be separately assessed. Statically indented panels and impacted panels have a combination of two damage types: facesheet damage and core damage. In order to separately examine the effects of these two damage types, it was necessary to manufacture and test sandwich panels with only (simulated) core damage and panels with only (simulated) facesheet damage. Effort was spent in the present work to design and manufacture these panels with the appropriate simulated damage type.

The simulated core damage specimens have a permanent dent/dimple with the same geometric profiles as those in the indented panels. In order to avoid damaging the facesheet, a special procedure is used to cure the facesheets of these simulated core damage specimens (see Chapter 5). In order to obtain core damage similar to that in the static indentation damage states, the core underneath the dimple is crushed with the same indentors to the same depth (3 mm) as that in the indented panels. Thus, specimens with simulated core damage have damage in the form of crushed core and an initially deformed facesheet.

The simulated facesheet damage specimens, on the other hand, are designed to include facesheet damage observed in the indentation damage states, but without the associated core damage. Hence, the fracture pattern observed in the indentation damage states is introduced in the simulated facesheet damage specimen by cutting through-thickness slits in the facesheets. The core of these simulated facesheet damage panels is undamaged and the specimens do not have a permanent dent in the facesheet. The manufacturing procedures of these simulated damage specimens are given in Chapter 5.

The contribution of the facesheet damage and the core damage is thus examined by comparing the failure mechanisms and failure loads of the

static indentation damage panels, the simulated core damage panels, and the simulated facesheet damage panels.

3.3 Failure Mechanisms

As discussed in Chapter 2, there has been little description of the failure mechanisms of impact-damaged sandwich panels under uniaxial compression, except for one specific configuration. Impacted and indented sandwich panels with thin (2 plies) fabric facesheets and honeycomb core were observed to fail via propagation of the initial dent/dimple. One of the objectives of the present investigation is to quantitatively characterize and examine this failure mechanism in relation to the final failure of the sandwich panel. A technique is thus required to measure the out-of-plane displacement of the panel as a function of the applied compressive stress. The quantitative experimental results thus obtained can also provide a basis for the verification of analytical models designed to predict the failure mechanisms of impact-damaged sandwich panels. Hence, compression tests of all the damaged panels are monitored by the shadow moiré method.

The shadow moiré method has two advantages over conventional strain gages: (i) it gives whole-field deformation patterns, (ii) it requires no physical contact with the specimens. The shadow moiré method is the simplest member of a family of metrological techniques collectively called moiré methods [71-73]. The more practical aspects of moiré methods are also given in most experimental handbooks, [e.g. 74, 75]. A comprehensive review on the subject was given by Sciammarella [76]. Sciammarella & Chiang [77] and Oplinger [78] provide examples of engineering applications of moiré methods. The shadow moiré method, in particular, has widely been used to observe buckling phenomena of various types: global buckling of

stiffened panels [54], local buckling of delaminated structures [79-81], and impact damage propagation [82]. The principle of the shadow moiré method and the experimental setup for the present work are described in Chapter 5.

3.4 Analyses

As indicated in Chapter 2, all existing models for predicting the compressive residual strength of impact damage sandwich panels account for only one of the two damage types: facesheet damage and core damage. In order to highlight the differences in damage types modelled and in the subsequent failure predictions, two existing analytical models are used to calculate the failure loads of all three types of damaged panels. The failure load predictions of both models will be compared with the experimental values to verify the applicability of the models to the three different damage states.

The first model is the Mar-Lin correlation originally derived for predicting residual tensile strength of notched composite laminates. The model only accounts for facesheet damage and is empirical in nature. Its usefulness in predicting the compressive residual strength of sandwich panels with visible facesheet damage has been demonstrated in Lie's work [28]. However, the exclusion of core damage in using the Mar-Lin correlation to predict residual strength of sandwich panels may render the method inadequate when the core damage is the more dominant damage type.

The second model is based on a model by Minguet [70]. This dimple propagation model only accounts for core damage and can simulate the aforementioned failure mechanisms of an impact-damaged thin-faced sandwich panel. However, the exclusion of the facesheet damage may

render the model inadequate when the facesheet damage is the more dominant damage type. Hence, the dimple evolution predicted by the dimple propagation model will be compared with the moiré measurements from the present investigation to verify the accuracy of the model.

Chapter 4

Analytical Methods

Two analytical techniques are used to predict the failure loads of damaged sandwich panels under uniaxial compression. The first one is the dimple propagation model based on a similar model by Minguet [70] which was used to predict the compressive residual strength of impact-damaged sandwich panels. The second technique is the Mar-Lin correlation [83] originally developed to predict tensile strength of notched composite laminates.

4.1 Dimple Propagation Model

The model considers the large deflections of a uniaxially-loaded orthotropic plate with initial curvatures resting on a foundation which provides supporting reaction characterized by two parameters. When the model is applied to sandwich panels with impact or indentation damage, the damaged facesheet of the sandwich panel is represented by the orthotropic plate while the core is modelled by the two-parameter foundation. The initial curvatures of the plate are used to model the shape of the dimple due to impact/indentation. Also included in the model are core damage due to impact/indentation and core damage due to subsequent dimple propagation. In the following subsections, the details of the model are described: the governing equations, the discretization procedures, the two-parameter foundation, and the incorporation of core damage. Finally, a sample problem is used to examine the convergence of the model.

As mentioned earlier, the dimple propagation model is based on a similar model by Minguet [70]. A brief explanation of the difference

between the two models is in order. In Minguet's model, the core of the sandwich panel is modelled as an orthotropic continuum while the present model uses a two-parameter foundation to model the core. The switch from the continuum to the two-parameter foundation is due to two reasons. First, it requires nine experimentally-determined elastic constants to characterize an orthotropic continuum. Such elastic constants do not exist for a honeycomb core because honeycombs have never been characterized as an orthotropic continuum, nor has it been proven that honeycombs can be characterized as such. The continuum representation of the core, therefore, may not be realistic. Furthermore, such a representation complicates the mathematics of the model. Second, in Minguet's model the deformation of the core is defined by the displacement variables in three orthogonal directions. In order to couple the facesheets to the core, the displacement variables in the core are expressed in terms of the displacements in the facesheets. However, the large deformation plate theory used for the facesheet is based on a stress function formulation. It is unclear to the author how the coupling between the facesheet and the core is achieved with the different variables used.

4.1.1 Governing equations

The governing differential equations are those for large deflections of an initially deformed orthotropic plate resting on an elastic foundation. The derivation of the equations can be found in most books on nonlinear plate theories, e.g. [84]. The coordinate system shown in Figure 4.1 is used where the origin is at a corner of the plate and the xy -plane is the mid-plane of the plate. The governing differential equations can thus be written as:

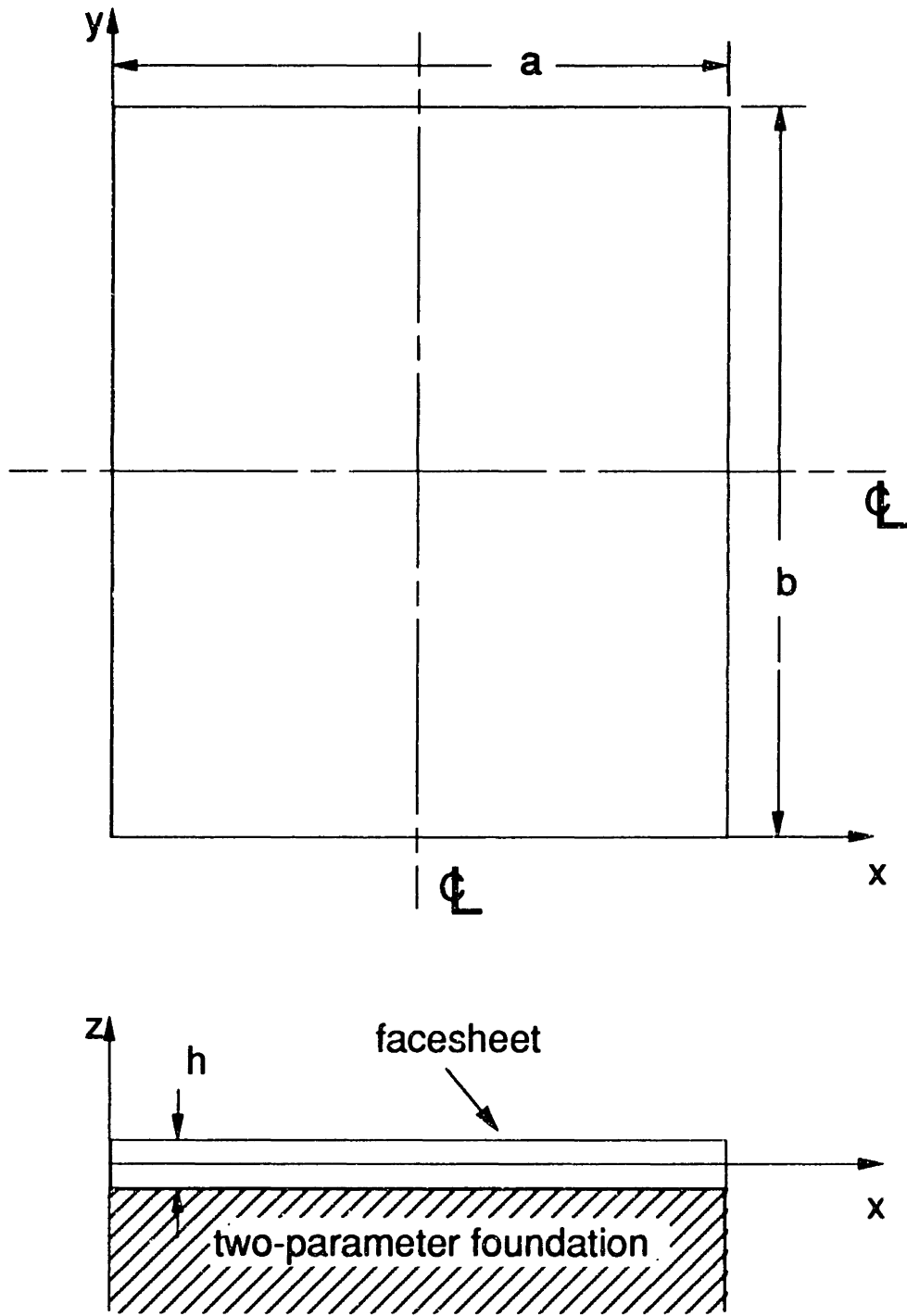


Figure 4.1 Coordinate system used for dimple propagation model.

$$D_{11}w_{,xxxx} + 2(D_{12} + 2D_{66})w_{,xxyy} + D_{22}w_{,yyyy} + k_1w + k_2\nabla^2w = h[F_{,yy}(\xi + w)_{,xx} + F_{,xx}(\xi + w)_{,yy} - 2F_{,xy}(\xi + w)_{,xy}] \quad (4.1)$$

and

$$h[A_{11}^*F_{,yyyy} + (2A_{12}^* + A_{66}^*)F_{,xxyy} + A_{22}^*F_{,xxxx}] = w_{,xy}^2 + 2\xi_{,xy}w_{,xy} - w_{,xx}w_{,yy} - \xi_{,yy}w_{,xx} - \xi_{,xx}w_{,yy} \quad (4.2)$$

where:

D_{ij} = elements of D-matrix in Classical Laminated Plate Theory (CLPT)

A_{ij}^* = elements of inverse of A-matrix in CLPT

$w(x,y)$ = out-of-plane displacement of plate

$F(x,y)$ = Airy stress function

$\xi(x,y)$ = initial deformation of the plate

h = thickness of the plate

k_1, k_2 = parameters that characterize the reaction of the foundation

$(),_x$ = partial derivatives with respect to the subscripted variable

Similarities between this set of equations and that of von Karman [85] for isotropic plates can readily be recognized. Equation 4.1 is the equilibrium equation in the thickness direction of the plate while Equation 4.2 is the compatibility equation. The Airy stress function $F(x,y)$ is related to the stress resultants N_{xx} , N_{yy} and N_{xy} in Classical Laminated Plate Theory by the following equations:

$$N_{xx} = hF_{,yy} \quad (4.3)$$

$$N_{yy} = hF_{,xx} \quad (4.4)$$

$$N_{xy} = -2hF_{,xy} \quad (4.5)$$

The initial dent shape $\xi(x,y)$ is assumed to be:

$$\xi(x,y) = \xi_0 \cos^2 \left[\frac{\pi}{2} \left(\frac{x - \frac{a}{2}}{R_x} \right) \right] \cos^2 \left[\frac{\pi}{2} \left(\frac{y - \frac{b}{2}}{R_y} \right) \right] \quad (4.6)$$

where:

ξ_0 = initial dent depth at the center of the panel

R_x, R_y = the in-plane dimensions of the dent

a = dimension of plate along x-axis

b = dimension of plate along y-axis

The values of ξ_0, R_x and R_y are chosen to best match the experimentally measured shape of the dimple.

4.1.2 Discretization of stress function and displacement function

The problem is discretized by assuming the following expansions for w, F , and ξ :

$$F(x,y) = \sum_i \sum_j F_{ij} \cos \frac{i\pi x}{a} \cos \frac{j\pi y}{b} + \bar{\sigma}_{xx} \frac{y^2}{2}; \quad i, j = 0, 2, 4, \dots \quad (4.7)$$

$$w(x,y) = \sum_i \sum_j w_{ij} \sin \frac{i\pi x}{a} \sin \frac{j\pi y}{b}; \quad i, j = 1, 3, 5, \dots \quad (4.8)$$

$$\xi(x,y) = \sum_i \sum_j \xi_{ij} \sin \frac{i\pi x}{a} \sin \frac{j\pi y}{b}; \quad i, j = 1, 3, 5, \dots \quad (4.9)$$

where $\bar{\sigma}_{xx}$ is the applied far-field stress while F_{ij} and w_{ij} are the unknown modal amplitudes for $F(x,y)$ and $w(x,y)$, respectively. The ξ_{ij} are the modal amplitudes of the initial deformation, given by:

$$\xi_{ij} = \frac{4}{ab} \int_0^a \int_0^b \xi(x,y) \sin \frac{i\pi x}{a} \sin \frac{j\pi y}{b} dx dy \quad (4.9a)$$

The symmetries of the problem require w , σ_{xx} , and σ_{yy} to be symmetric about $x=a/2$ and $y=b/2$. Hence, only even terms are needed for $F(x,y)$ and only odd terms for $w(x,y)$ and $\xi(x,y)$. Substituting Equations 4.7 through 4.9 into Equations 4.1 and 4.2, and collecting terms give:

$$\begin{aligned} \sum_i \sum_j \left[C_{ij} w_{ij} + h \bar{\sigma}_{xx} (\xi_{ij} + w_{ij}) \left(\frac{i\pi}{a} \right)^2 \right] \sin \frac{i\pi x}{a} \sin \frac{j\pi y}{b} = \\ \sum_i \sum_j \sum_m \sum_n \left\{ h G_{ijmn} F_{ij} (\xi_{mn} + w_{mn}) \sin \frac{m\pi x}{a} \sin \frac{n\pi y}{b} \cos \frac{i\pi x}{a} \cos \frac{j\pi y}{b} \right. \\ \left. - 2h H_{ijmn} F_{ij} (\xi_{mn} + w_{mn}) \sin \frac{i\pi x}{a} \sin \frac{j\pi y}{b} \cos \frac{m\pi x}{a} \cos \frac{n\pi y}{b} \right\} \end{aligned} \quad (4.10)$$

and

$$\begin{aligned} \sum_i \sum_j h I_{ij} F_{ij} \cos \frac{i\pi x}{a} \cos \frac{j\pi y}{b} = \sum_i \sum_j \sum_m \sum_n \\ \left\{ - \left[\left(\frac{i\pi}{a} \right)^2 \left(\frac{n\pi}{b} \right)^2 w_{ij} w_{mn} + G_{ijmn} w_{ij} \xi_{mn} \right] \sin \frac{i\pi x}{a} \sin \frac{j\pi y}{b} \sin \frac{m\pi x}{a} \sin \frac{n\pi y}{b} \right. \\ \left. + H_{ijmn} (2\xi_{mn} + w_{mn}) w_{ij} \cos \frac{i\pi x}{a} \cos \frac{j\pi y}{b} \cos \frac{m\pi x}{a} \cos \frac{n\pi y}{b} \right\} \end{aligned} \quad (4.11)$$

where:

$$C_{ij} = D_{11} \left(\frac{i\pi}{a} \right)^4 + 2(D_{12} + 2D_{66}) \left(\frac{i\pi}{a} \right)^2 \left(\frac{j\pi}{b} \right)^2 + D_{22} \left(\frac{j\pi}{b} \right)^4 + k_1 - k_2 \left[\left(\frac{i\pi}{a} \right)^2 + \left(\frac{j\pi}{b} \right)^2 \right] \quad (4.10a)$$

$$G_{ijmn} = \left(\frac{j\pi}{b} \right)^2 \left(\frac{m\pi}{a} \right)^2 + \left(\frac{i\pi}{a} \right)^2 \left(\frac{n\pi}{b} \right)^2 \quad (4.10b)$$

$$H_{ijmn} = \left(\frac{i\pi}{a} \right) \left(\frac{j\pi}{b} \right) \left(\frac{m\pi}{a} \right) \left(\frac{n\pi}{b} \right) \quad (4.10c)$$

$$I_{ij} = A_{11}^* \left(\frac{j\pi}{b} \right)^4 + (2A_{12}^* + A_{66}^*) \left(\frac{i\pi}{a} \right)^2 \left(\frac{j\pi}{b} \right)^2 + A_{22}^* \left(\frac{i\pi}{a} \right)^4 \quad (4.11a)$$

Using the three trigonometric identities:

$$\sin \frac{i\pi x}{a} \cos \frac{m\pi x}{a} = \frac{1}{2} \left[\sin \frac{(i+m)\pi x}{a} + \sin \frac{(i-m)\pi x}{a} \right],$$

$$\sin \frac{i\pi x}{a} \sin \frac{m\pi x}{a} = \frac{1}{2} \left[\cos \frac{(i-m)\pi x}{a} - \cos \frac{(i+m)\pi x}{a} \right], \text{ and}$$

$$\cos \frac{i\pi x}{a} \cos \frac{m\pi x}{a} = \frac{1}{2} \left[\cos \frac{(i-m)\pi x}{a} + \cos \frac{(i+m)\pi x}{a} \right],$$

the right hand sides of Equations 4.10 and 4.11 can be converted into the same form as the left hand sides. Hence, Equation 4.10 becomes:

$$\begin{aligned} \sum_i \sum_j \left(C_{ij} w_{ij} + h \bar{\sigma}_{xx} (\xi_{ij} + w_{ij}) \left(\frac{i\pi}{a} \right)^2 \right) \sin \frac{i\pi x}{a} \sin \frac{j\pi y}{b} &= \frac{h}{4} \sum_i \sum_j \sum_m \sum_n \\ \left\{ F_{ij} (\xi_{mn} + w_{mn}) \left[(G_{ijmn} - 2H_{ijmn}) \sin \frac{(i+m)\pi x}{a} \sin \frac{(j+n)\pi y}{b} \right. \right. \\ &- (G_{ijmn} + 2H_{ijmn}) \sin \frac{(i+m)\pi x}{a} \sin \frac{(j-n)\pi y}{b} \\ &- (G_{ijmn} + 2H_{ijmn}) \sin \frac{(i-m)\pi x}{a} \sin \frac{(j+n)\pi y}{b} \\ &\left. \left. + (G_{ijmn} - 2H_{ijmn}) \sin \frac{(i-m)\pi x}{a} \sin \frac{(j-n)\pi y}{b} \right] \right\} \end{aligned} \quad (4.12)$$

while Equation 4.11 becomes:

$$\begin{aligned}
 \sum_i \sum_j h l_{ij} F_{ij} \cos \frac{i\pi x}{a} \cos \frac{j\pi y}{b} &= \frac{1}{4} \sum_i \sum_j \sum_m \sum_n \\
 &\left\{ \left[\left[-\left(\frac{i\pi}{a}\right)^2 \left(\frac{n\pi}{b}\right)^2 + H_{ijmn} \right] w_{ij} w_{mn} + \left[-G_{ijmn} + 2H_{ijmn} \right] w_{ij} \xi_{mn} \right] \right. \\
 &\quad \left. \cos \frac{(i-m)\pi x}{a} \cos \frac{(j-n)\pi y}{b} + \right. \\
 &\left\{ \left[\left(\frac{i\pi}{a}\right)^2 \left(\frac{n\pi}{b}\right)^2 + H_{ijmn} \right] w_{ij} w_{mn} + \left[G_{ijmn} + 2H_{ijmn} \right] w_{ij} \xi_{mn} \right\} \\
 &\quad \left. \cos \frac{(i-m)\pi x}{a} \cos \frac{(j+n)\pi y}{b} + \right. \\
 &\left\{ \left[\left(\frac{i\pi}{a}\right)^2 \left(\frac{n\pi}{b}\right)^2 + H_{ijmn} \right] w_{ij} w_{mn} + \left[G_{ijmn} + 2H_{ijmn} \right] w_{ij} \xi_{mn} \right\} \\
 &\quad \left. \cos \frac{(i+m)\pi x}{a} \cos \frac{(j-n)\pi y}{b} + \right. \\
 &\left\{ \left[-\left(\frac{i\pi}{a}\right)^2 \left(\frac{n\pi}{b}\right)^2 + H_{ijmn} \right] w_{ij} w_{mn} + \left[-G_{ijmn} + 2H_{ijmn} \right] w_{ij} \xi_{mn} \right\} \\
 &\quad \left. \cos \frac{(i+m)\pi x}{a} \cos \frac{(j+n)\pi y}{b} \right\} \tag{4.13}
 \end{aligned}$$

Coefficients of like terms are equated to give two sets of nonlinear algebraic equations in F_{ij} and w_{ij} .

$$\begin{bmatrix} \ddots & & & & \\ & \ddots & & & \\ & & \ddots & & \\ & & & \ddots & \\ & & & & \ddots \end{bmatrix} \begin{Bmatrix} w_{11} \\ w_{13} \\ \vdots \\ w_{ij} \\ \vdots \end{Bmatrix} = \begin{Bmatrix} R_1^w(w_{ij}, F_{ij}, \xi_{ij}, \bar{\sigma}_{xx}) \\ R_2^w(w_{ij}, F_{ij}, \xi_{ij}, \bar{\sigma}_{xx}) \\ \vdots \\ R_k^w(w_{ij}, F_{ij}, \xi_{ij}, \bar{\sigma}_{xx}) \\ \vdots \end{Bmatrix} \tag{4.14}$$

$$\begin{bmatrix} \ddots & & & & \\ & \ddots & & & \\ & & \ddots & & \\ & & & \ddots & \\ & & & & \ddots \end{bmatrix} \begin{Bmatrix} F_{00} \\ F_{02} \\ \vdots \\ F_{ij} \\ \vdots \end{Bmatrix} = \begin{Bmatrix} R_1^F(w_{ij}, \xi_{ij}) \\ R_2^F(w_{ij}, \xi_{ij}) \\ \vdots \\ R_k^F(w_{ij}, \xi_{ij}) \\ \vdots \end{Bmatrix} \tag{4.15}$$

where $[M^w]$ and $[M^F]$ are diagonal matrices defined by:

$$M_{kt}^w = C_{ij} \quad (4.16)$$

and

$$M_{kt}^F = hI_{ij} \quad (4.17)$$

For a given value of the subscript k, the subscripts i and j are uniquely defined by the numbering system shown in Table 4.1. The right hand sides of Equations 4.14 and 4.15 are given by:

$$R_k^w = h\bar{\sigma}_{xx} \left(\xi_{pq} + w_{pq} \right) \left(\frac{p\pi}{a} \right)^2 + \frac{h}{4} \sum_i \sum_j \sum_m \sum_n \left\{ \begin{aligned} & F_{ij}(\xi_{mn} + w_{mn})(G_{ijmn} - 2H_{ijmn}) \Big|_{\substack{i+m=p \\ j+n=q}} \mp F_{ij}(\xi_{mn} + w_{mn})(G_{ijmn} + 2H_{ijmn}) \Big|_{\substack{i+m=p \\ |j-n|=q}} \\ & \mp F_{ij}(\xi_{mn} + w_{mn})(G_{ijmn} + 2H_{ijmn}) \Big|_{\substack{|i-m|=p \\ j+n=q}} + F_{ij}(\xi_{mn} + w_{mn})(G_{ijmn} - 2H_{ijmn}) \Big|_{\substack{|i-m|=p \\ |j-n|=q}} \end{aligned} \right\} \quad (4.18)$$

$$R_k^F = \sum_i \sum_j \sum_m \sum_n \left\{ \begin{aligned} & \left[\left(-\left(\frac{i\pi}{a} \right)^2 \left(\frac{n\pi}{b} \right)^2 + H_{ijmn} \right) w_{ij} w_{mn} + (-G_{ijmn} + 2H_{ijmn}) w_{ij} \xi_{mn} \right] \Big|_{\substack{|i-m|=p \\ |j-n|=q}} \\ & + \left[\left(-\left(\frac{i\pi}{a} \right)^2 \left(\frac{n\pi}{b} \right)^2 + H_{ijmn} \right) w_{ij} w_{mn} + (-G_{ijmn} + 2H_{ijmn}) w_{ij} \xi_{mn} \right] \Big|_{\substack{|i-m|=p \\ j+n=q}} \\ & + \left[\left(-\left(\frac{i\pi}{a} \right)^2 \left(\frac{n\pi}{b} \right)^2 + H_{ijmn} \right) w_{ij} w_{mn} + (-G_{ijmn} + 2H_{ijmn}) w_{ij} \xi_{mn} \right] \Big|_{\substack{i+m=p \\ |j-n|=q}} \\ & + \left[\left(-\left(\frac{i\pi}{a} \right)^2 \left(\frac{n\pi}{b} \right)^2 + H_{ijmn} \right) w_{ij} w_{mn} + (-G_{ijmn} + 2H_{ijmn}) w_{ij} \xi_{mn} \right] \Big|_{\substack{i+m=p \\ j+n=q}} \end{aligned} \right\} \quad (4.19)$$

Table 4.1 **Numbering system of the assumed modes for an N
by N analysis (for N>3)**

Single Index	Double Index (odd modes)		Double Index (even modes)	
k	i	j	i	j
1	1	1	0	0
2	1	3	0	2
3	1	5	0	4
:	:	:	:	:
k	2a-1	2b-1	2(a-1)	2(b-1)
:	:	:	:	:

$$a = [k/N]$$

$$b = k - N([k/N] - 1)$$

$[k/N]$ = smallest integer larger than or equal to the quotient k/N

For a given value of the subscript k , the subscripts p and q in Equations 4.18 and 4.19 are uniquely defined by the same numbering system shown in Table 4.1. The right hand sides of Equations 4.18 and 4.19 sum up terms of which the subscripted variables satisfy certain specific conditions as specified by the subscripted equations after the vertical bars ($|$). For example, the term

$$\frac{h}{4} \sum_i \sum_j \sum_m \sum_n F_{ij} (\xi_{mn} + w_{mn}) (G_{ijmn} - 2H_{ijmn}) \Big|_{\substack{i+m=p \\ j+n=q}}$$

on the right hand side of Equation 4.18 implies that only the terms where $(i+m=p)$ and $(j+n=q)$ are considered in the summation.

Since Equations 4.14 and 4.15 are nonlinear, an iterative solution procedure is required to solve them. The forms of Equations 4.14 and 4.15 readily suggest the solution method of fixed-point iterations [86], also known as the method of successive substitutions [87]. Based on these equations, the following iterative sequences are established:

$$\begin{Bmatrix} w_{11} \\ w_{13} \\ \vdots \\ w_{ij} \\ \vdots \end{Bmatrix}^{(n+1)} = \begin{Bmatrix} R_1^w / M_{11}^w \\ R_2^w / M_{22}^w \\ \vdots \\ R_k^w / M_{kk}^w \\ \vdots \end{Bmatrix}^{(n)} \quad (4.20)$$

and

$$\begin{Bmatrix} F_{00} \\ F_{02} \\ \vdots \\ F_{ij} \\ \vdots \end{Bmatrix}^{(n+1)} = \begin{Bmatrix} R_1^F \\ R_2^F / M_{22}^F \\ \vdots \\ R_k^F / M_{kk}^F \\ \vdots \end{Bmatrix}^{(n)} \quad (4.21)$$

At the n th iteration step, the differences between the current values of the modal amplitudes and the projected values, at the $(n+1)$ th step, are calculated:

$$\begin{Bmatrix} \delta w_{11} \\ \delta w_{13} \\ \vdots \\ \delta w_{ij} \\ \vdots \end{Bmatrix}^{(n)} = \begin{Bmatrix} w_{11} \\ w_{13} \\ \vdots \\ w_{ij} \\ \vdots \end{Bmatrix}^{(n)} - \begin{Bmatrix} w_{11} \\ w_{13} \\ \vdots \\ w_{ij} \\ \vdots \end{Bmatrix}^{(n+1)} \quad (4.22)$$

and

$$\begin{Bmatrix} \delta F_{00} \\ \delta F_{02} \\ \vdots \\ \delta F_{ij} \\ \vdots \end{Bmatrix}^{(n)} = \begin{Bmatrix} F_{00} \\ F_{02} \\ \vdots \\ F_{ij} \\ \vdots \end{Bmatrix}^{(n)} - \begin{Bmatrix} F_{00} \\ F_{02} \\ \vdots \\ F_{ij} \\ \vdots \end{Bmatrix}^{(n+1)} \quad (4.23)$$

Following common practice in numerical computation, the sums of the squares of δw_{ij} and δF_{ij} , defined as $|\delta w_{ij}|^2$ and $|\delta F_{ij}|^2$:

$$\left| (\delta w_{ij})^2 \right| = (\delta w_{11})^2 + (\delta w_{13})^2 + \dots \quad (4.24)$$

and

$$\left| (\delta F_{ij})^2 \right| = (\delta F_{00})^2 + (\delta F_{02})^2 + \dots \quad (4.25)$$

are used to monitor the convergence of the solution. When $|\delta w_{ij}|^2$ and $|\delta F_{ij}|^2$ reach certain prescribed tolerances, the iteration is stopped.

4.1.3 Two-parameter foundation model

To use the simple propagation model to analyze sandwich panels, a two-parameter foundation was chosen to model the elastic behavior of the

core. A description of the two-parameter foundation model is in order.

A number of researchers, especially those in civil engineering, have spent a considerable amount of effort examining various elastic foundation models [88-91]. The simplest of these models is the Winkler foundation model [92] where the foundation is modelled as a group of independent linear springs. At the other end of the spectrum are models where the foundation is treated as an anisotropic continuum. The two-parameter model used in the present investigation is, in complexity, between the Winkler foundation and the continuum foundations. The model was previously proposed by Filonenko-Borodich [93] and Pasternak [94]. The model provides a "membrane-type" interaction among the linear springs used in the Winkler model. Such interaction is governed by the curvatures at the surface of the foundation. The foundation reaction is characterized by:

$$\sigma_{zz}(x,y) = k_1 w(x,y) + k_2 \nabla^2 w(x,y) \quad (4.26)$$

The foundation parameters k_1 and k_2 are calculated as follows in the current work. An existing elasticity model [52] is used to calculate the stress distribution and displacement distribution at the interface between the core and the facesheet of the sandwich panel for a Hertzian contact loading on the facesheet. A least-squares fit of the form of Equation 4.26 is performed using the stress distribution and the displacement distribution in order to obtain the parameters k_1 and k_2 .

4.1.4 Core damage model

The formulation thus far has used an elastic foundation to model the core of the sandwich panel. In reality, the core underneath the dimple has been damaged by indentation or impact. The behavior of this initial region

of damaged/crushed core is not elastic and needs to be accounted for in the dimple propagation model. Also, as the dimple propagates, core crushing can occur outside the initial region. This progressive core crushing must be accounted for as well. The foundation is, therefore, assumed to behave in one of the following three ways. First, if the core is undamaged, it will behave elastically and the reaction, σ_{zz} , is given by Equation 4.26. Second, within the initial region of crushed core due to indentation or impact, the core sustains no reaction, i.e. σ_{zz} is equal to 0. Lastly, if the core is subsequently crushed (σ_{zz} is greater than the compressive strength) during the dimple propagation, the core sustains a constant reaction given by the "plateau stress" of the core. The "plateau stress" is the reaction of the core after it is crushed and its value is obtained from a flatwise compression test of the core [58]. Figure 4.2 is a sketch of the stress-strain curve of a bare core under flatwise compression which shows how the compressive strength and the plateau stress of the core are defined.

The initially crushed core due to indentation and the subsequently crushed core due to dimple propagation are modelled differently for the following reasoning. When the indentation load is released after the maximum indentation depth is reached, the facesheet will rebound and pull the buckled cell walls up from the maximum indentation depth. These "pulled-up" cell walls can support no load. On the other hand, the core subsequently crushed during the dimple propagation stays at the depth at which crushing occurs. The subsequently crushed core can, therefore, support a load in the same way as in a flatwise compression test as illustrated in Figure 4.2. It should be noted, however, that if the displacement within the initial region of crushed core exceeds that corresponding to the shape of the initial maximum indentation, the reaction

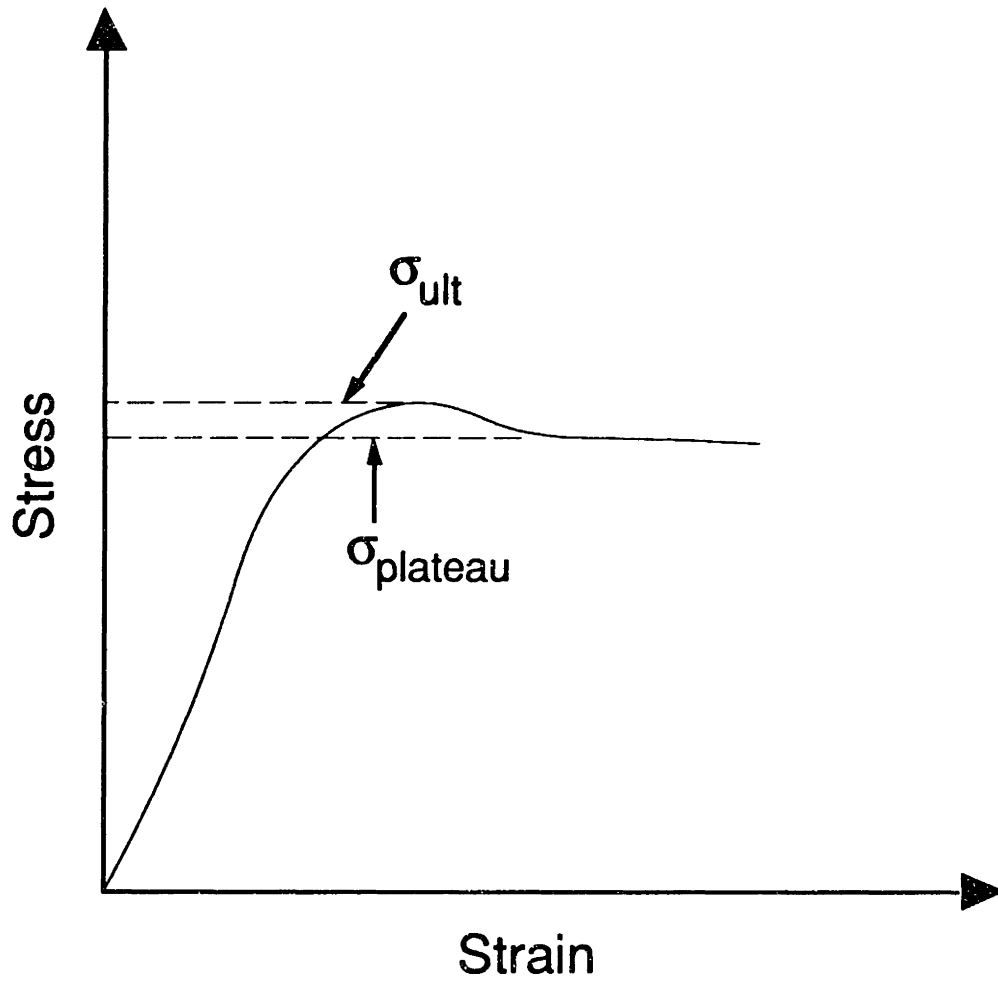


Figure 4.2 Sketch of stress-strain curve of flatwise compression test of bare Nomex honeycomb core (actual data can be found in [58]).

of the core should be equal to the plateau stress. However, such large displacement was never achieved in all the specimens tested.

The initially crushed core due to indentation and the subsequently crushed core due to dimple propagation are modelled differently for the following reasoning. When the indentation load is released after the maximum indentation depth is reached, the facesheet will rebound and pull the buckled cell walls up from the maximum indentation depth. These "pulled-up" cell walls can support no load. On the other hand, the core subsequently crushed during the dimple propagation stays at the depth at which crushing occurs. The subsequently crushed core can, therefore, support a load in the same way as in a flatwise compression test as illustrated in Figure 4.2. It should be noted, however, that if the displacement within the initial region of crushed core exceeds that corresponding to the shape of the initial maximum indentation, the reaction of the core should be equal to the plateau stress. However, such large displacement was never achieved in all the specimens tested.

The core damage is incorporated into the analytical model as follows. First, the facesheet is divided into a uniform grid and the reaction between the facesheet and the elastic foundation, σ_e , is calculated at the nodal points of the grid. Second, such reaction is modified at nodal points within the region of initial crushed core and at nodal points where σ_{ult} is exceeded. This is achieved by superimposing a complementary stress distribution, σ_c , onto the reaction between the facesheet and the elastic foundation such that the desired stress distribution is equal to the sum of σ_e and σ_c . Third, the complementary stress distribution is augmented into the equilibrium equation in the iteration process to ensure that equilibrium is satisfied once

convergence is achieved. The mathematical details of the above process are described next.

The facesheet is divided into a uniform rectangular grid with the same number of nodal points (x_i, y_j) as the number of modes used in the expansion (Equation 4.8) for the displacement function w . At each iteration step, σ_{zz} at the interface between the foundation and the facesheet is calculated at the nodal points assuming an elastic foundation. This is given by the reaction of the two-parameter foundation from Equation 4.26:

$$\begin{Bmatrix} \sigma_{zz}(x_1, y_1) \\ \sigma_{zz}(x_1, y_2) \\ \vdots \\ \sigma_{zz}(x_i, y_j) \\ \vdots \end{Bmatrix} = k_1 \begin{Bmatrix} w(x_1, y_1) \\ w(x_1, y_2) \\ \vdots \\ w(x_i, y_j) \\ \vdots \end{Bmatrix} + k_2 \nabla^2 \begin{Bmatrix} w(x_1, y_1) \\ w(x_1, y_2) \\ \vdots \\ w(x_i, y_j) \\ \vdots \end{Bmatrix} \quad (4.27)$$

Substituting the expansion for $w(x,y)$ of Equation 4.8 and performing the appropriate differentiations for the Laplace operator give:

$$\begin{Bmatrix} \sigma_{zz}(x_1, y_1) \\ \sigma_{zz}(x_1, y_2) \\ \vdots \\ \sigma_{zz}(x_i, y_j) \\ \vdots \end{Bmatrix} = \begin{bmatrix} \sin \frac{\pi x_1}{a} \sin \frac{\pi y_1}{b} & \sin \frac{\pi x_1}{a} \sin \frac{3\pi y_1}{b} & \dots & \sin \frac{m\pi x_1}{a} \sin \frac{n\pi y_1}{b} & \dots \\ \sin \frac{\pi x_1}{a} \sin \frac{\pi y_2}{b} & \sin \frac{\pi x_1}{a} \sin \frac{3\pi y_2}{b} & \dots & \sin \frac{m\pi x_1}{a} \sin \frac{n\pi y_2}{b} & \dots \\ \vdots & \vdots & & \vdots & \\ \sin \frac{\pi x_i}{a} \sin \frac{\pi y_j}{b} & \sin \frac{\pi x_i}{a} \sin \frac{3\pi y_j}{b} & \dots & \sin \frac{m\pi x_i}{a} \sin \frac{n\pi y_j}{b} & \dots \\ \vdots & \vdots & & \vdots & \end{bmatrix} \begin{Bmatrix} \sigma_{zz}^{(11)} \\ \sigma_{zz}^{(13)} \\ \vdots \\ \sigma_{zz}^{(mn)} \\ \vdots \end{Bmatrix} \quad (4.28)$$

where,

$$\begin{Bmatrix} \sigma_{zz}^{(11)} \\ \sigma_{zz}^{(13)} \\ \vdots \\ \sigma_{zz}^{(mn)} \\ \vdots \end{Bmatrix} = \begin{Bmatrix} \bar{k}_{11}w_{11} \\ \bar{k}_{13}w_{13} \\ \vdots \\ \bar{k}_{mn}w_{mn} \\ \vdots \end{Bmatrix} \quad (4.28a)$$

and

$$\bar{k}_{mn} = k_1 - k_2 \left[\left(\frac{m\pi}{a} \right)^2 + \left(\frac{n\pi}{b} \right)^2 \right] \quad (4.28b)$$

Equation 4.28 plays a very important role in the core damage model. It relates the "modal amplitudes" of the reaction stress of the core, $\sigma_{zz}^{(mn)}$, to the corresponding "nodal amplitudes" $\sigma_{zz}(x_i, y_j)$. Hence, the complementary stress distribution in the "nodal space" is evaluated and the corresponding modal amplitudes are obtained by inverting the matrix in Equation 4.28.

Based on the experimental measurement, an initial region of crushed core, R_0 , is identified. Note that the model can be adapted for other shapes of initial crushed core. At the nodal points within this region, complementary stresses are calculated as the negative of the reaction of the elastic foundation so that the sum of the elastic stress and the complementary stress is equal to the desired value of zero. The nodal points at which σ_{zz} exceeds the strength of the core, σ_{ult} , during subsequent loading are also identified. At these nodal points, the complementary stresses are calculated as the difference between the reaction of the elastic foundation and $\sigma_{plateau}$. The complementary stress distribution can be written as a stress vector:

$$\left\{ \begin{array}{c} \vdots \\ \sigma_{zz}(x_i, y_j) \\ \vdots \\ \sigma_{zz}(x_m, y_n) \\ \vdots \\ \sigma_{zz}(x_k, y_l) \\ \vdots \end{array} \right\}^c = - \left\{ \begin{array}{c} \vdots \\ \sigma_{zz}(x_i, y_j) \\ \vdots \\ \sigma_{zz}(x_m, y_n) - \sigma_{plateau} \\ \vdots \\ 0 \\ \vdots \end{array} \right\} \quad (4.29)$$

where the superscript "c" stands for "complementary". In this illustrative case, the nodal point (x_i, y_j) is within the initial region of crushed core, (x_m, y_n) is a nodal point at which the core strength is exceeded during subsequent loading, and (x_k, y_l) is a nodal point where the core still behaves elastically. The complementary stress vector shown in Equation 4.29 is then transformed back to the modal space using Equation 4.28:

$$\left\{ \begin{array}{c} \sigma_{zz}^{(11)} \\ \sigma_{zz}^{(13)} \\ \vdots \\ \sigma_{zz}^{(mn)} \\ \vdots \end{array} \right\}^c = \left[\begin{array}{cccc} \sin \frac{\pi x_1}{a} \sin \frac{\pi y_1}{b} & \sin \frac{\pi x_1}{a} \sin \frac{3\pi y_1}{b} & \dots & \sin \frac{m\pi x_1}{a} \sin \frac{n\pi y_1}{b} & \dots \\ \sin \frac{\pi x_1}{a} \sin \frac{\pi y_2}{b} & \sin \frac{\pi x_1}{a} \sin \frac{3\pi y_2}{b} & \dots & \sin \frac{m\pi x_1}{a} \sin \frac{n\pi y_2}{b} & \dots \\ \vdots & \vdots & & \vdots & \\ \sin \frac{\pi x_i}{a} \sin \frac{\pi y_j}{b} & \sin \frac{\pi x_i}{a} \sin \frac{3\pi y_j}{b} & \dots & \sin \frac{m\pi x_i}{a} \sin \frac{n\pi y_j}{b} & \dots \\ \vdots & \vdots & & \vdots & \end{array} \right]^{-1} \left\{ \begin{array}{c} \sigma_{zz}(x_1, y_1) \\ \sigma_{zz}(x_1, y_2) \\ \vdots \\ \sigma_{zz}(x_i, y_j) \\ \vdots \end{array} \right\}^c \quad (4.30)$$

These "modal amplitudes" of the complementary stress are augmented to the right hand side of the equilibrium equation, Equation 4.20, at each iteration step.

$$\begin{Bmatrix} w_{11} \\ w_{13} \\ \vdots \\ w_{ij} \\ \vdots \end{Bmatrix}^{(n+1)} = \begin{Bmatrix} R_1^w / M_{11}^w \\ R_2^w / M_{22}^w \\ \vdots \\ R_k^w / M_{kk}^w \\ \vdots \end{Bmatrix}^{(n)} - \begin{Bmatrix} \sigma_{zz}^{(11)} / M_{11}^w \\ \sigma_{zz}^{(13)} / M_{22}^w \\ \vdots \\ \sigma_{zz}^{(pq)} / M_{kk}^w \end{Bmatrix}^{(n)} \quad (4.31)$$

The iterative procedures are repeated until convergence is achieved.

4.1.5 Solution procedure

All components and relevant equations of the dimple propagation model have been described. For a given applied stress, $\bar{\sigma}_{xx}$, the model is used to solve for the modal amplitudes w_{ij} and F_{ij} which can then be used to calculate the stresses in the facesheet for damage prediction. The solution procedures are outlined as follows:

- (i) set all w_{ij} and F_{ij} to zero;
- (ii) evaluate the complementary stress vector using Equation 4.29;
- (iii) update the modal amplitudes w_{ij} using Equation 4.31;
- (iv) update the modal amplitudes F_{ij} using Equation 4.21 with new w_{ij} on the righthand side;
- (v) calculate the sum of the squares of the residuals $|(\delta w_{ij})^2|$ and $|(\delta F_{ij})^2|$ using Equations 4.24 and 4.25; and
- (vi) check magnitudes of $|(\delta w_{ij})^2|$ and $|(\delta F_{ij})^2|$; if they are greater than the tolerances, go back to (ii).

There are no absolute tolerances for $|(\delta w_{ij})^2|$ and $|(\delta F_{ij})^2|$. The tolerances change from case to case. However, there are two rules of thumb to help decide when to stop the iterative process. First, the value of $|(\delta F_{ij})^2|$ is always several orders of magnitude greater than the value of $|(\delta w_{ij})^2|$. Therefore, the tolerance for $|(\delta F_{ij})^2|$ should be several orders of magnitude greater than that for $|(\delta w_{ij})^2|$. Second, the asymptotic values of

$|\delta w_{ij}|^2$ and $|\delta F_{ij}|^2$ are usually four or five orders of magnitude smaller than their starting values. Thus, for all cases presented, the iterations are stopped after $|\delta w_{ij}|^2$ and $|\delta F_{ij}|^2$ have decreased by four orders of magnitudes.

It may happen that the iterative solution procedures described above fail to give a converged solution. When this is the case, a lower applied stress should be used to obtain a converged solution. Then the applied stress is increased with the modal amplitudes of the previous converged solution used as the starting point of the iterations. Such a process is repeated until the desired applied load is reached.

4.1.6 Failure prediction

The failure of a sandwich panel is defined herein as a significant loss of load-carrying capability. For undamaged sandwich panels, this usually means fracture in both facesheets. For impact-damaged or indented sandwich panels, failure usually means fracture of the initially damaged facesheet. The dimple propagation model described thus far has not addressed the failure of the facesheet due to uniaxial compression. A discussion of the issues and procedures involved in the failure prediction of the sandwich panels is given in the present section.

In the original model by Minguet [70], failure of the sandwich panels is defined as the unstable growth of the dimple perpendicular to the loading (The definition of failure is not given explicitly in Minguet's paper. The above definition is gathered by the author through private communication.). The unstable growth is caused by the progressive crushing of the core all the way to the edges of the sandwich panel. By adjusting the plateau stress of the honeycomb core, rather than using an actual measured value, Minguet managed to obtain fairly good correlation of the failure stress of

the impact-damaged panels. However, one important aspect of the damage prediction process was not examined carefully in Minguet's paper: the model predicts very high bending stress within the dimple. Such high bending stresses may have exceeded the strength of the facesheet material before the unstable growth sets in.

In the present work, the longitudinal stress σ_{xx} (loading is applied along the x-axis) is used for failure prediction. In particular, the laminate-level stress distribution σ_{xx} along the centerline perpendicular to the loading is evaluated at the top, middle, and bottom surfaces of the facesheet for the various applied stress levels. The peak values in the stress distributions are compared with the failure stress of the undamaged panels. This is, therefore, a laminate-level stress evaluation. This could be easily extended to a ply-by-ply scheme. However, such a scheme is not necessary herein due to the relatively thin facesheets and particular layups utilized.

4.1.7 Computer program

The formulation of the dimple propagation model has been implemented in a FORTRAN 77 computer program called GROWTH. The program is compiled with the DEC Fortran compiler for ULTRIX/RISC Systems v3.2 and is run on a DECstation 5000/133 workstation. A flowchart for program GROWTH is depicted in Figure 4.3. The entire program listing is given in Appendix A. Depending on the number of iterations and the number of modes used, the run time of GROWTH typically varies between 5 minutes for 23 by 23 modes with 40 iterations to 15 minutes for 23 by 23 modes with 100 iterations. The numbers of modes quoted here, and in all subsequent references, are the actual number of modes used in the computation. Hence, a 23 by 23-mode analysis utilizes 23

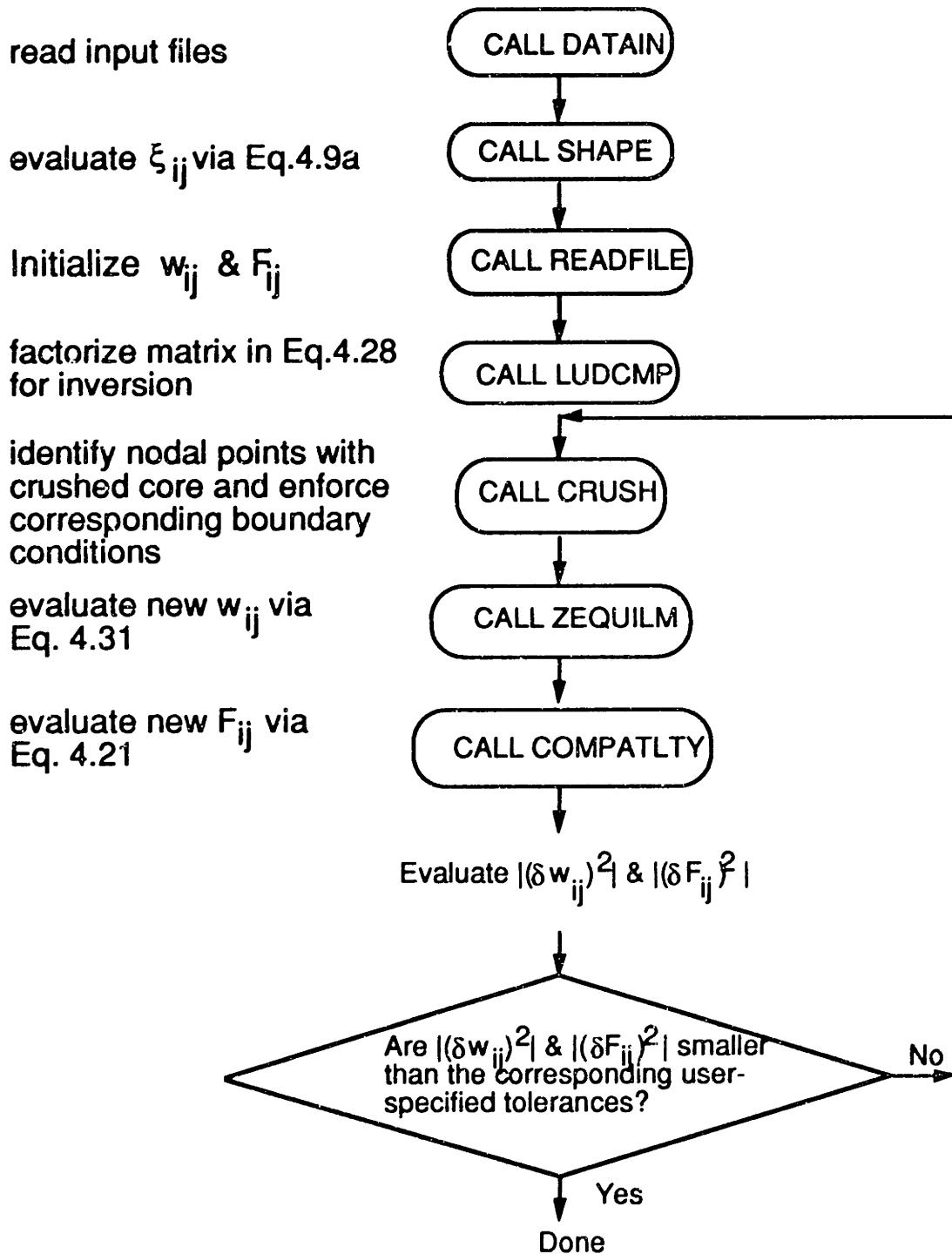


Figure 4.3 Flowchart for program GROWTH.

by 23 odd modes of the expansion for $w(x,y)$ and $\xi(x,y)$, but 23 by 23 even modes of the expansion for $F(x,y)$.

The main outputs of the program are the modal amplitudes for $w(x,y)$ and $F(x,y)$. Once the modal amplitudes for $w(x,y)$ and $F(x,y)$ are found, all stress and strain components in the facesheets can be calculated at any locations desired using Eqs. 4.3 through 4.5, which relate the stress resultants to the stress function $F(x,y)$, and Classical Laminated Plate Theory. The user of the program is free to decide what stress or strain components to use for failure prediction, along with the failure criterion chosen. Based on the failure mode observed (see Chapter 6) in the present work, the longitudinal stress component, σ_{xx} , along the specimen centerline perpendicular to the loading direction is chosen to correlate residual strengths of the specimens tested. The peak membrane value of σ_{xx} is identified by visual examination of the output file. The peak value is then compared with the failure strength of the corresponding undamaged specimens to decide whether failure has occurred. If the user of the program wants to use other stress or strain components for failure prediction, a new subroutine can easily be implemented to calculate the desired stress or strain components in terms of the modal amplitudes for $w(x,y)$ and $F(x,y)$.

4.1.8 Convergence studies

In the present dimple propagation model, there are two types of convergence that need to be delineated clearly. First, for a given number of modes used in the expansion series given in Equation 4.8, the iteration scheme described by Equations 4.31 and 4.21 drives the residuals δw_{ij} and δF_{ij} to approach zero and yields a converged solution. Such convergence is referred to as "local convergence". A locally converged solution satisfies the

governing differential equations and the prescribed boundary conditions at the nodal points for that particular number of modes.

Second, as the number of modes is changed, a different "locally converged" solution may be obtained. As the number of modes changes, so do the number and locations of the nodal points. Since the boundary condition at the plate-foundation interface is enforced at these nodal points, the effective boundary condition changes with the changes in the locations of the nodal points. As the number of modes is increased, these "locally converged" solutions will approach an asymptotic value, i.e. a "globally converged" solution. The results shown in this section are locally converged solutions for a given number of modes. A sample problem is examined to study the global convergence of the model as the number of modes is varied.

The sample problem chosen for the convergence studies is that of a 89 mm by 85 mm sandwich panel with (0/90) plain weave fabric facesheets and a Nomex honeycomb core. The fabric material system is AW193PW/3501-6, the properties of which are given in Chapter 6. The necessary input parameters for the computer program are given in Table 4.2. One variable is left out in Table 4.2: the radius of the initial region of crushed core R_0 . Two values of R_0 (5 mm and 10 mm) are examined in relation to the global convergence of the model. These two values of R_0 are typical measurements of the region of crushed core observed experimentally (see Chapter 6).

The dimensions of the model were chosen to reduce the number of required modes. In this analysis, more modes are required to obtain a converged solution as the in-plane dimensions increase. This is a direct consequence of approximating a localized function (i.e. the dimple profile) with a double Fourier series over a large domain (i.e. the dimensions of the model). In the present work, since the dimple propagation is primarily

Table 4.2 Input parameters for sample problem

Parameter	Value
a	89 mm
b	89 mm
R_x	11 mm
R_y	11 mm
ξ_0	-0.2 mm
h	0.35 mm
A_{11}	22.92 MNm ⁻¹
A_{12}	3.437 MNm ⁻¹
A_{16}	0.0 MNm ⁻¹
A_{22}	22.92 MNm ⁻¹
A_{26}	0.0 MNm ⁻¹
A_{66}	2.195 MNm ⁻¹
D_{11}	0.2339 Nm
D_{12}	0.0351 Nm
D_{16}	0.0 Nm
D_{22}	0.2339 Nm
D_{26}	0.0 Nm
D_{66}	0.0224 Nm
σ_{ult}	1.8 MPa
$\sigma_{plateau}$	1.4 MPa
k_1	20.53 GNm ⁻³
k_2	-28.27 kNm ⁻¹
$\bar{\sigma}_{xx}$	-250 MPa

along the direction perpendicular to the loading, the dimension chosen along the y-axis is the actual nominal width (89 mm) of the specimens tested. The dimension along the x-axis is also chosen to be 89 mm, which is smaller than the nominal gage length (203 mm) of the test specimen, to reduce the number of modes required to obtain a converged solution. Since virtually no propagation occurs in the x-direction, this should have no bearing on the results.

The dimple profiles (sum of initial deflections and additional out-of-plane displacements due to applied in-plane loads) along the centerline perpendicular to the loading for different numbers of modes used are shown in Figures 4.4 and 4.5 for the two different values of R_0 . Note that, for clarity, the y-axis has been shifted by $b/2$ so that the center of the panel is at y equal to 0. It can be seen from Figures 4.4 and 4.5 that a converged solution is obtained with 23 by 23 modes for both values of R_0 . A larger initial region (R_0 equal to 10 mm) of crushed core is seen to promote greater propagation of the dimple than a smaller initial region (R_0 equal to 5 mm) of crushed core. The resulting dimple is also deeper.

The distributions of the core reaction stress, σ_{zz} , along the centerline perpendicular to the loading are shown in Figures 4.6 and 4.7 for the two values of R_0 . It can be seen that the stress component, being related to the second derivatives of the stress function and the displacement function, is not as converged as the displacement. The model is, however, quite successful in enforcing the zero-reaction condition within the initial region of crushed core as indicated by the values of σ_{zz} near the center of the panel in these figures. The high compressive stress at the tips of the dimple explains why progressive core crushing occurs.

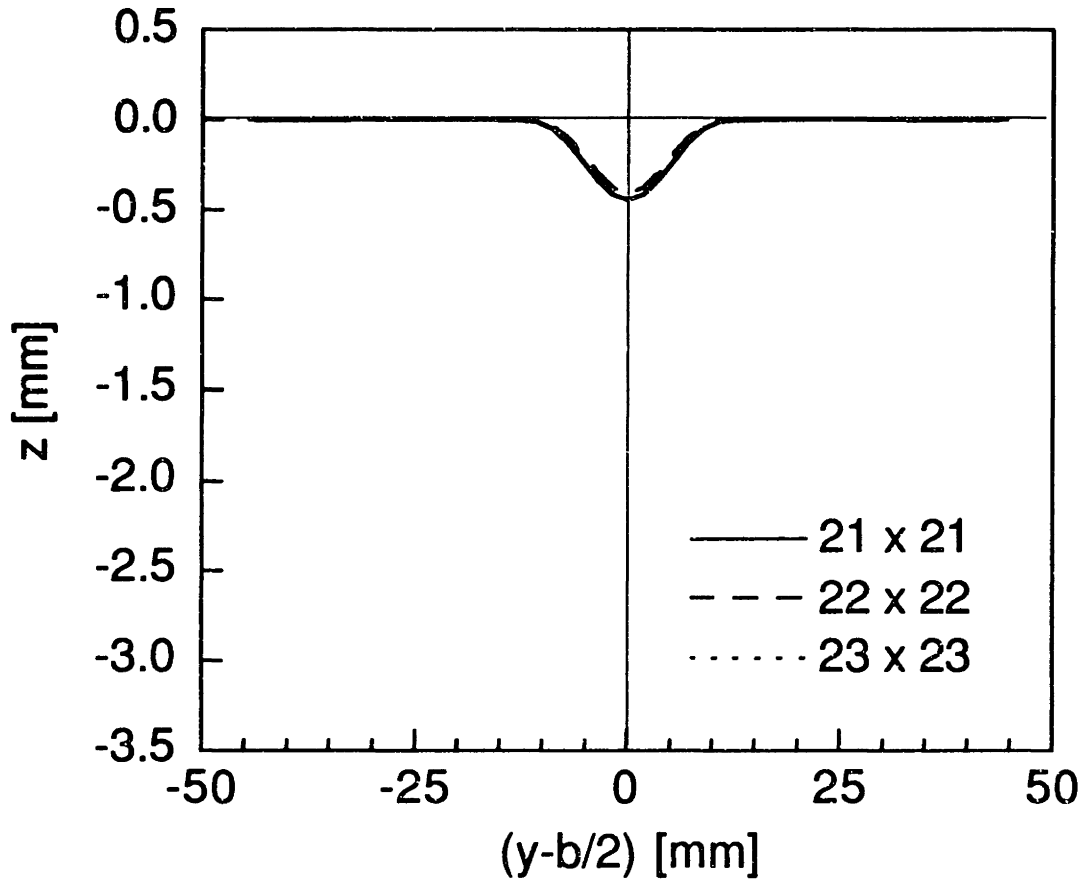


Figure 4.4 Predicted dimple profile, for various numbers of modes, along centerline perpendicular to loading in a (0/90) sandwich panel loaded to -250 MPa for an initial crushed core radius of 5 mm.

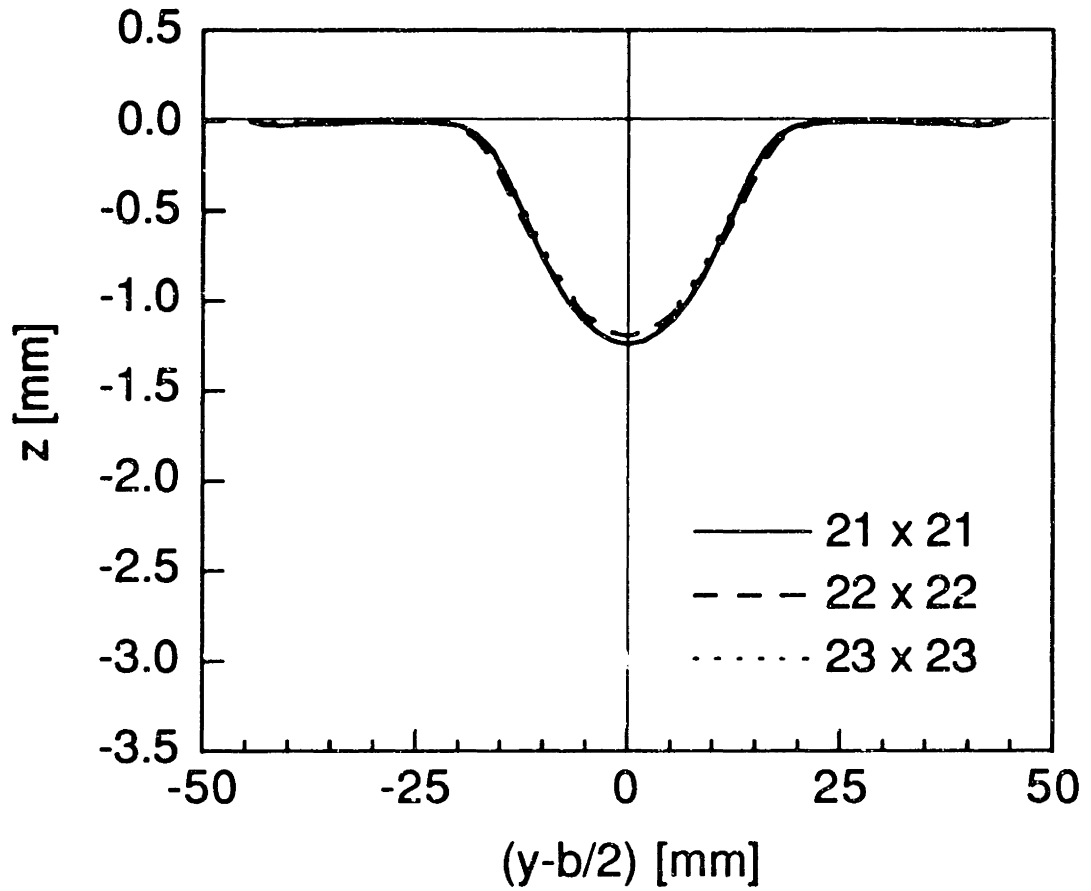


Figure 4.5 Predicted dimple profile, for various numbers of modes, along centerline perpendicular to loading in a (0/90) sandwich panel loaded to -250 MPa for an initial crushed core radius of 10 mm..

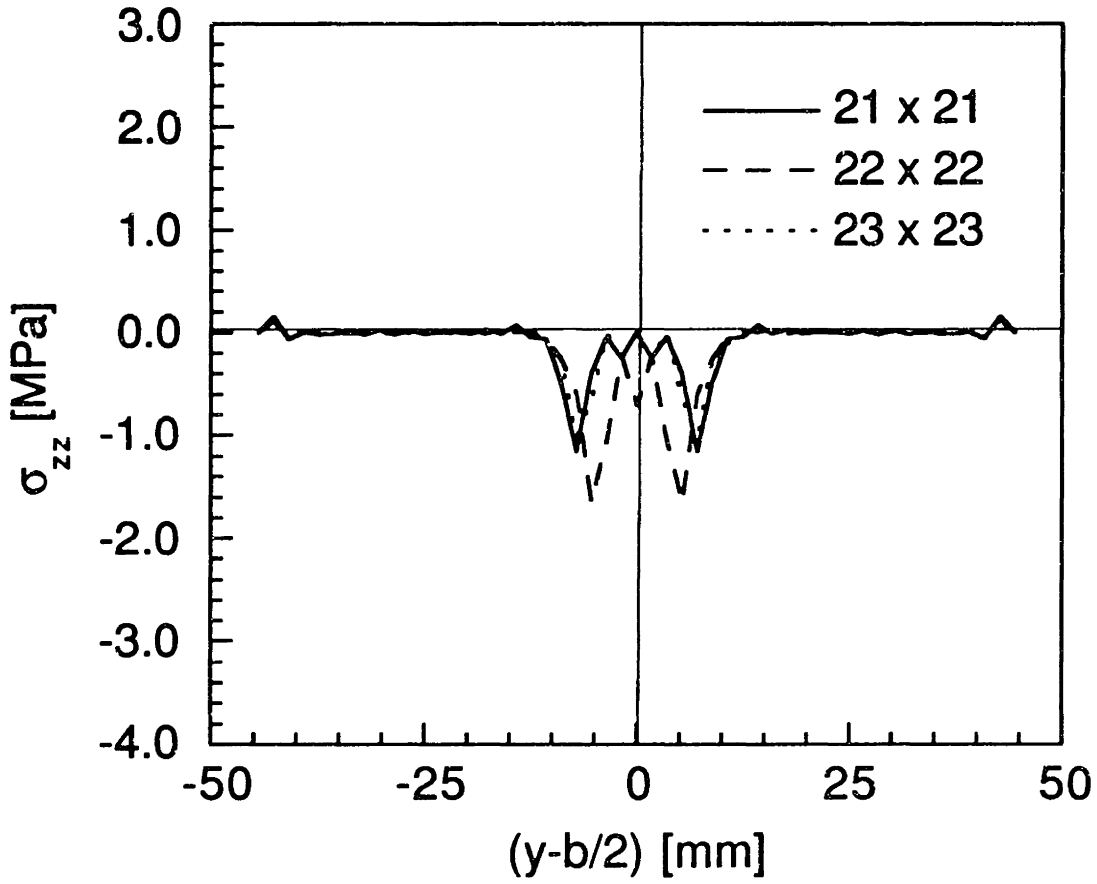


Figure 4.6 Predicted through-thickness stress (σ_{zz}) distribution, for various numbers of modes, at interface between core and facesheet along centerline perpendicular to loading in a (0/90) sandwich panel loaded to -250 MPa for an initial crushed core radius of 5 mm.

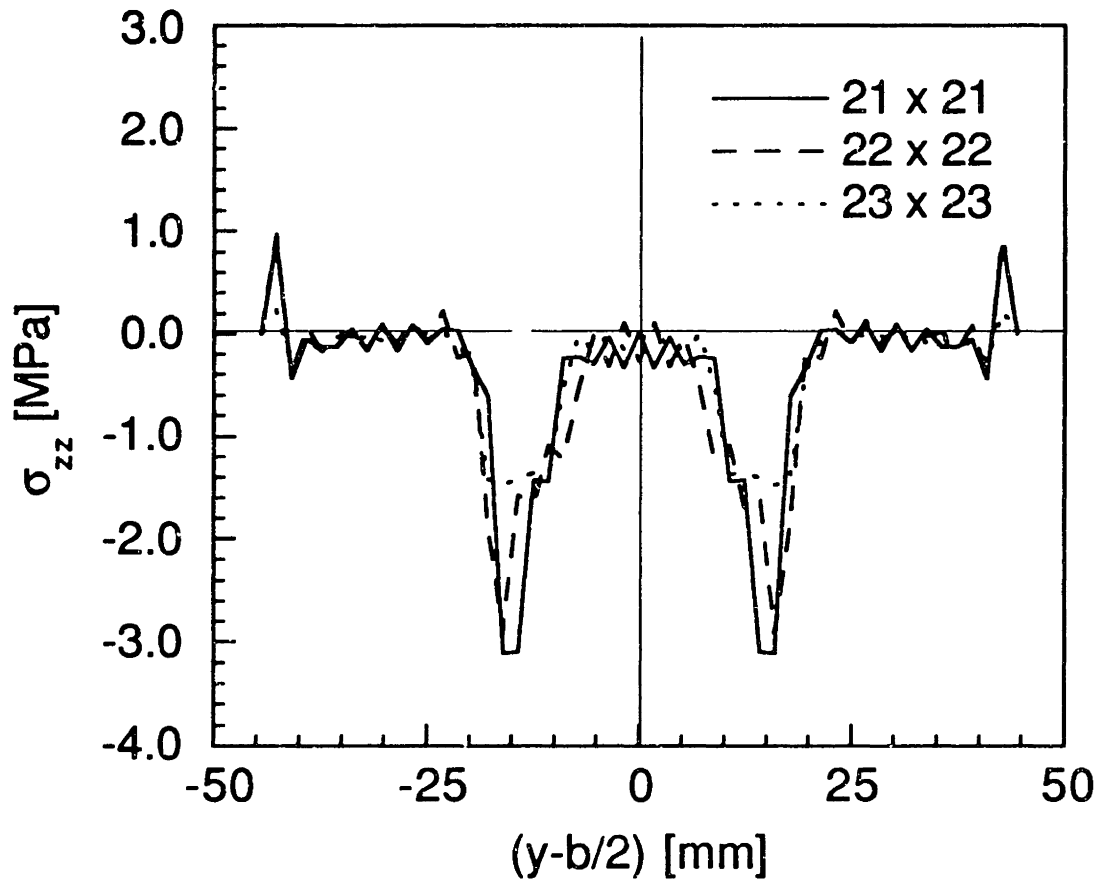


Figure 4.7 Predicted through-thickness stress (σ_{zz}) distribution, for various numbers of modes, at interface between core and facesheet along centerline perpendicular to loading in a (0/90) sandwich panel loaded to -250 MPa for an initial crushed core radius of 10 mm.

The longitudinal stress, σ_{xx} , distributions along the centerline perpendicular to the loading at the top surface of the facesheet are shown in Figures 4.8 and 4.9 for the two values of R_0 . The solution shows the redistribution of stress around the dimple and the recovery of uniform far-field stress. Lastly, the longitudinal stress, σ_{xx} , distributions along the centerline perpendicular to the loading at the bottom surface of the facesheet are shown in Figures 4.10 and 4.11.

This sample problem shows that the dimple propagation model is capable of simulating the propagation of the dimple, as observed in experiments, due to the applied in-plane compressive load. The model is also capable of incorporating core damage due to initial indentation and due to subsequent dimple propagation. The sample problem shows that a 23 by 23 modes analysis is sufficient to produce a converged solution for values of R_0 between 5 mm and 10 mm.

4.2 Mar-Lin Correlation

The Mar-Lin correlation [83] is a semi-empirical model originally proposed to predict the tensile strength of notched composite laminates. It has been used with reasonable success in correlating tensile strength of notched composite laminates with circular holes as well as those with slits. It has also been used to correlate compressive strength of sandwich panels with a circular hole in one of the facesheets [59] and compressive strength of sandwich panels with impact damage [28]. The Mar-Lin correlation can be expressed in the following form:

$$\sigma_f = H_c(2a)^{-m} \tag{4.32}$$

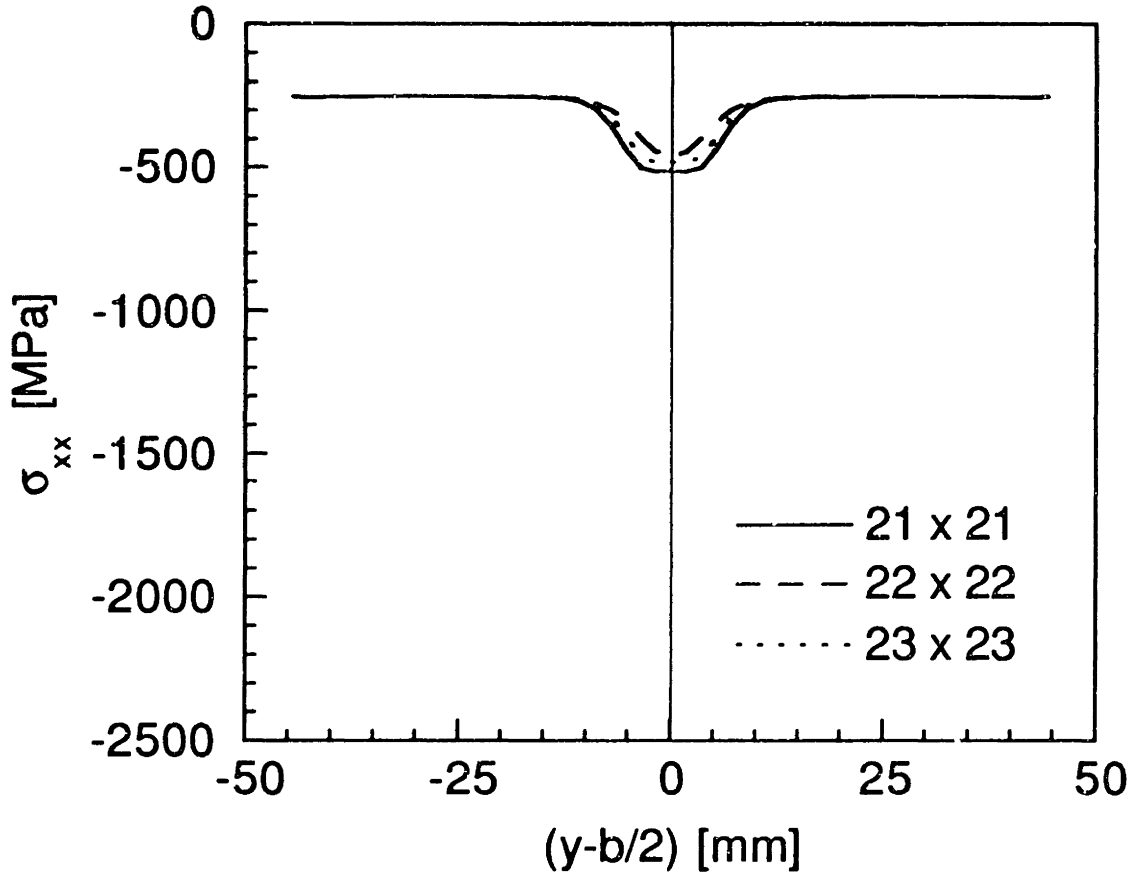


Figure 4.8 Predicted longitudinal stress (σ_{xx}) distribution, for various numbers of modes, at top surface of facesheet along centerline perpendicular to loading in an (0/90) sandwich panel loaded to -250 MPa for an initial crushed core radius of 5 mm.

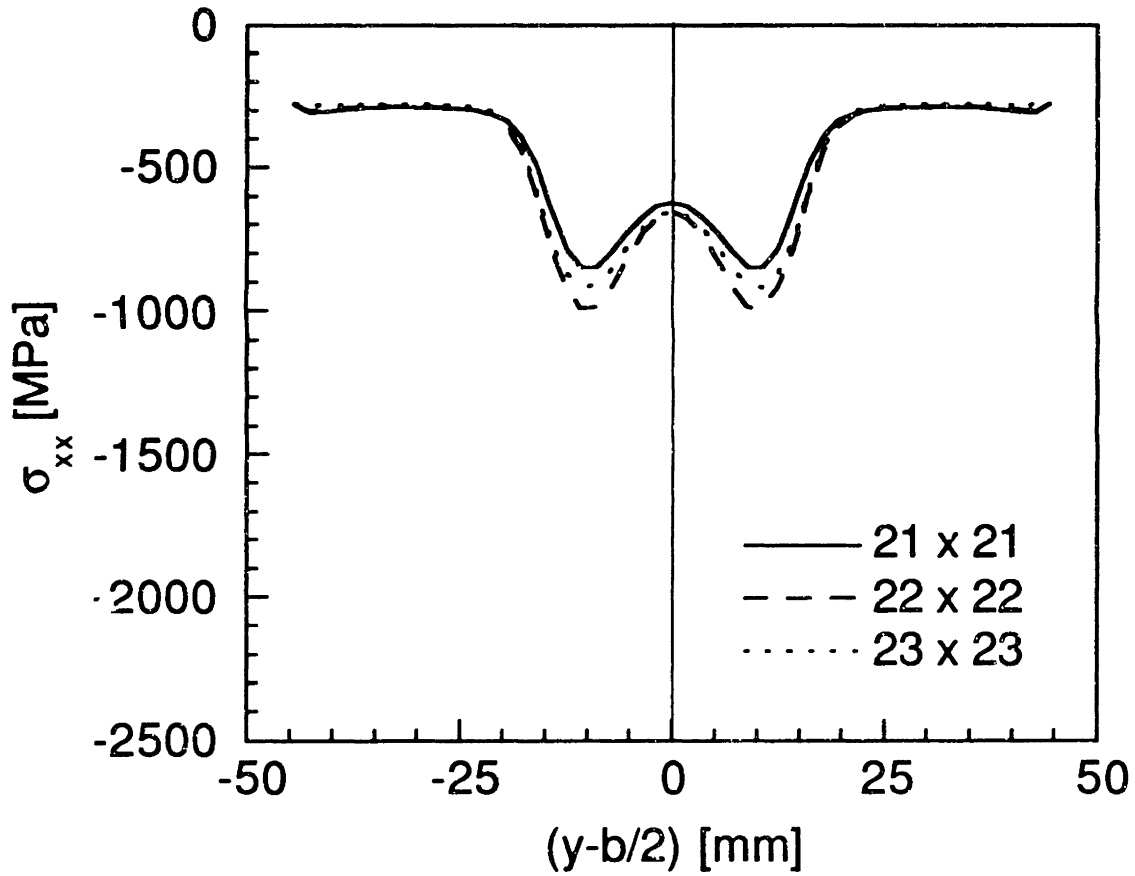


Figure 4.9 Predicted longitudinal stress (σ_{xx}) distribution, for various numbers of modes, at top surface of facesheet along centerline perpendicular to loading in an (0/90) sandwich panel loaded to -250 MPa for an initial crushed core radius of 10 mm.

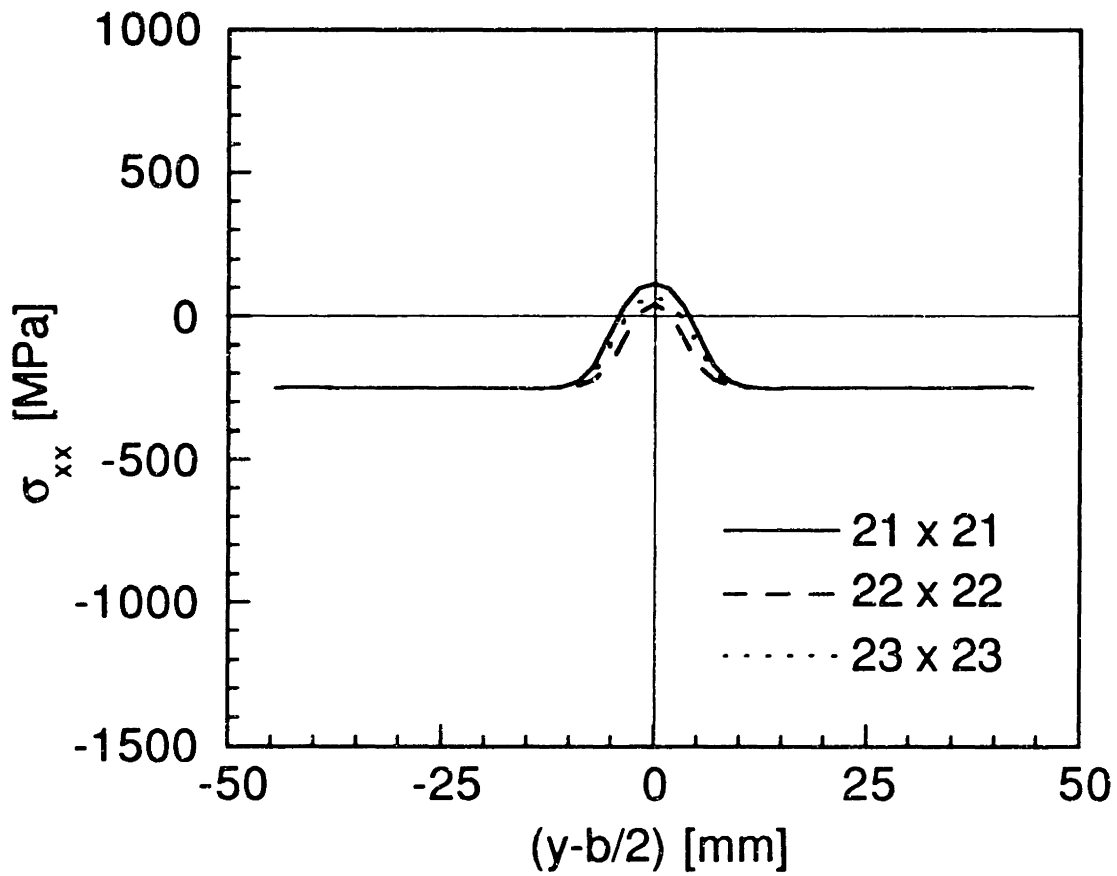


Figure 4.10 Predicted longitudinal stress (σ_{xx}) distribution, for various numbers of modes, at bottom surface of facesheet along centerline perpendicular to loading in an (0/90) sandwich panel loaded to -250 MPa for an initial crushed core radius of 10 mm.

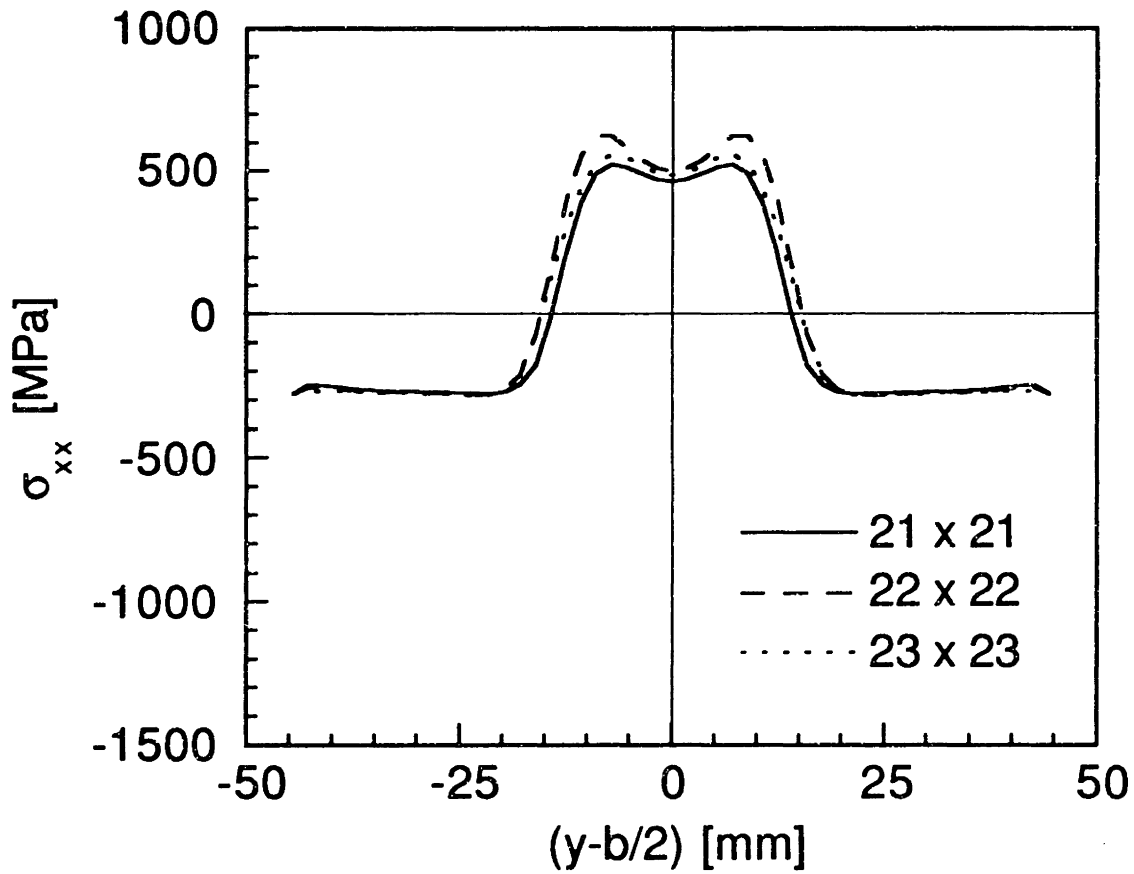


Figure 4.11 Predicted longitudinal stress (σ_{xx}) distribution, for various numbers of modes, at bottom surface of facesheet along centerline perpendicular to loading in an (0/90) sandwich panel loaded to -250 MPa for an initial crushed core radius of 10 mm.

where σ_f is the strength of the notched laminate, H_c is the composite fracture parameter, $2a$ is the length of the discontinuity (e.g. hole diameter, slit length), and m is related to the order of the singularity at the crack tip at a fiber/matrix interface [83]. The model is semi-empirical because the parameters H_c and m have to be calculated *a priori* from experimental data. This is usually accomplished by performing a least-squares fit on the experimental data in the logarithmic form of Equation 4.32:

$$\ln \sigma_f = \ln H_c - m \ln 2a \quad (4.33)$$

However, variation in the experimental data can cause wide swings in the derived value of m . Therefore, Lagace [95] adopted the theoretical value of m [96] for the particular material system and utilized Equation 4.32 as a one-parameter curve fit. In the present investigation, Equation 4.33 is used as a one-parameter fit with the theoretical value of m equal to 0.28 for the particular material system used [95]. The parameter $2a$ for the present investigation is the in-plane dimension of facesheet damage measured perpendicular to the loading direction from X-radiographs.

Chapter 5

Experimental Procedures

As stated in Chapter 3, a combination of experimental investigation and analytical modelling was used to achieve the research goals. The analytical models are described in Chapter 4 while the experimental procedures are presented in this chapter. The contents of this chapter include descriptions of the material system and specimen configuration, the test matrices, the manufacturing procedures of test specimens, the test procedures, the experimental setup, and techniques of damage characterization.

5.1 Specimen Description

The facesheets of all sandwich specimens are made of graphite/epoxy plain weave fabric AW193/PW3501-6 manufactured by Hercules¹. The material was received in preimpregnated form (prepreg) on a 1.22 m (48 inch)-wide roll. The fabric has white tracer fibers running in both the warp and the fill directions. The spacing between the tracer fibers in the warp direction is 229 mm while that between the tracer fibers in the fill direction is 305 mm. The fabric has a resin content of 34.6%, an areal weight of 191 g/m², and is a no-bleed material system. The nominal ply thickness is 0.35 mm. The 25.4 mm (1 inch)-thick Nomex honeycomb core used for all specimens is manufactured by Ciba-Geigy. The density and the cell size of the honeycomb core are 48.1 kg/m³ (3 pcf) and 3.18 mm (1/8 inch),

¹ A list of addresses and phone numbers for material and equipment suppliers is given in Appendix B

respectively. The film adhesive used to bond the facesheets and the core is FM123-2 manufactured by American Cyanamid. The density of the film adhesive is 290 g/m^2 (0.06 lb/ft^2). As explained in Chapter 3, these materials were chosen because previous work in TELAC [28, 33, 59] has established a fairly extensive data base on the impact resistance and damage tolerance of sandwich panels made of the same material system. The present work can therefore build on the results of this previous work.

All specimens tested under uniaxial compression are nominally 356 mm (14 inches) long and 89 mm (3.5 inches) wide. The loading is applied along the longer dimension. Loading tabs, 76 mm in length, are used to reduce stress concentrations at the grip, giving a test section which is 203 mm long. The generic specimen configuration is depicted in Figure 5.1. The core of the sandwich panels is made from three separate pieces as indicated in Figure 5.1. The high density (22.1 kg/m^3) aluminum honeycomb is needed to resist gripping pressure of the hydraulic testing machine. The two layups chosen for the facesheets are (0/90) and (± 45). The specimen configuration and layups chosen for the present investigation are the same as those used in previous work [28, 59].

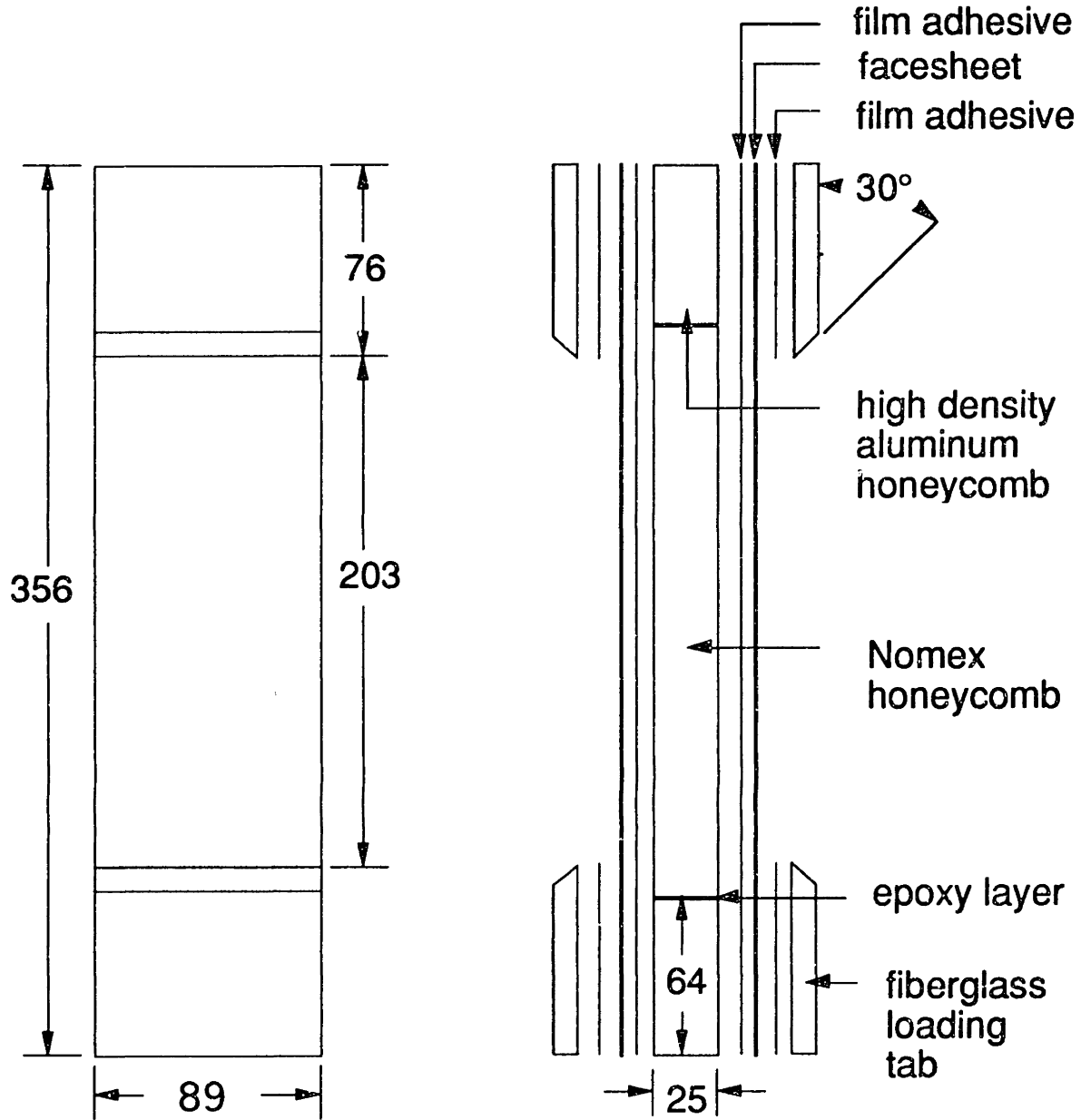
5.2 Test Matrices

Three groups of specimens were manufactured. Indentation damage was introduced in the first group of specimens which was used for damage characterization. The second group was tested to obtain basic material properties of the material system. The third group of specimens contain various damage types and was tested under uniaxial compression for the damage tolerance investigation.

One of the objectives of the present work is to characterize damage in sandwich panels due to impact/indentation loading. The approach, outlined in Chapter 3, is to create three damage states using three different hemispherical indentors, 12.7 mm, 25.4 mm, and 38.1 mm in diameter, driven to an indentation depth of 3 mm. Two sandwich panels, one with (0/90) facesheets and the other (± 45), were inflicted with these three damage states. These damage states were examined through a variety of damage inspection techniques (see Section 5.6) to characterize the different damage types present. A total of nine indentation tests were performed on each panel: three with each of the three indentors. The nine indentation tests were done on nine different locations spread out over the 356 mm by 305 mm area of the panels to avoid possible interaction between adjacent damage sites.

As explained in Chapter 3, the material system for the present work was chosen to continue to expand the database established in TELAC on the impact resistance and damage tolerance of sandwich panels. It is, therefore, important to ensure that the properties of the specimens used in the present work are comparable to those obtained previously. A group of sandwich specimens of the generic configuration shown in Figure 5.1 were tested under uniaxial compression to obtain material properties for the material system. These specimens and the properties sought are listed in Table 5.1.

The specimens tested in the damage tolerance part of the investigation are listed in Table 5.2. The undamaged specimens were tested as a control. The specimens with static indentation damage had the damage states characterized in the impact resistance part of the investigation. These damage states are referred to as SID1 (12.7 mm indenter), SID2 (25.4 mm indenter), and SID3 (38.1 mm indenter). After



all dimensions in mm

Figure 5.1 Illustration of specimen configuration.

Table 5.1 Test matrix for material property evaluation

Facesheet	Number of specimens	Properties measured
(0 ₂)	3	E _L , ν _{LT}
(90 ₂)	3	E _F , ν _{TL}
(±45)	3	G _{LT}

Table 5.2 Test matrix^a for damage tolerance investigation

Damage Type	Damage Level ^b			
	0	1	2	3
None	3	—	—	—
Static Indentation	—	3 ^c	3	3
Simulated Core	—	3	3	3
Simulated Facesheet	—	3	—	—

^a Matrix repeated for (0/90) and (± 45) facesheets

^b Damage key: level 0 - undamaged; level 1 - caused by 12.7-mm diameter indenter; level 2 - 25.4-mm diameter indenter; level 3 - 38.1-mm diameter indenter.

^c Number of specimens tested.

the damage characterization process and examination of the results (see Chapter 6), three more damage states were created to simulate the core damage observed in the indented panels. They are the simulated core damage (SCD) specimens and are labelled as SCD1 (simulating SID1), SCD2 (simulating SID2), and SCD3 (simulating SID3). A third set of specimens was created to simulate the facesheet damage observed in SID1. They are the specimens with simulated facesheet damage and are referred to as SFD1. Only one type of specimens with simulated facesheet damage was created because X-radiographs of the indented panels show no well-defined damage pattern in the facesheets indented by the 25.4 mm-diameter indenter and the 38.1 mm-diameter indenter. Thus, only the 12.7 mm-diameter indenter created facesheet damage that could be physically modelled

5.3 Manufacturing Procedures

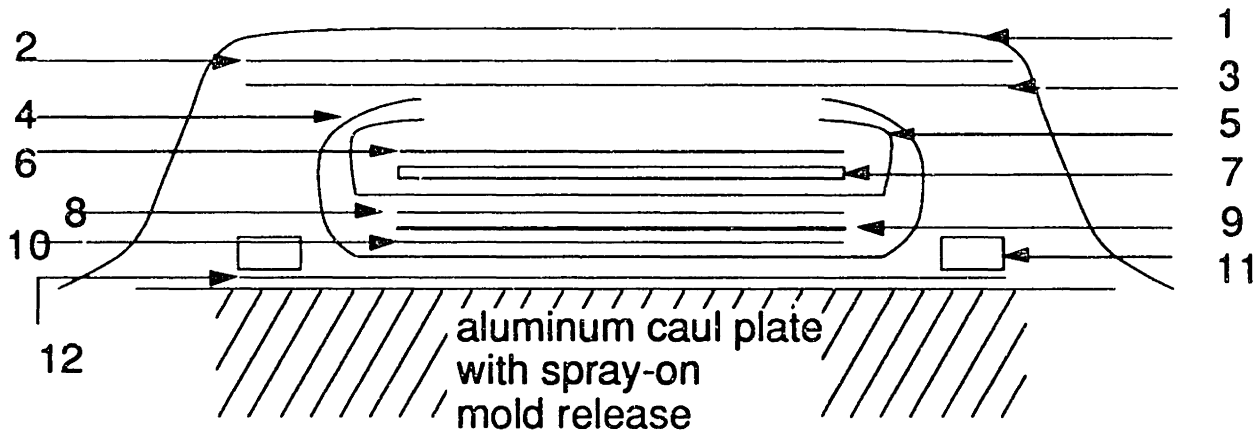
The general procedures presented in this section are those used to manufacture undamaged specimens. The manufacturing procedures of specimens with different damage types involve variations of, or additional steps to, the general procedures. These variations and additional steps are described in subsequent sections. The reader is reminded that the specimens with simulated core damage and the specimens with simulated facesheet damage were designed based on the damage characterization results of the indented specimens. Hence, the manufacturing procedures for the specimens with simulated core damage and for the specimens with simulated facesheet damage were decided after the results of the damage characterization of indented specimens (see Chapter 6) were examined.

5.3.1 General procedures

The manufacturing process of undamaged sandwich panels can be divided into five stages: layup, laminate cure, secondary bond cure, loading tab bond cure, and milling. In the remaining part of this section, these five stages are described in the order they were performed. The reader is reminded that this section is not a step-by-step instruction manual for manufacturing composite sandwich panels. The information contained herein should be complemented with additional details of the manufacturing procedures found in Ref. [97].

The prepreg was taken out of the freezer and allowed to warm up for 45 minutes to an hour. This prevents moisture in the air from condensing onto the prepreg. The prepreg is then taken out of the storage bag and laid out on a table. Individual plies are cut out from the fabric using Stanley utility knives. An aluminum template, 356 mm by 305 mm (14 inch by 12 inch), covered with teflon was used to facilitate accurate cutting. Plies with different orientations are put together to form the desired laminates. A 381 mm by 330 mm sheet of clear fluorocarbon release film was placed on the two surfaces of the laminate. The FEP A5000 release film is a product of DuPont and has a nominal thickness of 0.0254 mm. It is generally used for no-bleed material systems to minimize the loss of resin during the cure. After the release film is put on the laminates, it is trimmed along three sides of the facesheet while one of the shorter sides is left untrimmed for ease of handling. This concludes the process of layup.

The laminates, each sandwiched between two pieces of release film, are placed on an aluminum caul plate together with other curing materials as shown in Figure 5.2. A vacuum of 737 mm to 762 mm (29 inch to 30 inch) of mercury was maintained inside the vacuum bag throughout the cure.



- 1 = vacuum bag
- 2 = 3-4 layers of fiberglass cloth
- 3 = porous teflon
- 4 = guaranteed nonporous teflon (GNPT)
- 5 = GNPT
- 6 = GNPT
- 7 = aluminum top plate
- 8 = fluorocarbon release film
- 9 = graphite/epoxy prepreg
- 10 = fluorocarbon release film
- 11 = cork dam
- 12 = GNPT

Figure 5.2 Illustration of cure assembly for laminate (facesheet) cure of specimens with no damage, static indentation damage, and simulated facesheet damage.

The same cure cycle used for this system by previous researchers in TELAC [28, 58, 59] was used in the present work. The nominal temperature and pressure histories of the laminate cure are given in Figure 5.3. The cured laminates are then postcured for 8 hours at 350°F at ambient pressure. Details of the preparation of the caul plate and the operation of the autoclave can be found in Ref. [97].

The postcured laminates are trimmed along all four edges to remove epoxy "ridges". The trimming was done on a milling machine equipped with a diamond-grit cutting wheel and water cooling. Because the facesheets are thin, they are trimmed in pairs with a table feed of 279 mm /min (11 inch/min). The thickness of the trimmed laminates was measured at 27 locations with a micrometer as depicted in Figure 5.4. The average thickness of all laminates is 0.348 mm with a coefficient of variation of 3.6%. This value is consistent with the nominal value of 0.350 mm. The laminates are wiped with cheesecloth soaked with methanol to provide a grease-free surface for bonding. The laminates are now ready to be bonded to the honeycomb core.

A 356 mm by 305 mm by 25.4 mm thick honeycomb core was assembled from two pieces of high density (22.1 kg/m³) aluminum honeycomb and one piece of Nomex honeycomb. The high density aluminum honeycomb was cut into strips of 63.5 mm by 305 mm, with the ribbon direction along the 63.5 mm dimension, using a bandsaw. The 25.4 mm-thick Nomex honeycomb was cut into rectangular pieces measuring 305 mm by 229 mm with the ribbon direction along the 229 mm dimension using a bandsaw equipped with a wavy-edged blade. The two pieces of aluminum core and the piece of Nomex core were bonded together using Epoxi-Patch[®] produced by Dexter Corporation to form a core with nominal in-plane

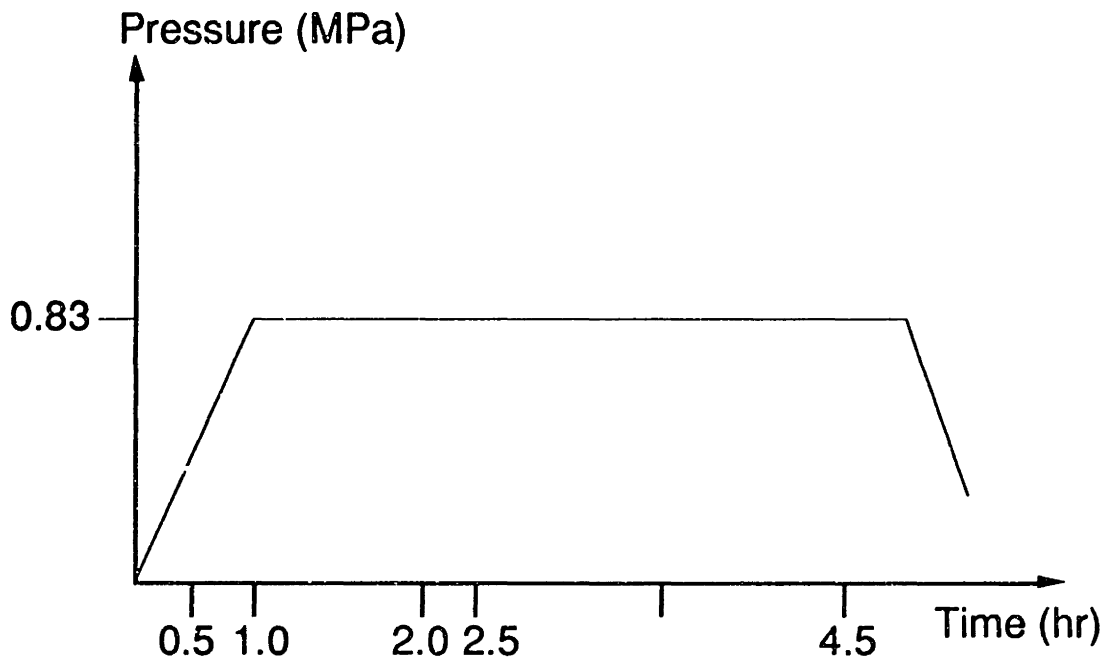
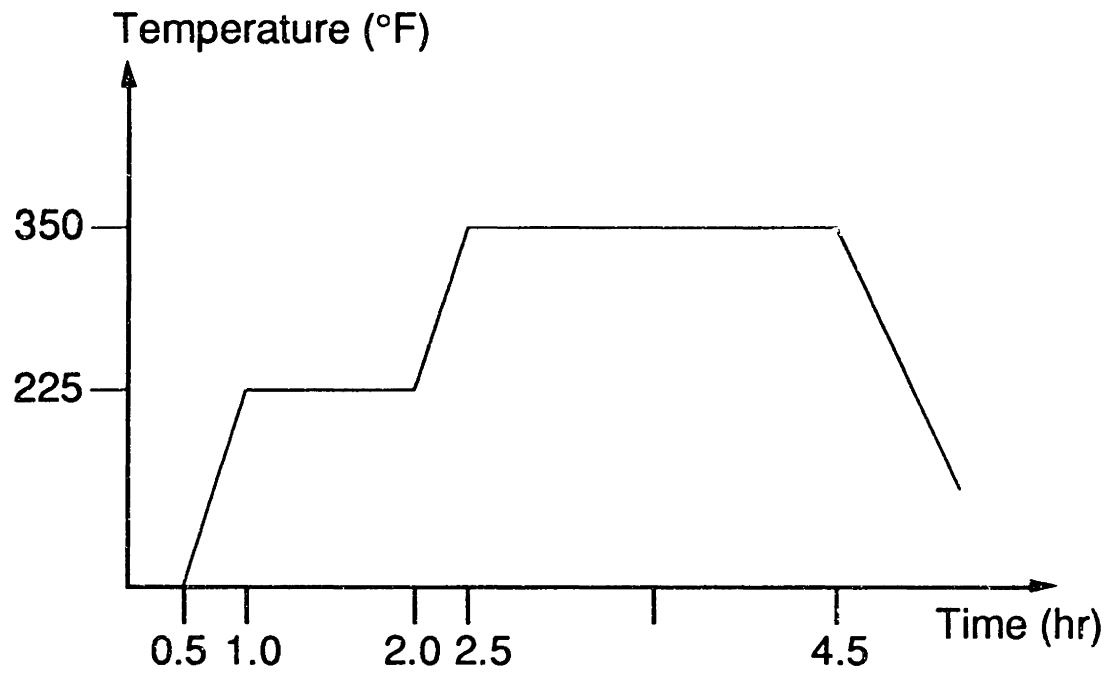
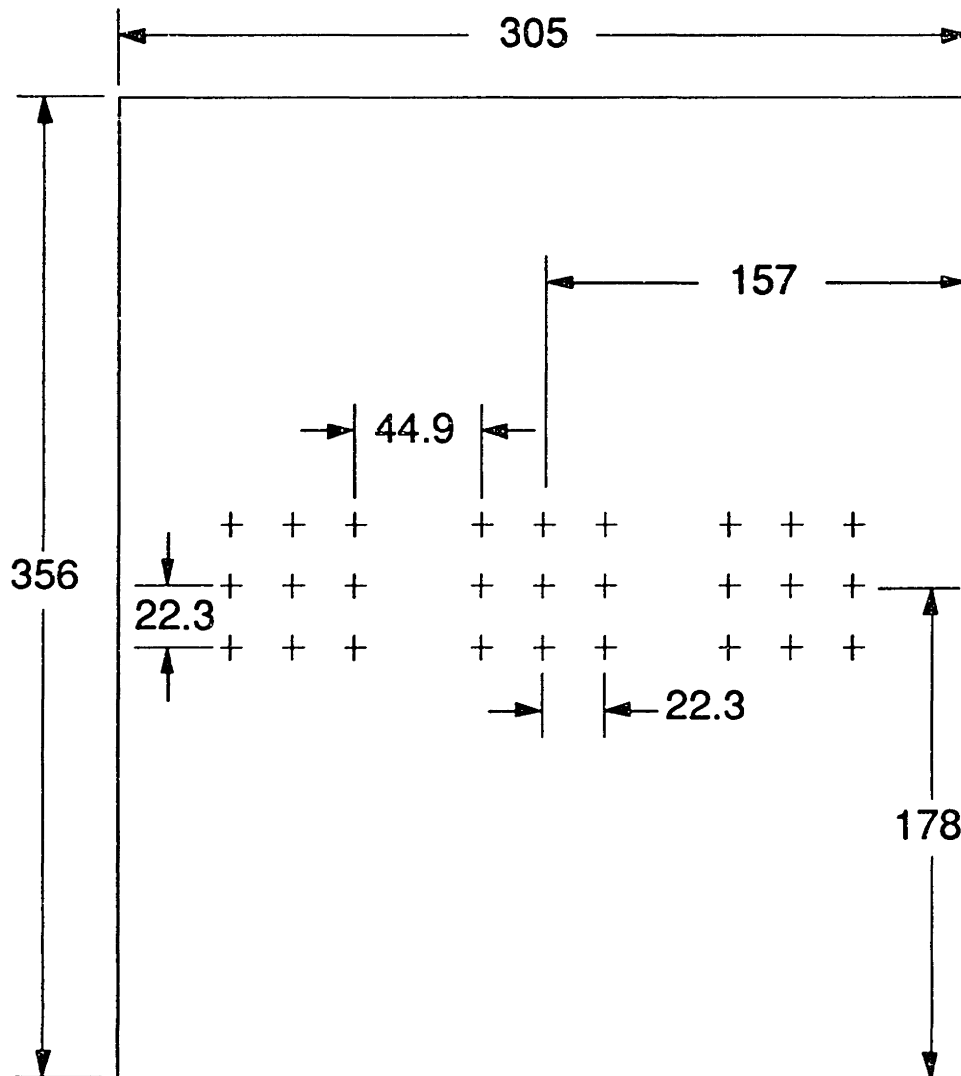


Figure 5.3 Nominal temperature and pressure histories for laminate cure.



+ location for thickness measurements

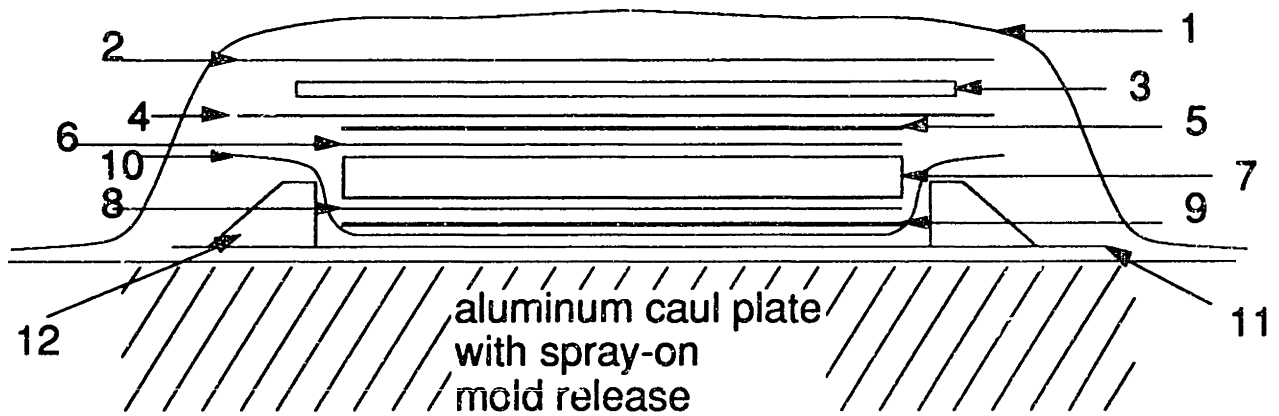
all dimensions in mm

Figure 5.4 Locations for thickness measurements of undamaged facesheets.

dimensions of 305 mm by 356 mm. The three pieces of core were placed in a core assembly jig which applies slight pressure to keep the separate pieces together when the epoxy is curing. The cure takes about four hours at room temperature.

The core was bonded to the facesheets with film adhesive in a secondary bond cure. The film adhesive used for the bond cure was taken out of the freezer and allowed to warm up for 45 minutes to an hour. This prevents moisture in the air from condensing onto the film adhesive. The film adhesive was then taken out of the storage bag and laid out on a table. The facesheets, having been degreased with methanol, are put onto the film adhesive and used as templates for cutting. The facesheets with the film adhesive on one side are then put on the two surfaces of the core. A great deal of care was exercised to align the facesheets relative to each other. The sandwich panels were then placed on an aluminum caul plate for the bond cure. Specially machined aluminum dams are placed around the sandwich panels as shown in Figure 5.5 to prevent the autoclave pressure from crushing the Nomex honeycomb along the edges. The dams also provide a gentle slope for the vacuum bag to conform to in going from the surface of the panels to the caul plate. The arrangement of the sandwich panels and the cure materials is shown in Figure 5.6. The nominal temperature and pressure histories for the bond cure are given in Figure 5.7. The vacuum bag is vented to atmospheric pressure for all bond cures. The cured panels are then ready to have fiberglass loading tabs put on them.

The loading tabs used are Scotchply™ 1002 manufactured by 3M and are made of fiberglass in a cross-ply layup. All loading tabs used for the present work are 7-ply thick (1.78 mm). The fiberglass was received in sheets of 381 mm by 305 mm. The sheets are cut into 308 mm by 76 mm



- 1 = vacuum bag
- 2 = 3-4 layers of fiberglass cloth
- 3 = steel top plate
- 4 = guaranteed nonporous teflon (GNPT)
- 5 = facesheet
- 6 = film adhesive
- 7 = honeycomb
- 8 = film adhesive
- 9 = facesheet
- 10 = GNPT
- 11 = GNPT
- 12 = aluminum dam

Figure 5.6 Illustration of cure assembly for secondary bond cure.

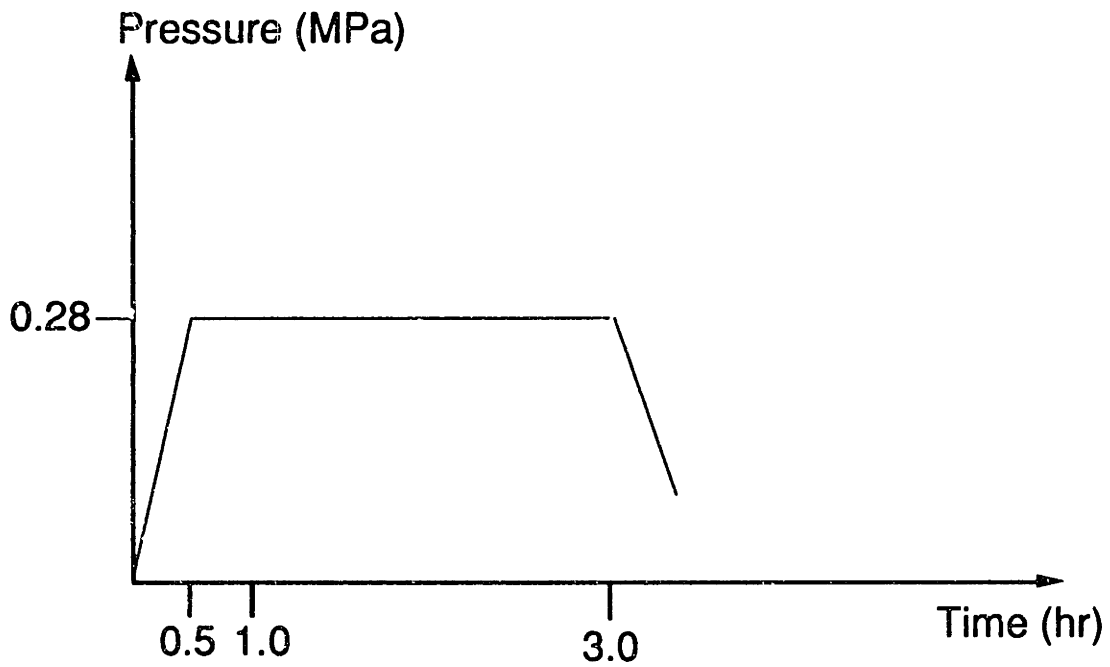
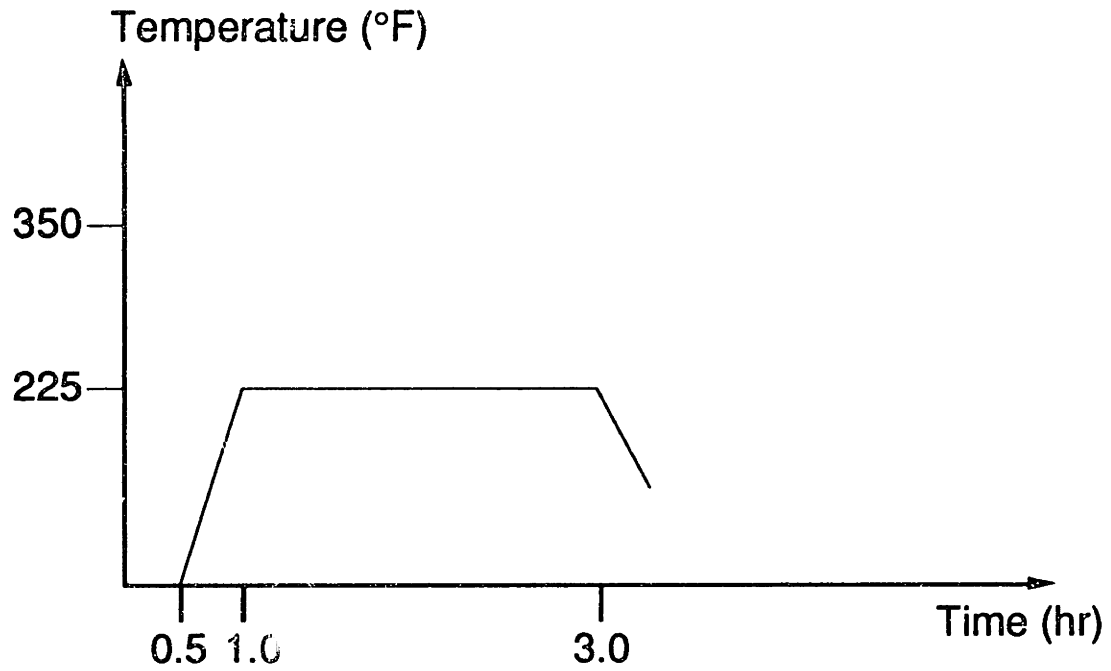


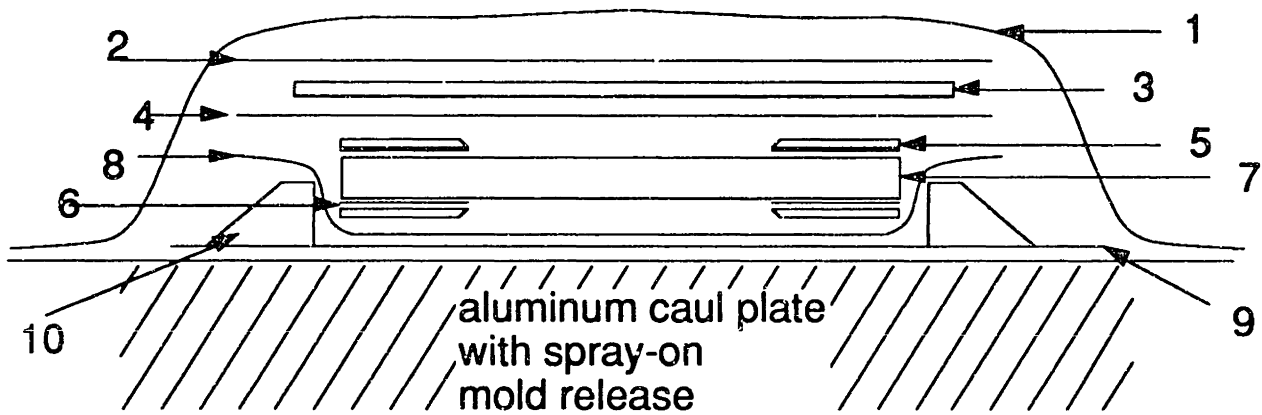
Figure 5.7 Nominal temperature and pressure histories for secondary bond cure and loading tab cure.

strips using a bandsaw equipped with a carbide cutting blade. One of the 308 mm sides was sanded to a 30° angle with a belt sander. The loading tabs were used as templates to cut the film adhesive. The loading tab strips, with film adhesive on one side, are placed on the sandwich panels 203 mm apart and the whole assembly is put on the caul plate surrounded by the same aluminum dams used for the bond cure. The layout of the loading tab cure is depicted in Figure 5.8. The temperature and pressure histories used for the tab cure are the same as those for the bond cure (see Figure 5.7). This cure cycle was copied from previous work on the same material system [28, 59]. It was later realized that the nominal pressure for the loading tab bond cure should have been scaled to account for the reduced contact area between the tabs and the steel plates. Since no abnormality was observed with specimens in the previous work, the cure cycle shown in Figure 5.7 was not changed. The vacuum bag is vented to atmospheric pressure for all loading tab bond cures.

The resulting 356 mm by 305 mm (14 inch by 12 inch) panels with loading tabs are cut into three 89 mm by 356 mm specimens using the same milling machine and diamond grit cutting wheel for trimming the facesheets. A table feed of 127 mm/min (5 inch/min) was used.

5.3.2 Specimens with Static Indentation Damage (SID)

The manufacturing procedures for specimens with static indentation damage are the same as those for undamaged panels (see Section 5.3.1). The indentation damage was subsequently introduced in the undamaged specimens via static indentation tests, the procedures of which are described in Section 5.5.1.



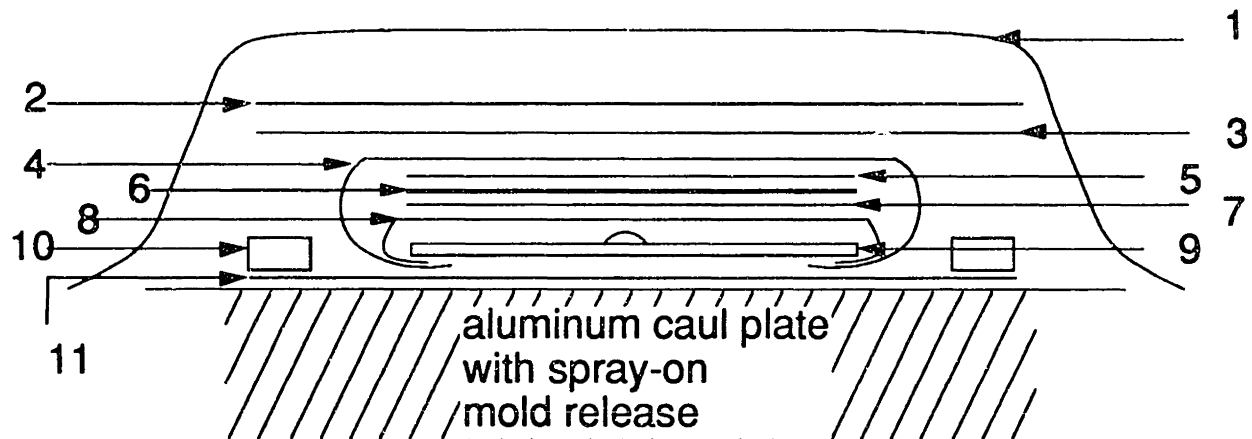
- 1 = vacuum bag
- 2 = 3-4 layers of fiberglass cloth
- 3 = steel top plate
- 4 = guaranteed nonporous teflon (GNPT)
- 5 = loading tab
- 6 = film adhesive
- 7 = sandwich panel
- 8 = GNPT
- 9 = GNPT
- 10 = aluminum dam

Figure 5.8 Illustration of assembly for loading tab cure.

5.3.3 Specimens with Simulated Core Damage (SCD)

The manufacturing procedures for the specimens with simulated core damage start with the preparation of a precrushed honeycomb core. Two pieces of high density aluminum honeycomb and a piece of Nomex honeycomb are bonded together the same way as for undamaged specimens, as described in Section 5.3.1, to form a core with nominal in-plane dimensions of 356 mm by 305 mm. The bare core is crushed locally at three locations before it is bonded to a dimpled facesheet with the indentations located such that they end up at the center of the three specimens which are eventually cut from the panel. A piece of double-sided tape, approximately 50 mm by 50 mm, was placed on the surface of the core at the locations where it was to be indented. The core was indented to a depth of 3 mm with the appropriate indenter following the procedures described in Section 5.5.1. The double-sided tape served two purposes. First, it provided membrane effect to spread out the crushed region. Second, it pulled up the crushed core during unloading. This allowed a better contour fit in the later bonding between the crushed core and the facesheet. The double-sided tape was removed from the honeycomb after the indentation tests.

The layup of the facesheets for the specimens with simulated core damage was done in exactly the same way as that for undamaged specimens and specimens with static indentation damage. However, for the laminate cure, the prepreg was placed on top of a specially designed cure plate, as described later. The purpose of the cure plate is to allow the facesheet to cure into a shape resembling that of the indented specimens, i.e. with a cured "dent". The assembly of the laminate cure is shown in Figure 5.9. The vacuum bag was carefully smoothed as the vacuum was pulled. This

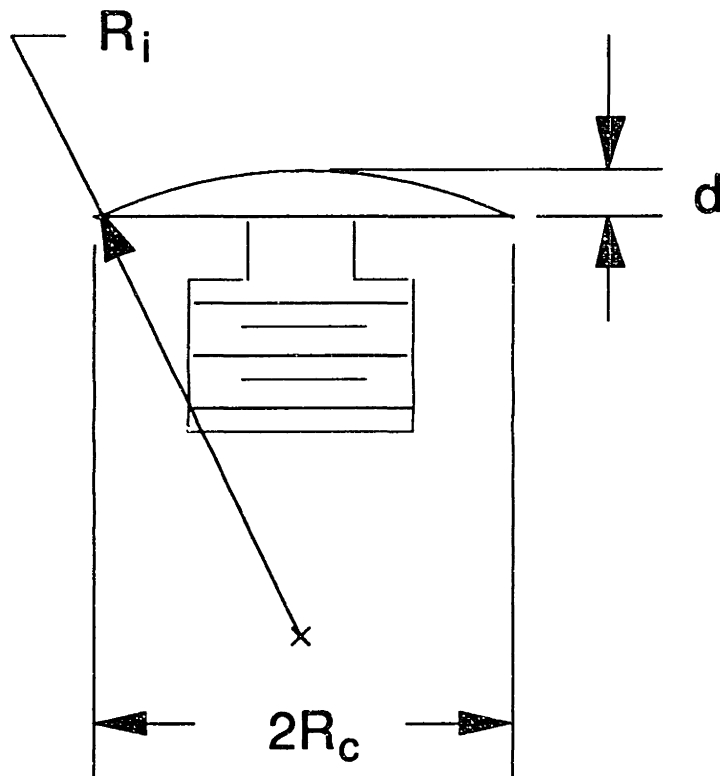


- 1 = vacuum bag
- 2 = 3-4 layers of fiberglass cloth
- 3 = porous teflon
- 4 = guaranteed nonporous teflon (GNPT)
- 5 = fluorocarbon release film
- 6 = graphite/epoxy prepreg
- 7 = fluorocarbon release film
- 8 = GNPT
- 9 = special cure plate
- 10 = cork dam
- 11 = GNPT

Figure 5.9 Illustration of cure assembly for facesheets used in specimens with simulated core damage.

was very important because the laminates did not have an aluminum top plate in order to ensure a wrinkle-free surface. A female top plate was not used because it is desirable to allow the facesheet to bridge over the boundary of the tups so that a smooth and gentle slope can be formed, similar to the profiles of the indented specimens. The same cure cycle for undamaged laminates (See Figure 5.3) was used for these "dimpled" laminates. Only one of the facesheets of for each specimen was cured this way. The other one was cured exactly like those for undamaged panels because only one facesheet of the specimens with static indentation damage was damaged. All facesheets were postcured for 8 hours at ambient pressure without the cure plates.

As indicated, two types of cure plates were used. The first type of cure plate is made of 6061-T6 aluminum and was used to simulate core damage induced by the 12.7 mm-diameter indenter and that by the 25.4 mm-diameter indenter. The cure plate is 356 mm long, 305 mm wide, and 9.6 mm (3/8 inch) thick. The cure plate has three detachable aluminum tups in it. The detachable tups and the aluminum cure plate are illustrated in Figures 5.10 and 5.11 respectively. The aluminum tups are screwed into the three tapped holes in the cure plate. The tups are of two sizes: one for simulating core damage induced by the 12.7 mm-diameter indenter and the other for simulating core damage induced by the 25.4 mm-diameter indenter. The SCD1 specimens simulate the core damage induced with the 12.7 mm-diameter indenter; SCD2 specimens simulates the core damage induced with the 25.4 mm-diameter indenter. The nose radii (R_i in Figure 5.10) are 6.35 mm and 12.7 mm for SCD1 and SCD2, respectively. The thicknesses (h in Figure 5.10) are 1 mm and 0.75 mm for SCD1 and SCD2 respectively. The base radii (R_c in Figure 5.10) are 3.42 mm and 4.30 mm

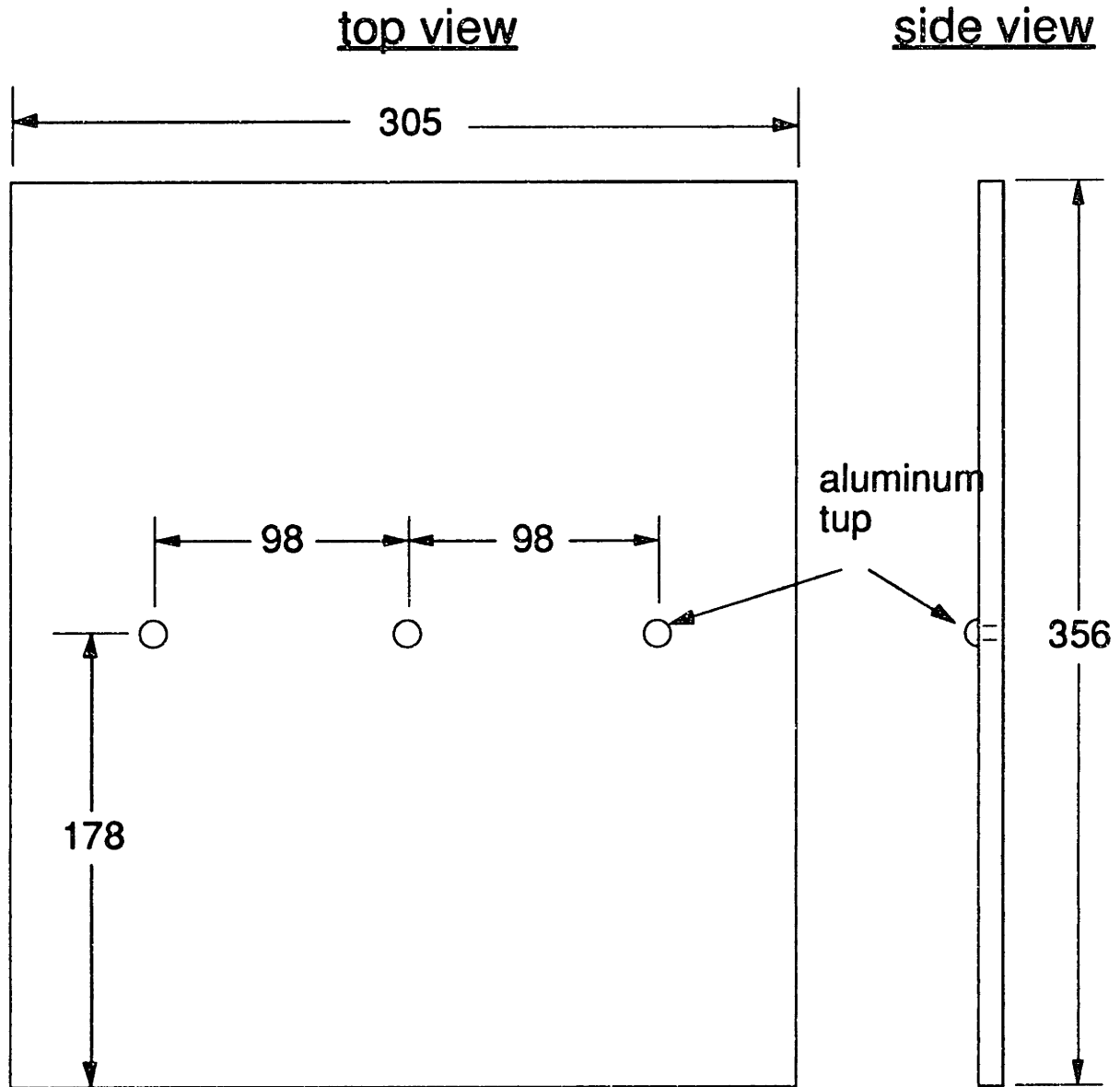


R_i = nose radius

d = thickness

R_c = base radius

Figure 5.10 Illustration of detachable tups for manufacturing SCD1 and SCD2 specimens.



all dimensions in mm

Figure 5.11 Illustration of special aluminum cure plate for manufacturing SCD1 and SCD2 specimens.

for SCD1 and SCD2 respectively. The tups were machined using a special radii-cutter manufactured by RALMIKE. It was not possible to machine the tup for the SCD3 specimens, which simulate core damage induced with the 38.1 mm-diameter indenter, because the tup required was too thin (0.2 mm). Therefore, a different method was used to manufacture the cure plates for the SCD3 specimens.

The second type of cure plate is made from a casting compound, DAPOCAST 38-3, produced by D-Aircraft. These cure plates were used to simulate core damage induced with the 38.1 mm-diameter indenter and were manufactured as follows. Two sandwich panels, one with (0/90) facesheets and the other with (± 45) facesheets, were indented at three locations with the 38.1 mm-diameter indenter, following test procedures described in Section 5.5.1. A dam was built around the edges of the panel with aluminum bars of cross-section 19.1 mm by 12.7 mm as shown in Figure 5.12. The aluminum bars were secured on the panel with double-sided tape. Mold release Mold Wiz[®] F57 produced by Axel was sprayed on the indented surface of the sandwich panel and the dam. The casting compound was poured into the mold formed by the panel and the dam. The casting compound was left at room temperature for 24 hours on a horizontal surface. This was followed by 2 hours at 150°F inside an oven. The casting compound, which had solidified at this point, was taken off the panel and replaced in the oven for another 4 hours at 350°F. The cured compound was then postcured for 4 hours at 400°F. The casting compound has the male shape of the female mold formed by the indented sandwich panel. This casting compound was used as a special cure plate for the SCD3 specimens.

The postcured dimpled facesheets were trimmed in the same way as for undamaged laminates. Care was exercised not to crush the dimples

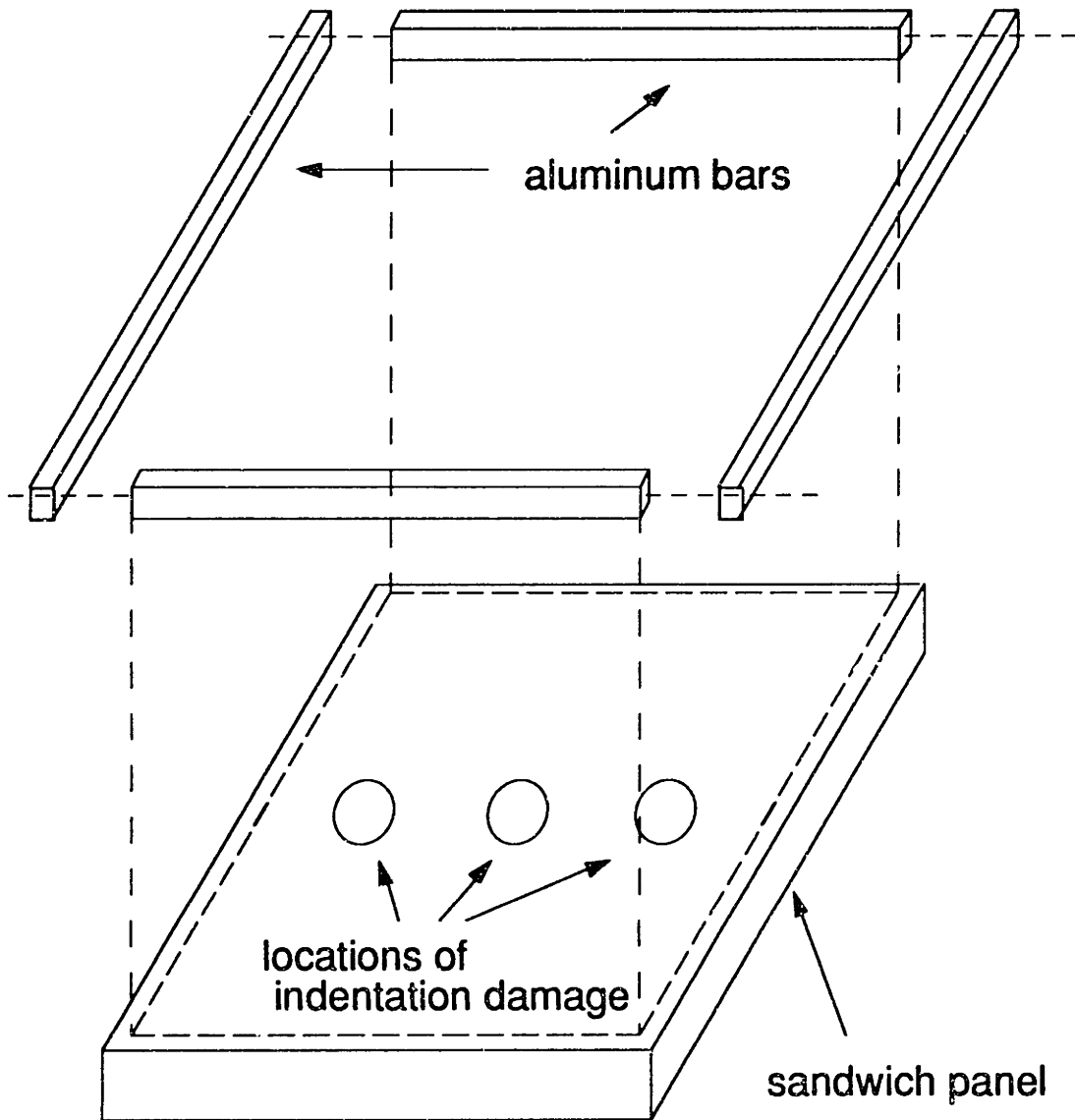
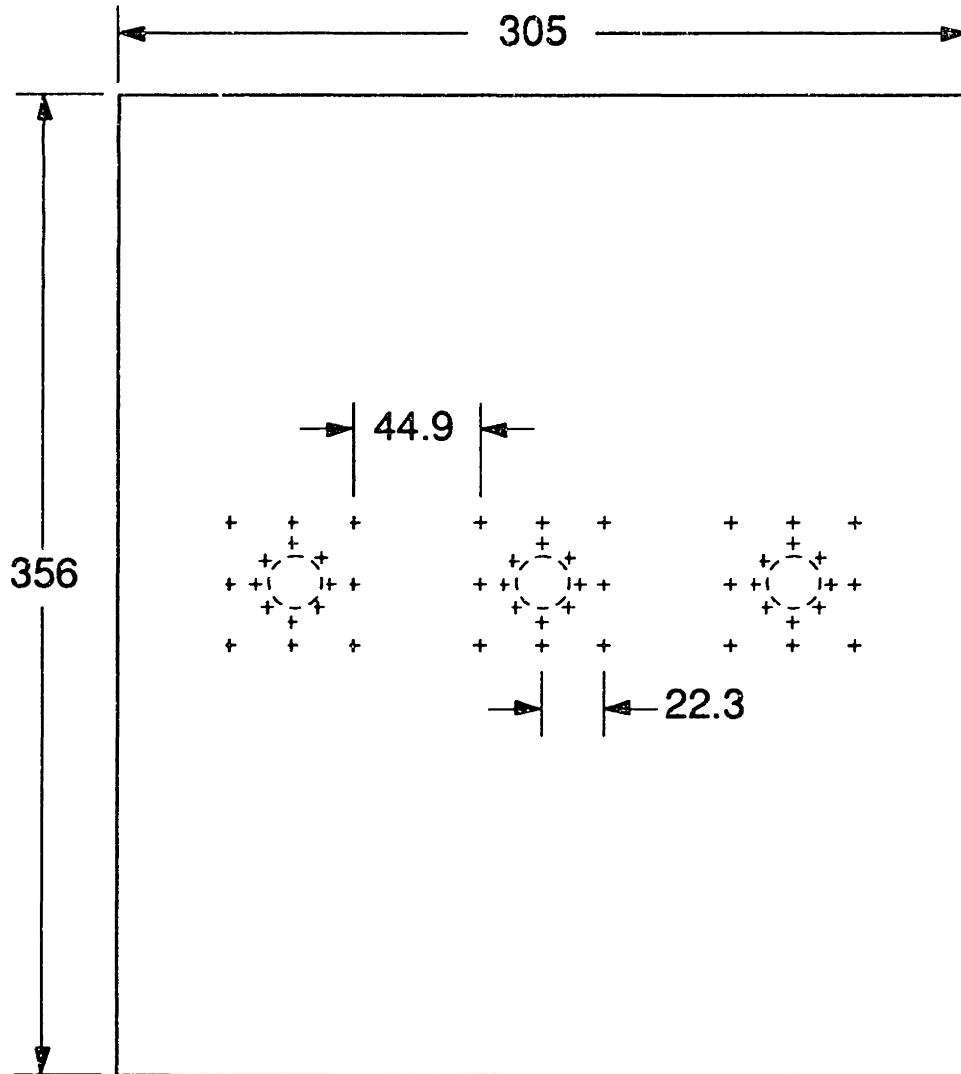


Figure 5.12 Illustration of mold for manufacturing special cure plates used in manufacture of SCD3 specimens.

when clamping the laminates on the milling machine table. Thickness measurements were made on the dimpled facesheets at locations shown in Figure 5.13. Measurements at the eight locations around the dimple were used to check any abnormality in the thickness of the facesheets due to the shape of the dimple. The average value of the thickness measurements around the circumference of the dimple is 0.353 mm with a coefficient of variation of 3.5%. This is consistent with the nominal value of 0.350 mm and basically the same thickness as for the flat facesheets.

The secondary bond cure of specimens with simulated core damage is different from that for the undamaged and static indentation specimens. The film adhesive was put on the dimpled facesheet and allowed to conform around the dimple with the help of a heat gun. The facesheet was then placed on the precrushed surface of the honeycomb core. A great deal of care was exercised to align the dimples in the facesheets with the crushed regions of the core. A masking tape was put on the facesheet through the center of each of the three dimples. The locations of the regions of crushed core were marked on the sides of the core. The facesheet was adjusted until the masking tapes were aligned with the marks at the sides of the core. For the secondary bond cure, the special cure plate used to cure the dimpled laminates were placed on top of the sandwich panels as shown in Figure 5.14. The same temperature and pressure histories (see Figure 5.7) for the secondary bond of undamaged panels were used.

The subsequent loading tab bond cure and the milling of the specimens with simulated core damage are the same as for the undamaged panels.

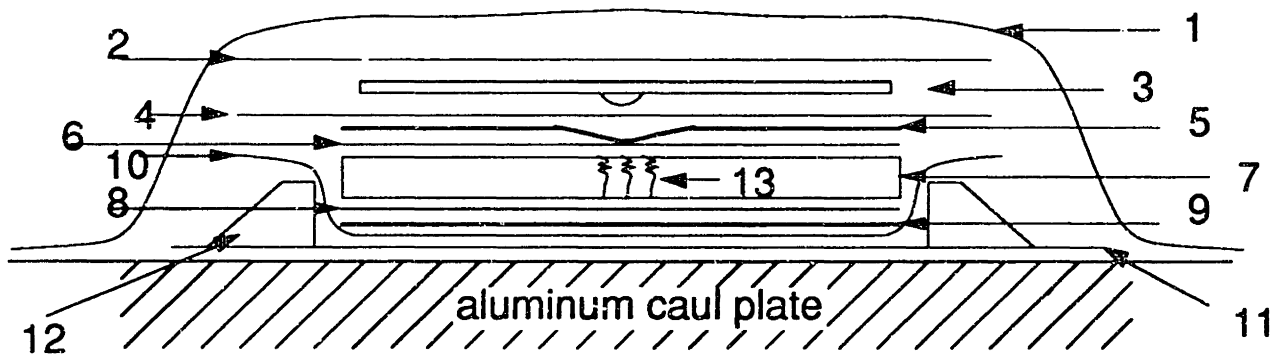


+ location for thickness measurements

○ simulated core damage

all dimensions in mm

Figure 5.13 Locations for thickness measurements for dimpled facesheets used in specimens with simulated core damage.



- 1 = vacuum bag
- 2 = 3-4 layers of fiberglass cloth
- 3 = special cure plate
- 4 = guaranteed nonporous teflon (GNPT)
- 5 = dimpled facesheet
- 6 = film adhesive
- 7 = precrushed Nomex honeycomb
- 8 = film adhesive
- 9 = undamaged facesheet
- 10 = GNPT
- 11 = GNPT
- 12 = aluminum dam
- 13 = region of precrushed core

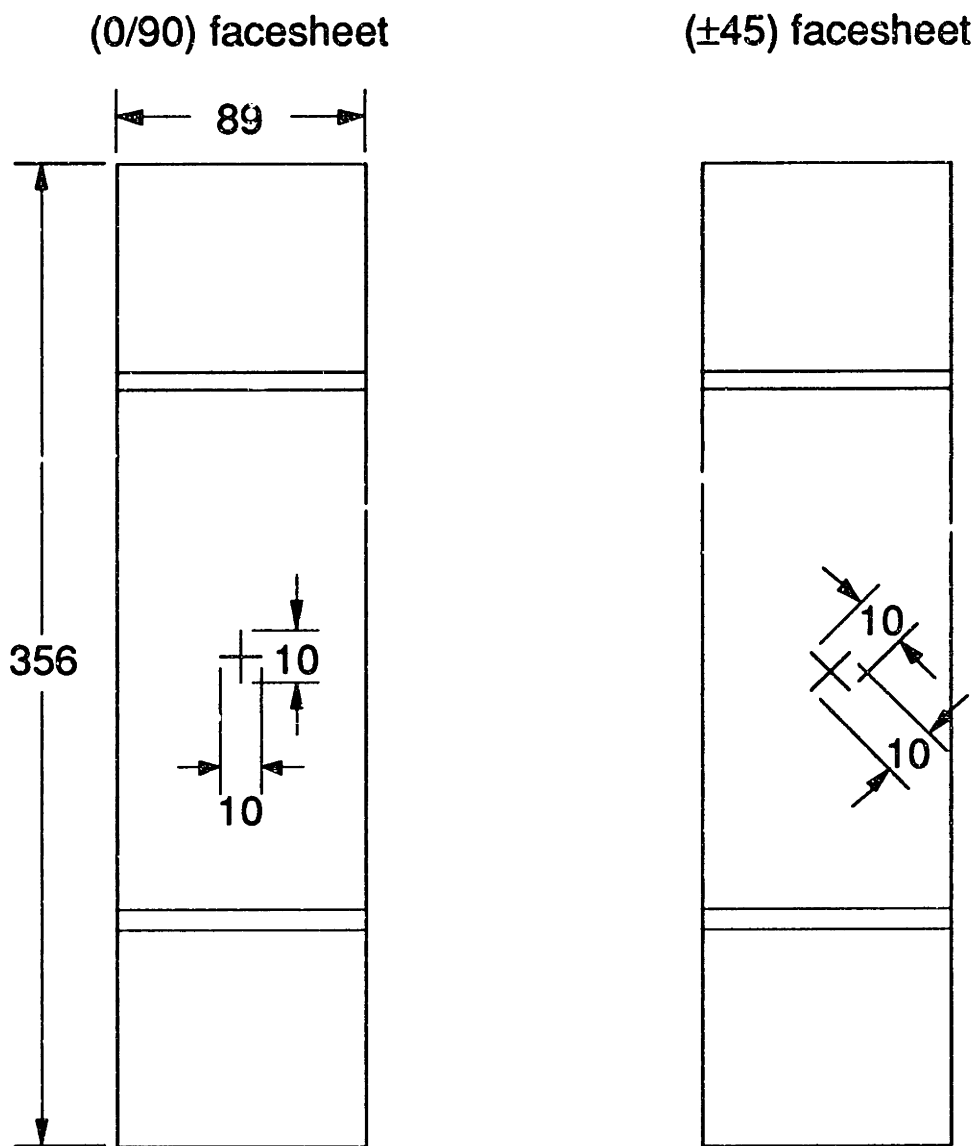
Figure 5.14 Cure assembly for secondary bond cure of panels with simulated core damage.

5.3.4 Specimens with Simulated Facesheet Damage (SFD)

The facesheets of specimens with simulated facesheet damage were manufactured in the same way as those of undamaged specimens. A pair of slits in the form of a cross was subsequently cut in the facesheets using a Dremel[®] Moto-Tool[®] equipped with a 25 mm diameter, 0.6 mm thick cutting blade (cut-off wheel #409). The lengths of the slits are all 10 mm and the slits are aligned with the tows of the fabric facesheets as shown in Figure 5.15. The Dremel Tool is mounted on a special jig (Figure 5.16) to facilitate accurate and stable cutting action. Since the cutting blade is circular, it does not cut through the facesheet near the tips of the slits. A jewelry saw was used to finish the tips to a pointed shape. The lengths of the slits were measured with a pair of calipers. The results are given in Chapter 6. The secondary bond cure and the loading tab cure are the same as the undamaged panels. On one of the specimens, film adhesive within the slit was removed with an X-acto knife before the bond cure so that the slit was not filled with adhesive after the bond cure. Test results show that the failure mode and failure load are not affected by the presence of film adhesive in the slits.

5.4 Instrumentation and Surface Preparation

Strain gages were put on the undamaged specimens used for material property evaluation (see Table 5.1) to obtain longitudinal and transverse strain measurements for evaluation of material properties. These gage locations are depicted in Figure 5.17. A pair of back-to-back gages were put on the undamaged specimens, specimens with static indentation damage, simulated core damage, and simulated facesheet damage (see Table 5.2) to check for any bending during the uniaxial compression tests. These gage



all dimensions in mm

Figure 5.15 Slit locations for specimens with simulated facesheet damage.

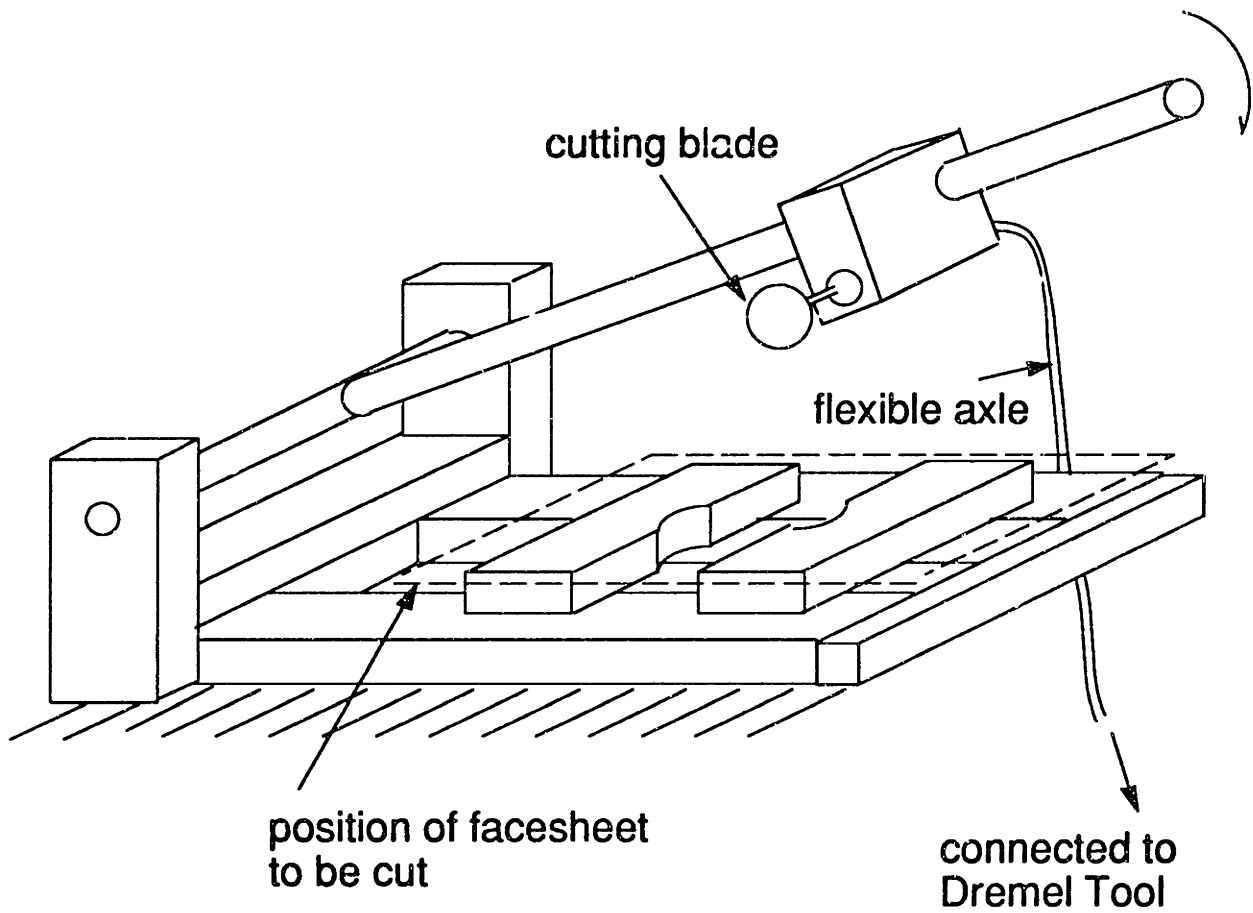


Figure 5.16 Illustration of jig used to cut slits in specimens with simulated facesheet damage.

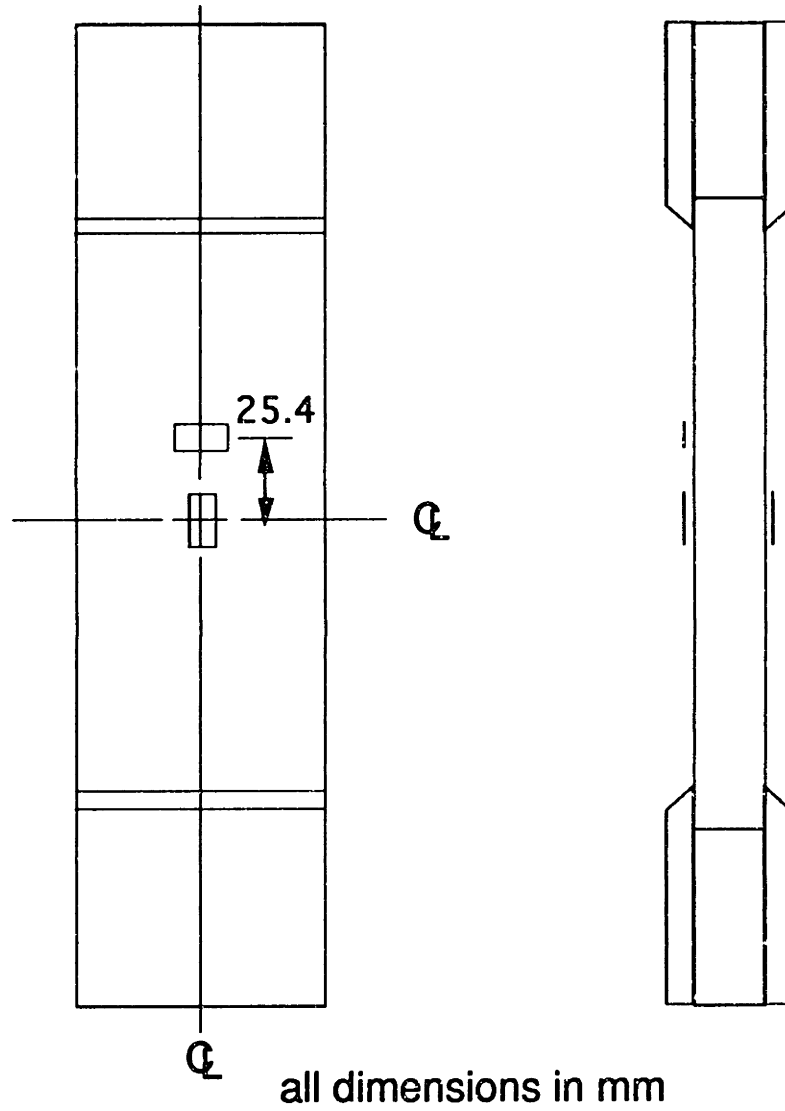


Figure 5.17 Strain gage locations for undamaged panels used to evaluate material properties.

locations are depicted in Figure 5.18 and are chosen such that the gages are not affected by the induced damage, the loading tab, and the free edge. These gages can therefore yield data to determine the modulus of each specimen and provide specimen quality check. All strain gages used were manufactured by the Micro-Measurements Division of Measurements Group, Inc. and of the type EA-06-125AD-120. Procedures for attaching strain gages can be found in Ref. [97].

The specimens with static indentation damage and those with simulated core damage which were tested under uniaxial compression were monitored by the shadow moiré method. In order to observe moiré fringes, the damaged surface of the sandwich panels was spray painted with matte white paint. The paint was applied in a few (between 3 to 5) thin layers. Each layer of paint was sprayed on after the previous layer was completely dry. The strain gage was covered with masking tape when the specimen was spray painted. The specimens with simulated facesheet damage were also spray painted to help identify the fracture pattern at failure.

5.5 Test Procedures

Two types of tests were performed: static indentation tests and uniaxial compression tests. The test procedures, test setups, and procedures of data reduction are described in this section.

5.5.1 Static Indentation Tests

All static indentation tests were performed using an MTS 810 uniaxial testing machine equipped with hydraulic grips. The load cell (Model 661-23A-02) of the testing machine has a maximum calibrated capacity of 444.8 kN (100,000 lb). In order to increase the resolution of the load data, a smaller load cell was used. The smaller load cell (Model

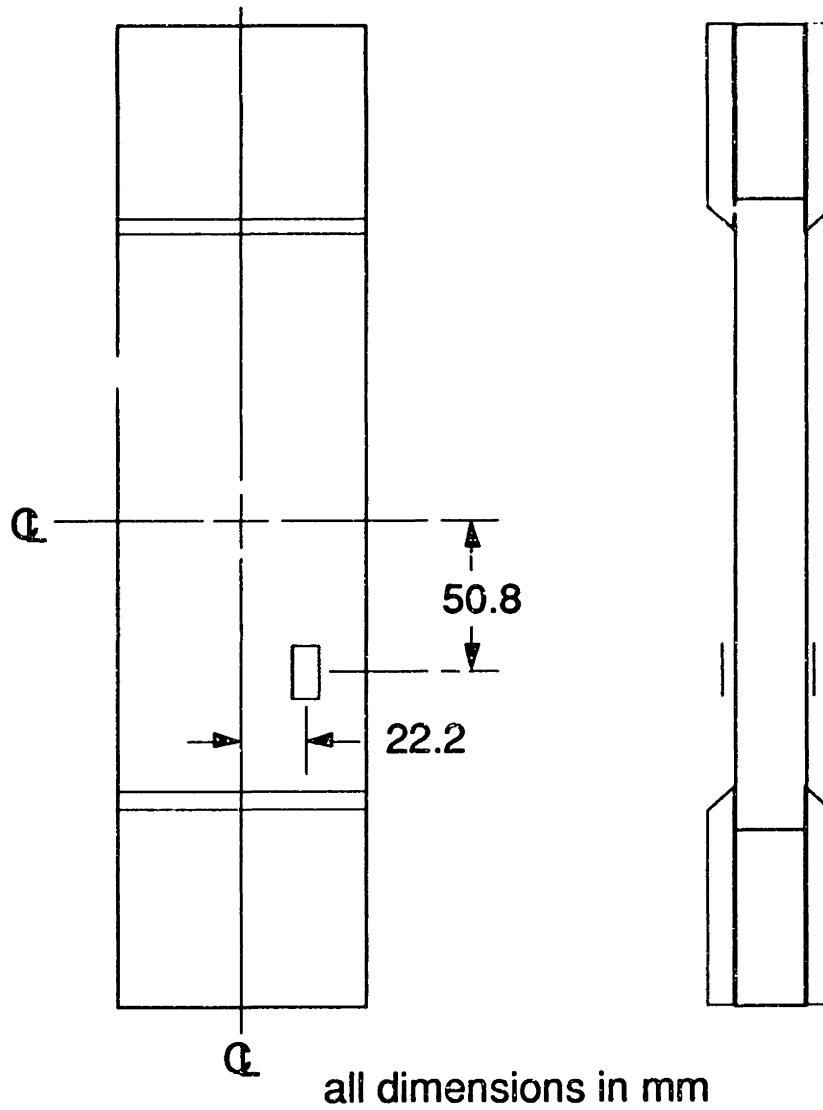


Figure 5.18 Strain gage locations for specimens with static indentation damage, simulated core damage, and simulated facesheet damage.

661.13A-04) has a maximum calibrated capacity of 8896 N (2000 lb). The assembly of this load cell and the indenter is depicted in Figure 5.19. The hydraulic actuator (series 204) of the testing machine has a maximum calibrated range of 127 mm (5 inches) and a maximum stroke rate of 31.3 mm/sec (74 inches/min).

As explained in Chapter 3, three indentors made of stainless steel were used to create three different damage states. The indentors have hemispherical nose diameters of 12.7 mm, 25.4 mm, and 38.1 mm respectively. Although the present investigation does not include impact testing, all three indentors were machined to a constant mass of 216 g so that they could easily be used for future impact work. A scale drawing of the three indentors is given in Figure 5.20. The tapped hole in the base of the indentors allows them to be attached to a 25.4 mm diameter aluminum rod which is placed in the hydraulic grips of the testing machine.

In the indentation tests, the sandwich specimens were placed on a 0.38 mm-thick steel plate which rests upon the lower grip of the testing machine. The steel plate was in direct contact with the bottom facesheet of the sandwich specimen so that no global bending of the sandwich structure was allowed during the indentation tests. The upper grip was lowered until the indenter was about 10 mm away from the surface of the sandwich panel. The lower grip was then raised using the "zero" dial on the signal conditioner of the load channel until the specimen surface was about 1 mm away from the indenter. A piece of paper was then placed between the indenter and the sandwich panel. The lower grip was raised even further using the "set point" dial until the paper could barely be pulled out. At this point the indenter is approximately a paper thickness (0.1 mm) away from the surface of the sandwich panel and the test was ready to begin.

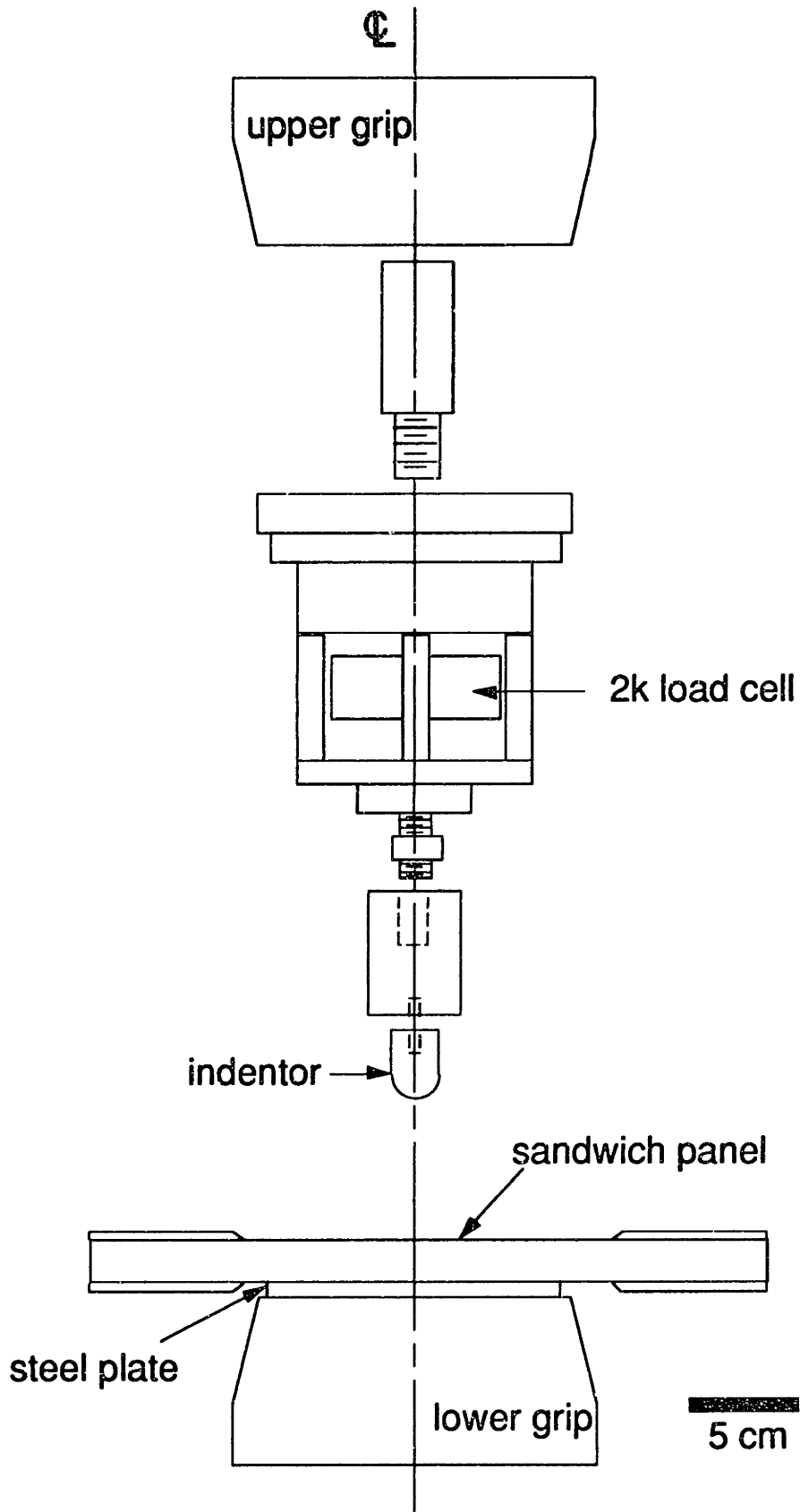


Figure 5.19 Illustration of experimental setup for static indentation tests.

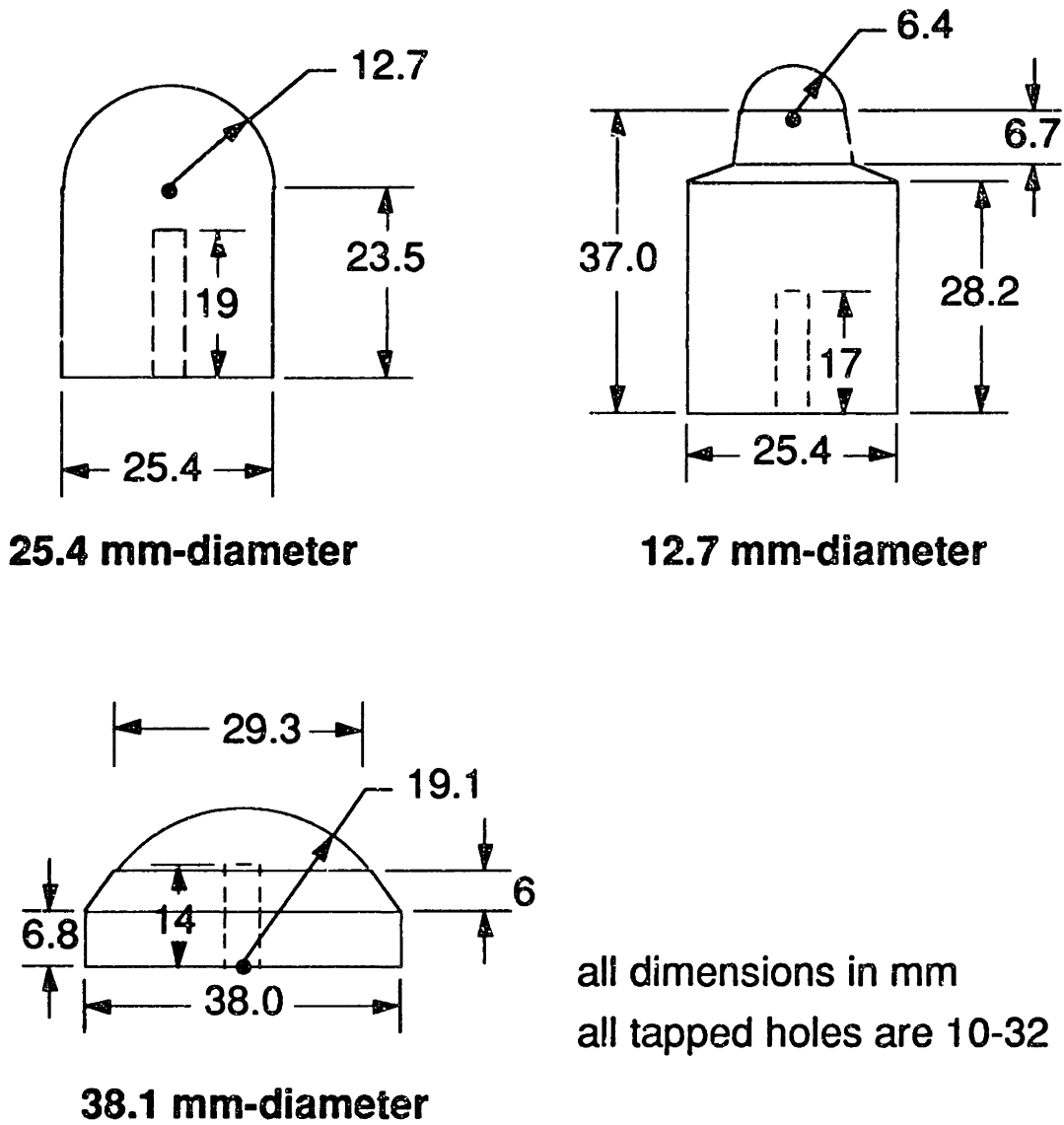


Figure 5.20 Illustration of indentors used for static indentation tests.

The tests were run under stroke control at a stroke rate of 3 mm/min (0.002 inch/sec). The tests were stopped manually when the indentation reached 3 mm. The specimen was then unloaded at the same rate. Two channels of data were recorded: load and stroke. The analog-digital board used for data acquisition was MacADIOS II/16 manufactured by GW Instruments, while the data acquisition software used was LabVIEW™ manufactured by National Instruments. The data acquisition system is implemented in a Macintosh IIx computer with 8MB RAM and an 80MB harddrive. The 10% range on the smaller load cell gives a load resolution of 0.435 N per computer unit (0.435 N/c.u.). The 10% range on the stroke transducer gives a stroke resolution of 0.0062 mm/c.u. The sampling rate was 3 Hz. Both the loading and unloading of the indentation process were recorded.

5.5.2 Uniaxial Compression Tests

All the uniaxial compression tests were conducted in the same testing machine as for the indentation tests. The test procedures for the compression tests of the undamaged specimens and damaged specimens are essentially the same. These general procedures are described in the present section. However, the compression tests of the damaged panels were also monitored by the shadow moiré method as described in the next section.

The specimen was put in the upper grip first. A grip pressure of 3.45 MPa (500 psi) was applied. A set square was used to align the specimen so that it was perpendicular to the grip. The specimen was then lowered until the bottom end was inside the lower grip. The back-to-back strain gages were calibrated and zeroed with the specimen hanging from the upper grip. When the lower grip was closed, the back-to-back strain gages were

carefully monitored. If the difference between the two strain gage readings differed by more than 200 microstrain for (0/90) specimens or 500 microstrain for (± 45) specimens, masking tape was stuck on the lower loading tabs to compensate for the misalignment. This ensures that the initial "bending strain" is less than 5% of the failure strain of the corresponding undamaged specimens. The stroke rate used for all compression tests was 3 mm/min (0.002 in/sec), the same as the stroke rate used in previous work [28, 59]. Since the nominal gage length of the specimens is 203 mm (8 inches), the corresponding strain rate is approximately 250 microstrain/sec.

Recorded data include load data, stroke data, and strain gage data. Sampling frequencies used were 10 Hz for the (0/90) specimens and 5 Hz for the (± 45) specimens. The same data acquisition system was used as for the static indentation tests. The compression tests were stopped manually when the specimens failed. Failure was defined as a significant load drop (by more than 40%) and was always accompanied by a loud bang and visible facesheet fracture. Although one of the facesheets might still be intact, the test was stopped after this first failure. The damage mode of the specimen was examined visually and sketched in the log book before the specimen was unloaded. Photographs of the failed specimens were taken after they were taken out of the testing machine.

5.5.3 Shadow moiré method

The shadow moiré method utilizes the interference between a set of closely spaced lines and its shadow to measure out-of-plane displacement. In practice, a light beam is shined on a moiré grating at an angle. The grating is held closely to the surface of which the out-of-plane deformation is

to be measured. The beam casts a shadow of the grating on the observed surface. The interference between the grating and its shadow gives rise to interference, or moiré, fringes. These moiré fringes are out-of-plane displacement contours of the observed surface. An example of these moiré fringes is shown in Figure 5.21. The fringes correspond to a dimple/dent machined in an aluminum plate using a ball-end mill.

The theory of the shadow moiré method and its applications in various engineering disciplines can be found in the references given in Section 3.2. The out-of-plane displacement is calculated by the following "field" equation:

$$w = \frac{Np}{\tan \alpha} \quad (5.1)$$

where w is the out-of-plane displacement, p the pitch of the grating, α the angle of incidence, and N the fringe order. The pitch of a grating is the distance between the centers of two consecutive dark fringes. The angle of incidence is the angle between the surface normal and the light source. The zeroth order fringe is the datum from which the out-of-plane displacement is measured. In the present investigation, the periphery of the dimple is used as the datum and hence the outermost fringe that defines the circumference of the dimple is the zeroth order fringe. The fringe next to the zeroth-order fringe is the first-order fringe, and so on. The sample fringe pattern shown in Figure 5.21, therefore, has eleven fringes from order zero to order ten. In the present work, p is equal to 0.127 mm and α is equal to 35° . Thus, the resolution for w (i.e. difference in w of one fringe order) is 0.181 mm for the present setup.

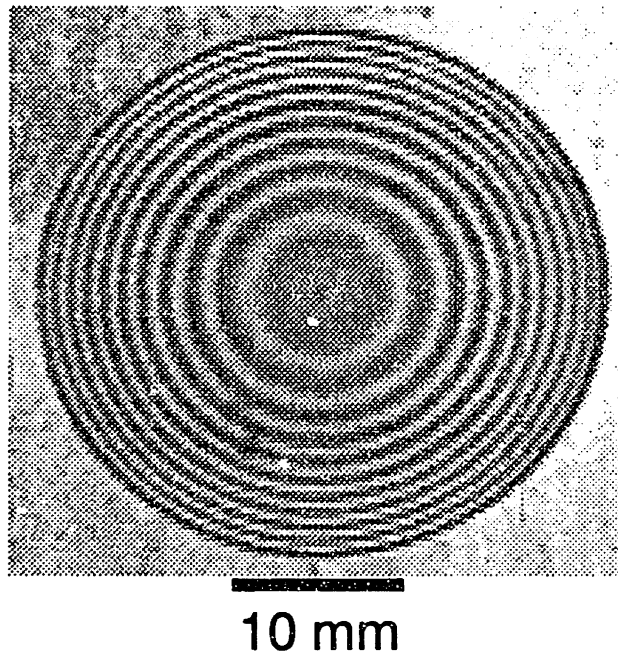


Figure 5.21 Photograph of moiré fringes of a hemispherical dimple, 16 mm in radius and 2 mm deep, machined in an aluminum plate with a ball-end mill.

The moiré setup used in the present work consists of four components: moiré gratings, grating holder, video camera, and light source. Moiré gratings are essentially glass plates with black lines etched on the surface. They are commercially referred to as "Ronchi rulings". Ronchi rulings of density up to 1000 lines per inch are readily available from most optical equipment suppliers. The Ronchi ruling used for the present work is a 50% grating (equal opaque and transparent areas) with 200 lines per inch (7.87 lines per mm). This gives the pitch of 12.7 mm indicated earlier. The grating is 3.89 mm thick and 102 mm by 102 mm (4 inch by 4 inch). It was purchased from Edmund Scientific, Inc. When the specimen failed, debris would hit the grating which was placed very close to the surface of the specimen. In order to avoid breaking a master grating in every test, duplicates of the master grating were photographically reproduced and used in the actual testing. Photo-sensitive glass plates (technical pan plates) manufactured by Kodak were used for the reproduction. These glass plates were 10.2 cm by 12.7 cm by 0.15 cm (4 inch by 5 inch by 0.06 inch) and were received in a light-tight box of 36 plates. The master grating was reproduced via a contact print onto the photo-plates.

The gratings were held in front of the sandwich panel by a specially designed grating holder. The grating holder is made of aluminum and is depicted in Figure 5.22. The jig sits on a linear translation stage which allows two degrees of freedom: in-out and left-right as seen in the front view. The side arm can be moved vertically along and rotated about the support rod. The grating was first centered relative to the specimen by adjusting the linear translation stage. It was then moved slowly toward the specimen. Fringes would start to appear when the grating was about 1 cm from the specimen because the grating was not parallel to the surface of the

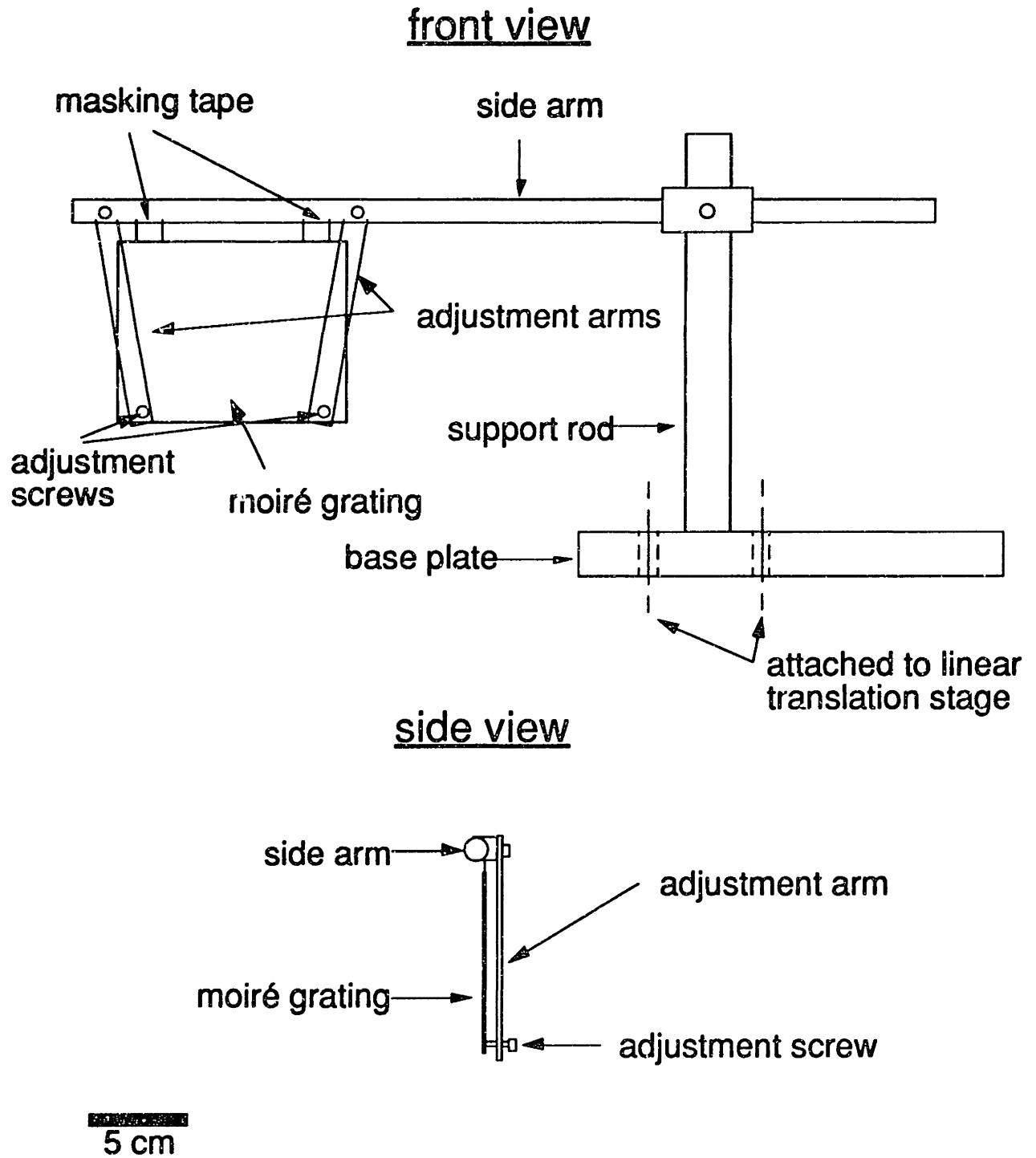


Figure 5.22 Illustration of grating holder for the shadow moiré setup.

specimen. The side arm was then rotated about the support rod until all the fringes appeared horizontal. At this point the grating was parallel to the specimen along the horizontal axis. The adjustment screws were adjusted slowly until the horizontal fringes disappeared. At that point, the grating was parallel to the surface of the sandwich panel. As the screws were being adjusted, the grating was gradually moved closer to the specimen. The grating was eventually placed as close to the surface of the sandwich panel as possible without touching the panel. The distance between the grating and the specimen must be small, otherwise blurry fringes result.

The light source is a commercial slide projector. It was placed on a ladder at about the same height as the test specimen and about 2 meters from the testing machine. Since the distance between the projector and the specimen is much greater than the width of the specimen, the light from the projector can be regarded as approximately collimated (i.e. a point source at infinity). The axis of the slide projector was inclined at an angle of 35° with respect to the surface of the sandwich panel. Incidence angles larger than 35° cause excessive shadow on the dimple while angles smaller than 35° give lower resolution. The angle of incidence was measured by the angle finder shown in Figure 5.23.

The entire compression test was recorded by a camcorder up to the point of failure. The camcorder used is a Cannon A1 MarkII 8 mm model. It was placed on a tripod in front of the testing machine at a distance of about 1.2 m (four feet) from the test specimen. The axis of the camcorder is normal to the surface of the specimen. The camcorder was connected to a television so that the dimple propagation process could be viewed simultaneously by the two experimenters who controlled the data

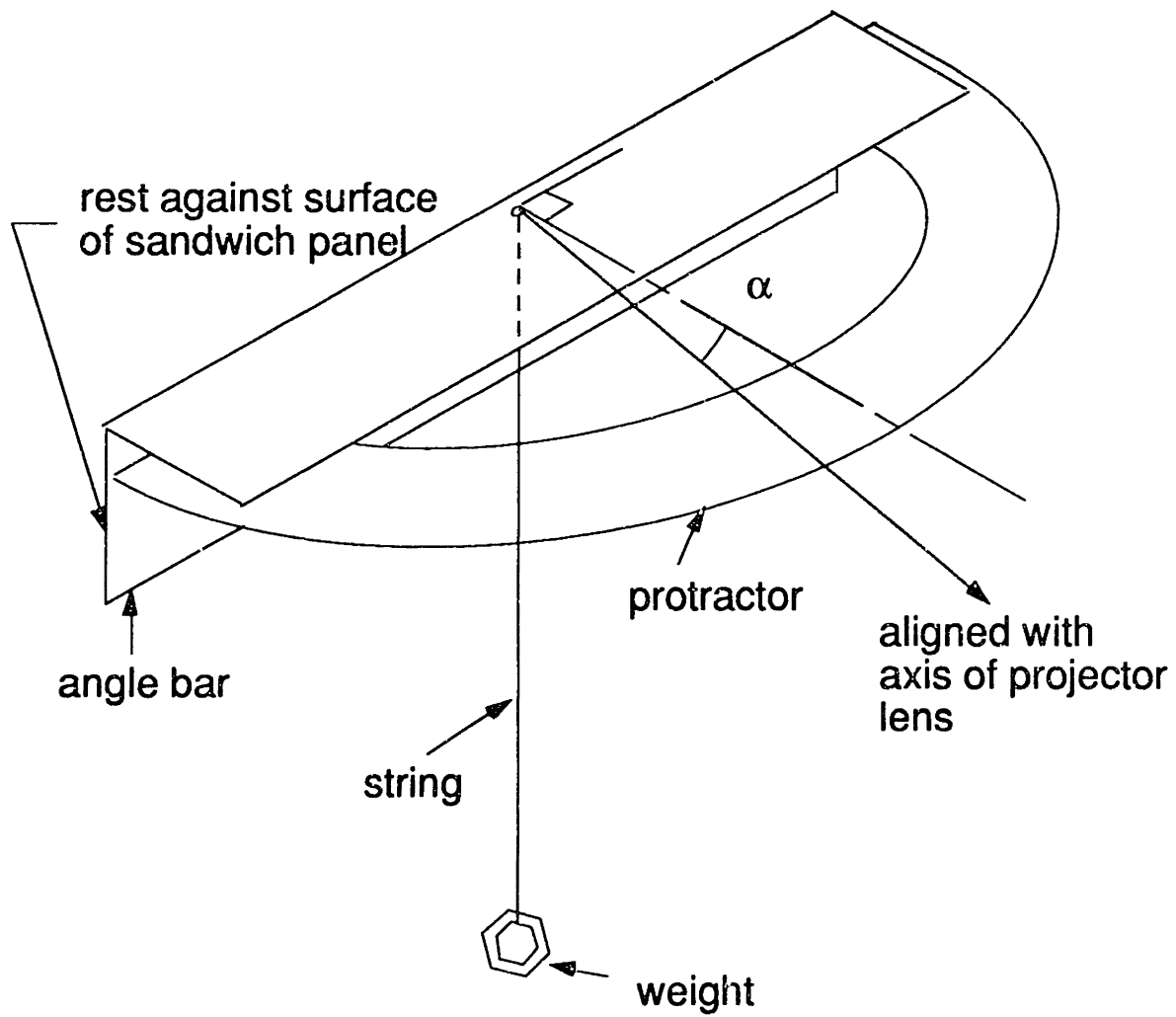


Figure 5.23 Illustration of angle finder used for measuring angle of incidence of light source for shadow moiré method.

acquisition and the testing machine respectively. The schematic of the moiré setup is depicted in Figure 5.24.

5.5.4 Data reduction

All data were taken in English units and then converted to SI units. For the indentation tests, the load data were plotted against the stroke data to give the load-indentation curves of the specimens. For the uniaxial compression tests, stress data were obtained by dividing the load data with the total measured cross-sectional area of the facesheets. The slope of the stress-strain curves yields the modulus of the specimens.

The videos of the moiré fringes were played back on a television. Given the sampling frequency used in the compression tests and using the tape counter on the TV screen, the load data were synchronized with the video images. Selected video images at different loads were digitized using ComputerEyes™ by Digital Vision and subsequently stored on computer disks. These digitized images were eventually printed out and the spacings between the fringes measured along the x-axis (loading axis) and the y-axis using a pair of Vernier calipers. By combining the measurements of the fringe spacings and calculating w via Equation 5.1, the profiles of the dimple along the x-axis and the y-axis are obtained for any given load. For example, the measured profile along the horizontal axis (x-axis) of the dimple shown in Figure 5.21 is given in Figure 5.25. Measurements taken with a dial gage, as described in Section 5.6.4, are also included.

5.6 Damage characterization

Three damage inspection techniques were used to characterize specimen damage: X-radiography, microscopic inspection, thermal deply, and dial gage measurements. X-radiography provides integrated in-plane

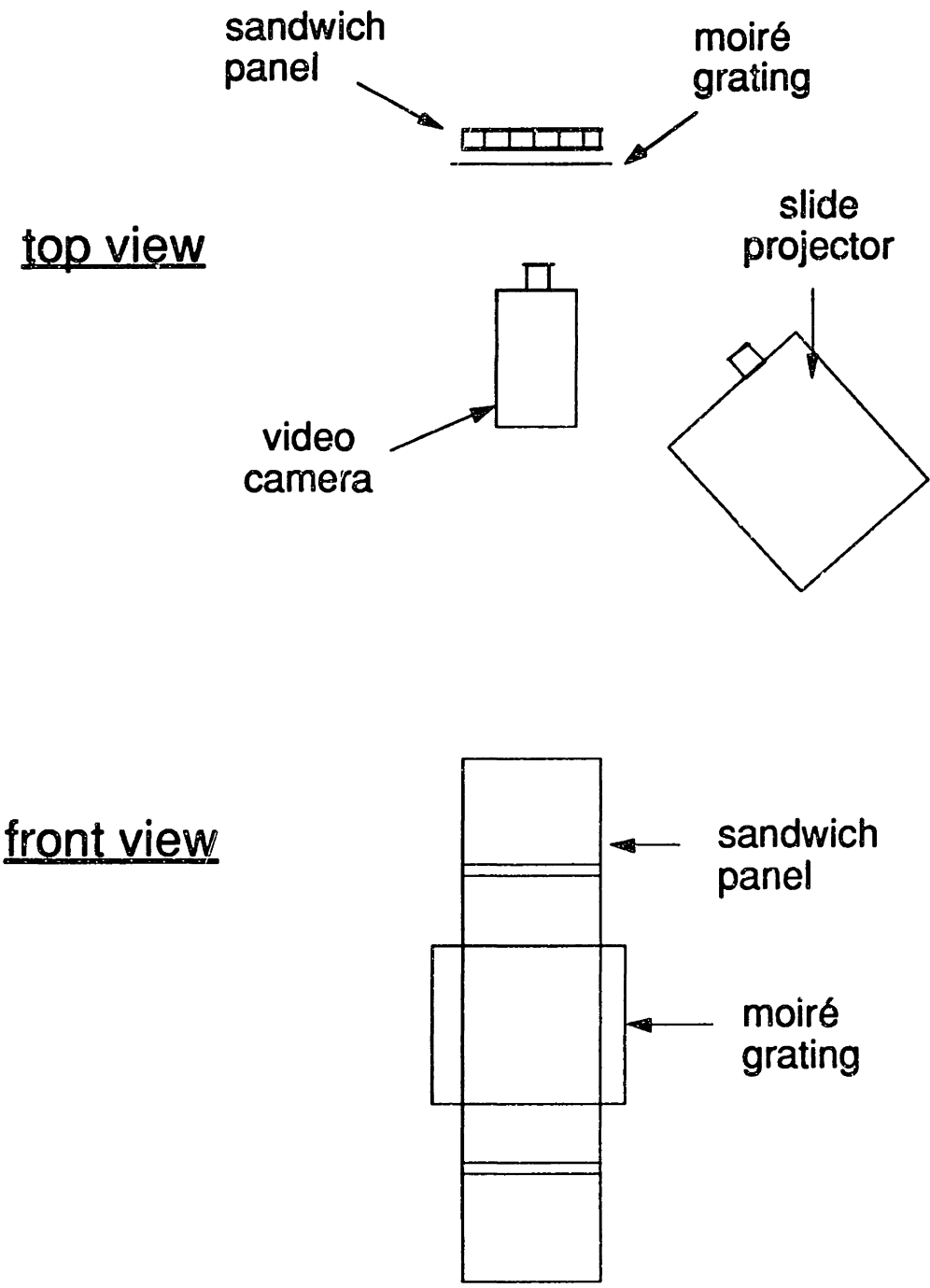


Figure 5.24 Schematic of the moiré setup.

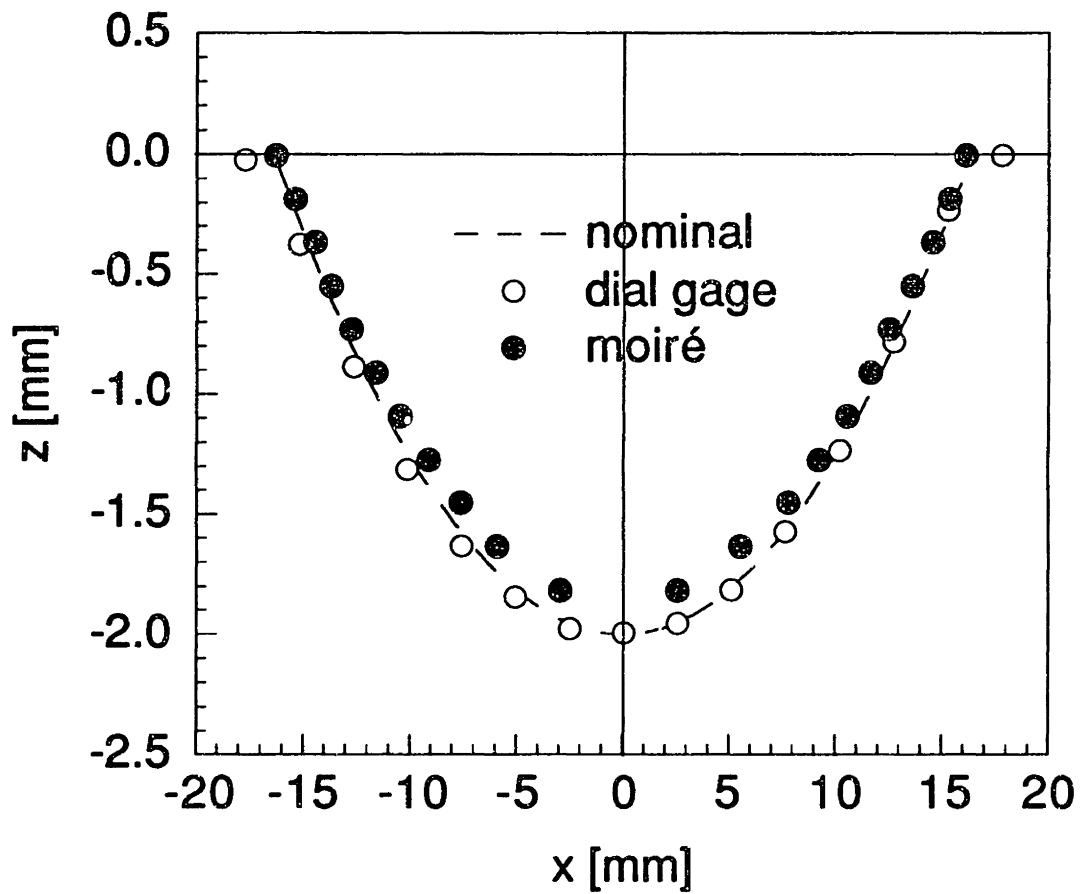


Figure 5.25 Moiré measurements of a hemispherical dimple, 16 mm in radius and 2 mm deep, machined in an aluminum plate with a ball-end mill (finge pattern shown in Figure 5.21).

dimensions of the facesheet damage. Microscopic inspection of cross-sections of the damage location provides through-thickness information on both facesheet and core damage. Thermal deply can reveal hard-to-detect fiber damage which usually occurs away from the surface of the facesheet. A dial gage was used to measure the dimple profiles.

5.6.1 X-radiography

The X-ray machine used was the Torrex 150D X-ray inspection system manufactured by Scanray Corporation. For all the X-radiographs taken in the present work, the operating voltage was set at 50 kV and the current at 3 mA. The Timerad operating mode was used for all inspection. In this operating mode, a sensor inside the X-ray chamber stops the exposure when a specified dosage of radiation is detected. The specified dosage for all X-radiographs was set at 260 mR. The specimen was placed on top of a radiation sensor and a Polaroid Type 52 film placed between the sensor and the specimen. An X-ray opaque dye (1,4-diiodobutane) was injected into the damage location and allowed to soak for 30 minutes. For visible and barely visible facesheet damage, the dye was applied to the surface with a syringe. For cases with no visible facesheet damage, holes of diameter 0.6 mm were drilled in the facesheet to a depth just above the adhesive layer. The twist drill bit was secured in a hand-held drill. The handle of the hand-held drill was inserted into the chuck of a drill press. The drill bit was marked at 0.35 mm from the tip to help gage the depth of the hole. The drilling process was interrupted frequently to check that the hole had not gone through the adhesive layer between the facesheet and the core. The dye was introduced into the facesheet through these holes. It is important not to flood the damage area with too much dye because it will

mask the details in the X-radiographs. Vernier calipers were used to measure the damage lengths, if observable, in the X-radiographs. Typical X-radiographs are shown in Figure 5.26.

5.6.2 Microscopic inspection

In order to examine the cross-sections, damaged specimens were sectioned along the warp direction through the center of the damage using the same milling machine described in Section 5.3.1. The cross-sections were examined with an Olympus SZ-Tr zoom-stereo microscope. The total magnification of the microscope is the product of the eye-piece magnification, the zoom magnification, and the objective magnification. For a given total magnification, the resolution increases with the objective magnification and not with the eye-piece magnification. In the current investigation, 10X eyepieces were used in combination with a 1X objective. The zoom magnification was varied between 0.7X and 4X which yields a total magnification between 7X and 40X. The extent of core damage through the thickness and at the interface between the facesheet and the core was noted. The damage in the facesheet was also examined. A small scale (5 mm) printed on a strip of paper was placed near the damage site to help obtain quantitative measurements.

Although the Olympus microscope serves well for visual inspection, it has problems taking photomicrographs with the Olympus OM2 camera. There are two reasons for the problem. First, the Olympus OM2 camera is very difficult to focus when mounted on top of the microscope. Second, the quality of photomicrographs is very dependent on good lighting conditions which require considerable trial-and-error. Since the photographs require development time, the results were not seen until after a few days. By that

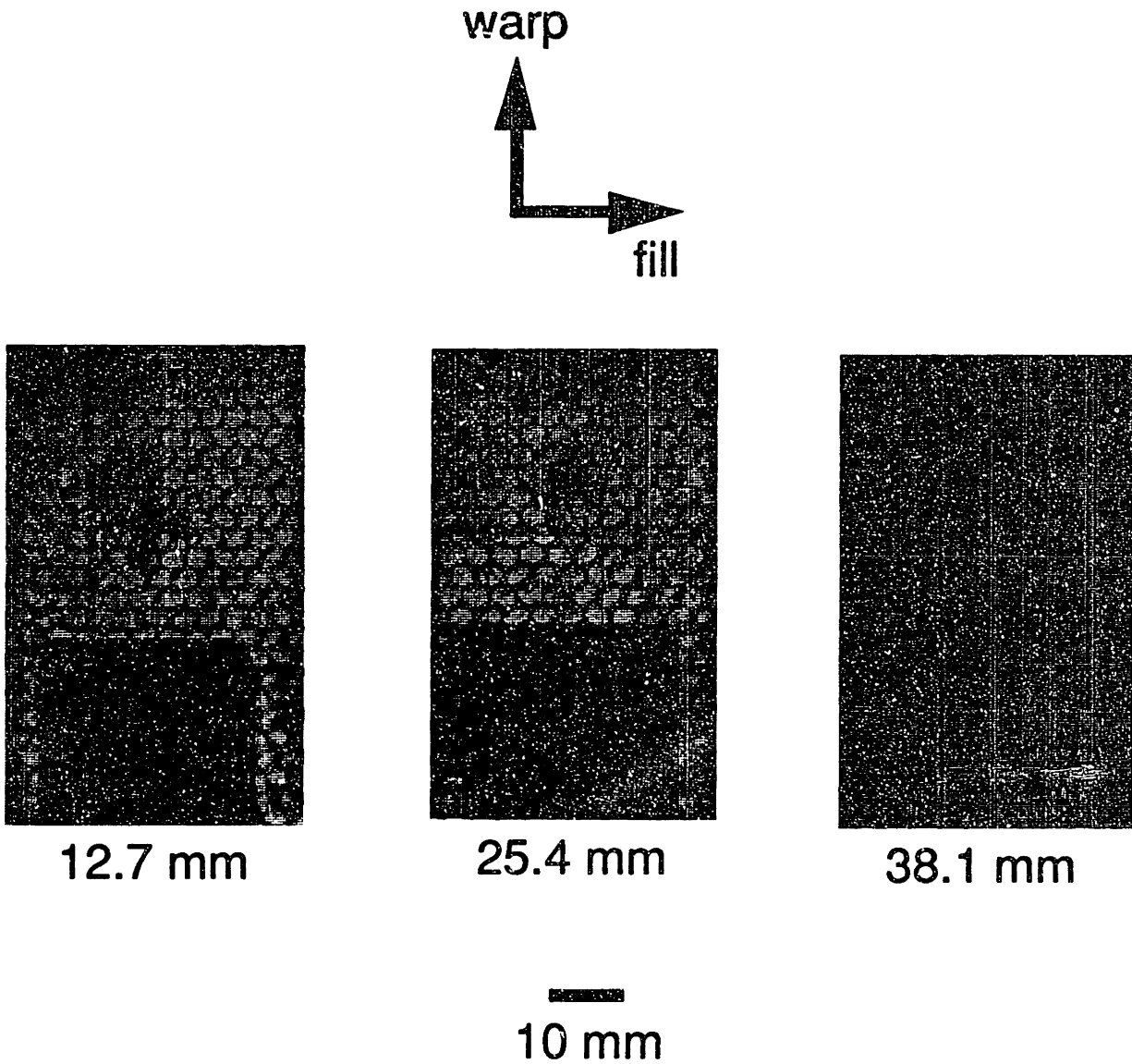


Figure 5.26 Typical X-radiographs of the specimens with (0/90) facesheets indented with the three different indentors.

time, it was often difficult to reproduce the same lighting conditions, let alone to improve on it. Therefore, another camera, the Polaroid MP-3 Land Camera, was used to take pictures of selected cross-sections. Although the Polaroid camera has a lower magnification power (between 2X and 10X) than the Olympus camera, it has the advantage of allowing instant photography and it is easier to focus. A photograph of a typical cross-section is shown in Figure 5.27. Note that the Polaroid camera was used to document the qualitative appearance of the cross-section only. Quantitative damage characterization was done via the Olympus microscope as described in the previous paragraph.

5.6.3 Thermal deply

In the thermal deply method, the resin is burned off at high temperature so that the plies can be separated for examining fiber damage in the facesheet. For the current work, a 50 mm by 50 mm square of the sandwich specimen around the indentation damage was cut out and put on a steel wire mesh. The specimen and the mesh were put in a furnace for 5 minutes at 1000° F. The specimen was then taken out of the furnace and allowed to cool down. At that point the core would be completely charred and separated from the facesheet. The individual plies of the facesheet were carefully separated by hand and then examined under the microscope.

The locations of fiber damage were noted. The thermal deply method was very effective in locating facesheet damage that might be overlooked by X-radiography and sectioning. This type of fiber damage usually occurred in the bottom ply away from the indented surface. A sketch of typical fiber damage is shown in Figure 5.28. The number of "checkerboard squares" which contained fiber damage was recorded.

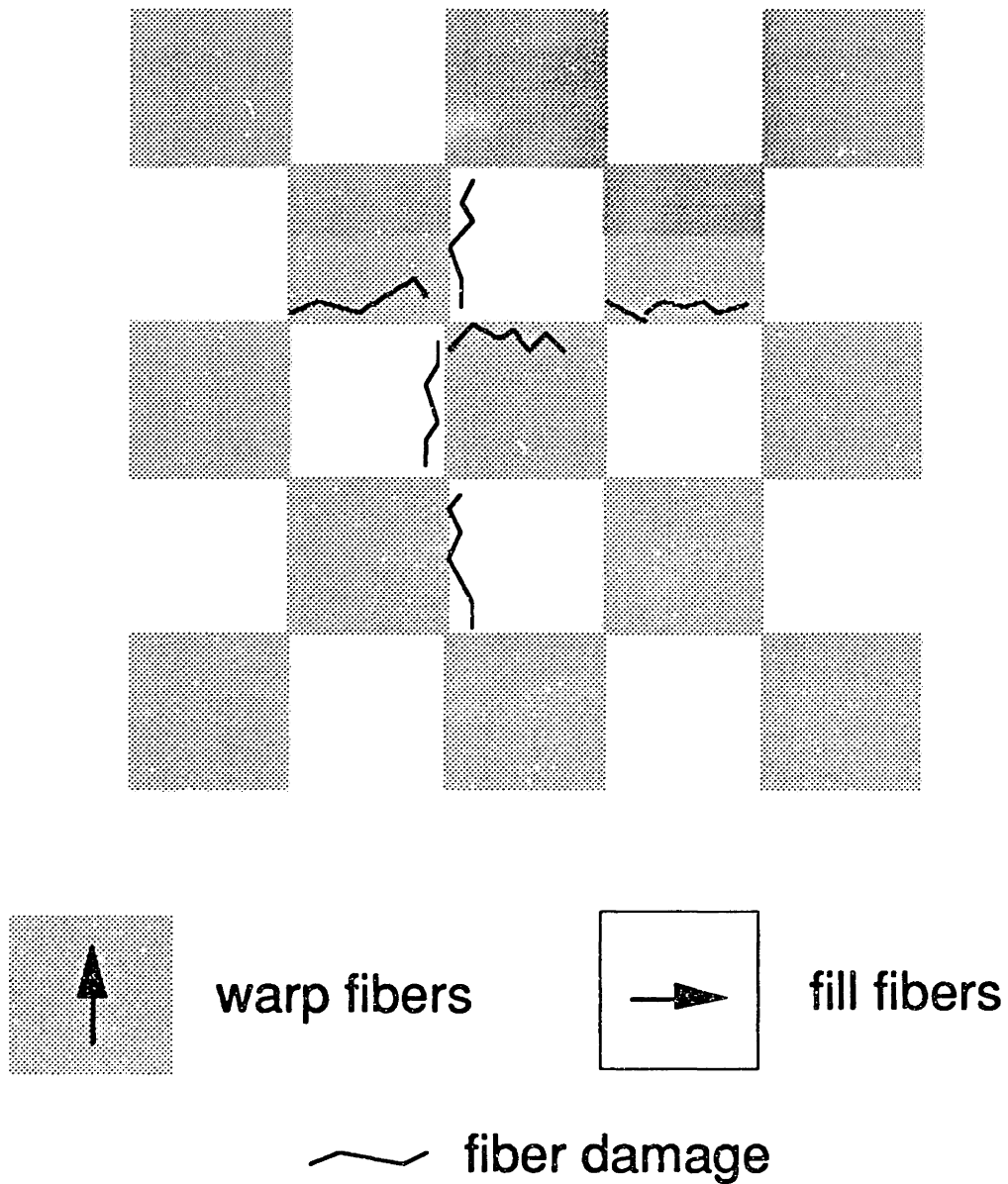


Figure 5.27 Typical sketch of fiber damage due to indentation as observed in individual plies of the facesheets after thermal deply.

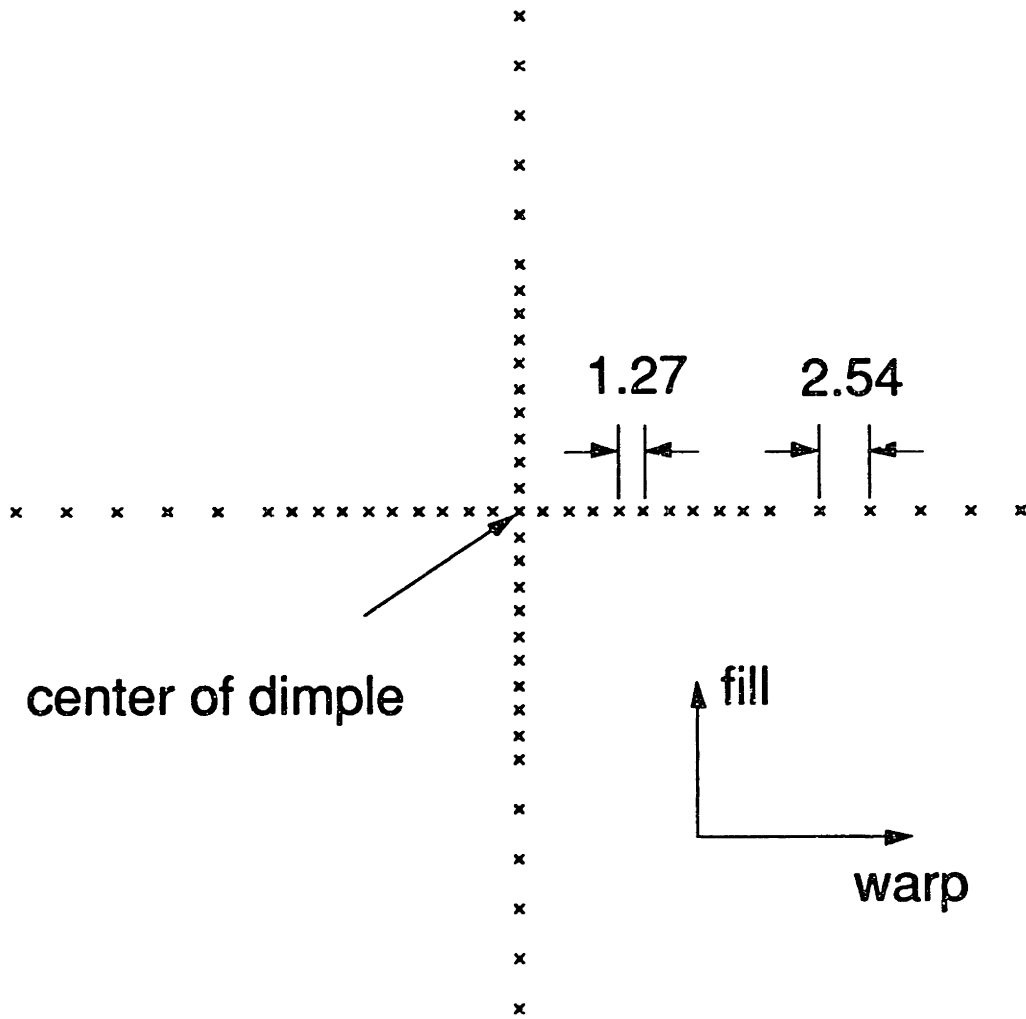


5 mm

Figure 5.28 Photograph of typical cross-section of a specimen with (0/90) facesheets indented with the 12.7 mm-diameter indenter.

5.6.4 Dial gage measurements

The shapes of the dimples in specimens with static indentation damage and specimens with simulated core damage are characterized by profile measurements along the tows of the fabric. The measurements were made by means of a dial gage mounted on a milling machine. The sandwich panels were placed on the milling machine table equipped with a digital display for the table feed. The lowest point of the dimple was first located. The milling machine table was then moved along each of the two tow directions in ten 1.27 mm (0.05 inch) intervals, followed by five 2.54 mm (0.1 inch) intervals. These locations for the dial gage measurements are depicted in Figure 5.29. The readings of the dial gage were recorded by hand at each stop.



× location for dial gage measurement

all dimensions in mm

Figure 5.29 Locations for dial gage measurements of the dimple profiles.

Chapter 6

Results

All experimental results and selected analytical results are presented in this chapter. The results presented are divided into two categories: impact resistance and damage tolerance. The impact resistance results are all experimental and consist of load-indentation data and damage characterization of indented specimens and of specimens with simulated damage. The damage tolerance results consist of both analytical and experimental results. Experimental results include far-field stress-strain data, dimple evolution data obtained by measuring moiré fringes, postmortem inspection of failed specimens, and compressive strength of the specimens. Analytical results presented include predictions of the evolving dimple profiles, through-thickness stress distributions at the interface between the core and the facesheet, and longitudinal stress distributions in the facesheet. Where appropriate, analytical predictions are compared with the corresponding experimental results. Data of all specimens tested under uniaxial compression are given in Appendix C.

As explained in Chapter 3, the current material system was chosen to continue to build on an existing data base in TELAC. In Chapter 5, a set of material property evaluation tests was described. These tests were used to verify that the material and manufacturing procedures used in the current research are comparable with those in earlier works [28, 59]. The material properties obtained from these material property evaluation tests are shown in Table 6.1. Also listed in Table 6.1 are the material properties obtained by

Table 6.1 Measured material properties of AW193/3501-6

	Present	Lie [28]
E_L [GPa]	63.8 (2.7%) ^a	63.0 (2.2%)
E_T [GPa]	63.6 (6.4%)	59.9 (2.8%)
ν_{LT}	0.15 (13.6%)	0.07 (26.2%)
ν_{TL}	0.11 (36.7%)	0.10 (15.3%)
G_{LT} [GPa]	6.27 (0.3%)	4.83 (-)

^anumbers in parentheses are coefficients of variation

Lie [28] on the same material system. The two sets of results are the same within the scatter of experimental data.

6.1 Impact Resistance

Load-indentation data are presented first, followed by characterization of the indentation damage, of the simulated core damage, and of the simulated facesheet damage. Load-indentation data are a measure of the contact stiffness of the sandwich panel. This information is necessary for dynamic modelling of the impact of the panels. The purpose of the damage characterization of indented sandwich panels is to provide information on the damage types and the amount of each damage type present in those panels. Such information was used to design simulated damage types for the damage tolerance investigation.

6.1.1 Load-indentation data

The load-indentation data are very repeatable for a given facesheet layup and indenter size. Therefore, only one set of results is presented for each combination of facesheet layup and indenter size. In particular, for each facesheet layup, three load-indentation curves are presented: one for the 12.7 mm-diameter indenter, one for the 25.4 mm-diameter indenter, and one for the 38.1 mm-diameter indenter. Both the loading and unloading parts of the indentation tests are presented. Since the indentation tests were started with the indenter at approximately 0.1 mm away from the surface of the panel (see Section 5.5.1), the initial part of the loading curve registers no load.

Typical load-indentation curves of specimens with (0/90) facesheets indented with the three indentors are given in Figure 6.1. The loading part of the curves are the same for indentations less than 1 mm. Beyond 1 mm,

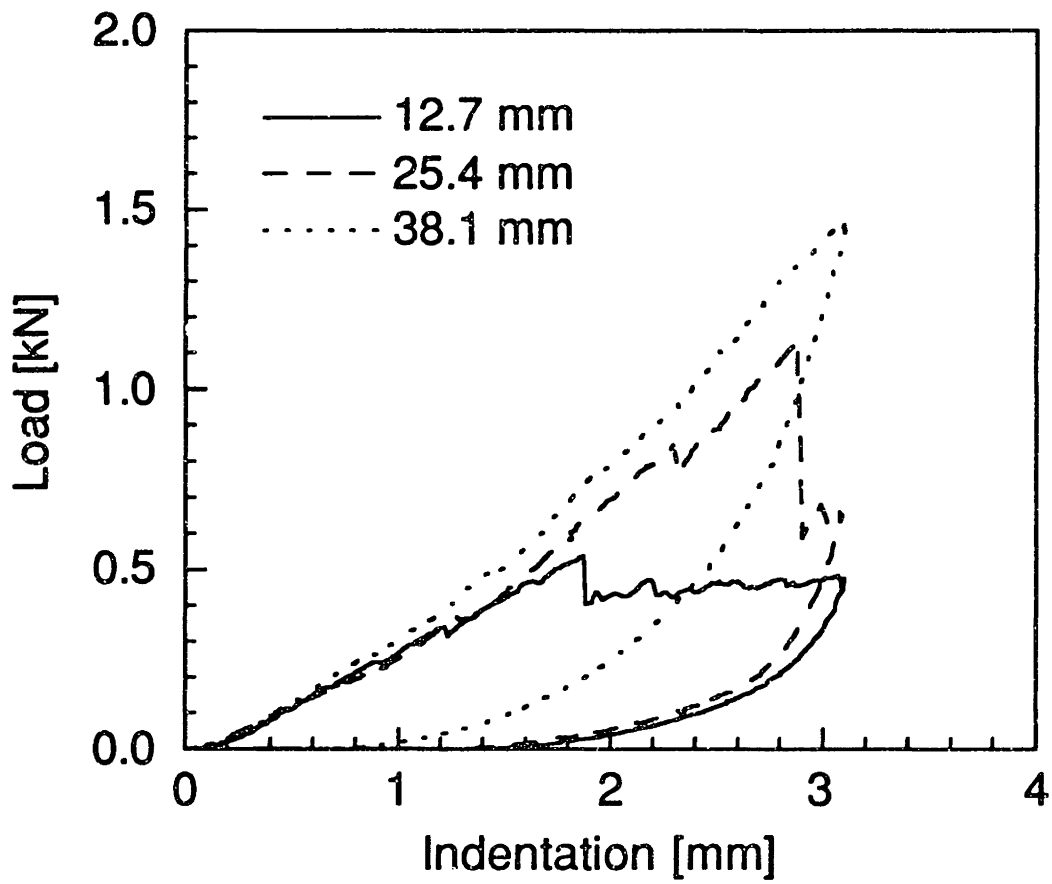


Figure 6.1 Typical load-indentation curves of specimens with (0/90) facesheets for different indenter diameters.

the curve for the 38.1 mm-diameter indenter starts to stiffen more than the ones for the 12.7 mm-diameter indenter and the 25.4 mm-diameter indenter. At about 550 N, the curve for the 12.7 mm-diameter indenter shows a load drop and then stays approximately at a constant load of 450 N. A similar load drop occurs at about 1150 N for the case of the 25.4 mm-diameter indenter. No load drop is observed for the case of the 38.1 mm-diameter indenter and a maximum load of approximately 1450 N was achieved, which corresponds to the maximum indentation depth of 3 mm. When the indentation reached 3 mm (about 3.1 mm in the figure because of the gap between the indenter and the sandwich panel at the start of the test), the indentation test was stopped and the testing machine started to unload the specimen. All three indentors have an unloading curve different from the loading curve. For a given indentation, the load is smaller when the indenter is unloading. The load reaches zero at an indentation of about 1.4 mm for the cases of the 12.7 mm-diameter indenter and the 25.4 mm-diameter indenter. For the case of the 38.1 mm-diameter indenter, the load reaches zero at an indentation of about 0.8 mm.

Typical load-indentation curves of specimens with (± 45) facesheets indented with the three indentors are given in Figure 6.2. The loading part of the curves are the same for indentations less than 1 mm. As in the case of specimens with (0/90) facesheets, beyond 1 mm, the curve for the case of the 38.1 mm-diameter indenter starts to stiffen more than the ones for the case of the 12.7 mm-diameter indenter and the case of the 25.4 mm-diameter indenter. Beyond 450 N, the load for the case of the 12.7 mm-diameter indenter remains approximately constant. A load drop occurs at about 1000 N for the case of the 25.4 mm-diameter indenter. No load drop is observed for the case of the 38.1 mm-diameter indenter and a maximum

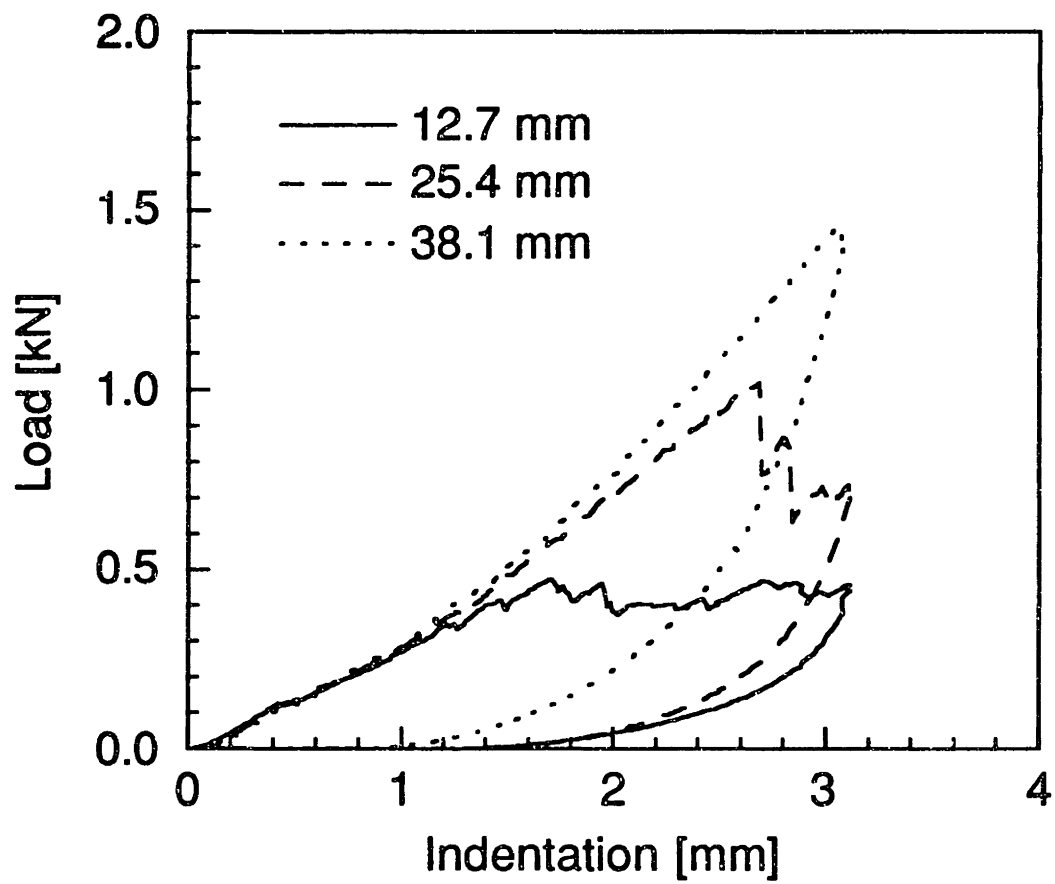


Figure 6.2 Typical load-indentation curves of specimens with (± 45) facesheets for different indenter diameters.

load of approximately 1450 N was achieved, which corresponds to the maximum indentation depth of 3 mm. When the indentation reached 3 mm (about 3.1 mm in the figure because of the gap between the indenter and the sandwich panel at the start of the test), the indentation test was stopped and the testing machine started to unload the specimen. All three indentors have an unloading curve different from the loading curve. For a given indentation, the load is smaller when the indenter is unloading. The load reaches zero at an indentation of about 1.4 mm for the cases of the 12.7 mm-diameter indenter and the 25.4 mm-diameter indenter. For the case of the 38.1 mm-diameter indenter, the load reaches zero at an indentation of about 0.8 mm.

The load-indentation curves of specimens with (0/90) and (± 45) facesheets are compared in Figures 6.3 through 6.5 for the three different indenter diameters. The load-indentation curves are essentially the same within the scatter of the experimental data.

6.1.2 Characterization of static indentation damage

The results presented include photographs and sketches of damage patterns in the indented facesheets, in-plane X-radiographs of indented facesheets, photographs of cross-sections through the damage site, dial gage measurements of dimple profiles, and amounts of fiber damage revealed by the thermal depley method.

(0/90) specimens

The indented facesheets were examined both visually and under a microscope. Permanent dents/dimples were seen in all indented facesheets at the point of indentation. The boundary of the dents were approximately

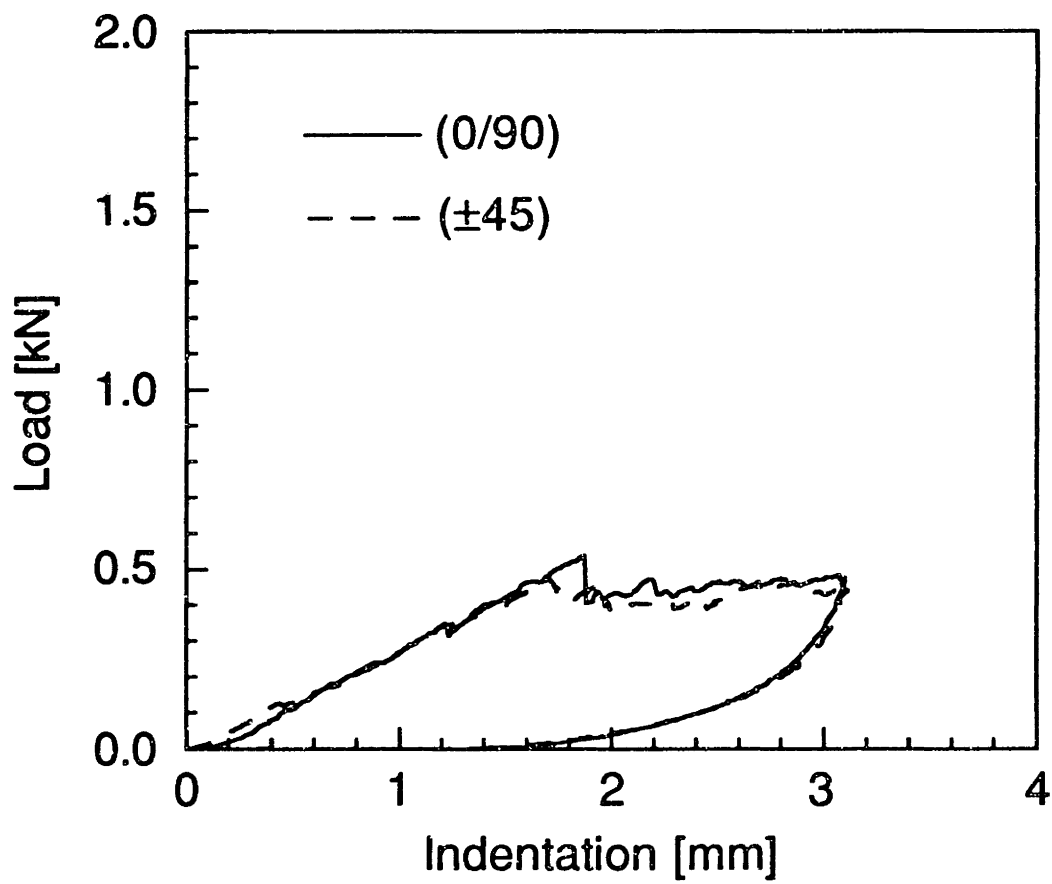


Figure 6.3 Load-indentation curves of specimens with (0/90) facesheets and with (±45) facesheets indented with the 12.7 mm-diameter indenter.

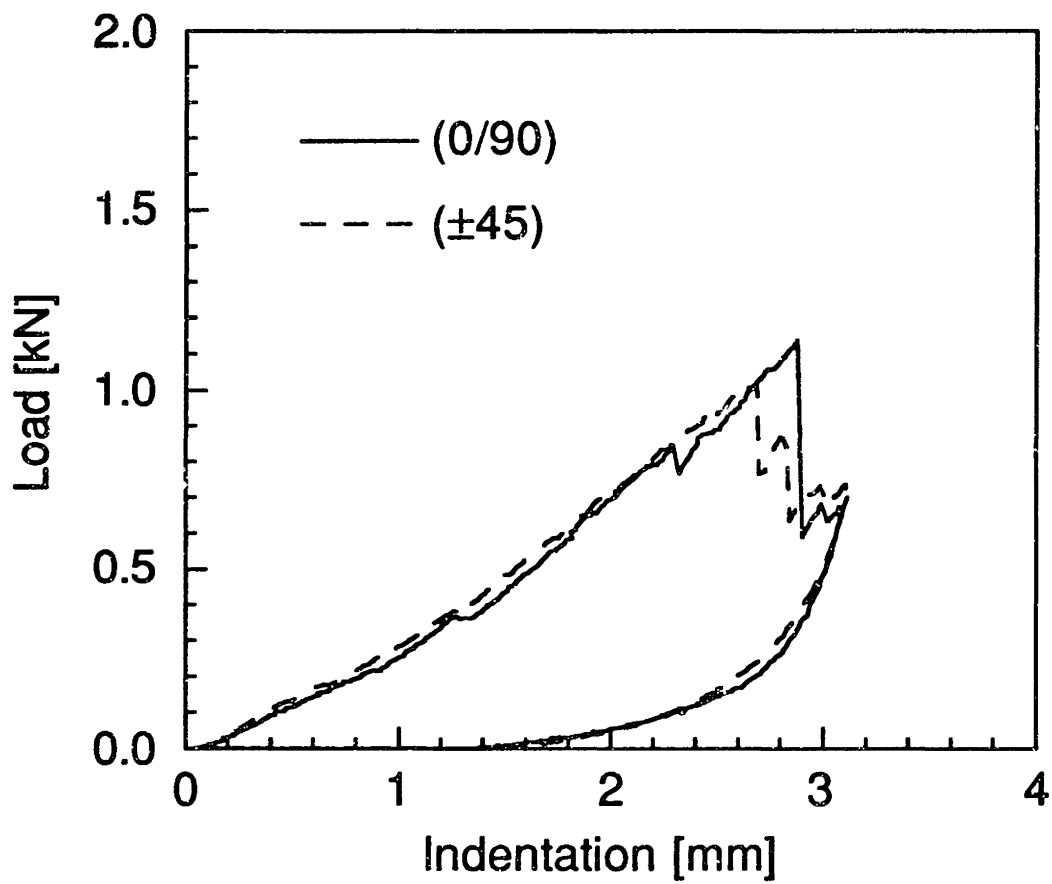


Figure 6.4 Load-indentation curves of specimens with (0/90) facesheets and with (±45) facesheets indented with the 25.4 mm-diameter indenter.

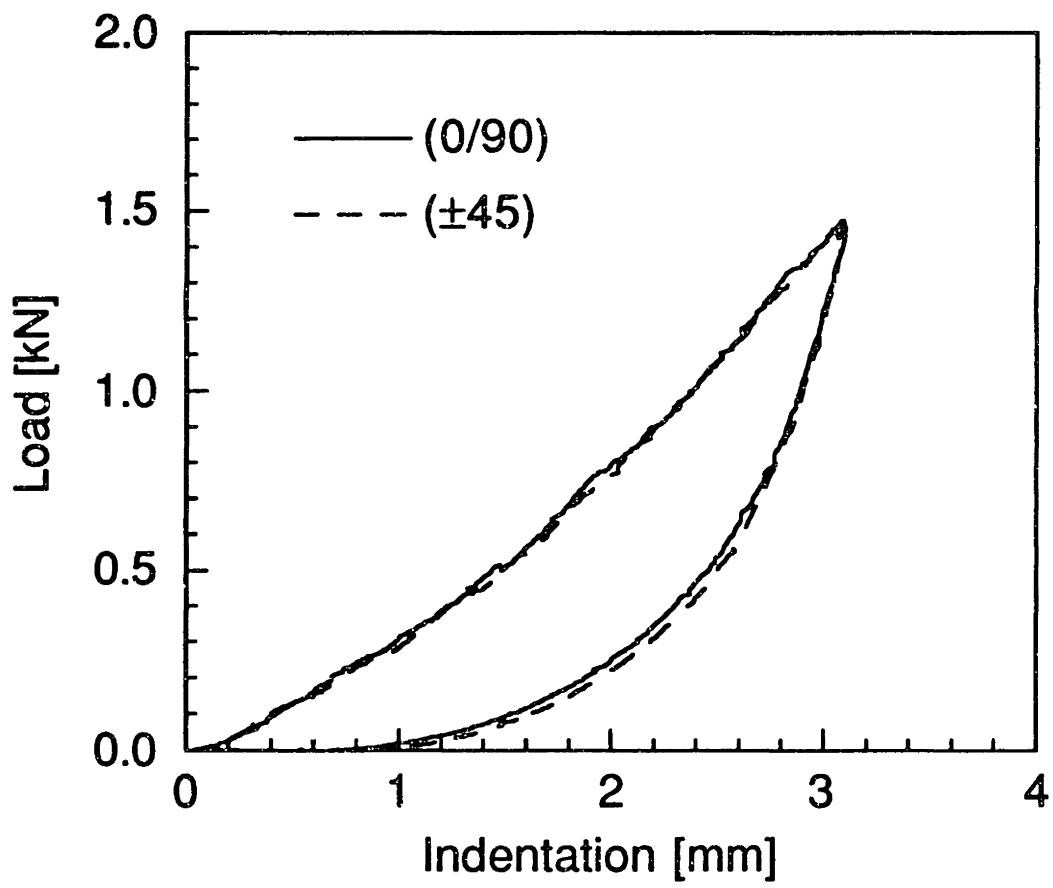
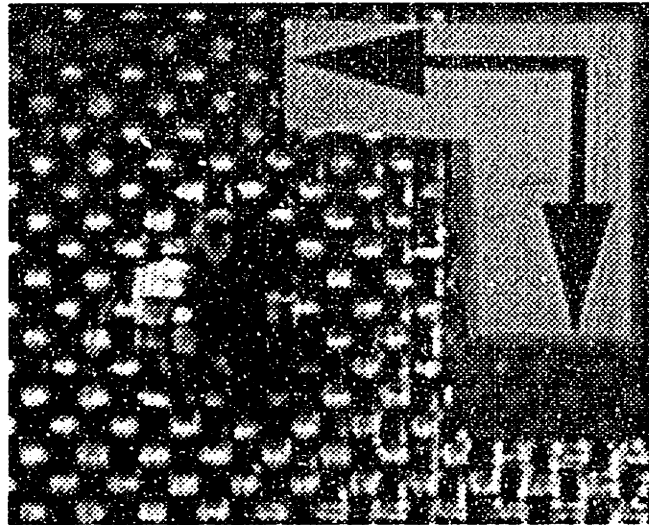


Figure 6.5 Load-indentation curves of specimens with (0/90) facesheets and with (±45) facesheets indented with the 38.1 mm-diameter indenter.

rectangular with the diagonals of the dents aligned with the tows of the fabric facesheet as shown in Figures 6.6 through 6.8.

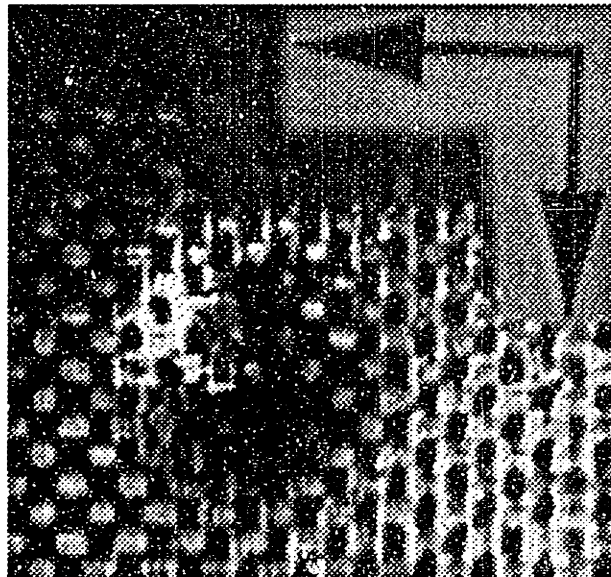
Under the microscope, matrix cracks could be seen extensively within the dimple in the case of indentation with the 12.7 mm-diameter indenter. No facesheet damage was observed outside the dimple. These matrix cracks were bounded within the "checkerboard squares" (referred to as "squares" in this section) formed by the interweave of the tows. Each square is, thus, formed by a tow of fibers. Fiber damage was seen mainly along borders between two adjacent tows as illustrated in Figure 6.9. The fiber damage sites within individual squares coalesce to form two "fractures" in the form of a cross (see Figure 6.9). The fractures always run between two adjacent tows and along the tow directions. A photograph of this typical fracture pattern in specimens with (0/90) facesheets for the case of indentation with the 12.7 mm-diameter indenter is shown in Figure 6.10. The facesheet damage inflicted by indentation with the 25.4 mm-diameter indenter looks similar to that for the case of the 12.7 mm-diameter indenter except that fewer matrix cracks and less fiber damage were observed in the former case. No facesheet damage was seen in the case of the 38.1 mm-diameter indenter.

Typical X-radiographs of specimens with (0/90) facesheets indented with the three different indentors are shown in Figure 6.11. A cross-shaped fracture pattern can clearly be identified for the case of indentation with the 12.7 mm-diameter indenter. This pattern is aligned with the tows of the fabric facesheet. The tow directions of the facesheet are identified by the tracer fibers running vertically and horizontally in the X-radiographs. Facesheet damage can also be observed for the 25.4 mm-diameter indenter but the cross-shaped fracture pattern can no longer be clearly identified. No



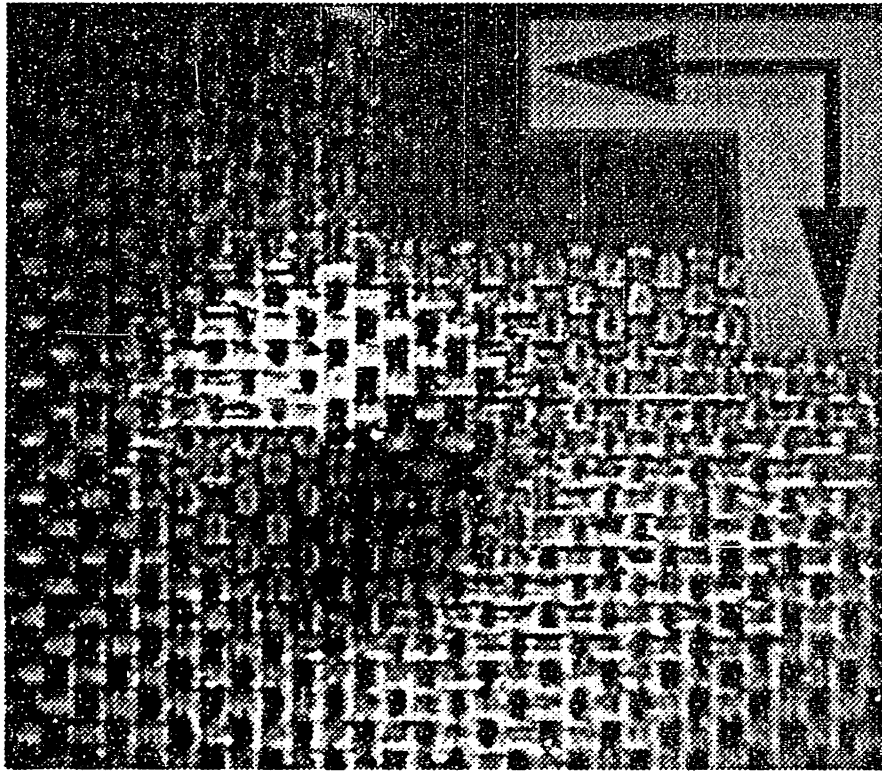
10 mm

Figure 6.6 Permanent dent/dimple due to indentation with the 12.7 mm-diameter indenter in a specimen with (0/90) facesheets.



10 mm

Figure 6.7 Permanent dent/dimple due to indentation with the 25.4 mm-diameter indenter in a specimen with (0/90) facesheets.



10 mm

Figure 6.8 Permanent dent/dimple due to indentation with the 38.1 mm-diameter indenter in a specimen with (0/90) facesheets.

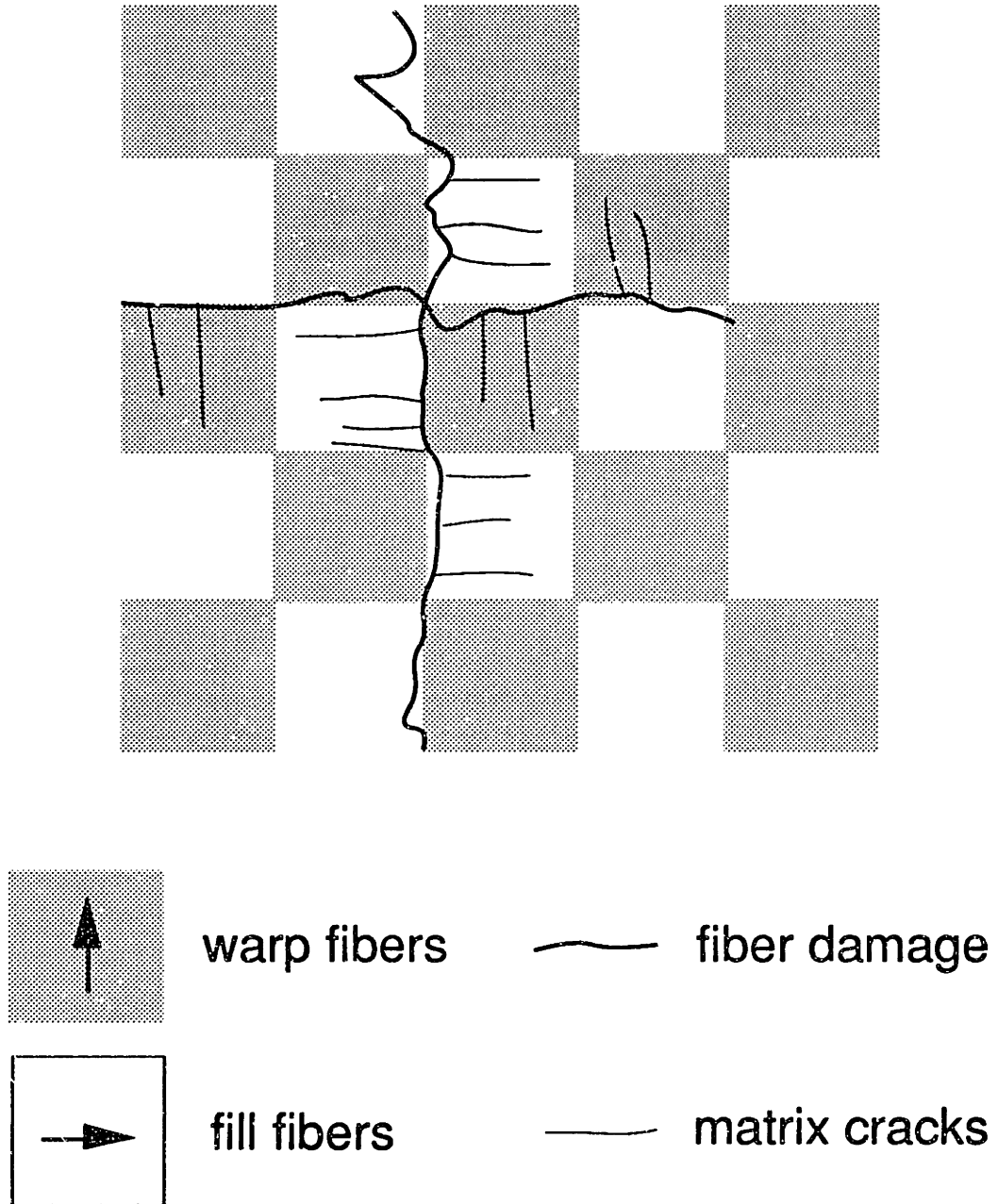
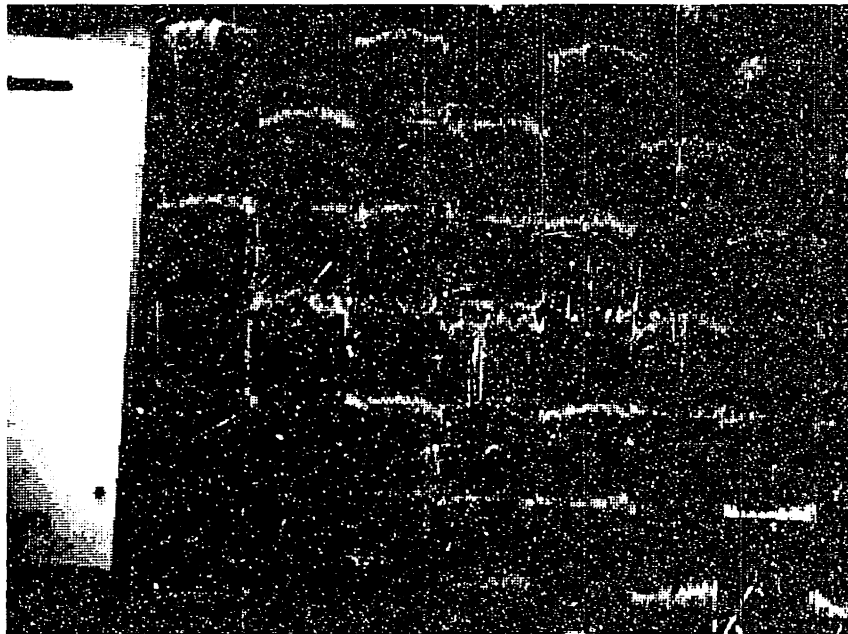


Figure 6.9 Sketch of facesheet damage due to indentation in specimens with (0/90) facesheets.



10 mm

Figure 6.10 Photograph of facesheet damage due to indentation with the 12.7 mm-diameter indenter in a specimen with (0/90) facesheets.

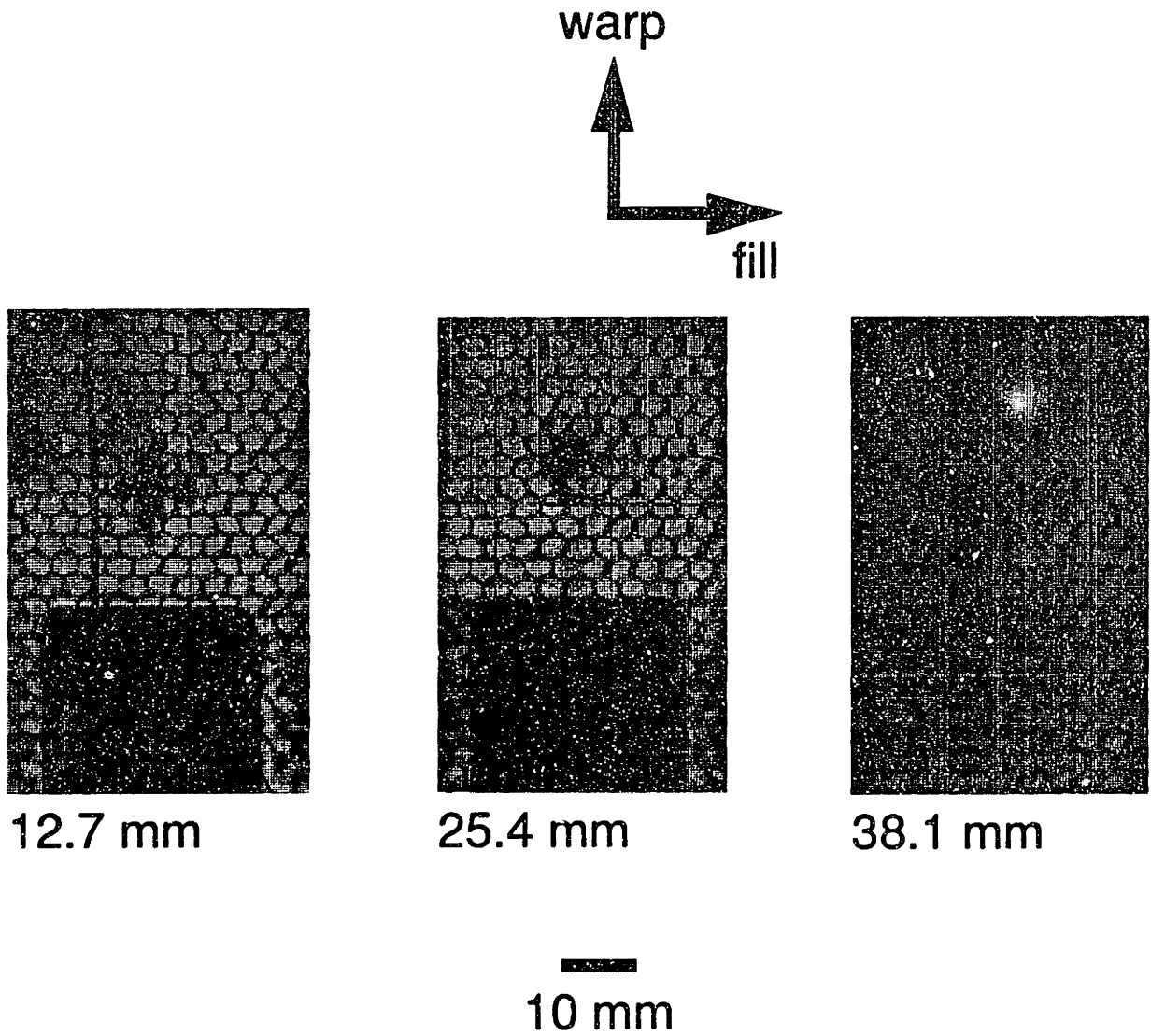


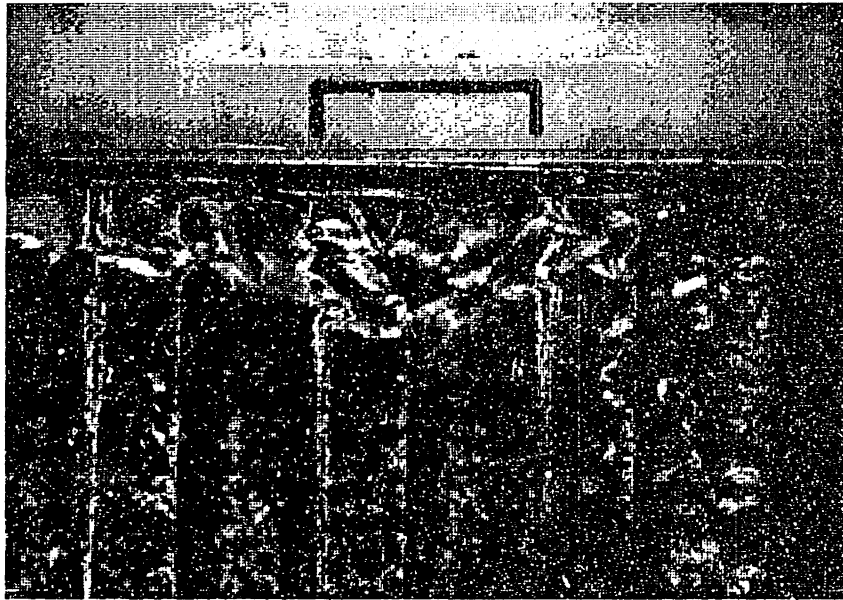
Figure 6.11 Typical X-radiographs of the specimens with (0/90) facesheets indented with the three different indentors.

facesheet damage is observed in the X-radiograph for the 38.1 mm-diameter indenter.

Some indented specimens were sectioned along the warp direction of the facesheet through the center of the dimple. These cross-sections are shown in Figures 6.12 through 6.14. Core damage is manifested mainly as buckled/crushed cell walls. For the case of indentation with the 12.7 mm-diameter indenter, some cell walls split along the thickness direction. The in-plane extent of core damage, as measured along the interface between the core and the facesheet, is 10 mm for the case of the 12.7 mm-diameter indenter, 13 mm for the case of the 25.4 mm-diameter indenter, and 16 mm for the case of the 38.1 mm-diameter indenter. It should be pointed out that quantitative measurements of core damage made on cross-sections should only be used in a relative sense because the measurements are affected by factors that are difficult to control. First, the location of a section is difficult to control precisely because of the use of visual alignment on the milling machine table and the finite thickness (1.2 mm) of the cutting wheel. Second, the honeycomb core is not a continuum and, hence, the resolution of the measurements of core damage is limited by the size of the cells (3.18 mm).

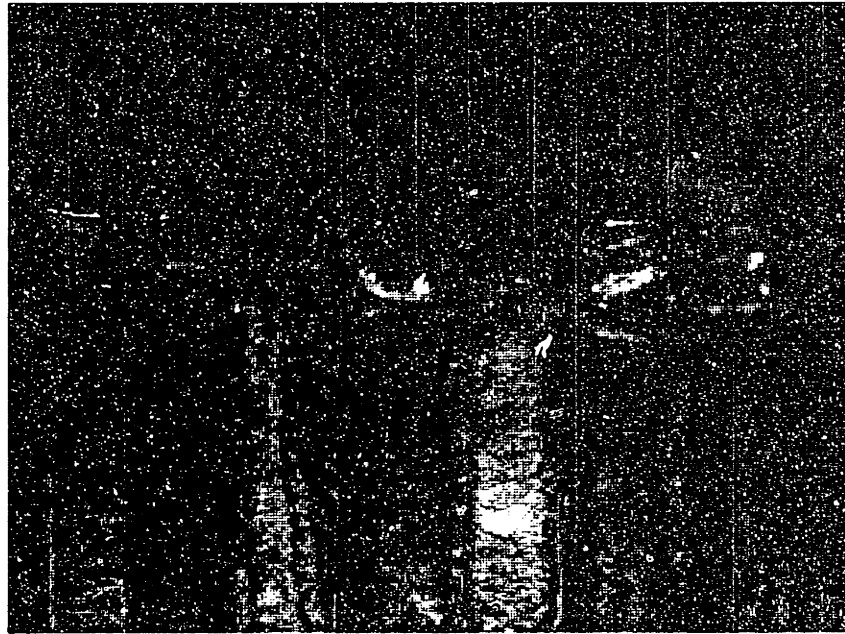
Significant rebound of the indented facesheet from the 3 mm indentation depth is observed for all three indenter diameters. The 38.1 mm-diameter shows the most rebound, followed by the 25.4 mm-diameter indenter and the 12.7 mm-diameter indenter. Quantitative measurements of the dimple profiles are presented later in Section 6.1.3.

Fiber breakage and a pair of delaminations can be observed in the facesheet of the specimen indented with the 12.7 mm-diameter indenter. Each of these delaminations is less than 5 mm long and they are located



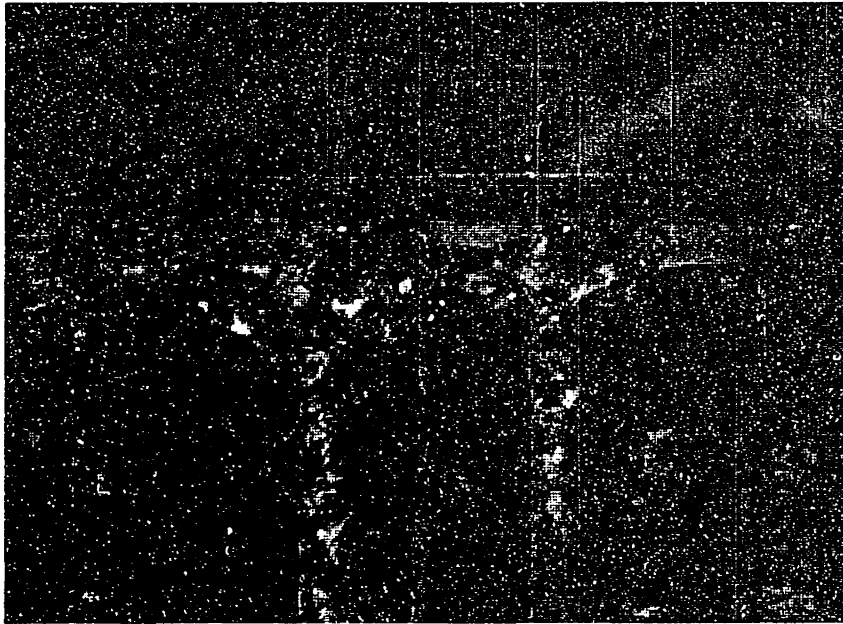
5 mm

Figure 6.12 Photograph of cross-section of a specimen with (0/90) facesheets indented with the 12.7 mm-diameter indenter.



5 mm

Figure 6.13 Photograph of cross-section of a specimen with (0/90) facesheets indented with the 25.4 mm-diameter indenter.



5 mm

Figure 6.14 Photograph of cross-section of a specimen with (0/90) facesheets indented with the 38.1 mm-diameter indenter.

symmetrically about the point of indentation. They are about 1 mm apart and are separated by a region of fiber damage. In the case of the 25.4 mm-diameter indenter, the facesheet sustains smaller (less than 3 mm) delaminations which are, again, located symmetrically about the point of indentation and about 1 mm apart. No facesheet damage was found in cross-sections of specimens indented with the 38.1 mm-diameter indenter.

Results from thermal depey show that the top ply of the indented facesheet always has less fiber damage than the bottom ply. The cross-shaped fracture pattern observed in the X-radiograph of the specimen indented with the 12.7 mm-diameter indenter consists of fiber breakage in both plies in the indented facesheet. The top ply of the facesheet indented with the 12.7 mm-diameter indenter has fiber damage in 4 to 6 squares near the center of the dimple while the bottom ply has fiber damage in 6 to 8 squares. The top ply of the facesheet indented with the 25.4 mm-diameter indenter has fiber damage in 2 to 4 squares near the center of the dimple while the bottom ply has fiber damage in 4 to 6 squares. The top ply of the facesheet indented with the 38.1 mm-diameter indenter has no fiber damage while the bottom ply has some fiber damage within one square near the center of the dimple.

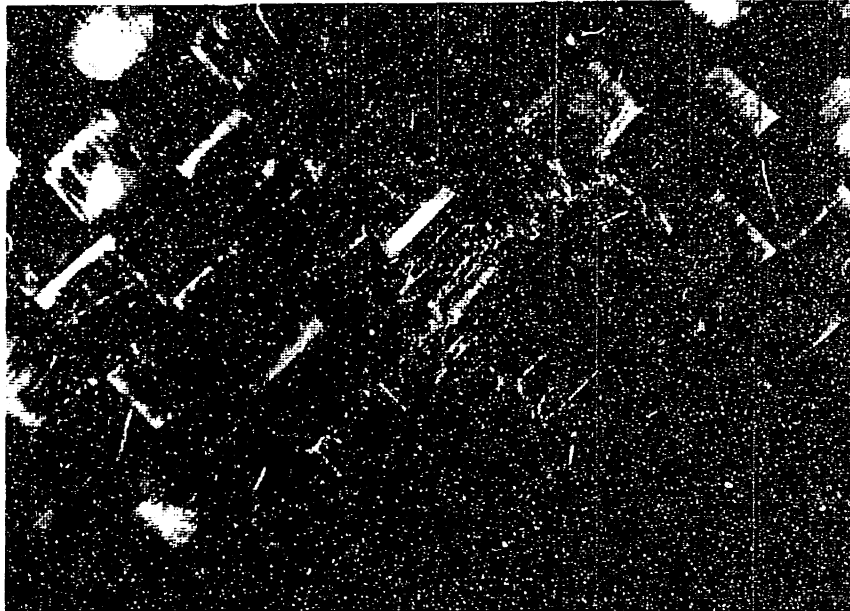
(±45) specimens

The indented facesheets were examined both visually and under a microscope. Permanent dents/dimples were seen in all indented facesheets at the point of indentation. The boundary of the dents were approximately rectangular with the diagonals aligned with the tows of the fabric facesheet in a manner similar to the specimens with (0/90) facesheets.

Under the microscope, matrix cracks could be seen extensively within the dimple in the case of indentation with the 12.7 mm-diameter indenter.

No facesheet damage was observed outside the dimple. These matrix cracks were again bounded within the "checkerboard squares" formed by the interweave of the tows. Each square is, thus, formed by a tow of fibers. Fiber damage was seen mainly along borders between two adjacent tows. The fiber damage sites within individual squares coalesce to form two "fractures" in the form of a cross. The fractures always run between two adjacent tows and along the tow directions. A photograph of the typical fracture pattern in a specimen with (± 45) facesheets for the case of indentation with the 12.7 mm-diameter indenter is shown in Figure 6.15. The facesheet damage inflicted by indentation with the 25.4 mm-diameter indenter looks similar to that for the case of the 12.7 mm-diameter indenter except that fewer matrix cracks and less fiber damage were observed in the former case. Once again, no facesheet damage was seen in the case of the 38.1 mm-diameter indenter. Apart from being rotated by 45° , the fracture patterns of the specimens with (± 45) facesheets are not distinguishable from the corresponding cases of the specimens with (0/90) facesheets.

Typical X-radiographs of specimens indented with (± 45) facesheets by the three different indentors are shown in Figure 6.16. A cross-shaped fracture pattern can again be seen for the case of the 12.7 mm-diameter indenter. The cross is again aligned with the tows of the fabric facesheet. The directions of the tows can be recognized by the tracer fibers running at 45° angles. There are also tracer fibers running vertically and horizontally in Figure 6.16. They belong to the bottom facesheet which has a (0/90) layup. The cross-shaped fracture pattern is no longer recognizable for the case of the 25.4 mm-diameter indenter although there continues to be facesheet damage. No facesheet damage is observed in the X-radiograph for the case of the 38.1 mm-diameter indenter.



10 mm

Figure 6.15 Photograph of facesheet damage due to indentation with the 12.7 mm-diameter indenter in a specimen with (± 45) facesheets.

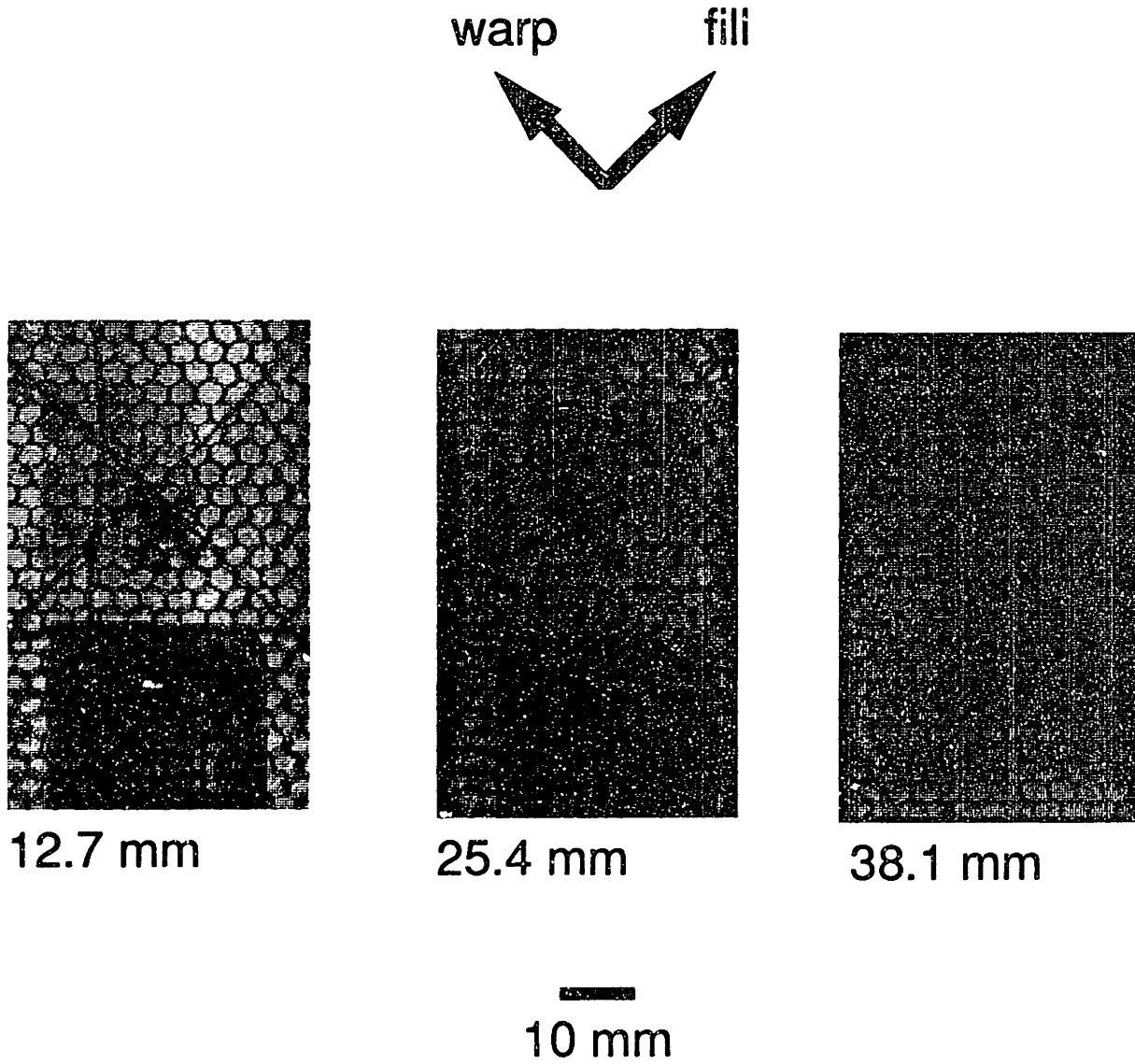
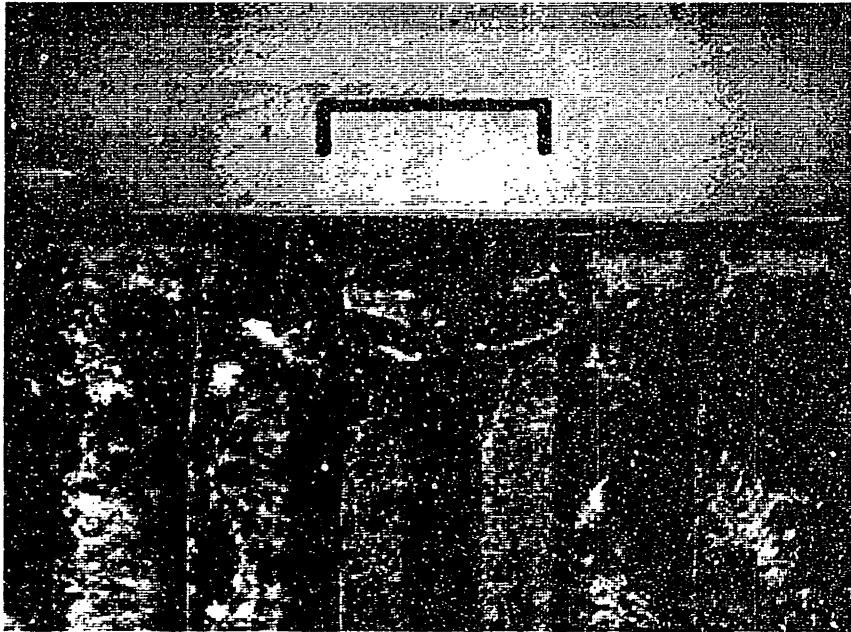


Figure 6.16 Typical X-radiographs of specimens with (± 45) facesheets indented with the three different indentors.

Some indented specimens were sectioned along the warp direction through the center of the dimple. These cross-sections are shown in Figures 6.17 through 6.19. Core damage is again manifested mainly as buckled/crushed cell walls. For the case of indentation with the 25.4 mm-diameter indenter, some cell walls split along the thickness direction. The in-plane extent of core damage, as measured along the interface between the core and the facesheet, is 12 mm for the case of the 12.7 mm-diameter indenter, 14 mm for the case of the 25.4 mm-diameter indenter, and 17 mm for the case of the 38.1 mm-diameter indenter. The measurements are the same, within accuracy of the measuring method, as those made in the corresponding specimens with (0/90) facesheets. It should again be noted that quantitative measurements made on cross-sections should only be used in a relative sense.

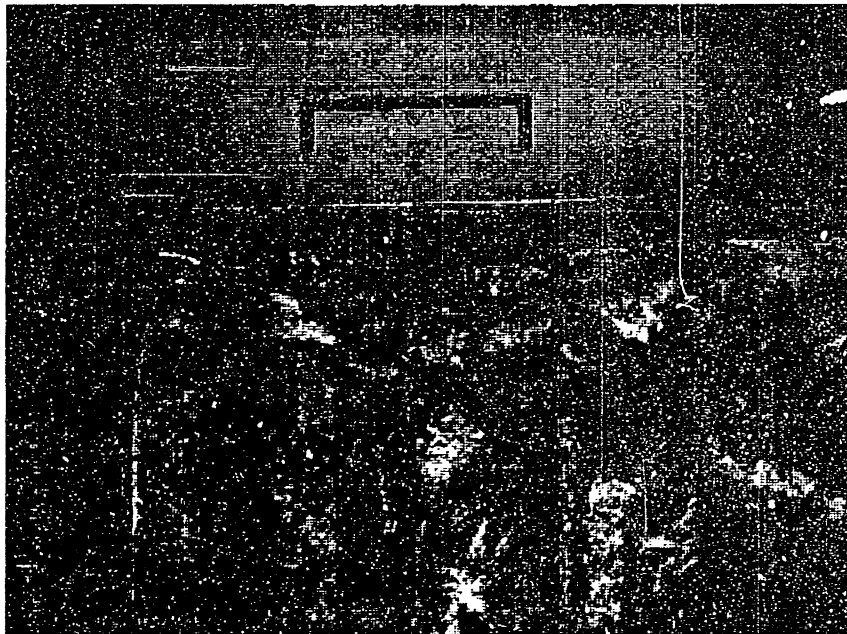
Once again, significant rebound of the indented facesheet from the 3 mm indentation depth is observed for all three indenter diameters. The specimen indented with the 38.1 mm-diameter indenter had the most rebound from the maximum indentation depth of 3 mm, followed by the specimen indented with the 25.4 mm-diameter indenter and the 12.7 mm-diameter indenter. Again, quantitative measurements of the dimple profiles are presented later in Section 6.1.3.

Fiber breakage and a pair of delaminations can be seen in specimens indented with the 12.7 mm-diameter indenter. Similar to the case of specimens with (0/90) facesheets, each of these delaminations is less than 5 mm long and they are located symmetrically about the point of indentation. They are about 1 mm apart and separated by a region of fiber breakage. The facesheet indented with the 25.4 mm-diameter sustains smaller (less than 3 mm long) delaminations which are, again, located symmetrically



5 mm

Figure 6.17 Photograph of cross-section of a specimen with (± 45) facesheets indented with the 12.7 mm-diameter indenter.



5 mm

Figure 6.18 Photograph of cross-section of a specimen with (± 45) facesheets indented with the 25.4 mm-diameter indenter.



5 mm

Figure 6.19 Photograph of cross-section of a specimen with (± 45) facesheets indented with the 38.1 mm-diameter indenter.

about the point of indentation about 1 mm apart. A couple of delaminations, about 2 mm long, were found in the cross-section of a specimen indented with the 38.1 mm-diameter indenter. Matrix cracks were also seen within one tow in the bottom ply near the point of indentation but without connection to the delamination.

Results from thermal depley show that the top ply of the indented facesheet always has less fiber damage than the bottom ply. The cross-shaped fracture pattern observed in the X-radiograph of specimens indented with the 12.7 mm-diameter indenter consists of fiber breakage in both plies in the indented facesheet. The top ply of the facesheet indented with the 12.7 mm-diameter indenter has fiber damage in 4 to 6 squares near the center of the dimple while the bottom ply has fiber damage in 6 to 8 squares. The top ply of the facesheet indented with the 25.4 mm-diameter indenter has fiber damage in 2 to 4 squares near the center of the dimple while the bottom ply has fiber damage in 4 to 6 squares. The top ply of the facesheet indented with the 38.1 mm-diameter indenter has no fiber damage while the bottom ply has some fiber damage within one square near the center of the dimple. The fiber damage revealed by the thermal depley method for specimens with (± 45) facesheets is again basically the same as that for specimens with (0/90) facesheets, when viewed relative to the tow directions.

6.1.3 Simulated Damage Types

The results from the characterization process of static indentation damage were used to design specimens with simulated core damage and specimens with simulated facesheet damage. These simulated damage types were examined via some of the damage characterization techniques

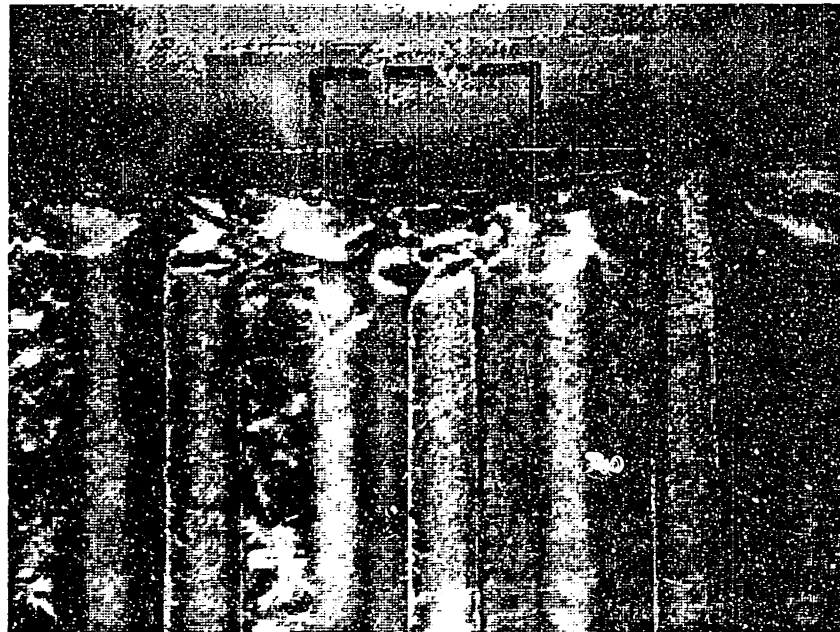
used for indented specimens. The results are compared with the corresponding static indentation damage to verify that these simulated damage types are good physical representations of the facesheet damage and the core damage observed in the indented specimens.

Three specimens with simulated core damage and (0/90) facesheets were inspected by some of the techniques used for the static indentation damage described in Section 6.1.2. These specimens represent the three different damage levels used to simulate the core damage in specimens indented with the 12.7 mm-diameter indenter (SCD1), specimens indented with the 25.4 mm-diameter indenter (SCD2), and specimens indented with the 38.1 mm-diameter indenter (SCD3). No facesheet damage was observed in the X-radiographs of these specimens with simulated core damage. The cross-sections of these specimens are shown in Figures 6.20 through 6.22. The in-plane extent of core damage, as measured along the interface between the core and the facesheet, is 10 mm for the case of SCD1, 12 mm for the case of SCD2, and 14 mm for the case of SCD3. The core damage in the specimens with simulated core damage, thus, show the same trend as that in the specimens with static indentation damage where measurements of 10 mm, 13 mm, and 16 mm were obtained. The core damage in the specimens with simulated core damage is, however, more localized than the corresponding one in the specimens with static indentation damage in the sense that the depth of crushed core decreases more quickly away from the point of indentation, as illustrated in Figure 6.23. The bondline between the crushed core and the facesheet is good for all three specimens with simulated core damage. The method of double-sided tape succeeded in pulling the crushed cell walls up from the maximum indentation depth in order to allow it to bond with the facesheet. No facesheet damage was



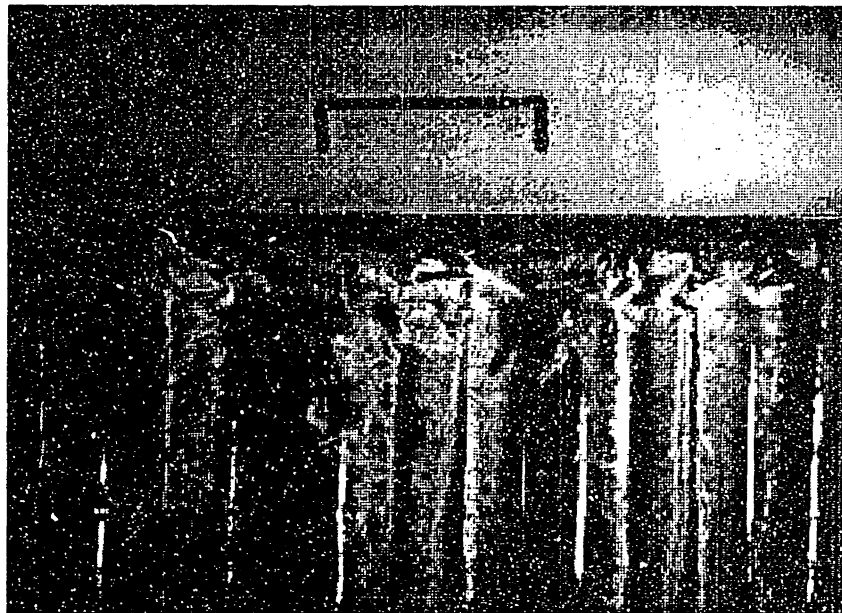
5 mm

Figure 6.20 Photograph of cross-section of a specimen with level 1 simulated core damage and (0/90) facesheets.



5 mm

Figure 6.21 Photograph of cross-section of a specimen with level 2 simulated core damage and (0/90) facesheets.



5 mm

Figure 6.22 Photograph of cross-section of a specimen with level 3 simulated core damage and (0/90) facesheets.

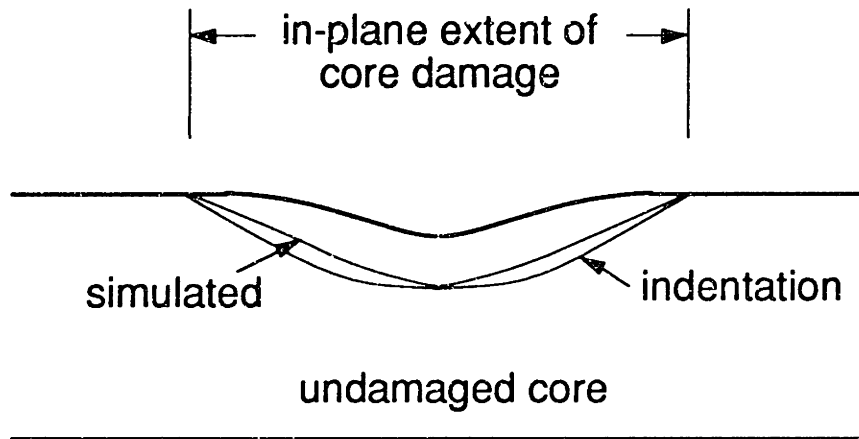


Figure 6.23 Sketch illustrating relative in-plane extent and through-thickness distribution of core damage in specimens with simulated core damage versus those with static indentation damage.

observed in the cross sections of any of these specimens with simulated core damage.

One of the key issues in the specimens with simulated core damage is to simulate the profile of the dimple caused by static indentation. The profiles of the dimples of both types of specimens were measured along the tow directions of the facesheet through the center of the dimple by means of a dial gage as described in Section 5.6.4. The comparisons between the profiles along the x-axis (warp direction) and the y-axis (fill direction) are shown in Figures 6.24 through 6.29. A good correlation exists in all cases between the specimens with static indentation damage and the specimens with simulated core damage. Note that the axis system shown in these figures has been shifted relative to the one used for the dimple propagation model. The origin of the axis system in Figures 6.24 through 6.29 is at the center of the dimple while that for the model is at one of the corners of the panel.

In order to conserve the prepreg for further manufacturing and due to the satisfactory results shown by the specimens with (0/90) facesheets which had simulated core damage, no specimens with simulated core damage and (± 45) facesheets were manufactured for sectioning. However, the profiles of the dimples were again measured along the tow directions of the (± 45) facesheets through the center of the dimple in these specimens. The profiles along the x-axis (warp direction) and the y-axis (fill direction) are given in Figures 6.30 through 6.35. The axis system in these figures is shifted such that the origin is at the center of the dimple. Once again, a good correlation between the specimens with static indentation damage and the specimens with simulated core damage is observed in all three cases.

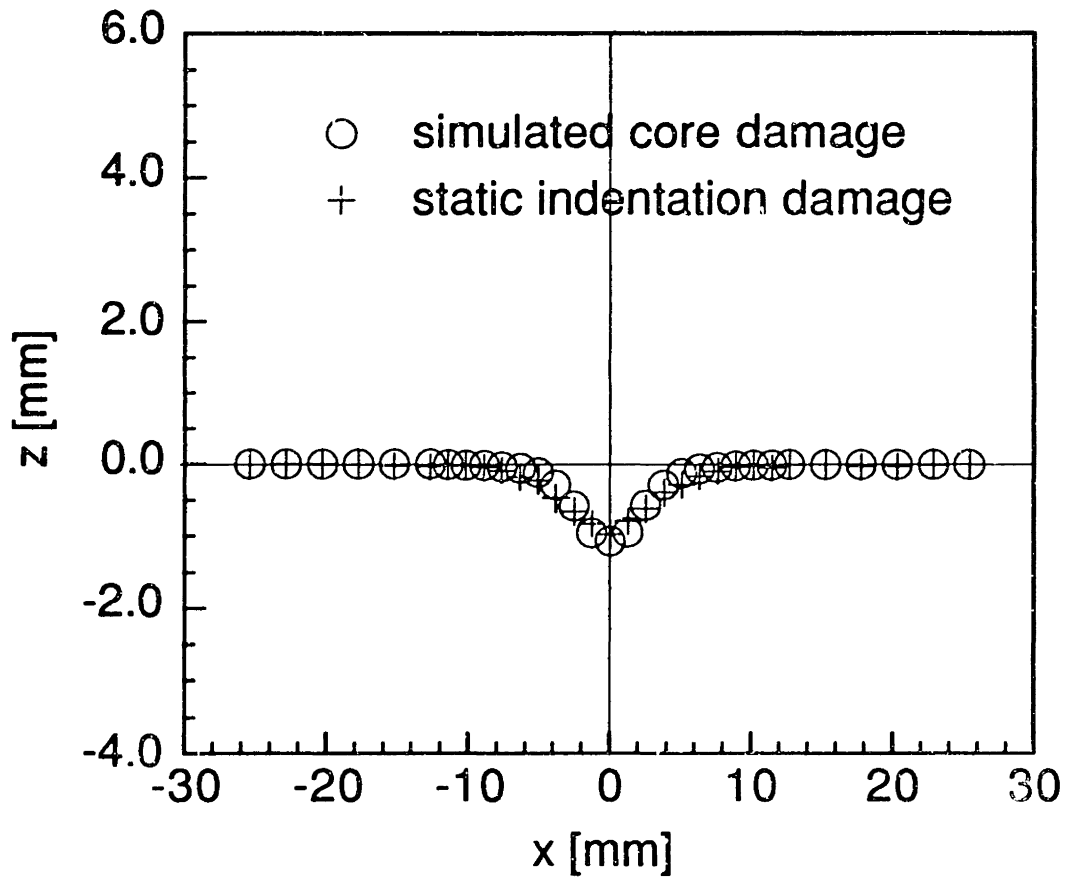


Figure 6.24 Dimple profiles along the warp direction of specimens with (0/90) facesheets and level 1 static indentation damage and level 1 simulated core damage.

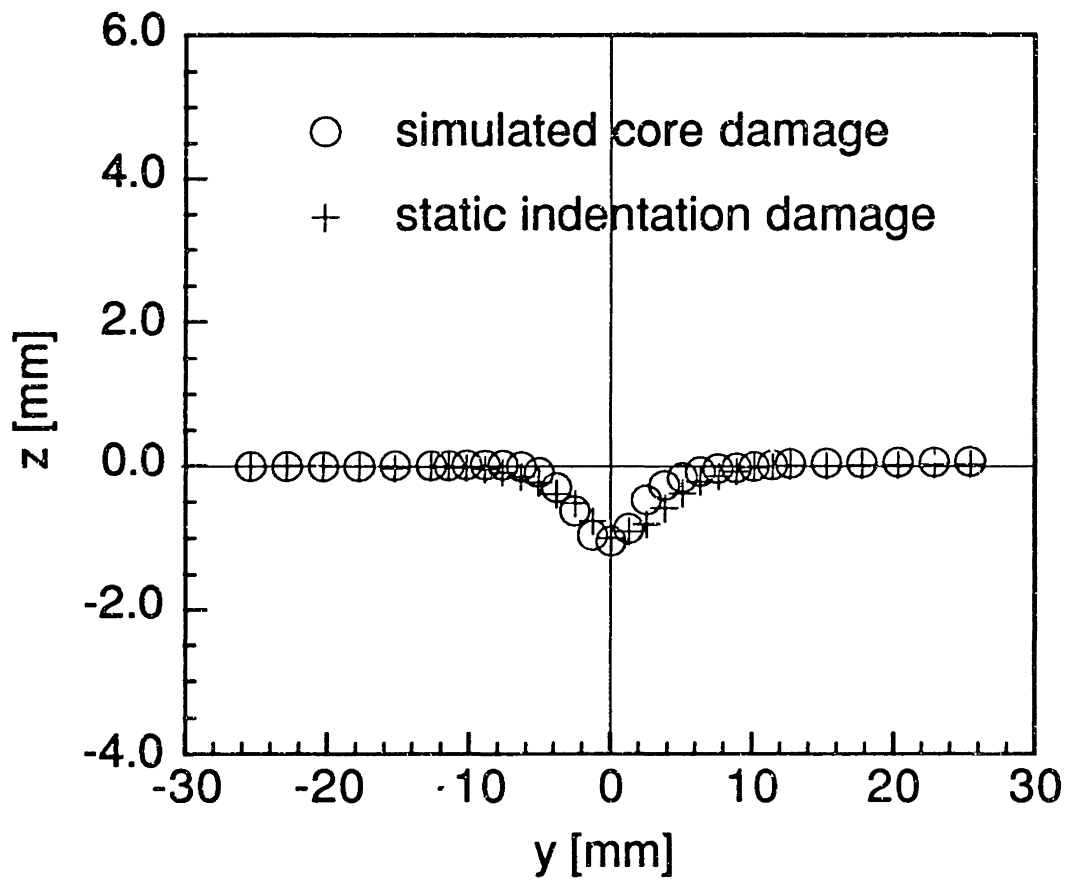


Figure 6.25 Dimple profiles along the fill direction of specimens with (0/90) facesheets and level 1 static indentation damage and level 1 simulated core damage.

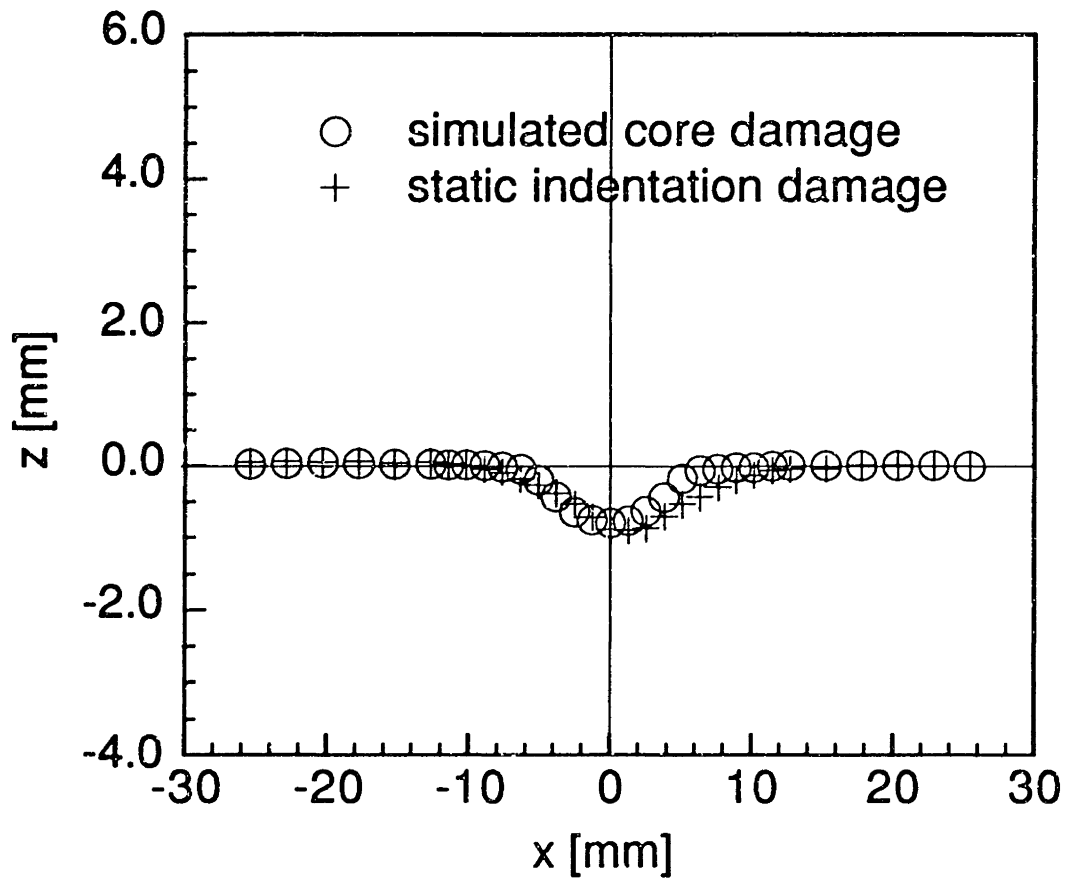


Figure 6.26 Dimple profiles along the warp direction of specimens with (0/90) facesheets and level 2 static indentation damage and level 2 simulated core damage.

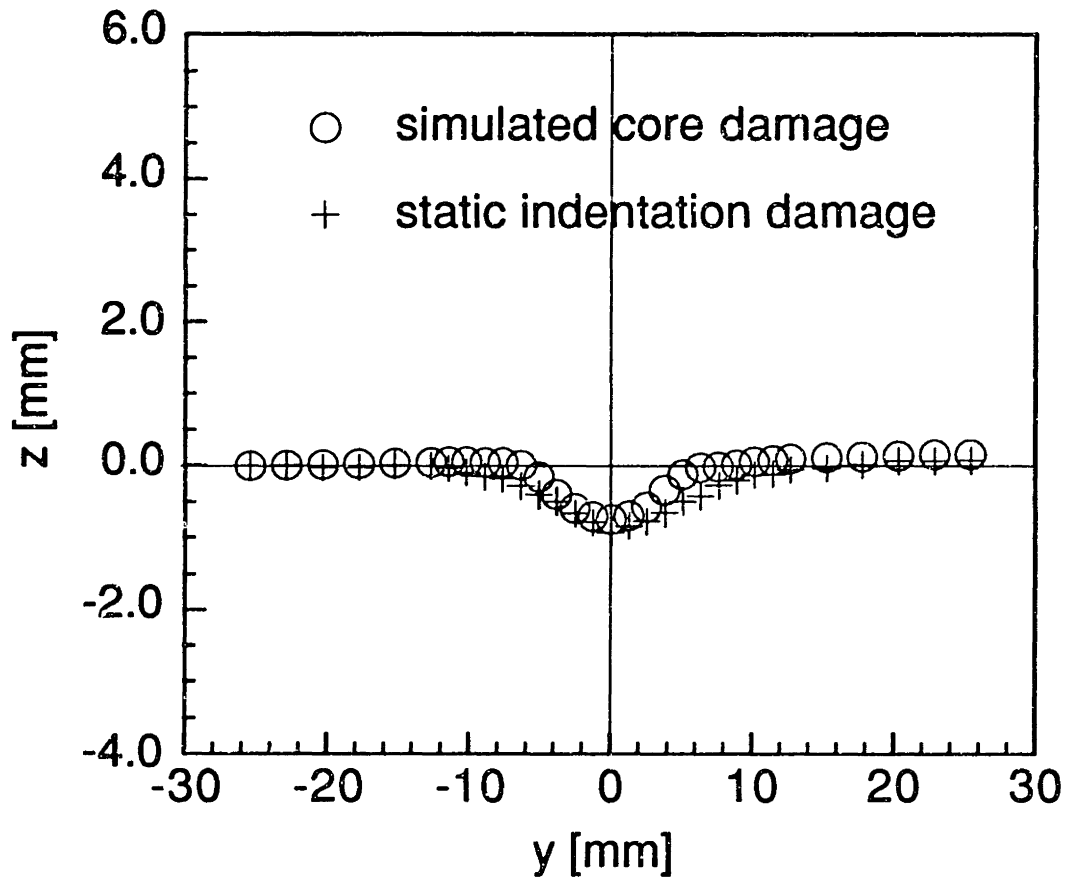


Figure 6.27 Dimple profiles along the fill direction of specimens with (0/90) facesheets and level 2 static indentation damage and level 2 simulated core damage.

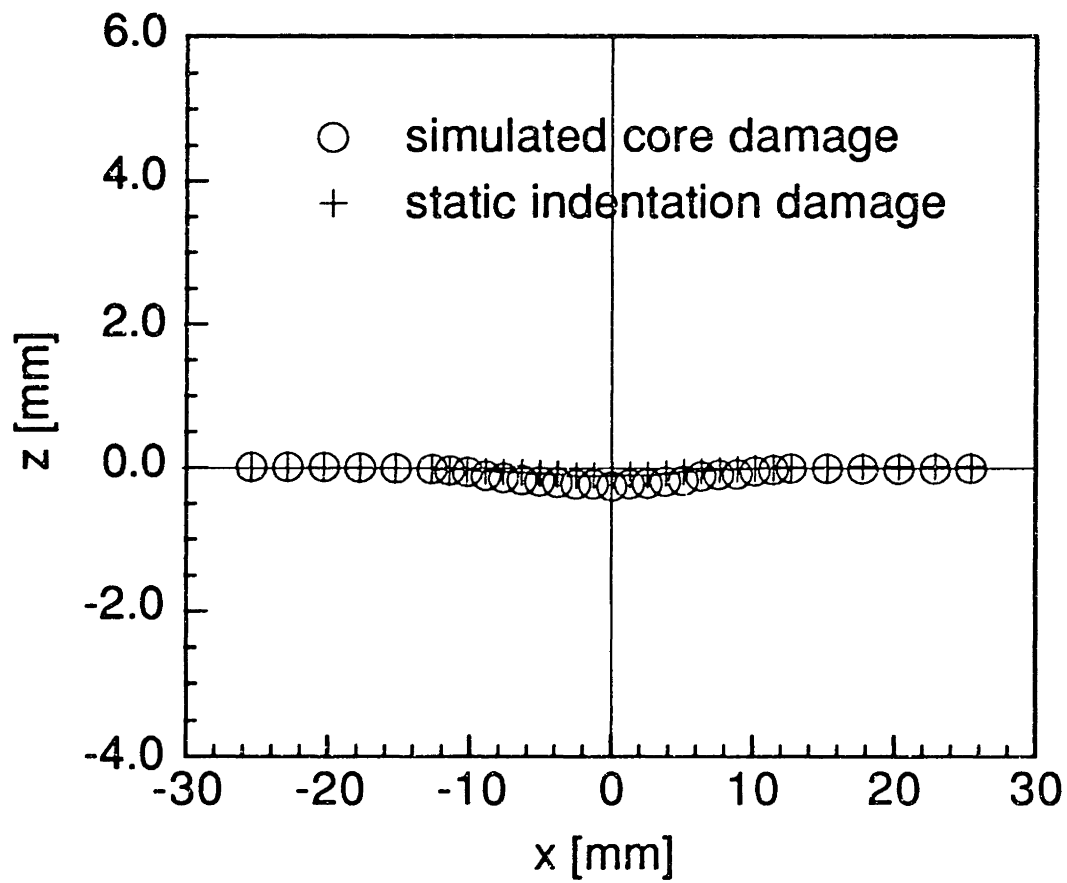


Figure 6.28 Dimple profiles along the warp direction of specimens with (0/90) facesheets and level 3 static indentation damage and level 3 simulated core damage.

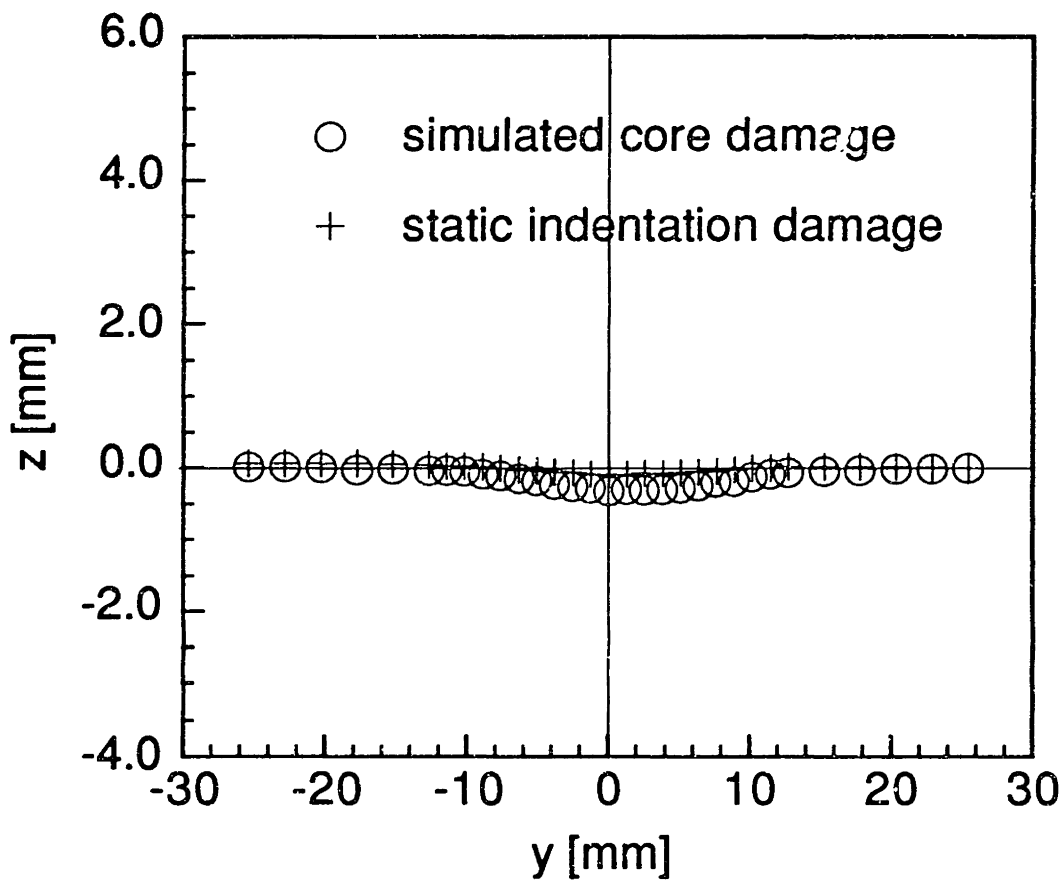


Figure 6.29 Dimple profiles along the fill direction of specimens with (0/90) facesheets and level 3 static indentation damage and level 3 simulated core damage.

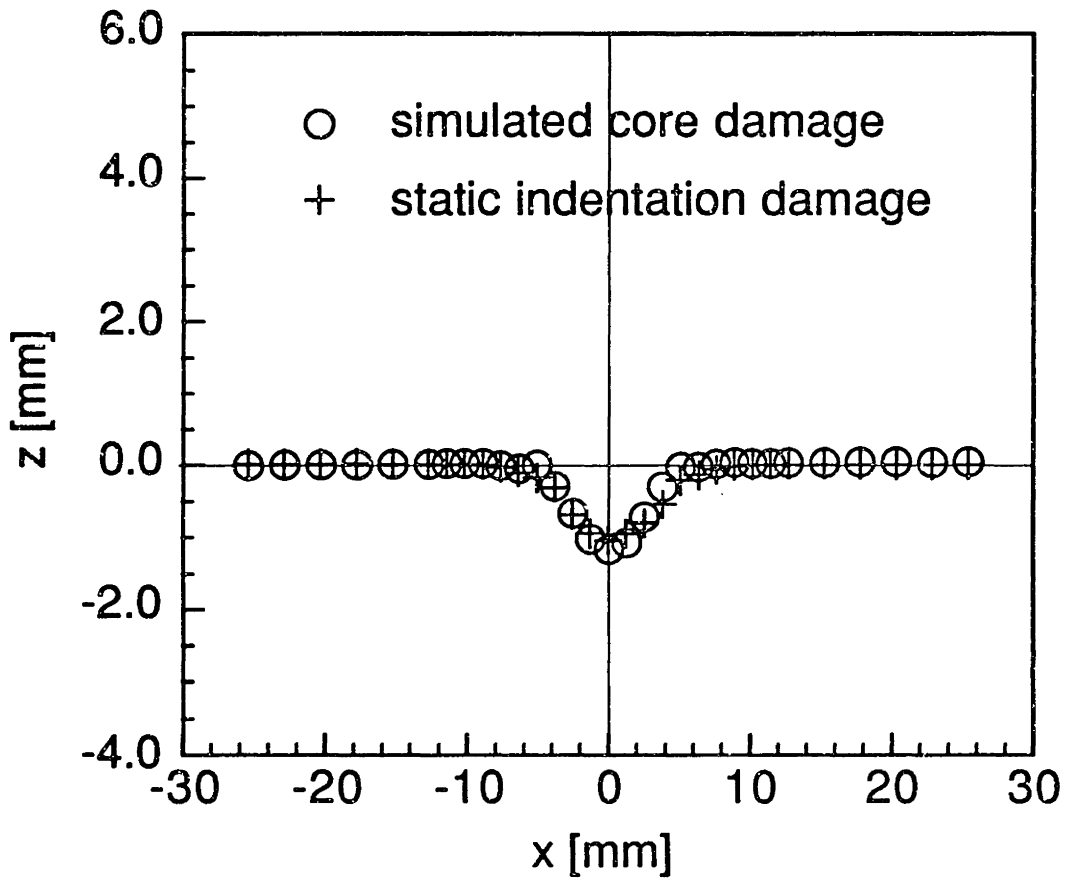


Figure 6.30 Dimple profiles along the warp direction of specimens with $(\pm 45^\circ)$ facesheets and level 1 static indentation damage and level 1 simulated core damage.

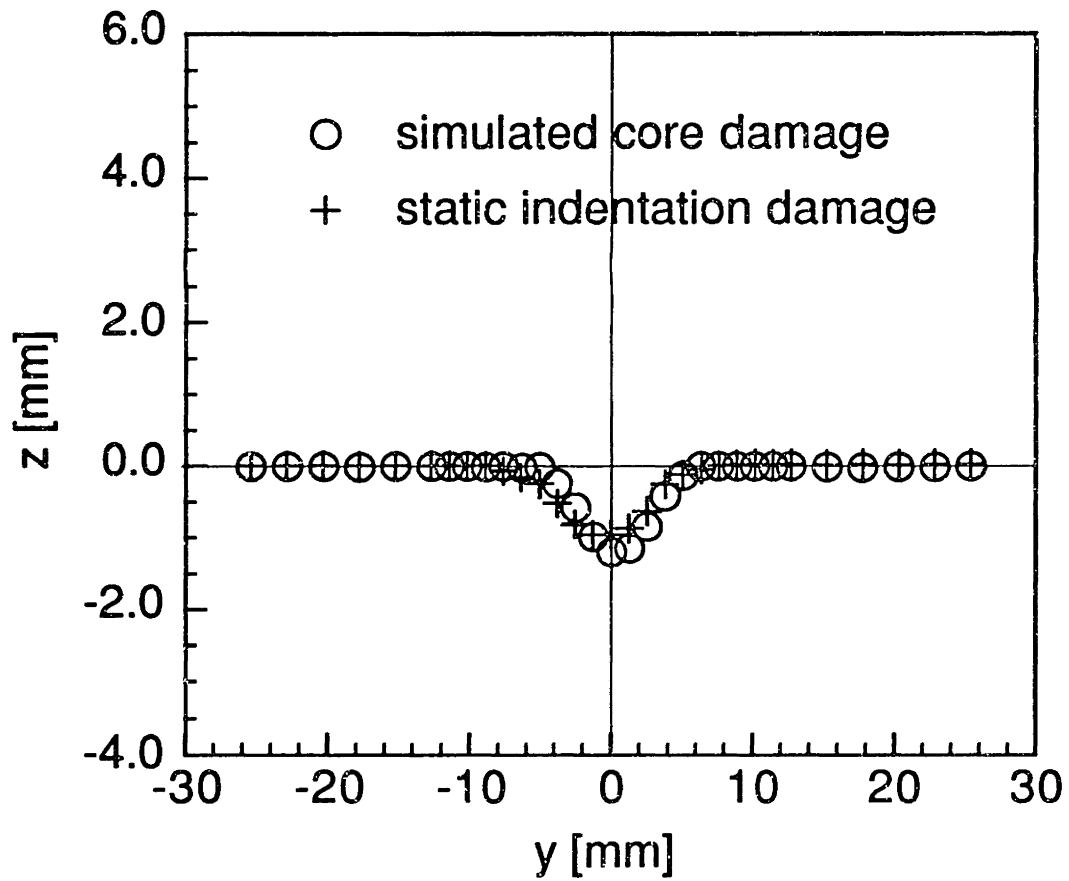


Figure 6.31 Dimple profiles along the fill direction of specimens with (± 45) facesheets and level 1 static indentation damage and level 1 simulated core damage.

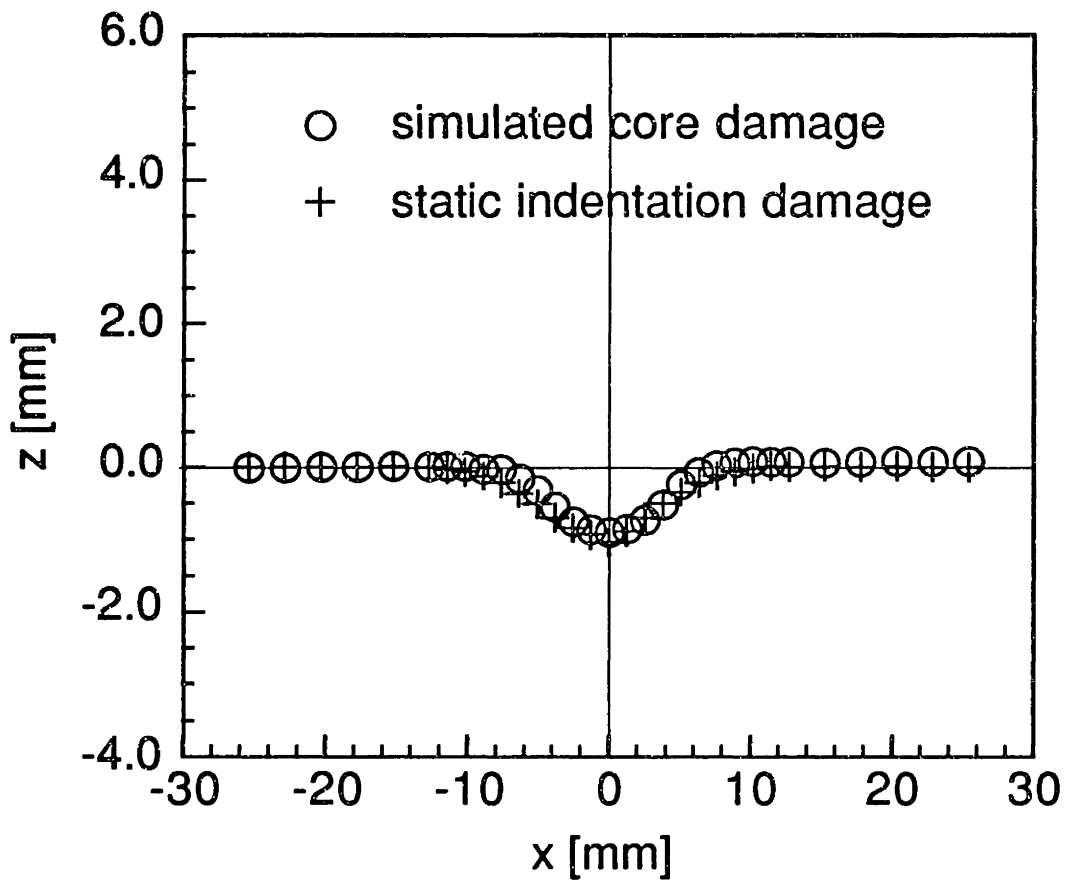


Figure 6.32 Dimple profiles along the warp direction of specimens with (± 45) facesheets and level 2 static indentation damage and level 2 simulated core damage.

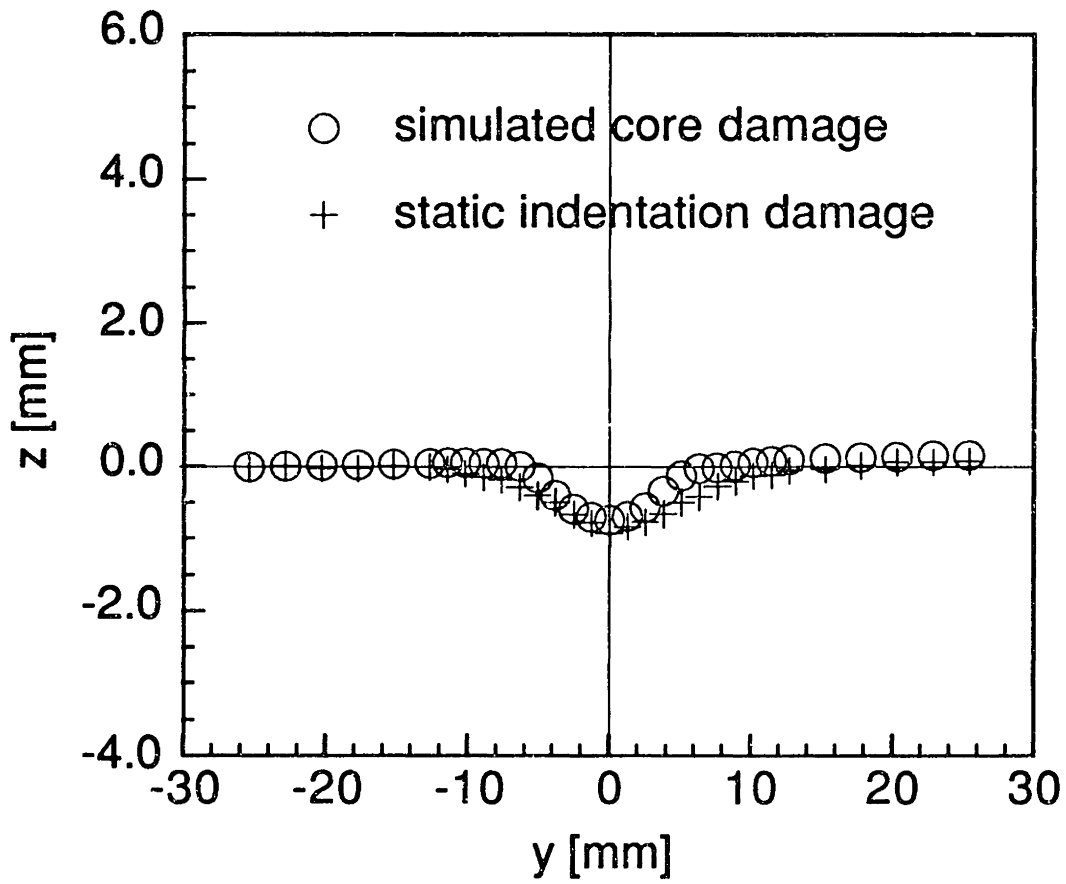


Figure 6.33 Dimple profiles along the fill direction of specimens with (± 45) facesheets and level 2 static indentation damage and level 2 simulated core damage.

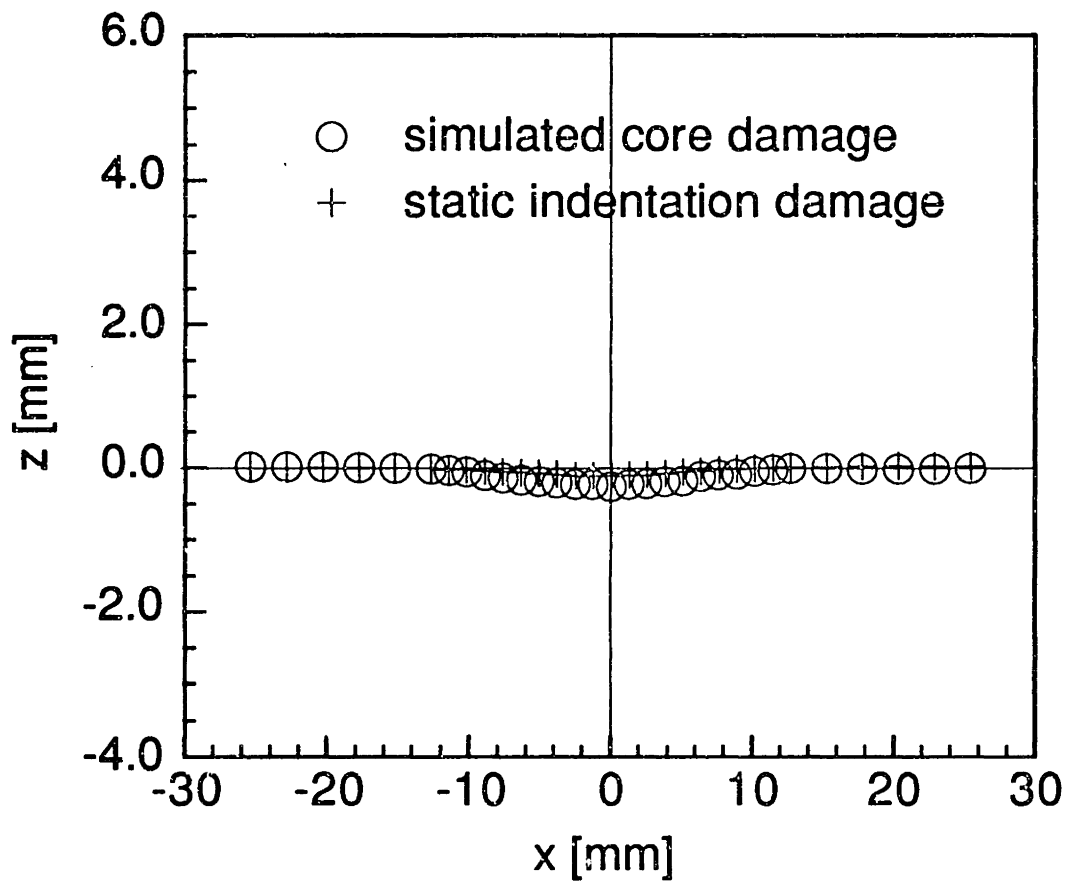


Figure 6.34 Dimple profiles along the warp direction of specimens with (± 45) facesheets and level 3 static indentation damage and level 3 simulated core damage.

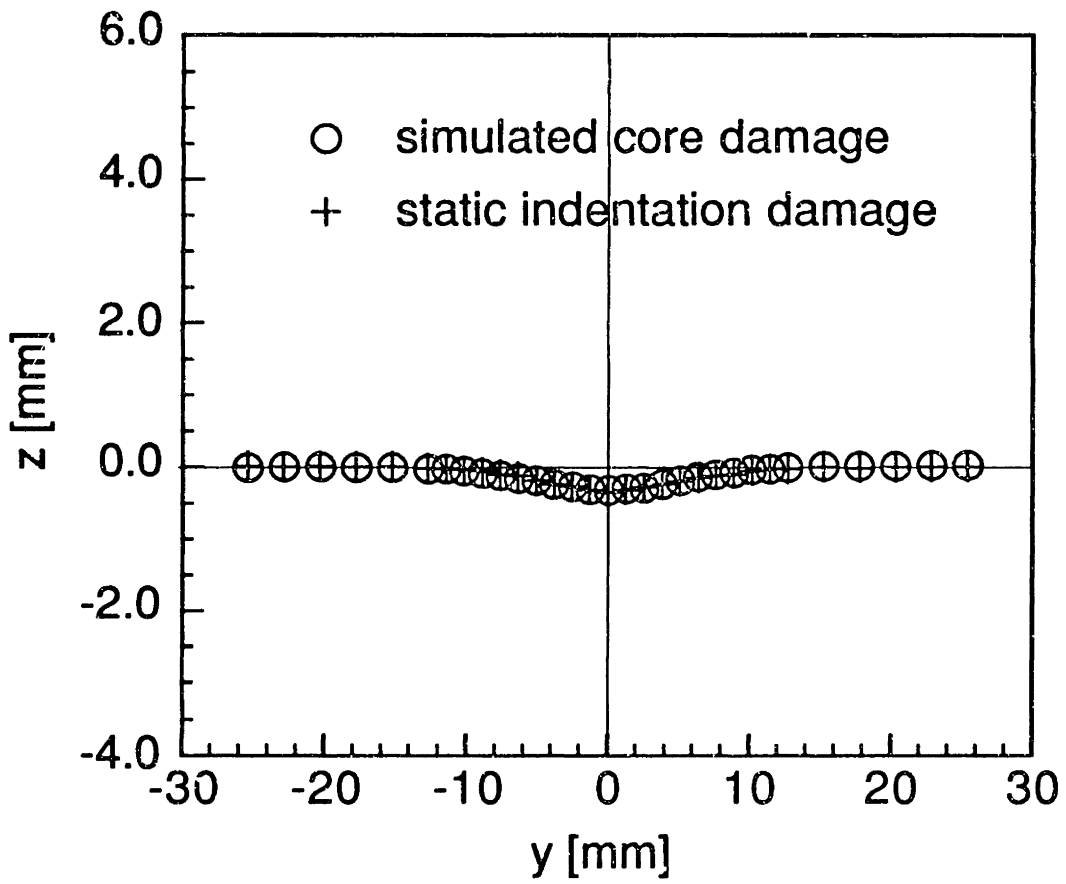


Figure 6.35 Dimple profiles along the fill direction of specimens with (± 45) facesheets and level 3 static indentation damage and level 3 simulated core damage.

Specimens with simulated facesheet damage

Characterization of the static indentation damage (see Section 6.1.2) shows that only the 12.7 mm-diameter indenter created a well-defined damage pattern in the facesheet. Therefore, only one set of specimens with simulated facesheet damage was manufactured to simulate this case. As described in Chapter 5, a pair of slits in the form of a cross was cut in the facesheet. In accordance with the characteristics of the fracture pattern observed in the specimens indented with the 12.7 mm-diameter indenter, the cross is aligned with the tows of the fabric and runs between two adjacent tows. The lengths of the slits were measured by a pair of Vernier calipers and are given in Table 6.2. The measured lengths are all within 4% of the nominal length of 10 mm. Typical photographs of these slits before the bond cure are shown in Figures 6.36 and 6.37.

6.2 Damage Tolerance

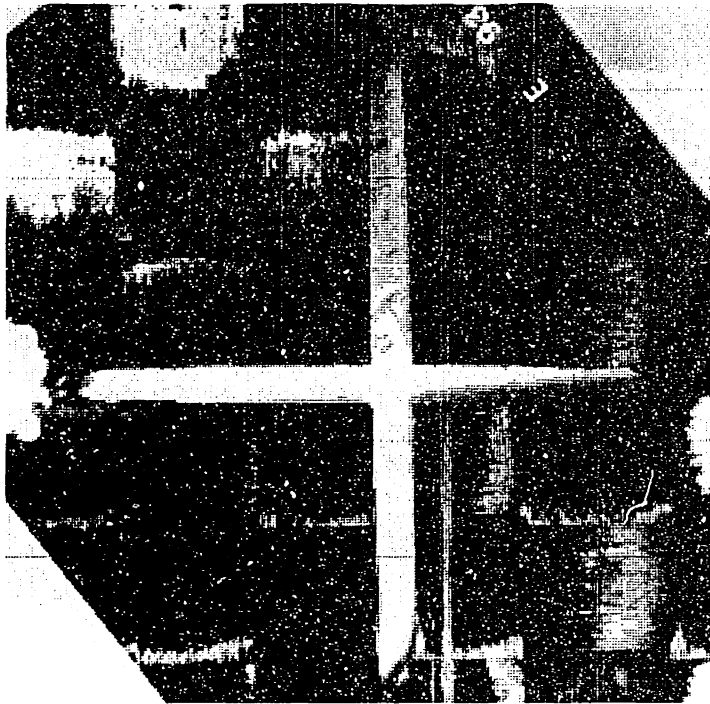
This section, which is divided into six subsections, contains both analytical results and experimental results. In Section 6.2.1, the values of the input parameters for the dimple propagation model are chosen based on the characterization results of the specimens with different damage types. Results of a parametric study of the effect of σ_{plateau} on the predictions of the model are also presented. In Sections 6.2.2 through 6.2.5, results of the uniaxial compression tests are presented. Results from these compression tests include far-field stress-strain data, dimple evolution data, post-mortem inspection of failed specimens, and compressive strength data. A total of 54 specimens were tested to failure under uniaxial compression. Some of the compression tests were monitored by the shadow moiré method to give quantitative measurements of the dimple propagation. Appropriate

Table 6.2 Measured slit lengths of specimens with simulated facesheet damage

Facesheet ID	Tow direction	
	Warp [mm]	Fill [mm]
d21-1 ^a	9.6	10.7
d21-2	10.1	9.8
d21-3	9.6	9.7
c2-1 ^b	11.0	9.8
c2-2	10.4	10.1
c2-3	9.6	10.0

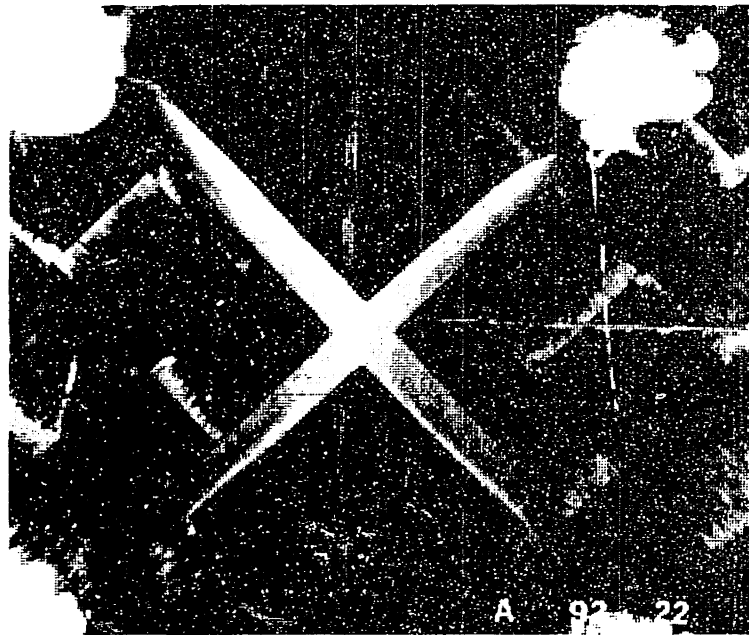
^a all "d" facesheets are (0/90)

^b all "c" facesheets are (± 45)



1 mm

Figure 6.36 Photograph of simulated facesheet damage in (0/90) facesheet.





1 mm

Figure 6.37 Photograph of simulated facesheet damage in (± 45) facesheet.

analytical results are included in Section 6.2.3 for comparison with the experimental results on the dimple propagation. In Section 6.2.6, longitudinal stress distributions as predicted by the dimple propagation model are examined in an attempt to correlate the residual strength of the damage specimens.

6.2.1 Input parameters for the dimple propagation model

A convergence study was conducted in Chapter 4 (Section 4.1.8). It was found that a 23 by 23-mode analysis was sufficient to obtain a converged solution for the displacement $w(x,y)$ with the particular values of the parameters chosen for the problem. After the results of damage characterization were reviewed, some of the values of the parameters given in Table 4.2 were adjusted to better represent the behavior of the sandwich panels tested.

The initial in-plane dimensions of the dimple are defined by the parameters R_x and R_y , while the initial depth of the dimple is given by ξ_0 . The values of these parameters for the specimens with simulated core damage are shown in Tables 6.3 and 6.4. The same set of values were used for the corresponding specimens with static indentation damage since it has been shown (see Section 6.1.3) that the profiles of the dimples in these two types of specimens correlate well. In Figures 6.38 through 6.43, the assumed shapes of the various dimples are compared with measurements along the tows of the fabric facesheets through the center of the dimple.

In the dimple propagation model, the initial region of crushed core is assumed to be circular with a radius of R_0 . The values of R_0 used for specimens with different types of damage are given in Table 6.5. The values of R_0 for specimens with simulated core damage are half of the extent of

Table 6.3 Values of initial dimple parameters (R_x , R_y , and ξ_0)^a which best match the experimentally measured dimple profiles in specimens with (0/90) facesheets

	Damage Level		
	1	2	3
R_x	7	9	13
R_y	7	9	13
ξ_0	-1.00	-0.75	-0.20

^aall dimensions in mm

Table 6.4 Values of initial dimple parameters (R_x , R_y , and ξ_0)^a which best match the experimentally measured dimple profiles in specimens with (± 45) facesheets

	Damage Level		
	1	2	3
R_x	9	11	13
R_y	9	11	13
ξ_0	-1.00	-0.80	-0.30

^aall dimensions in mm

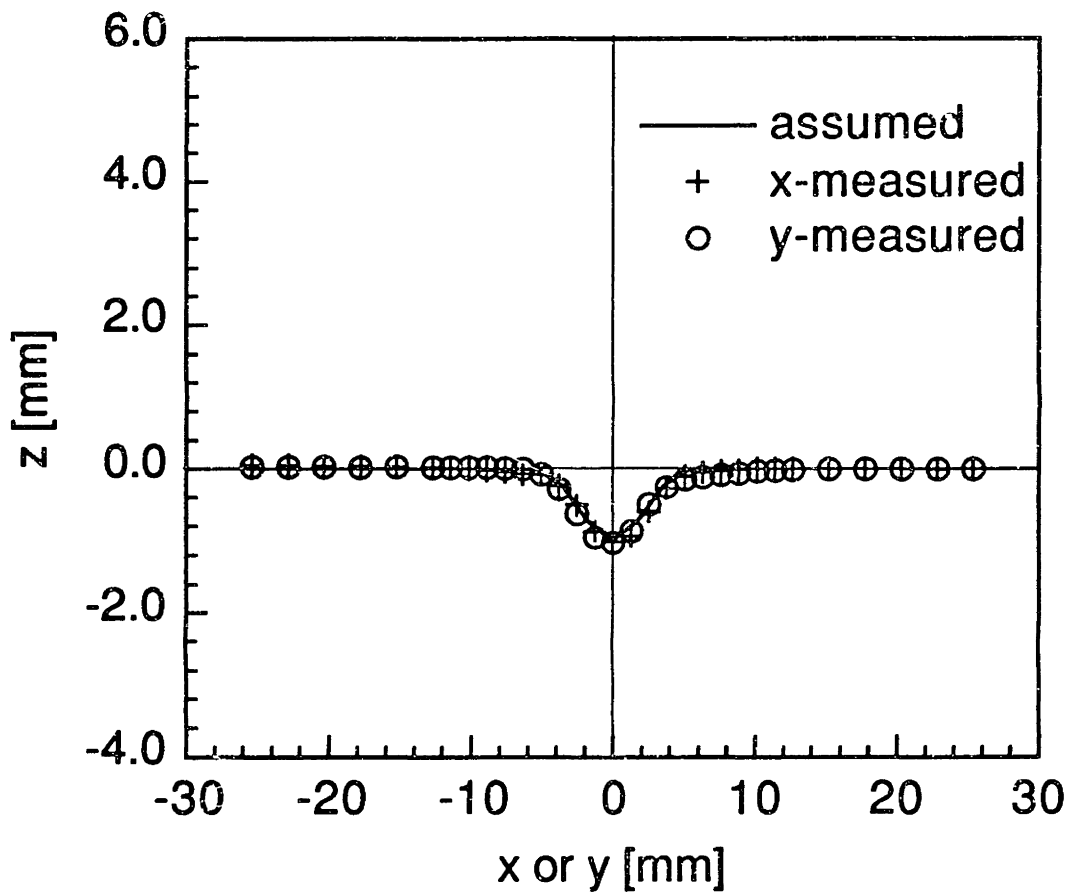


Figure 6.38 Assumed and measured shapes of the dimple in specimens with (0/90) facesheets and level 1 simulated core damage.

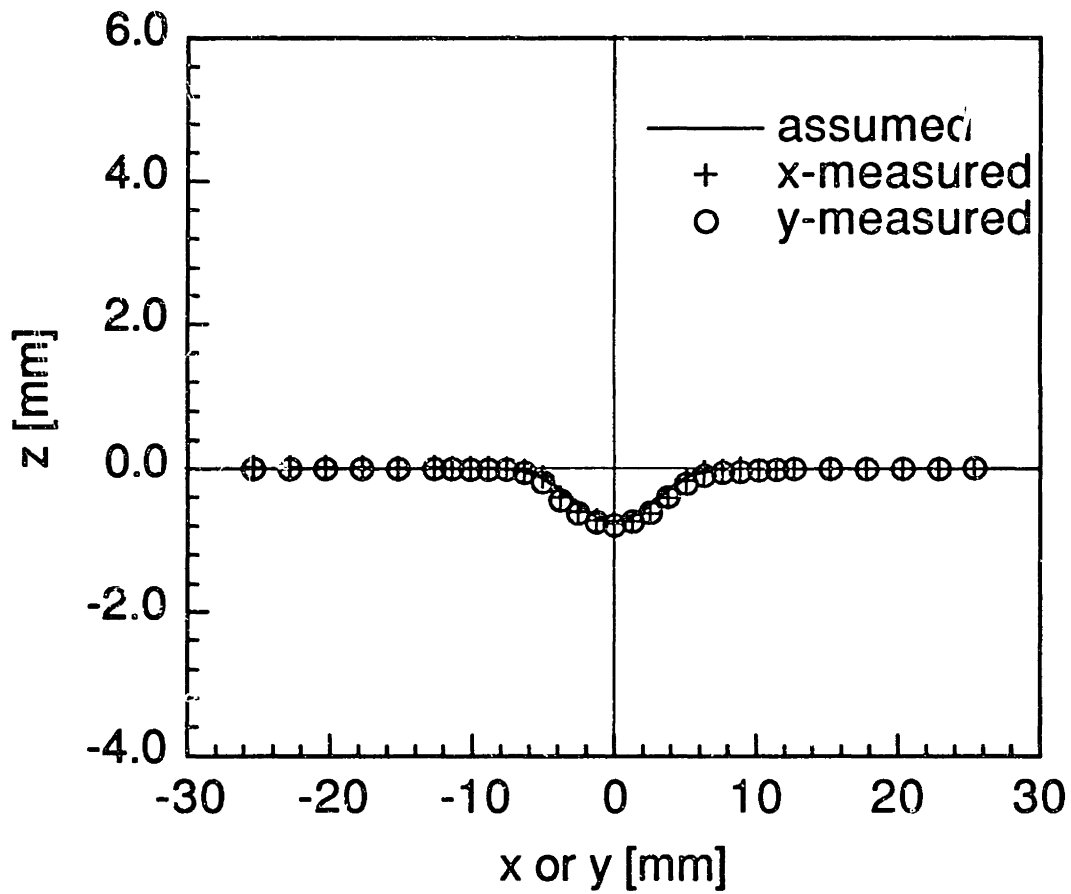


Figure 6.39 Assumed and measured shapes of the dimple in specimens with (0/90) facesheets and level 2 simulated core damage.

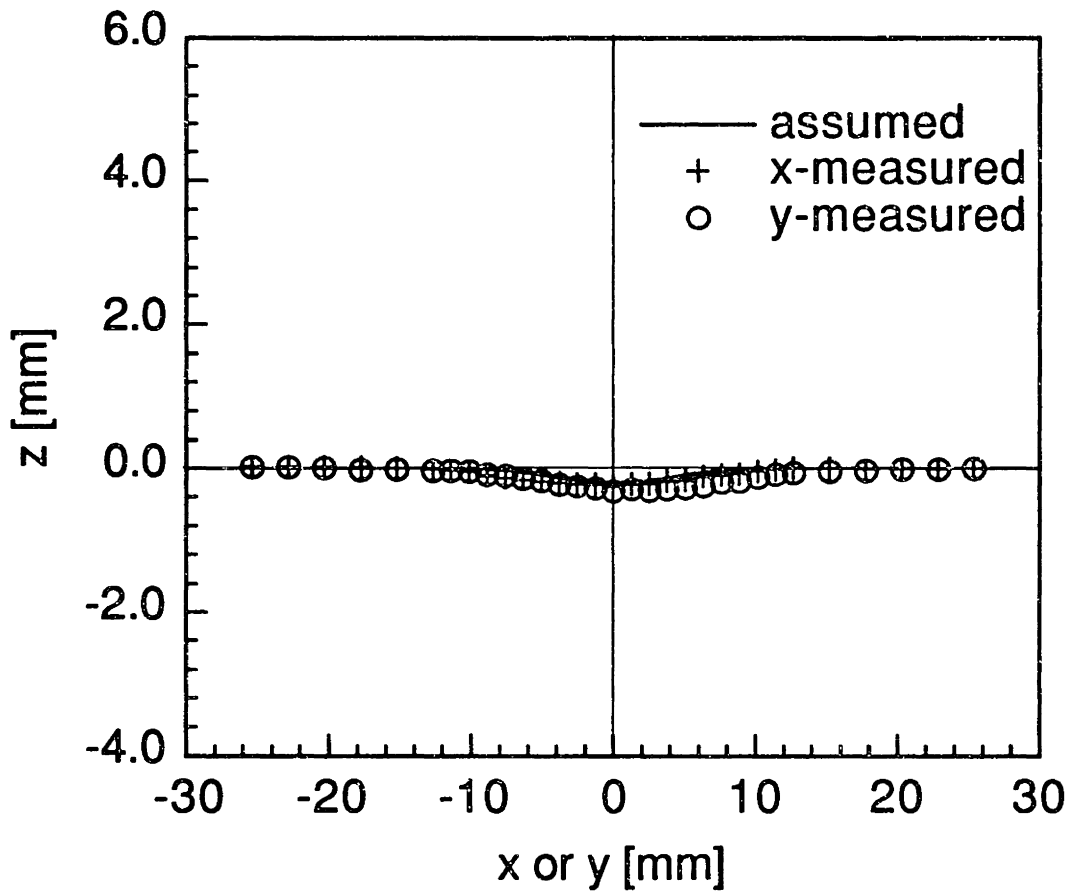


Figure 6.40 Assumed and measured shapes of the dimple in specimens with (0/90) facesheets and level 3 simulated core damage.

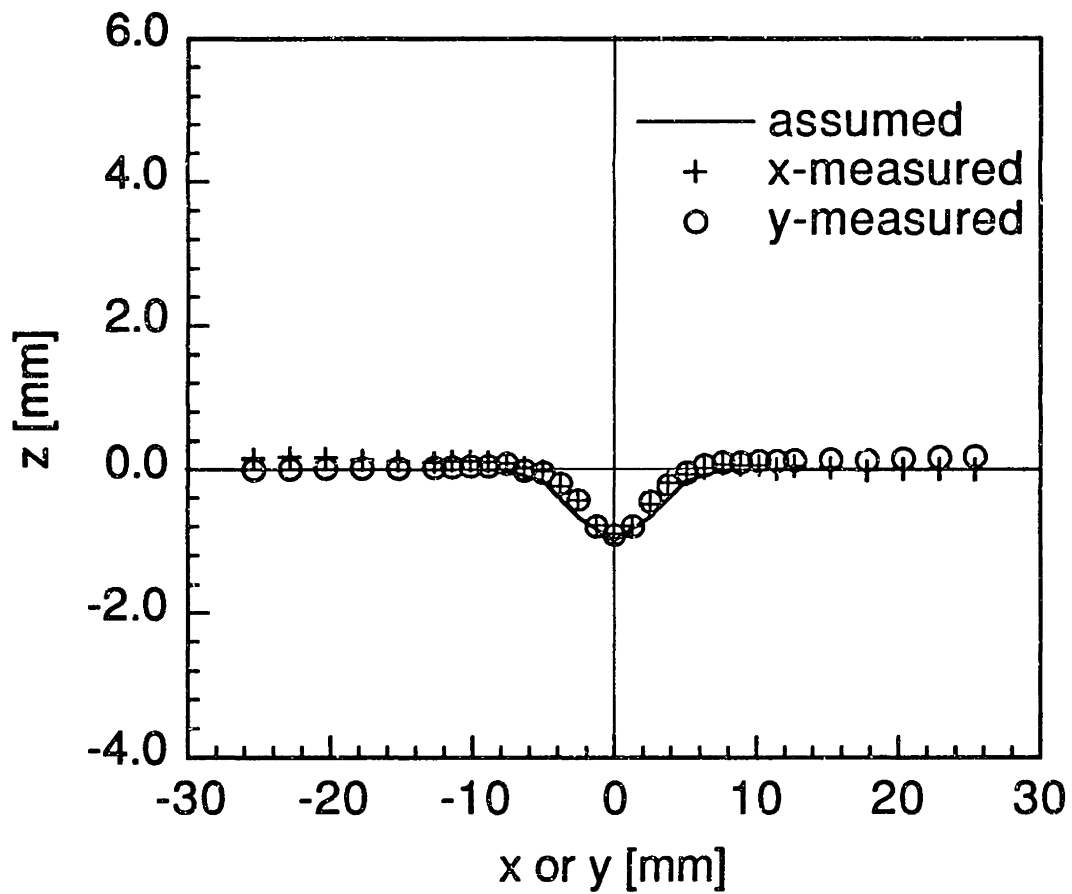


Figure 6.41 Assumed and measured shapes of the dimple in specimens with (± 45) facesheets and level 1 simulated core damage.

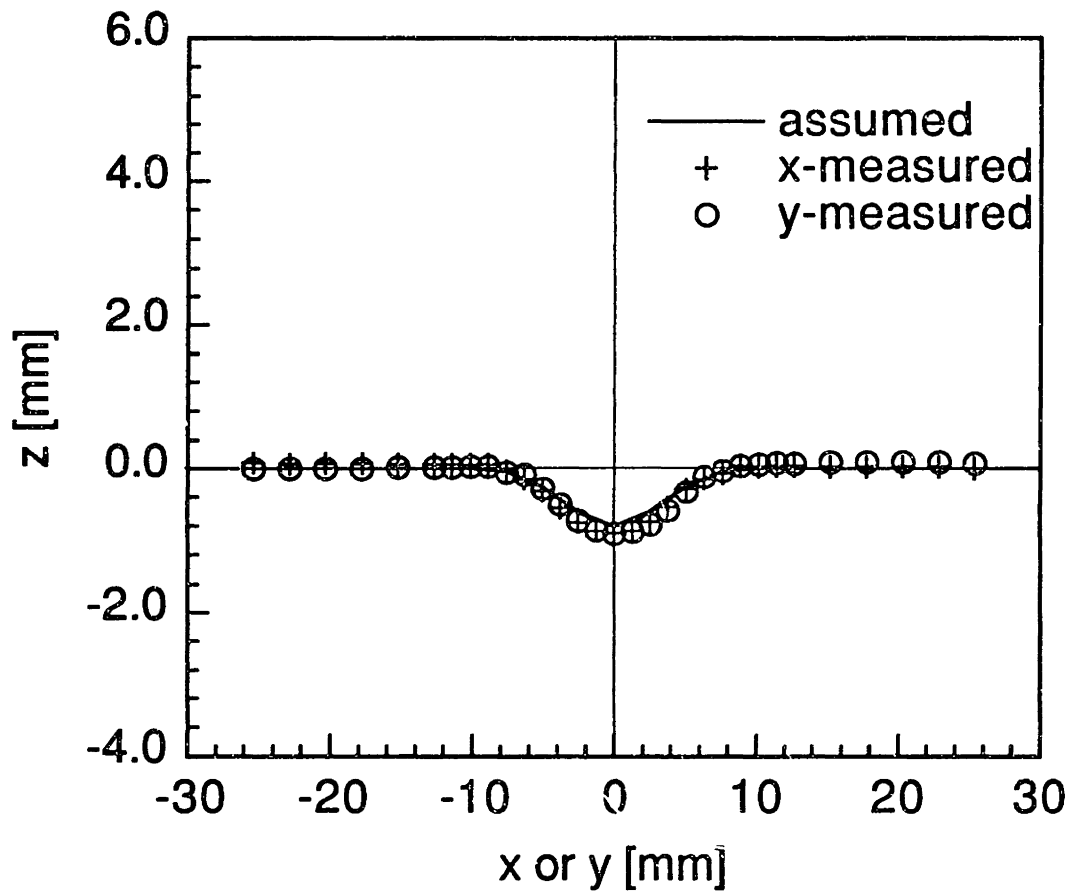


Figure 6.42 Assumed and measured shapes of the dimple in specimens with (± 45) facesheets and level 2 simulated core damage.

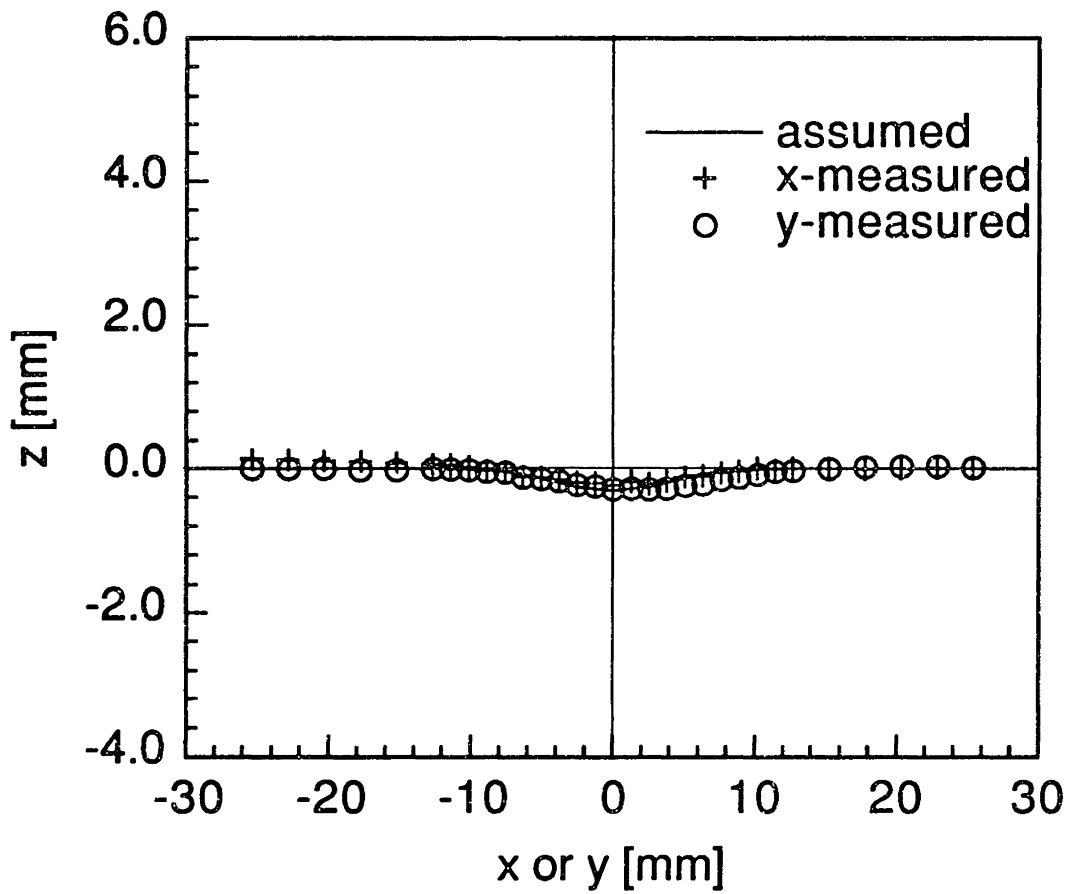


Figure 6.43 Assumed and measured shapes of the dimple in specimens with (± 45) facesheets and level 3 simulated core damage.

Table 6.5 Values^a of the radius of the initial region of crushed core, R_0 , used in the dimple propagation model for specimens with (0/90) facesheets and those with (± 45) facesheets

	Damage Level		
	1	2	3
Static Indentation	6 ^a	7	8
Simulated Core	5	6	7

^a all values in mm

core damage observed in the cross-sections inspected as described in Section 6.1.3. Slightly higher values of R_0 are used for specimens with static indentation damage because these specimens had slightly more extensive core damage than the corresponding specimens with simulated core damage (see Section 6.1.3). Although the more extensive core damage observed in specimens with static indentation damage is manifested in the through-thickness distribution of the crushed core rather than the in-plane extent of the crushed core, the dimple propagation model can only account for such difference by using a different value of R_0 .

The values of the parameters σ_{ult} and $\sigma_{plateau}$ used in the convergence study are 1.8 MPa and 1.4 MPa respectively. These values were obtained by Williamson [58] from flatwise compression tests on bare 25.4 mm-thick Nomex honeycomb core. Later, it was realized that a higher value of σ_{ult} would be obtained if the core was "stabilized" by bonding it to two facesheets. Thus, the manufacturer's value of 2.4 MPa for the stabilized strength is used for σ_{ult} in all analytical predictions presented in this chapter.

Since the manufacturer does not provide data on the plateau stress $\sigma_{plateau}$, the same value as that of the bare core, 1.4 MPa, is used. A parametric study of the effect of $\sigma_{plateau}$ on the results of the model was performed with three values of $\sigma_{plateau}$: 1.2 MPa, 1.4 MPa, and 1.6 MPa for the case of a specimen with (0/90) facesheets and level 3 simulated core damage. The applied stress used is -310 MPa which is high enough to cause significant progressive core crushing beyond the initial region of crushed core. The dimple profiles, the through-thickness stress, σ_{zz} , distribution at the interface between the core and the facesheet, and the longitudinal stress, σ_{xx} , distributions are given in Figures 6.44 through 6.47. The

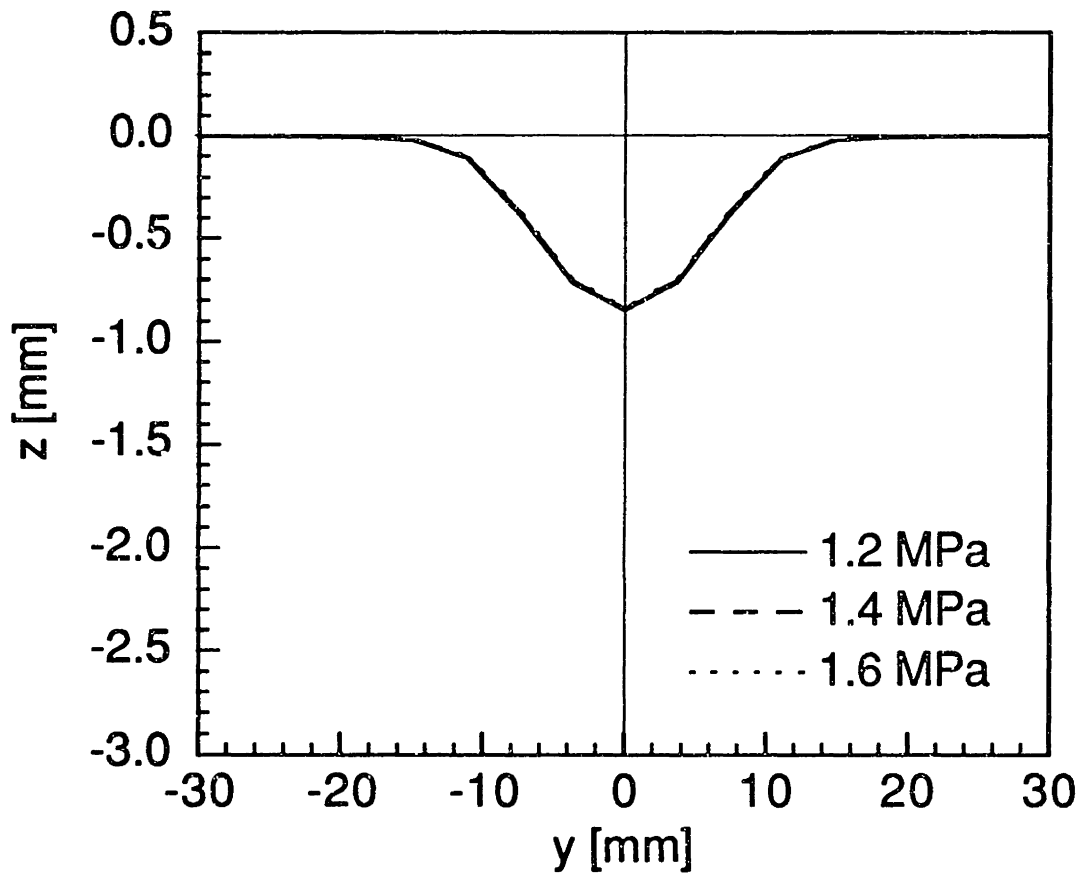


Figure 6.44 Predicted dimple profiles of a specimen with (0/90) facesheets and level 3 simulated core damage at an applied stress of -310 MPa for three values of σ_{plateau} .

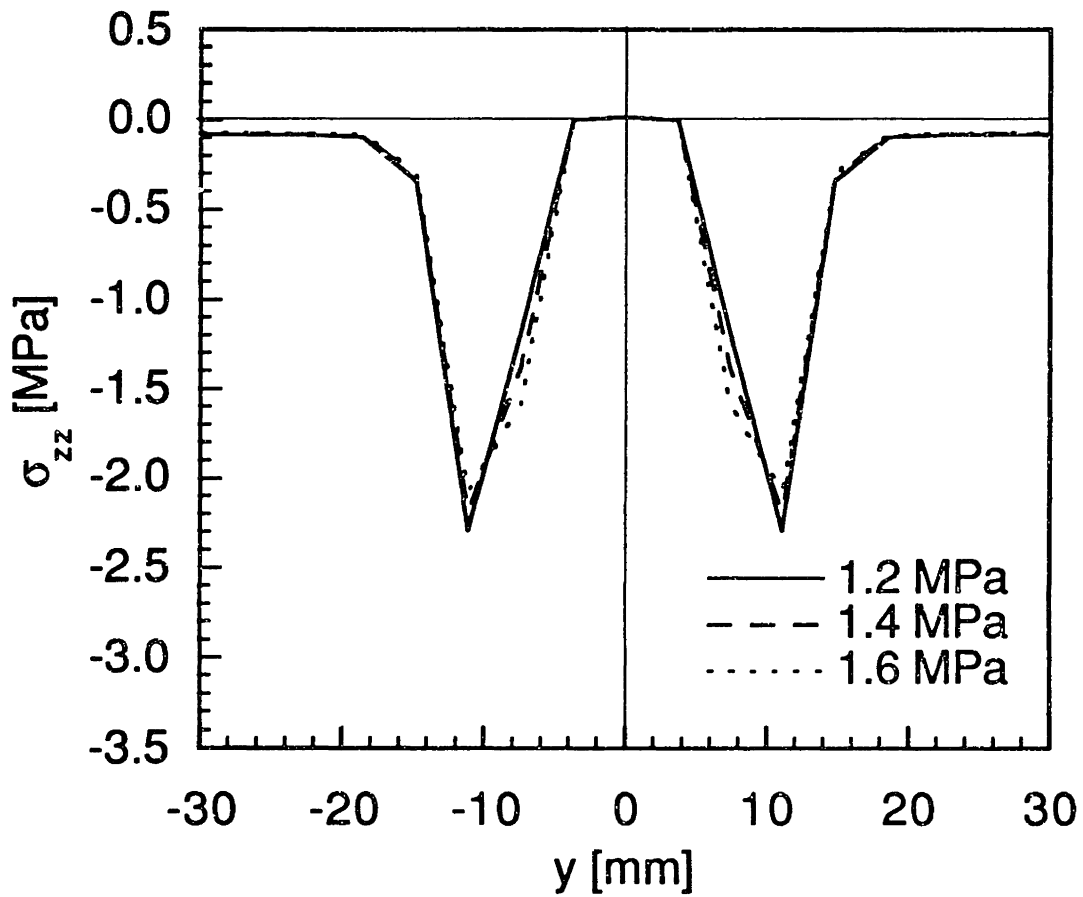


Figure 6.45 Predicted through-thickness stress distribution of a specimen with (0/90) facesheets and level 3 simulated core damage at an applied stress of -310 MPa for three values of σ_{plateau} .

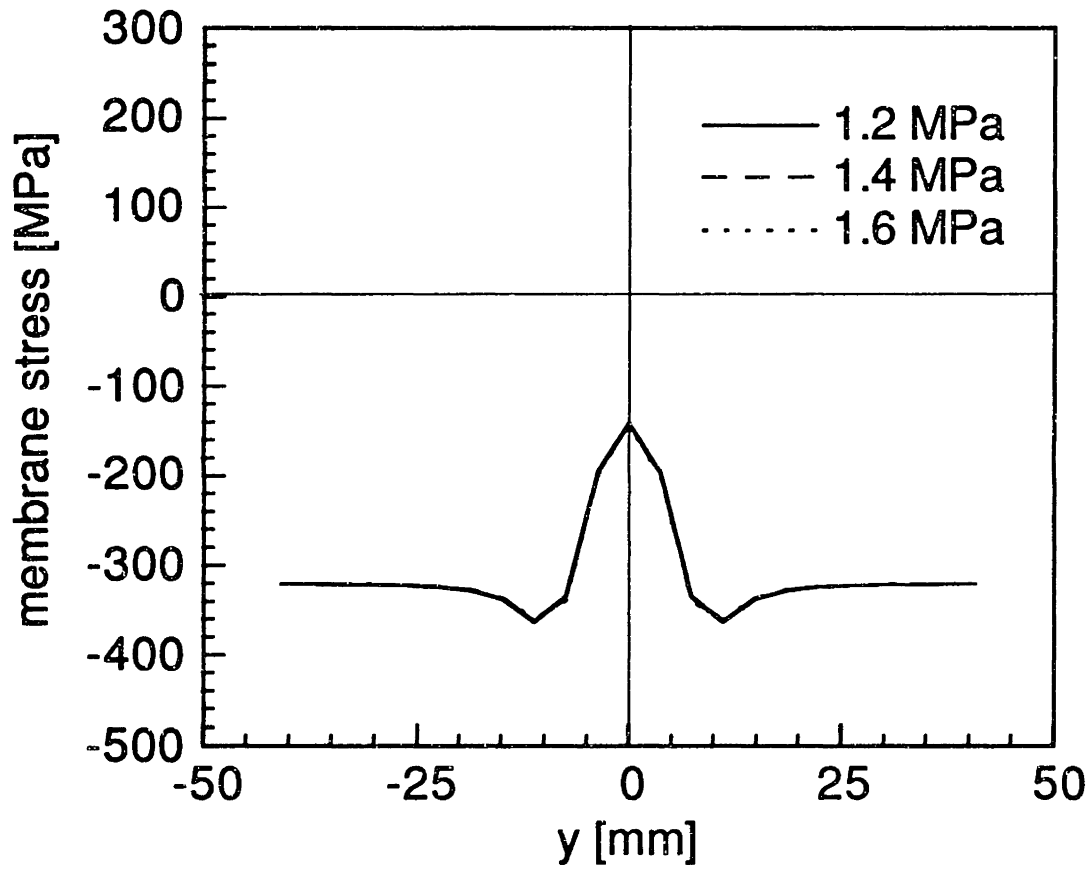


Figure 6.46 Predicted membrane stress distribution of a specimen with (0/90) facesheets and level 3 simulated core damage at an applied stress of -310 MPa for three values of σ_{plateau} .

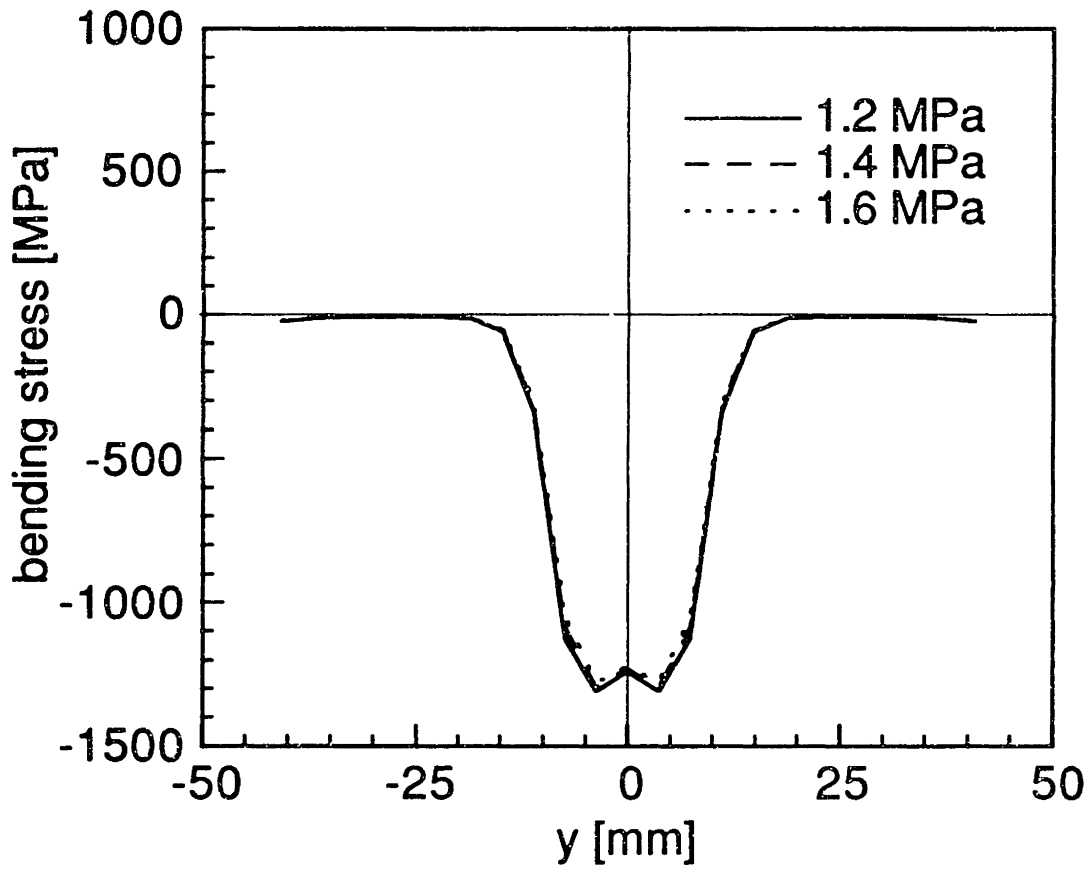


Figure 6.47 Predicted bending stress distribution of a specimen with (0/90) facesheets and level 3 simulated core damage at an applied stress of -310 MPa for three values of σ_{plateau} .

results indicate that the range of values for σ_{plateau} has little influence on the predictions of the model.

The values of the input parameters to the dimple propagation model for specimens with (0/90) and (± 45) facesheets are summarized in Tables 6.6 and 6.7.

6.2.2 Far-field stress-strain data

Far-field back-to-back strain gages were placed on all specimens to check for bending during the uniaxial compression tests as well as to determine the modulus of the specimens. Typical stress-strain results are presented in this section. Slopes of these stress-strain curves are calculated as the moduli of the specimens. Average values of the moduli of the specimens with different damage types are also compared.

For specimens with (0/90) facesheets, typical stress-strain results of an undamaged specimen, a specimen with static indentation damage, a specimen with simulated core damage, and a specimen with simulated facesheet damage are shown in Figures 6.48 through 6.51. Data beyond the point of failure were deleted from these figures. All stress-strain curves are linear up to the point of failure. The average moduli of the specimens are given in Table 6.8. The overall average value of 65.9 MPa is consistent with that predicted via Classical Laminated Plate Theory (64.0 GPa) using the material properties from the material property evaluation tests. The data also show that the various damage types did not affect the far-field strain of the sandwich panels. In all but two cases, the difference between the moduli of the two facesheets of a specimen is less than 10%.

For specimens with (± 45) facesheets, typical stress-strain results of an undamaged specimen, a specimen with static indentation damage, a

Table 6.6 Input parameters for the dimple propagation model used for specimens with (0/90) facesheets

Parameter	Value
a	89 mm
b	89 mm
R_x	see Table 6.3
R_y	see Table 6.3
ξ_0	see Table 6.3
R_0	see Table 6.5
h	0.35 mm
A_{11}	22.92 MNm ⁻¹
A_{12}	3.437 MNm ⁻¹
A_{16}, A_{26}	0.0 MNm ⁻¹
A_{22}	22.92 MNm ⁻¹
A_{66}	2.195 MNm ⁻¹
D_{11}	0.2339 Nm
D_{12}	0.0351 Nm
D_{16}, D_{26}	0.0 Nm
D_{22}	0.2339 Nm
D_{66}	0.0224 Nm
σ_{ult}	2.4 MPa
$\sigma_{plateau}$	1.4 MPa
k_1	20.53 GNm ⁻³
k_2	-28.27 kNm ⁻¹
$\bar{\sigma}_{xx}$	-250 MPa

Tables 6.7 Input parameters for the dimple propagation model used for specimens with (± 45) facesheets

Parameter	Value
a	89 mm
b	89 mm
R_x	see Table 6.4
R_y	see Table 6.4
ξ_0	see Table 6.4
R_0	see Table 6.5
h	0.35 mm
A_{11}	15.37 MNm ⁻¹
A_{12}	10.98 MNm ⁻¹
A_{16}, A_{26}	0.0 MNm ⁻¹
A_{22}	15.37 MNm ⁻¹
A_{66}	9.739 MNm ⁻¹
D_{11}	0.1569 Nm
D_{12}	0.1121 Nm
D_{16}, D_{26}	0.0 Nm
D_{22}	0.1569 Nm
D_{66}	0.0994 Nm
σ_{ult}	2.4 MPa
$\sigma_{plateau}$	1.4 MPa
k_1	20.53 GNm ⁻³
k_2	-28.27 kNm ⁻¹
$\bar{\sigma}_{xx}$	-250 MPa

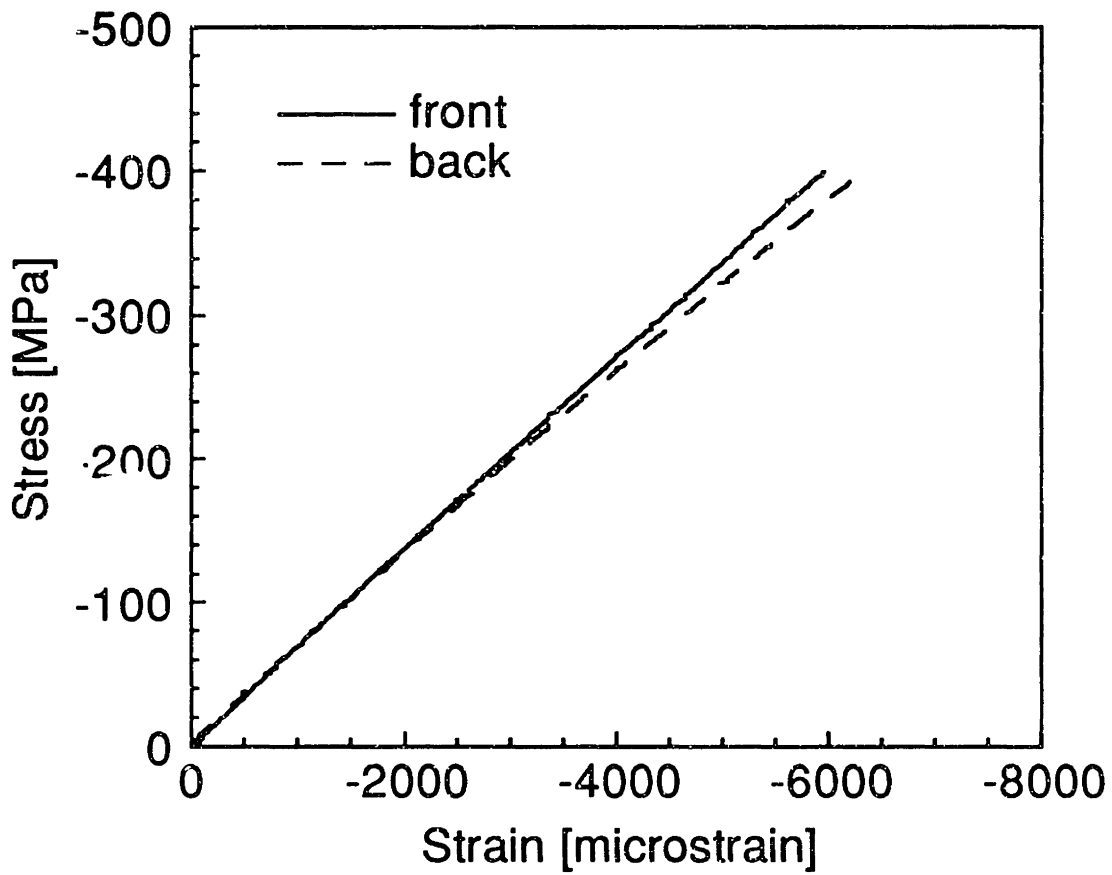


Figure 6.48 Typical stress-strain results of an undamaged specimen with (0/90) facesheets.

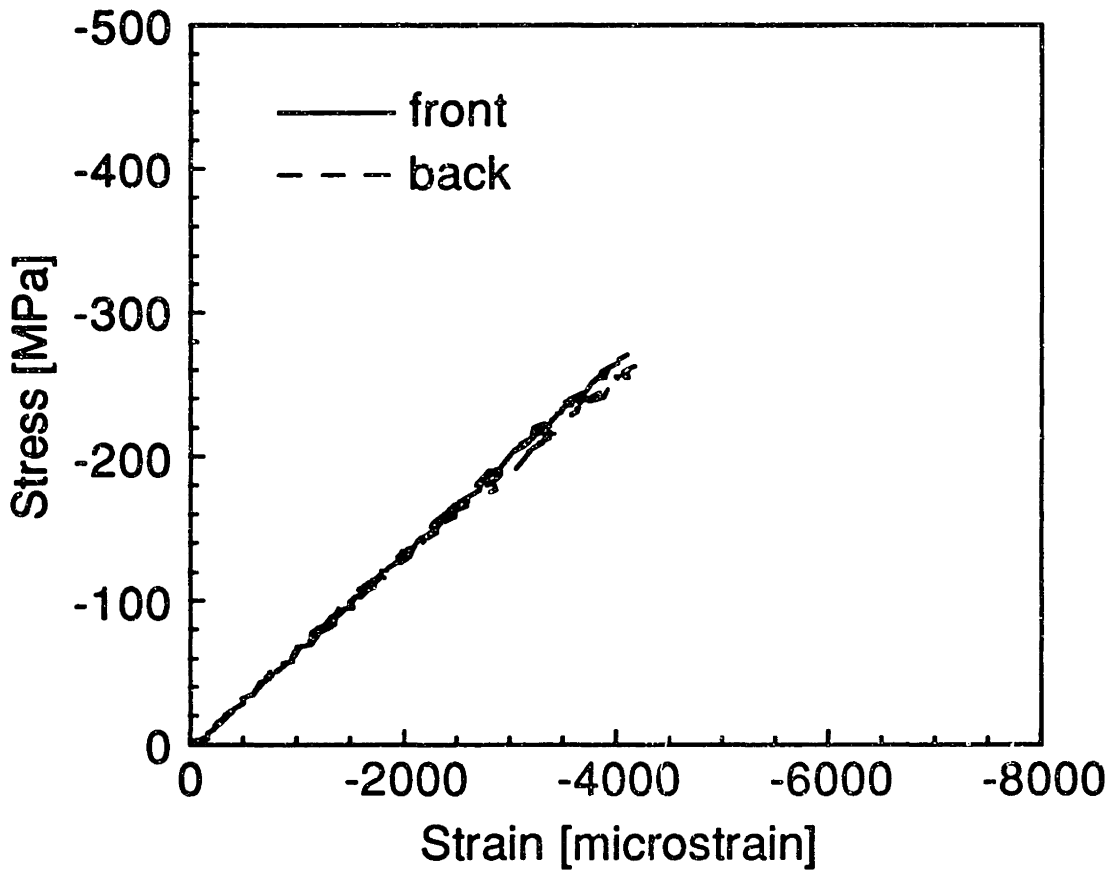


Figure 6.49 Typical stress-strain results of a specimen with (0/90) facesheets and static indentation damage.

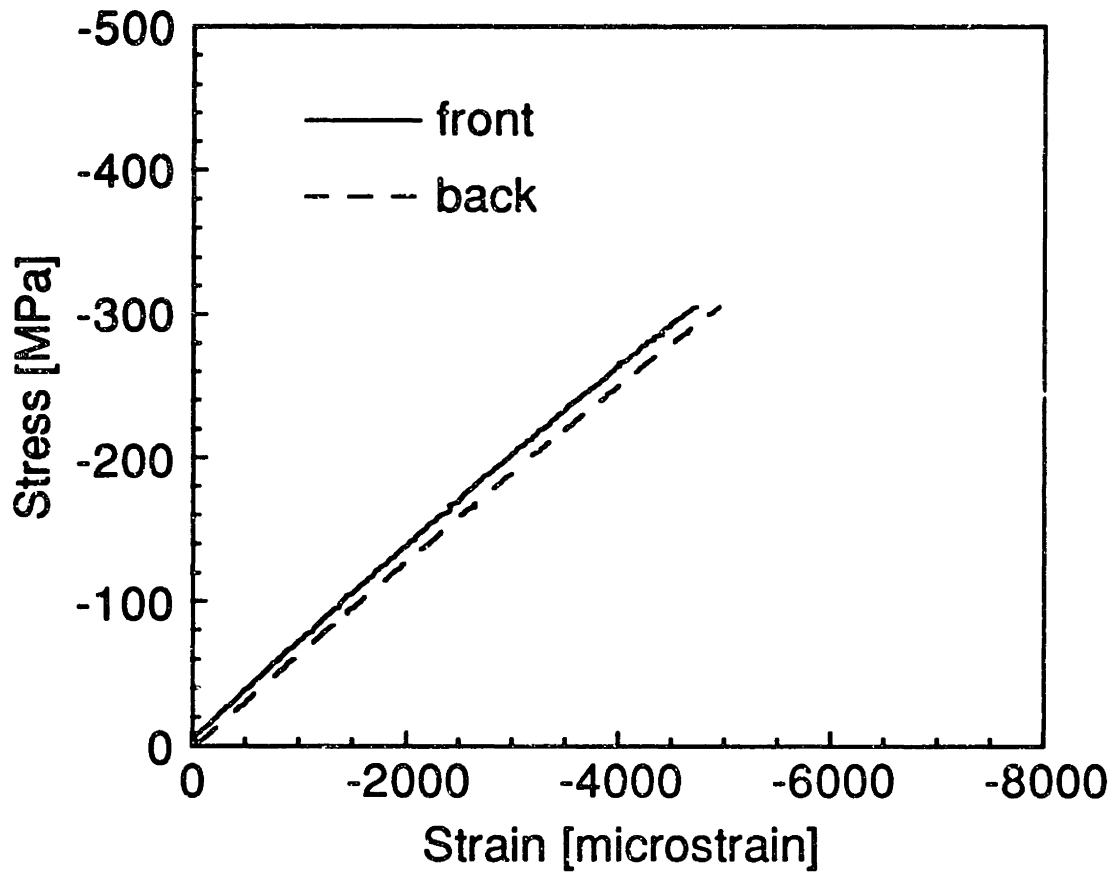


Figure 6.50 Typical stress-strain results of a specimen with (0/90) facesheets and simulated core damage.

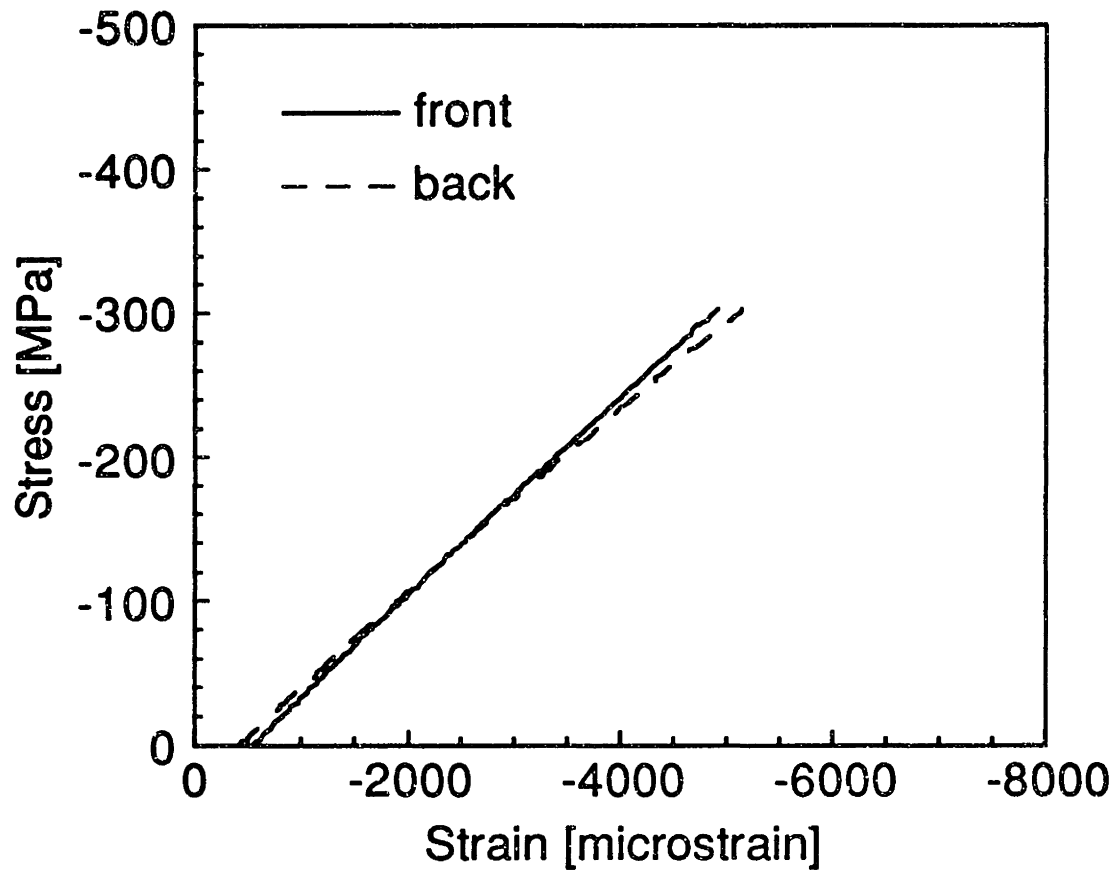


Figure 6.51 Typical stress-strain results of a specimen with (0/90) facesheets and simulated facesheet damage.

Table 6.8 Compressive moduli of specimens with (0/90) facesheets

Damage Type	Modulus [GPa]
None	66.2 (4.3%) ^a
Static Indentation	65.5 (4.4%)
Simulated Core	65.1 (6.4%)
Simulated Facesheet	66.9 (5.1%)

^anumbers in parentheses are coefficients of variation

simulated core damage specimen, and a specimen with simulated facesheet damage are shown in Figures 6.52 through 6.55. All stress-strain curves are nonlinear and show a softening characteristic as the load increases. Such behavior is consistent with observations made by other researchers [59, 98]. The first linear section of the stress-strain curves was identified by the computer program LIN6 [99]. The moduli of the specimens, defined as the slope of the first linear section, are given in Table 6.9. The overall average value of 22.9 MPa is consistent with that predicted via Classical Laminated Plate Theory (21.5 GPa) using the material properties from the material property evaluation tests. The data also show that the various damage types did not affect the far-field strain of the sandwich panels. In all but one case, the difference between the moduli of the two facesheets of a specimen is less than 10%.

6.2.3 Dimple propagation

As described in Section 5.5.4, the uniaxial compression tests of some damaged panels were monitored by the shadow moiré method. These include most of the specimens with static indentation damage and all the specimens with simulated core damage. The first specimen with simulated facesheet damage tested was monitored by the shadow moiré method and no out-of-plane deformation was observed. All subsequent specimens were, therefore, not monitored using the shadow moiré method.

Moiré fringes developed as the dimple propagated and the evolution of these moiré fringes was recorded with a camcorder. Selected video images were digitized and measured. The video images were selected at intervals of approximately every two new fringes generated. Moiré measurements of the dimple profiles are compared with the corresponding

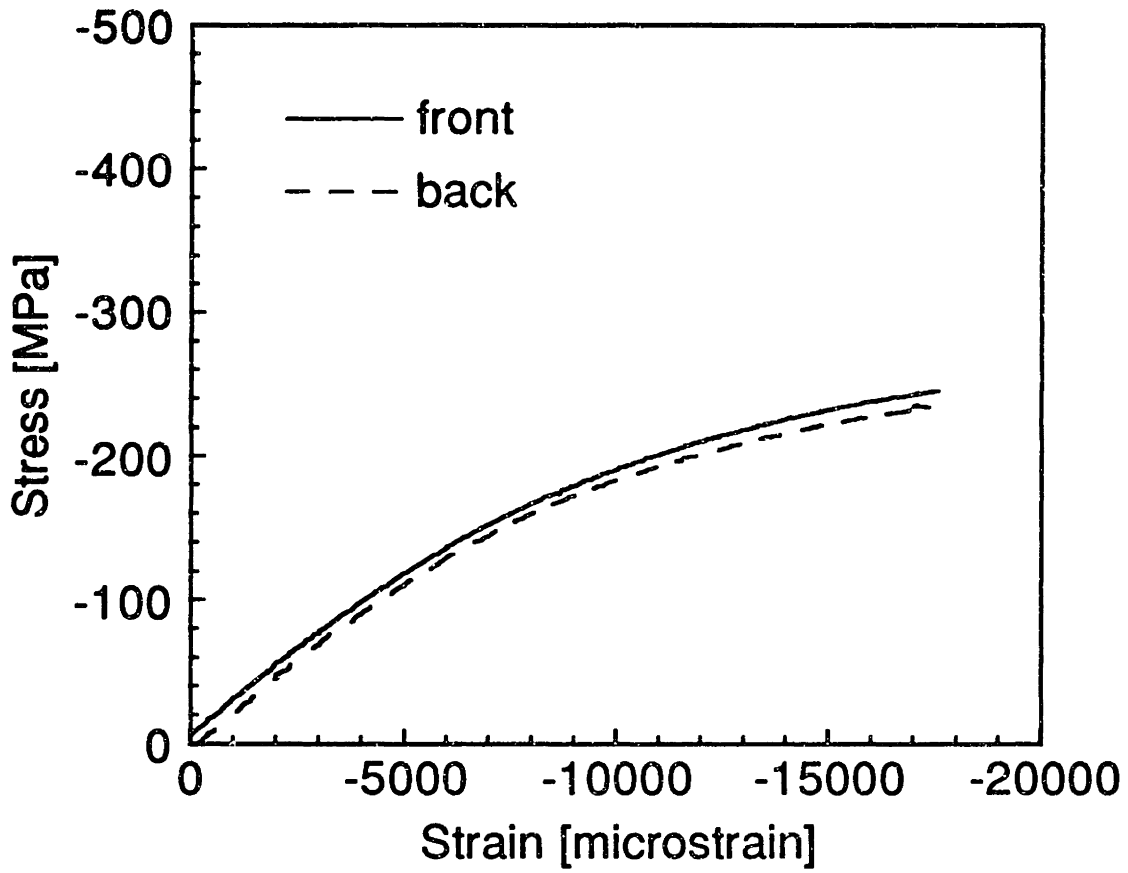


Figure 6.52 Typical stress-strain results of an undamaged specimen with (± 45) facesheets.

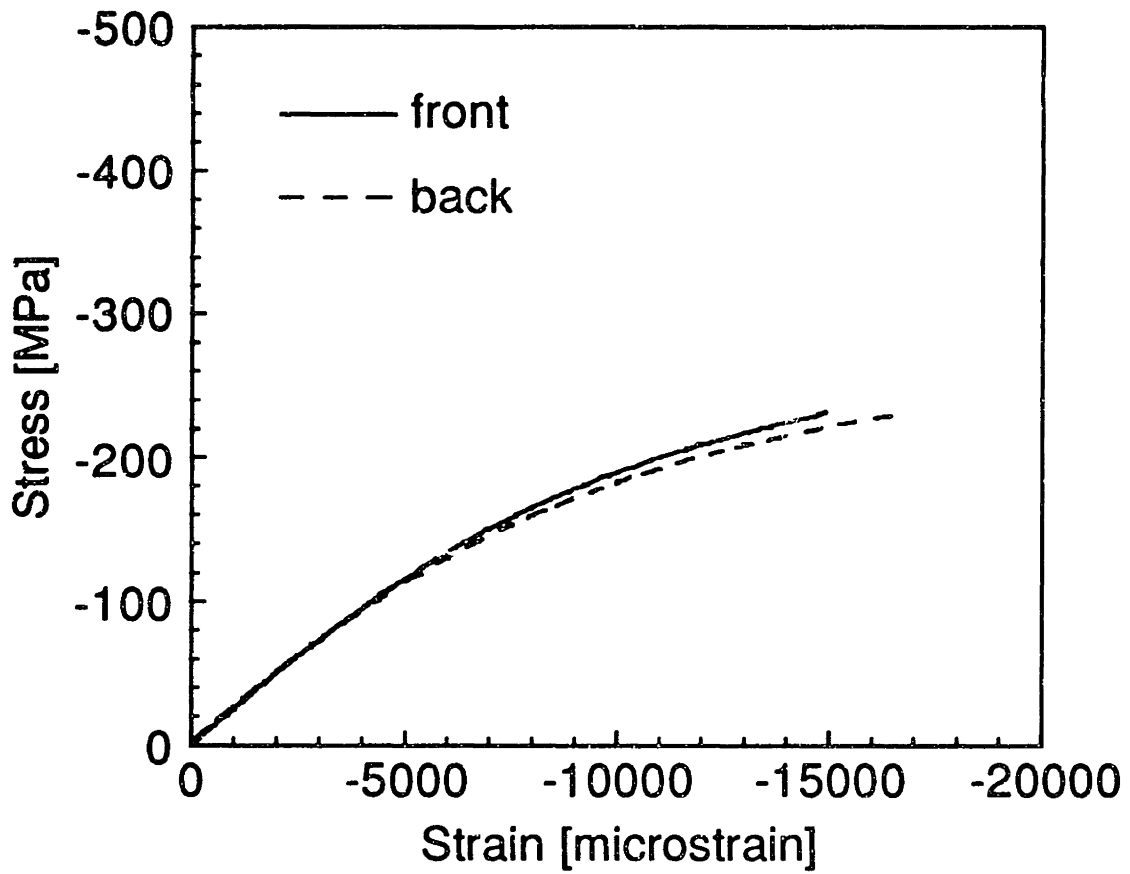


Figure 6.53 Typical stress-strain results of a specimen with (± 45) facesheets and static indentation damage.

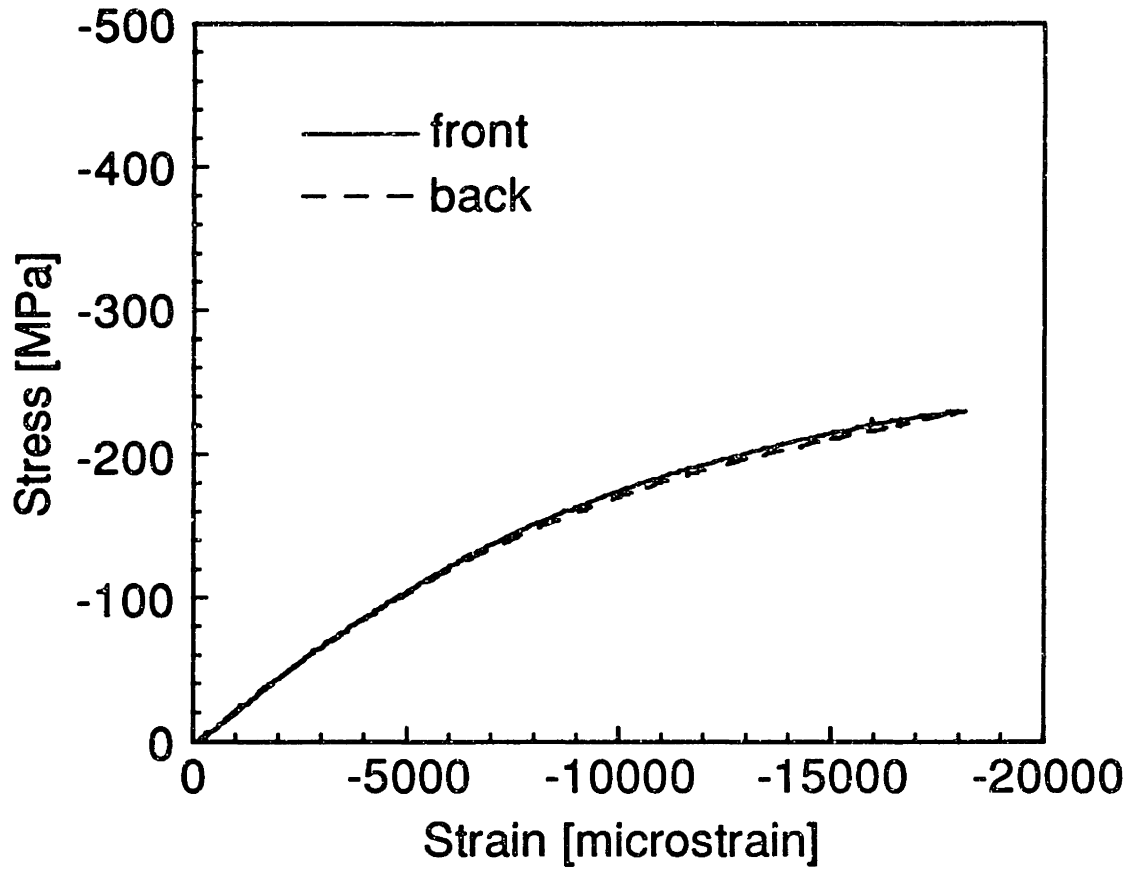


Figure 6.54 Typical stress-strain results of a specimen with (± 45) facesheets and simulated core damage.

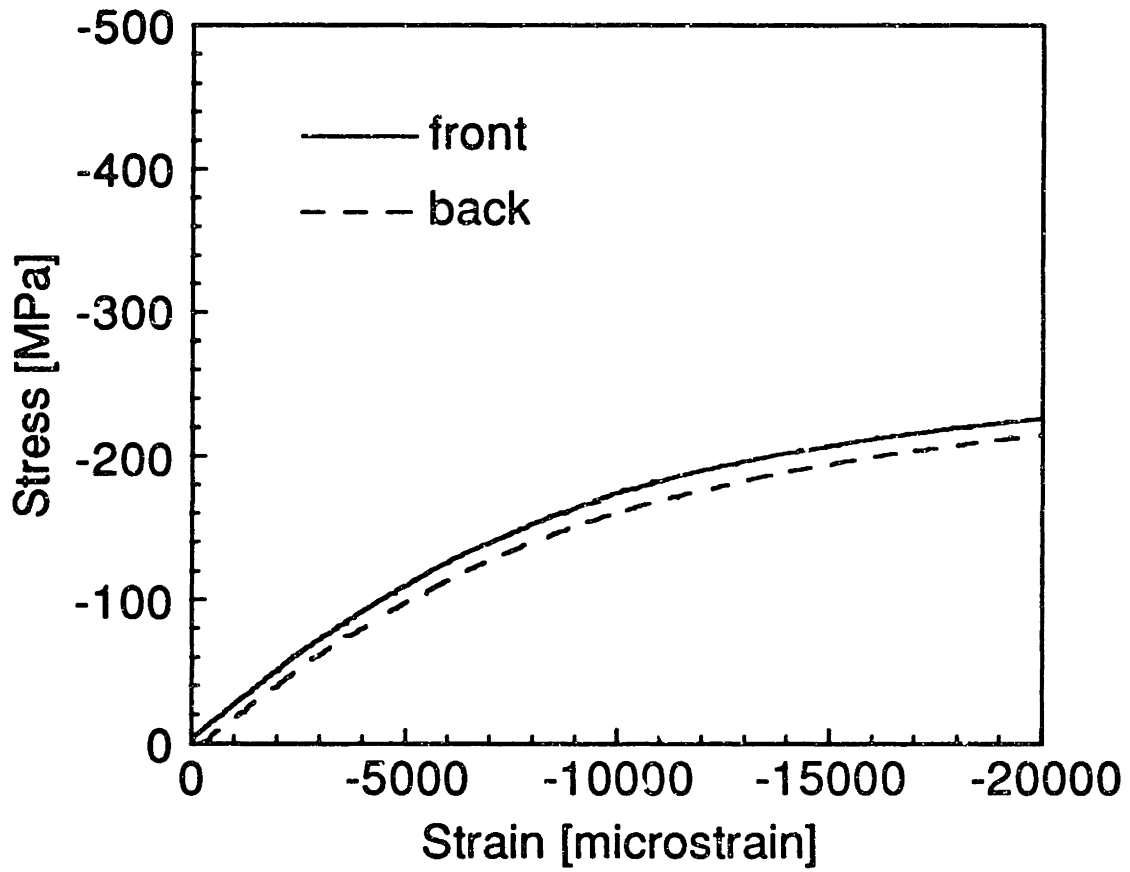


Figure 6.55 Typical stress-strain results of a specimen with (± 45) facesheets and simulated facesheet damage.

Table 6.9 Compressive moduli of specimens with (± 45) facesheets

Damage Type	Modulus [GPa]
None	22.6 (6.3%) ^a
Static Indentation	23.1 (6.4%)
Simulated Core	22.8 (2.6%)
Simulated Facesheet	23.0 (2.3%)

^anumbers in parentheses are coefficients of variation

analytical predictions at various applied stress levels. In all profile data shown, the symbols are the experimental results while the lines are the corresponding predictions of the dimple propagation model. The highest applied stress level shown is always the failure stress of the specimen. Hence, the corresponding dimple profiles are those just before catastrophic failure occurred. Occasionally, some data points are missing from the experimental results because the fringes are too blurry to be measured. It should also be noted that, for the presentation of the profile data, the x-axis and the y-axis are shifted so that the origin is at the center of the dimple.

A typical set of digitized fringe patterns is shown in Figure 6.56 for a specimen with (0/90) facesheets and indented with the 12.7 mm-diameter indenter. The loading axis in such figures is along the vertical direction. In agreement with observations by other researchers [28, 41], the dimples propagated mostly perpendicular to the loading. The shape of the initial dent/dimple changes from circular to elliptical and finally to an elongated diamond with rounded corners. Similar evolution patterns are also observed in specimens with simulated core damage as shown in Figure 6.57. The characteristics of the dimple propagation do not change qualitatively with damage levels. The moiré measurements made along the x-axis (loading direction) and the y-axis (perpendicular to loading direction) are given in Figures 6.58 and 6.59 for the fringe patterns shown in Figure 6.56. It can be seen from the moiré measurements that negligible propagation occurred in the loading direction (i.e. along the x-axis).

Additional dimple profiles of specimens with various levels of static indentation damage are shown in Figures 6.60 through 6.65 for specimens with (0/90) facesheets. The corresponding analytical predictions by the dimple propagation model are also included. It can be seen from these

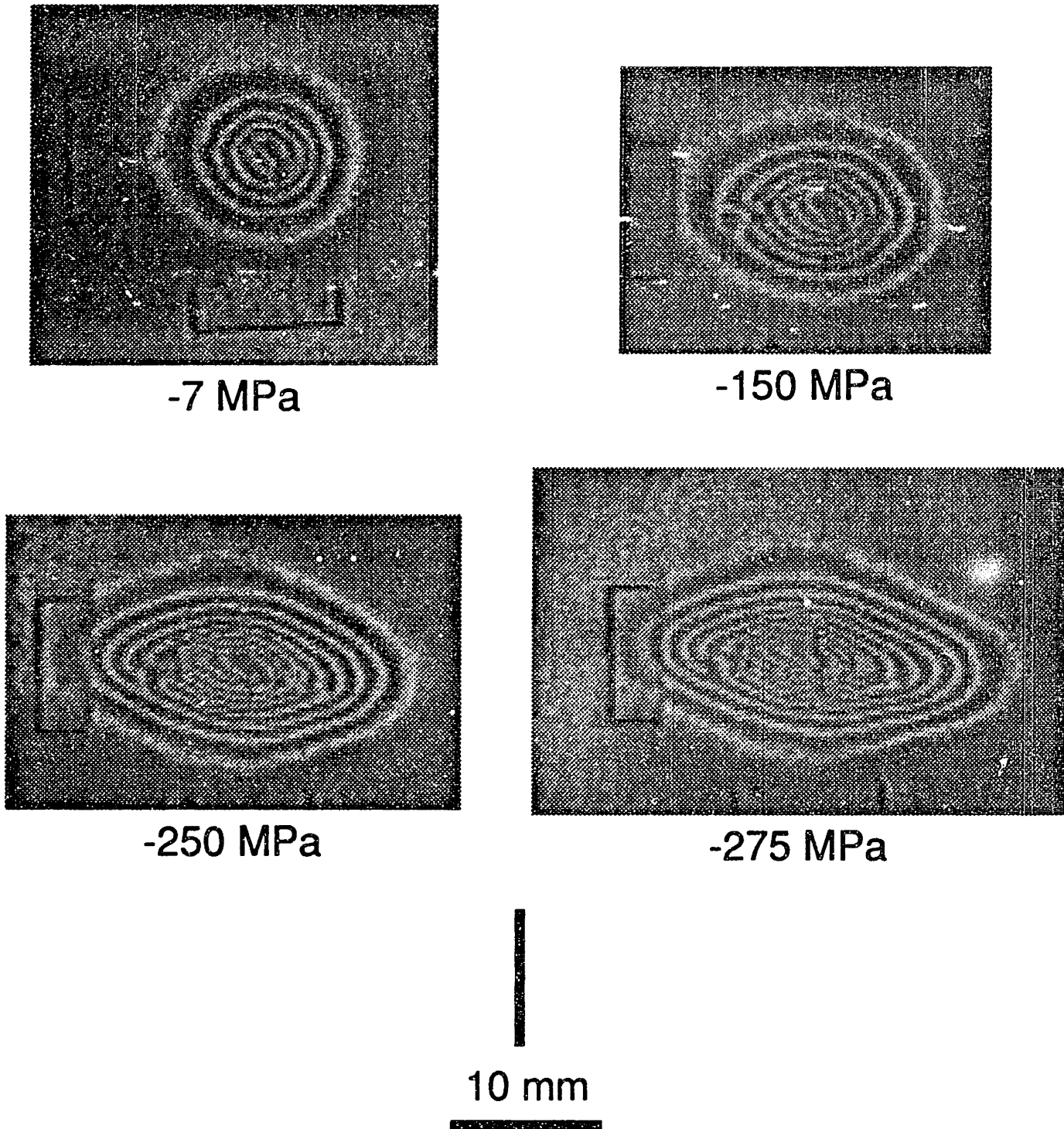


Figure 6.56 Digitized moiré fringe patterns at various applied stress levels for a specimen with (0/90) facesheets and indentation damage inflicted with a 12.7 mm-diameter indenter.

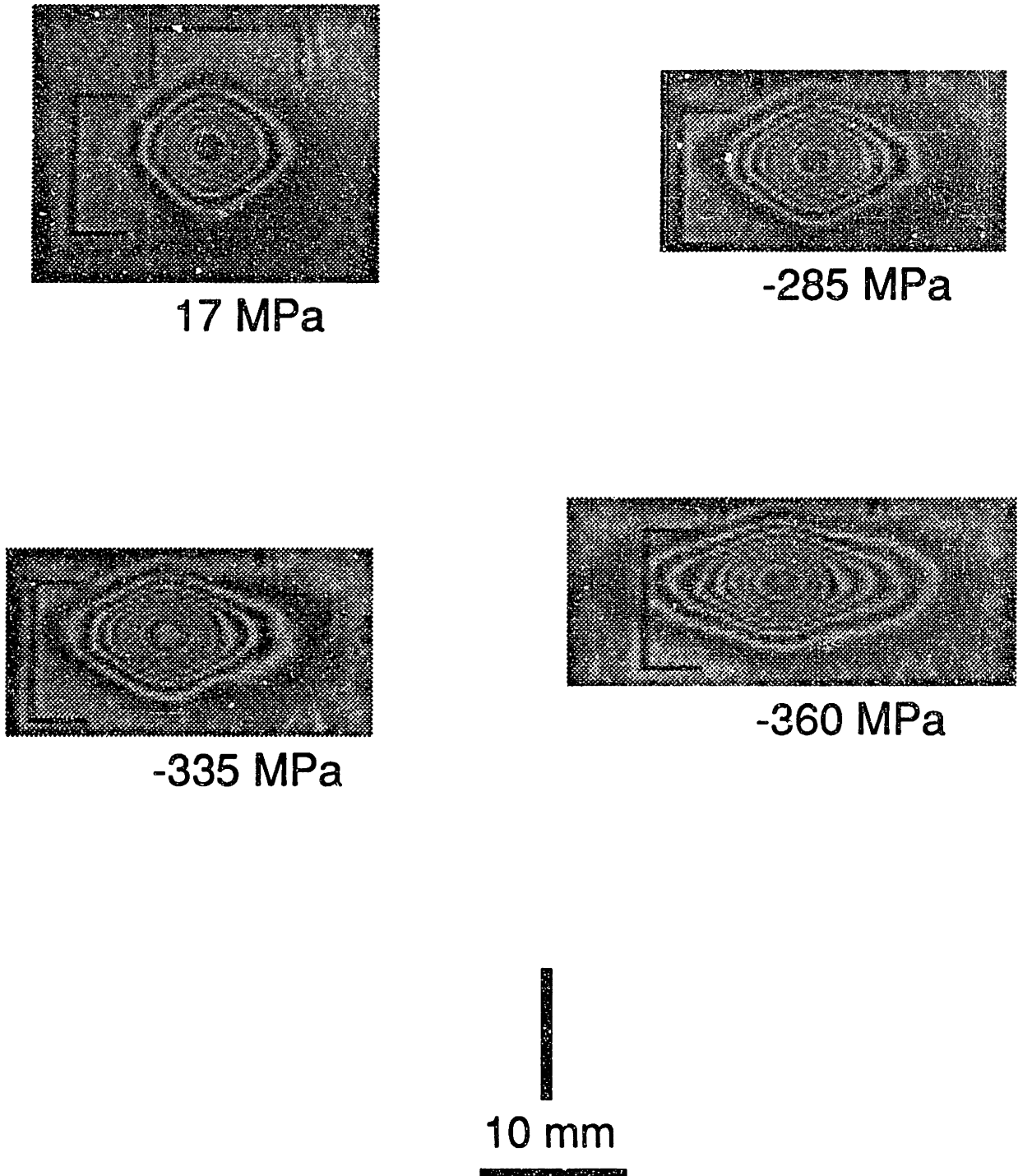


Figure 6.57 Digitized moiré fringe patterns at various applied stress levels for a specimen with (0/90) facesheets and level 1 simulated core damage.

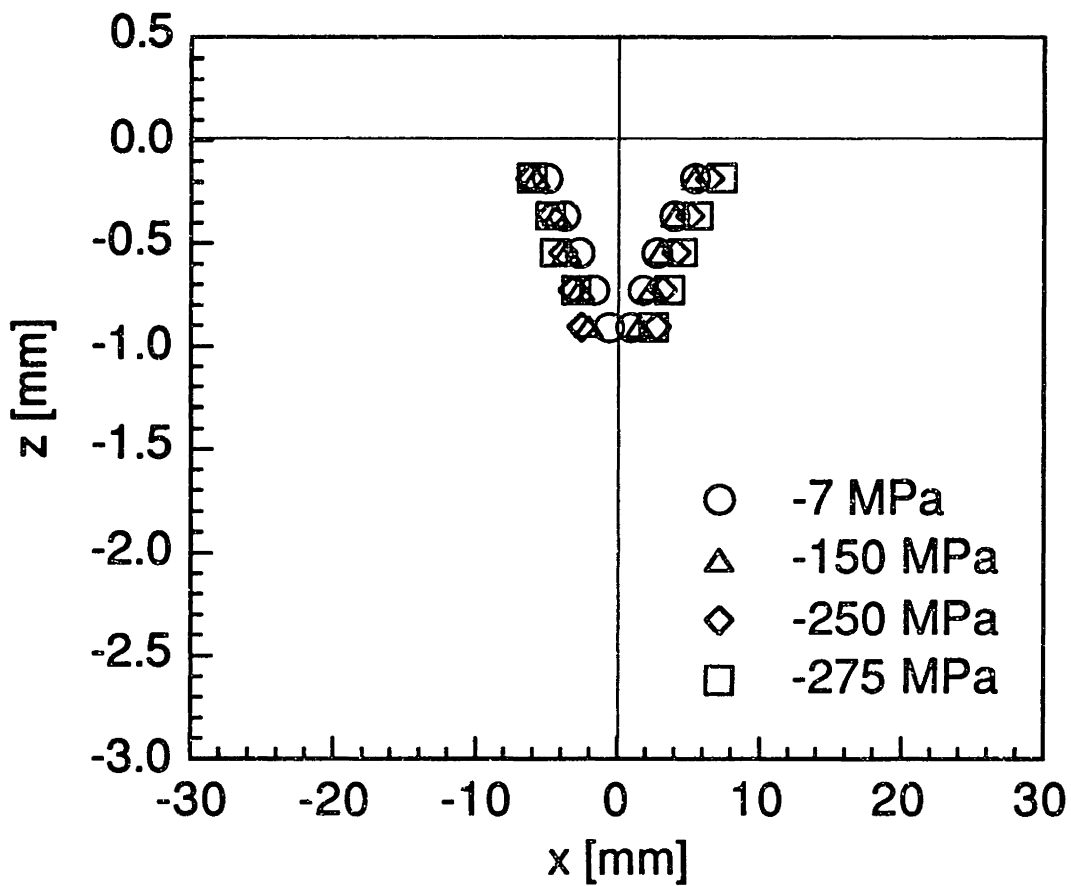


Figure 6.58 Measured dimple profiles along centerline in loading direction at various loads for a specimen with (0/90) facesheets and level 1 static indentation damage (corresponding moiré fringe patterns shown in Figure 6.56).

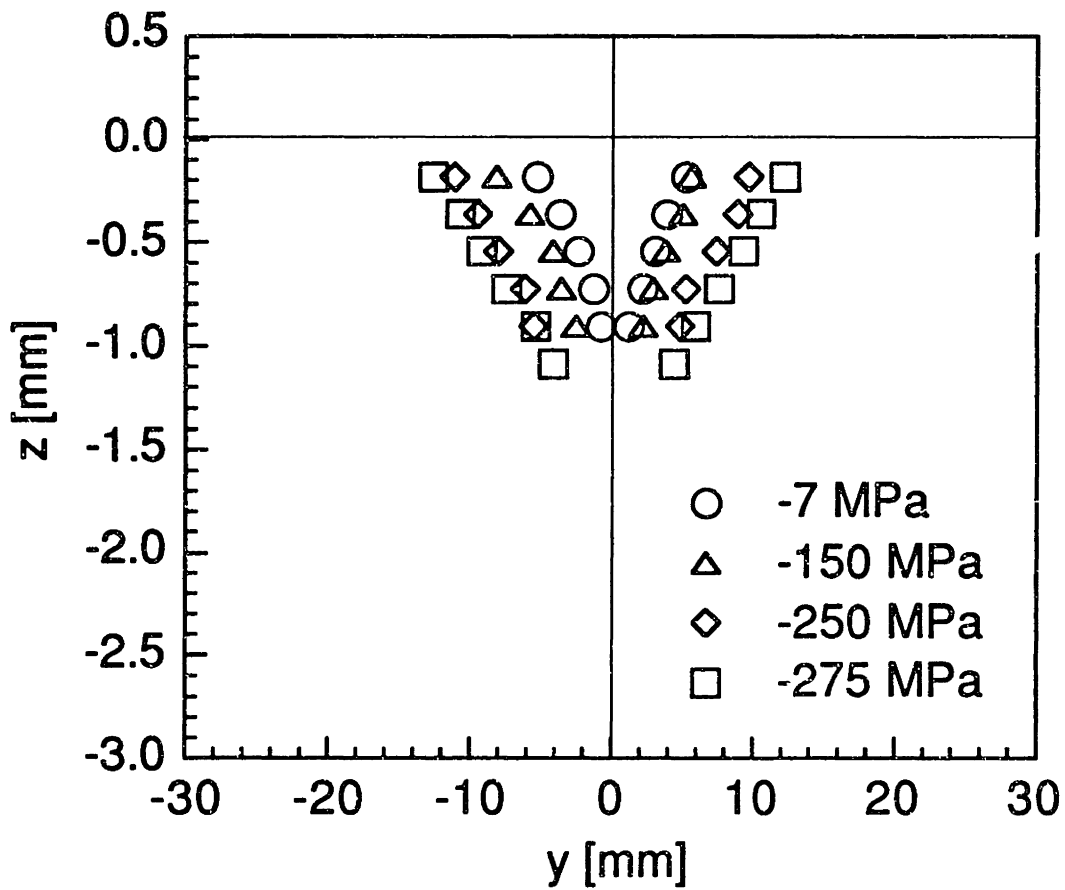


Figure 6.59 Measured dimple profiles along centerline perpendicular to loading direction at various loads for a specimen with (0/90) facesheets and level 1 static indentation damage (corresponding moiré fringe patterns shown in Figure 6.56).

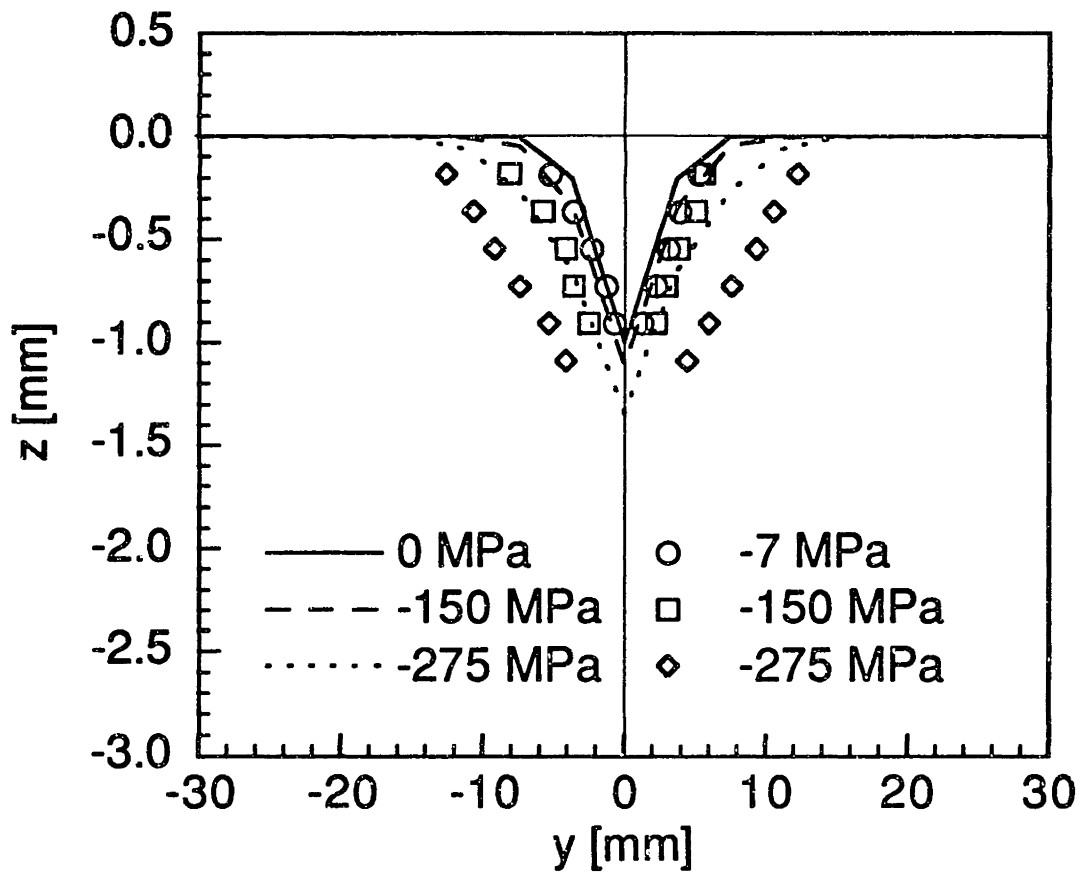


Figure 6.60 Experimental and predicted dimple profiles along centerline perpendicular to loading direction at various loads for a specimen with (0/90) facesheets and with level 1 static indentation damage.

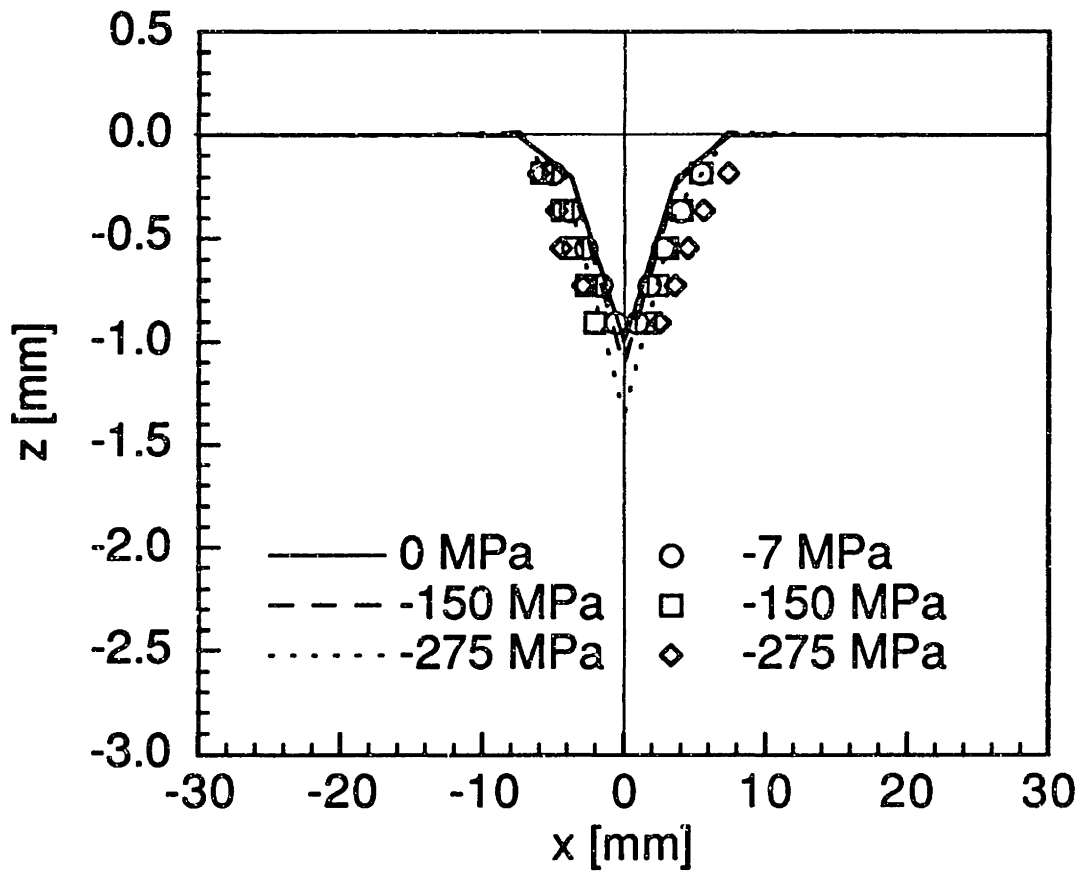


Figure 6.61 Experimental and predicted dimple profiles along centerline in loading direction at various loads for a specimen with (0/90) facesheets and with level 1 static indentation damage.

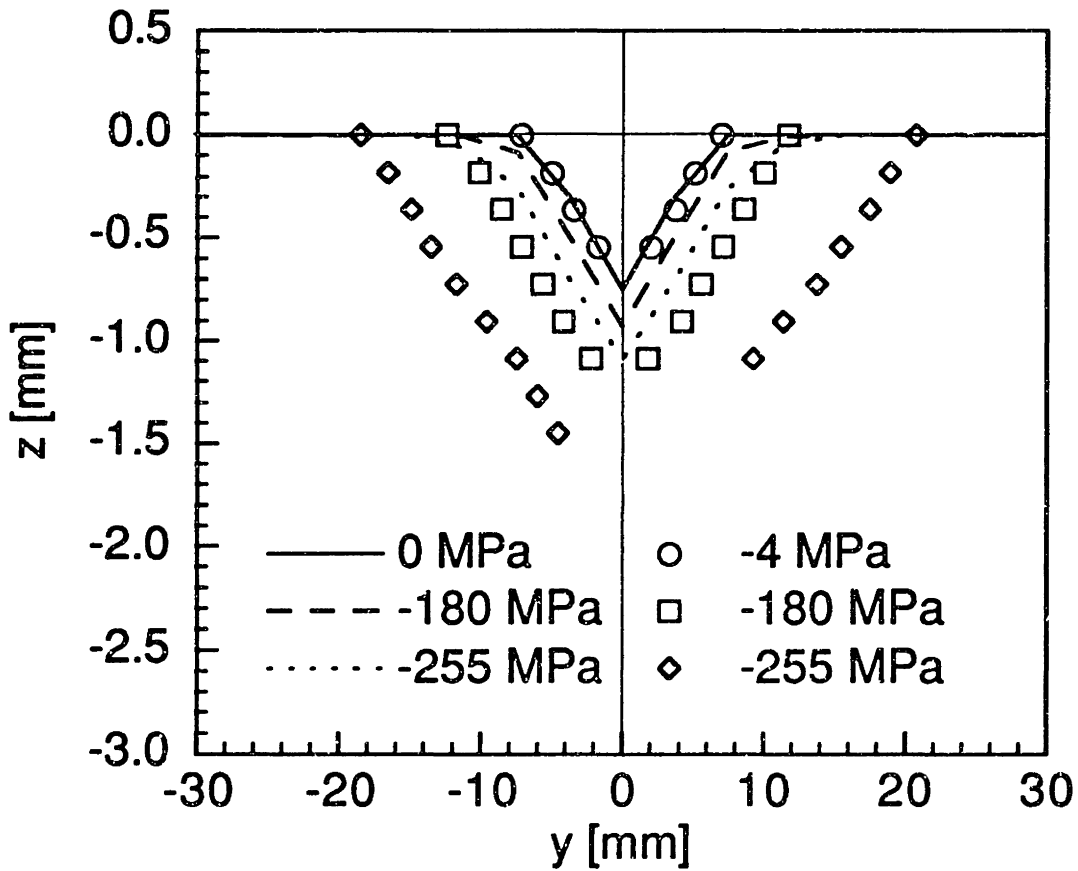


Figure 6.62 Experimental and predicted dimple profiles along centerline perpendicular to loading direction at various loads for a specimen with (0/90) facesheets and with level 2 static indentation damage.

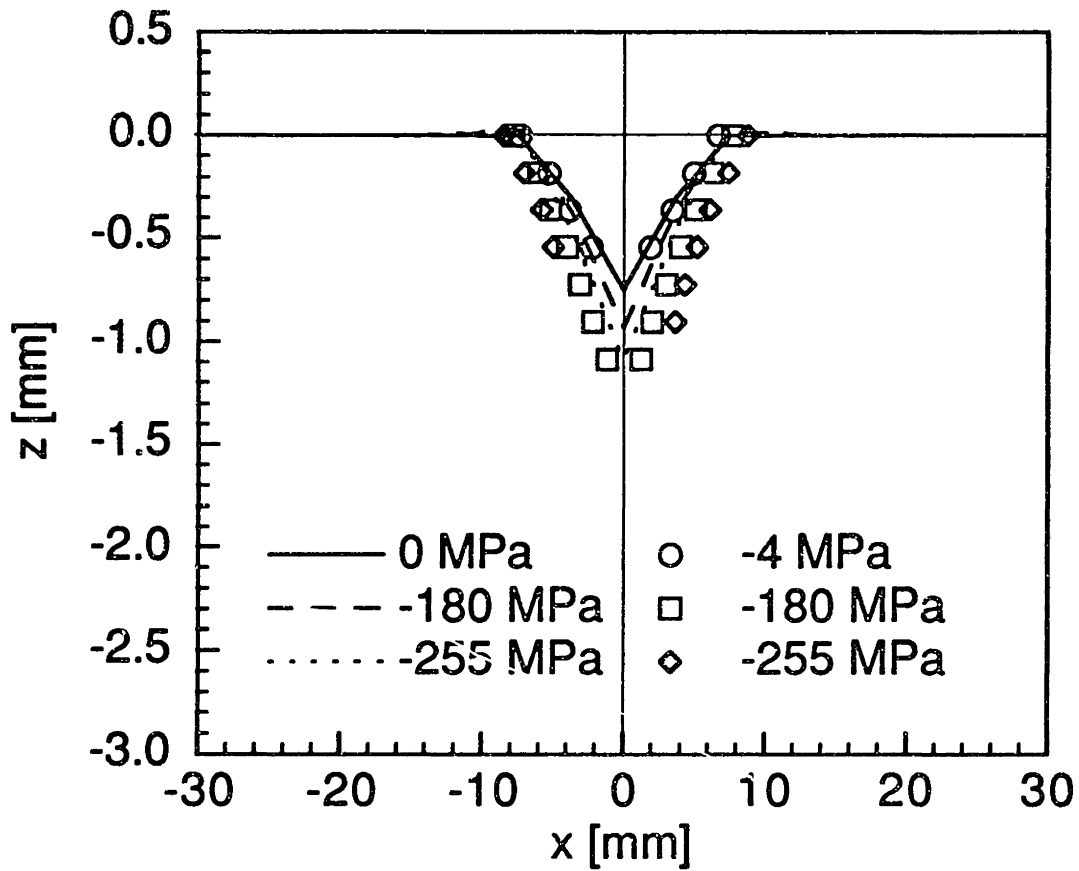


Figure 6.63 Experimental and predicted dimple profiles along centerline in loading direction at various loads for a specimen with (0/90) facesheets and with level 2 static indentation damage.

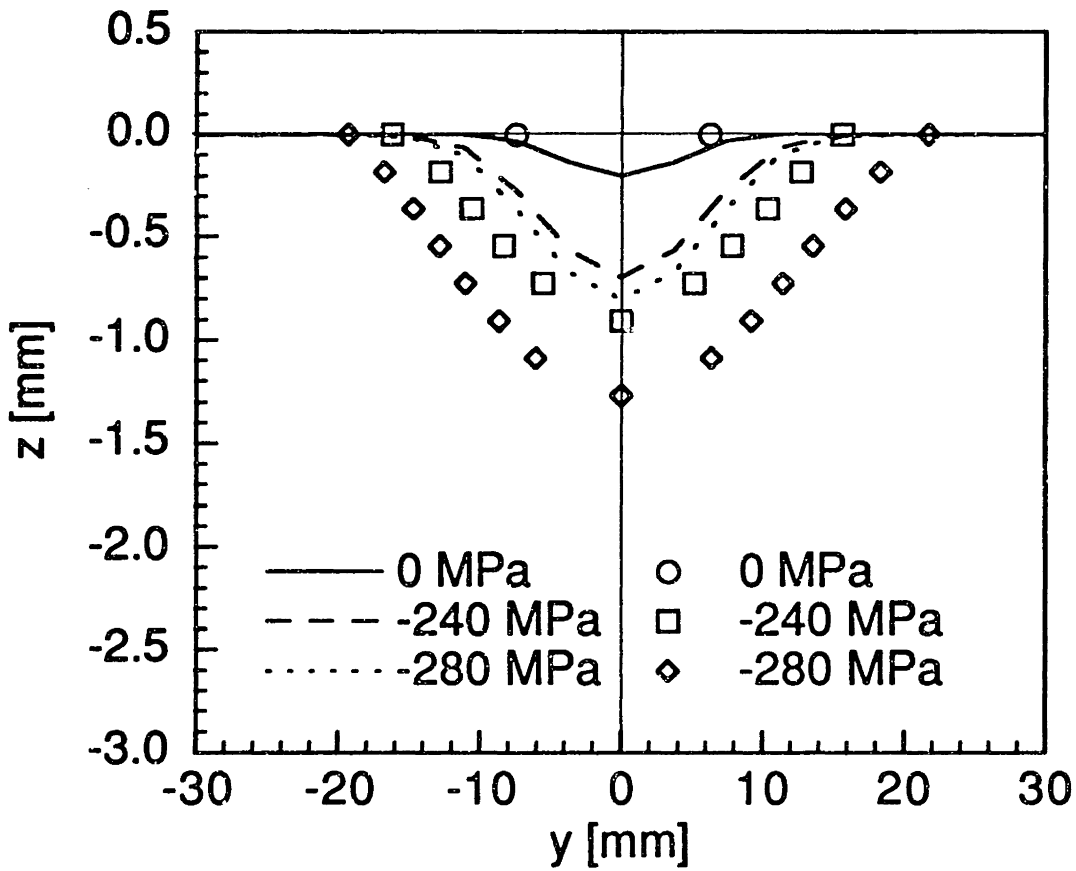


Figure 6.64 Experimental and predicted dimple profiles along centerline perpendicular to loading direction at various loads for a specimen with (0/90) facesheets and with level 3 static indentation damage.

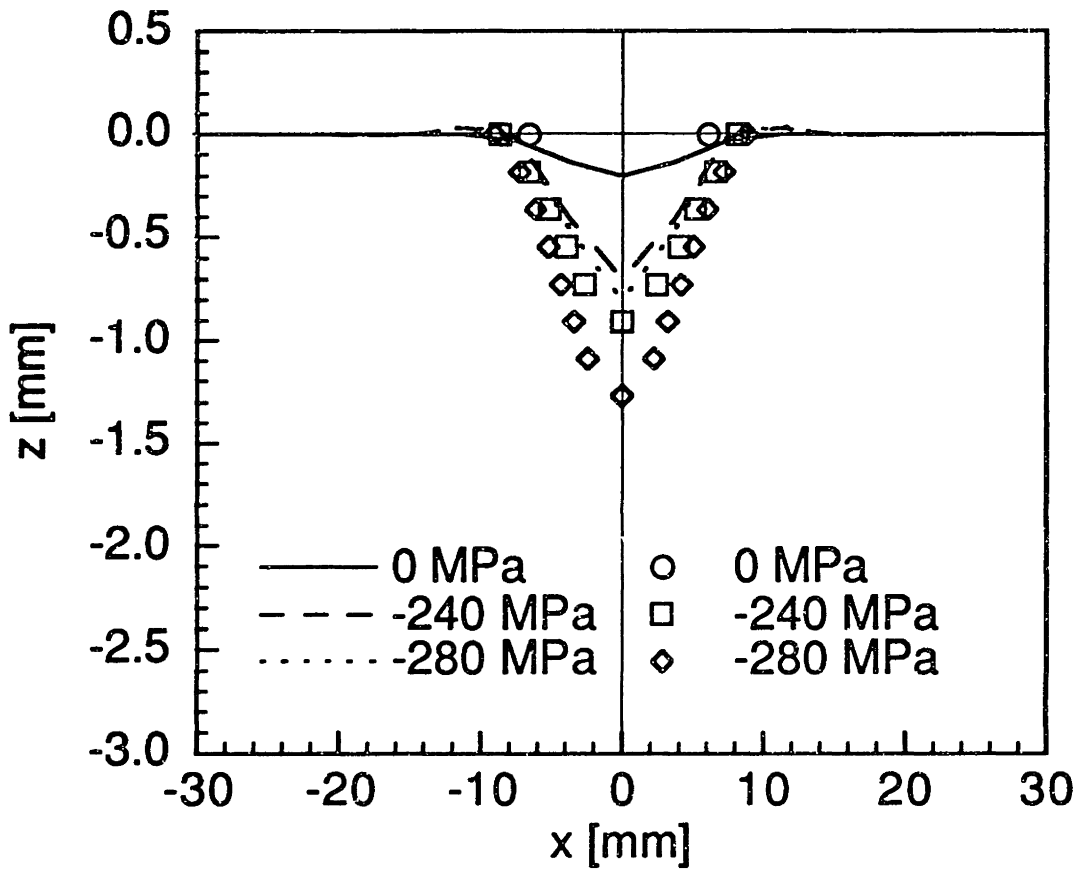


Figure 6.65 Experimental and predicted dimple profiles along centerline in loading direction at various loads for a specimen with (0/90) facesheets and with level 3 static indentation damage.

figures that the dimple primarily propagates perpendicular to the loading direction (i.e. along the y-axis) regardless of the damage level. The dimple propagation model shows the same trend as that of the experimental data, but underpredicts the propagation of the dimple for all three damage levels.

Additional dimple profiles of specimens with various levels of simulated core damage are shown in Figures 6.66 through 6.71 for specimens with (0/90) facesheets. The corresponding analytical predictions by the dimple propagation model are also included. Once again, the dimples propagate primarily along the y-axis regardless of the damage level. The predictions of the dimple propagation model match fairly well with the experimental results. In the case of level 3 simulated core damage, the model requires an applied stress of -320 MPa to match the measured profiles at an applied stress of -310 MPa. The dimple propagates further before catastrophic failure in the specimens with static indentation damage than in the corresponding specimens with simulated core damage for all damage levels. This observation is quantitatively examined later in this section when the dimensions of the dimples just before catastrophic failure are compared between these two groups of specimens.

The dimple propagation data can be presented in an alternative way by plotting the applied stress level against the dimension of the dimple perpendicular to the loading direction, the primary direction of propagation. The dimension of the dimple is measured at the first-order fringe of the moiré patterns. The first-order fringe is chosen over the zeroth-order fringe because it can be measured more accurately than the zeroth-order fringe. Sometimes in level 3 damage, the first order fringe is not measurable because the dimple is too shallow and its maximum nominal depth of 0.2 mm is very close to the resolution of the moiré measurements (0.181 mm).

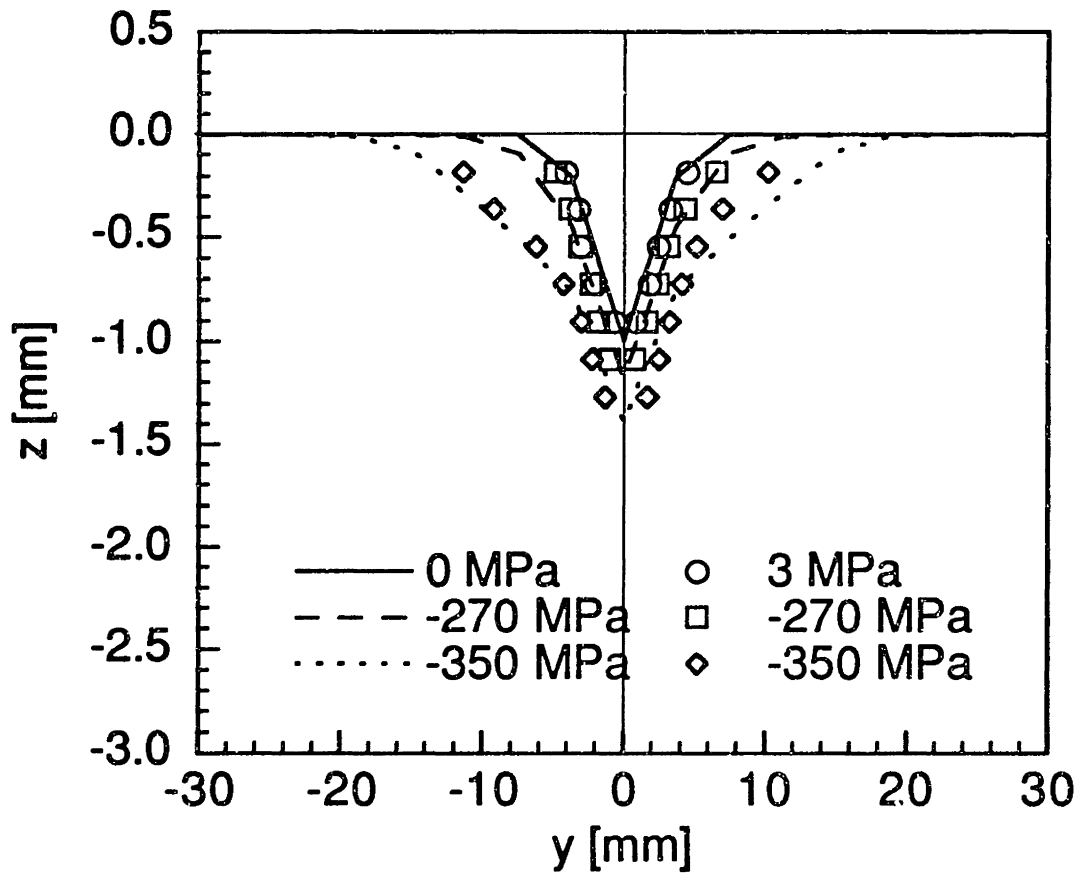


Figure 6.66 Experimental and predicted dimple profiles along centerline perpendicular to loading direction at various loads for a specimen with (0/90) facesheets and with level 1 simulated core damage.

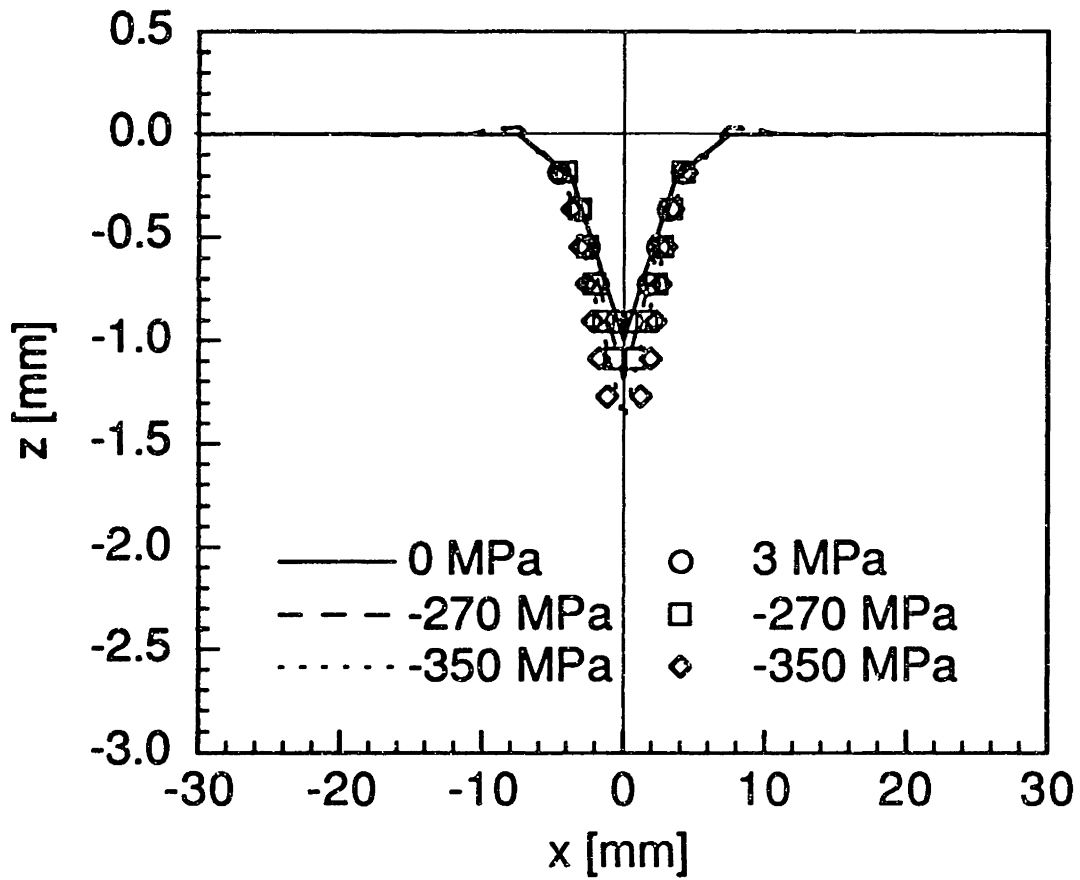


Figure 6.67 Experimental and predicted dimple profiles along centerline in loading direction at various loads for a specimen with (0/90) facesheets and with level 1 simulated core damage.

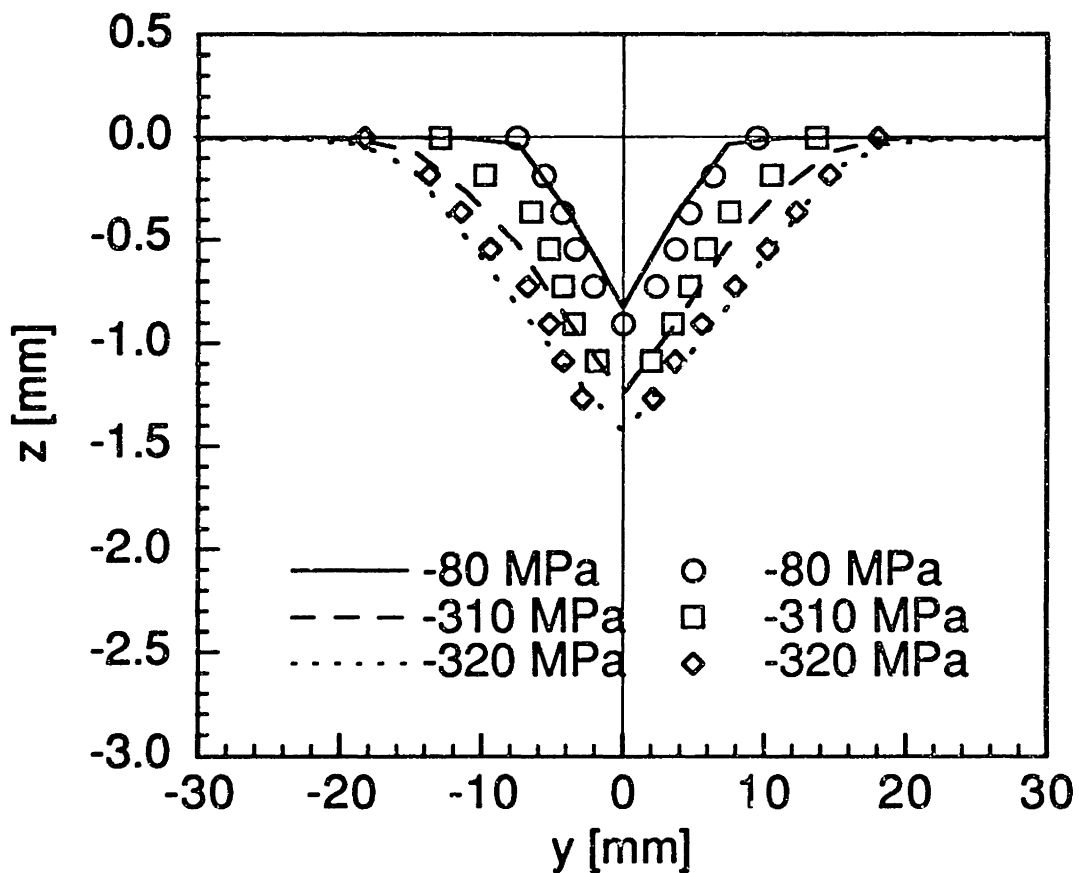


Figure 6.68 Experimental and predicted dimple profiles along centerline perpendicular to loading direction at various loads for a specimen with (0/90) facesheets and with level 2 simulated core damage.

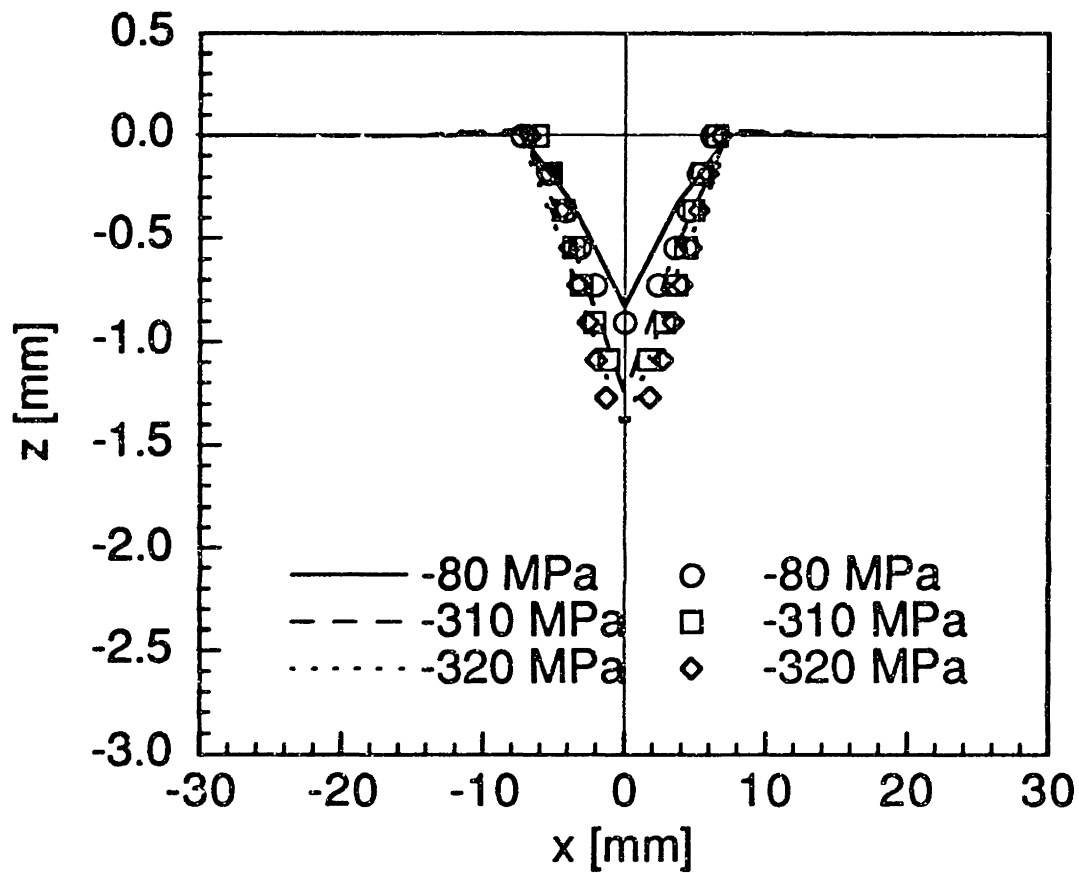


Figure 6.69 Experimental and predicted dimple profiles along centerline in loading direction at various loads for a specimen with (0/90) facesheets and with level 2 simulated core damage.

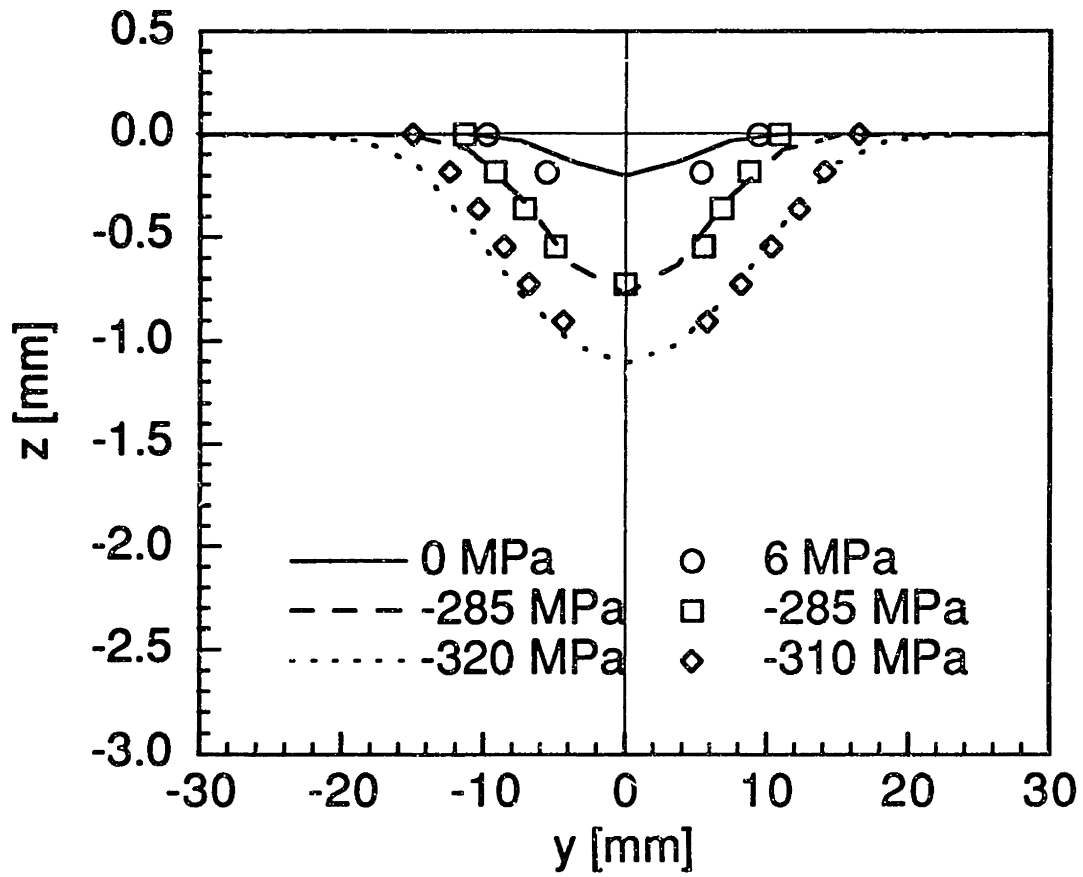


Figure 6.70 Experimental and predicted dimple profiles along centerline perpendicular to loading direction at various loads for a specimen with (0/90) facesheets and with level 3 simulated core damage.

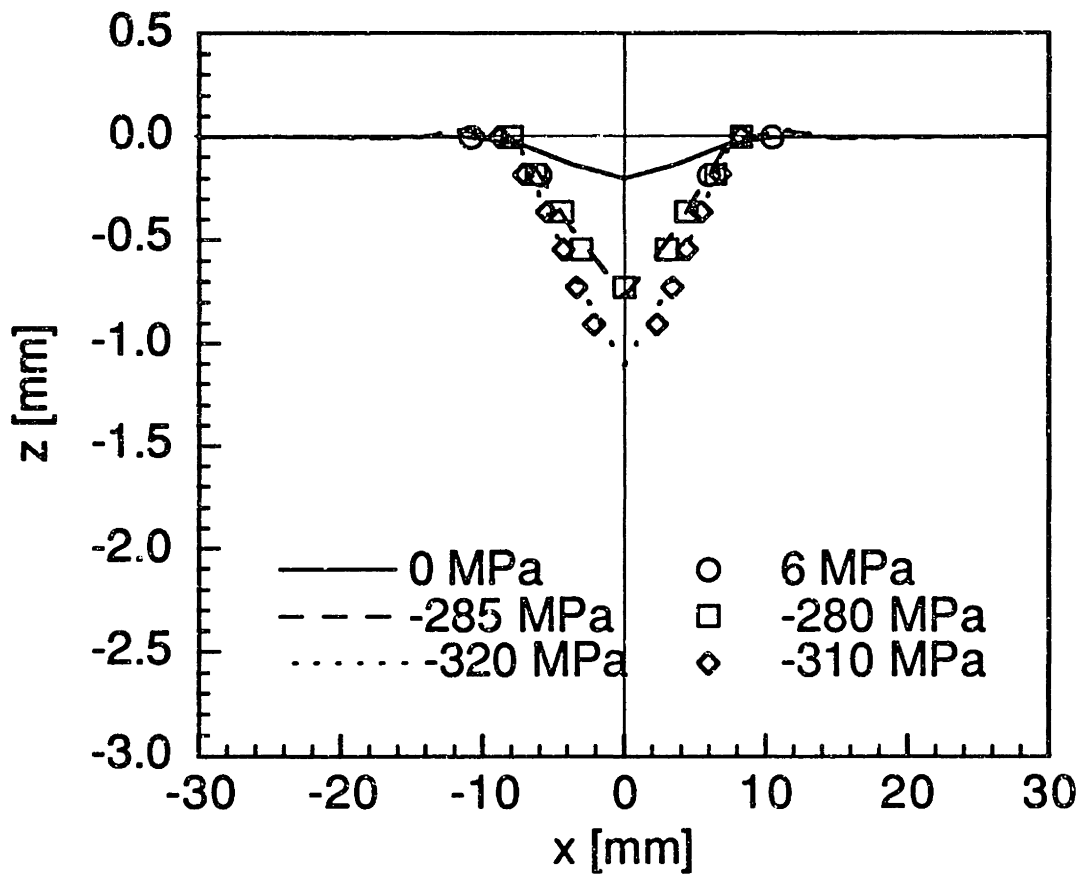


Figure 6.71 Experimental and predicted dimple profiles along centerline in loading direction at various loads for a specimen with (0/90) facesheets and with level 3 simulated core damage.

In those cases, the value of zero is assigned to the dimension of the dimple as defined by the boundary of the first order fringe.

The applied stress level is plotted against the dimension of the dimple perpendicular to the loading direction in Figures 6.72 through 6.74 for a group of specimens with (0/90) facesheets and various levels of static indentation damage and simulated core damage. The corresponding analytical predictions for specimens with simulated core damage is also included. It can be seen from these figures that specimens with static indentation damage have greater propagation for a given applied stress level than the corresponding specimens with simulated core damage. The analytical predictions also match the corresponding experimental data fairly well and correctly show the trend of propagation observed in the experiments. The dimple profile data are plotted in Figures 6.75 and 6.76 according to the damage types in specimens with (0/90) facesheets. It can be seen in Figure 6.76 that specimens with level 2 and level 3 simulated core damage have very similar dimple evolution.

A typical set of digitized fringe patterns is shown in Figure 6.77 for a specimen with (± 45) facesheets and indented with the 12.7 mm-diameter indenter. As in the case of (0/90) facesheets, the initial dent/dimple changes from circular to elliptical and finally to an elongated diamond with rounded corners. Similar evolution patterns are also observed in specimens with simulated core damage as shown in Figure 6.78. The characteristics of the dimple propagation do not change qualitatively with damage levels.

Dimple profiles of specimens with various levels of static indentation damage are shown in Figures 6.79 through 6.84 for specimens with (± 45) facesheets. The corresponding analytical predictions by the dimple propagation model are also included. The dimples again propagated

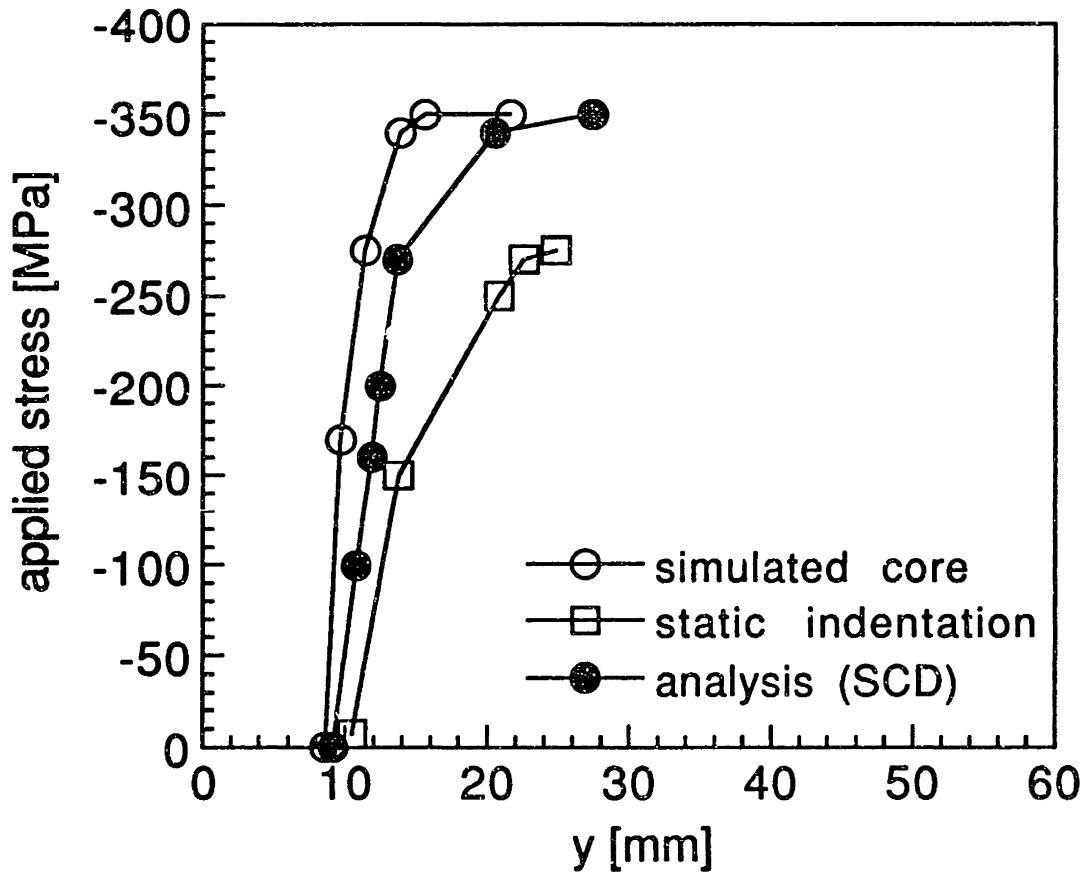


Figure 6.72 Predicted and measured dimension of dimple along centerline perpendicular to loading at various applied stress levels for specimens with (0/90) facesheets and level 1 damage.

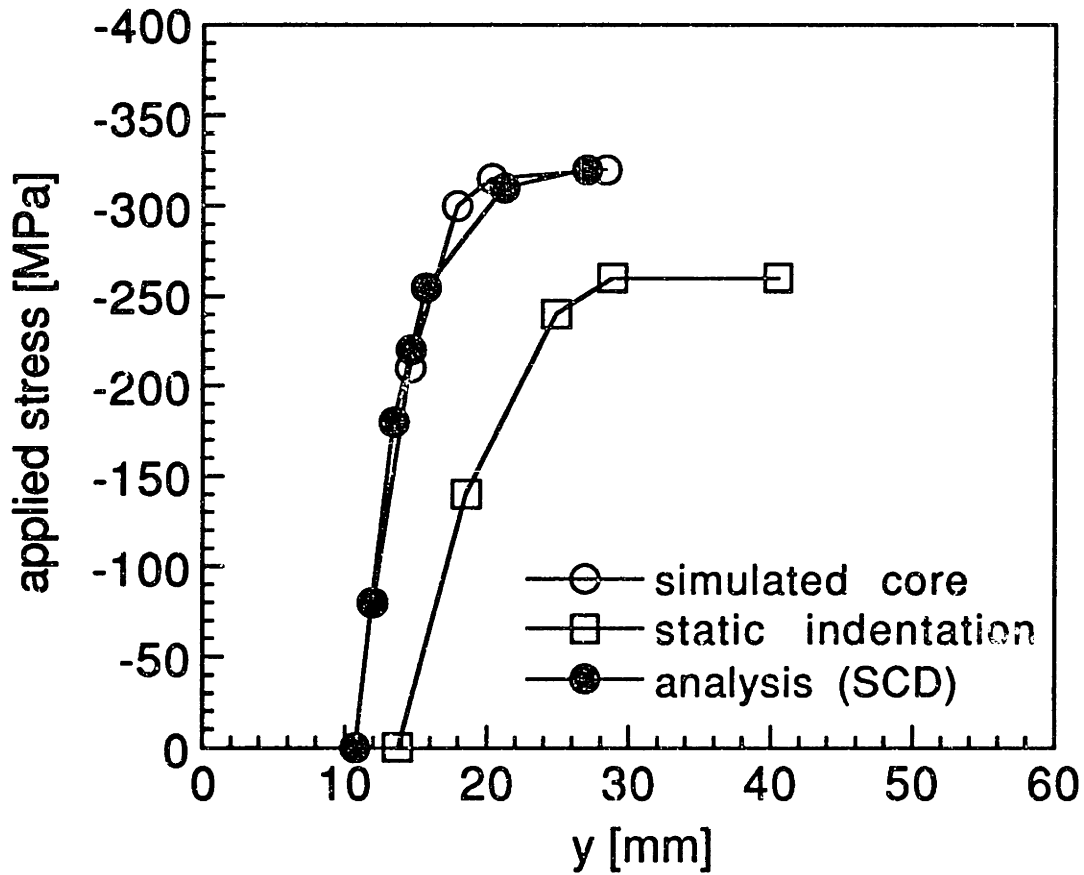


Figure 6.73 Predicted and measured dimension of dimple along centerline perpendicular to loading at various applied stress levels for specimens with (0/90) facesheets and level 2 damage.

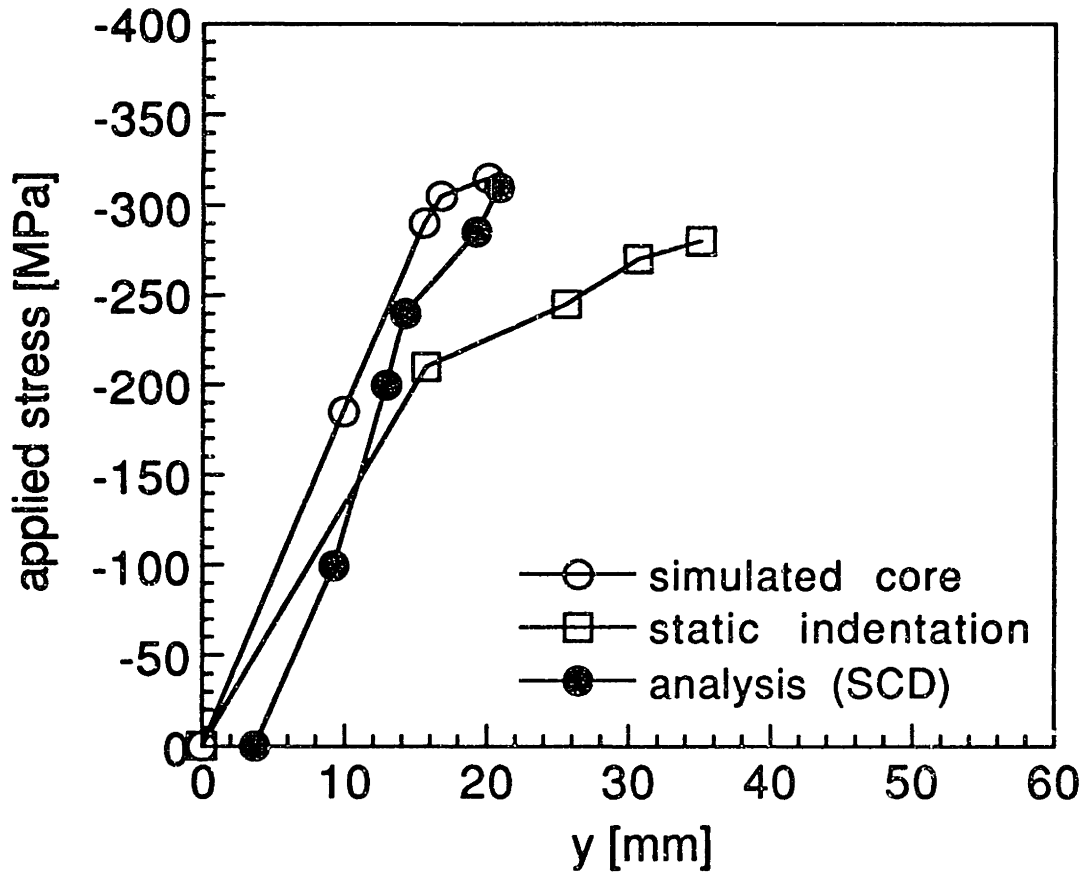


Figure 6.74 Predicted and measured dimension of dimple along centerline perpendicular to loading at various applied stress levels for specimens with (0/90) facesheets and level 3 damage.

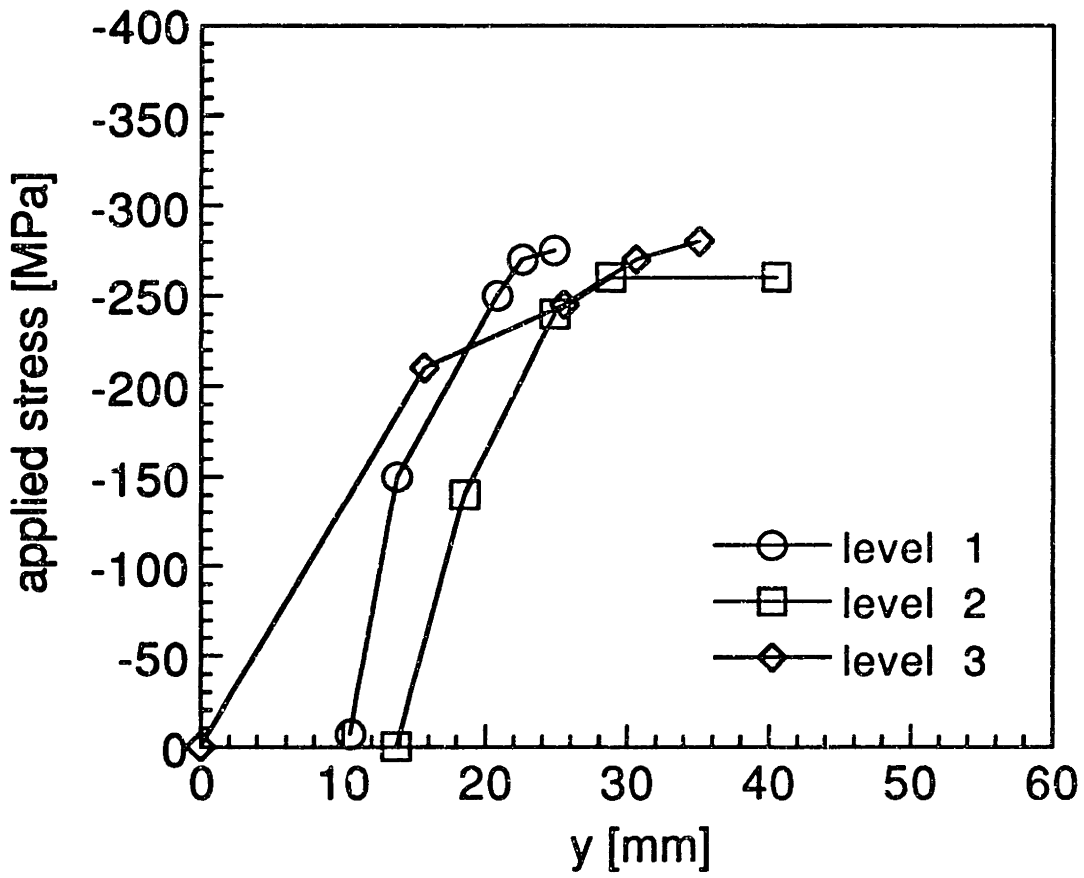


Figure 6.75 Dimension of dimple along centerline perpendicular to loading at various applied stress levels for specimens with (0/90) facesheets and static indentation damage.

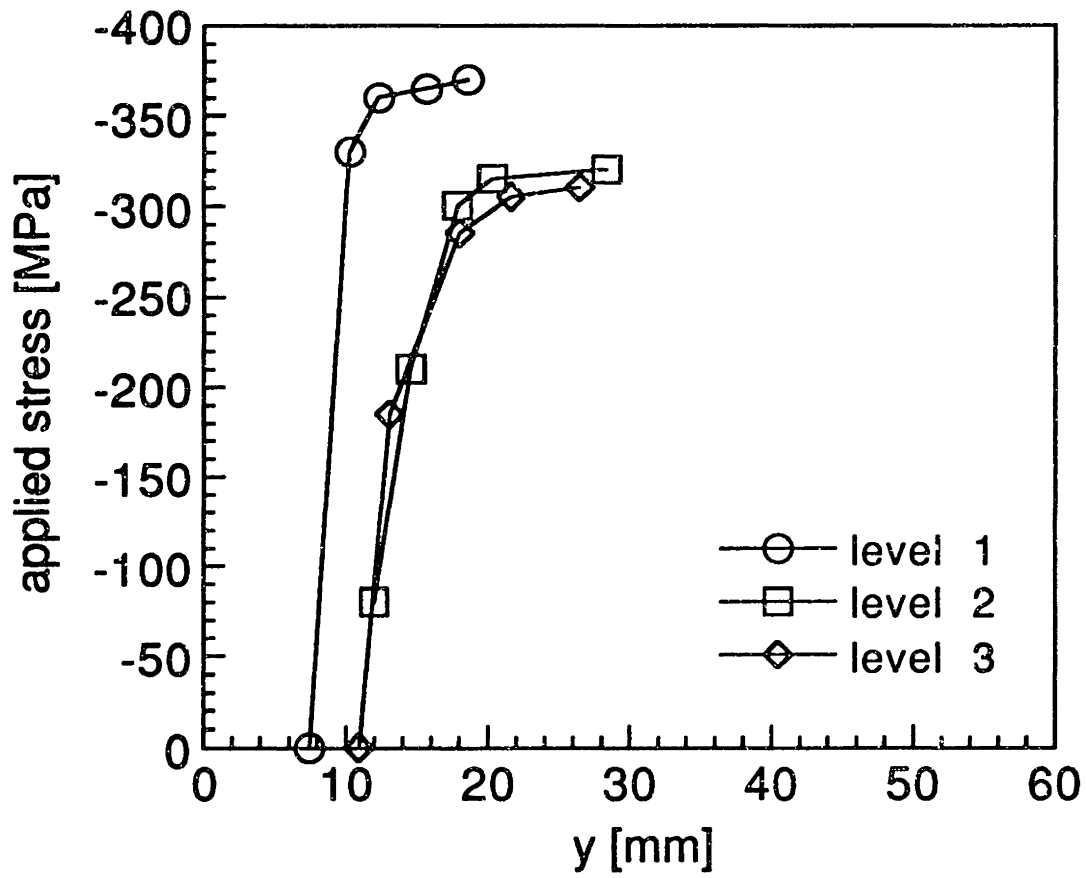


Figure 6.76 Dimension of dimple along centerline perpendicular to loading at various applied stress levels for specimens with (0/90) facesheets and simulated core damage.

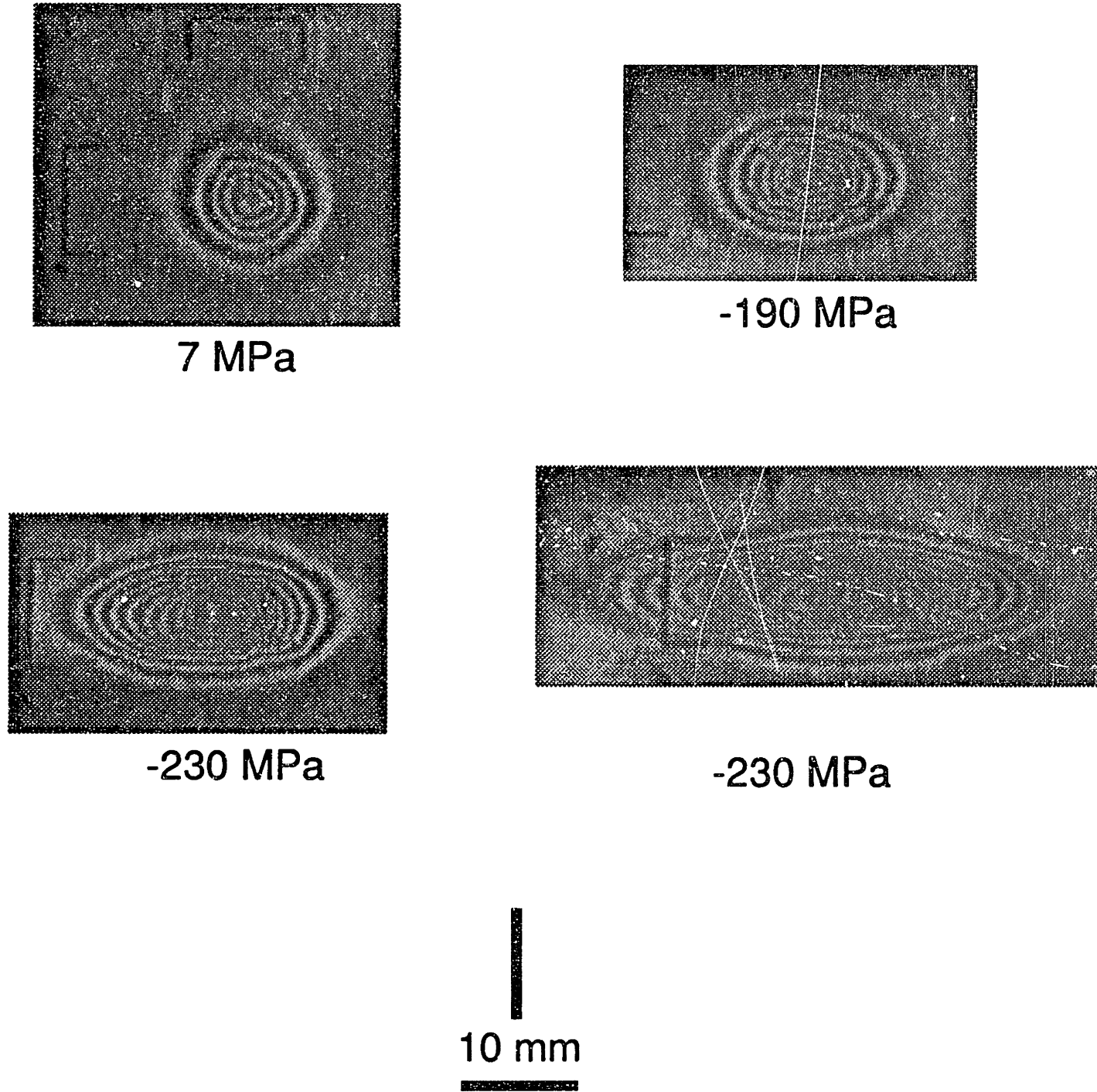


Figure 6.77 Digitized moiré fringe patterns at various applied stress levels for a specimen with (± 45) facesheets and indentation damage inflicted with a 12.7 mm-diameter indenter.

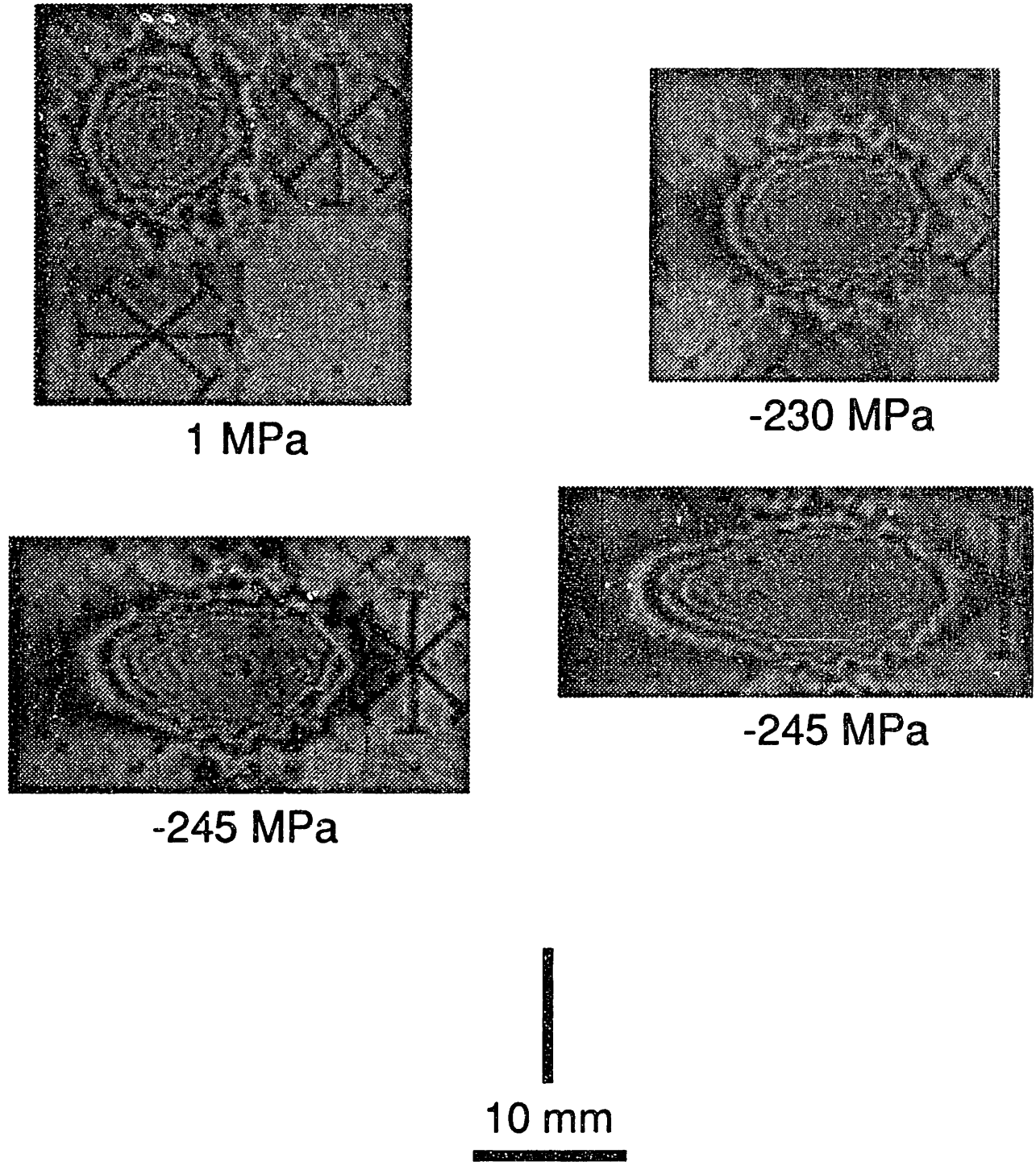


Figure 6.78 Digitized moiré fringe patterns at various applied stress levels for a specimen with (± 45) facesheets and level 1 simulated core damage.

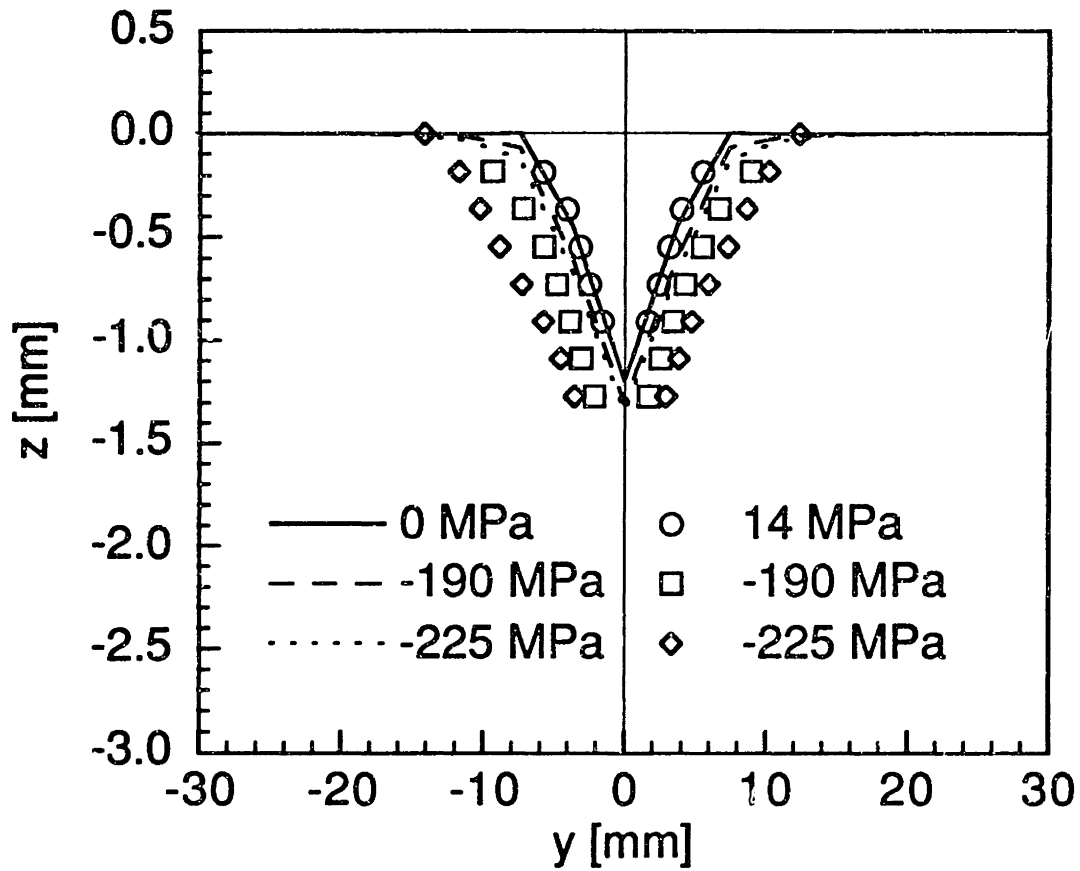


Figure 6.79 Experimental and predicted dimple profiles along centerline perpendicular to loading direction at various loads for a specimen with (± 45) facesheets and with level 1 static indentation damage.

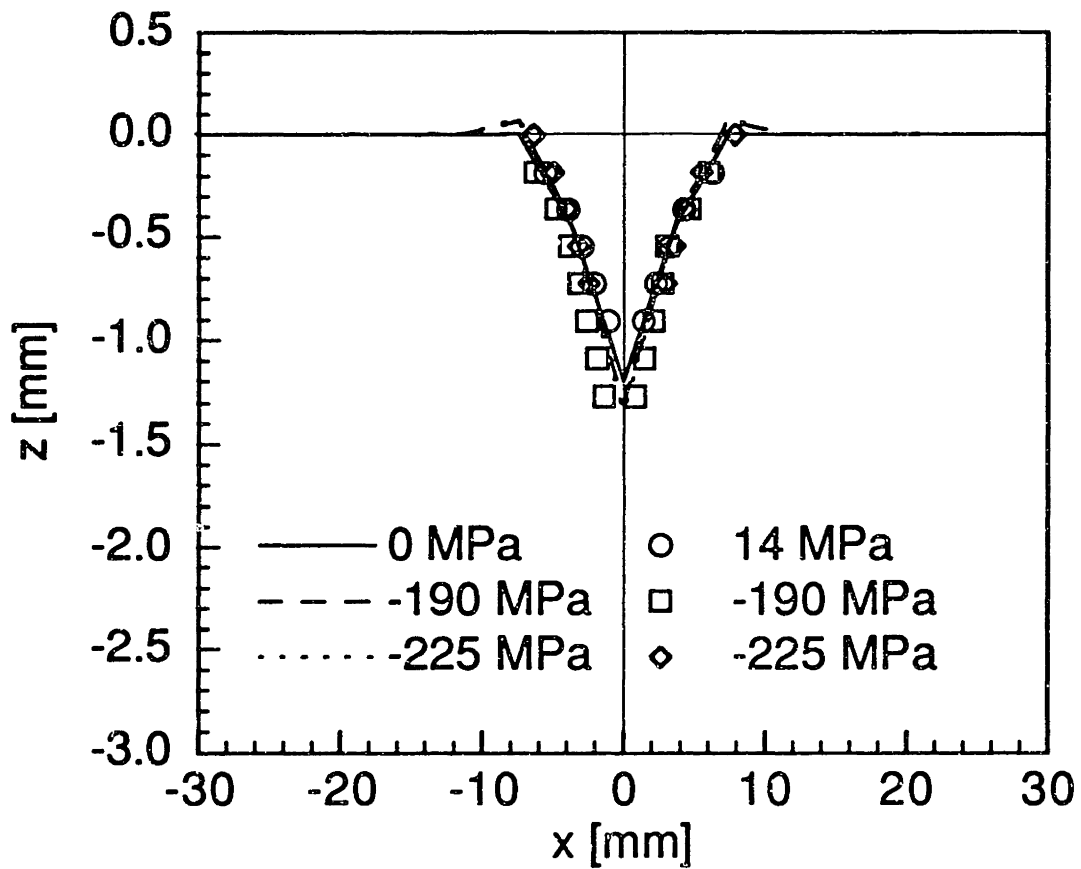


Figure 6.80 Experimental and predicted dimple profiles along centerline in loading direction at various loads for a specimen with (± 45) facesheets and with level 1 static indentation damage.

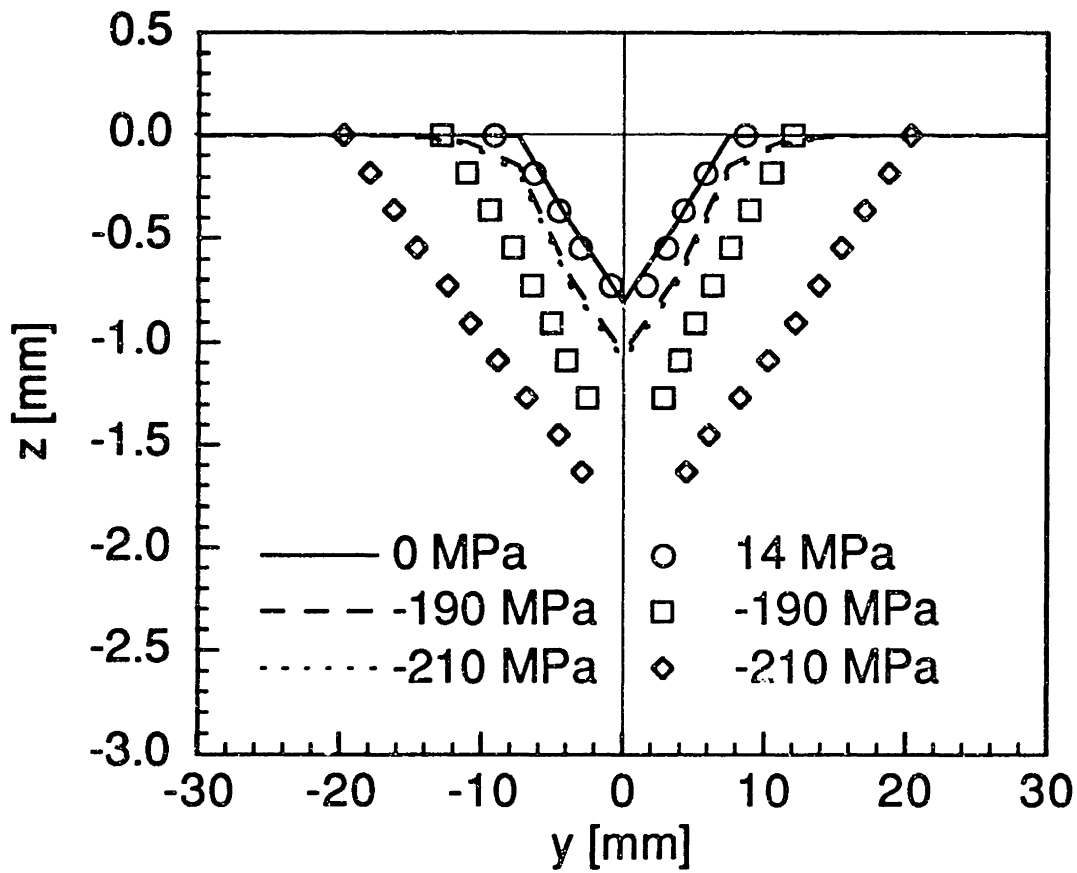


Figure 6.81 Experimental and predicted dimple profiles along centerline perpendicular to loading direction at various loads for a specimen with (± 45) facesheets and with level 2 static indentation damage.

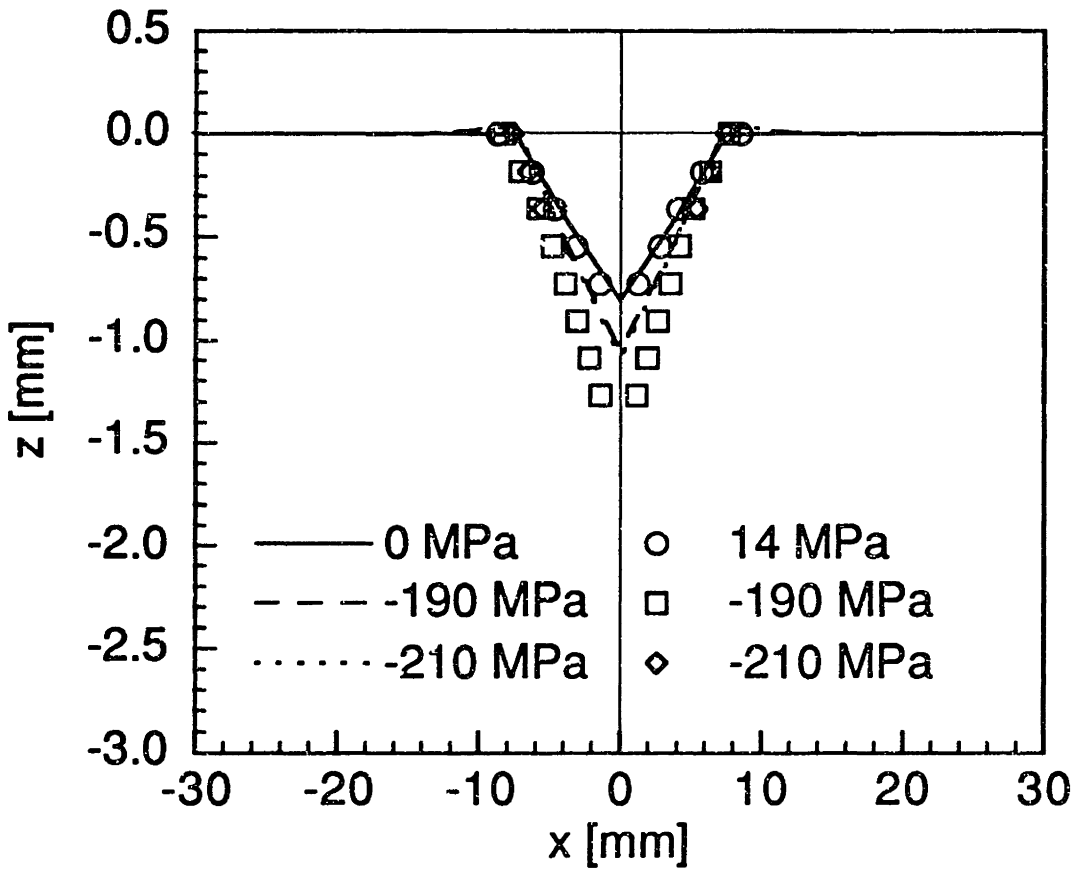


Figure 6.82 Experimental and predicted dimple profiles along centerline in loading direction at various loads for a specimen with (± 45) facesheets and with level 2 static indentation damage.

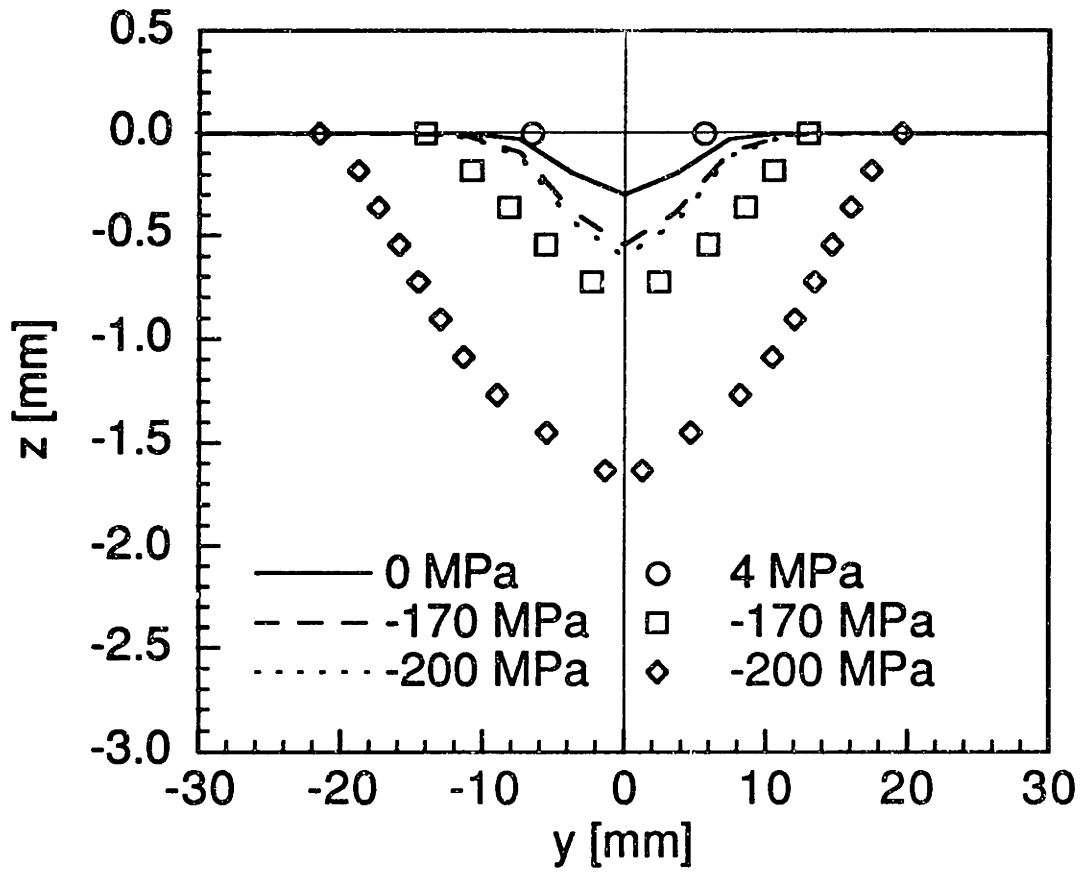


Figure 6.83 Experimental and predicted dimple profiles along centerline perpendicular to loading direction at various loads for a specimen with (± 45) facesheets and with level 3 static indentation damage.

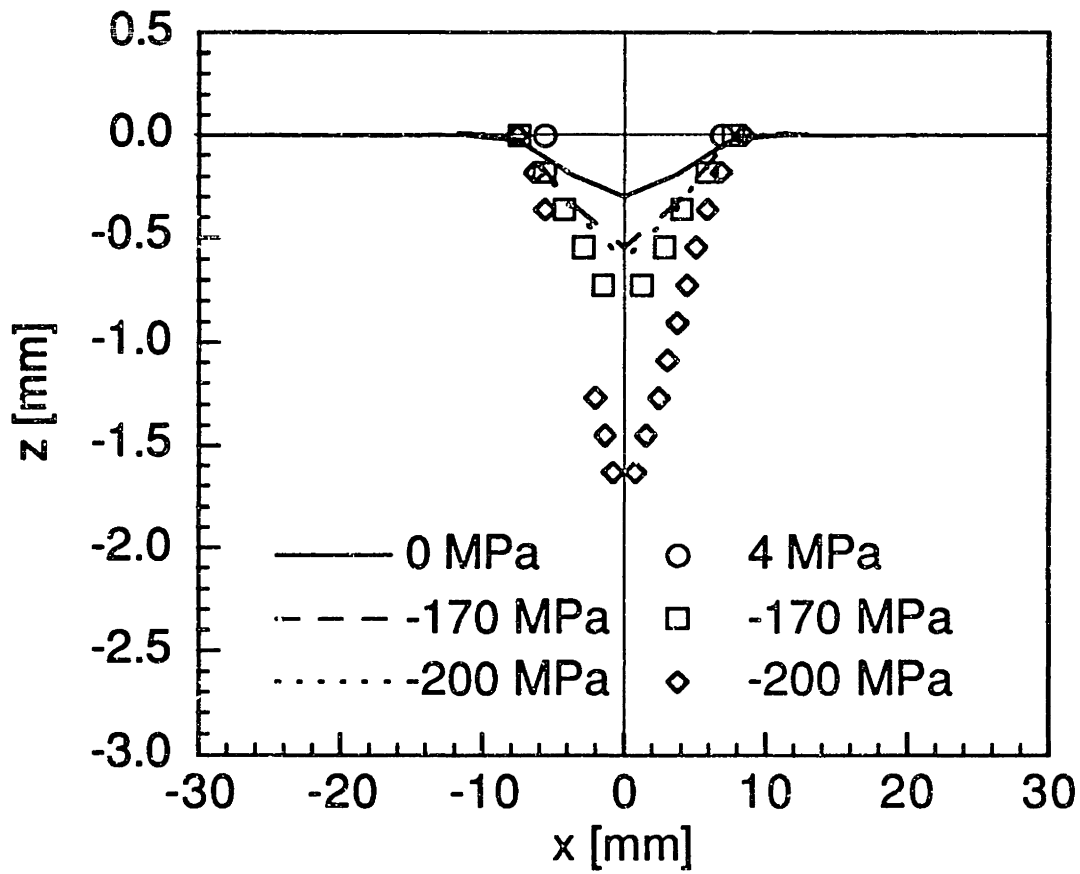


Figure 6.84 Experimental and predicted dimple profiles along centerline in loading direction at various loads for a specimen with (± 45) facesheets and with level 3 static indentation damage.

primarily along the y-axis regardless of the damage levels. The dimple propagation model predicts the same trend, but underpredicts the dimple propagation as it did for the case of specimens with (0/90) facesheets and static indentation damage.

Additional dimple profiles of specimens with various levels of simulated core damage are shown in Figures 6.85 through 6.90 for specimens with (± 45) facesheets. The corresponding analytical predictions by the dimple propagation model are also included. Once again, the dimple propagates primarily perpendicular to the loading direction (i.e. along the y-axis) for all damage levels. The analytical predictions match the experimental results quite well for intermediate load levels: -205 MPa for level 1 simulated core damage, -190 MPa for level 2 simulated core damage, and -220 MPa for level 3 simulated core damage. However the model underpredicts the dimple propagation at the experimental failure stress for specimens with level 2 and level 3 simulated core damage. The dimple in specimens with level 1 simulated core damage showed very little propagation before failure. Therefore, it is not possible to evaluate the accuracy with which the model predicts this particular dimple propagation. Once again, the dimple propagates further before catastrophic failure in the specimens with static indentation damage than in the corresponding specimens with simulated core damage. This observation is quantitatively examined later by comparing the dimensions of the dimples just before catastrophic failure for different specimen types.

The applied stress level is plotted against the dimension of the dimple perpendicular to the loading direction in Figures 6.91 through 6.93 for a group of specimens with (± 45) facesheets and various damage levels. Once again, specimens with static indentation damage have more extensive

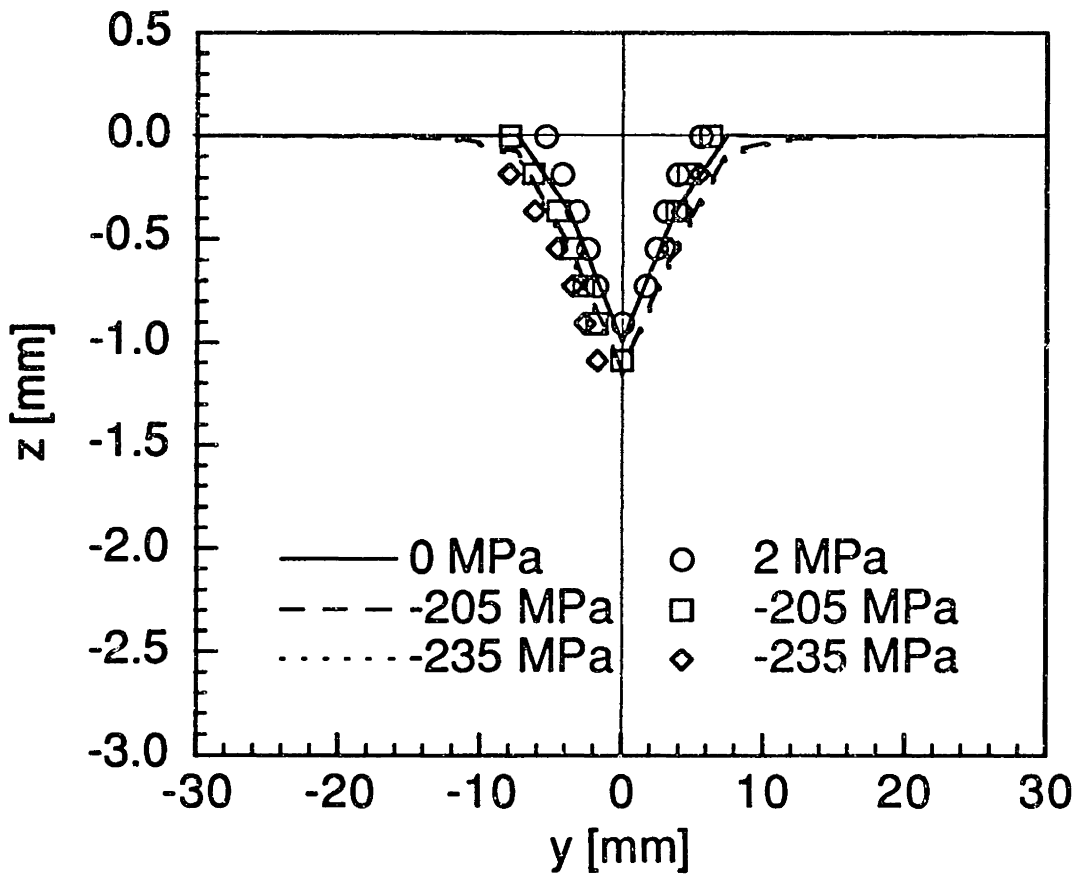


Figure 6.85 Experimental and predicted dimple profiles along centerline perpendicular to loading direction at various loads for a specimen with (± 45) facesheets and with level 1 simulated core damage.

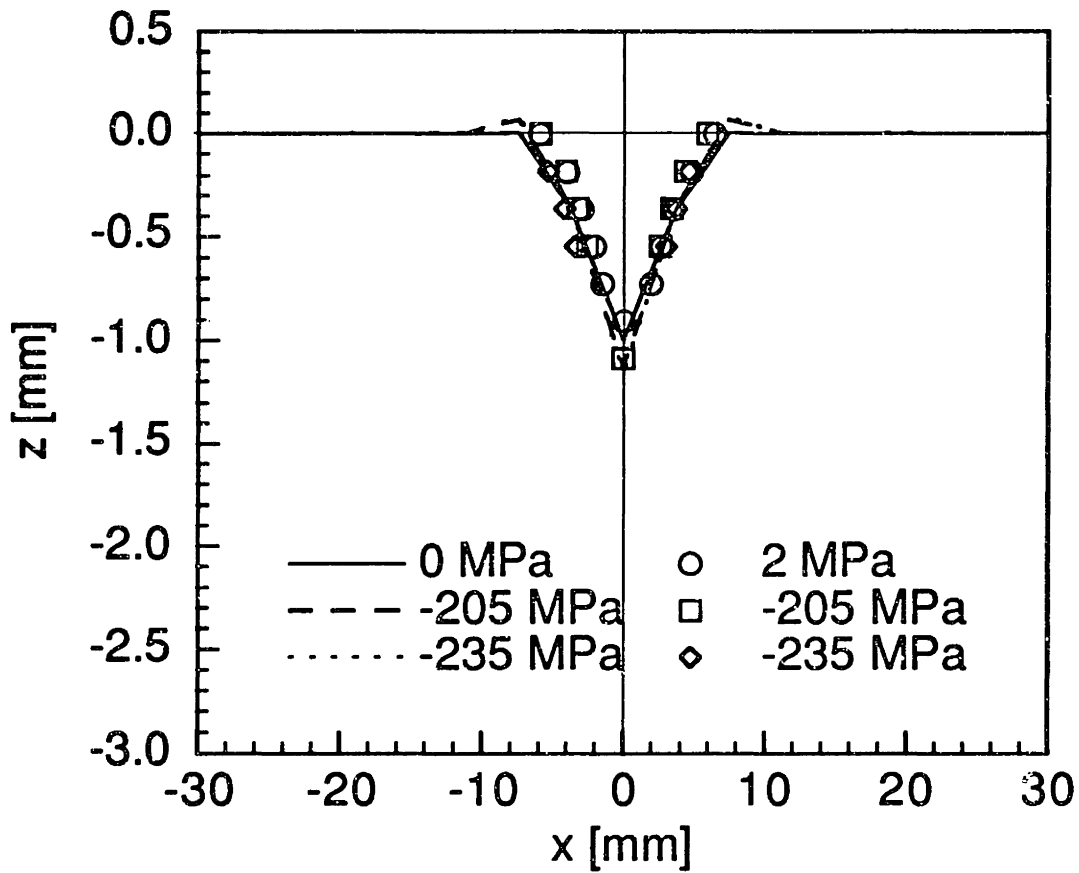


Figure 6.86 Experimental and predicted dimple profiles along centerline in loading direction at various loads for a specimen with (± 45) facesheets and with level 1 simulated core damage.

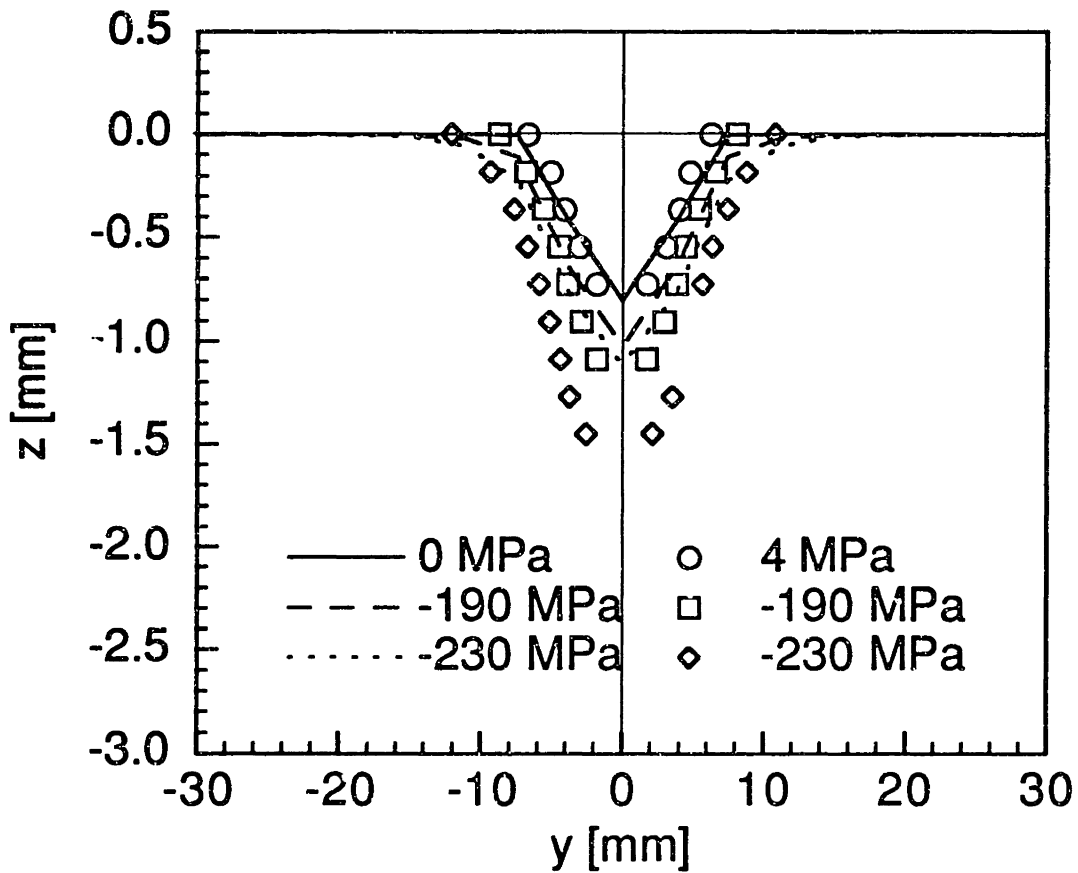


Figure 6.87 Experimental and predicted dimple profiles along centerline perpendicular to loading direction at various loads for a specimen with (± 45) facesheets and with level 2 simulated core damage.

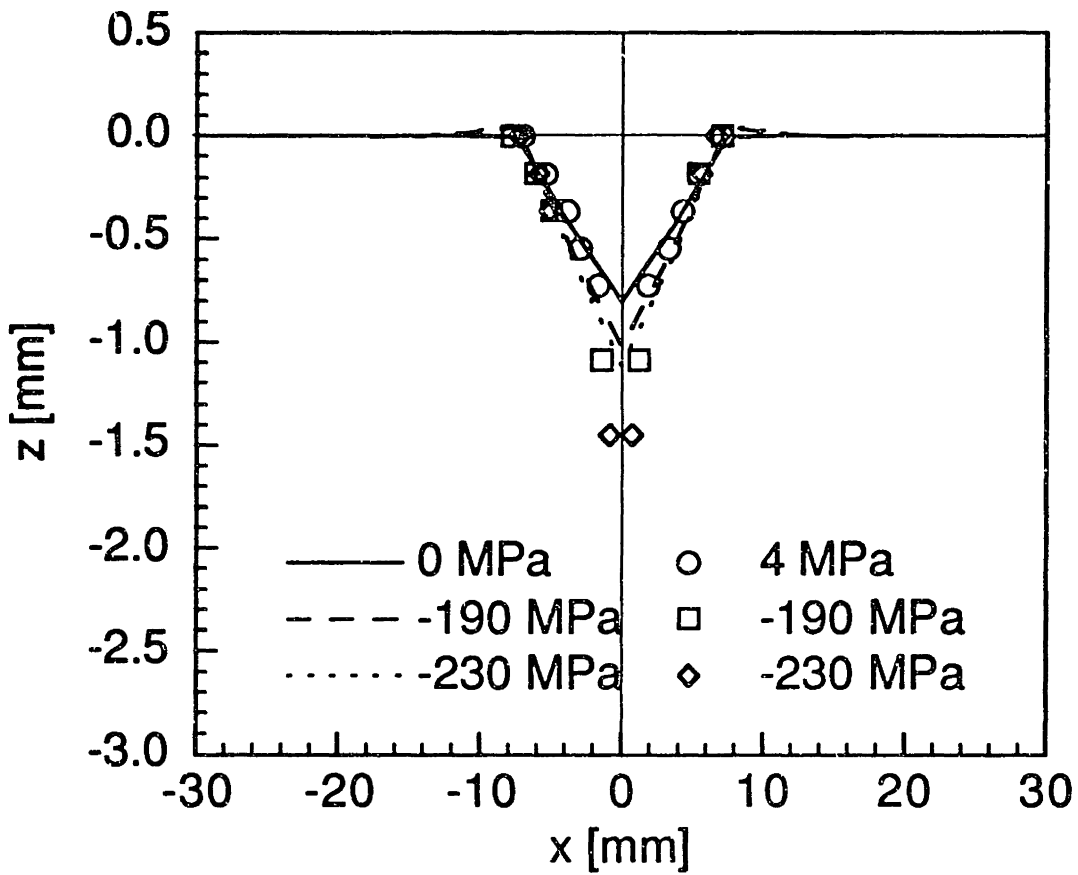


Figure 6.88 Experimental and predicted dimple profiles along centerline in loading direction at various loads for a specimen with (± 45) facesheets and with level 2 simulated core damage.

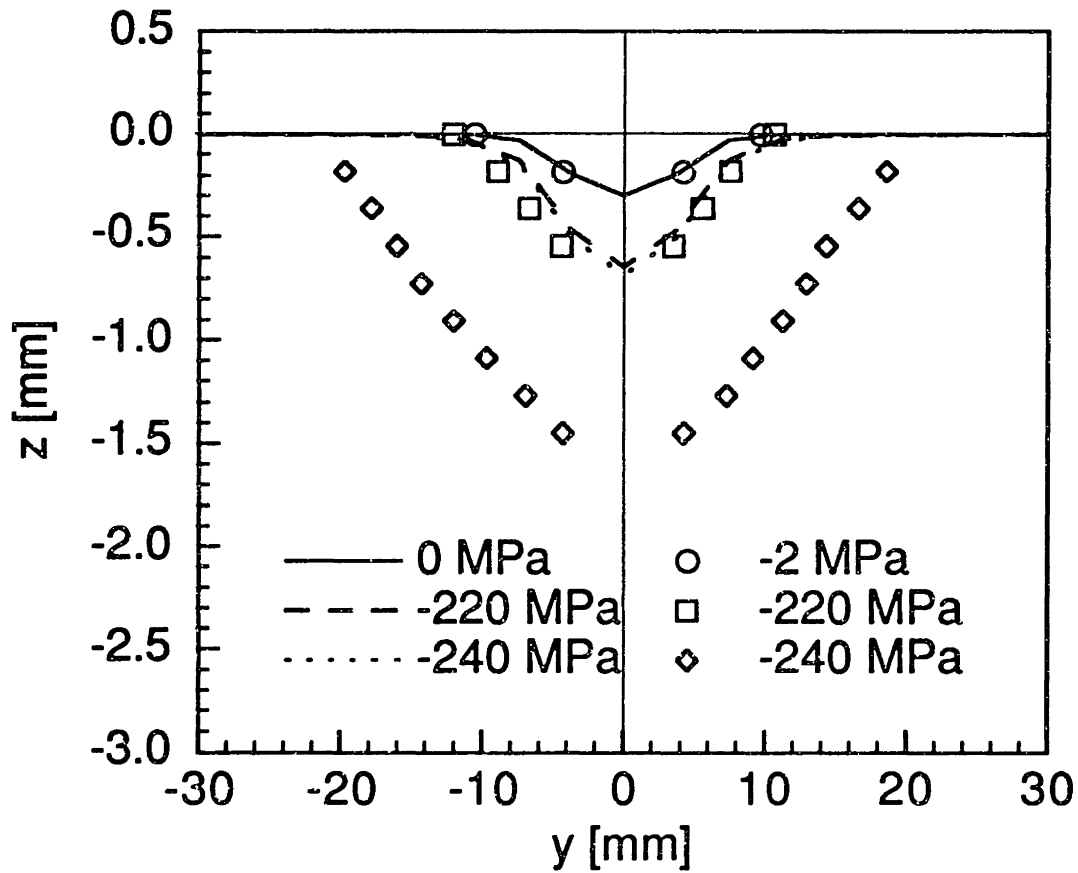


Figure 6.89 Experimental and predicted dimple profiles along centerline perpendicular to loading direction at various loads for a specimen with (± 45) facesheets and with level 3 simulated core damage.

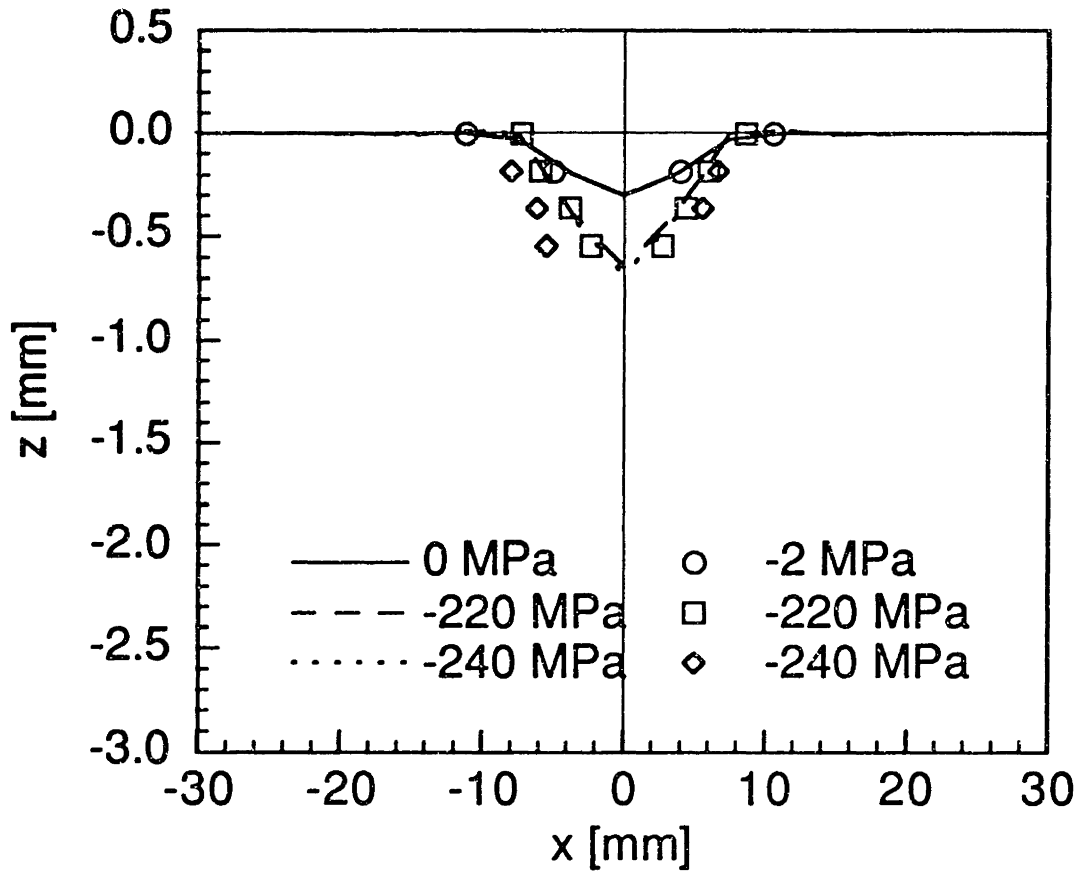


Figure 6.90 Experimental and predicted dimple profiles along centerline in loading direction at various loads for a specimen with (± 45) facesheets and with level 3 simulated core damage.

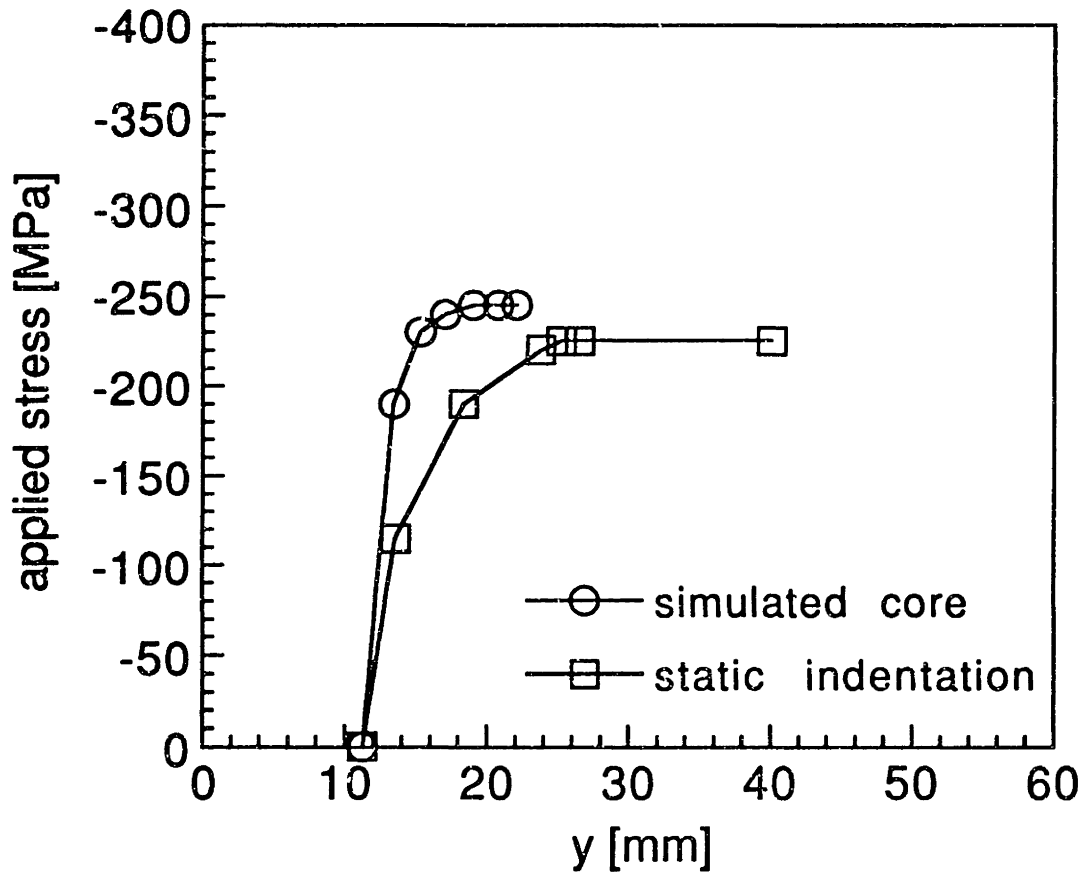


Figure 6.91 Dimension of dimple along centerline perpendicular to loading at various applied stress levels for specimens with (± 45) facesheets and level 1 damage.

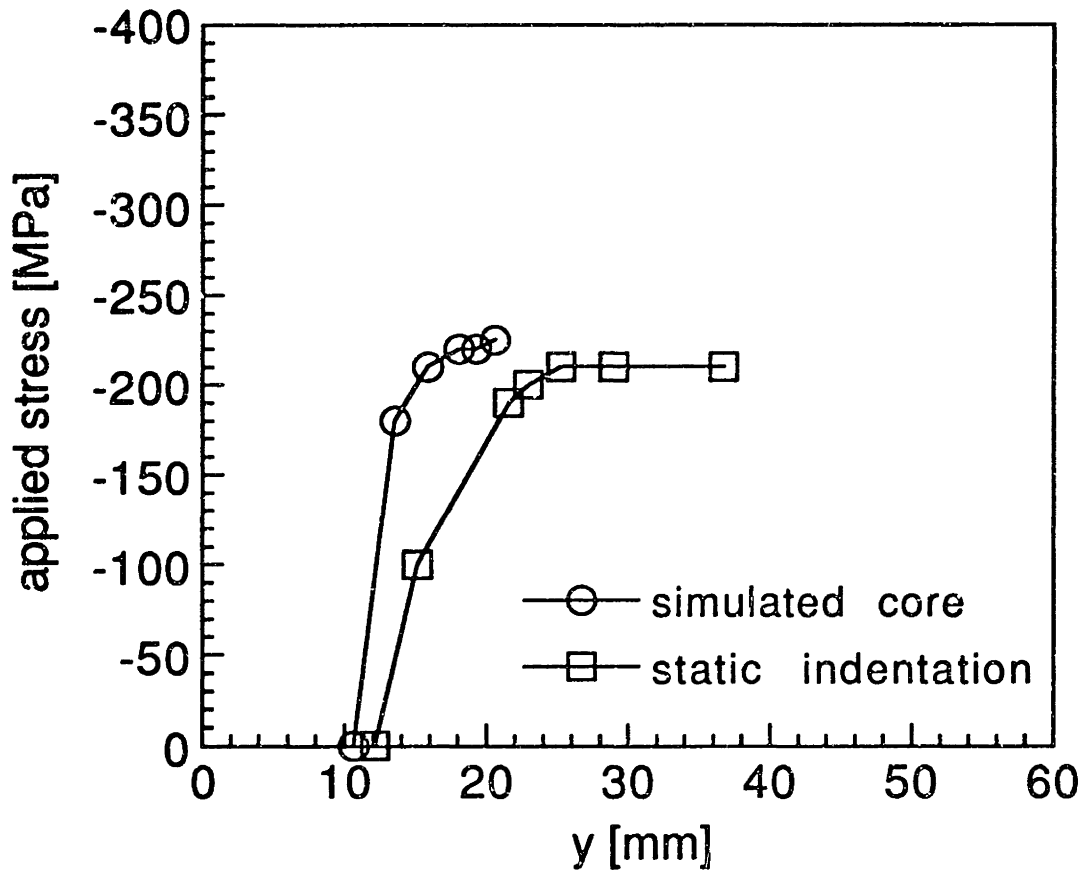


Figure 6.92 Dimension of dimple along centerline perpendicular to loading at various applied stress levels for specimens with (± 45) facesheets and level 2 damage.

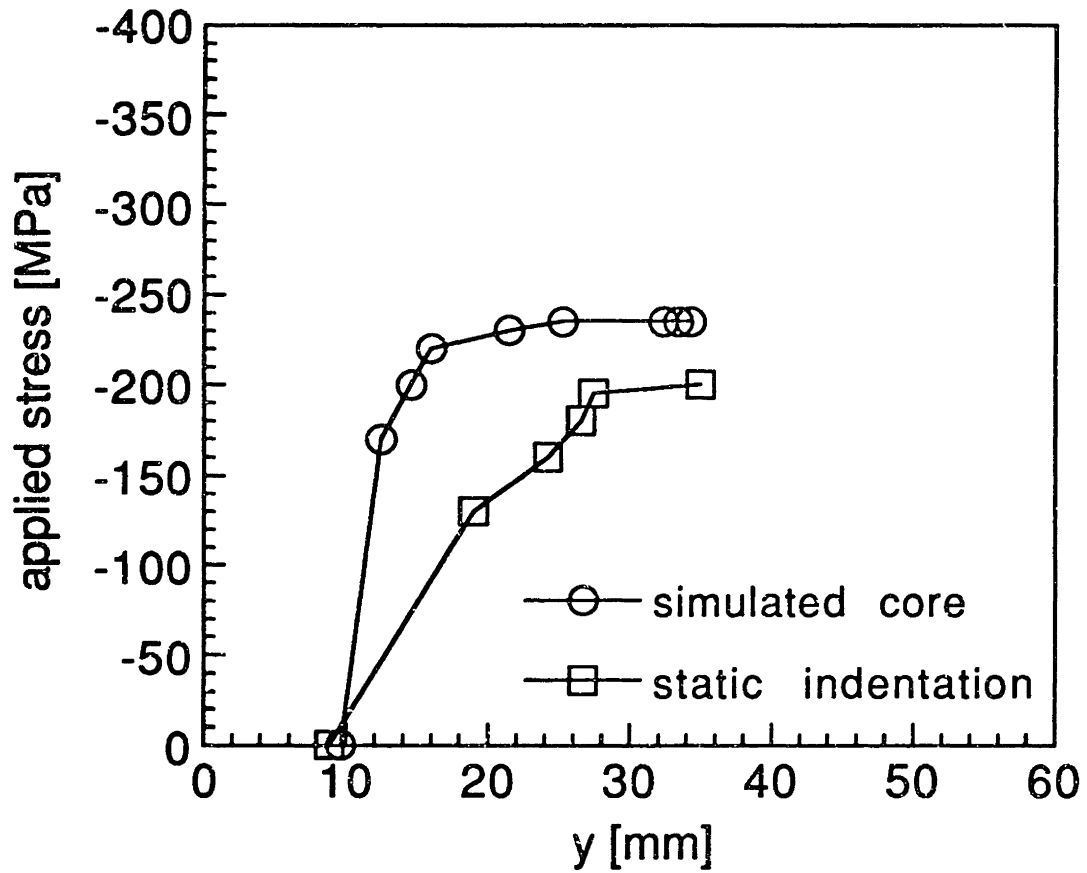


Figure 6.93 Dimension of dimple along centerline perpendicular to loading at various applied stress levels for specimens with (± 45) facesheets and level 3 damage.

dimple propagation at a given applied stress level than the corresponding specimens with simulated core damage for all damage levels. This dimple profile data is also plotted in Figures 6.94 and 6.95 according to damage types. It can be seen in Figures 6.94 and 6.95 that specimens with different levels of simulated core damage can have very similar starting points and subsequent dimple propagation. It is important to note that the in-plane dimension of the dimple measured at the surface of the specimens, as indicated by the dial gage measurements in Section 6.1.3, differs more among the different damage levels: level 3 has the largest dimple, followed by level 2 and level 1 damage, than do the measurements shown in Figures 6.94 and 6.95. This is due to the fact that the dimple for level 3 damage has the smallest slope at the surface while that for level 1 damage has the greatest slope. Hence, the dimensions of the dimple measured at the depth of the first-order fringe for the three different damage levels are closer to one another than the corresponding measurements made at the depth of the zeroth-order fringe.

Two additional parameters are used to compare the dimple propagation in the specimens with static indentation damage and the specimens with simulated core damage. The first parameter, y_{crit} , is the dimension of the dimple along the y-axis just before catastrophic failure occurred. The second parameter, z_{crit} , is the depth of the dimple just before catastrophic failure occurred. Catastrophic failure is defined on the videotape of the moiré fringe patterns by the transition from a well-defined moiré fringe pattern to an across-width fracture within one video frame (i.e., 1/30 second).

The values of y_{crit} of specimens with (0/90) facesheets and of specimens with (± 45) facesheets are shown in Figures 6.96 and 6.97,

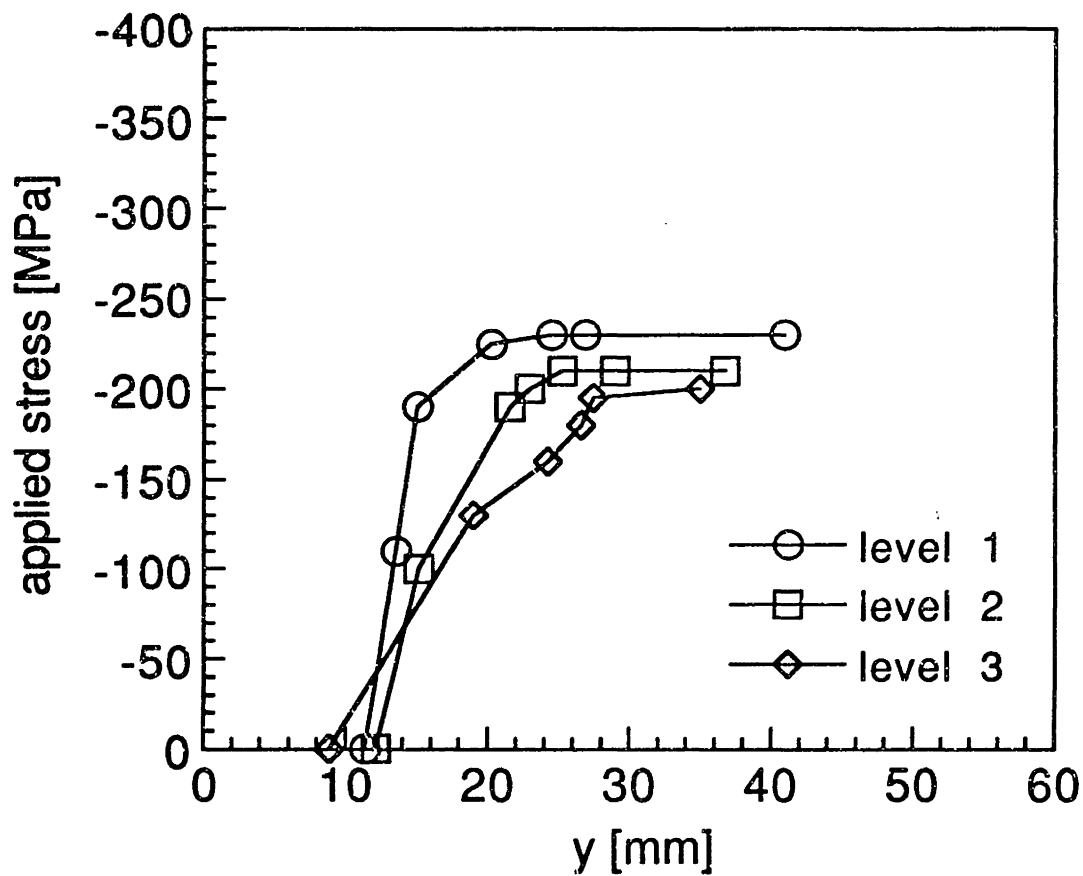


Figure 6.94` Dimension of dimple along centerline perpendicular to loading at various applied stress levels for specimens with (± 45) facesheets and static indentation damage.

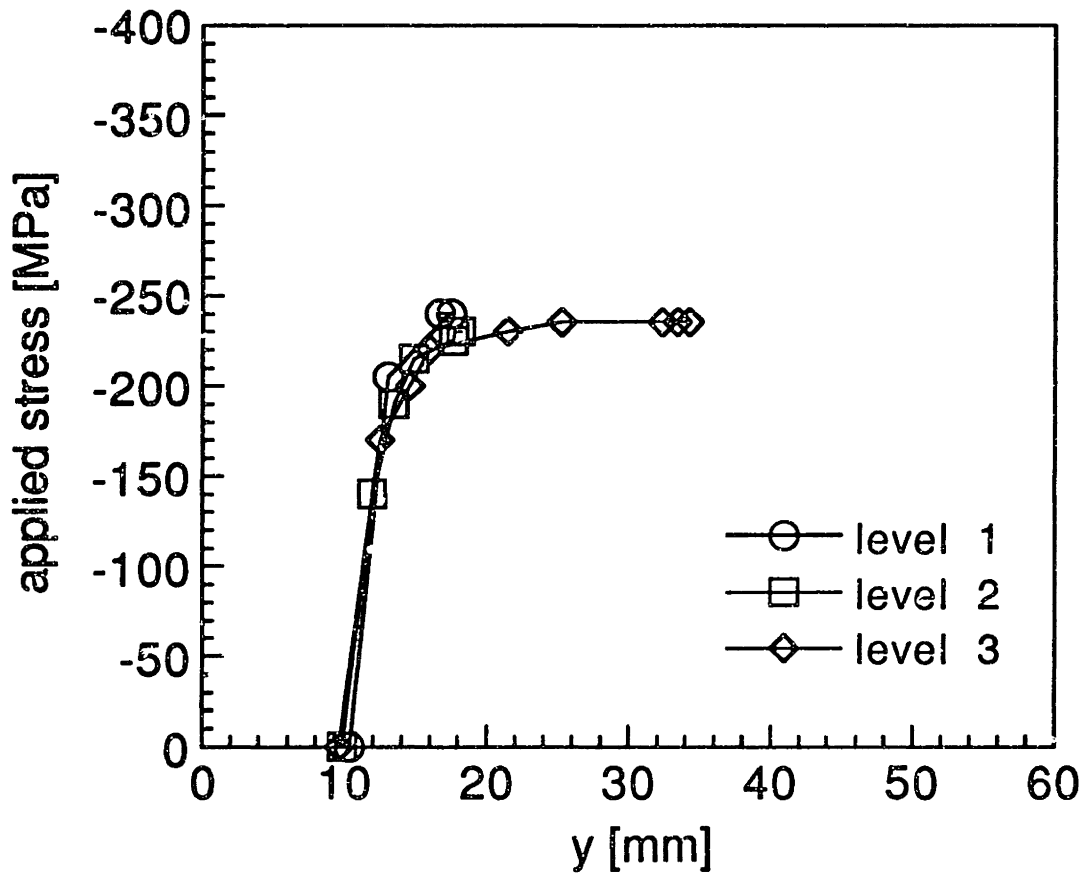


Figure 6.95 Dimension of dimple along centerline perpendicular to loading at various applied stress levels for specimens with (± 45) facesheets and simulated core damage.

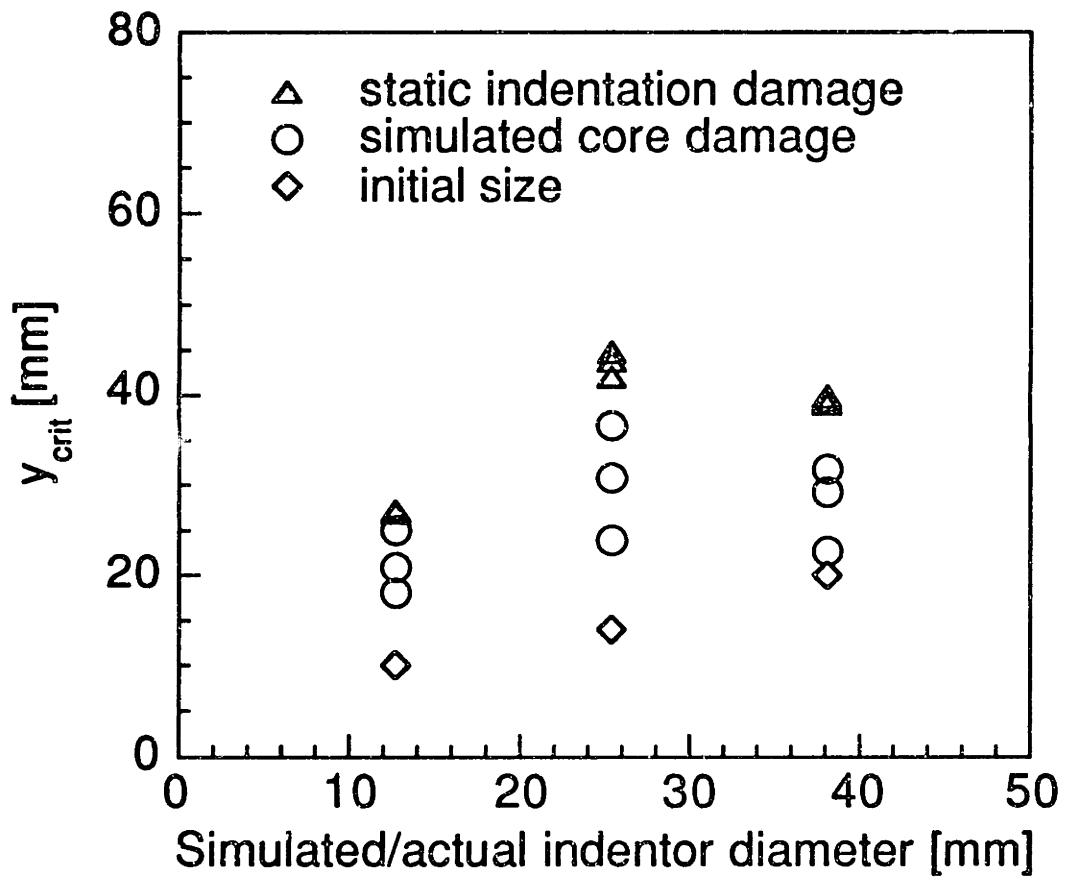


Figure 6.96 Dimension of dimple perpendicular to loading direction just before catastrophic failure, y_{crit} , for specimens with (0/90) facesheets versus simulated/actual indenter diameter.

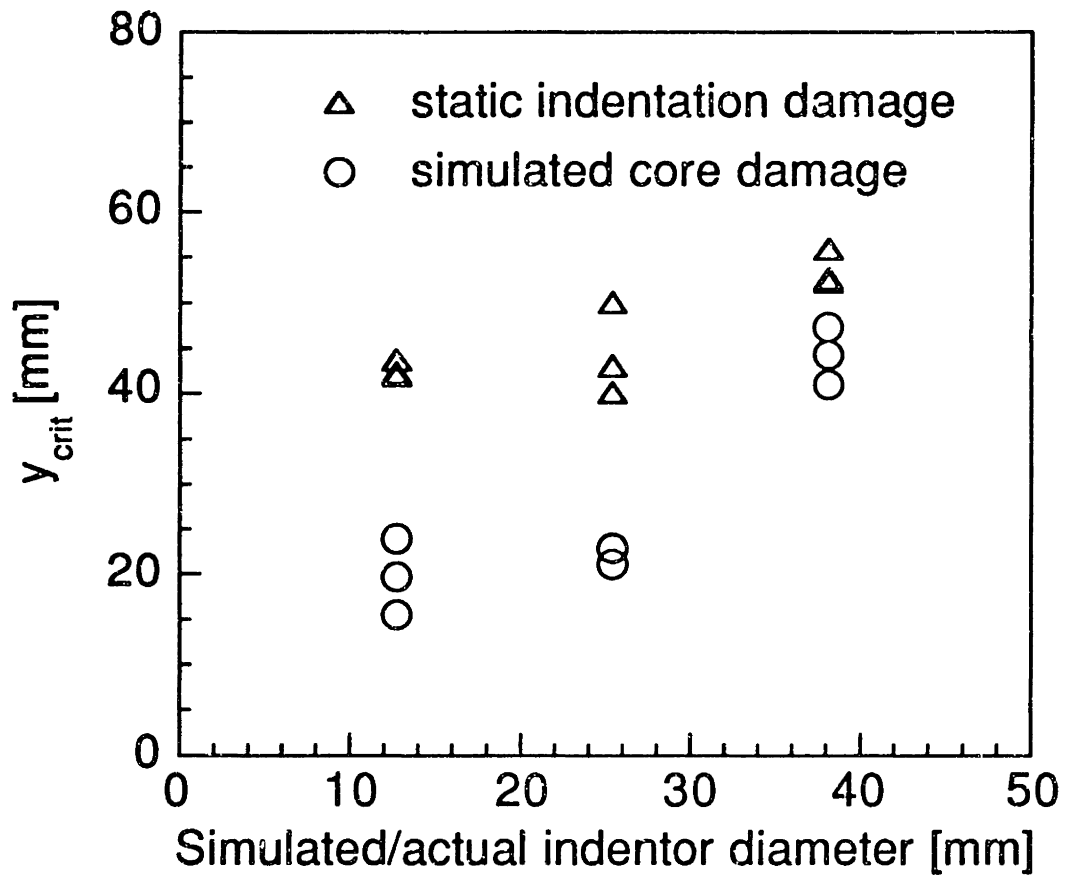


Figure 6.97 Dimension of dimple perpendicular to loading direction just before catastrophic failure, y_{crit} , for specimens with (± 45) facesheets versus simulated/actual indenter diameter.

respectively. Also included in Figure 6.96 are the initial dimensions of the dimples as measured with the dial gage. The results for specimens with simulated core damage show more scatter than those for static indentation specimens, with the exception of specimens with (± 45) facesheets indented with the 25.4 mm-diameter indenter (level 2 damage). The static indentation specimens always have greater values of y_{crit} than the corresponding specimens with simulated core damage for both facesheet layups. Among specimens with (0/90) facesheets and static indentation damage, damage level 1 has the lowest average y_{crit} value of 27 mm while level 2 has the highest average of 44 mm and level 3 has the intermediate average of 39 mm. For specimens with (0/90) facesheets and simulated core damage, damage level 1 has the lowest average of 21 mm, followed by level 3 with 28 mm, and level 2 with 31 mm. Among specimens with (± 45) facesheets and static indentation damage, damage level 1 has the lowest average value of 43 mm followed by level 2 with 44 mm and level 3 with 54 mm. For specimens with (± 45) facesheets and simulated core damage, damage level 1 has the lowest average of 20 mm, followed by level 2 with 22 mm, and level 3 with 44 mm.

The values of z_{crit} of specimens with (0/90) facesheets and of specimens with (± 45) facesheets are shown in Figures 6.98 and 6.99, respectively. Specimens with (0/90) facesheets and static indentation damage show greater values of z_{crit} than the corresponding specimens with simulated core damage for the case of the 25.4 mm-diameter indenter and the case of the 38.1 mm-diameter indenter (level 3 damage). Specimens with (± 45) facesheets and static indentation damage show greater values of z_{crit} than the corresponding specimens with simulated core damage for the case of the 38.1 mm-diameter specimens. For specimens with simulated

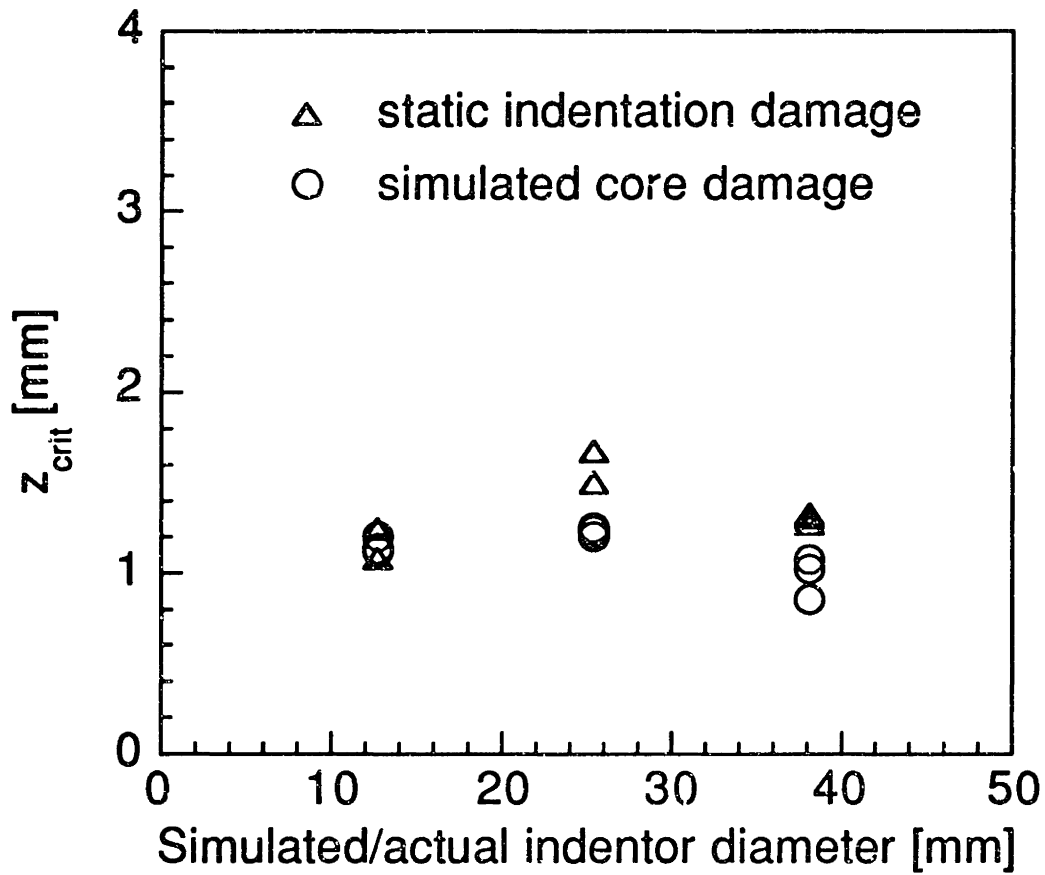


Figure 6.98 Depth of dimple just before catastrophic failure, z_{crit} , for specimens with (0/90) facesheets versus simulated/actual indenter diameter.

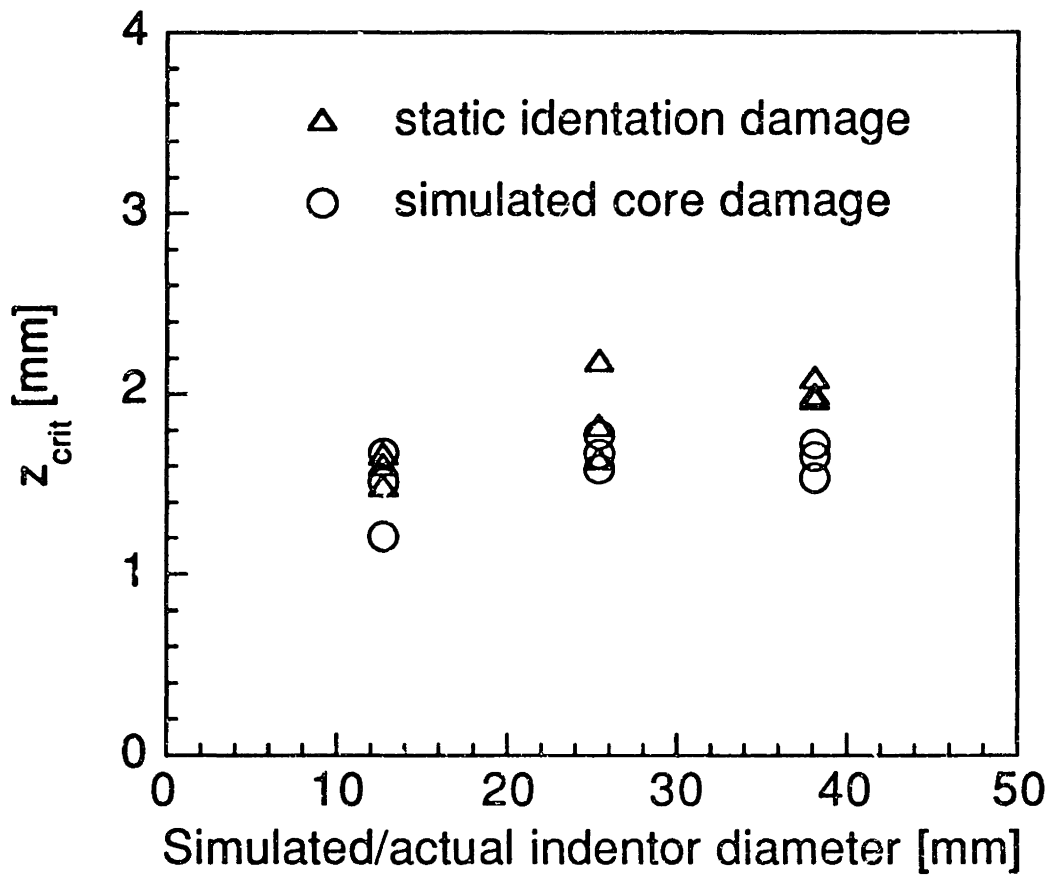


Figure 6.99 Depth of dimple just before catastrophic failure, z_{crit} , for specimens with (± 45) facesheets versus simulated/actual indenter diameter.

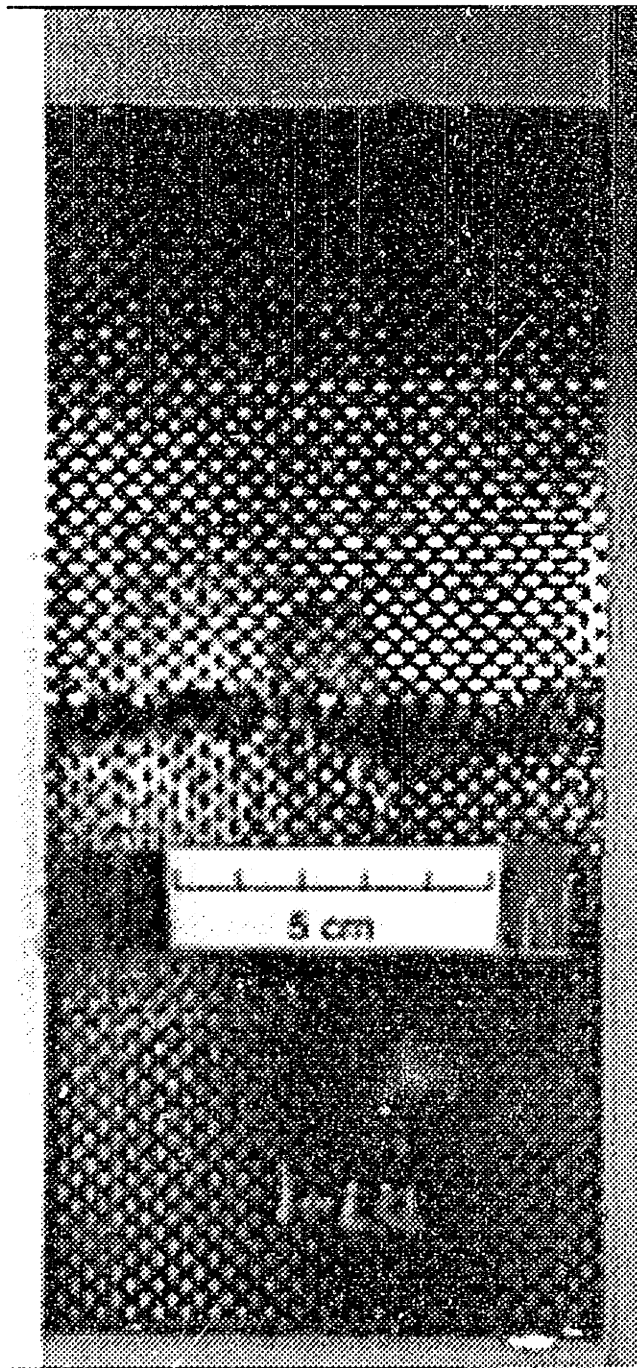
core damage, the values of z_{crit} are approximately the same for all three damage levels and both facesheet layups. For specimens with (0/90) facesheets and static indentation damage, damage level 2 has slightly higher z_{crit} than damage levels 1 and 3. For specimens with (± 45) facesheets and static indentation damage, the value of z_{crit} increases slightly in going from damage level 1 to level 2, and finally to level 3.

6.2.4 Post-mortem inspection of failed specimens

All specimens were tested to failure. Failure always occurred with a sudden load drop and the emission of a loud noise. Results of post-mortem examination of failed specimens are presented in this section. The phrase "failure modes" is used in this section to refer to the final damage state of the failed specimens. It is different from "failure mechanism" which is the process that leads to final failure of the damaged specimens, i.e. the dimple propagation described in Section 6.2.3 for specimens with static indentation damage and those with simulated core damage.

(0/90) specimens

The failure mode of the undamaged specimens with (0/90) facesheets is facesheet fracture perpendicular to the loading direction as shown in Figure 6.100. Both facesheets failed in all the undamaged specimens. The fracture went through both plies in the facesheets. Two different failure modes were observed in the core. Little or no core damage was observed from the edges of the panels beneath the fracture in one of the facesheets. On the other hand, core tearing was evident beneath the fracture in the other facesheet. Core tearing is a tension failure of the core in the thickness direction as illustrated in Figure 6.101. Such core tearing failure is a secondary failure caused by bending when the front facesheet fails [59].




10 mm

Figure 6.100 Photograph of failure mode of an undamaged specimen with (0/90) facesheets

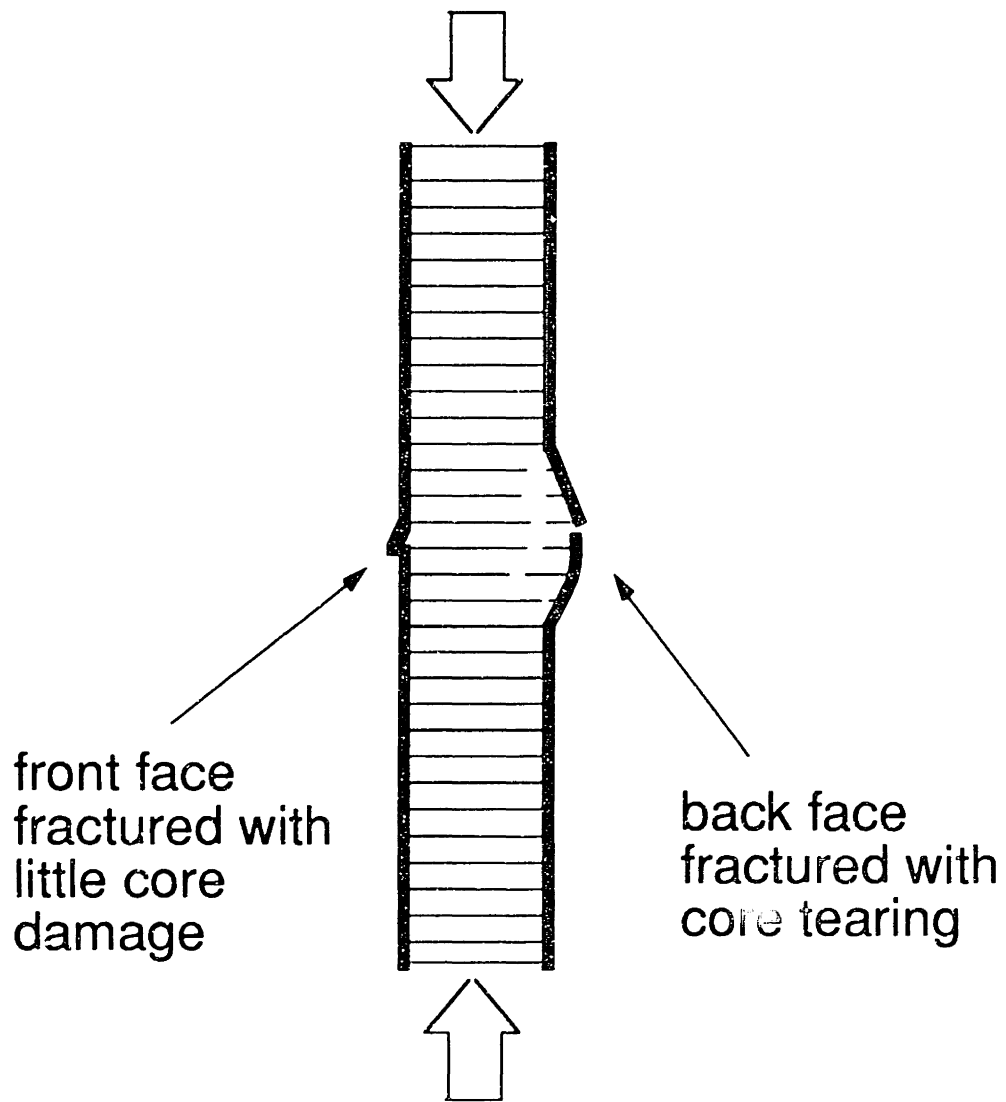


Figure 6.101 Sketch of core tearing observed in failed sandwich panels.

The failure modes of the specimens with static indentation damage and those with simulated core damage are similar. Damage inspection before the specimens were unloaded revealed the presence of a depression as a result of the dimple propagation. The depression/dimple extended completely to the edges in specimens with level 3 simulated core damage while it only extended part way for other damage types. These two different failure modes are illustrated in Figure 6.102. Core tearing and core crushing could be observed from the sides of the specimens when the dimple extended completely to the edges as illustrated in Figure 6.103. The "humps" depicted in the figure was formed as a result of the core tearing when the specimen failed. Such humps were not observed during the dimple propagation.

The final failure is a straight fracture across the width of the specimen in the damaged facesheet as shown in Figure 6.104, for a typical specimen with static indentation damage, and in Figure 6.105, for a typical specimen with simulated core damage. This final failure mode is unchanged with initial damage level. The white paint at the center section of the specimen was used to enhance the contrast of the moiré fringes (see Section 5.4). In all specimens with static indentation damage, the back facesheet was still intact after the front facesheet (i.e. the facesheet with the indentation damage) failed. In all but two of the specimens with simulated core damage, the back facesheet was still intact after the front facesheet (i.e. the facesheet with the simulated core damage) failed.

As briefly stated in the beginning of Section 6.2.3, the failure mechanism of specimens with simulated facesheet damage is different from that of the other two types of specimens. No out-of-plane deformation was observed in the specimens with simulated facesheet damage. The failure

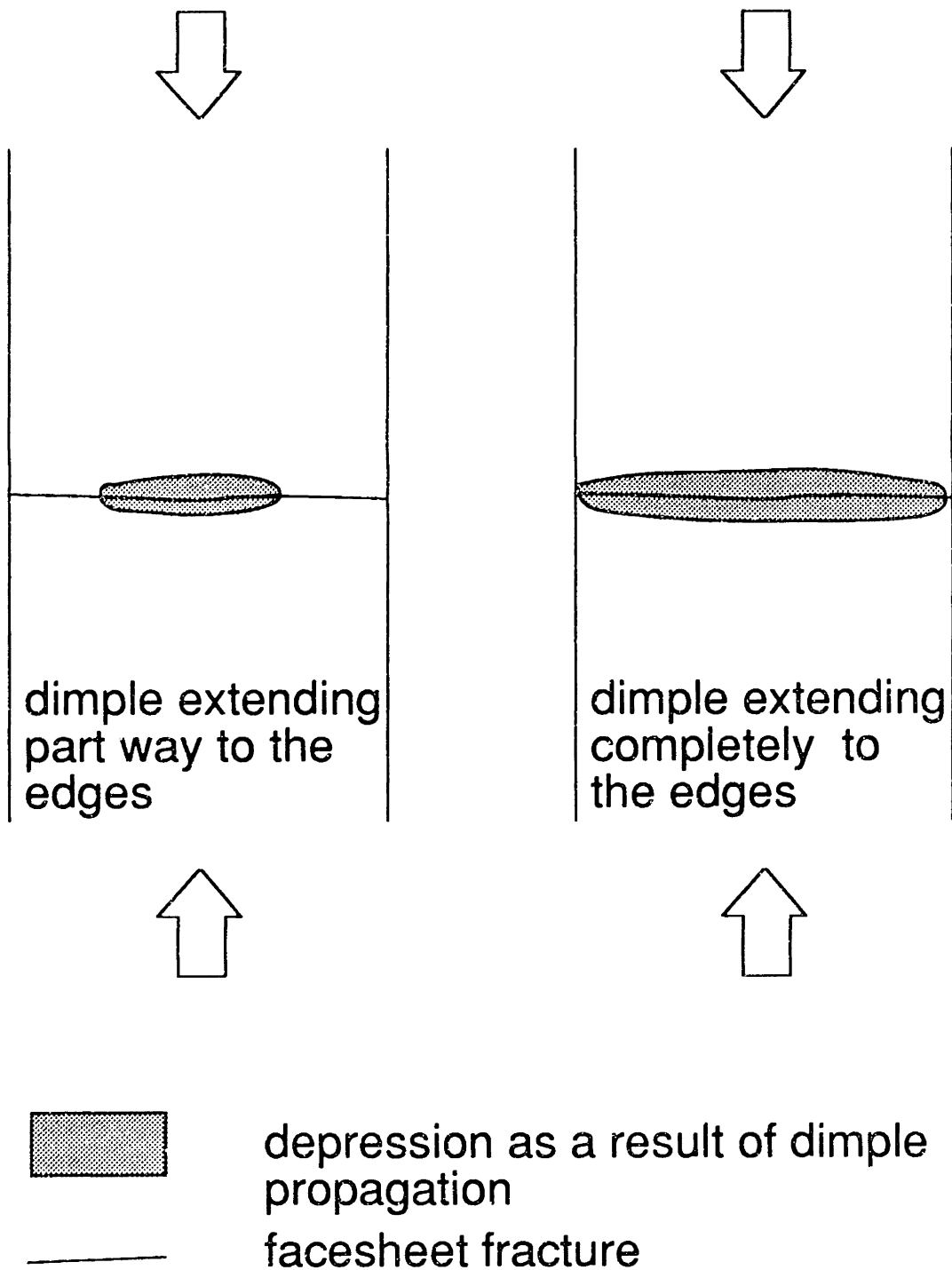


Figure 6.102 Sketch of failure modes in specimens with (0/90) facesheets and static indentation damage as well as specimens with simulated core damage.

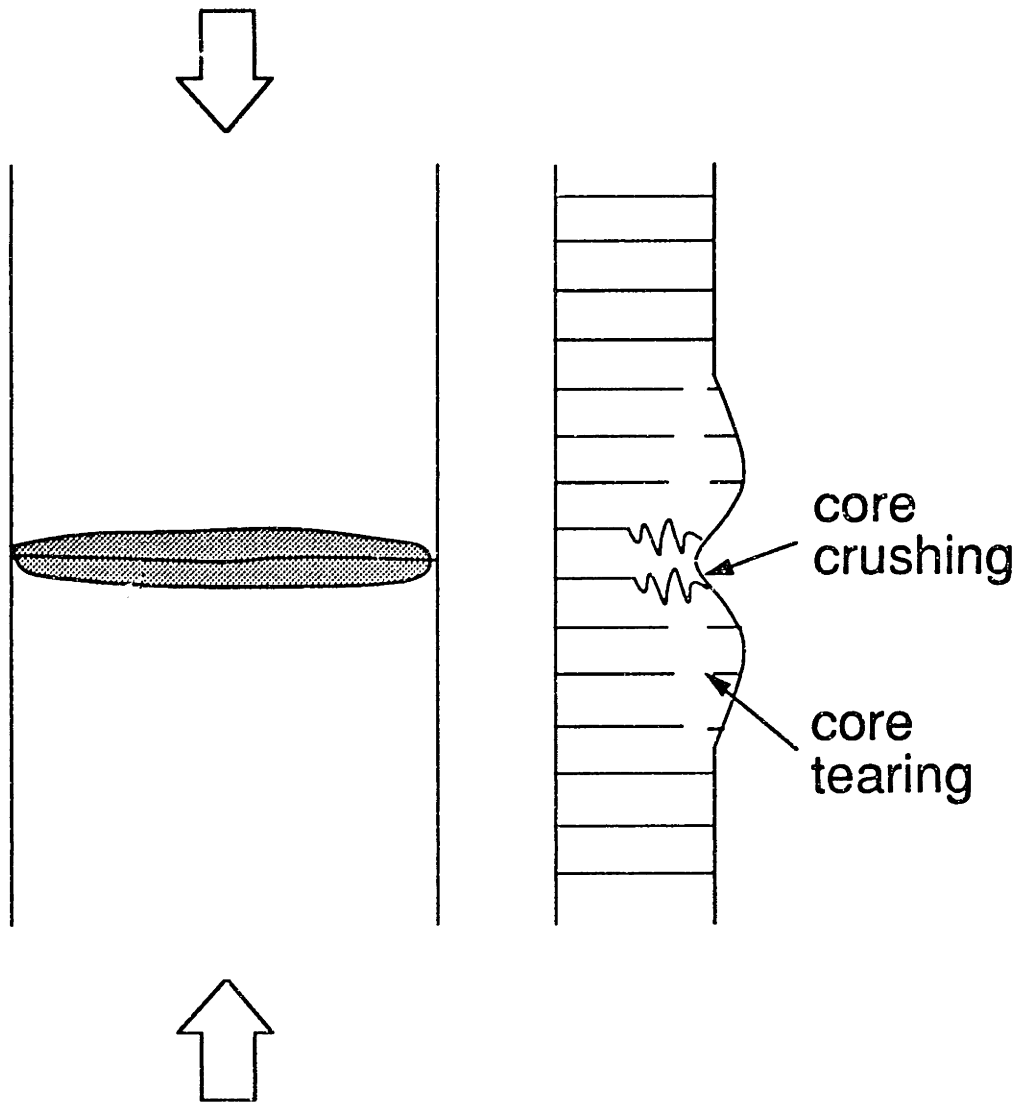
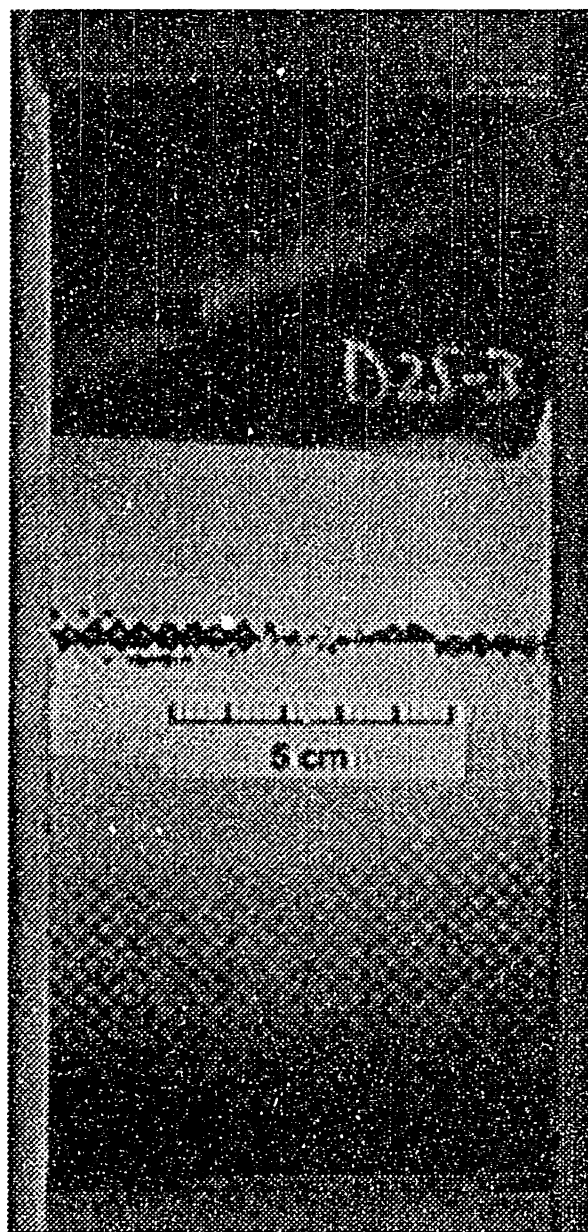
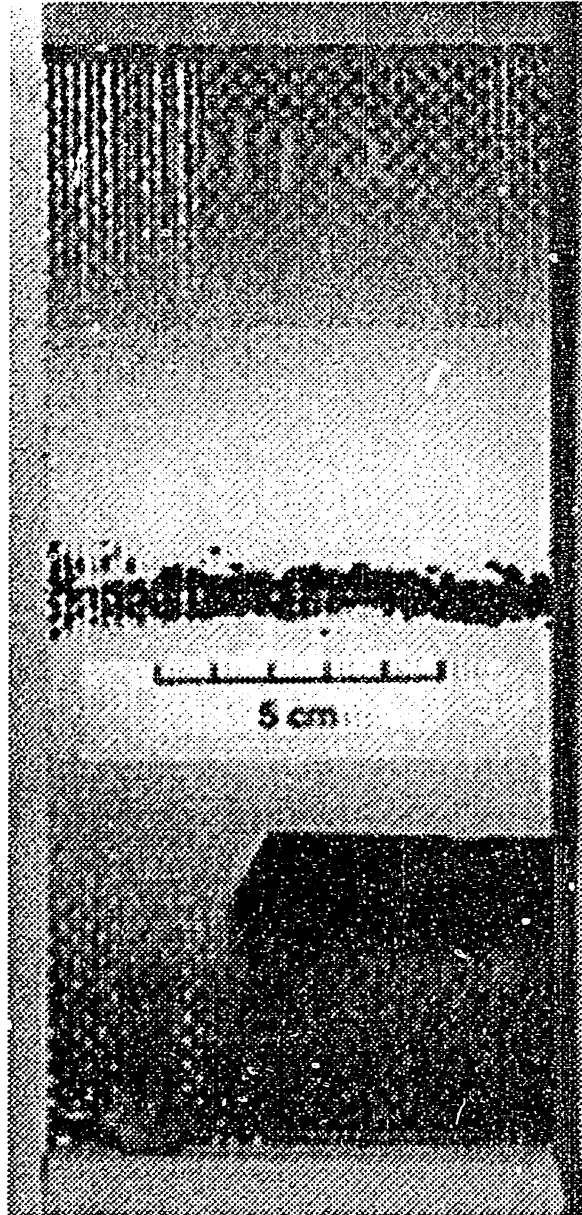


Figure 6.103 Sketch of core tearing and core crushing observed at edges of some failed specimens with static indentation damage and specimens with simulated core damage when dimple propagated to the edges.



10 mm

Figure 6.104 Photograph of a typical straight-line fracture perpendicular to the loading direction for a specimen with (0/90) facesheets and static indentation damage.



 10 mm

Figure 6.105 Photograph of a typical straight-line fracture perpendicular to the loading direction for a specimen with (0/90) facesheets and simulated core damage.

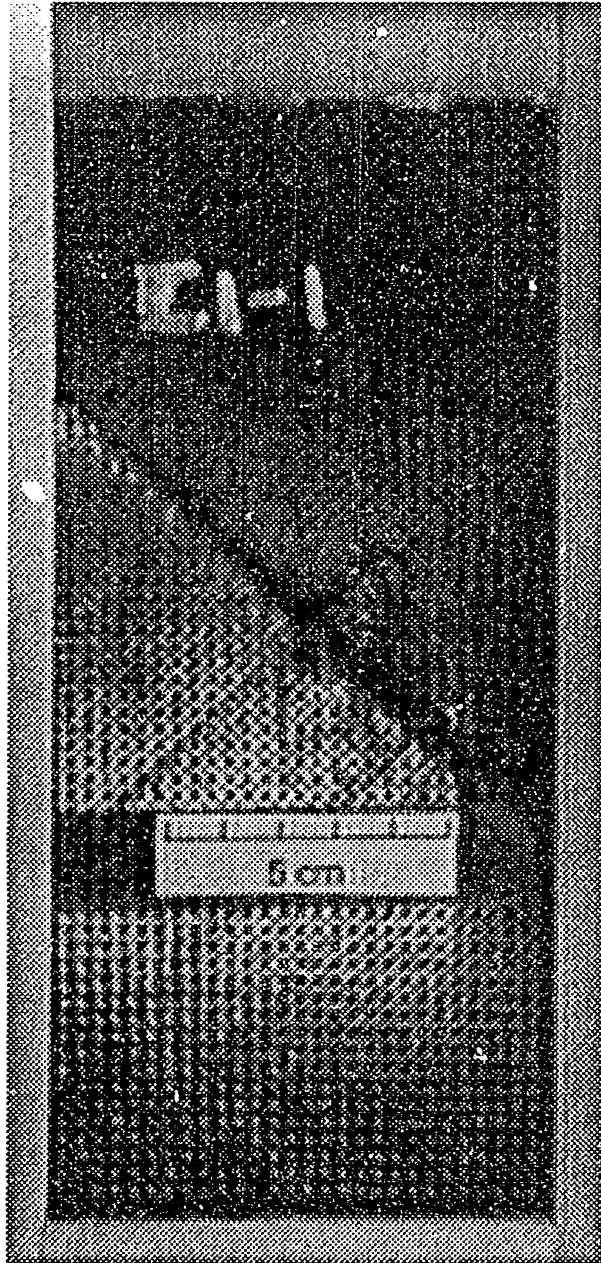
mode of these specimens, however, is not distinguishable from those with static indentation damage and simulated core damage described earlier. These specimens with simulated facesheet damage failed by developing a fracture across the width in a catastrophic manner. The fracture always originated from the tips of the horizontal slit. A photograph of a typical specimen after failure is shown in Figure 6.106.

(±45) specimens

The failure mode of the undamaged specimens with (±45) facesheets is facesheet fracture at 45° angles to the loading direction (i.e. along the tows of the fabric facesheet). The fracture could be a straight line, as shown in Figure 6.107, or it could be in a "zig-zag" pattern, as shown in Figure 6.108. Both facesheets failed in all the undamaged specimens. Two different failure modes were observed in the core. Little or no core damage was observed from the edges of the panel beneath one of the facesheet. Core tearing was evident beneath the fracture in the other facesheet.

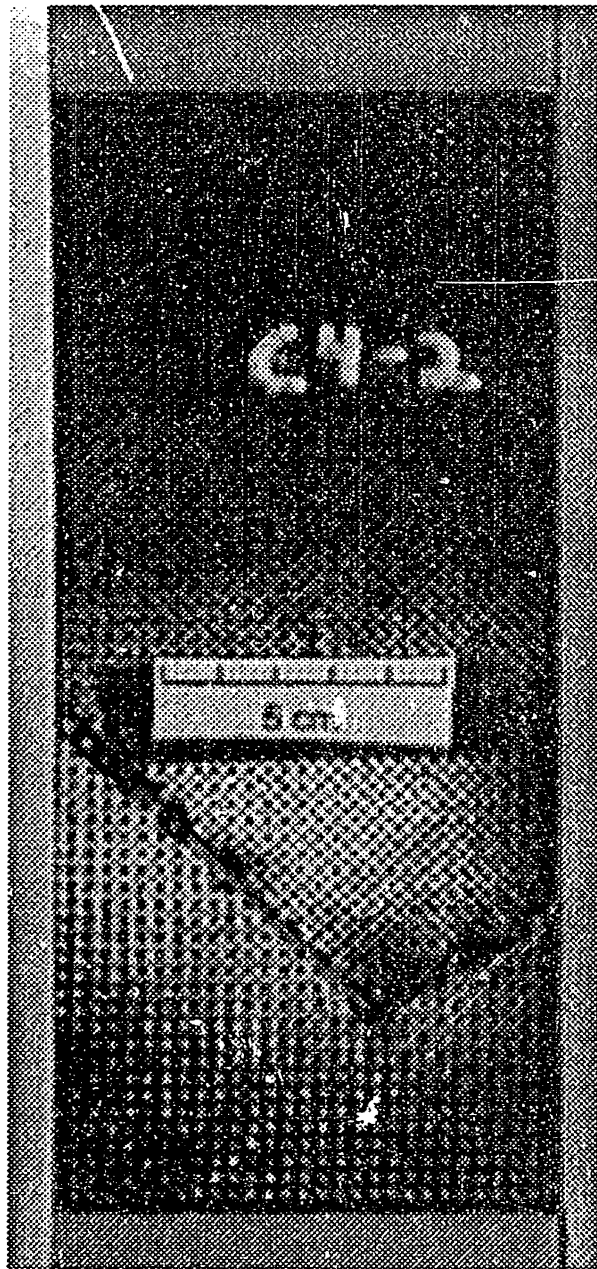
Once again, the failure modes of the specimens with static indentation damage and those with simulated core damage are similar. Damage inspection before the specimen was unloaded again revealed the presence of a depression as a result of dimple propagation. The dimple/depression extended completely to the edges in specimens with all three levels of static indentation damage and those with level 3 simulated core damage. These two failure modes are illustrated in Figure 6.109. Core tearing and core crushing could sometimes be observed from the sides of the specimens when the dimple extended to the edges.

The final failure is a fracture across the width of the specimen in the damaged facesheet. When the dimple extended completely to the edges of the specimen, a straight line fracture completely across the width of the




10 mm

Figure 6.107 Photograph of failure mode of an undamaged specimen with (± 45) facesheets showing a straight-line fracture along one of the tow directions.




10 mm

Figure 6.108 Photograph of failure mode of an undamaged specimen with (± 45) facesheets showing a "zig-zag" fracture along one of the tow directions.

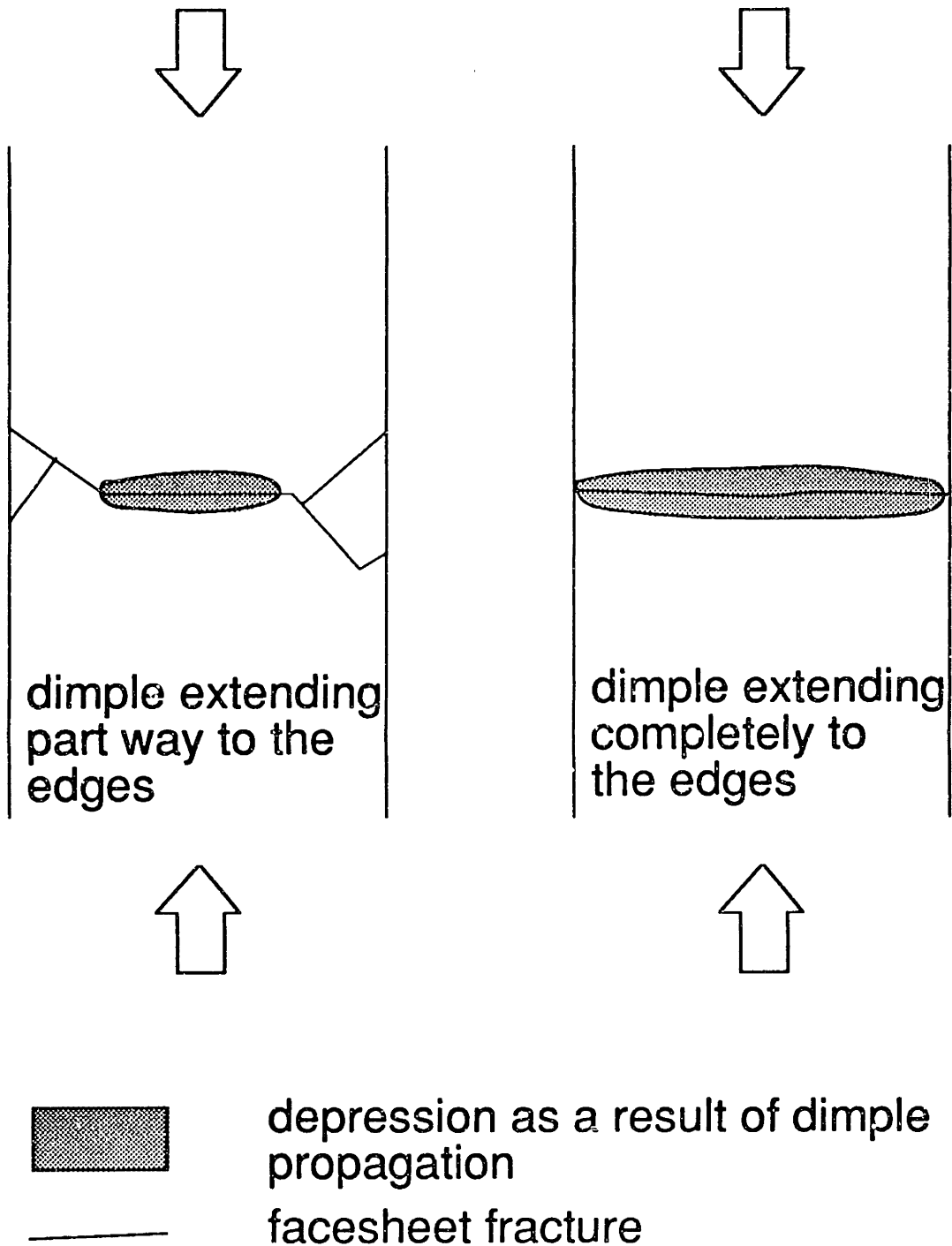
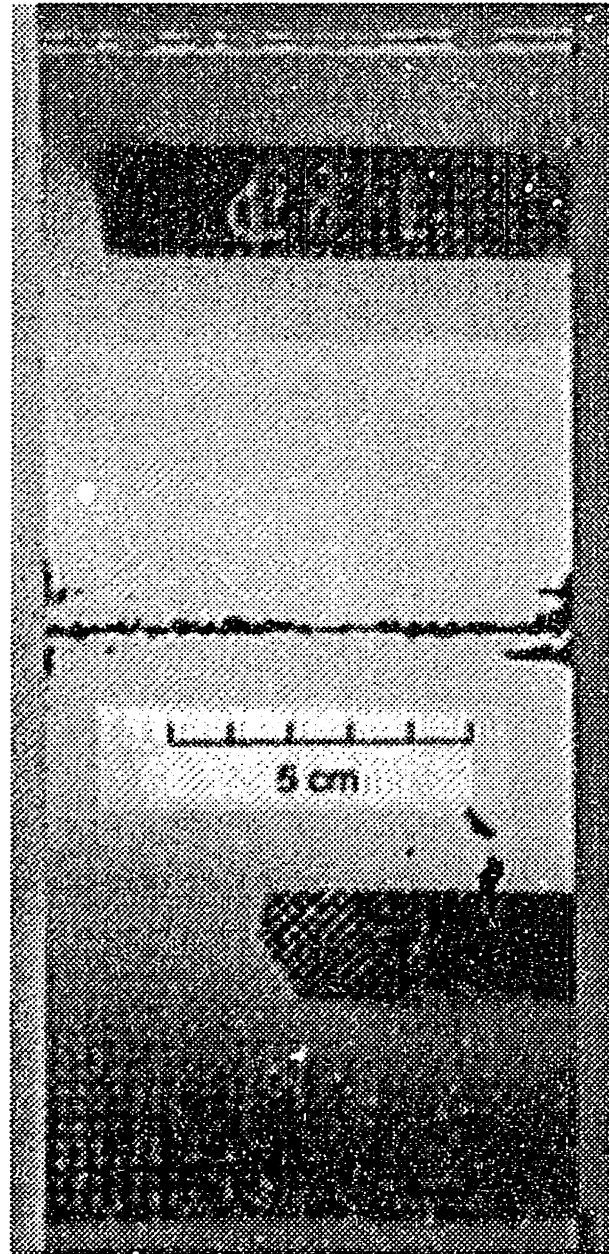


Figure 6.109 Sketch of failure mode in specimens with (± 45) facesheets and static indentation damage or simulated core damage.

specimen resulted as shown in Figure 6.110, for a typical specimen with static indentation damage, and in Figure 6.111, for a typical specimen with simulated core damage. If the dimple did not extend completely to the edges, a straight line fracture occurred at the bottom of the depression and branched out at 45° angles beyond the extent of the depression as shown in Figures 6.112 and 6.113. In all specimens with static indentation damage, the back facesheet was still intact after the front facesheet (i.e. the facesheet with the indentation damage) failed. In all but five specimens with simulated core damage, the back facesheet was still intact after the front facesheet (i.e. the facesheet with the simulated core damage) failed.

As briefly stated in the beginning of Section 6.2.3, the specimens with simulated facesheet damage failed via a different mechanism from the specimens with static indentation damage and specimens with simulated core damage as no out-of-plane deformation was observed. Two of the three specimens with simulated facesheet damage failed by developing fracture at 45° angles to the loading direction as shown in Figure 6.114. This is in contrast with the failure mode of specimens with simulated core damage and that of specimens with static indentation damage which has straight-line fracture perpendicular to the loading direction. The fracture always originated from the tips of the slits in a stable manner first, followed by catastrophic failure. The stable growth of the slits was captured on the videotape while the catastrophic failure occurred within one video frame (i.e. 1/30 second). During the stable growth, the slits extended in short increments (less than 10 mm) in a zig-zag manner at 45° angles, as illustrated in Figure 6.115. One specimen with simulated facesheet damage failed in the facesheet without the slits. The sketch shown in Figure 6.116 highlights the different failure modes in the specimens with simulated




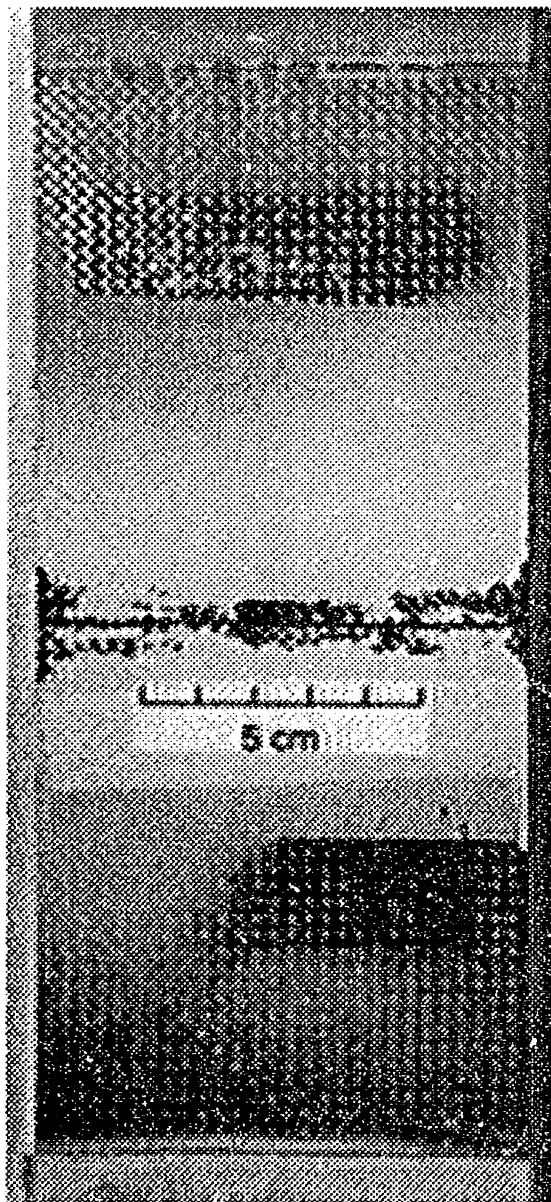
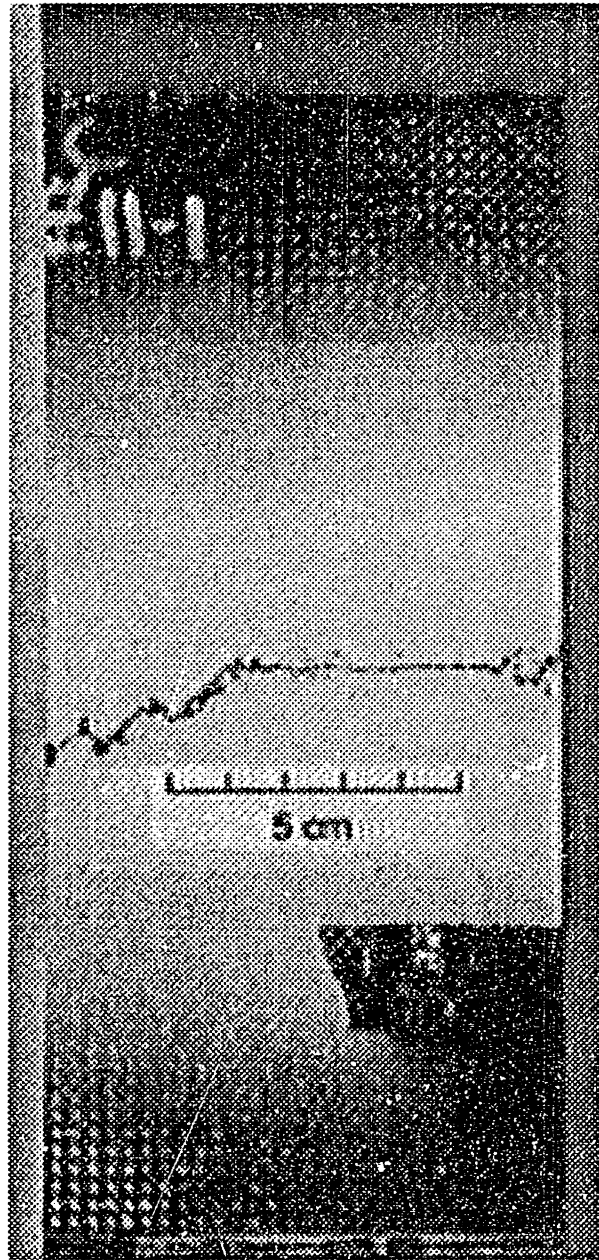

10 mm

Figure 6.110 Photograph of failure mode of a specimen with static indentation damage and (± 45) facesheets showing a straight-line fracture perpendicular to the loading direction.



 10 mm

Figure 6.111 Photograph of failure mode of a specimen with (± 45) facesheets and simulated core damage showing a straight-line fracture perpendicular to the loading direction.




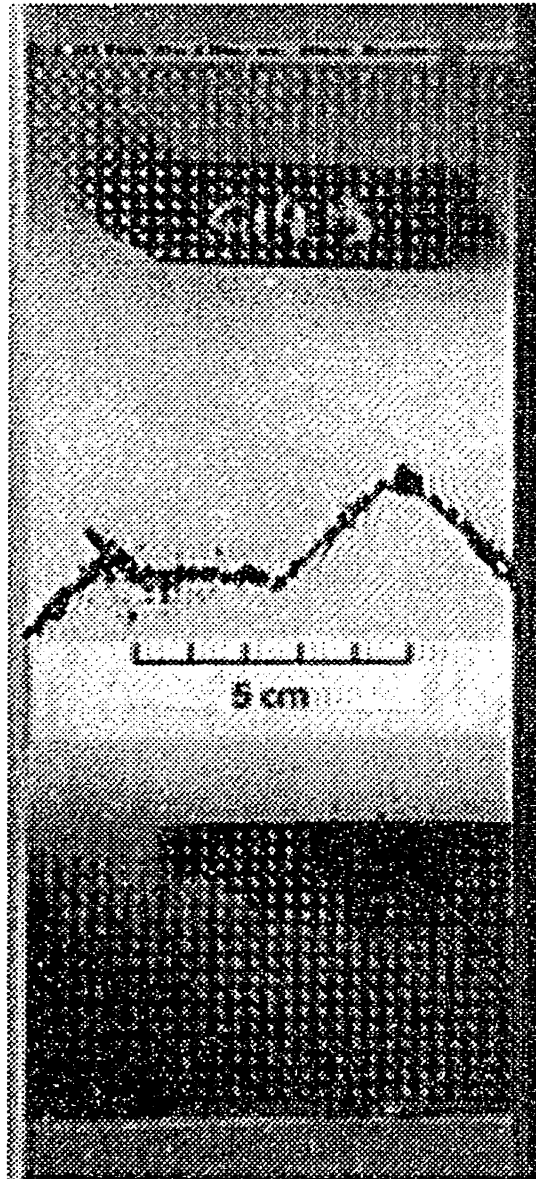
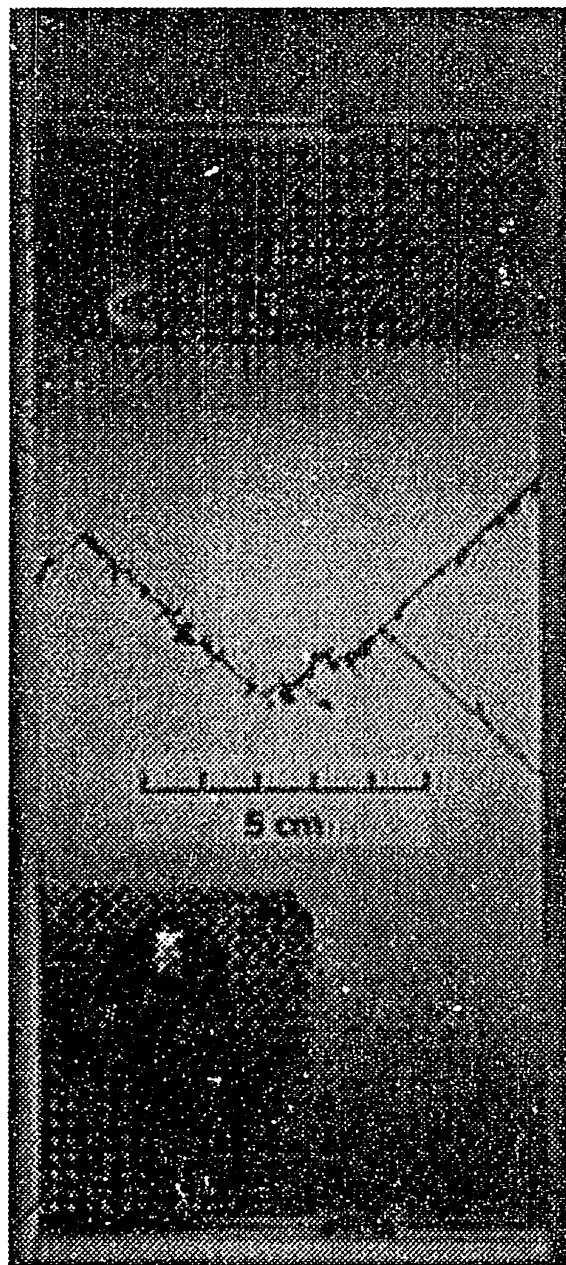

10 mm

Figure 6.112 Photograph of failure mode of a specimen with (± 45) facesheets and static indentation damage showing a straight-line fracture at center and "branched" fracture beyond the extent of the dimple propagation.




10 mm

Figure 6.113 Photograph of failure mode of a specimen with (± 45) facesheets and simulated core damage showing a straight-line fracture at center and "branched" fracture beyond the extent of the dimple propagation.




10 mm

Figure 6.114 Photograph of fracture pattern of a specimen with (± 45) facesheets and simulated facesheet damage.

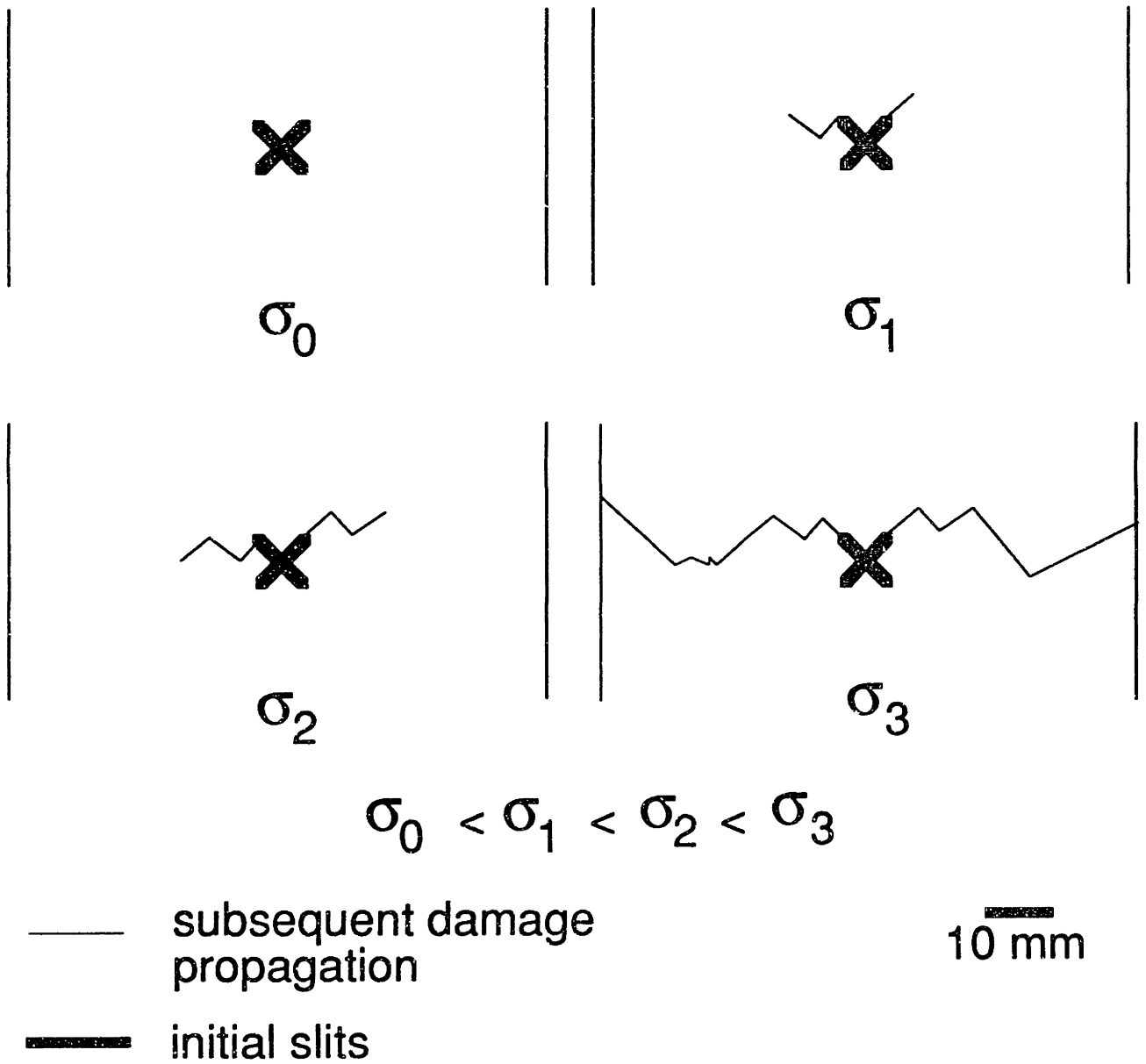


Figure 6.115 Sketch of the propagation of the slits in specimens with (± 45) facesheets and simulated facesheet damage.

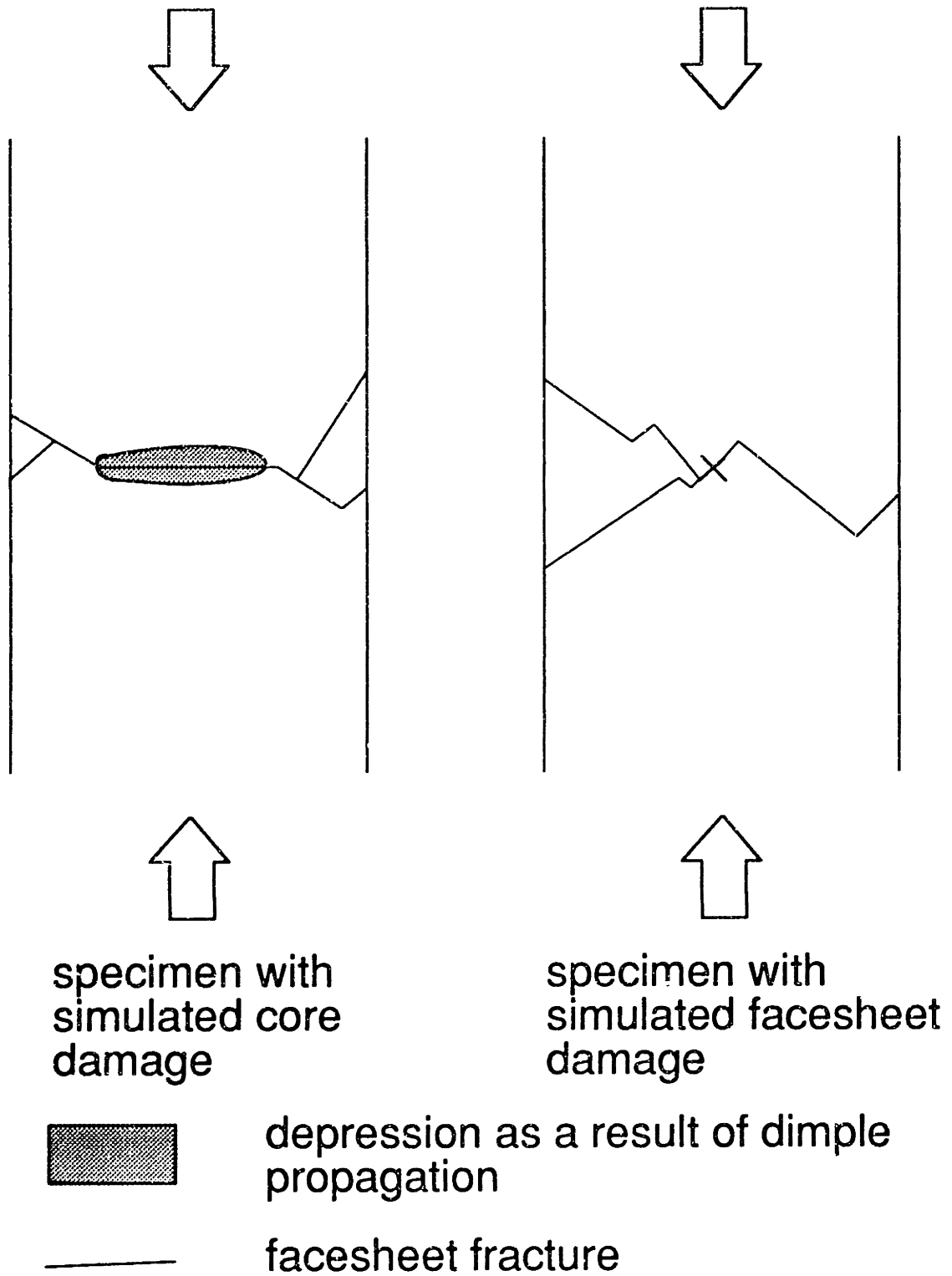


Figure 6.116 Sketch of failure modes of specimens with (± 45) facesheets and simulated facesheet damage and specimens with simulated core damage.

facesheet damage and in the specimens with simulated core damage and with the dimple extending part way across the width.

6.2.5 Compressive strength results

The compressive strength data of specimens with (0/90) facesheets are presented first, followed by those of specimens with (± 45) facesheets. The strength is calculated by dividing the failure load by the measured cross-sectional area (thickness times width) of the facesheets.

The compressive strength of all specimens with (0/90) facesheets are shown in Table 6.10 and Figure 6.117. The coefficients of variation are all below 7% except for the specimens with level 1 static indentation damage. An explanation for this higher coefficient of variation is given later. Among the specimens with simulated core damage, those with level 1 damage (SCD1) have the highest average failure stress of 360 MPa. The specimens with level 2 and level 3 damage (SCD2 and SCD3) have approximately the same average failure stress of 315 MPa and 309 MPa respectively. The specimens with static indentation damage have approximately the same residual strength of 267 MPa for level 1 damage, 264 MPa for level 2 damage, and 265 MPa for level 3 damage. One of the specimens with level 1 static indentation damage failed by developing in-plane fracture on one side, as shown in Figure 6.118, instead of by dimple propagation like all other specimens. This specimen has the lowest failure stress among all specimens with level 1 static indentation damage. If the failure load of this specimen is ignored, the average failure stress for the remaining two specimens is 281 MPa (5.28%). All specimens with static indentation damage have lower failure stresses than the corresponding specimens with simulated core damage. The specimens with level 1 simulated facesheet damage have

Table 6.10 Compressive strengths of specimens with (0/90) facesheets

Damage Type	Level			
	None	1	2	3
None	403 (1.4%) ^a	—	—	—
Static Indentation	—	267 (11.7%)	264 (2.1%)	265 (4.0%)
Simulated Core	—	360 (2.4%)	315 (1.4%)	309 (1.5%)
Simulated Facesheet	—	291 (6.1%)	--	—

^anumbers in parentheses are coefficients of variation

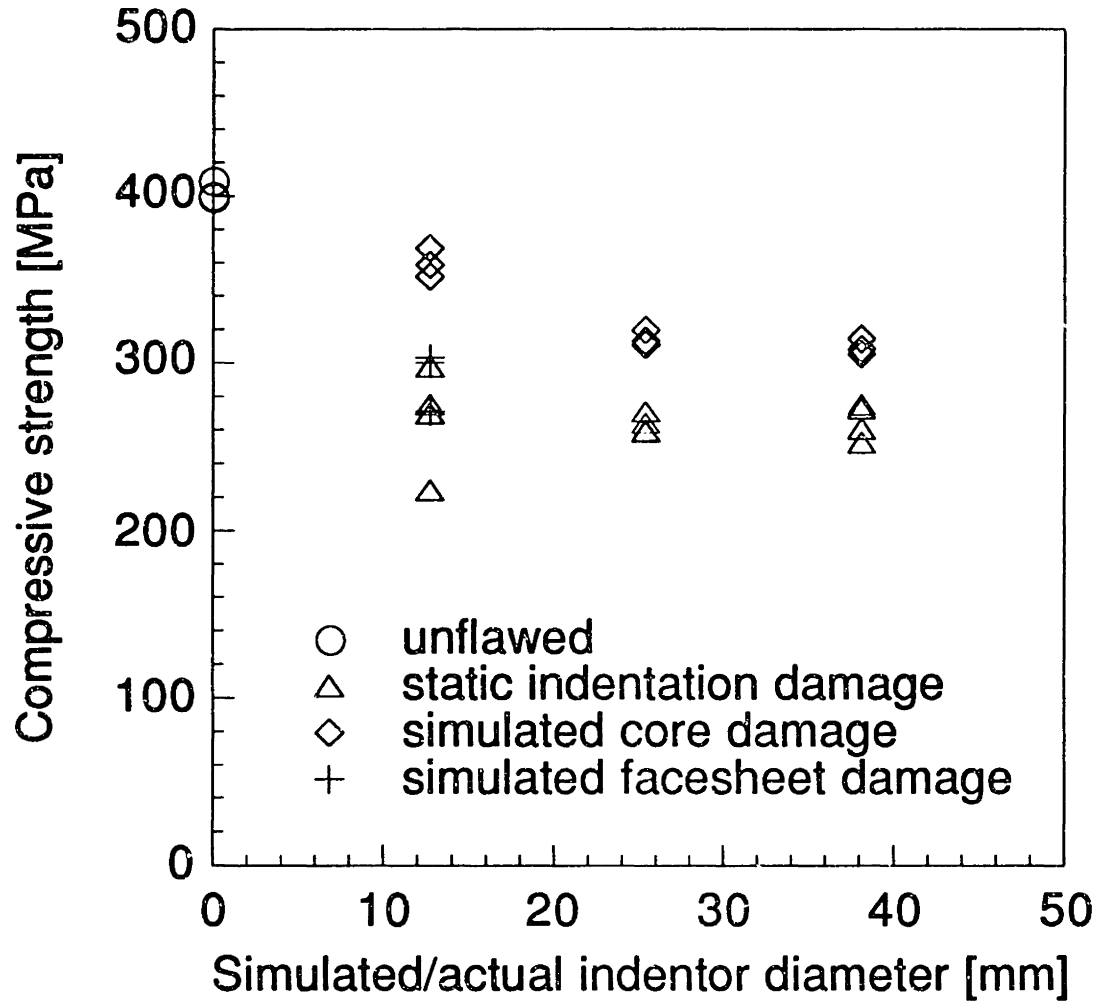
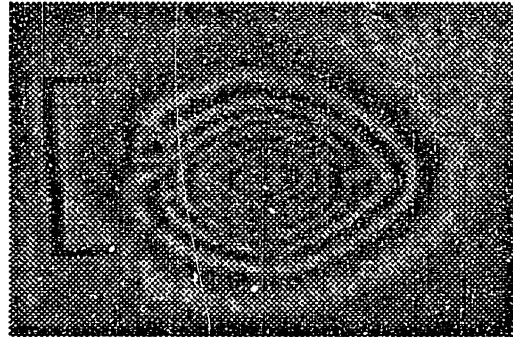
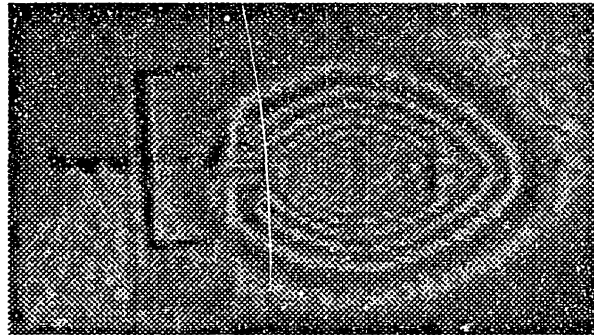
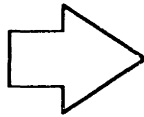


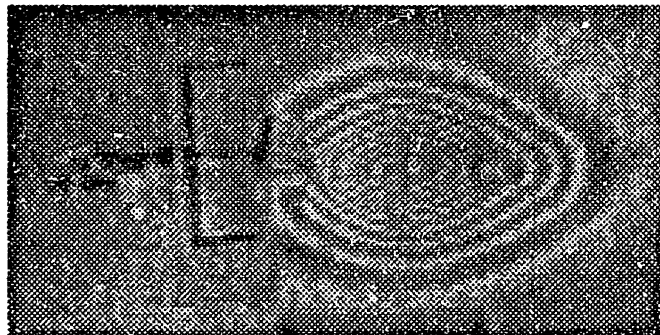
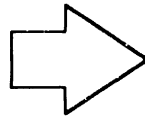
Figure 6.117 Compressive strength of specimens with (0/90) facesheets versus simulated/actual indenter diameter.



215 MPa



220 MPa



225 MPa

Figure 6.118 Digitized video image of the specimen with (0/90) facesheets and level 1 static indentation damage that failed by developing a fracture on one side of the dimple.

approximately the same residual strength as those with level 1 static indentation damage.

The compressive strength of all specimens with (± 45) facesheets are shown in Table 6.11 and Figure 6.119. The coefficients of variation are all below 6% except for the specimens with level 3 indentation damage. An explanation of this higher coefficient of variation is given later. The specimens with simulated core damage have approximately the same failure strength. The static indentation specimens show a decline in strength with greater simulated/actual indenter diameter. One of these specimens with level 3 damage failed with the dimple propagating to the edge on one side only while the other two of these specimens with level 3 damage failed with the dimple propagating to the edge on both sides. This former specimen has the highest failure stress of 229 MPa among the three. If the failure load of this specimen is ignored, the average failure stress for the remaining two specimens is 196 MPa (2.02%). All specimens with simulated core damage show slightly higher residual strength than the corresponding specimens with static indentation damage. The specimens with level 1 simulated facesheet damage have approximately the same residual strength as those with level 1 static indentation damage.

6.2.6 Predicted stress distributions and prediction of failure stress

In Chapter 4, the convergence study showed that significant longitudinal stresses, σ_{xx} , can develop along the centerline through the dimple and perpendicular to the loading. Such a finding is consistent with the final failure mode of specimens with static indentation damage and those with simulated core damage, which is facesheet fracture, generally perpendicular to the loading direction and through the center of the dimple.

Table 6.11 Compressive strength of specimens with (± 45) facesheets

Damage Type	Level			
	None	1	2	3
None	247 (0.92%) ^a	—	—	—
Static Indentation	—	221 (4.9%)	211 (5.5%)	204 (8.2%)
Simulated Core	—	240 (1.5%)	226 (1.3%)	234 (1.7%)
Simulated Facesheet	—	221 (3.1%)	—	—

^anumbers in parentheses are coefficients of variation

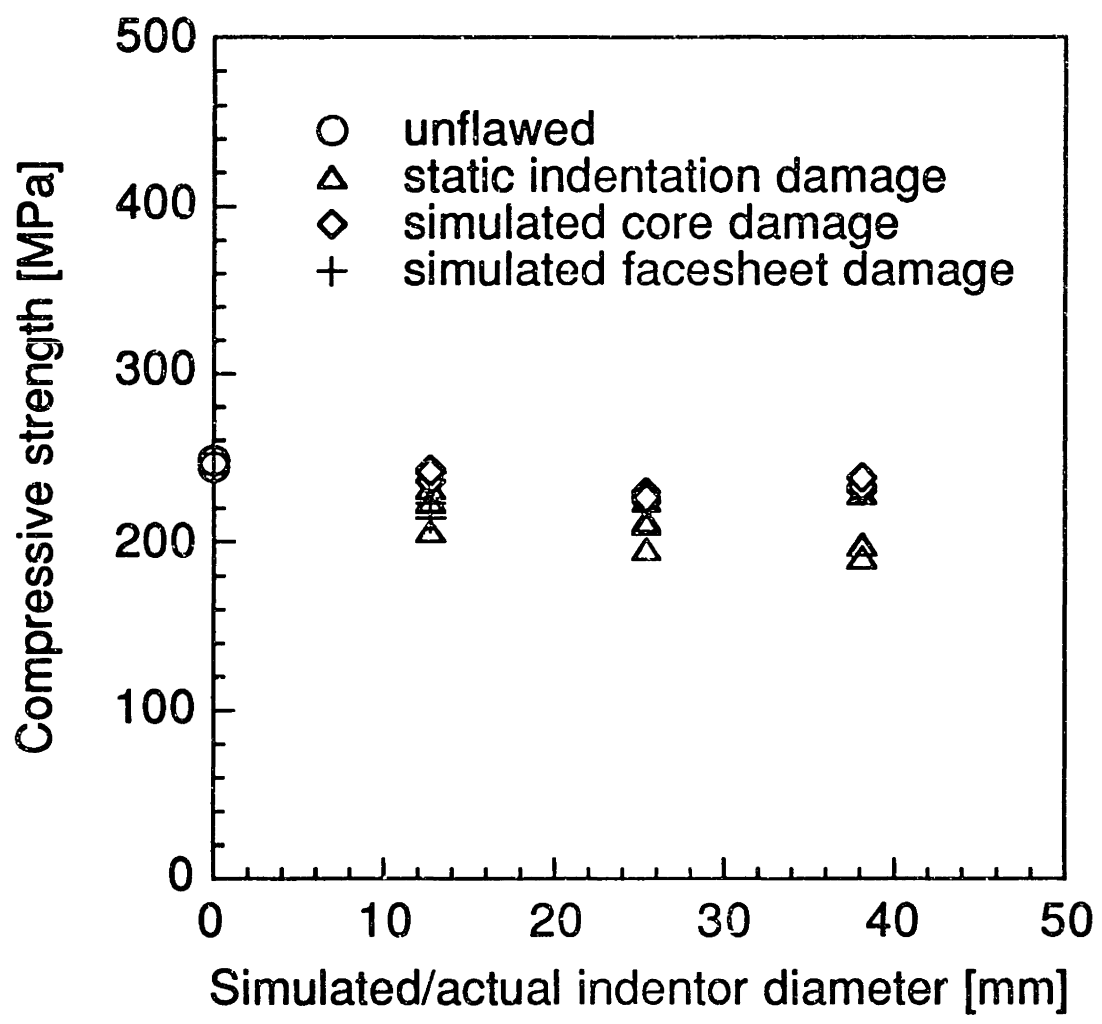


Figure 6.119 Compressive strength of specimens with (± 45) facesheets versus simulated/actual indenter diameter.

Such a fracture would most likely be attributable to the longitudinal stress. It is, therefore, suggested that the longitudinal stress distribution be examined to predict the residual strengths of the damaged panels under uniaxial compression.

The longitudinal stress distributions are thus calculated along the centerline through the center of the dimple and examined in an attempt to correlate failure of the damaged sandwich panels. Two components, the membrane stress and the bending stress, of the longitudinal stress are examined as well as the total longitudinal stress. The membrane stress is related to the stress resultant, N_{xx} , which can be calculated from the stress function, $F(x,y)$, as defined in Chapter 4:

$$\sigma_{xx}^{membrane} = N_{xx} / h = F_{,yy} \quad (6.1)$$

The bending stress is related to the moment resultant, M_{xx} , which can be calculated at any through-thickness location z in the laminate from the curvatures, $w_{,xx}$ and $w_{,yy}$, as in Classical Laminated Plate Theory:

$$\sigma_{xx}^{bending} = \frac{12M_{xx}}{h^3} z = \frac{12z}{h^3} (D_{11}w_{,xx} + D_{12}w_{,yy}) \quad (6.2)$$

for the particular laminates utilized herein and where h is the laminate thickness. The total longitudinal stress is the sum of the membrane component and the bending component.

Twelve cases are examined in this section, six with (0/90) facesheets and six with (± 45) facesheets. For each facesheet layup, results for all three levels of simulated core damage and all three levels of static indentation damage are presented, including distributions of the membrane stress, the bending stress, and the total longitudinal stress. The bending stress is

calculated at the top surface of the facesheet, where z is equal to $h/2$, while the total stress is calculated at both the top and bottom surfaces of the facesheet, where z is equal to $h/2$ and $-h/2$, respectively. In each case, the stress distributions are shown at two applied stress levels for which the particular dimple profiles were presented earlier in this chapter. The higher of these two applied stress levels is the residual strength of the corresponding specimen.

The longitudinal stress distributions in the specimens with (0/90) facesheets and simulated core damage are shown in Figures 6.120 through 6.128. The membrane stress distributions show a redistribution of stress around the dimple and an increase in magnitude near the boundary of the dimple along the y -axis for both applied stress levels. On the other hand, stress relaxation can be observed within the dimple. For all three damage levels, the magnitude of the stress relaxation increases as the applied stress level increases such that the stress level at the center of the dimple remains approximately the same. The magnitudes of the maximum membrane stress are approximately 400 MPa for level 1 damage, 420 MPa for level 2 damage, and 400 MPa for level 3 damage when the applied stress levels are equal to the corresponding residual strengths of the specimens (i.e. at failure). These values are very close to the average compressive strength of the undamaged specimens (403 MPa), as given in Table 6.5. In other words, the maximum membrane stress levels at failure correlates well with the residual strengths of these specimens with (0/90) facesheets and simulated core damage. The locations of the maximum membrane stress at failure for all three levels of simulated core damage occurred at about 15 mm from the center of the dimple, or 30 mm apart. The moiré measurements show that the average width of the dimple, measured at the depth of the zeroth order

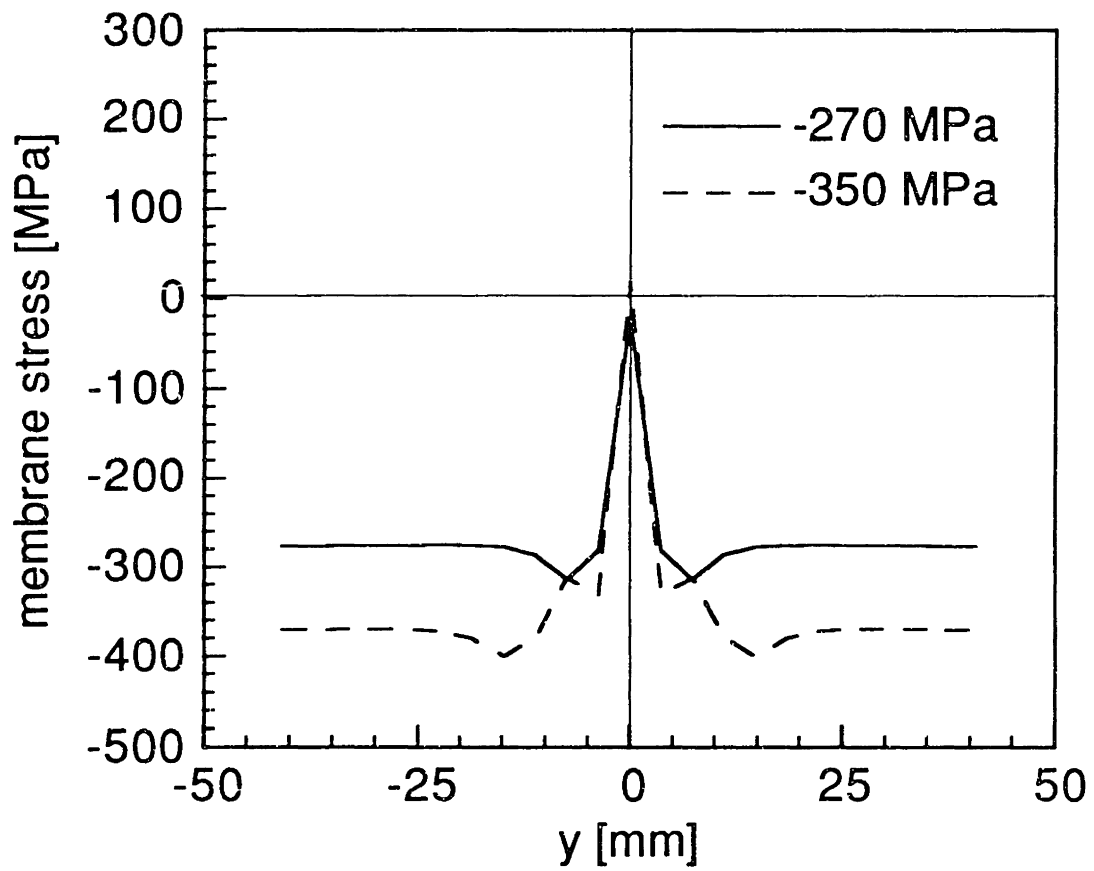


Figure 6.120 Membrane stress distribution at two applied stress levels in a specimen with (0/90) facesheets and level 1 simulated core damage.

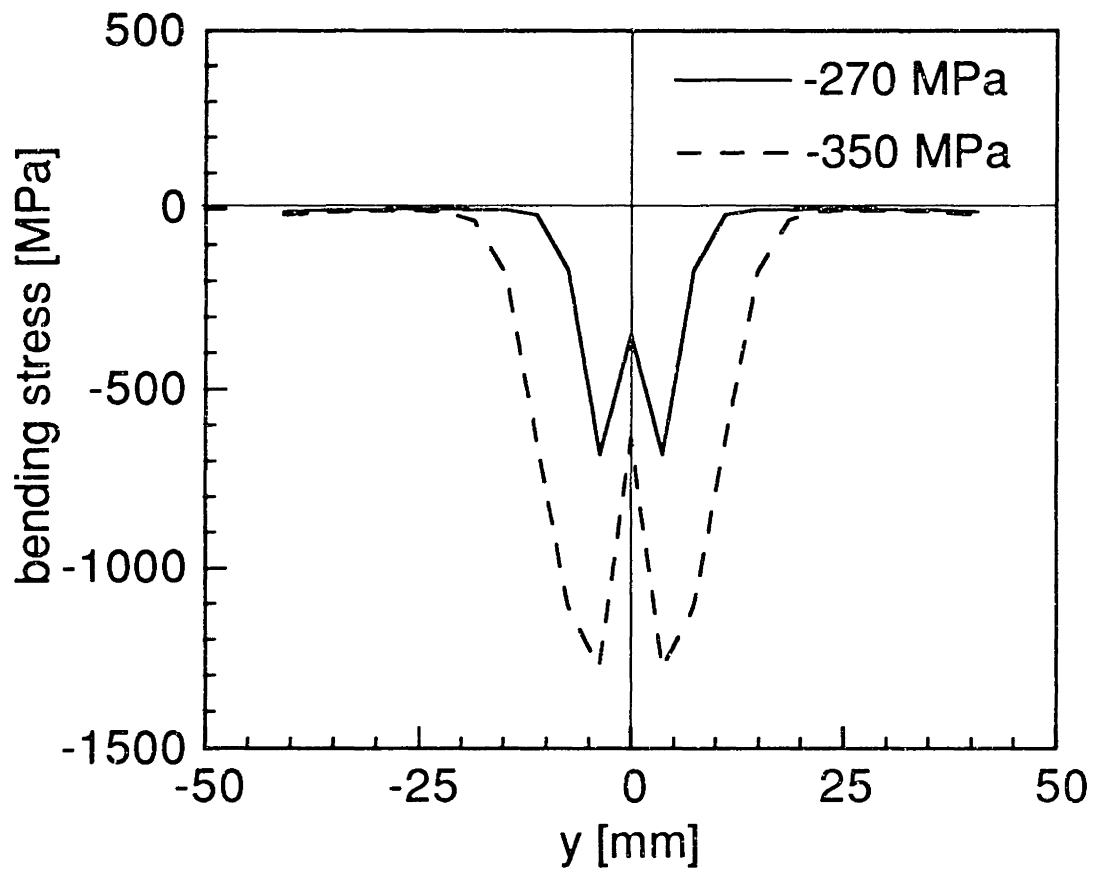


Figure 6.121 Bending stress distribution at top surface for two applied stress levels in a specimen with (0/90) facesheets and level 1 simulated core damage.

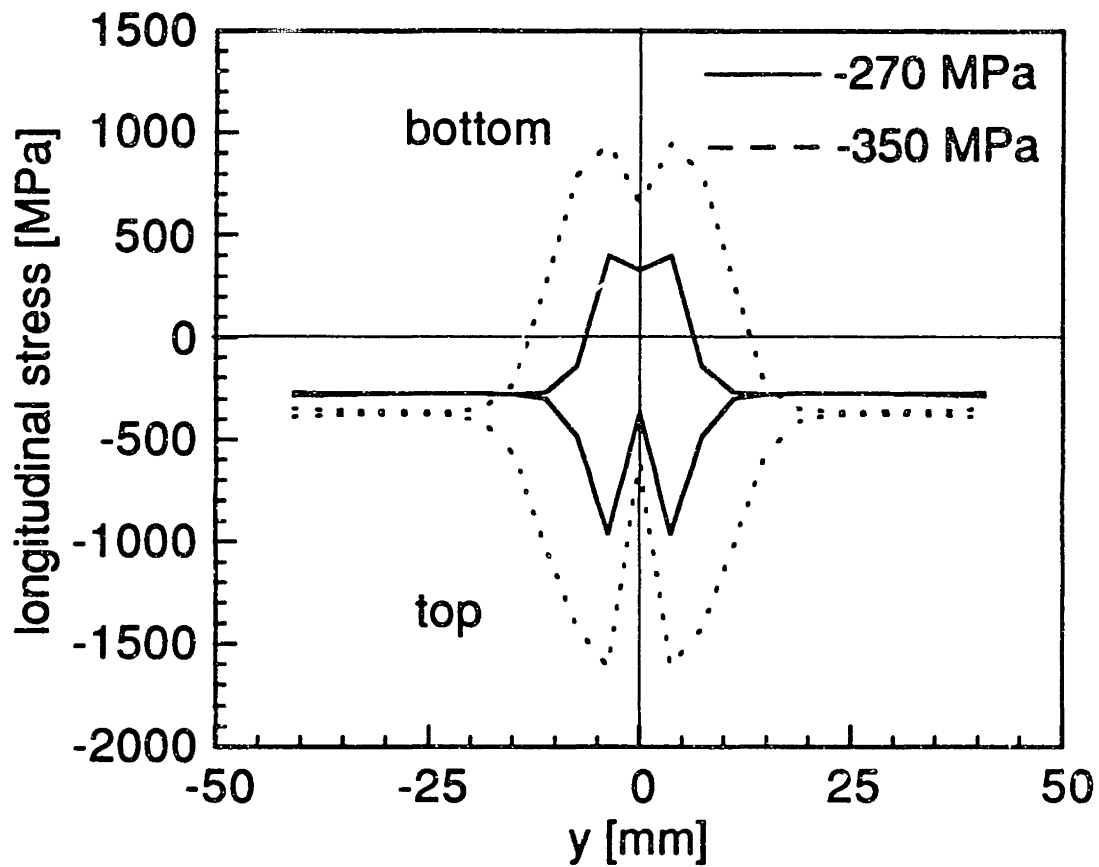


Figure 6.122 Total longitudinal stress distribution at top and bottom surfaces for two applied stress levels in a specimen with (0/90) facesheets and level 1 simulated core damage.

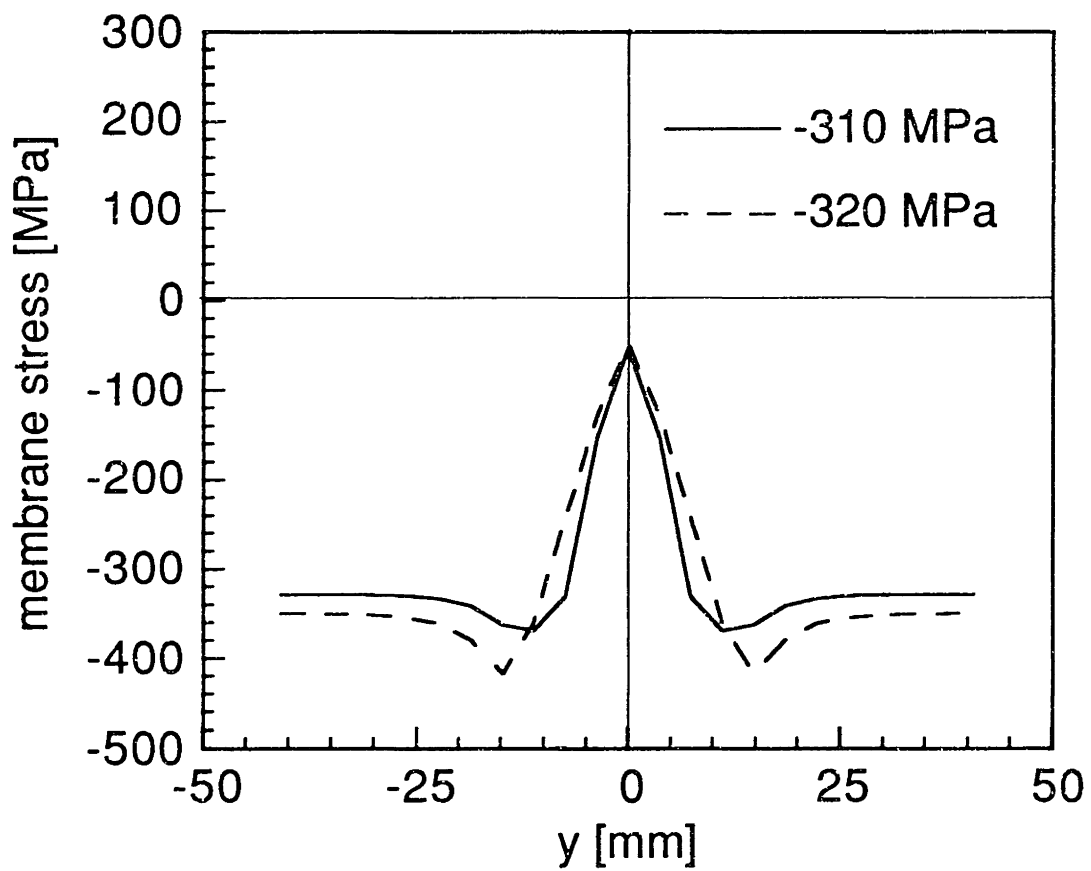


Figure 6.123 Membrane stress distribution at two applied stress levels in a specimen with (0/90) facesheets and level 2 simulated core damage.

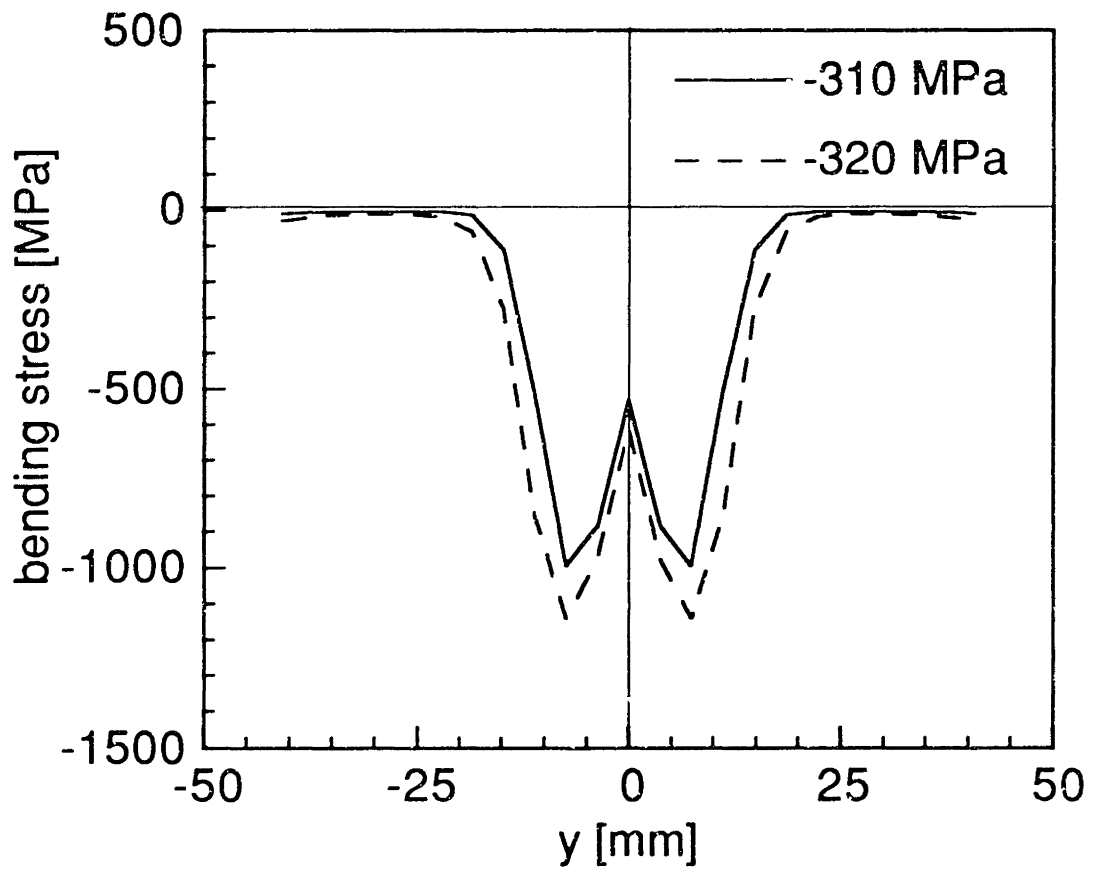


Figure 6.124 Bending stress distribution at top surface for two applied stress levels in a specimen with (0/90) facesheets and level 2 simulated core damage.

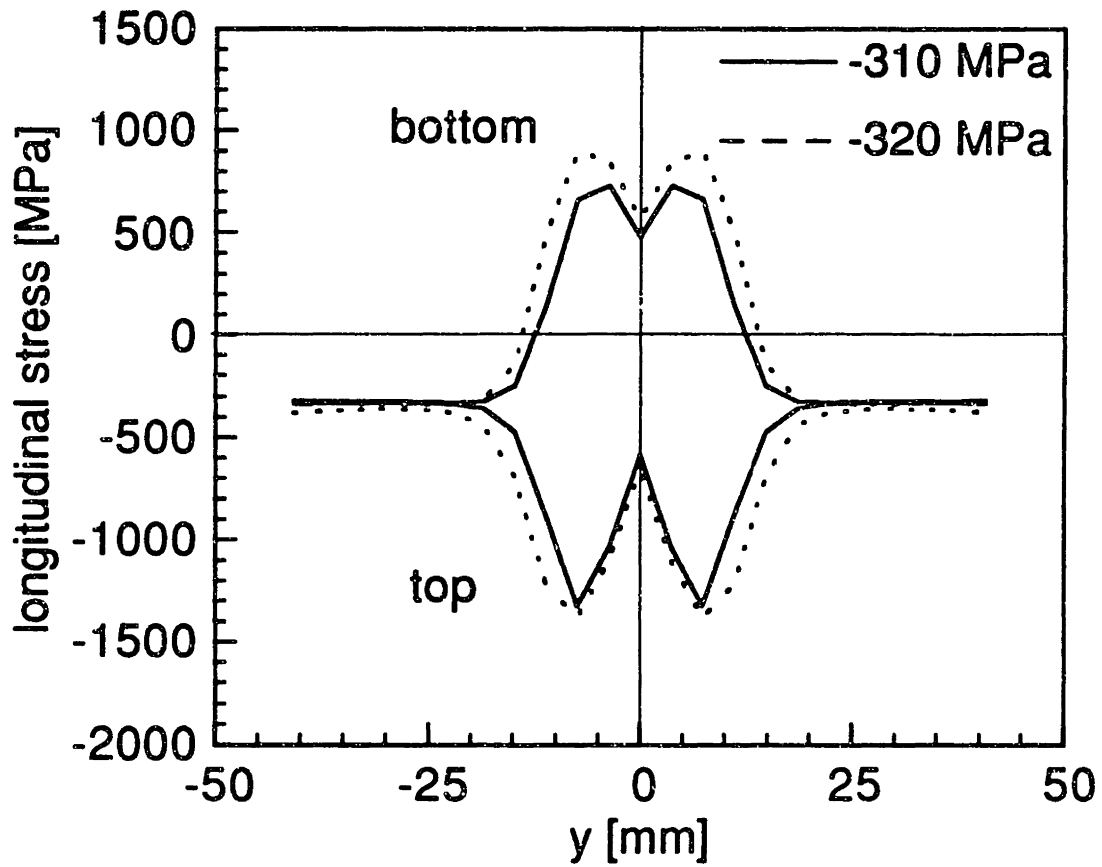


Figure 6.125 Total longitudinal stress distribution at top and bottom surfaces for two applied stress levels in a specimen with (0/90) facesheets and level 2 simulated core damage.

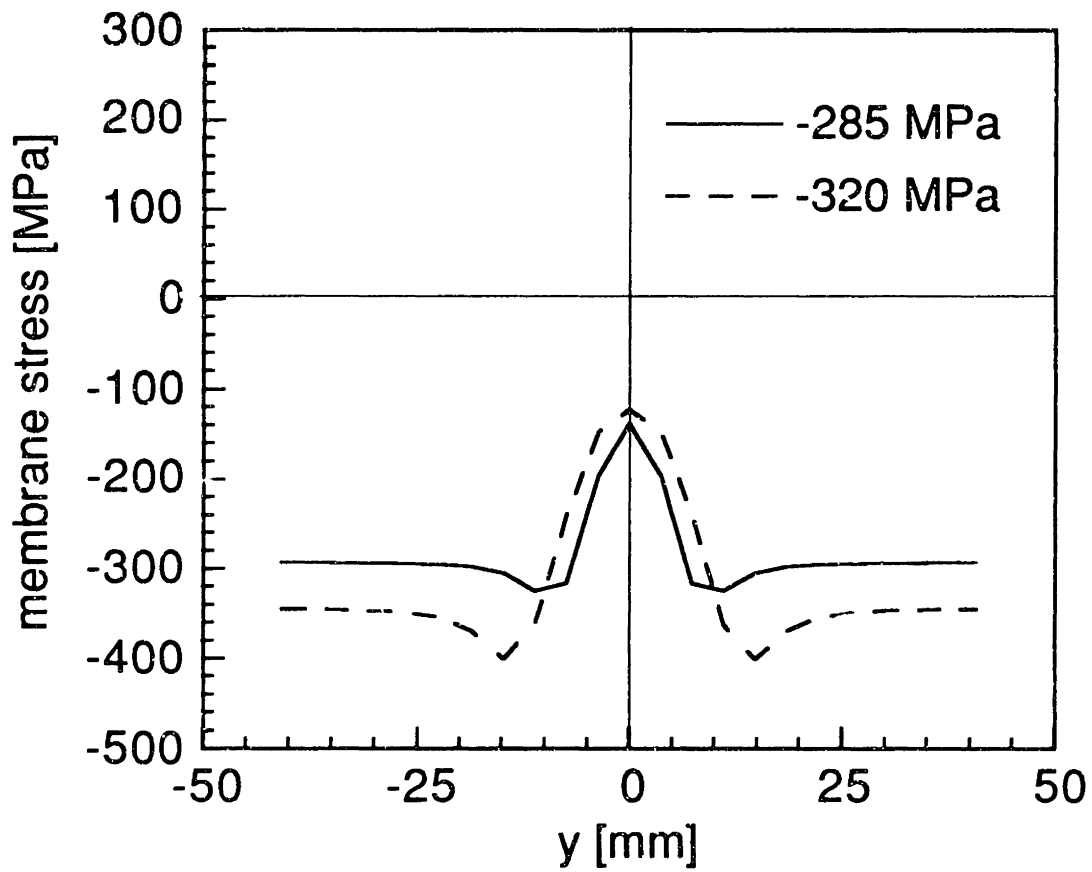


Figure 6.126 Membrane stress distribution at two applied stress levels in a specimen with (0/90) facesheets and level 3 simulated core damage.

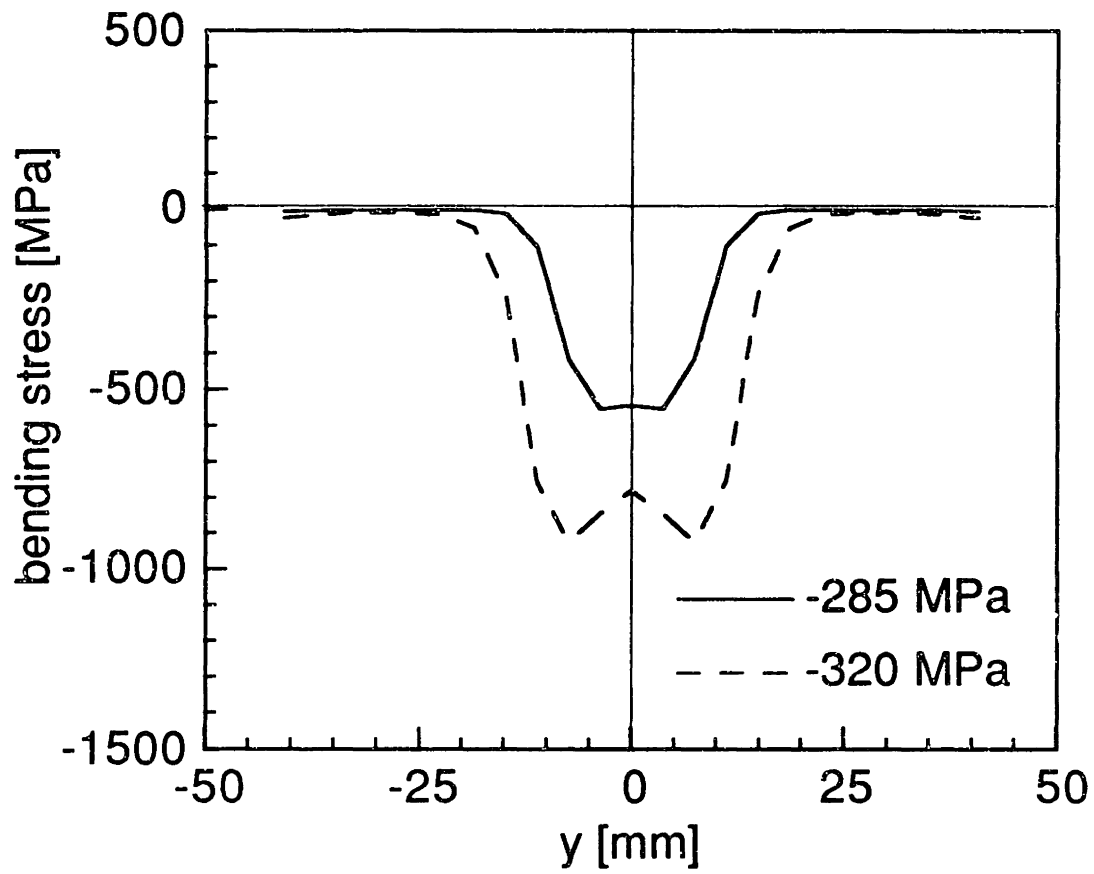


Figure 6.127 Bending stress distribution at top surface for two applied stress levels in a specimen with (0/90) facesheets and level 3 simulated core damage.

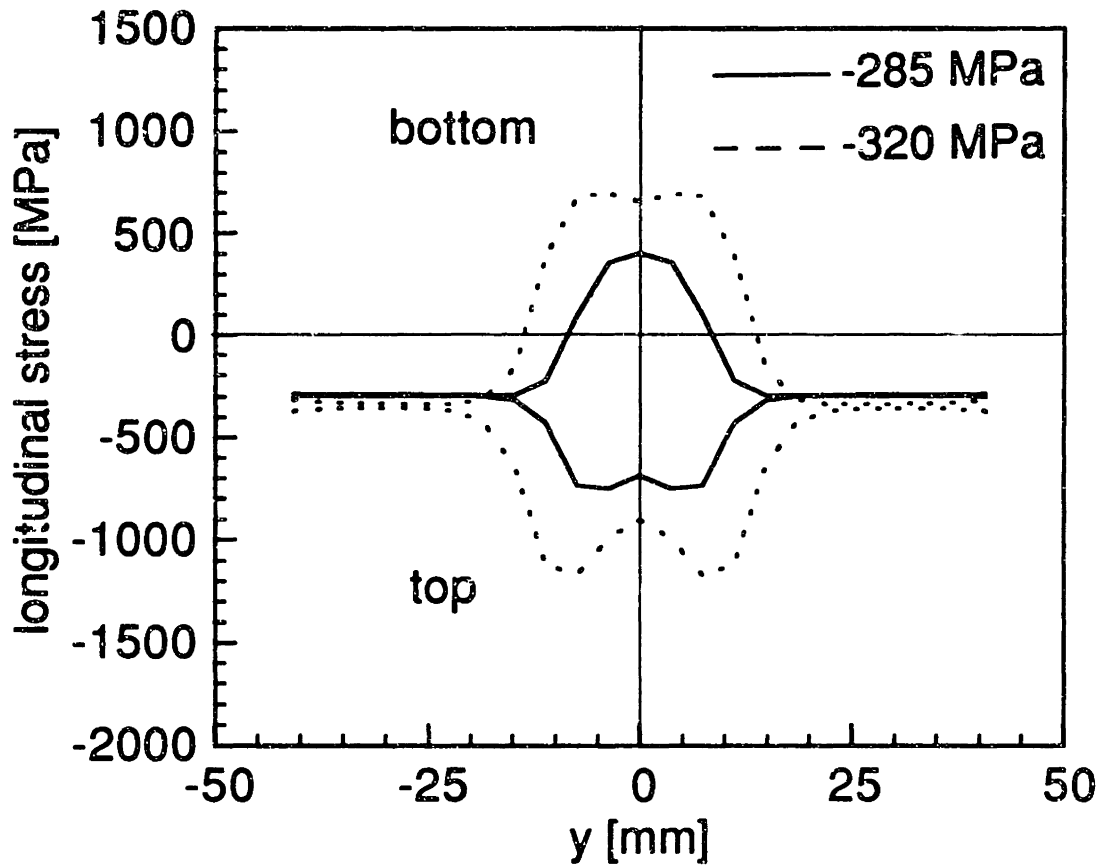


Figure 6.128 Total longitudinal stress distribution at top and bottom surfaces for two applied stress levels in a specimen with (0/90) facesheets and level 3 simulated core damage.

fringe, just before catastrophic failure in these specimens with (0/90) facesheets and simulated core damage is 21 mm for level 1 damage, 31 mm for level 2 damage, and 28 mm for level 3 damage. The locations of calculated peak stress are, therefore, outside or very close to the extent of the dimple propagation as measured experimentally. Note, however, that these locations of maximum membrane stress occur within the calculated extent of the dimple propagation.

The bending stress distributions at both applied stress levels for specimens with level 1 and level 2 simulated core damage show a bimodal shape symmetric about the center of the specimen. For the specimen with level 3 simulated core damage, only the distribution at failure shows the bimodal shape. At failure, the magnitudes of the maximum bending stress are approximately 1200 MPa for level 1 damage, 1100 MPa for level 2 damage, and 900 MPa for level 3 damage. The corresponding locations of the maximum bending stress are about 4 mm from the center of the dimple for level 1 damage, and 7 mm for levels 2 and 3 damage. These locations of maximum bending stress are well within the extent of the dimple propagation.

The longitudinal stress distributions in the specimens with (0/90) facesheets and static indentation damage are shown in Figures 6.129 through 6.137. Once again, the membrane stress distributions show a redistribution of stress around the dimple and an increase in magnitude near the boundary of the dimple along the y-axis for both applied stress levels. Stress relaxation is again observed within the dimple. The magnitudes of the maximum membrane stress at failure are approximately 320 MPa for level 1 damage, 320 MPa for level 2 damage, and 330 MPa for level 3 damage. The magnitudes of the maximum membrane stress are all

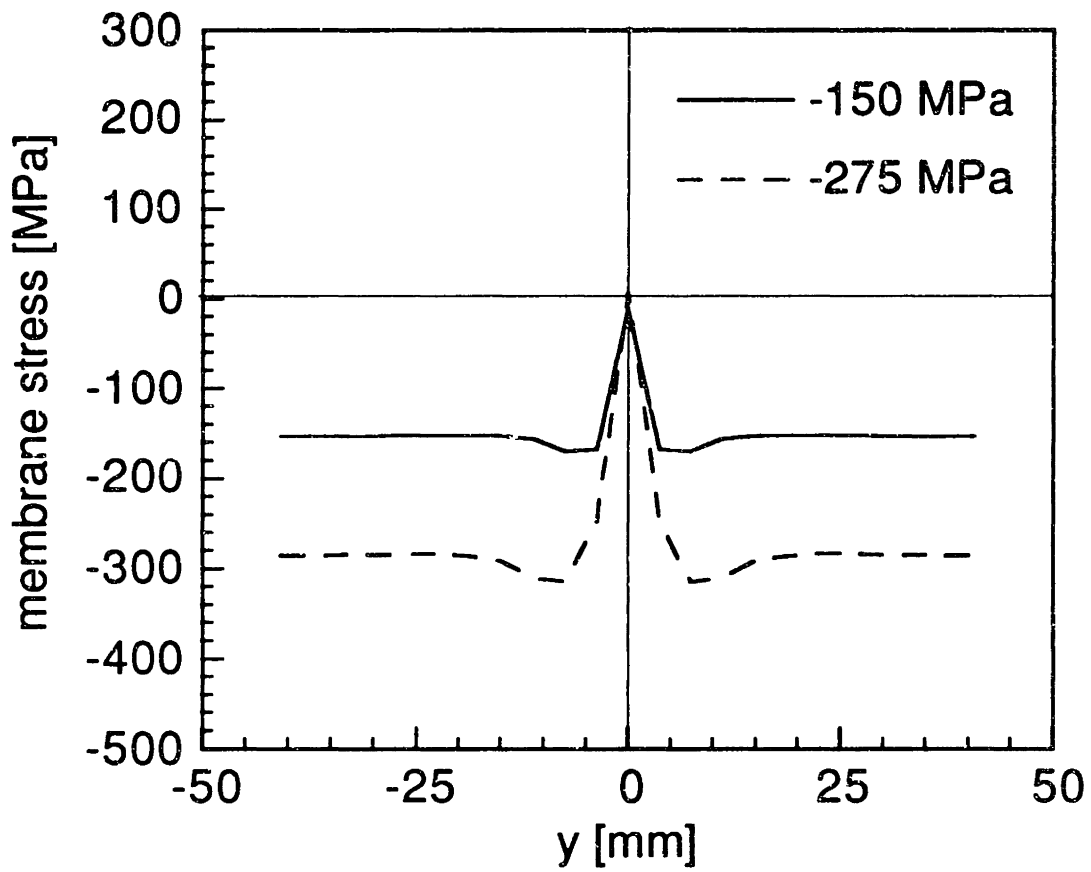


Figure 6.129 Membrane stress distribution at two applied stress levels in a specimen with (0/90) facesheets and level 1 static indentation damage.

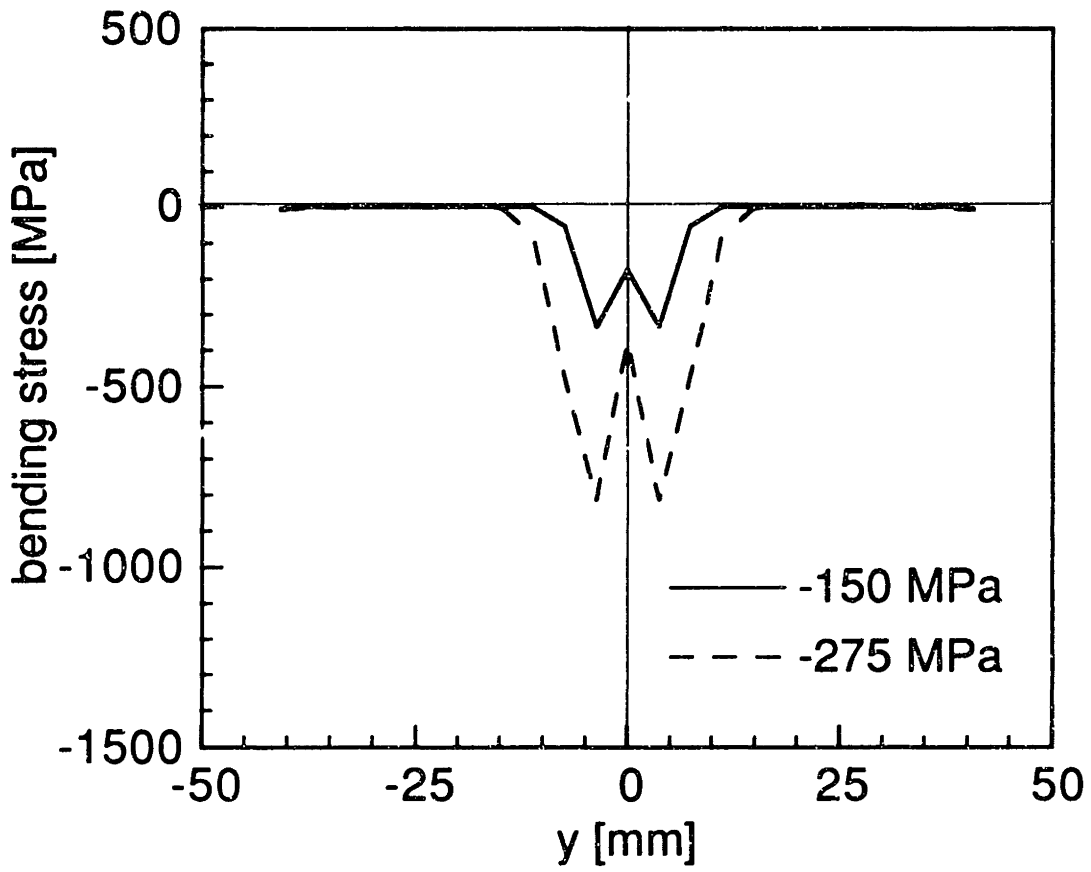


Figure 6.130 Bending stress distribution at top surface for two applied stress levels in a specimen with (0/90) facesheets and level 1 static indentation damage.

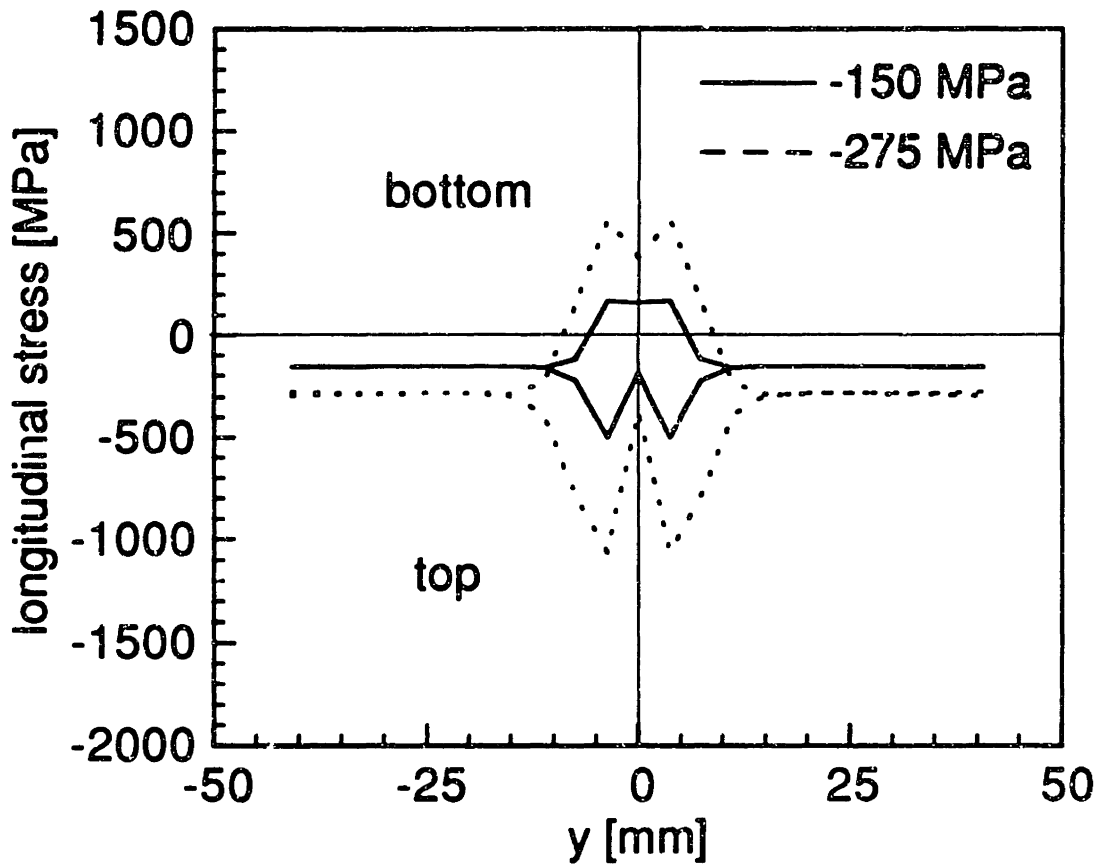


Figure 6.131 Total longitudinal stress distribution at top and bottom surfaces for two applied stress levels in a specimen with (0/90) facesheets and level 1 static indentation damage.

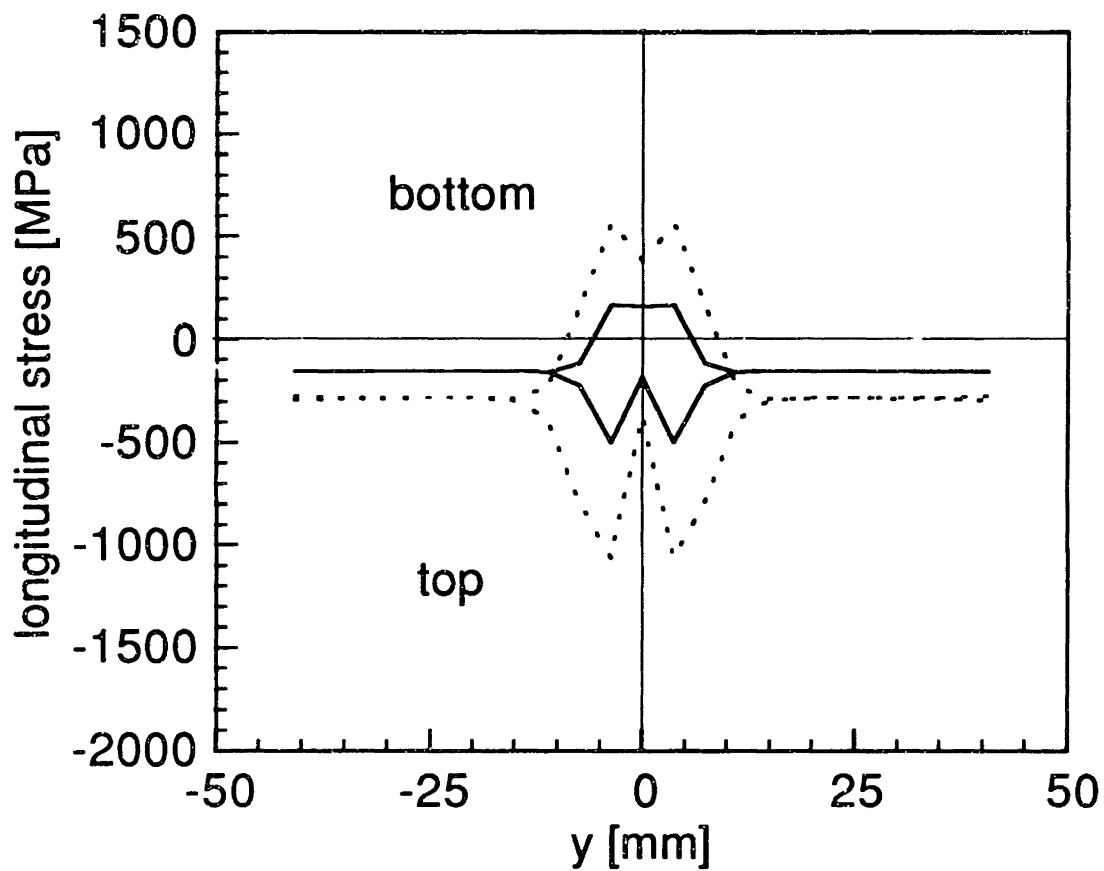


Figure 6.131 Total longitudinal stress distribution at top and bottom surfaces for two applied stress levels in a specimen with (0/90) facesheets and level 1 static indentation damage.

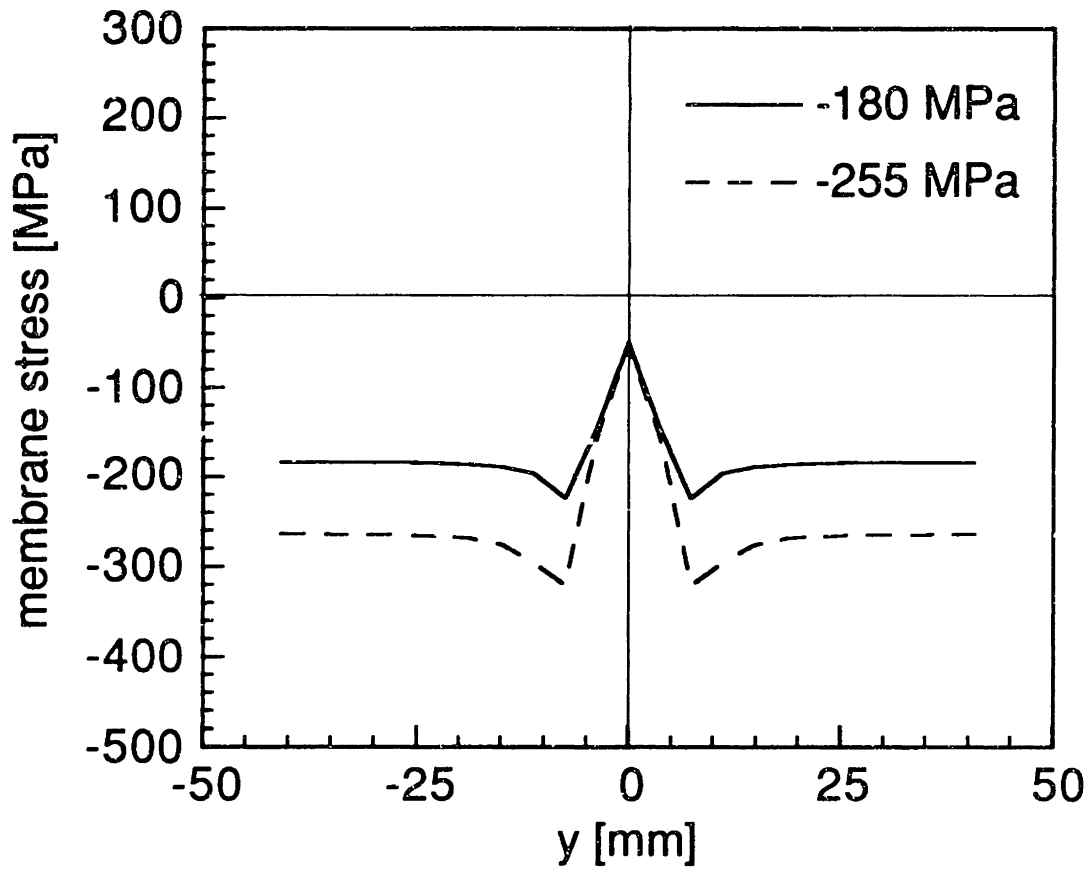


Figure 6.132 Membrane stress distribution at two applied stress levels in a specimen with (0/90) facesheets and level 2 static indentation damage.

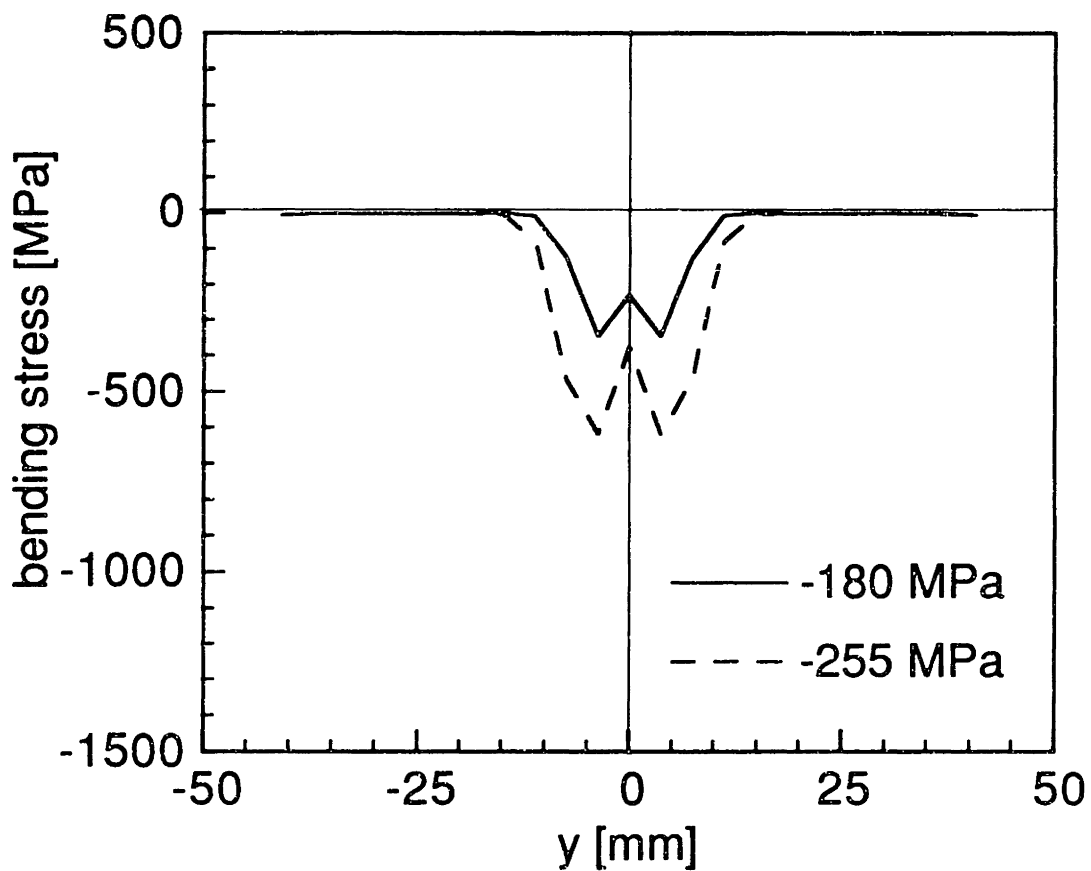


Figure 6.133 Bending stress distribution at top surface for two applied stress levels in a specimen with (0/90) facesheets and level 2 static indentation damage.

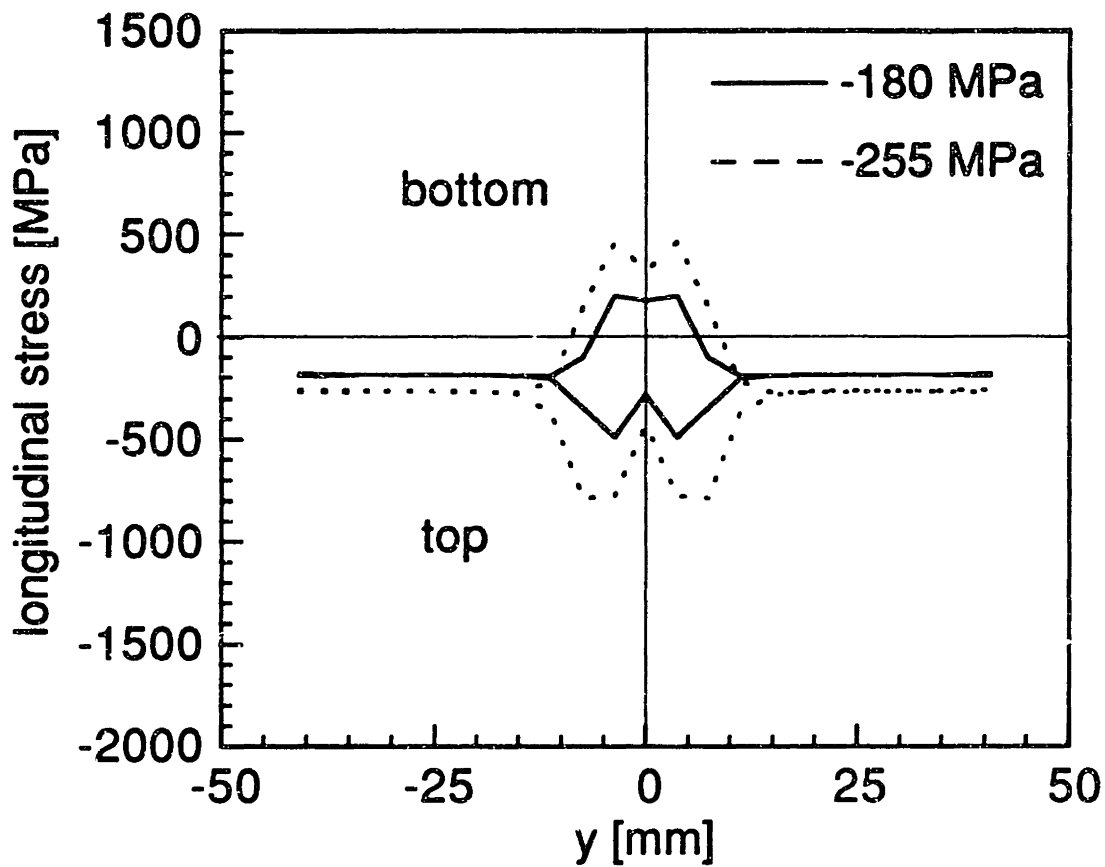


Figure 6.134 Total longitudinal stress distribution at top and bottom surfaces for two applied stress levels in a specimen with (0/90) facesheets and level 2 static indentation damage.

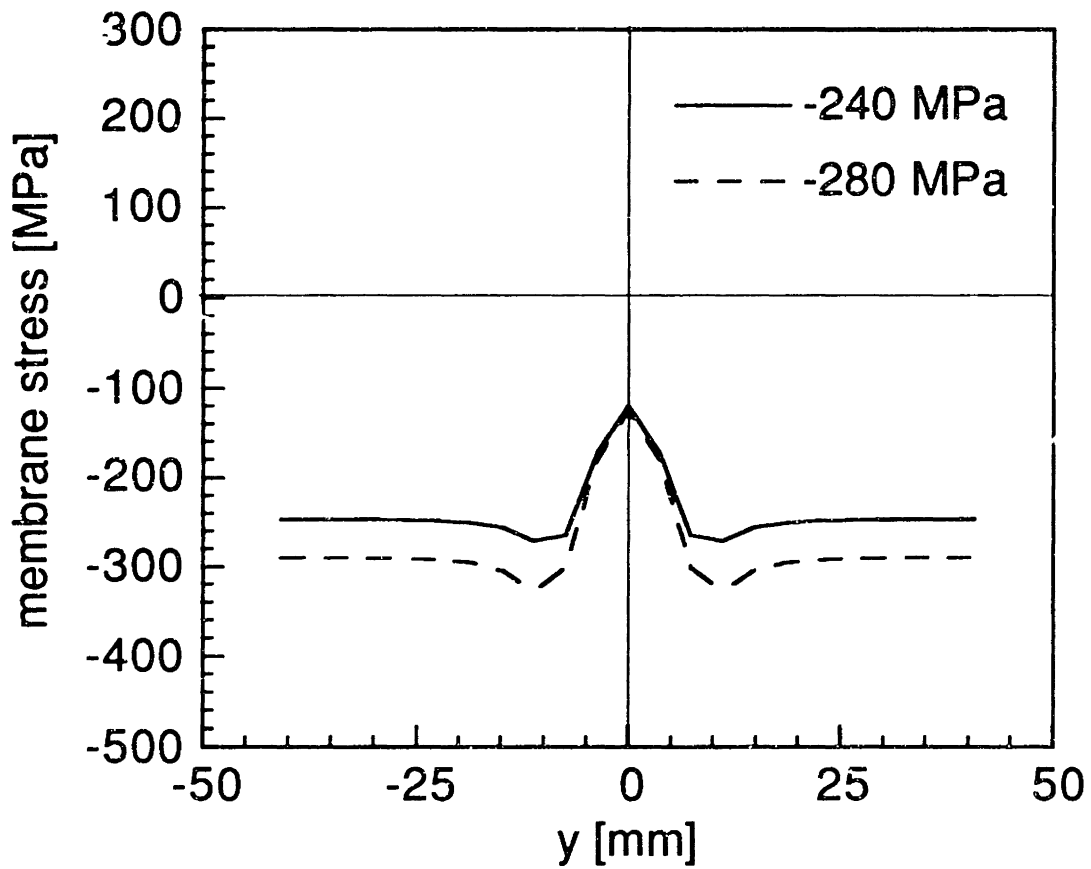


Figure 6.135 Membrane stress distribution at two applied stress levels in a specimen with (0/90) facesheets and level 3 static indentation damage.

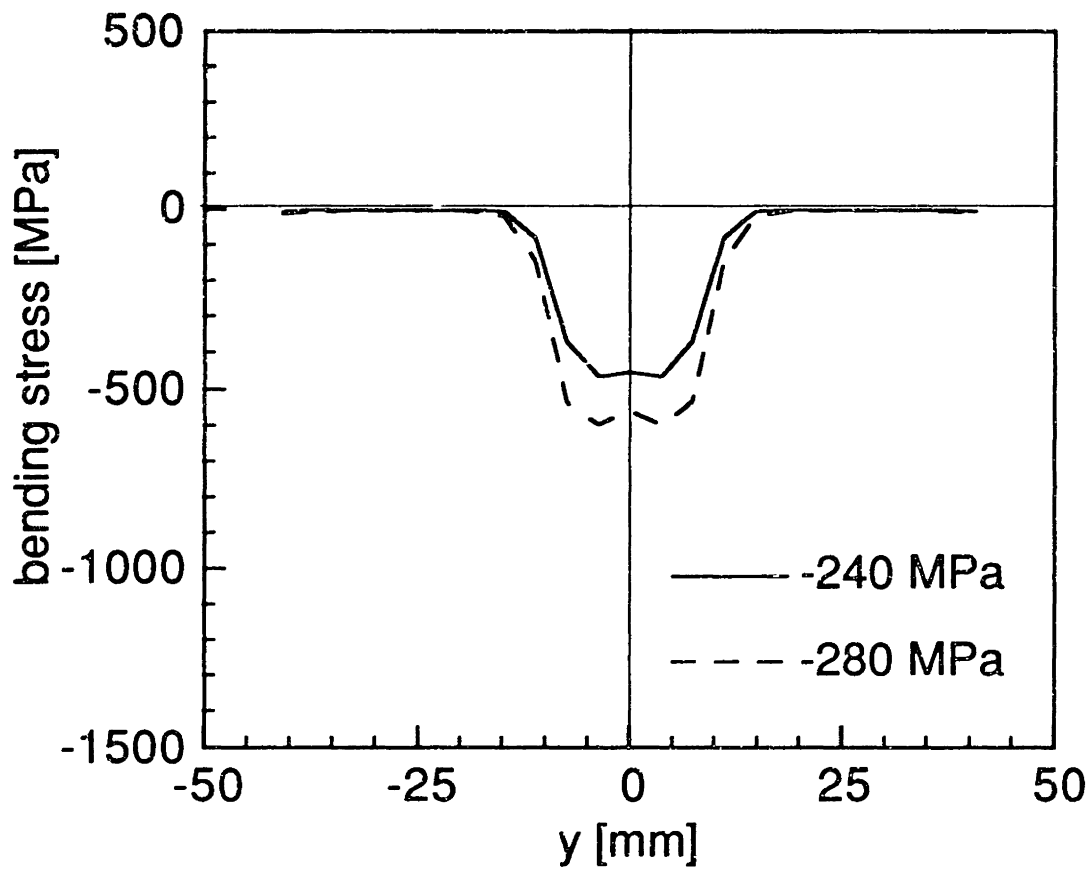


Figure 6.136 Bending stress distribution at top surface for two applied stress levels in a specimen with (0/90) facesheets and level 3 static indentation damage.

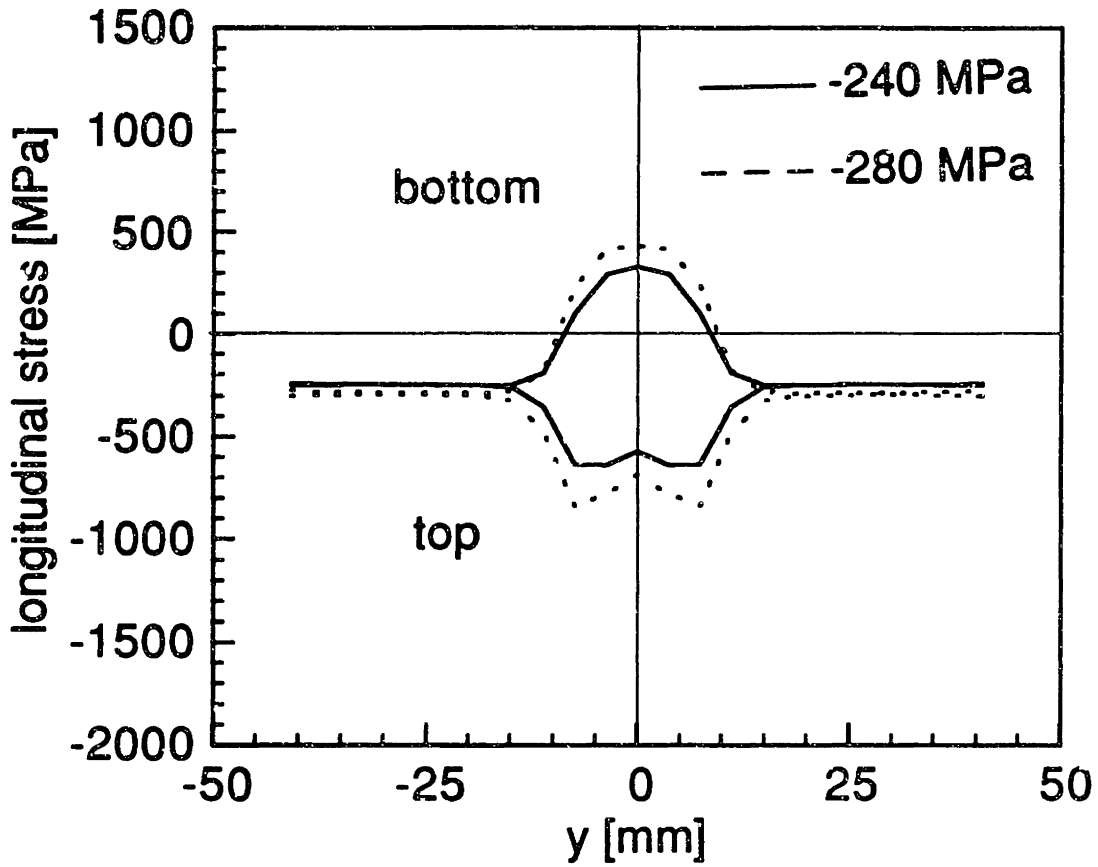


Figure 6.137 Total longitudinal stress distribution at top and bottom surfaces for two applied stress levels in a specimen with (0/90) facesheets and level 3 static indentation damage.

considerably lower than the average failure stress of the undamaged panels (403 MPa). In other words, the dimple propagation model overpredicts the residual strength of the indented specimens if the membrane stress is used to correlate the residual strength as it would require further loading to increase the maximum membrane stress to the strength of the undamaged specimens. This is not surprising since the dimple propagation model underpredicts the propagation of the dimple in such specimens with static indentation damage. The locations of the maximum membrane stress at failure are approximately 7 mm from the center of the dimple for damage levels 1 and 2, and 11 mm for level 3 damage. The moiré measurements, as shown in Figure 6.96, show that the average width of the dimple just before catastrophic failure in specimens with (0/90) facesheets and static indentation damage is 27 mm for level 1 damage, 44 mm for level 2 damage, and 39 mm for level 3 damage.

The bending stress distributions show similar bimodal shape as those for specimens with simulated core damage. The maximum bending stress levels at failure are about 810 MPa for level 1 static indentation damage, 620 MPa for level 2, and 600 MPa for level 3. All these values, again, exceed the average failure stress of the undamaged specimens which is 403 MPa. The corresponding locations of maximum bending stress are approximately 4 mm from the center of the dimple for all three damage levels.

The longitudinal stress distributions are plotted along the centerline perpendicular to the loading in Figures 6.138 through 6.146 for specimens with (± 45) facesheets and simulated core damage. Once again, stress concentration is observed in the membrane stress distributions near the boundary of the dimple while stress relaxation is seen further within the

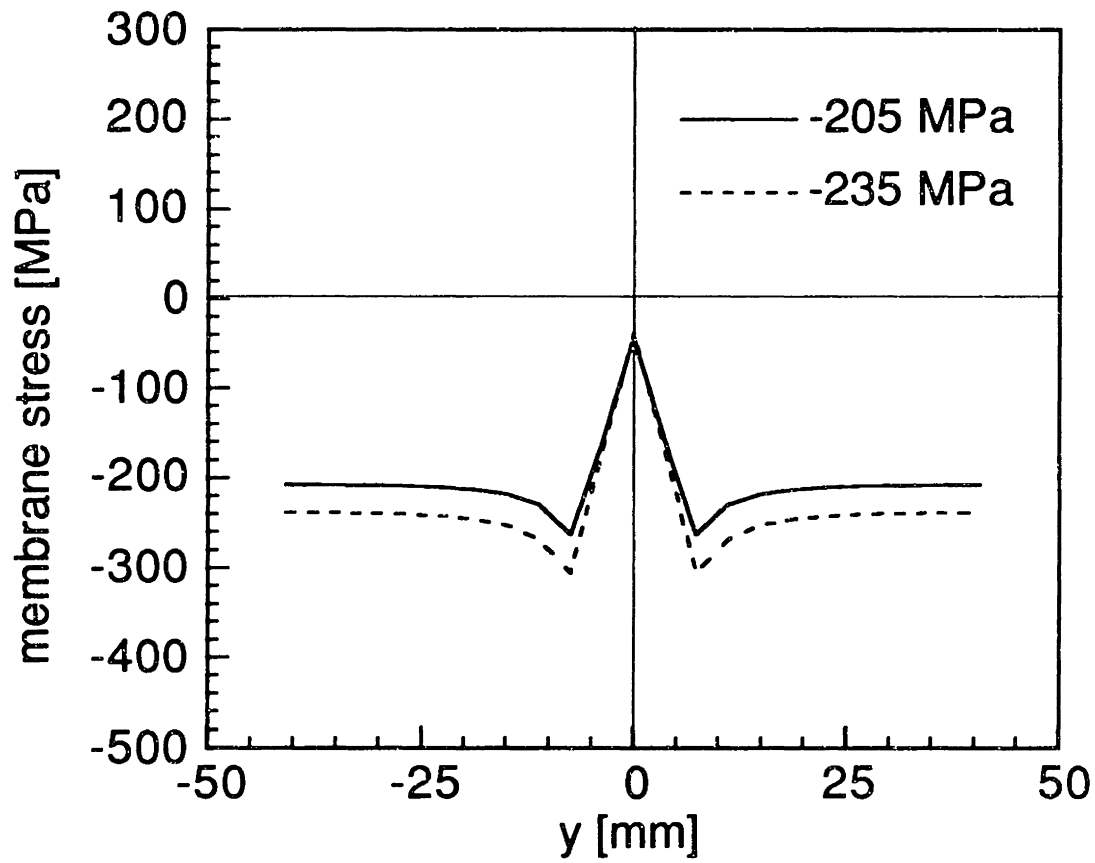


Figure 6.138 Membrane stress distribution at two applied stress levels in a specimen with (± 45) facesheets and level 1 simulated core damage.

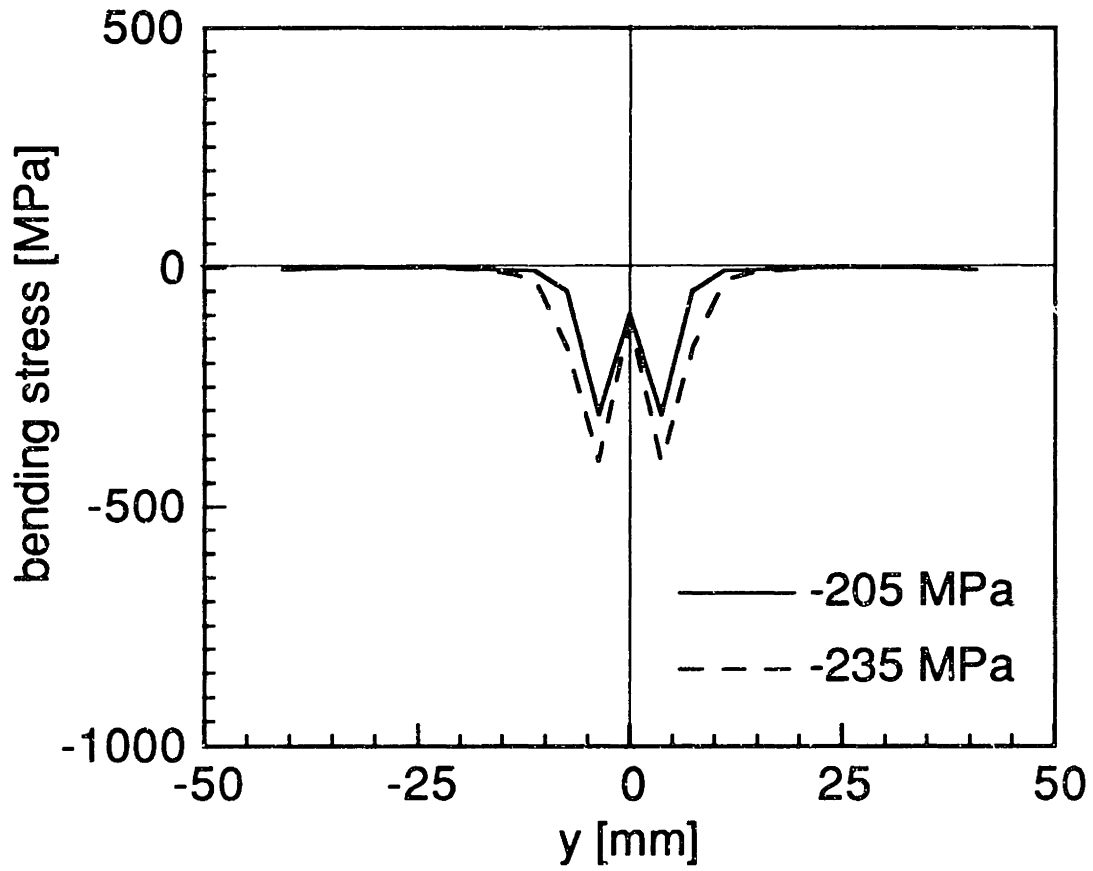


Figure 6.139 Bending stress distribution at top surface for two applied stress levels in a specimen with (± 45) facesheets and level 1 simulated core damage.

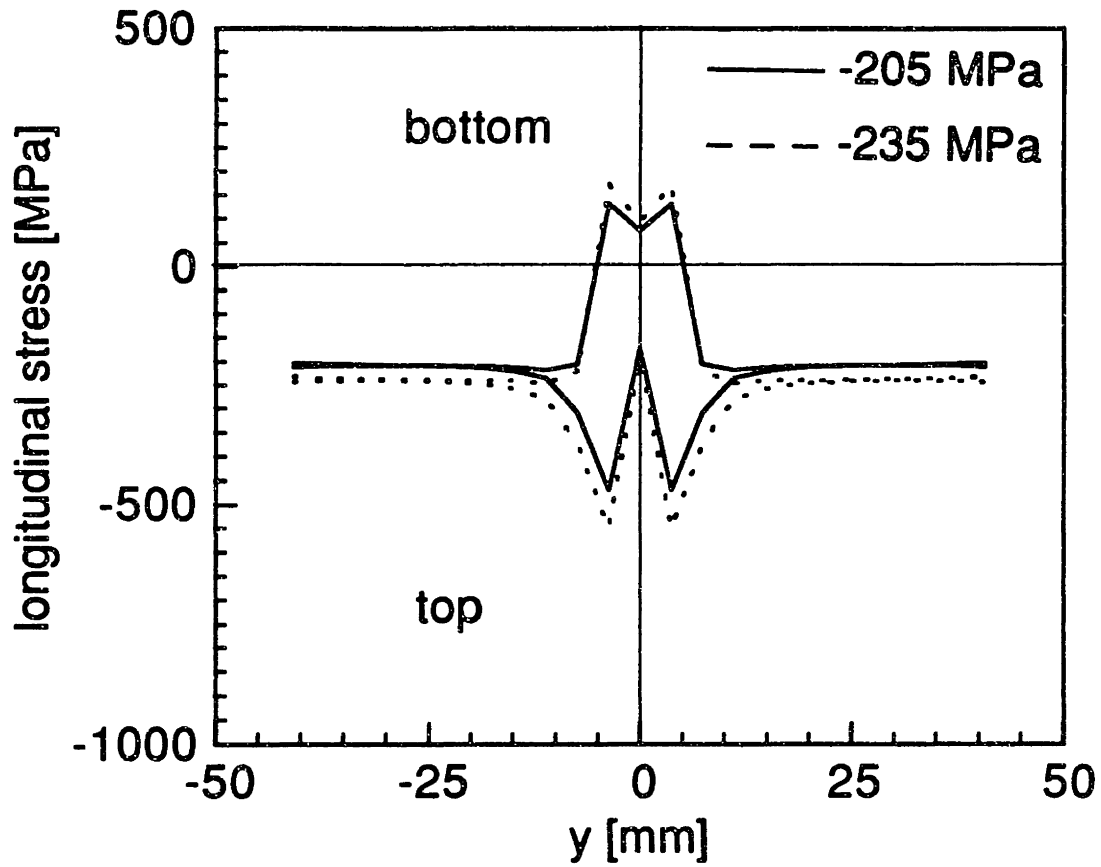


Figure 6.140 Total longitudinal stress distribution at top and bottom surfaces for two applied stress levels in a specimen with (± 45) facesheets and level 1 simulated core damage.

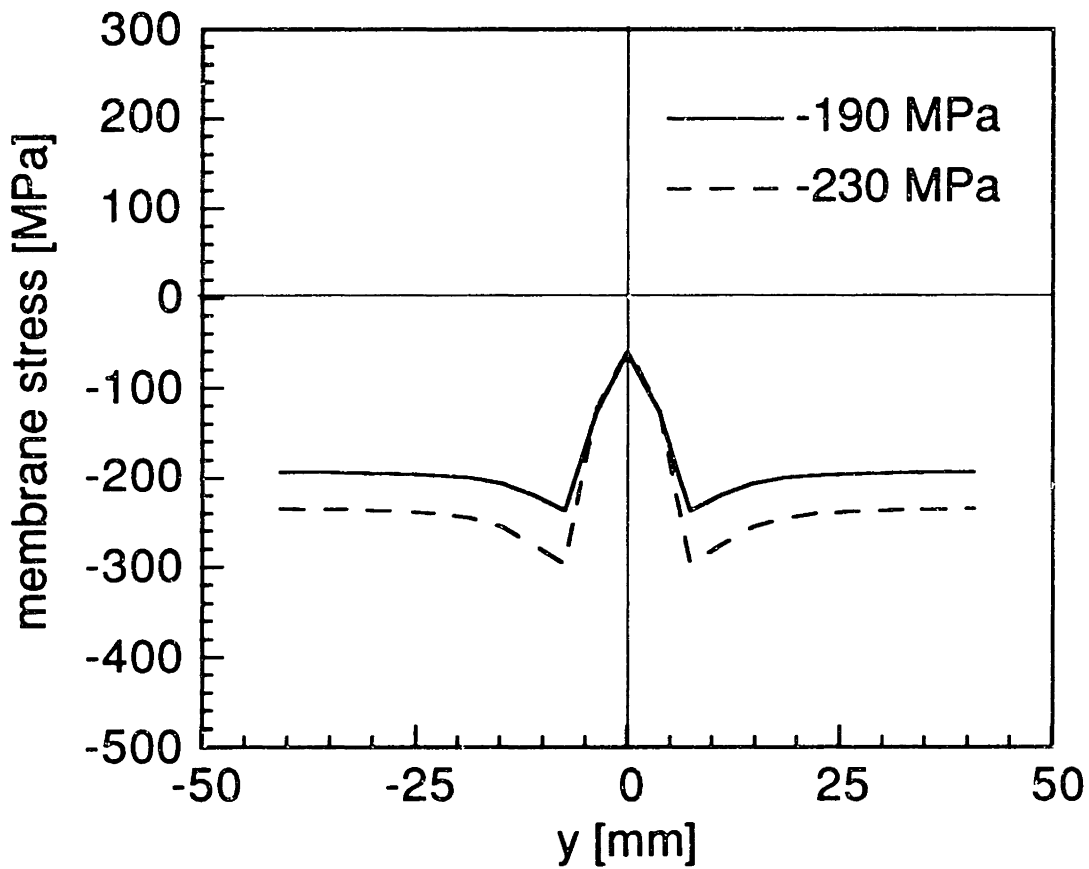


Figure 6.141 Membrane stress distribution at two applied stress levels in a specimen with (± 45) facesheets and level 2 simulated core damage.

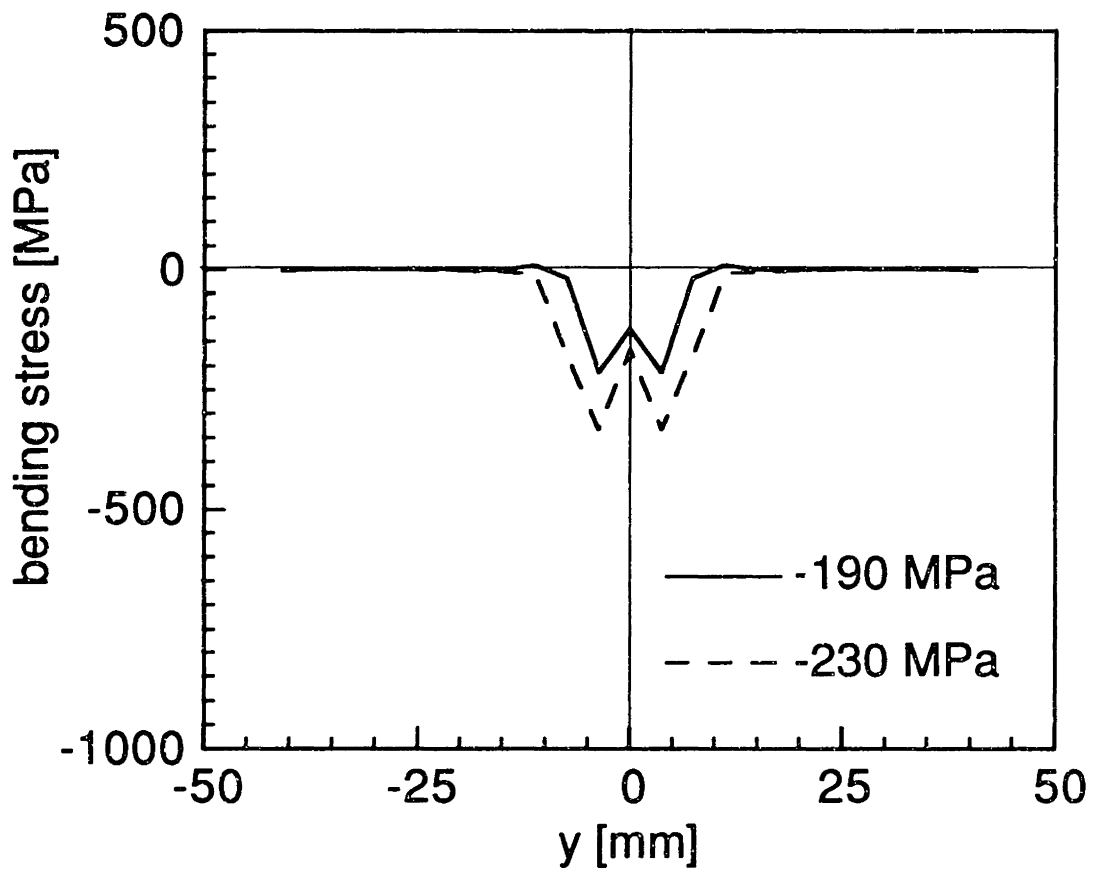


Figure 6.142 Bending stress distribution at top surface for two applied stress levels in a specimen with (± 45) facesheets and level 2 simulated core damage.

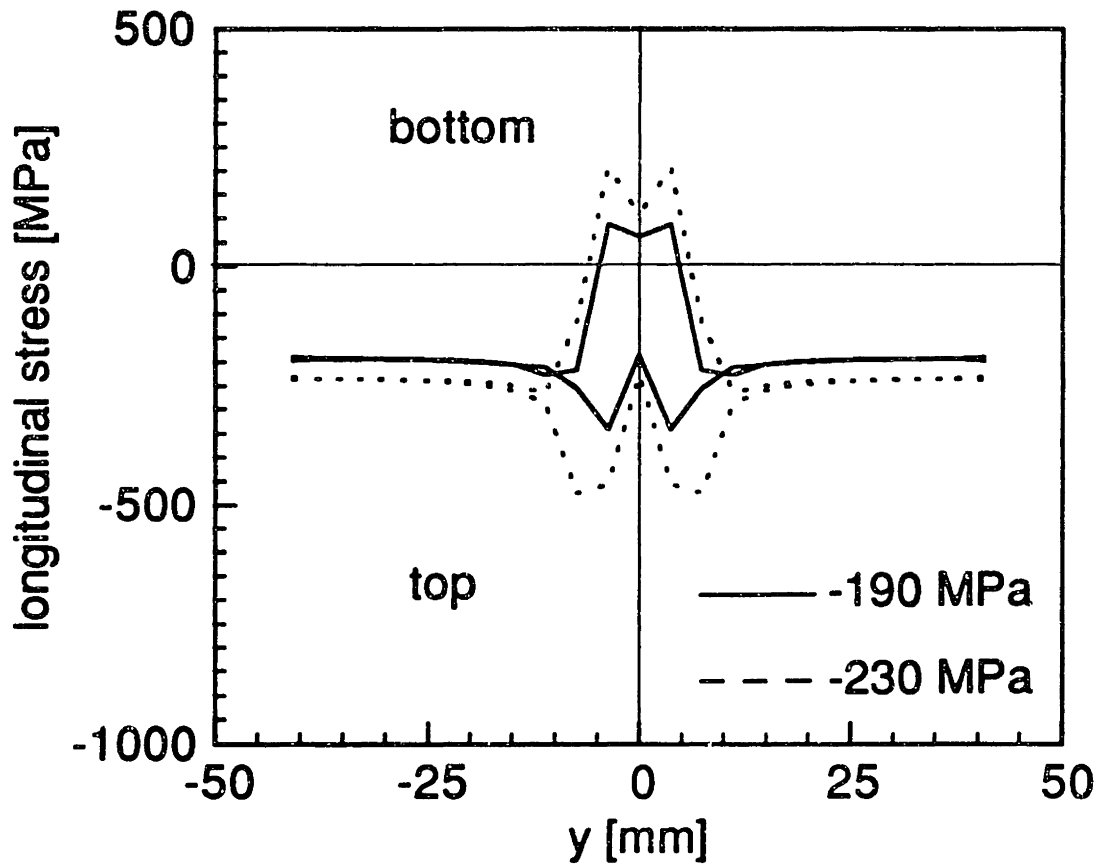


Figure 6.143 Total longitudinal stress distribution at top and bottom surfaces for two applied stress levels in a specimen with (± 45) facesheets and level 2 simulated core damage.

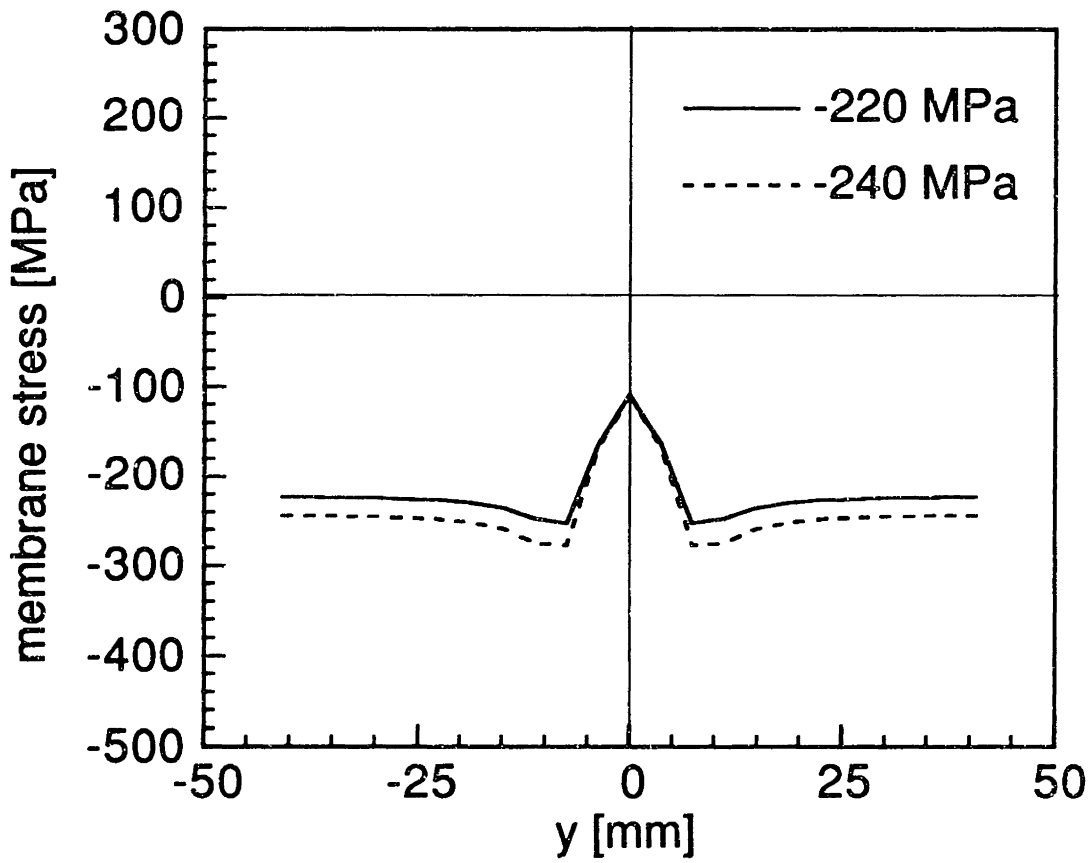


Figure 6.144 Membrane stress distribution at two applied stress levels in a specimen with (± 45) facesheets and level 3 simulated core damage.

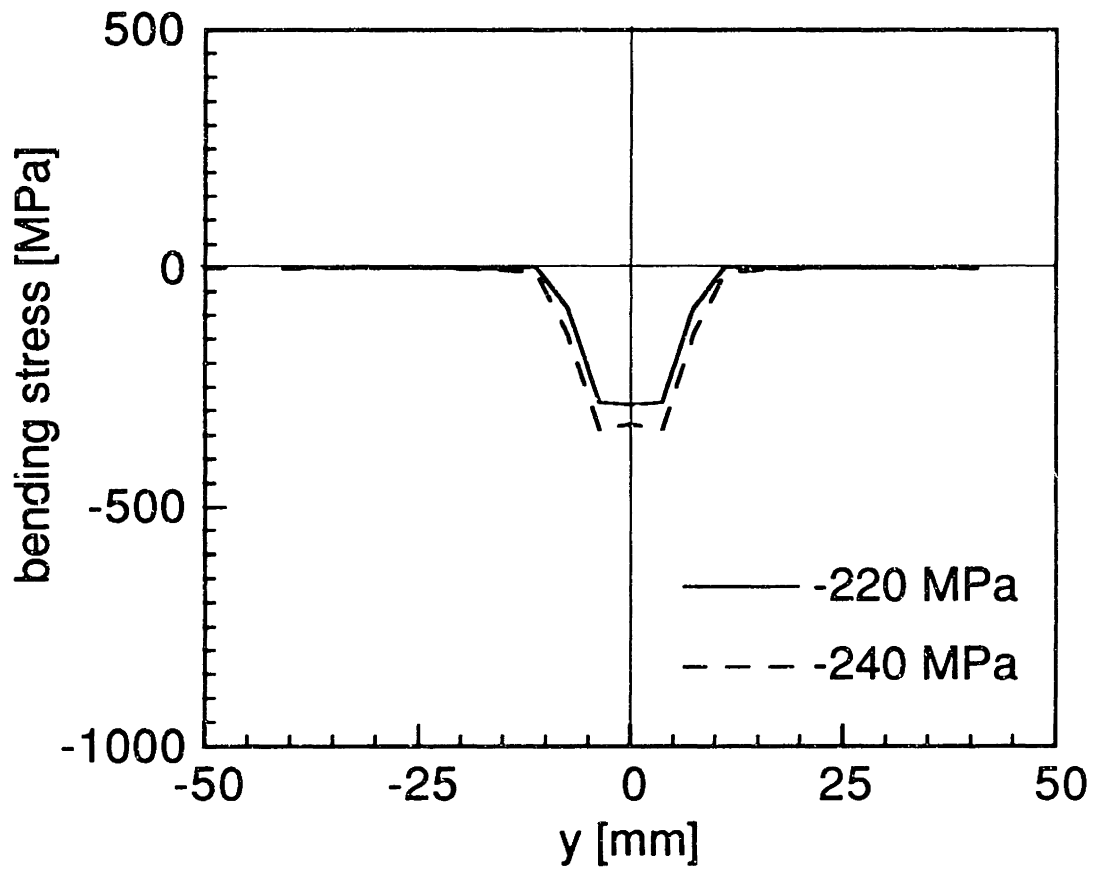


Figure 6.145 Bending stress distribution at top surface for two applied stress levels in a specimen with (± 45) facesheets and level 3 simulated core damage.

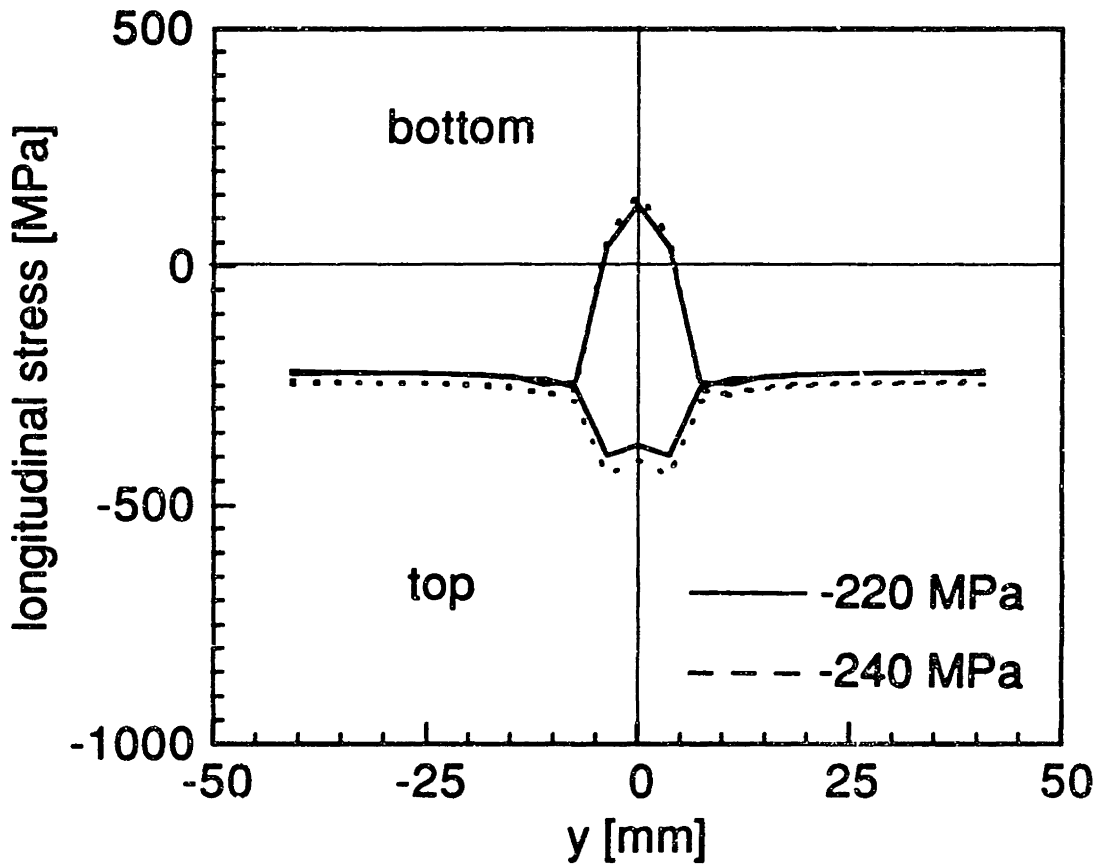


Figure 6.146 Total longitudinal stress distribution at top and bottom surfaces for two applied stress levels in a specimen with (± 45) facesheets and level 3 simulated core damage.

dimple. The maximum membrane stress levels at failure are 300 MPa for damage levels 1 and 2, and 270 MPa for level 3 damage. Hence, at failure, the maximum membrane stress predicted by the dimple propagation model is higher than the average failure stress of the corresponding undamaged specimens (250 MPa). In other words, the dimple propagation model underpredicts the residual strengths if the peak membrane stress is used as the basis for comparison. The corresponding locations of the peak membrane stress are about 7 mm from the center of the dimple for all three damage level. The moiré measurements show that the average width of the dimple just before catastrophic failure in these specimens with (± 45) facesheets and simulated core damage is 20 mm for level 1 damage, 22 mm for level 2 damage, and 44 mm for level 3 damage.

The bending stress distribution at failure shows a bimodal shape for level 1 and level 2 damage. The maximum bending stress at failure is 360 MPa for damage level 1, 330 MPa for level 2, and 280 MPa for damage level 3. The corresponding locations of the peak stress are about 4 mm from the center of the dimple for damage levels 1 and 2, and at the center of the dimple for level 3.

Finally, the longitudinal stress distribution is plotted along the centerline perpendicular to the loading in Figures 6.147 through 6.155 for specimens with (± 45) facesheets and static indentation damage. Once again, stress concentration is observed in the membrane stress distributions near the boundary of the dimple while stress relaxation is seen further within the dimple. The maximum membrane stress levels at failure are 290 MPa for damage levels 1, 270 MPa for damage level 2, and 220 MPa for level 3 damage. The corresponding locations of the peak stress are about 7 mm from the center of the dimple for all three damage levels. The moiré

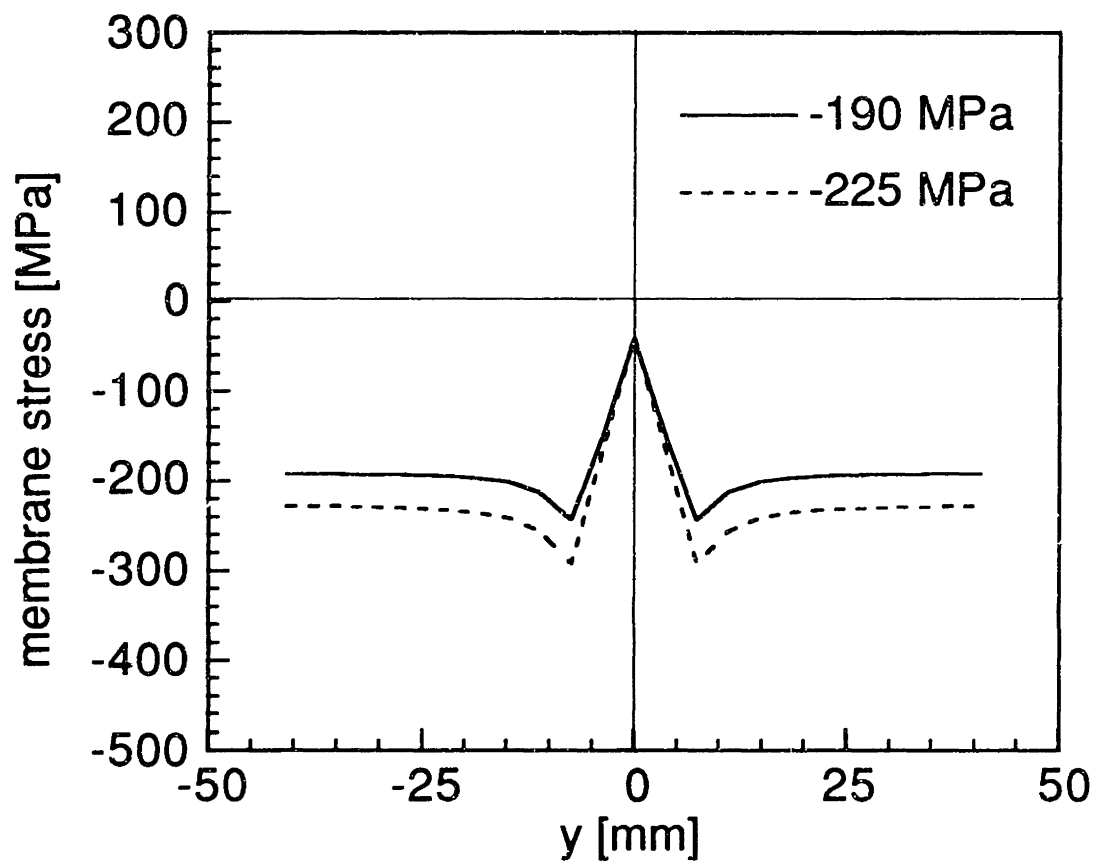


Figure 6.147 Membrane stress distribution at two applied stress levels in a specimen with (± 45) facesheets and level 1 static indentation damage.

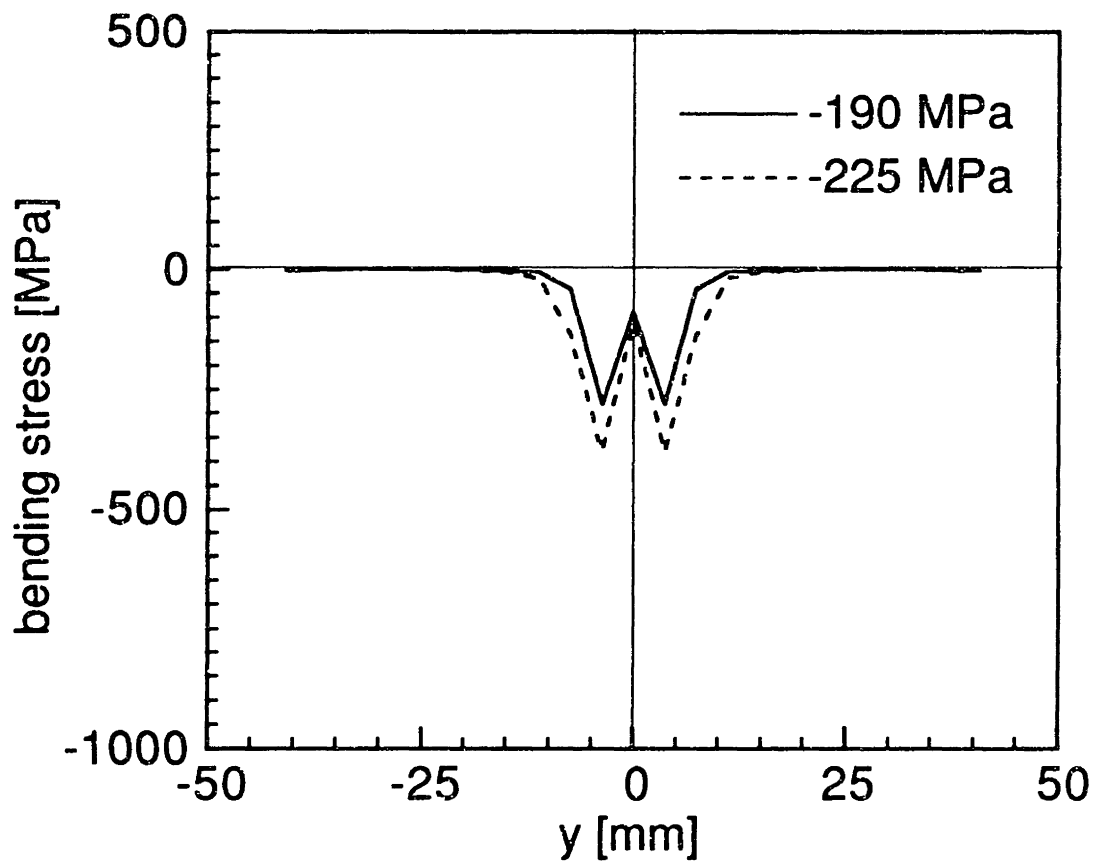


Figure 6.148 Bending stress distribution at top surface for two applied stress levels in a specimen with (± 45) facesheets and level 1 static indentation damage.

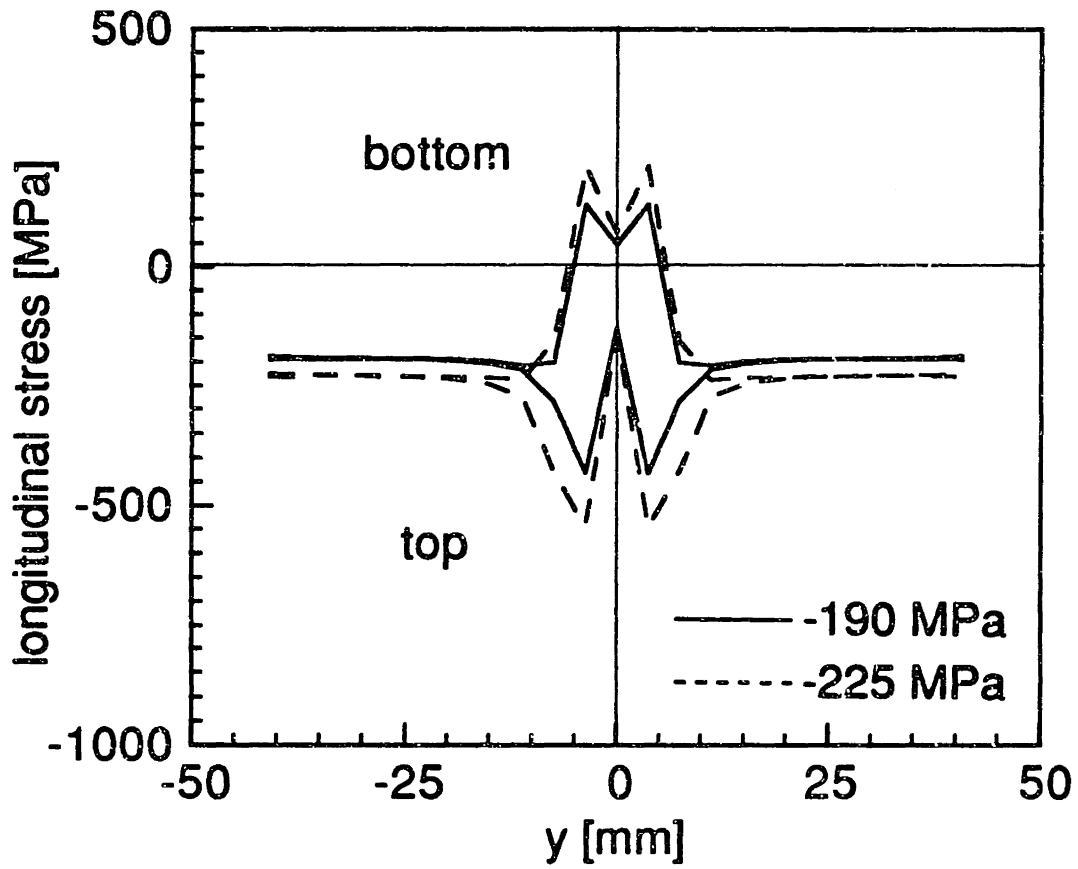


Figure 6.149 Total longitudinal stress distribution at top and bottom surfaces for two applied stress levels in a specimen with (± 45) facesheets and level 1 static indentation damage.

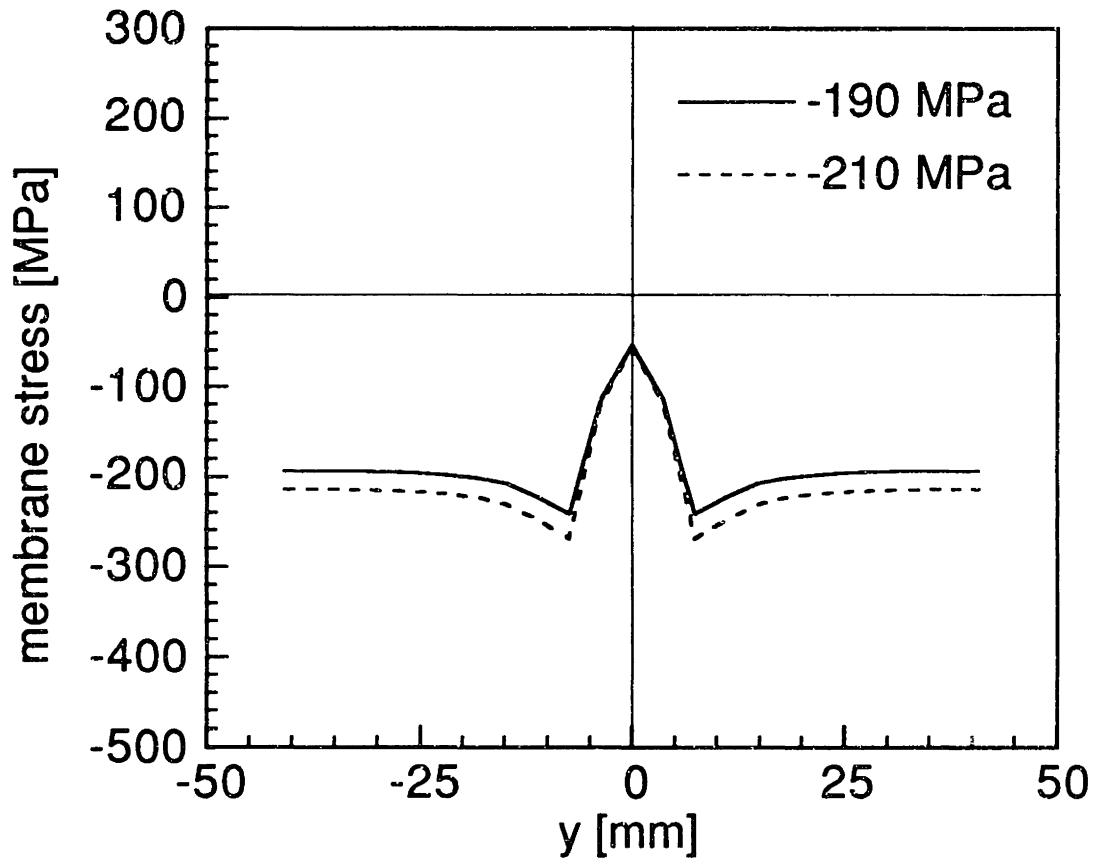


Figure 6.150 Membrane stress distribution at two applied stress levels in a specimen with (± 45) facesheets and level 2 static indentation damage.

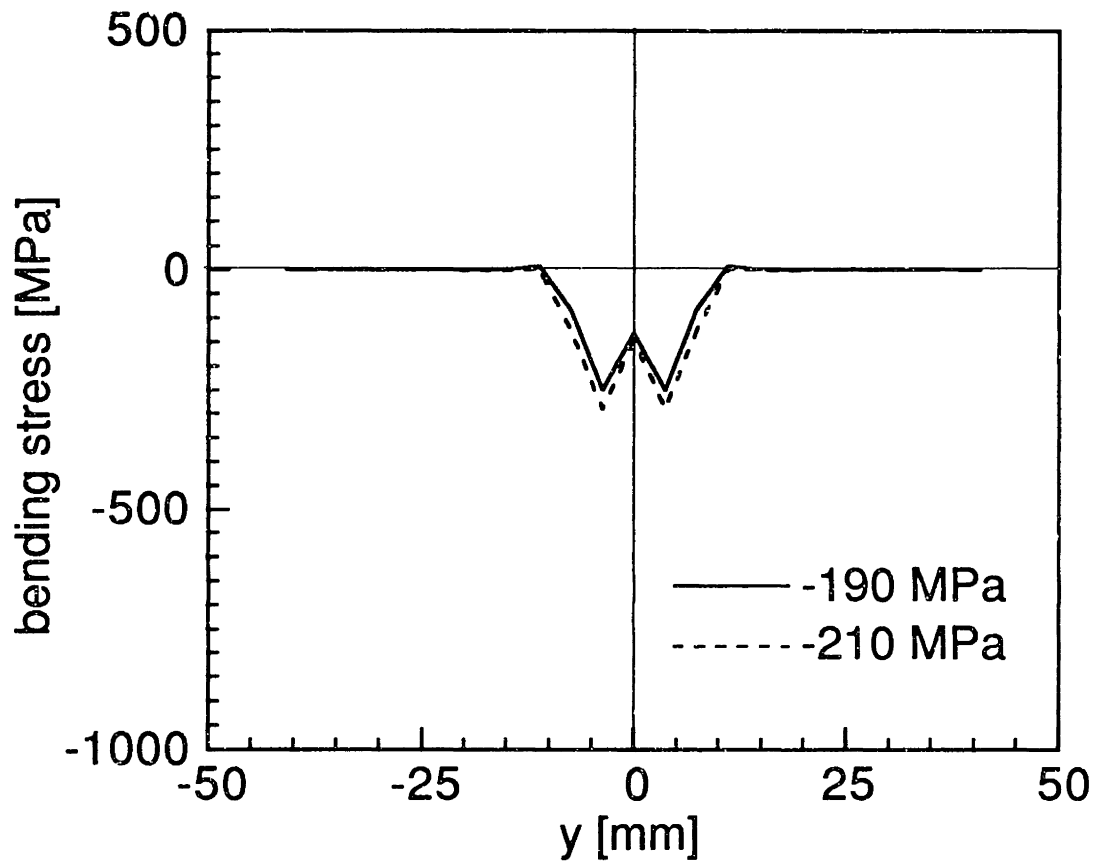


Figure 6.151 Bending stress distribution at top surface for two applied stress levels in a specimen with (± 45) facesheets and level 2 static indentation damage.

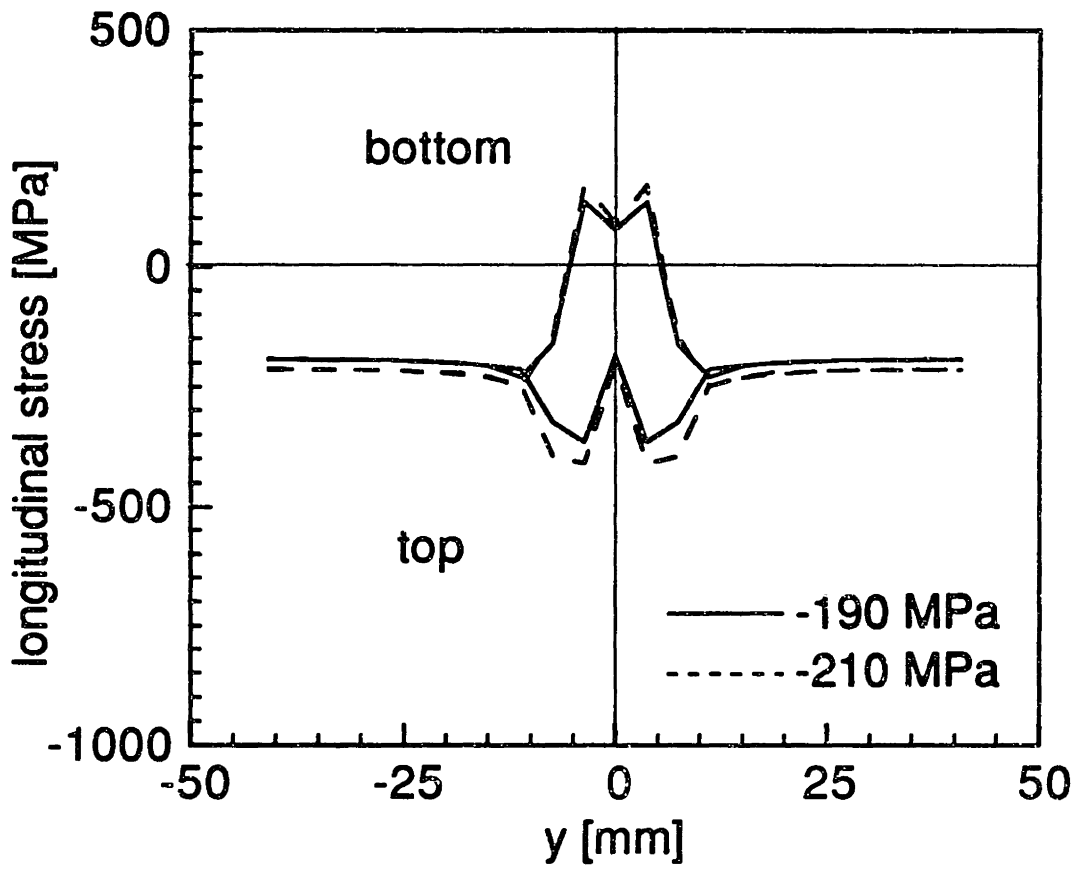


Figure 6.152 Total longitudinal stress distribution at top and bottom surfaces for two applied stress levels in a specimen with (± 45) facesheets and level 2 static indentation damage.

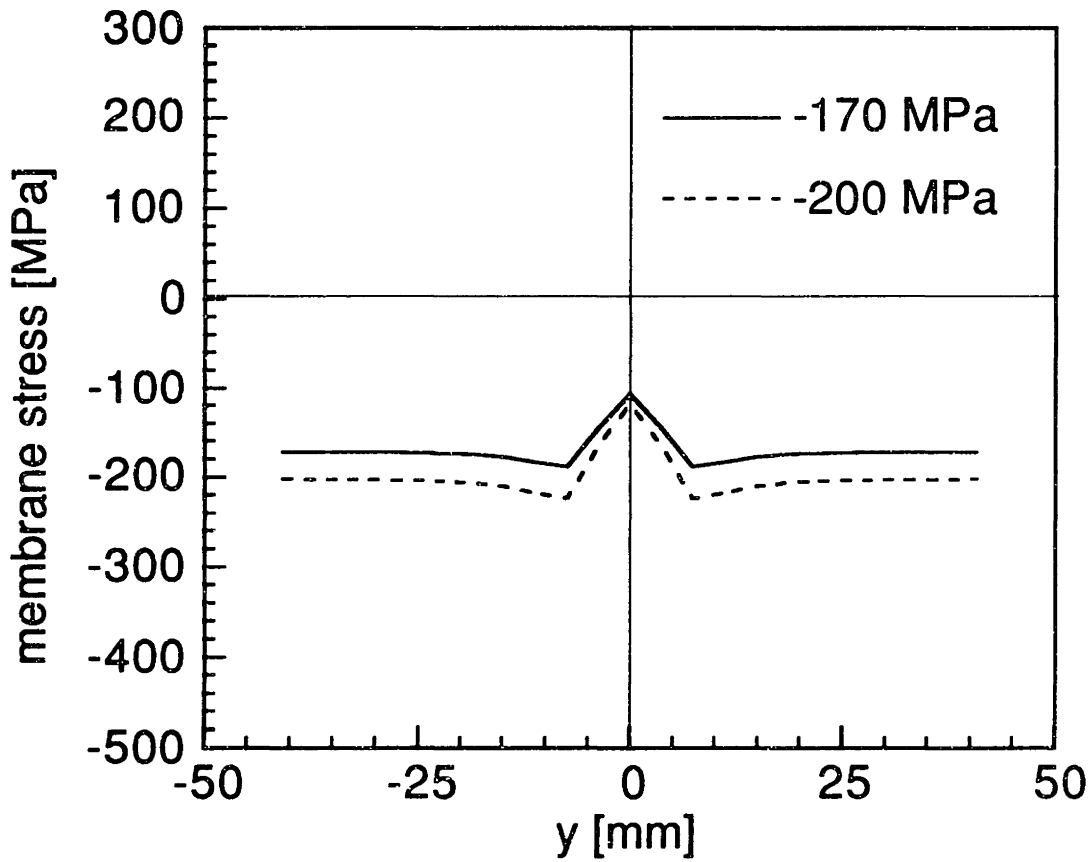


Figure 6.153 Membrane stress distribution at two applied stress levels in a specimen with (± 45) facesheets and level 3 static indentation damage.

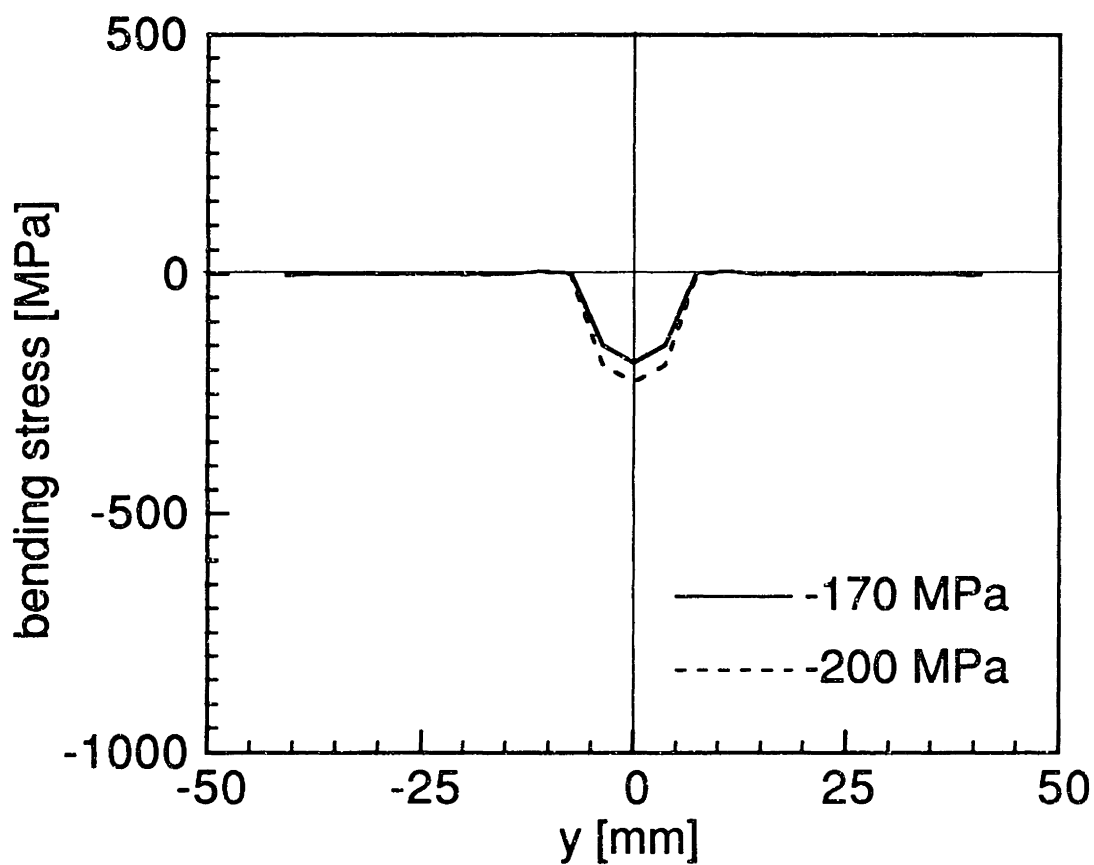


Figure 6.154 Bending stress distribution at top surface for two applied stress levels in a specimen with (± 45) facesheets and level 3 static indentation damage.

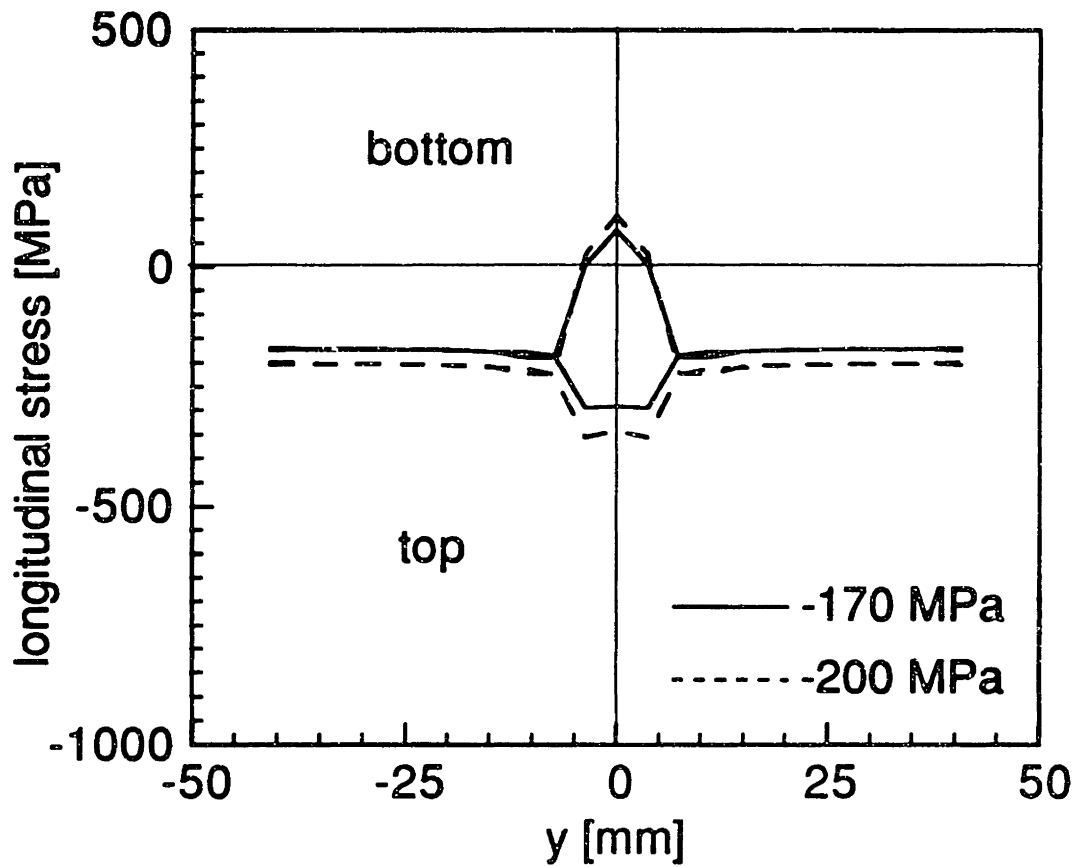


Figure 6.155 Total longitudinal stress distribution at top and bottom surfaces for two applied stress levels in a specimen with (± 45) facesheets and level 3 static indentation damage.

measurements show that the average width of the dimple just before catastrophic failure in these specimens with (± 45) facesheets and static indentation damage is 43 mm for level 1 damage, 44 mm for level 2 damage, and 54 mm for level 3 damage.

The bending stress distribution of these specimens with (± 45) facesheets and static indentation damage at failure shows a bimodal shape for level 1 and level 2 damage. The maximum bending stress at failure is 380 MPa for damage level 1, 290 MPa for level 2, and 230 MPa for damage level 3. The corresponding locations of the peak stress are about 4 mm from the center of the dimple for damage levels 1 and 2, and at the center of the dimple for level 3.

Chapter 7

Discussion

Important findings of the present investigation are discussed in this chapter. Relevant results presented in Chapter 6 are used to provide evidence for the discussion. The discussion is oriented towards assessing the progress made in achieving the four research goals listed in Chapter 3. These research goals are: (i) to characterize the damage in the sandwich panels due to indentation/impact loading, (ii) to characterize failure mechanisms of such damaged panels under uniaxial compression, (iii) to investigate separately the contributions to the failure mechanism and final failure of facesheet damage and core damage, and (iv) to predict the failure mechanism and failure load of such damaged panels. The first research goal is addressed in Section 7.1 where results of the impact resistance part of the present investigation is discussed. The remaining three research goals are addressed in Section 7.2 where results of the damage tolerance part of the investigation is discussed.

7.1 Impact Resistance

Three controlled damage states were created by means of static indentation tests. Damage characterization results of these indented damage states show that they have the desirable characteristics of having different combinations of facesheet damage and core damage. In particular, indentation damage inflicted with the 12.7 mm-diameter indenter has a very localized and deep dimple shape in combination with significant facesheet damage. On the other hand, indentation damage inflicted with the 38.1 mm-diameter indenter has a more spread-out and shallow dimple

shape in combination with virtually no facesheet damage. Such resulting combinations of geometric profile of the dent/dimple and the corresponding amount of facesheet damage are explained as follows. If significant facesheet damage occurs in the indentation process, the facesheet becomes more compliant locally around the point of indentation. The more compliant the facesheet, the less capable it is to rebound to the originally flat position. Hence, the deepest dent is accompanied by the most extensive facesheet damage in the case of the 12.7 mm-diameter indenter while the shallowest dent is accompanied by the least facesheet damage in the case of the 38.1 mm-diameter indenter. As shown in the results of the damage tolerance study, these different damage states are instrumental in isolating the effects of core damage and facesheet damage on the failure mechanism and on the residual strength of indented/impacted thin-faced sandwich panels.

Besides having different combinations of facesheet damage and core damage, the three different damage states have detectability ranges from easily visible (Level 1) to barely visible (Level 3). However, such categorization of damage is not indicative of the extent (depth and width) of the core damage in the specimens since the core was crushed to the same depth (3 mm) for all three damage levels. Moreover, the barely visible damage state (Level 3) can cause equally significant or greater reduction in the compressive strength of the sandwich panels as the easily visible damage state (Level 1); this is demonstrated in the damage tolerance part of the investigation. The use of visibility as an indicator of the amount of damage is, therefore, questionable in the context of damage tolerance.

The indenter diameter is another possible metric to be used in regard to the impact/indentation damage. The dimensions of the dimple perpendicular to the loading direction is plotted against the indenter

diameter in Figure 7.1 for specimens with (0/90) facesheets and static indentation damage. Also included in Figure 7.1 is a straight line of unit slope. It can be seen from the figure that the relative increase in the indenter diameter for the three damage levels is larger than the corresponding increase in the in-plane dimension of the dimple. In other words, the in-plane dimension of the dimple does not increase proportionately with the diameter of the indenter. If the dimension of the dimple is measured at the depth (0.181 mm) of the first-order fringe, the difference among the three different indenter sizes or damage levels becomes even smaller, as illustrated by the initial measurements in the load-y plots shown in Chapter 6 (Figures 6.76 and 6.95). Also, the subsequent propagation of the dimple as measured at the depth of the first-order fringe can be very similar for the different damage levels. Thus, the use of indenter diameter as a metric in damage tolerance studies should be exercised with caution.

The special manufacturing procedures described in Section 5.3.3, for specimens with simulated core damage and those with simulated facesheet damage are mostly proven successful. For example, specimens with simulated core damage had dimples that closely resemble the dimple shapes in corresponding indented specimens as verified by the dial gage measurements of the profiles. Also, these specimens with simulated core damage show no sign of any facesheet damage and, hence, succeed in isolating the core damage observed in the indented specimens. However, the core damage in specimens with simulated core damage is more localized than in the corresponding indented specimens. This is due to the different methods by which the core damage was introduced in these two types of specimens. In the indented specimens, the core was crushed by pressure of

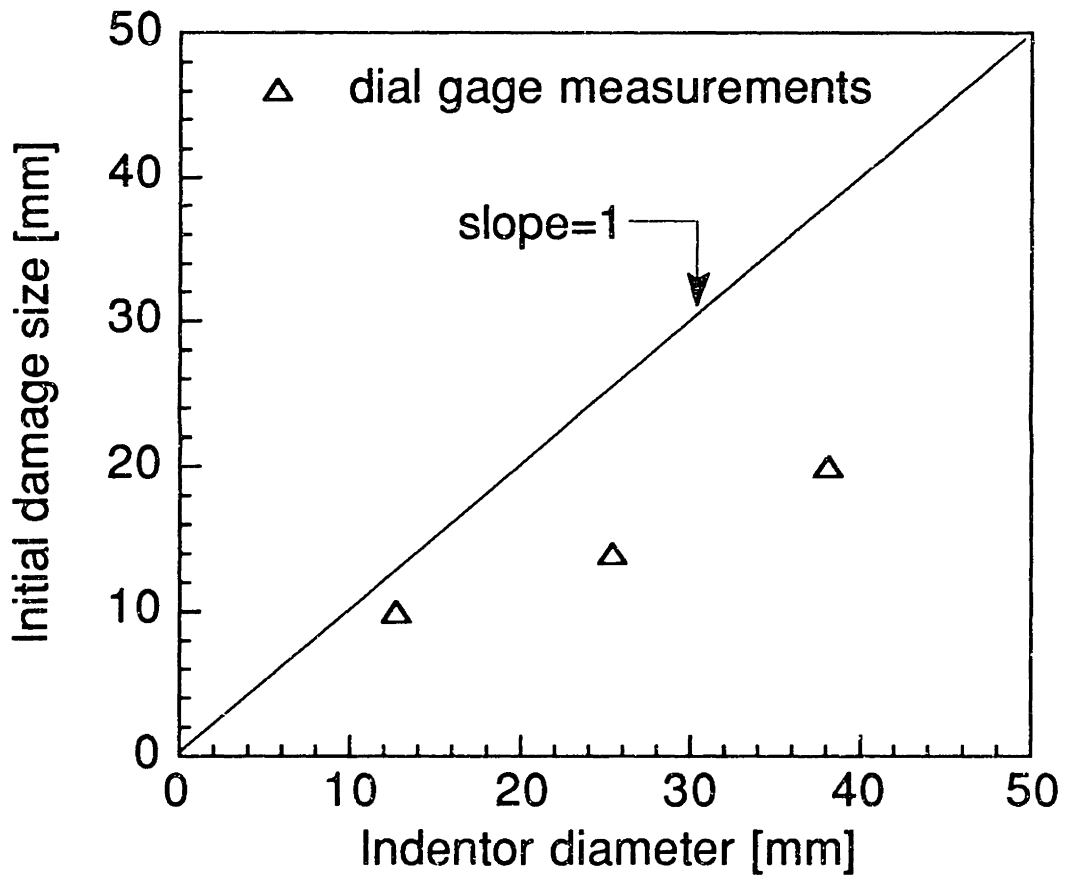


Figure 7.1 Initial dimension of the dimple perpendicular to loading direction versus indenter diameter for specimens with (0/90) facesheets and static indentation damage.

the indenter transmitted via the facesheet while in the specimens with simulated core damage, the core was crushed by pressure of the indenter transmitted via the double-sided tape before the core was bonded to the facesheets (see Section 5.3.3). The graphite/epoxy facesheet induces a more uniformly-distributed pressure than the double-sided tape which has a much lower bending stiffness than the facesheet.

Another less than ideal situation occurred for specimens with simulated facesheet damage which were designed to simulate the facesheet damage pattern of the indented specimens. Ideally, three levels of simulated facesheet damage should be used to model separately the facesheet damage in the three levels of indentation damage. However, the facesheet damage pattern in level 2 indentation damage is not well defined while that in level 3 indentation damage was barely detectable. Hence, only the facesheet damage pattern inflicted with the 12.7 mm-diameter indenter was possible to simulate physically. These specimens with level 1 simulated facesheet damage had slits which are a fairly good representation of the facesheet damage in specimens indented with the 12.7 mm-diameter indenter. The lengths of the slits were close (within 4%) to the nominal length (10 mm) of the cross-shaped fracture pattern measured in the indented specimens. The slits were cut along boundaries between two adjacent tows, consistent with the location of the fiber damage observed in the indented specimen. However, the slits were wider than the cross-shaped fractures in the indented panels due to the finite thickness of the cutting wheel (0.6 mm). This is not considered as a significant limitation on the effectiveness of these specimens with simulated facesheet damage in modelling the facesheet damage in the corresponding indented specimens since earlier work on notched strength of composite laminates has shown

that the critical characteristic is the dimension of the notch perpendicular to the loading and not the actual shape of the notch [83]. However, since the slits were cut through the thickness of the facesheet, the two plies of the facesheet have essentially the same amount of fiber damage while the bottom ply of an indented facesheet has more fiber damage than the top ply. Such a "gradient" in damage through the thickness of the facesheet is due to the bending stress induced by the indentation. The distribution of damage through the thickness in monolithic composite laminate has been shown to be dependent on the thickness of the laminates [100]. Through-thickness variations of damage distribution are also observed in the facesheets of sandwich panels with different facesheet thicknesses [58]. The effect of the through-thickness damage distribution on the failure mechanism of these damaged sandwich panels needs to be further investigated, possibly by testing sandwich panels with thicker facesheets.

Thus far, the damage types in the sandwich panels have been categorized as either facesheet damage and core damage. The initial out-of-plane deformation, i.e. the dent/dimple, has been associated with the core damage. As later discussion illustrates, the categorization by facesheet damage and core damage is not sufficient to explain the failure mechanism of these sandwich panels. A more thorough categorization is herein proposed which consists of three different damage types: material facesheet damage, geometric facesheet damage, and core damage. Material facesheet damage includes the more "traditional" facesheet damage such as fiber damage, delaminations, and matrix cracks, while geometric facesheet damage refers to the (initial) out-of-plane deformation, i.e. the shape of the dimple/dent. Core damage includes mainly buckled/crushed cell walls. Under this new categorization, specimens with simulated core damage

actually also contain geometric facesheet damage while specimens with simulated facesheet damage contain only material facesheet damage.

In summary, static indentation tests were successfully used to create three damage states with the desirable combinations of facesheet damage and core damage. These damage states were thoroughly examined, including three dimensional characterization of the dent shape and extent of core damage. The simulated damage types are capable of simulating separately the important characteristics of the facesheet damage and the core damage observed in the indented panels.

7.2 Damage Tolerance

The dimple propagation model is assessed qualitatively in Section 7.2.1 while quantitative predictions of the model are compared with the corresponding experimental results in Sections 7.2.2 and 7.2.3. The effects of the facesheet damage and core damage on the failure mechanism and the final failure of the damaged sandwich panels are discussed in Sections 7.2.2 and 7.2.3, respectively.

7.2.1 Assessment of the dimple propagation model

The analytical results alone show that the dimple propagation model can qualitatively simulate the propagation of the dimple which is mostly perpendicular to the loading direction. The model predicts a redistribution of longitudinal stress around the dimple resulting in stress concentration near the edges of the dimple. High compressive through-thickness stresses at the interface between the core and the facesheet are also predicted at the edges of the dimple along the centerline perpendicular to the loading direction. These results are consistent with those predicted with the model by Minguet [70]. The combination of in-plane load redistribution and the

initial out-of-plane deformation, i.e. geometric facesheet damage, causes local bending within the dimple. This local bending, in turn, triggers the progressive crushing of the core and, hence, the propagation of the dimple perpendicular to the loading direction. The quantitative comparison between the predicted dimple propagation and the corresponding experimental data is discussed in Section 7.2.2.

The load redistribution around the dimple gives rise to high longitudinal stress along the centerline through the center of the dimple and perpendicular to the loading direction. The presence of these high longitudinal stresses is consistent with the fact that most specimens with simulated core damage and static indentation damage failed through the center of the dimple and perpendicular to the loading direction. Quantitative failure predictions based on the longitudinal stress distributions are discussed in Section 7.2.2.

There are a few implicit assumptions in the dimple propagation model for which justification is provided by some of the experimental observations. The dimple propagation ignores the global bending of the sandwich panel by modelling only the damaged facesheet. The strain gage data of the back-to-back far-field gages verifies that global bending was indeed negligible for all specimens tested under uniaxial compression. Global bending, however, might be an issue for sandwich panels with thinner cores. The effect of such global bending on the failure mechanism and the final failure of sandwich panels needs to be examined. Also, the model assumes that there is an initial region of crushed core which provides zero supporting reaction to the facesheet. The load-indentation curves of the specimens indicate that during unloading the indentation load reaches zero before the indented facesheet rebounds to the corresponding depths of

the permanent dimple. Lastly, the consistent values for the modulus of the sandwich specimens obtained from the far-field gages indicates that the various damage types did not affect the far-field stress/strain. This experimental observation justifies the application of a uniform far-field applied stress in the dimple propagation model.

7.2.2 Dimple propagation

The previously identified failure mechanism of dimple propagation in impact-damaged thin-faced sandwich panels was successfully quantified by the shadow moiré method. The major limitation of the current moiré setup is the loss of accuracy when the surface slope of the dimple becomes too small or too big. When the surface slope is too small (e.g. for most cases herein with level 3 damage where the resulting dimples are very shallow), only one or two fringes were observed. These fringes are usually very wide and possess fuzzy boundaries. These factors make it very difficult, sometimes impossible, to obtain in-plane measurements of the locations of the fringes. On the other hand, when the surface slope is too big (e.g. near the center of the dimple in specimens with level 1 damage at high applied stress levels), the fringes become so close to one another that it is not possible to resolve them visually.

Comparing the failure mechanism of specimens with simulated facesheet damage and that of specimens with static indentation damage indicates that material facesheet damage alone did not cause dimple propagation; the permanent dent, i.e. geometric facesheet damage, and initial core damage are necessary to induce the dimple propagation observed in indented/impacted sandwich panels. However, the dent shape and core damage are not the only factors that affect the dimple propagation as shown

by the quantitative difference in the failure mechanism between specimens with static indentation damage and those with simulated core damage. The quantitative difference is reflected in the rate of propagation with respect to the applied stress. The plots of applied stress against the dimension of the dimple perpendicular to the loading (load-y plots) show a greater slope for specimens with simulated core damage, indicating less propagation per unit increase in applied stress level. Also the propagation became unstable (i.e. the slope of the load-y plots approaches zero) at a lower applied stress level for specimens with static indentation damage than for specimens with simulated core damage. This difference in the dimple propagation process between specimens with static indentation damage and those with simulated core damage reduces as the damage goes from level 1 to level 3 for specimens with (0/90) facesheets. This is clearly a consequence of the material facesheet damage being present in the specimens with static indentation damage; level 1 static indentation damage has the most extensive material facesheet damage while level 3 static indentation damage has virtually no material facesheet damage.

The effect of the material facesheet damage is further demonstrated by the fact that the predictions of the dimple propagation model match the experimental data well for specimens with (0/90) facesheets and simulated core damage but underpredicts the dimple propagation in specimens with (0/90) facesheets and indentation damage since the dimple propagation model does not include any material facesheet damage. It is hypothesized that the material facesheet damage around the point of indentation causes a local reduction of stiffness in the indented facesheet, which in turn promotes further redistribution of longitudinal stress around the dimple. In the presence of the dimple, such a redistribution of longitudinal stress provides

further momentum for local bending within the dimple and, hence, for dimple propagation. The effect of facesheet damage on the local stiffness of the indented facesheet was also used in Section 7.1 to explain the rebounding of the indented facesheets.

For specimens with (± 45) facesheets, the dimple propagation model underpredicts the dimple propagation of both the indented specimens and those with simulated core damage. While the discrepancy in the case of indented specimens may be attributable to the presence of material facesheet damage in the indented specimens, the discrepancy in the case of specimens with simulated core damage appears puzzling since the model works well with specimens with simulated core damage and (0/90) facesheets. This originally unexpected observation is explained by the nonlinear stress-strain response of the specimens with (± 45) facesheets. All the stress-strain data of the specimens with (± 45) facesheets show a softening characteristic. The resultant shear stress in an undamaged specimen with (± 45) facesheets under uniaxial compression is plotted against the shear strain in Figure 7.2. The tangent shear modulus, defined as the slope of the curve at a given point on the curve, decreases with increasing shear stress. Since the resultant shear stress is half of the applied uniaxial compressive stress, the data imply that the shear modulus of the fabric facesheet decreases with increasing applied stress. If the shear modulus of the facesheet is reduced, different elements of the A-matrix and D-matrix are generated. This change in the input parameters to the dimple propagation model is likely to affect the predictions of the dimple propagation model, as shown in the following example.

The shear modulus at an applied stress of 240 MPa is about 1 MPa (cf. an initial value of 6.27 MPa). The elements of the D-matrix and A-

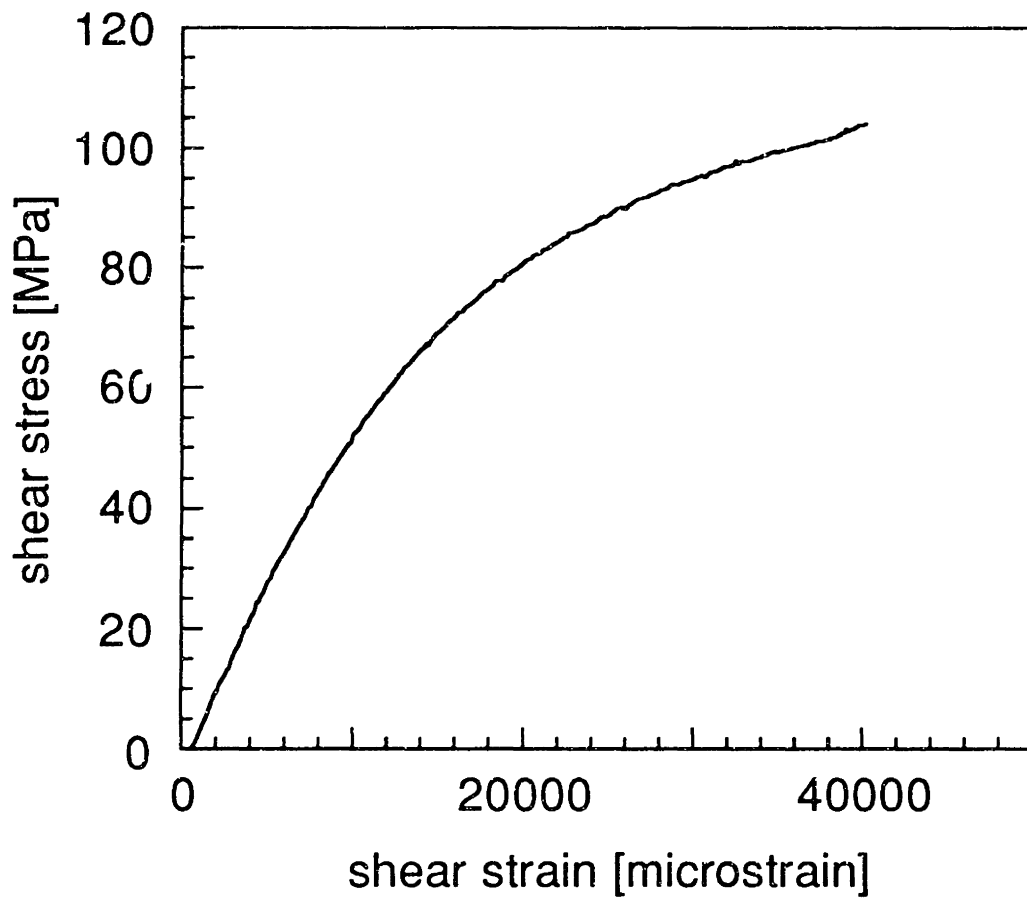


Figure 7.2 Shear stress versus shear strain in an undamaged specimen with (± 45) facesheets loaded under uniaxial compression.

matrix corresponding to this reduced shear modulus are given in Tables 7.1 and 7.2 respectively. The new values of D_{11} and A_{11} represent a reduction of approximately 12% from the old values given in Table 6.7. The prediction of the dimple propagation model with this new set of inputs is compared with the corresponding experimental result as well as with the original prediction in Figure 7.3 for the case of level 3 simulated core damage. It can be seen that with the new set of inputs, the model gives results which are closer to the experimental data. However, the analytical prediction is still not satisfactory. This is likely due to the fact that the local variation of the stress field around the dimple requires a nonuniform adjustment of the shear modulus.

The above calculation demonstrates the effect of global reduction in the stiffness of the facesheet on the dimple propagation process. It is safe to assume that a local reduction in the stiffness of the facesheet would have a similar effect on the dimple propagation process. Hence, the fundamental effect of facesheet damage in specimens with (0/90) facesheets and indentation damage is the same as that of nonlinear stress-strain behavior in specimens with (± 45) facesheets: the local reduction in the stiffness of the facesheet which causes further redistribution of the longitudinal stress and thereby increases the propensity of the dimple to propagate, as explained earlier. Since the dimple propagation model does not account for this local reduction in the stiffness of the facesheet, it underpredicts the dimple propagation for all specimens with (± 45) facesheets and for specimens with (0/90) facesheets and static indentation damage. Implementation of local reduction in facesheet stiffness is, thus, necessary for better analytical predictions and further study of this phenomenon is warranted.

Table 7.1 Elements of D-matrix of a (± 45) facesheet with a reduced shear modulus of 1.0 GPa

Matrix element	Value [Nm]
D_{11}	0.1381
D_{22}	0.1381
D_{66}	0.0994
D_{12}	0.1309
D_{16}	0.0
D_{26}	0.0

Table 7.2 Elements of A-matrix of a (± 45) facesheet with a reduced shear modulus of 1.0 GPa

Matrix element	Value [MNm^{-1}]
A_{11}	13.53
A_{22}	13.53
A_{66}	9.74
A_{12}	12.83
A_{16}	0.0
A_{26}	0.0

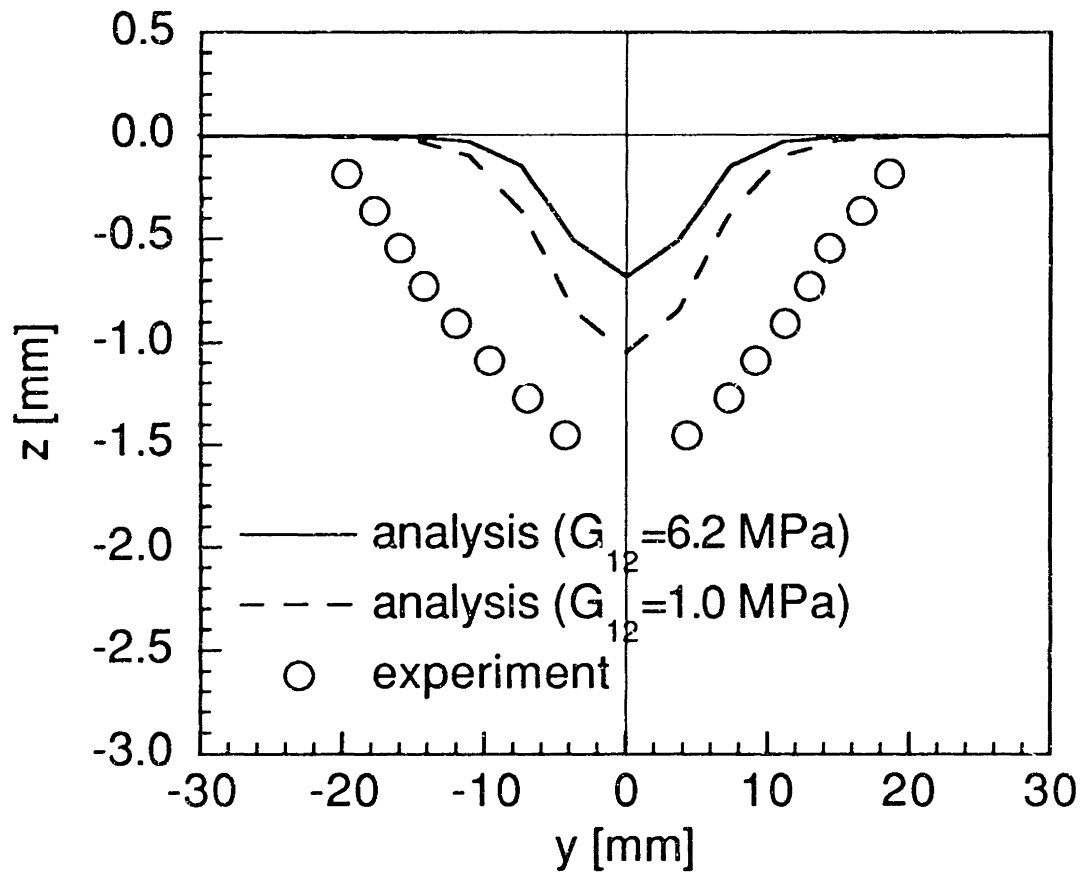


Figure 7.3 Experimental and predicted dimple profiles along centerline perpendicular to loading direction at an applied stress level of -240 MPa for a specimen with (± 45) and level 3 simulated core damage; the predicted results are based on nominal (6.2 GPa) and reduced (1.0 GPa) values of the shear modulus.

7.2.3 Final failure

The discussion of the dimple propagation in the previous section covers the failure mechanism up to the point of catastrophic failure. Since the catastrophic failure happens within one video frame, the only experimental information about the final failure of these specimens is obtained via post-mortem inspection. The depression revealed by post-mortem inspection of specimens with static indentation damage and those with simulated core damage is a measure of the final in-plane extent of the dimple propagation. Experimental data suggest that this final extent of the dimple propagation differs for the two different layups. The specimens with (± 45) facesheets tend to propagate completely to the edges more often than specimens with (0/90) facesheets. For the specimens with (± 45) facesheets, the dimple propagated completely to the edges in the cases with all three levels of static indentation damage, and in the case with level 3 simulated core damage. For specimens with (0/90) facesheets, only those with level 3 simulated core damage propagated completely to the edges. This difference in the final extent of the dimple propagation between the two layups is likely related to the material nonlinearity of the (± 45) facesheets which, as explained earlier, causes local reduction in the stiffness of these facesheets resulting in more severe redistribution of longitudinal stress around the dimple and, hence, further dimple propagation. However, the more significant implication of the results of the post-mortem inspection is the possible presence of finite width effects in some of the specimens tested.

Finite width effects have traditionally been related to testing of notched specimens with a finite dimension perpendicular to the loading direction. Although the dimple due to indentation/impact is different from a

notch or an open hole, it has a similar effect of redirecting the load path around itself and hence giving rise to stress concentrations. The presence of stress concentrations may interact with the free edges of the specimen and, thus, the rate of propagation and the residual strength of the damaged specimens may vary with the specimen width. It is unclear, with the available experimental data from the present investigation, how the residual strength of the specimens is affected by the finite width of the specimen. From the analytical predictions, which have accounted for the finite width of the specimens in determining the stress distributions, if the far-field longitudinal stress is recovered beyond the extent of the dimple perpendicular to the loading at the failure stress, it is safe to assume that the residual strength is not affected by the finite width of the specimen, as in specimens with (0/90) facesheets and level 1 simulated core damage. However, if the model predicts a dimple propagation completely to the edges of the specimen at the failure stress, further investigation is required to assess the effects of finite width. One option is to increase the in-plane dimensions of the model and check if the results are affected by such an increase. However, as explained in Chapter 4, that requires more modes to achieve a converged solution. Another option is to perform experiments on specimens with different widths and compare their residual strengths.

Specimens with simulated facesheet damage showed a very different failure mechanism from that of specimens with static indentation; no out-of-plane deformation was observed in specimens with simulated facesheet damage for both facesheet layups. For specimens with (0/90) facesheets, this results in similar failure modes between specimens with static indentation damage and those with simulated facesheet damage, both of which consist of an across-width fracture. For specimens with (± 45)

facesheets, however, the two different failure mechanisms lead to very different failure modes in specimens with static indentation damage and those with simulated facesheet damage. The former exhibits straight-line fracture within the extent of the dimple propagation while the latter shows a fracture pattern at 45° angles. The case of specimens with (± 45) facesheets illustrates the significant influence of failure mechanisms on the final failure modes. The local bending within the dimple during propagation alters the stress state in the facesheet and creates high longitudinal stress to cause failure.

The importance of understanding the failure mechanism of these damaged sandwich specimens is further verified by comparing the residual strengths of specimens with simulated facesheet damage with those with static indentation damage. As mentioned earlier, material facesheet damage alone does not induce the dimple propagation as specimens with simulated facesheet damage did not have the same failure mechanism as specimens with static indentation damage. However, despite the very different failure mechanisms, specimens with simulated facesheet damage have approximately the same failure stress as those with level 1 static indentation damage. Such an observation may explain why some researchers have had some success in correlating residual strength of impact-damaged sandwich panels with analytical models that only account for facesheet damage. Material facesheet damage may be the critical in determining the residual strength of specimens with level 1 static indentation damage. Models like that by Mar and Lin may be sufficient to correlate this residual strength on an engineering basis. However, such models can predict nonconservative residual strength for specimens with other damage states, as for level 2 and level 3 static indentation damage in

the current work. This argument is further substantiated by the simple calculations in the next paragraph.

If the data for level 1 static indentation damage in specimens with (0/90) facesheets are used to evaluate the composite fracture parameter, H_c , in the Mar-Lin correlation, a value of $535 \text{ MPamm}^{-0.28}$ is obtained. If this value of H_c is used to correlate the residual strength of specimens with level 2 static indentation damage, the value of 341 MPa is obtained, compared to the experimental value of 264 MPa. For specimens with level 3 static indentation damage, the material facesheet damage is so small (fiber damage within one tow) that these specimens should have the same strength of 403 MPa as the undamaged specimens, compared to the experimental value of 265 MPa. This is because the damage width parameter, $2a$, for level 3 indentation damage is smaller than the "critical damage size". The critical damage size is defined as the value of $2a$ at which the Mar-Lin correlation curve intersects with the horizontal line representing the strength of the undamaged specimens [95]. Hence, the residual strength of these panels with level 2 and level 3 indentation damage are significantly overestimated. Different correlation parameters are clearly required for different indenter sizes. More importantly, models like the Mar-Lin correlation should only be used on data that are representative of the failure mechanism upon which the model is based on. In the case of the Mar-Lin correlation, only the material facesheet damage is accounted for while the geometric facesheet damage is completely ignored.

For (0/90) and (± 45) facesheets alike, the strength of specimens with static indentation damage are always lower than those of the corresponding specimens with simulated core damage. This is most likely due to the

presence of facesheet damage which reduces the local stiffness. As explained earlier, this local reduction in facesheet stiffness causes more severe load redistribution, local bending, and hence further dimple propagation. However, the similarity between the two layups ends at that. For specimens with (0/90) facesheets, the interaction between facesheet damage and core damage plays a role in the residual strengths of specimens with indentation/impact damage. The strength results of specimens with simulated core damage show that the dent shape and the core damage in specimens with level 1 static indentation damage should give the highest residual strength among specimens with static indentation specimens. However, the presence of material facesheet damage in specimens with static indentation damage reduces the residual compressive strength of these specimens (281 MPa) with only core damage closer to the same level as those with level 2 (264 MPa) and level 3 (265 MPa) damage. The largest reduction (79 MPa) with respect to the strength of corresponding specimens with simulated core damage is observed in specimens with level 1 static indentation damage which also have the most extensive material facesheet damage. The corresponding reductions for level 2 and level 3 damage are 51 MPa and 44 MPa, respectively.

The residual strength results of specimens with (± 45) facesheets suggest that the interaction between the facesheet damage and the core damage is less significant in that particular facesheet layup as the failure strengths of all three groups of specimens fall within a fairly narrow band along the strength axis. Such an observation may be related to the notch insensitivity of the facesheet layup shown by other researchers [59, 95] who have shown that the presence of an open hole in (± 45) laminates/facesheets causes a reduction of tensile/compressive strength proportional to the

reduction of the cross-sectional area. It appears that this layout is also insensitive to the presence of other types of damage as encountered in this work.

The membrane stress distributions for specimens with simulated core damage and (0/90) facesheets show stress concentrations near and within the boundary of the dimple. The stress concentrations cause stress to rise to a value close to the strength of the undamaged specimens. Hence, the membrane stress is used to correlate failure in the specimens with simulated core damage as follows. The maximum membrane stress is calculated by the dimple propagation model at an applied stress level slightly below the experimental failure stress. The applied stress level is then increased at 5 MPa increments with the corresponding maximum membrane stress recorded. The maximum membrane stress is plotted against the applied stress level and examined in the next two paragraphs for specimens with (0/90) facesheets.

The maximum membrane stress along the centerline perpendicular to the loading is plotted against the applied stress in Figure 7.4 for specimens with simulated core damage and (0/90) facesheets. The horizontal line representing the strength of undamaged specimens intersects the data for level 1 simulated core damage at about -350 MPa, at about -315 MPa for level 2 simulated core damage, and at about -320 MPa for level 3 simulated core damage. These predictions are consistent with the experimental failure stress for these specimens as given in Table 6.9 which are -360 MPa for level 1 damage, -315 MPa for level 2 damage, and -309 MPa for level 3 damage.

The maximum membrane stress along the centerline perpendicular to the loading is plotted against the applied stress in Figure 7.5 for specimens

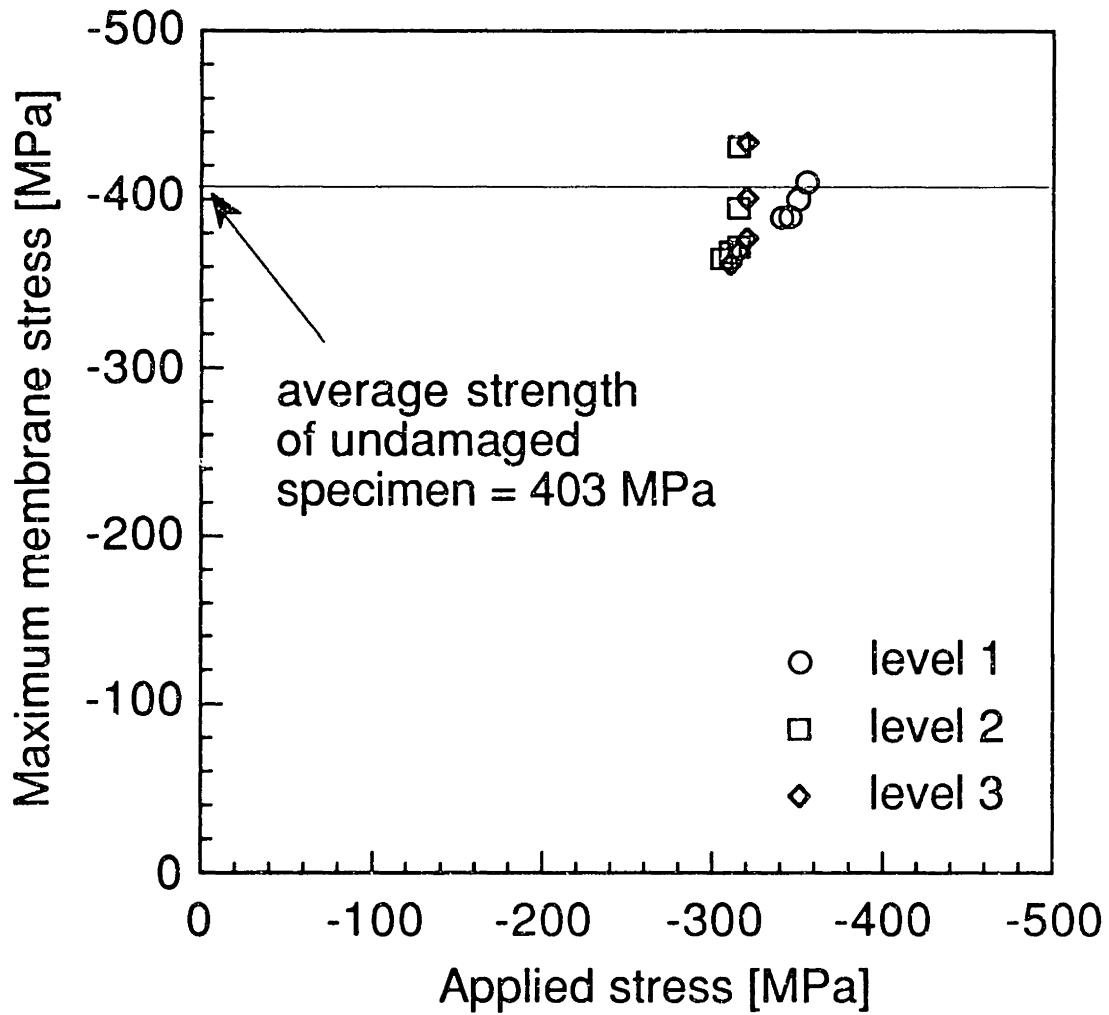


Figure 7.4 Calculated maximum membrane stress versus applied stress for specimens with (0/90) facesheets and various levels of simulated core damage.

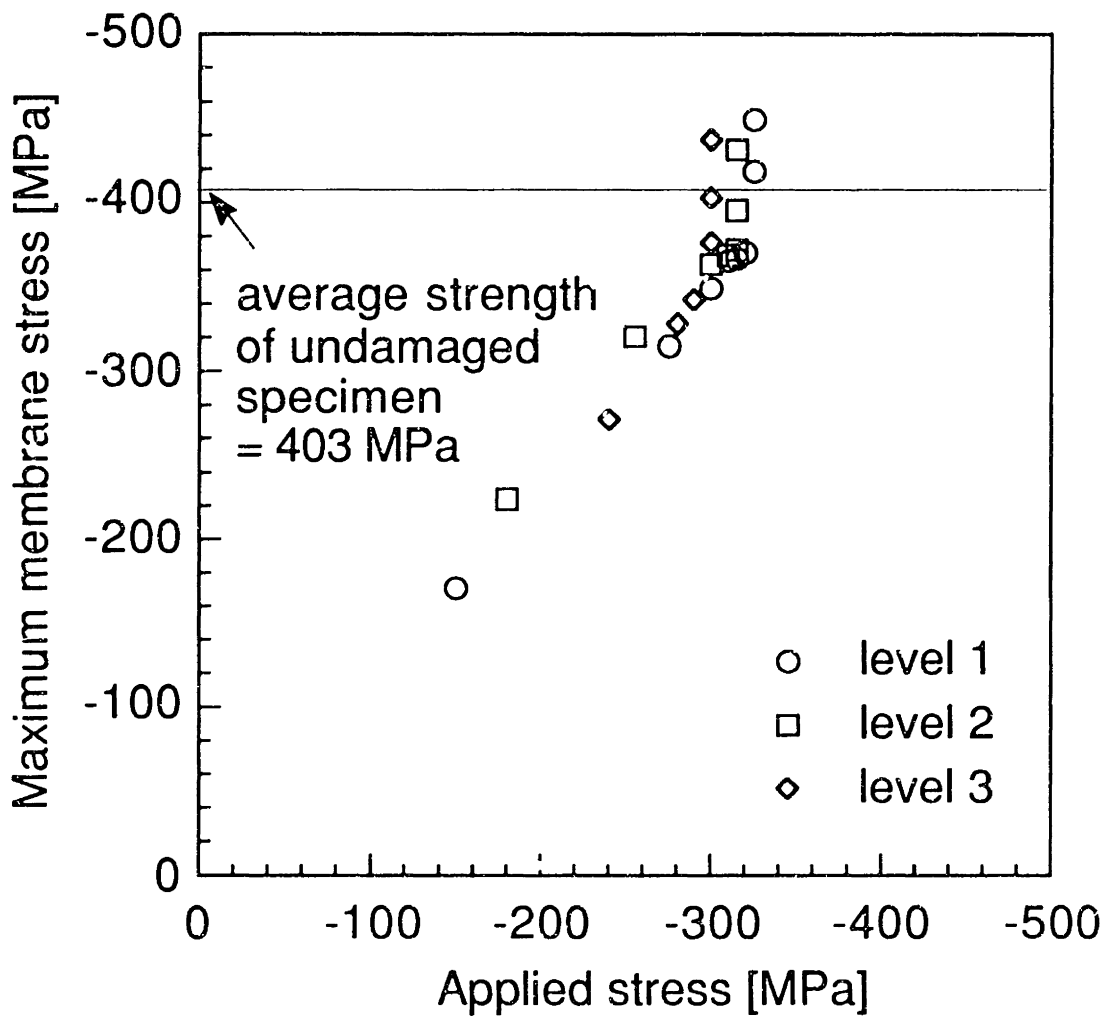


Figure 7.5 Calculated maximum membrane stress versus applied stress for specimens with (0/90) facesheets and various levels of static indentation damage.

with (0/90) facesheets and static indentation damage. The horizontal line representing the strength of undamaged specimens intersects the data for level 1 static indentation damage at about -325 MPa, at about -315 MPa for level 2 static indentation damage, and at about -300 MPa for level 3 static indentation damage. These predictions are higher than the experimental failure stress for these specimens shown in Table 6.9 which are -267 MPa, -264 MPa, and -265 MPa respectively for level 1, level 2, and level 3 damage. The highest difference is for the specimen with level 1 damage which also have the most extensive material facesheet damage.

In correlating the residual strength of damage specimens using the maximum membrane stress, the bending stress has been implicitly ignored. A word of explanation is in order. The bending stress distributions at failure for all specimens have peak values much higher (two to three times as high) than the strength of the corresponding undamaged specimens. It suggests that the specimens would fail at a much lower applied stress level if the bending stress is the critical stress component. Furthermore, the high magnitude of the bending stress indicates that there is a severe stress gradient through the thickness of the facesheet, particularly since these facesheets are relatively thin. Such a stress state is very different from that in the facesheets of a specimen under uniaxial compression. Since the failure strengths of the undamaged specimens are obtained under uniaxial compression where there is little/no stress gradient through the thickness, comparing the predicted peak bending stress within the dimple with these failure strengths of the undamaged specimen might not be appropriate. In general, researchers have not had much success in applying pointwise failure criteria in regions where high stress gradients, either in-plane or through-thickness, exist. More work needs to be done on understanding the

implications of these high stress gradients in the context of failure prediction.

The discussion on the dimple evolution of (± 45) has indicated the significant effect of material nonlinearity on the predictions of the dimple propagation. Since such nonlinear effect is not included in the dimple propagation model, it is not fruitful to try to correlate the residual strength of these panels via the same procedures as for specimens with (0/90) facesheets.

In summary, the failure mechanism of impacted/indented sandwich panels with thin (2-ply) facesheets is via the propagation of the initial dent/dimple mostly perpendicular to the loading direction. The propagation of the dimple causes stress concentrations near the edges of the dimple which, in turn, trigger the final failure in the form of catastrophic facesheet fracture. The combination of the initial dimple (i.e. geometric facesheet damage) in the facesheet and core damage is necessary to cause the dimple propagation. The presence of the material facesheet damage causes a local reduction in facesheet stiffness which induces more severe load redistribution around the dimple and, hence, promotes further dimple propagation. Existing analytical models are not sufficient to predict residual strength of impacted/indented specimens in general because they are not able to include both facesheet damage and core damage.

The results of the damage tolerance part of the investigation also bear important implications on the impact damage resistance part. In particular, all the possible damage types, including initial dent shape (i.e. geometric facesheet damage), extent of core damage, and material facesheet damage, affect the failure mechanism and final failure of impacted/indented specimens. Three-dimensional characterization of the geometric facesheet

and core damage should, therefore, be integrated in the impact damage resistance study. Moreover, as mentioned earlier in Section 7.1, visibility alone is not a good metric for damage tolerance studies since barely visible damage can cause equally significant or larger reduction in compressive strength than easily visible damage. Thus, the characterization results on geometric facesheet damage, material facesheet damage, and core damage have to be considered together to provide a full three-dimensional picture of the damage state in order to properly assess damage tolerance.

Chapter 8

Conclusions and Recommendations

The present work was conducted to investigate the impact damage resistance and damage tolerance of thin-faced composite sandwich panels. In particular, the research goals were (i) to characterize the damage in the sandwich panels due to indentation/impact loading, (ii) to characterize failure mechanisms of such damaged panels under uniaxial compression, (iii) to investigate separately the contributions of facesheet damage and core damage to the failure mechanism and final failure of such damaged panels, and (iv) to predict the failure mechanism and failure load of such damaged panels. In this chapter, conclusions are drawn from the findings of the present investigation and directions for future work are recommended.

8.1 Conclusions

The discussion presented in Chapter 7 leads to the following conclusions from the present work:

1. Damage types in indented/impacted sandwich panels are categorized as: geometric facesheet damage, material facesheet damage, and core damage. Geometric facesheet damage refers to the three-dimensional shape of the permanent dent/dimple in the indented/impacted facesheet. Material facesheet damage refers to the "traditional" damage types in the facesheet, e.g. delaminations, fiber breakage, and matrix cracks, while core damage consists mainly of crushed/buckled cell wall.
2. For a given indentation depth, indentors with different diameters induce very different damage states in thin-faced sandwich panels.

Indentors with smaller diameters tend to leave a localized and deep permanent dent with significant material facesheet damage while indentors with larger diameters tend to cause a spread-out and shallow permanent dent with little or no material facesheet damage.

3. Visibility of surface damage is not a good metric of damage for damage tolerance study because barely visible damage can cause equally significant or greater reduction in strength as easily visible damage.
4. Damage characterization of impacted/indented sandwich configurations should include, among other parameters, measurements of the three-dimensional shape of the permanent dent/dimple (i.e. geometric facesheet damage) and the extent of the core damage because they both affect the failure mechanism of these damaged panels.
5. The failure mechanism of impacted/indented thin-faced sandwich panels subjected to uniaxial compression is via dimple propagation perpendicular to the loading direction, followed by catastrophic failure via facesheet fracture across the width of the specimens.
6. As verified by the failure mechanism of specimens with simulated facesheet damage, material facesheet damage alone is not sufficient to cause dimple propagation; the combination of core damage and geometric facesheet damage, i.e. dent/dimple, is necessary.
7. The dimple propagation model, adapted from another existing analytical model, indicates that the driving force of such a propagation is the redistribution of the longitudinal stress within the dimple and the presence of eccentricity which causes local bending and, hence, dimple propagation.

8. Specimens with static indentation damage show further dimple propagation than the corresponding specimens with simulated core damage because of the presence of material facesheet damage which reduces the local stiffness of the facesheets and, hence, causes more severe load redistribution and local bending within the dimple.
9. The predicted dimple profiles at various applied stress levels match well with the experimental results for specimens with (0/90) facesheets and simulated core damage.
10. The dimple propagation model underpredicts the dimple propagation in specimens with (0/90) facesheets and static indentation damage as well as specimens with (± 45) facesheets because it does not account for the local reduction of facesheet stiffness caused by material facesheet damage and nonlinear stress-strain behavior. As explained earlier, such local reduction of facesheet stiffness causes more severe load redistribution and local bending within the dimple, thus resulting in further dimple propagation.
11. Post-mortem inspection of failed specimens showed some dimples propagated completely to the edges of the specimens. The stress redistribution around the dimple may interact with the free edges of the specimens, i.e. finite width effects. Such interaction can affect the rate of propagation and failure stress of the specimens. Hence, the residual strengths of the impacted/indented sandwich panels may vary with the width of the panels.
12. The final failure of specimens with static indentation damage and those with simulated core damage is facesheet fracture due to high longitudinal stresses caused by dimple propagation/local bending.

13. The geometric profile of the dimple (i.e. the geometric facesheet damage) and the corresponding core damage under the dimple affect the failure stress of specimens with simulated core damage. Dimples with more localized and deeper profiles fail at higher applied stresses than dimples with more spread-out and shallower profiles because the latter causes more severe load redistribution and, hence, higher stress concentrations.
14. Specimens with different combinations of facesheet damage and core damage can fail at approximately the same applied stress level because the effect of the dent shape (i.e. geometric facesheet damage) and the associated core damage as mentioned in (13) may be balanced by the effect of material facesheet damage.
15. Specimens with simulated facesheet damage failed at approximately the same failure stress as the corresponding indented specimens although the failure mechanisms are very different; the former failed via in-plane propagation of facesheet fracture while the latter failed via dimple propagation which is essentially a local bending phenomenon leading to final facesheet failure due to high longitudinal stress.
16. Correlative models should only be used to correlate strength data resulting from a failure mechanism upon which the model is based. Data representing different failure mechanisms cannot be correlated using only one model.
17. For specimens with (0/90) facesheets and simulated core damage, the applied stress at which the peak membrane stress along the centerline through the dimple and perpendicular to the loading reaches the strength of the undamaged specimens correlates well with the residual strength of the specimens.

18. The residual strength of specimens with (± 45) facesheets is insensitive to various damage levels. This is similar to the notch insensitive characteristics demonstrated by that particular layup.

8.2 Recommendations

The present work raises a number of issues which require further investigation. The following recommendations are therefore made:

1. Effective nondestructive inspection techniques need to be developed to characterize core damage reliably since the present work has demonstrated the influence of core damage on the failure mechanism and final failure of indented/impacted sandwich panels.
2. An appropriate and relative set of damage metrics needs to be developed for all three damage types: geometric facesheet damage, material facesheet damage, and core damage, in order to properly characterize damage for better assessment of damage tolerance.
3. Work should be conducted on other discretization methods, e.g. finite difference or some kind of global-local discretization techniques, which may be more efficient in solving the governing equations of the dimple propagation model, especially when the dimensions of the model/structure are large compared with those of the dimple.
4. Local reduction in facesheet stiffness around the dimple needs to be further investigated and also included in the analysis due to the presence of facesheet damage and/or due to the nonlinear stress-strain behavior of the facesheets.
5. There is a need to study the failure mechanisms and final failure modes of sandwich panels with different combinations of core thickness

and facesheet thickness because the effects of global bending and through-thickness damage distribution in the facesheet may affect the failure mechanism of dimple propagation or induce different mechanisms (e.g. global buckling, delamination buckling).

6. There is a need to understand the implications of high through-thickness stress gradients in predicting failure within regions where severe bending stresses exist.
7. The effects of finite width on the dimple propagation and the residual strength of impacted/indented panels should be studied by conducting experiments on panels of various widths and performing analyses to determine the variation of the stress fields around the dimple as the width of the specimen changes.

References

1. Allen, H. G., "The Story of Sandwich Construction", *1st Core Conference*, Zürich, Switzerland, 1988, pp. 1-24.
2. Allen, H. G., "Sandwich Construction Today and Tomorrow", in *Sandwich Construction 1 (1st International Conference)*, ed. Olsson, K. A. and Richard, R. P., Engineering Materials Advisory Services, 1989, pp. 3-22.
3. Hooper, E., "Starship: A Model for Future Design", *1st Core Conference*, Zürich, Switzerland, 1988, pp. 1-5.
4. Abbott, R., "Design and Certification of the All-Composite Airframe", *Aerospace Technology Conference and Exposition*, Anaheim, California, 1989, pp. 1-8.
5. Joy, V. A., Murphy, K. N., and Krishnadas Nair, C. G., "Technological Excellence in Honeycomb Sandwich and Composite Structures for Aerospace Applications", *Journal of Aeronautical Society of India*, Vol. 43, No. 2, May, 1991, pp. 101-112.
6. Van Veggel, L. H., "Impact and Damage Tolerance Properties of CFRP Sandwich Panels -- An Experimental Parameter Study For the Fokker 100 CA-EP Flap", *New Materials and Fatigue Resistant Aircraft Design; proceedings of the 14th symposium of the international committee on aeronautic fatigue*, Ottawa, Canada, 1987, pp. 557-583.
7. Saporito, J., "Sandwich Structures on Aerospaciale Helicopters", *34th International SAMPE Symposium*, Reno, NV, 1989, pp. 2506-2513.
8. Llorente, S., "Honeycomb Sandwich Primary Structure Applications on the Boeing Model 360 Helicopter", *34th International SAMPE Symposium*, Reno, NV, 1989, pp. 824-838.
9. Schulze, E. J. and Kesack, W. J., "Honeycomb Sandwich Composite Structures Used on the V-22 Osprey Fuselage", *22nd International SAMPE Technical Conference*, 1990, pp. 1051-1069.
10. Bansemir, H. and Haider, O., "Strength and Deformation Behaviour of Kevlar and Carbon Composite Sandwich Structures for Space Applications", *International Conference on Spacecraft Structures and Mechanical Testing*, Noordwijk, The Netherlands, 1991, pp. 421-426.

11. Zvanik, M., "Using GRP Sandwich Construction in the Marine Environment: Past, Present, and the Future", *Marine Composites Symposium*, Savannah, GA, 1993, pp. F21- 1-9.
12. "Military Specification: Airplane Damage Tolerance Requirements", MIL-A-83444, USAF, July, 1974.
13. "Damage-Tolerance and Fatigue Evaluation of Structure", FAR Advisory Circular 25.571, FAA, September, 1978.
14. Lincoln, J. W., "Damage Tolerance - USAF Experience", *13th ICAF Symposium*, Pisa, Italy, 1985, pp. 265-295.
15. Lincoln, J. W., "Damage Tolerance for Commuter Aircraft", *International Conference on Aging Aircraft and Structural Airworthiness*, NASA Langley Research Center, 1991, pp. 187-201.
16. Kan, H. P., Whitehead, R. S., and Kautz, E., "Damage Tolerance Certification Methodology for Composite Structures", *8th DOD/NASA/FAA Conference on Fibrous Composites in Structural Design*, NASA, Langley Research Center, 1990, pp. 479-494.
17. Lincoln, J. W., "Damage Tolerance for Helicopters", *15th ICAF Symposium*, Jerusalem, Israel, 1989, pp. 263-290.
18. Cairns, D. S. and Lagace, P. A., "A Consistent Engineering Methodology for the Treatment of Impact in Composite Materials", *Journal of Reinforced Plastics and Composites*, Vol. 11, April, 1992, pp. 395-412.
19. Ishai, O. and Shragai, A., "Effect of Impact Loading on Damage and Residual Compressive Strength of CFRP Laminated Beams", *Composite Structures*, Vol. 14, No. 4, 1990, pp. 319-337.
20. Sjöblom, P. and Hwang, B., "Compression-After-Impact: The \$5000 Data Point!", *34th International SAMPE Symposium*, Reno, NV, 1989, pp. 1411-1421.
21. de Jonge, J. B., "The Requirement of Damage Tolerance", TR 77005, NLR, February, 1976.
22. Hull, D. and Shi, Y. B., "Damage Mechanism Characterization in Composite Damage Tolerance Investigations", *Composite Structures*, Vol. 23, No. 2, 1993, pp. 99-120.

23. Reifsnider, K. L., "Service Induced Damage in Composite Structures", in *Handbook of Composites*, ed. al, C. T. H. e., Elsevier Science Publishers B. V., Amsterdam, 1989, pp. 231-262.
24. Cantwell, W. J. and Morton, J., "The Impact Resistance of Composite Materials — a Review", *Composites*, Vol. 22, No. 5, September, 1991, pp. 347-362.
25. Abrate, S., "Impact on Laminated Composite Materials", *Appl. Mech. Rev.*, Vol. 44, No. 4, 1991, pp. 155-189.
26. Steinmann, A. E., "Damage Tolerance of Thin Skin Sandwich Panels", U.S. Air Force Materials Lab. Report AFML-TR-76, Wright Patterson, Ohio, February, 1977.
27. Slepetz, J. M., Oplinger, D. W., Parker, B. S., and Tremblay, R. T., "Impact Damage Tolerance of Graphite/Epoxy Sandwich Panels", AMMRC TR 74-20, Army Materials and Mechanics Research Center, Watertown, MA, September, 1974.
28. Lie, S. C., "Damage Resistance and Damage Tolerance of Thin Composite Facesheet Honeycomb Panels", TELAC Report 89-3, Massachusetts Institute of Technology, Cambridge, MA, March, 1989.
29. Lagace, P. A., Williamson, J. E., Tsang, P. H. W., Wolf, E., and Thomas, S., "A Preliminary Proposition for a Test Method to Measure (Impact) Damage Resistance", *Journal of Reinforced Plastics and Composites*, Vol. 12, No. 5, May, 1993, pp. 584-601.
30. Labor, J. D. and Bhatia, N. M., "Impact Resistance of Graphite and Hybrid Configurations", *Nondestructive Evaluation and Flaw Criticality for Composite Materials (Symposium)*, ASTM STP 696, ASTM, 1979, pp. 101-117.
31. Nettles, A. T. and Hodge, A. J., "Impact Testiong of Glass/Phenolic Honeycomb Panels with Graphite/Epoxy Facesheets", *35th International SAMPE Symposium*, 1990, pp. 1430-1440.
32. Bernard, M. L. and Lagace, P. A., "Impact Resistance of Composite Sandwich Plates", *Journal of Reinforced Plastics and Composites*, Vol. 8, September, 1989, pp. 432-445.
33. Williamson, J. E. and Lagace, P. A., "Response Mechanisms in the Impact of Graphite/Epoxy Honeycomb Sandwich Panels", *Proceedings of the American Society for Composites Eighth Technical Conference on Composite Materials*, Cleveland, OH, 1993, pp. 287-297.

34. Palm, T. E., "Impact Resistance and Residual Compression Strength of Composite Sandwich Panels", *Composites: Design, Manufacture, & Application: Proceedings of 8th International Conference on Composite Materials*, Honolulu, HI, 1991, pp. 3-G-1 to 3-G-14.
35. Levin, K., "Damage Tolerance of CFRP Sandwich Panels", The Aeronautical Research Institute of Sweden, 1988.
36. Kim, C.-G. and Jun, E.-J., "Impact Characteristics of Composite Laminated Sandwich Structures", *Composites: Design, Manufacture, & Application: Proceedings of the 8th International Conference on Composite Materials*, Honolulu, HI, 1991, pp. 32-G-1 to 32-G-8.
37. Rhodes, M. D., "Impact Fracture of Composite Sandwich Structures", *AIAA Paper 75-748*, 1975.
38. Shih, W. K. and Jang, B. Z., "Instrumented Impact Testing of Composite Sandwich Panels", *Journal of Reinforced Plastics and Composites*, Vol. 8, May, 1989, pp. 270-298.
39. Llorente, S. and Gunther, C., "Damage Tolerance Evaluation of Sandwich Shear Panels", *National Technical Specialists' Meeting on Advanced Rotorcraft Structures*, Williamsburg, VA, 1988, pp. 1-12.
40. Wardle, M. W. and Zahr, G. E., "Instrumented Impact Testing of Aramid-Reinforced Composite Materials", *Instrumented Impact Testing of Plastics and Composite Materials*, ASTM STP 936, ASTM, 1987, pp. 219-235.
41. Llorente, S., Weems, D., and Fay, R., "Evaluation of Advanced Sandwich Structure Designed for Improved Durability and Damage Tolerance", *46th Annual Forum of the American Helicopter Society*, Washington, D. C., 1990, pp. 825-831.
42. Rhodes, M. D., Williams, J. G., and Starnes, J. H. J., "Effect of Impact Damage on the Compression Strength of Filamentary-Composite Hat-Stiffened Panels", *23rd SAMPE National Symposium and Exhibition*, Anaheim, CA, 1978, pp. 300-319.
43. Wolf, E., "Impact Damage Mechanisms in Several Laminated Material Systems", TELAC Report 92-3, Massachusetts Institute of Technology, March, 1992.

44. Akay, M. and Hanna, R., "A comparison of honeycomb-core and foam-core carbon-fibre/epoxy sandwich panels", *Composites*, Vol. 21, No. 4, 1990, pp. 325-331.
45. Tsang, P. H. W. and Dugundji, J., "Damage Resistance of Graphite/Epoxy Sandwich Panels under Low Speed Impact", *Journal of the American Helicopter Society*, January, 1992, pp. 75-81.
46. Chen, C.-H., Chen, M.-Y., and Chen, J.-P., "The Residual Shear Strength and Compressive Strength of C/E Composite Sandwich Structure After Low Velocity Impact", *36th International SAMPE Symposium*, San Diego, CA, 1991, pp. 932-943.
47. Koller, M. G., "Elastic impact of spheres on sandwich plates", *Journal of Applied Mathematics and Physics*, Vol. 37, March, 1986, pp. 256-269.
48. Sun, C. T. and Wu, C. L., "Low Velocity Impact of Composite Sandwich Panels", *AIAA/ASME/ASCE/AHS/ASC 32nd Structures, Structural Dynamics & Materials Conference*, Baltimore, MD, 1991, pp. 1123-1129.
49. Lee, L. J., Huang, K. Y., and Fan, Y. J., "Dynamic Responses of Composite Sandwich Plate Subjected to Low Velocity Impact", *Composites: Design, Manufacture, & Application: Proceedings of the 8th International Conference on Composite Materials*, Honolulu, HI, 1991, pp. 32-D-1 to 32-D-10.
50. Nemes, J. A. and Simmonds, K. E., "Low-Velocity Impact Response of Foam-Core Sandwich Composites", *Journal of Composite Materials*, Vol. 26, No. 4, 1990, pp. 500-519.
51. Stanton, E. L. and Crain, L. M., "Interlaminar Stress Gradients and Impact Damage", *Fibrous Composites in Structural Design*, San Diego, CA, 1978, pp. 423-439.
52. Tsang, P. H. W., "Impact Resistance of Graphite/Epoxy Sandwich Panels", TELAC Report 89-12, Massachusetts Institute of Technology, Cambridge, MA, August, 1989.
53. Gottesman, T., Bass, M., and Samuel, A., "Criticality of Impact Damage in Composite Sandwich Structures", *The 6th International Conference on Composite Materials and the 2nd European Conference on Composite Materials*, Imperial College of Science & Technology, London, England, 1987, pp. 3.27-3.35.

54. Card, M. F. and Rhodes, M. D., "Graphite-Epoxy Panel Compression Strength Reduction Due to Local Impact", *50th Meeting of the AGARD Structures and Materials Panel*, 1980, pp. 1-11.
55. Sharma, A. V., "Low-Velocity Impact Tests on Fibrous Composite Sandwich Structures", *Test Methods and Design Allowables for Fibrous Composites, ASTM STP 734*, ASTM, 1981, pp. 54-70.
56. Caldwell, M. S., Borris, P. W., and Falabella, R., "Impact Damage Tolerance Testing of Bonded Sandwich Panels", *22nd International SAMPE Technical Conference*, Boston, MA, 1990, pp. 509-520.
57. Charles, J.-P. and Guedra-Degeorges, D., "Impact Damage Tolerance of Helicopter Sandwich Structures", *International SAMPE Technical Conference*, Vol. 23, 1991, pp. 51-61.
58. Williamson, J. W., "Response Mechanisms in the Impact of Graphite/Epoxy Honeycomb Sandwich Panels", TELAC Report 91-12, Massachusetts Institute of Technology, August, 1991.
59. Marmorini, L., "The Contribution of Face Wrinkling to the Compressive Strength of Thin Composite Facesheet Sandwich Panels", TELAC Report 90-16, Massachusetts Institute of Technology, Cambridge, MA, July, 1990.
60. 't Hart, W. G. J., "The Effect of Impact Damage on the Tension-Compression Fatigue Properties of Sandwich Panels with Face Sheets of Carbon/Epoxy", National Aerospace Laboratory, December, 1981.
61. Adsit, N. R. and Waszczak, J. P., "Effect of Near-Visual Damage on the Properties of Graphite/Epoxy", *Composite Materials: Testing and Design (Fifth Conference)*, ASTM STP 674, ASTM, 1979, pp. 101-117.
62. Bernard, M. L., "Impact Resistance and Damage Tolerance of Composite Sandwich Plates", TELAC Report 87-11, Massachusetts Institute of Technology, May, 1987.
63. Whitcomb, J. D., "Mechanics of Instability-Related Delamination Growth", *Composite Materials: Testing and Design (9th Volume)*, ASTM STP 1059, ASTM, 1990, pp. 215-230.
64. Kassapoglou, C., "Buckling, Post-Buckling and Failure of Elliptical Delaminations in Laminates under Compression", *Composite Structures*, Vol. 9, 1988, pp. 139-159.

65. Kardomateas, G. A., "Effect of an Elastic Foundation on the Buckling and Postbuckling of Delaminated Composites Under Compressive Loads", *Journal of Applied Mechanics*, Vol. 55, March, 1988, pp. 238-241.
66. Hwu, C. and Hu, J. S., "Delamination Buckling of Honeycomb Sandwich with Laminated Faces", *Composites: Design, Manufacture, & Application: 8th International Conference on Composite Materials*, Honolulu, 1991, pp. 3-B-1 to 3-B-10.
67. Peck, S. O. and Springer, G. S., "The Behavior of Delaminations in Composite Plates -- Analytical and Experimental Results", *Journal of Composite Materials*, Vol. 25, July, 1991, pp. 907-929.
68. Kassapoglou, C. and Abbott, R., "A Correlation Parameter for Predicting the Compressive Strength of Composite Sandwich Panels after Low Speed Impact", *AIAA/ASME/ASCE/AHS/ASC 29th Structures, Structural Dynamics & Materials Conference*, 1986, pp. 642-650.
69. Kassapoglou, C., Jonas, P. J., and Abbott, R., "Compressive Strength of Composite Sandwich Panels After Impact Damage : An Experimental and Analytical Study", *Journal of Composites Technology and Research*, Vol. 10, Summer, 1988, pp. 65-73.
70. Minguet, P. J., "A Model for Predicting the Behavior of Impact-Damaged Minimum Gage Sandwich Panels under Compression", *AIAA/ASME/ASCE/AHS/ASC 32nd Structures, Structural Dynamics & Materials Conference*, Baltimore, MD, 1991, pp. 1112-1122.
71. Theocaris, P. S., *Moiré Fringes in Strain Analysis*, Pergamon Press, Oxford, NY, 1969, pp. 415.
72. Kafri, O. and Glatt, I., *The Physics of Moiré Metrology*, Wiley, New York, 1990, pp. 1-17.
73. Durelli, A. J. and Parks, V. J., *Moiré Analysis of Strain*, Prentice-Hall, Englewood Cliffs, N. J., 1970, pp. 251-256.
74. Kobayashi, A. S., *Handbook on Experimental Mechanics*, Prentice-Hall, Englewood Cliffs, NJ, 1987, pp. 282-313.
75. Doyle, J. F. and Phillips, J. W., *Manual on Experimental Stress Analysis (5th Edition)*, Society for Experimental Mechanics, Bethel, CT, 1989, pp. 107-135.

76. Sciammarella, C. A., "The Moiré Method -- A Review", *Experimental Mechanics*, November, 1982, pp. 418-433.
77. Sciammarella, C. A. and Chiang, F.-P., "The Moiré Method Applied to Three-Dimensional Elastic Problems", *Experimental Mechanics*, Vol. 4, November, 1964, pp. 313-319.
78. Oplinger, D. W., "Application of moiré methods to evaluation of structural performance of composite materials", *Optical Engineering*, Vol. 21, No. 4, July/August, 1982, pp. 626-632.
79. Jones, R., Broughton, W., Mousley, R. F., and Potter, R. T., "Compression Failures of Damaged Graphite Epoxy Laminates", *Composite Structures*, Vol. 3, 1985, pp. 167-186.
80. Mousley, R. F., "A Shadow Moiré Technique for the Measurement of Damage in Composites", *Composite Structures*, Vol. 4, 1985, pp. 231-244.
81. Cairns, D. S., Minguet, P. J., and Abdallah, M. G., "Theoretical and Experimental Response of Composite Laminates with Delaminations Loaded in Compression", *Proceedings of the AIAA/ASME/ASCE/AHS/ASC SDM Conference*, Dallas, TX, 1992, pp. 1-9.
82. Chia, H., Knauss, W. G., and Babcock, C. D., "Observation of Damage Growth in Compressively Loaded Laminates", *Experimental Mechanics*, Vol. 23, No. 3, September, 1983, pp. 329-337.
83. Mar, J. W. and Lin, K. Y., "Fracture of Boron/Aluminum Composites with Discontinuities", *Journal of Composite Materials*, Vol. 11, October, 1977, pp. 405-421.
84. Chia, C.-Y., *Nonlinear Analysis of Plates*, McGraw-Hill, Inc., 1980, pp. 1-422.
85. Timoshenko, S. J., *Theory of Plates and Shells*, 1965.
86. Mathews, J. H., *Numerical Methods for Computer Science, Engineering & Mathematics*, Prentice-Hall, Inc, Englewood Cliffs, NJ, 1987.
87. Hildebrand, F. B., *Introduction to Numerical Analysis*, Dover Publications, New York.

88. Herrmann, L. R. and Mason, W. E., "Response of Reinforcing Wires to Compressive States of Stress", *Journal of Composite Materials*, Vol. 1, 1967, pp. 212-226.
89. Fletcher, D. Q. and Hermann, L. R., "Elastic Foundation Representation of Continuum", *Journal of the Engineering Mechanics Division, Proceedings of the ASCE*, Vol. EM1, February, 1971, pp. 95-107.
90. Scott, R. F., *Foundation Analysis*, Prentice-Hall, Inc., Englewood Cliffs, NJ, 1981.
91. Selvadurai, A. P. S., *Elastic Analysis of Soil-Foundation Interaction*, Elsevier Scientific Publishing Company, 1979, pp. 1-543.
92. Winkler, E., *Die Lehre von der Elastizitat und Festigkeit*, Dominicus, Prague, 1867.
93. Filonenko-Borodich, M. M., "Some Approximate Theories of the Elastic Foundation", *Uch. Zap. Mosk. Gos. Univ. Mekh. (in Russian)*, Vol. 46, 1940, pp. 3-18.
94. Pasternak, P. L., "On a New Method of Analysis of an Elastic Foundation by Means of Two Foundational Constants", *Gosudarstvennoe Izdatelstvo Literaturi po Stroitelstvu Arkhitekture, Moscow (in Russian)*, 1954.
95. Lagace, P. A., "Notch Sensitivity and Stacking Sequence of Laminated Composites", *Composite Materials: Testing and Design (Seventh Conference)*, ASTM STP 893, ASTM, 1986, pp. 161-176.
96. Fenner, D. N., "Stress Singularities in Composite Materials with an Arbitrarily Oriented Crack Meeting an Interface", *International Journal of Fracture*, Vol. 12, No. 5, October, 1976, pp. 705-721.
97. Lagace, P. A., Brewer, J. C., and Varnerin, C., "TELAC Manufacturing Course Notes", TELAC Report 88-4B, Massachusetts Institute of Technology, 1990.
98. Lagace, P. A., "Nonlinear Stress-Strain Behavior of Graphite/Epoxy Laminates", *AIAA Journal*, Vol. 23, No. 10, 1985.
99. Vizzini, A. J., "An Efficient Algorithm to Characterize Stress-Strain Data Using Piecewise Linear Curves", *Journal of Testing and Evaluation*, Vol. 20, No. 2, March, 1992, pp. 126-131.

100. Cantwell, W. J. and Morton, J., "Geometrical Effects in the Low Velocity Impact Response of CFRP", *Composite Structures*, Vol. 12, 1989, pp. 39-59.

Appendix A

Program Listing

The entire listing of the program GROWTH is given in this appendix. The program is written in FORTRAN 77 and compiled on a DECstation 5000/133 workstation installed with the DEC FORTRAN compiler for ULTRIX/RISC System v3.2.


```
c
write(6,*)'does modal amplitudes for initial dent shape ',
&      'already exist? (y/n)'
read(5,103)ans
if (ans.eq.'y') then
write(6,*)'enter filename for modal amplitudes'
read(5,103)fname
open (unit=21,file=fname,status='old')
ij=0
do 50 i=1,nwx
do 50 j=1,nwy
ij=ij+1
50  read(21,*)zeta(ij)
continue
endif
if (ans.eq.'n') then
write(6,*)'evaluating modal amplitudes for initial dent shape...'
if (layup.eq.45)
& call shape45 (zeta,a,b,rx,ry,wdent,nwx,nwy)
if (layup.eq.90)
& call shape90 (zeta,a,b,rx,ry,wdent,nwx,nwy)
write(6,*)'do you want to save modal amplitudes for future use ',
&      '? (y/n)'
read(5,103)ans1
if (ans1.eq.'y') then
write(6,*)'enter filename to store modal amplitudes'
read(5,103)fname
open (unit=21,file=fname,status='unknown')
ij=0
do 60 i=1,nwx
do 60 j=1,nwy
ij=ij+1
60  write(21,*)zeta(ij)
continue
endif
endif

c
c read in modal amplitudes w2(ij) and f(ij) or initialize them
c
c call readfile (w2,f,nwx,nwy,nfx,nfy)
c
c read nodes at which sigma plateau is enforced
c
c call readnode (fix,nwx,nwy,mbad,nbad,np)
c
c read in other parameters
c
rlxf=1.
rlxw=1.
flag='y'
write(6,*)'input load ratio'
read(5,*)alpha
write(6,*)'input no. of iterations desired'
read(5,*)ni
write(12,*)'rlxf,rlxw,ni,alpha'
write(12,101)rlxf,rlxw,ni,alpha
write(6,*)'writes every n iterations where n is:'
read(5,*)nit
```

```
c
c   factorize matrix that relates modal amplitudes and nodal amplitudes
c
c   call factor (a,b,nwx,nwy,fft,indx)
c
c   start of loop to solve the coupled nonlinear equations
c
c   write(6,*)'iterating to solve coupled nonlinear equations...'
c   istep=1
5   continue
c   wnorm=0.
c   fnorm=0.
c
c   initialize rhs of compatability and z-equilibrium equations
c
c   ij=0
c   do 15 i=1,nfx
c   do 15 j=1,nfy
c     ij=ij+1
c     rhsf(ij)=0.
15  continue
c   ij=0
c   do 17 i=1,nwx
c   do 17 j=1,nwy
c     ij=ij+1
c     rhsw(ij)=0.
17  continue
c
c   calculate residual due to core crushing
c
c   call crush (fft,indx,w2,f,wd,a,b,nwx,nwy,ifail,jfail,flag,
c   &          kbad,lbad,bad,fix)
c
c   calculate rhs of z-equilibrium equation
c
c   call zequilm (w2,f,zeta,wd,a,b,nfx,nfy,nwx,nwy,rhsw,aload,alpha)
c
c   update modal amplitudes w2(ij)
c
c   ij=0
c   do 35 i=1,nwx
c   do 35 j=1,nwy
c     ij=ij+1
c     wnorm=wnorm+(w2(ij)-rhsw(ij))**2
c     w2(ij)=rlxw*rhsw(ij)
35  continue
c
c   calculate rhs of compatability equation
c
c   call compatlty (w2,f,zeta,a,b,nfx,nfy,nwx,nwy,rhsf)
c
c   update modal amplitudes f(ij)
c
c   ij=0
c   do 30 i=1,nfx
c   do 30 j=1,nfy
c     ij=ij+1
c     fnorm=fnorm+(f(ij)-rhsf(ij))**2
```



```
      f(ij)=rlxf*rhsf(ij)
30  continue
c
c  write norm of change of modal amplitudes at each iteration step
c
      if (mod(istep,nit).eq.0.or.istep.eq.1)
&   write(6,102)istep,wnorm,fnorm
c
c  identify locations of crushed core at the end of iterations
c
      if (istep.eq.ni) then
        write(6,*)'...iterations done'
        write(12,*)'initial core failure at:'
        do 90 i=1,np
          write(16,*)mbad(i),nbad(i)
90      continue
        write(6,*)'subsequent core failure at:'
        write(12,*)'subsequent core failure at:'
        do 80 i=1,jfail
          write(12,104)i,kbad(i),lbad(i),bad(i)
          write(6,104)i,kbad(i),lbad(i)
          write(16,*)kbad(i),lbad(i)
80      continue
        else
c
c      otherwise continue to loop
c
          istep=istep+1
          goto 5
        endif
c
c  calculate output along center-lines
c
      call centerl (f,w2,zeta,nwx,nwy,nfx,nfy,a,b,aload)
      write(12,103)'ifail,jfail'
      write(12,*)ifail,jfail
c
c  write modal amplitudes to files
c
      ij=0
      do 20 i=1,nwx
        do 20 j=1,nwy
          ij=ij+1
          write(13,*)w2(ij)
20      continue
          ij=0
          do 25 i=1,nfx
            do 25 j=1,nfy
              ij=ij+1
              write(14,*)f(ij)
25      continue
c
101  format (2e13.4,i4,f8.3)
102  format (i5,2e17.6)
103  format (a)
104  format (3i6,f8.2)
      stop
      end
```

```
c-----  
      subroutine datain (cc,tc,a,b,nfx,nfy,nwx,nwy,wdent,  
      & rx,ry,aload,layup)  
c  
c      This subroutine reads in mechanical properties of the facesheets  
c      and the core from the input files and writes them  
c      to appropriate output files.  
c  
      implicit real*8 (a-h,o-z)  
      real*8 cc(6,6)  
  
      character*50 title0,title1,title2,title3,title4  
      common/fprop/alli,a22i,a12i,a66i,d11,d22,d12,d66,tf1,tf2  
      common/cprop/fs1,fs2,fult1,fult2,rcrush  
c  
c      read face properties  
c  
      read(11,101)title4  
      read(11,101)title0  
      read(11,101)title1  
      read(11,*)a11,a12,a16,a22,a26,a66  
      read(11,101)title2  
      read(11,*)d11,d12,d16,d22,d26,d66  
      read(11,101)title3  
      read(11,*)tf1,tf2,layup  
c  
c      write face properties to output file  
c  
      write(12,101)title4  
      write(12,*)  
      write(12,101)title0  
      write(12,101)title1  
      write(12,102)a11,a12,a16,a22,a26,a66  
      write(12,101)title2  
      write(12,102)d11,d12,d16,d22,d26,d66  
      write(12,101)title3  
      write(12,103)tf1,tf2,layup  
c  
c      read core properties  
c  
      read(11,101)title0  
      read(11,101)title1  
      read(11,*)e11,e22,e33  
      read(11,101)title2  
      read(11,*)g23,g13,g12  
      read(11,101)title3  
      read(11,*)pnu23,pnu13,pnu12  
      read(11,101)title4  
      read(11,*)tc,fult1,fult2  
c  
c      write core properties to output file  
c  
      write(12,*)  
      write(12,101)title0  
      write(12,101)title1  
      write(12,104)e11,e22,e33  
      write(12,101)title2  
      write(12,104)g23,g13,g12
```

```
write(12,101)title3
write(12,105)pnu23,pnu13,pnu12
write(12,101)title4
write(12,104)tc,fult1,fult2
c
c   read other parameters
c
   read(11,101)title0
   read(11,101)title1
   read(11,*)a,b,nfx,nfy,nwx,nwy
   read(11,101)title2
   read(11,*)wdent,rx,ry
   read(11,101)title3
   read(11,*)aload,rcrush
c
c   write other parameters to output file
c
   write(12,*)
   write(12,101)title0
   write(12,101)title1
   write(12,107)a,b,nfx,nfy,nwx,nwy
   write(12,101)title2
   write(12,104)wdent,rx,ry
   write(12,101)title3
   write(12,106)aload,rcrush
c
c   read foundation stiffnesses
c
   read(11,101)title3
   read(11,*)fs1,fs2
c   fs1=e33/tc
   write(12,101)title3
   write(12,106)fs1,fs2
101 format(a)
102 format(6e13.4)
103 format(2e13.4,i4)
104 format(3e13.4)
105 format(3f8.3)
106 format(2e13.4)
107 format(2e13.4,4i5)
c
c   define core stiffness matrix cc(6,6)
c
   do 20 i=1,6
     do 20 j=1,6
       cc(i,j)=0.
20  continue
   pnu32=e33*pnu23/e22
   pnu31=e33*pnu13/e11
   pnu21=e22*pnu12/e11
   delta=1.-pnu12*pnu21-pnu23*pnu32-pnu31*pnu13-2.*pnu21*pnu32*pnu13
   cc(1,1)=(1.-pnu23*pnu32)*e11/delta
   cc(1,2)=(pnu21+pnu31*pnu23)*e11/delta
   cc(1,3)=(pnu31+pnu21*pnu32)*e11/delta
   cc(2,1)=cc(1,2)
   cc(2,2)=(1.-pnu13*pnu31)*e22/delta
   cc(2,3)=(pnu32+pnu12*pnu31)*e22/delta
   cc(3,1)=cc(1,3)
```

```
cc(3,2)=cc(2,3)
cc(3,3)=(1.-pnu12*pnu21)*e33/delta
cc(4,4)=g23
cc(5,5)=g13
cc(6,6)=g12
c
c calculate inverse of a-matrix
c
det=a11*a22-a12**2
a11i=a22/det
a22i=a11/det
a12i=-a12/det
a66i=1./a66
return
end
c-----
c subroutine readfile (w2,f,nwx,nwy,nfx,nfy)
c
c This subroutine reads in the modal amplitudes for w and F from the
c previous iteration.
c
implicit real*8 (a-h,o-z)
parameter (nfxmax=30,nfymin=30,nwxmax=30,nwymax=30,
& nnfmax=nfxmax*nfymin,nnwmax=nwxmax*nwymax)
real*8 w2(nnwmax),f(nnfmax)
character ans,fnwij*11,fnfij*11
write(6,*)'do you want to read modal amplitudes from input files?'
& , '(y/n) '
read(5,103)ans
if (ans.eq.'y') then
write(6,*)'input filename for wij'
read(5,103)fnwij
write(6,*)'input filename for fij'
read(5,103)fnfij
open (unit=17,file=fnwij,status='old')
open (unit=18,file=fnfij,status='old')
ij=0
do 40 i=1,nwx
do 40 j=1,nwy
ij=ij+1
read(17,*)w2(ij)
40 continue
ij=0
do 50 i=1,nfx
do 50 j=1,nfy
ij=ij+1
read(18,*)f(ij)
50 continue
else
ij=0
do 7 i=1,nfx
do 7 j=1,nfy
ij=ij+1
f(ij)=0.
7 continue
ij=0
do 10 i=1,nwx
do 10 j=1,nwy
```

```

        ij=ij+1
        w2(ij)=0.
10      continue
      endif
103     format(a)
        return
      end
c-----
      subroutine readnode (fix,nwx,nwy,mbad,nbad,np)
c
c      This subroutine reads in coordinates of the nodal points where the
c      core is crushed.
c
      implicit real*8 (a-h,o-z)
      parameter (nfxmax=30,nfyymax=30,nwxmax=30,nwymax=30,
&              nnfmax=nfxmax*nfyymax,nnwmax=nwxmax*nwymax)
      character fix(nnwmax),fname*11
      integer mbad(nnwmax),nbad(nnwmax)
      ij=0
      do 5 i=1,nwx
      do 5 j=1,nwy
        ij=ij+1
        fix(ij)='n'
5      continue
      write(6,*)'enter no. of nodes you want to relax'
      read(5,*)np
      if (np.ne.0) then
        write(6,*)'enter filename for failed nodes'
        read(5,102)fname
        open(unit=15,file=fname,status='unknown')
        do 10 i=1,np
          read(15,*)k,l
          mbad(i)=k
          nbad(i)=l
          kl=(k-1)*nwy+1
          fix(kl)='y'
10      continue
        endif
102     format(a)
        return
      end
c-----
      subroutine shape90 (zeta,a,b,rx,ry,wdent,nwx,nwy)
c
c      This subroutine calculates the modal amplitudes of the initial
c      dimple shape for specimens with (0/90) facesheets.
c
      implicit real*8 (a-h,o-z)
      parameter (nwxmax=30,nwymax=30,nnwmax=nwxmax*nwymax)
      real*8 zeta(nnwmax)
      pi=acos(-1.d0)
      r=.5*sqrt(rx**2+ry**2)
      s=ry/2./r
      c=rx/2./r
      s2=2.*s*c
      nx=int(a/2./rx)
      ny=int(b/2./ry)
      ij=0
```

```
do 10 i=1,nwx
  pia=(2*i-1)*pi/a
  nipx=2*(nx+2*i-1)
  delx=2.*r/nipx
  do 10 j=1,nwy
    pjb=(2*j-1)*pi/b
    nipy=2*(ny+2*j-1)
    dely=2.*r/nipy
    ij=ij+1
    zeta(ij)=0.
    do 20 k=0,nipx
      x=-r+k*delx
      if (k.eq.0.or.k.eq.nipx) then
        coefx=1.
      else
        coefx=2.*(mod(k,2)+1)
      endif
      do 20 l=0,nipy
        y=-r+l*dely
        xx=(c*x-c*y)+a/2.
        yy=(s*x+s*y)+b/2.
        dumx=pi*x/2./r
        dumy=pi*y/2./r
        fxy=wdent*(cos(dumx)*cos(dumy))**2
        if (l.eq.0.or.l.eq.nipy) then
          coefy=1.
        else
          coefy=2.*(mod(l,2)+1)
        endif
        zeta(ij)=zeta(ij)+coefx*coefy*fxy*sin(pia*xx)*sin(pjb*yy)
20      continue
      zeta(ij)=zeta(ij)*delx*dely/9.*4./a/b*s2
10    continue
  return
end
```

```
c-----
c      subroutine shape45 (zeta2,a,b,rx,ry,wdent,nwx,nwy)
c
c      This subroutine calculates modal amplitudes of the initial dimple
c      shape for specimens with (+45) facesheets.
c
c      implicit real*8 (a-h,o-z)
c      parameter (nfxmax=30,nfyymax=30,nwxmax=30,nwymax=30,
c      &          nnfmax=nfxmax*nfyymax,nnwmax=nwxmax*nwymax)
c      real*8 zeta2(nnwmax)
c      pi=acos(-1.)
c
c      analogy between shape and shape45 only works for rx=ry
c
c      rxx=rx/sqrt(2.)
c      ryy=ry/sqrt(2.)
c      ij=0
c      do 10 i=1,nwx
c        do 10 j=1,nwy
c          io=2*i-1
c          jo=2*j-1
c          ij=ij+1
c          cl=io*pi/a
```

```

c2=pi/rxx+io*pi/a
c3=pi/rxx-io*pi/a
c4=pi*a/2./rxx
x1=a/2.-rxx
x2=a/2.+rxx
if (abs(c3).le.1.e-8) then
  fx=.5*x2*sin(c4)-.5/c2*cos(c4-c2*x2)-cos(c1*x2)/c1-
&   .5*x1*sin(c4)+.5/c2*cos(c4-c2*x1)+cos(c1*x1)/c1
else
  fx=.5/c3*cos(c4-c3*x2)-.5/c2*cos(c4-c2*x2)-cos(c1*x2)/c1-
&   .5/c3*cos(c4-c3*x1)+.5/c2*cos(c4-c2*x1)+cos(c1*x1)/c1
endif
c1=jo*pi/b
c2=pi/ryy+jo*pi/b
c3=pi/ryy-jo*pi/b
c4=pi*b/2./ryy
x1=b/2.-ryy
x2=b/2.+ryy
if (abs(c3).le.1.e-8) then
  fy=.5*x2*sin(c4)-.5/c2*cos(c4-c2*x2)-cos(c1*x2)/c1-
&   .5*x1*sin(c4)+.5/c2*cos(c4-c2*x1)+cos(c1*x1)/c1
else
  fy=.5/c3*cos(c4-c3*x2)-.5/c2*cos(c4-c2*x2)-cos(c1*x2)/c1-
&   .5/c3*cos(c4-c3*x1)+.5/c2*cos(c4-c2*x1)+cos(c1*x1)/c1
endif
zeta2(ij)=wdent*fx*fy/a/b
c   zeta2(ij)=0.
10  continue
return
end

```

```

-----
c   subroutine factor (a,b,nwx,nwy,fft,indx)
c
c   This subroutine factorizes the matrix relating the modal amplitudes
c   and the nodal amplitudes using algorithms taken from Numerical
c   Recipes.
c
c   implicit real*8 (a-h,o-z)
c   parameter (nfxmax=30,nfyman=30,nwxmax=30,nwymax=30,
&   nnfmax=nfxmax*nfyman,nnwmax=nwxmax*nwymax)
c   real*8 vv(nnwmax),fft(nnwmax,nnwmax)
c   integer indx(nnwmax)
c   character fact,fact2,fname*10,fname2*10
c   pi=acos(-1.)
c   nnw=nwx*nwy
c   dela=a/(nwx+1)
c   delb=b/(nwy+1)
c   write(6,*)'factorizing matrix...'
c   kl=0
c   do 60 k=1,nwx
c   do 60 l=1,nwy
c     kl=kl+1
c     ij=0
c     x=k*dela
c     y=l*delb
c     do 70 i=1,nwx
c     do 70 j=1,nwy
c       pia=(2*i-1)*pi/a

```

```

    pjb=(2*j-1)*pi/b
    ij=ij+1
    fft(kl,ij)=sin(pia*x)*sin(pjb*y)
70  continue
60  continue
    call ludcmp (fft,nnw,nnwmax,indx,vv)
    return
    end
c-----
    subroutine crush (fft,indx,w2,f,wd,a,b,nwx,nwy,ifail,jfail,flag,
&                    kbad,lbad,bad,fix)
c
c  This subroutine enforces boundary conditions at nodal points
c  where the core is crushed.
c
    implicit real*8 (a-h,o-z)
    parameter (nfxmax=30,nfymax=30,nwxmax=30,nwymax=30,
&            nnfmax=nfxmax*nfymax,nnwmax=nwxmax*nwymax)
    real*8 w2(nnwmax),wd(nnwmax),f(nnfmax),fft(nnwmax,nnwmax),
&        bad(nnwmax)
    integer indx(nnwmax),kbad(nnwmax),lbad(nnwmax)
    character flag,fix(nnwmax)
    common/fprop/alli,a22i,a12i,a66i,d11,d22,d12,d66,tf1,tf2
    common/cprop/fs1,fs2,fult1,fult2,rcrush
    pi=acos(-1.)
    dela=a/(nwx+1)
    delb=b/(nwy+1)
    nnw=nwx*nwy
c
c  calculate discrete modal amplitudes wd(ij)
c
    ifail=0
    jfail=0
    kl=0
    do 20 k=1,nwx
    do 20 l=1,nwy
        kl=kl+1
        dum1=0.
        dum2=0.
        ij=0
        x=k*dela
        y=l*delb
        rxy=sqrt((x-a/2)**2+(y-b/2)**2)
        do 10 i=1,nwx
        do 10 j=1,nwy
            pia=(2*i-1)*pi/a
            pjb=(2*j-1)*pi/b
            ss=sin(pia*x)*sin(pjb*y)
            ij=ij+1
            dum1=dum1+w2(ij)*ss
            dum2=dum2-w2(ij)*(pia**2+pjb**2)*ss
10    continue
        sigma=dum1*fs1+dum2*fs2
        gain=abs(sigma)/sigma
c
c  enforce zero-reaction boundary condition
c
    if (flag.eq.'y') then
```



```
c
c   identify points within initial region of crushed core
c
c   if (rxy.lt.rcrush) then
c     wd(kl)=-sigma
c     ifail=ifail+1
c   elseif (fix(kl).eq.'y') then
c     wd(kl)=(fult2-abs(sigma))*gain
c
c   identify points at which sigmazz is above compressive strength of
c   core
c
c   elseif (-sigma.gt.fult1) then
c     wd(kl)=0.
c     jfail=jfail+1
c     kbad(jfail)=k
c     lbad(jfail)=1
c     bad(jfail)=gain
c   else
c     wd(kl)=0.
c   endif
c endif
c
c do not enforce zero-reaction boundary condition
c
c if (flag.eq.'n') then
c
c   identify points within initial region of crushed core
c
c   if (rxy.lt.rcrush) then
c     wd(kl)=-sigma-fult2
c     ifail=ifail+1
c   elseif (fix(kl).eq.'y') then
c     wd(kl)=(fult2-abs(sigma))*gain
c
c   identify points at which sigmazz is above compressive strength of
c   core
c
c   elseif (-sigma.gt.fult1) then
c     wd(kl)=0.
c     jfail=jfail+1
c     kbad(jfail)=k
c     lbad(jfail)=1
c     bad(jfail)=gain
c   else
c     wd(kl)=0.
c   endif
c endif
20 continue
   if (ifail.eq.0.and.jfail.eq.0) then
     return
   else
c
c   transform back to modal amplitudes
c
c   call lubksb (fft,nnw,nnwmax,indx,wd)
c   endif
101 format (3e13.4)
```



```
        endif
19      continue
        return
        end
c-----
      subroutine lubksb(a,n,np,indx,bb)
c
c      This subroutine performs backsubstitution after the l-u decomposition
c      (taken from Numerical Recipes).
c
      implicit real*8 (a-h,o-z)
      integer indx(n)
      real*8 a(np,np),bb(n)
      ii=0
      do 12 i=1,n
        ll=indx(i)
        sum=bb(ll)
        bb(ll)=bb(i)
        if (ii.ne.0)then
          do 11 j=ii,i-1
            sum=sum-a(i,j)*bb(j)
11          continue
          else if (sum.ne.0.) then
            ii=i
          endif
          bb(i)=sum
12      continue
      do 14 i=n,1,-1
        sum=bb(i)
        do 13 j=i+1,n
          sum=sum-a(i,j)*bb(j)
13      continue
        bb(i)=sum/a(i,i)
14      continue
      return
      end
c-----
      subroutine zequilm (w2,f,zeta,wd,a,b,nfx,nfy,nwx,nwy,rhsw,aload,
&                          alpha)
c
c      This subroutine sets up the matrix equation resulting from the
c      equilibrium equation.
c
      implicit real*8 (a-h,o-z)
      parameter (nfxmax=30,nfymax=30,nwxmax=30,nwymax=30,
&              nnfmax=nfxmax*nfymax,nnwmax=nwxmax*nwymax)
      real*8 w2(nnwmax),zeta(nnwmax),f(nnfmax),rhsw(nnwmax),wd(nnwmax)
      common/fprop/alli,a22i,a12i,a66i,d11,d22,d12,d66,tf1,tf2
      common/cprop/fs1,fs2,fult1,fult2,rcrush
      pi=acos(-1.)
c
c      evaluate rhs of z-equilibrium equation
c
      kl=0
      do 70 k=1,nfx
      do 70 l=1,nfy
        ke=2*(k-1)
        le=2*(l-1)
```

```

k1=k1+1
mn=0
do 10 m=1,nwx
do 10 n=1,nwy
  mo=2*m-1
  no=2*n-1
  mn=mn+1
  c1=ke*le*mo*no*pi**4/a**2/b**2
  c2=(ke*no*pi**2/a/b)**2
  c3=(le*mo*pi**2/a/b)**2
  c4=c2+c3
  ii=ke+mo
  jj=le+no
  if ((ii+1)/2.gt.nwx.or.(jj+1)/2.gt.nwy) goto 30
  ii=(ii+1)/2
  jj=(jj+1)/2
  ij=(ii-1)*nwy+jj
c    write(14,101)ke+mo,le+no,ii,jj,ij
  c5=c4-2.*c1
30  rhsw(ij)=rhsw(ij)+.25*f(k1)*(zeta(mn)+w2(mn))*c5
  ii=ke+mo
  jj=le-no
  if ((ii+1)/2.gt.nwx.or.(abs(jj)+1)/2.gt.nwy) goto 40
  c5=-c4-2.*c1
  if (jj.lt.0) c5=-c5
  ii=(ii+1)/2
  jj=(abs(jj)+1)/2
  ij=(ii-1)*nwy+jj
c    write(14,101)ke+mo,le-no,ii,jj,ij
  rhsw(ij)=rhsw(ij)+.25*f(k1)*(zeta(mn)+w2(mn))*c5
40  ii=ke-mo
  jj=le+no
  if ((abs(ii)+1)/2.gt.nwx.or.(jj+1)/2.gt.nwy) goto 50
  c5=-c4-2.*c1
  if (ii.lt.0) c5=-c5
  ii=(abs(ii)+1)/2
  jj=(jj+1)/2
  ij=(ii-1)*nwy+jj
c    write(14,101)ke-mo,le+no,ii,jj,ij
  rhsw(ij)=rhsw(ij)+.25*f(k1)*(zeta(mn)+w2(mn))*c5
50  ii=ke-mo
  jj=le-no
  if ((abs(ii)+1)/2.gt.nwx.or.(abs(jj)+1)/2.gt.nwy) goto 10
  c5=c4-2.*c1
  if (jj.lt.0) c5=-c5
  if (ii.lt.0) c5=-c5
  ii=(abs(ii)+1)/2
  jj=(abs(jj)+1)/2
  ij=(ii-1)*nwy+jj
c    write(14,101)ke-mo,le-no,ii,jj,ij
  rhsw(ij)=rhsw(ij)+.25*f(k1)*(zeta(mn)+w2(mn))*c5
10  continue
70  continue
c
c    add terms with aload and residuals due to crushed core
c
k1=0
do 60 k=1,nwx

```

```

do 60 l=1,nwy
  kl=kl+1
  rshw(kl)=tf1*(rshw(kl)
&          -aload*(zeta(kl)+(1.-alpha)*w2(kl))*((2.*k-1.)*pi/a)**2)
&          -wd(kl)
60 continue
c
c divide rhs of zequilibrium equation by 'stiffness term' on lhs
c
  ij=0
  do 20 i=1,nwx
  do 20 j=1,nwy
    pia=pi*(2.*i-1.)/a
    pjb=pi*(2.*j-1.)/b
    ij=ij+1
    dentr=d11*pia**4+(2.*d12+4.*d66)*(pia*pjb)**2+d22*pjb**4
&        +fs1-fs2*(pia**2+pjb**2)+tf1*alpha*aload*pia**2
    rshw(ij)=rshw(ij)/dentr
20 continue
101 format(5i6)
    return
    end
c-----
c
c subroutine compatlty (w2,f,zeta,a,b,nfx,nfy,nwx,nwy,rhsf)
c
c This subroutine sets up the matrix equation resulting from the
c compatibility equation.
c
  implicit real*8 (a-h,o-z)
  parameter (nfxmax=30,nfymax=30,nwxmax=30,nwymax=30,
&          nnfmax=nfxmax*nfymax,nnwmax=nwxmax*nwymax)
  real*8 w2(nnwmax),zeta(nnwmax),f(nnfmax),rhsf(nnfmax)
  common/fprop/alli,a22i,a12i,a66i,d11,d22,d12,d66,tf1,tf2
  common/cprop/fs1,fs2,fult1,fult2,rcrush
  pi=acos(-1.)
c
c evaluate rhs of compatability equation
c
  kl=0
  do 10 k=1,nwx
  do 10 l=1,nwy
    ko=2*k-1
    lo=2*l-1
    kl=kl+1
    mn=0
    do 10 m=1,nwx
    do 10 n=1,nwy
      mo=2*m-1
      no=2*n-1
      mn=mn+1
      c1=ko*lo*mo*no*pi**4/a**2/b**2
      c2=(ko*no*pi**2/a/b)**2
      c3=(lo*mo*pi**2/a/b)**2
      c4=c2+c3
      ii=abs(ko-mo)/2
      jj=abs(lo-no)/2
      if ((ii+1).gt.nfx.or.(jj+1).gt.nfy) goto 30
      ij=ii*nfy+jj+1

```

```

c      write(15,101)ko-mo,lo-no,ii,jj,ij
      rhsf(ij)=rhsf(ij)+.25*w2(kl)*(c1*(w2(mn)+2.*zeta(mn))-
&          c2*w2(mn)-c4*zeta(mn))
30     ii=abs(ko-mo)/2
      jj=(lo+no)/2
      if ((ii+1).gt.nfx.or.(jj+1).gt.nfy) goto 40
      ij=ii*nfy+jj+1
c      write(15,101)ko-mo,lo+no,ii,jj,ij
      rhsf(ij)=rhsf(ij)+.25*w2(kl)*(c1*(w2(mn)+2.*zeta(mn))+
&          c2*w2(mn)+c4*zeta(mn))
40     ii=(ko+mo)/2
      jj=abs(lo-no)/2
      if ((ii+1).gt.nfx.or.(jj+1).gt.nfy) goto 50
      ij=ii*nfy+jj+1
c      write(15,101)ko+mo,lo-no,ii,jj,ij
      rhsf(ij)=rhsf(ij)+.25*w2(kl)*(c1*(w2(mn)+2.*zeta(mn))+
&          c2*w2(mn)+c4*zeta(mn))
50     ii=(ko+mo)/2
      jj=(lo+no)/2
      if ((ii+1).gt.nfx.or.(jj+1).gt.nfy) goto 10
      ij=ii*nfy+jj+1
c      write(15,101)ko+mo,lo+no,ii,jj,ij
      rhsf(ij)=rhsf(ij)+.25*w2(kl)*(c1*(w2(mn)+2.*zeta(mn))-
&          c2*w2(mn)-c4*zeta(mn))
10    continue
c
c      divide rhs of compatability equation by 'stiffness term' on lhs
c
c      ij=0
      do 20 i=1,nfx
      do 20 j=1,nfy
      pia=pi*2.*(i-1)/a
      pjb=pi*2.*(j-1)/b
      ij=ij+1
      dum=alli*pjb**4+(2.*a12i+a66i)*pia**2*pjb**2+a22i*pia**4
      if (dum.ne.0.) rhsf(ij)=rhsf(ij)/dum/tf1
20    continue
101  format(5i6)
      return
      end
c-----
c      subroutine centerl (f,w2,zeta,nwx,nwy,nfx,nfy,a,b,aload)
c
c      This subroutine calculates desired outputs along the centerlines
c      of the panel.
c
c      implicit real*8 (a-h,o-z)
      parameter (nfxmax=30,nfymax=30,nwxmax=30,nwymax=30,
&          nnfmax=nfxmax*nfymax,nnwmax=nwxmax*nwymax)
      real*8 w2(nnwmax),f(nnfmax),zeta(nnwmax)
      common/fprop/alli,a22i,a12i,a66i,d11,d22,d12,d66,tf1,tf2
      common/cprop/fs1,fs2,fult1,fult2,rcrush
      pi=acos(-1.)
      write(19,102)aload/1.e+6,fs1/1.e+9,fs2/1.e+3,rcrush*1000
c
c      calculate deformed profile and sigmazz along x=a/2
c
c      x=a/2.

```

```
dely=b/(nwy+1)
smax=0.
do 10 l=1,nwy
  z=0.
  zd=0.
  dum1=0.
  dum2=0.
  dum3=0.
  dum4=0.
  dum5=0.
  dum6=0.
  dum7=0.
  dum8=0.
  ij=0
  y=l*dely
  do 20 i=1,nwx
  do 20 j=1,nwy
    ij=ij+1
    pia=(2*i-1)*pi/a
    pjb=(2*j-1)*pi/b
    cc=cos(pia*x)*cos(pjb*y)
    ss=sin(pia*x)*sin(pjb*y)
    dum2=dum2-(zeta(ij)+w2(ij))*pia**2*ss
    dum4=dum4-(zeta(ij)+w2(ij))*pjb**2*ss
    dum6=dum6+(zeta(ij)+w2(ij))*pia*pjb*cc
    dum7=dum7-ss*w2(ij)*
    &      (d11*pia**4+pia**2*pjb**2*(2.*d12+4.*d66)+d22*pjb**4)
    dum8=dum8+w2(ij)*(d11*pia**2+d12*pjb**2)*ss
    zd=zd+(w2(ij)+zeta(ij))*ss
    z=z+zeta(ij)*ss
20  continue
    ij=0
    do 30 i=1,nfx
    do 30 j=1,nfy
      ij=ij+1
      pia=2.*(i-1)*pi/a
      pjb=2.*(j-1)*pi/b
      cc=cos(pia*x)*cos(pjb*y)
      ss=sin(pia*x)*sin(pjb*y)
      dum1=dum1-f(ij)*pjb**2*cc
      dum3=dum3-f(ij)*pia**2*cc
      dum5=dum5-2.*f(ij)*pia*pjb*ss
30  continue
    sxxm=dum1+aload
    sxxb=dum8*6./tf1**2
    szz=tf1*(sxxm*dum2+dum3*dum4+dum5*dum6)+dum7
    sxx1=sxxm+sxxb
    sxx2=sxxm-sxxb
    if (1.eq.(nwy+1)/2) write(6,103)zd
c
c  displacements in [mm], stresses in [MPa]
c
    write(19,101)(y-b/2.)*1000.,z*1000.,zd*1000.,
    & szz/1.e+6,sxx1/1.e+6,sxx2/1.e+6,sxxm/1.e+6
c
c  locate max sxxm
c
    if (abs(sxxm).gt.abs(smax)) then
```

```
        smax=sxxm
        ymax=y-b/2.
    endif
10  continue
    write(6,*)ymax,smax/1.e+6
c
c  calculate deformed profile and sigmazz along y=b/2
c
    write(20,102)aload/1.e+6,fs1/1.e+9,fs2/1.e+3,rcrush*1000.
    y=b/2.
    delx=a/(nwx+1)
    do 50 l=1,nwx
        z=0.
        zd=0.
        dum1=0.
        dum2=0.
        dum3=0.
        dum4=0.
        dum5=0.
        dum6=0.
        dum7=0.
        dum8=0.
        ij=0
        x=l*delx
        do 60 i=1,nwx
            do 60 j=1,nwy
                ij=ij+1
                pia=(2*i-1)*pi/a
                pjb=(2*j-1)*pi/b
                cc=cos(pia*x)*cos(pjb*y)
                ss=sin(pia*x)*sin(pjb*y)
                dum2=dum2-(zeta(ij)+w2(ij))*pia**2*ss
                dum4=dum4-(zeta(ij)+w2(ij))*pjb**2*ss
                dum6=dum6+(zeta(ij)+w2(ij))*pia*pjb*cc
                dum7=dum7-ss*w2(ij)*
                &      (d11*pia**4+pia**2*pjb**2*(2.*d12+4.*d66)+d22*pjb**4)
c      dum8=dum8+w2(ij)*(d11*pia**2+d12*pjb**2)*ss
                zd=zd+(w2(ij)+zeta(ij))*ss
                z=z+zeta(ij)*ss
60      continue
        ij=0
        do 70 i=1,nfx
            do 70 j=1,nfy
                ij=ij+1
                pia=2.*(i-1)*pi/a
                pjb=2.*(j-1)*pi/b
                cc=cos(pia*x)*cos(pjb*y)
                ss=sin(pia*x)*sin(pjb*y)
                dum1=dum1-f(ij)*pjb**2*cc
                dum3=dum3-f(ij)*pia**2*cc
                dum5=dum5-2.*f(ij)*pia*pjb*ss
70      continue
        szz=tf1*((dum1+aload)*dum2+dum3*dum4+dum5*dum6)+dum7
c
c  displacements in [mm], stresses in [MPa]
c
        write(20,101)(x-a/2.)*1000.,z*1000.,zd*1000.,szz/1.e+6
50  continue
```



```
101 format(7e14.5)
102 format('zone="aload=',f7.1,' MPa, fs1=',f8.2,' GN/m/m/m, fs2='
&          ,f8.2,' kN/m, rcrush=',f5.1,' mm"')
103 format(1x,'zd=',e12.4)
    return
    end
```

Appendix B

Information on Material and Equipment Supplier

The addresses and phone numbers of material and equipment suppliers referred to in Chapter 5 are listed as follows:

Hercules, Magna, UT. Tel: 801-250-5911

Ciba-Geigy, Miami, FL. Tel: 1-800-854-1869

American Cyanamid Company, Havre de Grace, MD. Tel: 410-939-1910

DuPont Company, Wilmington, DE. Tel: 1-800-453-8527

Dexter Corporation, Adhesive & Structural Material Division, Seabrook, NH. Tel: 603-474-5541

3M Company, Springfield, MO. Tel: 1-800-235-2376

RALMIKE's[®] Tool-A-Rama[®], South Plainfield, NJ.

D-Aircraft Products Co., Anaheim, CA. Tel: 714-632-8444

Axel Plastics Research Laboratories, Inc. Woodside, NY. Tel: 718-672-8300

Measurements Group, Raleigh, NC.

MTS Systems Corporation, Minneapolis, MN. Tel: 612-944-4000

Lebow Associates, Inc., Troy, MI.

GW Instruments, Inc., Medford, MA. Tel: 617-625-4096.

National Instruments Corporation, Austin, TX. Tel: 1-800-433-3488

Edmund Scientific, Inc. Barrington, NJ. Tel: 609-573-6260

Kodak Co., Rochester, NY. Tel: 1-800-242-2424

Digital Vision, Inc., Dedham, MA. 617-329-5400

Scanray Corporation, Harbor City, CA.

Appendix C

Specimen Data

Data for all specimens tested under uniaxial compression tests are presented in Tables C.1 and C.2. The abbreviation SID indicates specimens with static indentation damage, SCD indicates specimens with simulated core damage, and SFD indicates specimens with simulated facesheet damage. The number at the end of the abbreviations represents the damage levels. Level 1 indentation damage is induced with the 12.7 mm-diameter indenter while Levels 2 and 3 are induced with the 25.4 mm-diameter indenter and the 38.1 mm-diameter indenter, respectively. The simulated damage levels have the appropriate damage as observed in the statically indented specimens.

Table C.1 Experimental data for specimens with (0/90) facesheets

Damage Type	Width [mm]	Thickness [mm]		Modulus [GPa]		Failure Stress [MPa]	Failure Strain [$\mu\epsilon$]
		Front	Back	Front	Back		
none	89.63	0.34	0.35	—	50.7	400	7680
	89.67	0.35	0.35	67.2	63.0	399	6160
	89.43	0.35	0.35	68.4	—	409	6010
SID1	89.29	0.34	0.34	71.2	67.8	275	3920
	88.82	0.34	0.34	67.6	63.7	270	4110
	89.03	0.32	0.32	68.3	67.2	224	3480
	87.34	0.34	0.35	.	—	298	4540
SID2	89.14	0.32	0.33	67.8	65.1	271	3980
	88.73	0.34	0.34	62.4	65.6	259	4110
	89.20	0.34	0.33	64.3	65.5	260	4010
	89.38	0.35	0.35	67.2	62.1	264	4120
SID3	89.20	0.36	0.36	63.6	59.4	253	4000
	89.07	0.35	0.35	62.7	64.4	275	4400
	89.20	0.34	0.36	65.6	66.7	261	3960
	89.00	0.35	0.34	70.0	61.9	273	3680
SCD1	89.24	0.33	0.33	67.8	71.0	358	5185
	88.95	0.33	0.34	71.7	65.6	351	4980
	89.35	0.31	0.34	70.2	68.7	369	5460
SCD2	89.04	0.35	0.39	58.7	59.8	313	5280
	89.00	0.36	0.34	62.7	65.0	320	5000
	89.25	0.35	0.35	63.0	62.4	311	4930
SCD3	89.29	0.34	0.39	59.7	60.9	308	5080
	89.15	0.35	0.36	64.4	62.5	305	4730
	89.50	0.33	0.34	69.7	67.6	314	4460
SFD1	89.50	0.34	0.34	68.1	68.0	271	3760
	89.70	0.34	0.34	69.4	64.3	303	4920
	89.24	0.34	0.35	70.3	61.3	300	4100

Table C.2 Experimental data for specimens with (± 45) facesheets

Damage Type	Width [mm]	Thickness [mm]		Modulus [GPa]		Failure Stress [MPa]	Failure Strain [$\mu\epsilon$]
		Front	Back	Front	Back		
none	88.87	0.35	0.35	24.3	24.9	245	17400
	88.50	0.35	0.35	24.5	22.5	249	19810
	88.90	0.34	0.36	27.3	24.2	248	16050
SID1	88.66	0.34	0.36	24.4	24.4	232	14900
	88.26	0.36	0.35	24.2	24.4	224	14400
	88.62	0.35	0.35	24.6	23.1	224	14200
	89.21	0.36	0.34	23.1	—	206	14700
SID2	89.04	0.35	0.34	24.9	23.9	213	11750
	88.61	0.35	0.34	23.5	22.5	225	13250
	88.64	0.34	0.37	24.3	23.8	211	12200
	89.40	0.35	0.36	23.9	22.5	196	12500
SID3	88.50	0.36	0.35	21.8	22.9	199	14400
	88.66	0.36	0.36	21.8	22.0	198	—
	88.70	0.34	0.36	19.6	19.2	229	—
	89.53	0.34	0.33	23.2	22.4	192	12050
SCD1	88.67	0.36	0.35	22.2	22.4	243	17425
	88.62	0.35	0.34	23.7	23.8	236	15550
	88.72	0.38	0.35	22.0	21.9	242	19560
SCD2	88.54	0.36	0.36	23.4	22.4	230	18200
	88.83	0.37	0.35	22.6	23.4	224	17340
	88.60	0.36	0.35	22.4	23.5	226	17300
SCD3	88.60	0.35	0.35	—	22.8	233	—
	88.66	0.36	0.35	22.4	23.3	230	17900
	88.70	0.35	0.35	22.8	22.7	238	18900
SFD1	89.37	0.34	0.35	22.4	23.1	214	17650
	89.31	0.35	0.35	23.1	22.6	223	19800
	89.38	0.35	0.34	23.8	—	227	20125

Appendix D

Experimental Dimple Propagation Data

In this appendix, plots are presented showing the applied stress level versus the dimension of the dimple perpendicular to the loading direction for specimens with simulated core damage and those with static indentation damage. The dimension of the dimple (variable y in the graphs presented) is defined as the width of the dimple as measured at the depth of the first-order moiré fringe (0.18 mm). The orders of the fringes essentially represent the contour levels of the out-of-plane displacement. The zeroth-order fringe is the outermost fringe and represents no out-of-plane displacement. The fringe next to the zeroth-order fringe is the first-order fringe. An example of moiré fringe patterns and a description of how fringe orders are determined is given in Section 5.5.3 of Chapter 5. The legends of the graphs are the codes used to identify individual specimens. It should be noted that for some cases of level 3 damage, zero is assigned to the initial value of y because the first-order fringe either does not exist or could not be measured accurately.

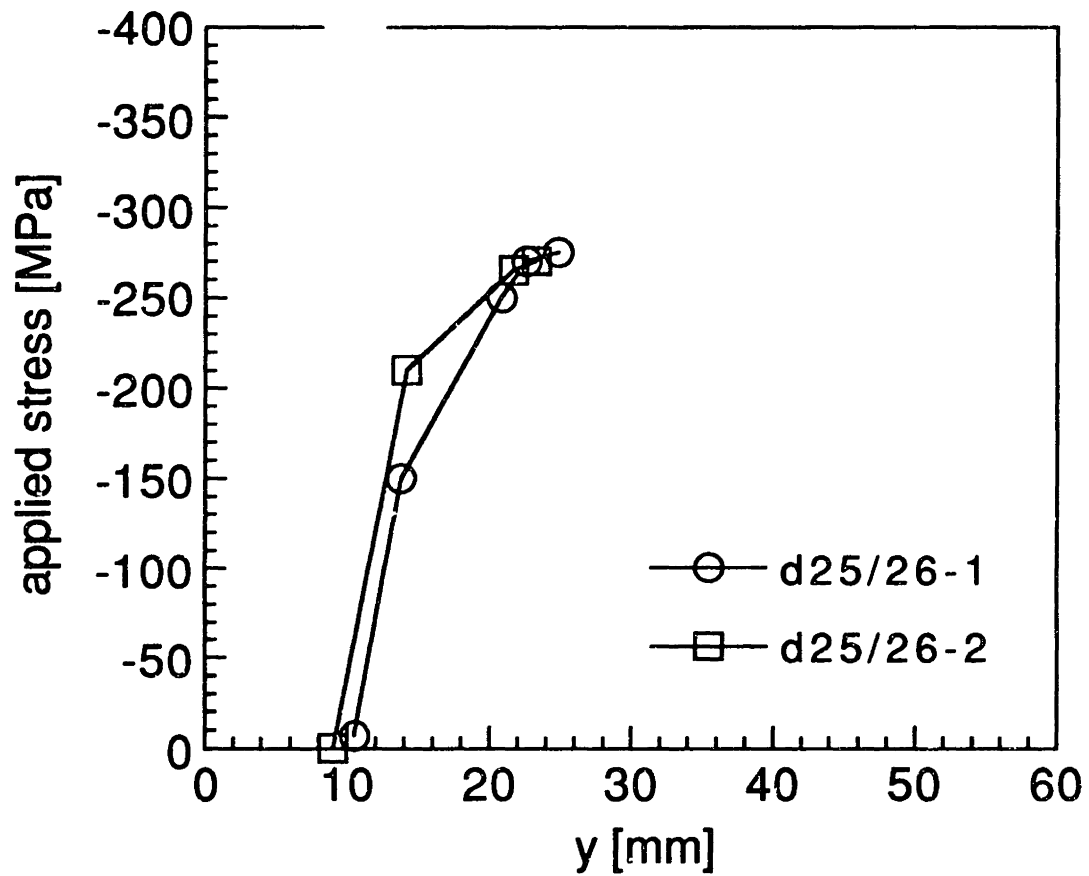


Figure D.1 Measured dimension of dimple along centerline perpendicular to loading at various applied stress levels for specimens with (0/90) facesheets and level 1 static indentation damage.

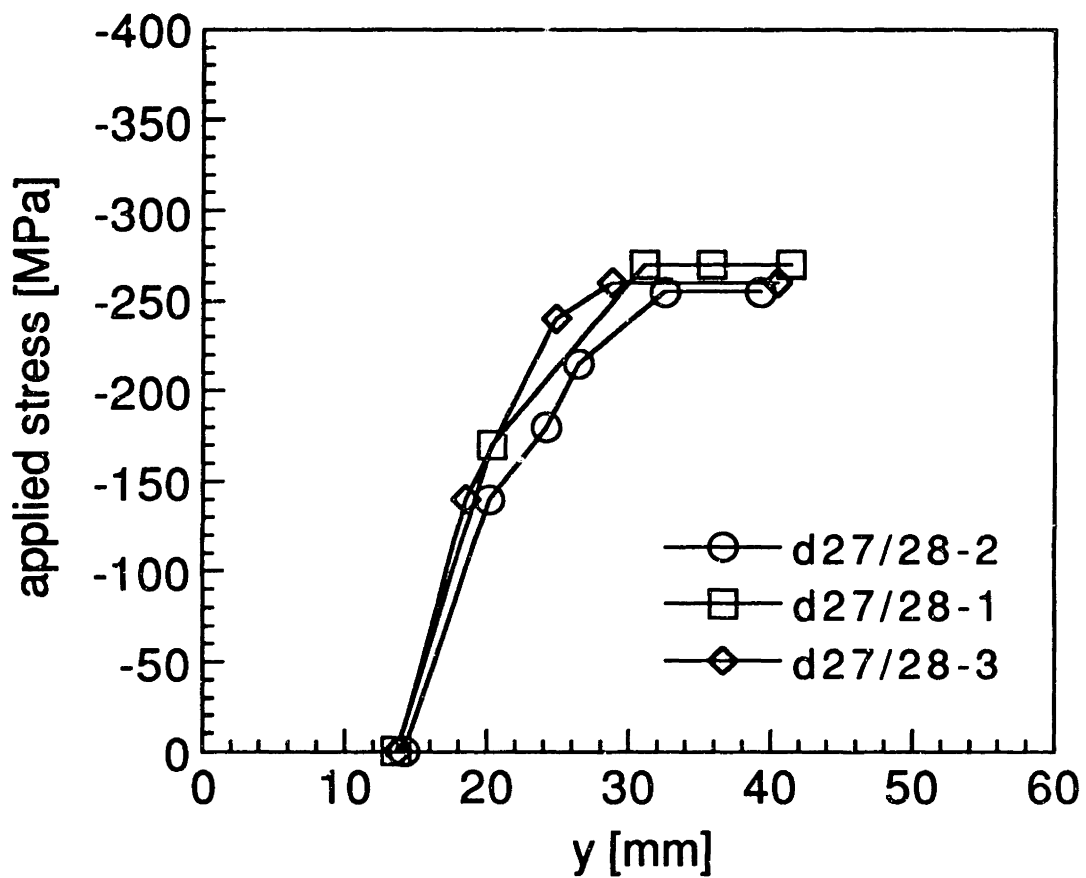


Figure D.2 Measured dimension of dimple along centerline perpendicular to loading at various applied stress levels for specimens with (0/90) facesheets and level 2 static indentation damage.

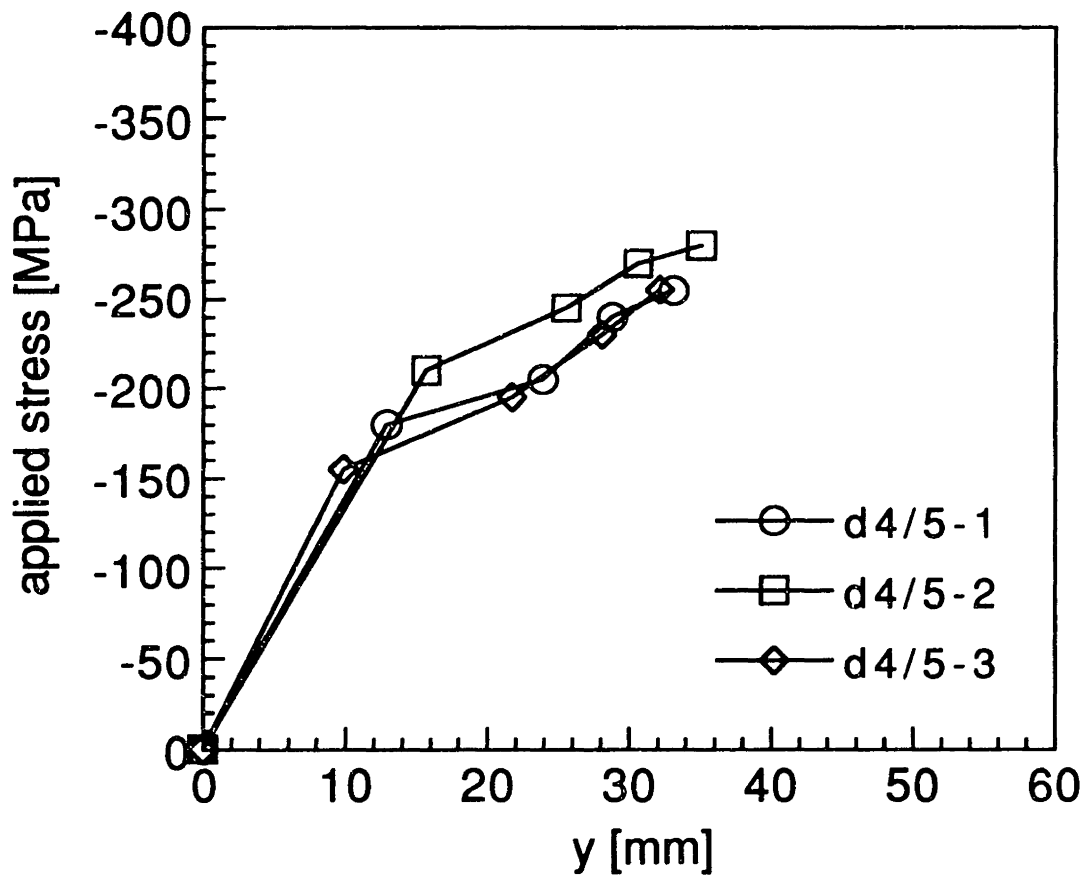


Figure D.3 Measured dimension of dimple along centerline perpendicular to loading at various applied stress levels for specimens with (0/90) facesheets and level 3 static indentation damage.

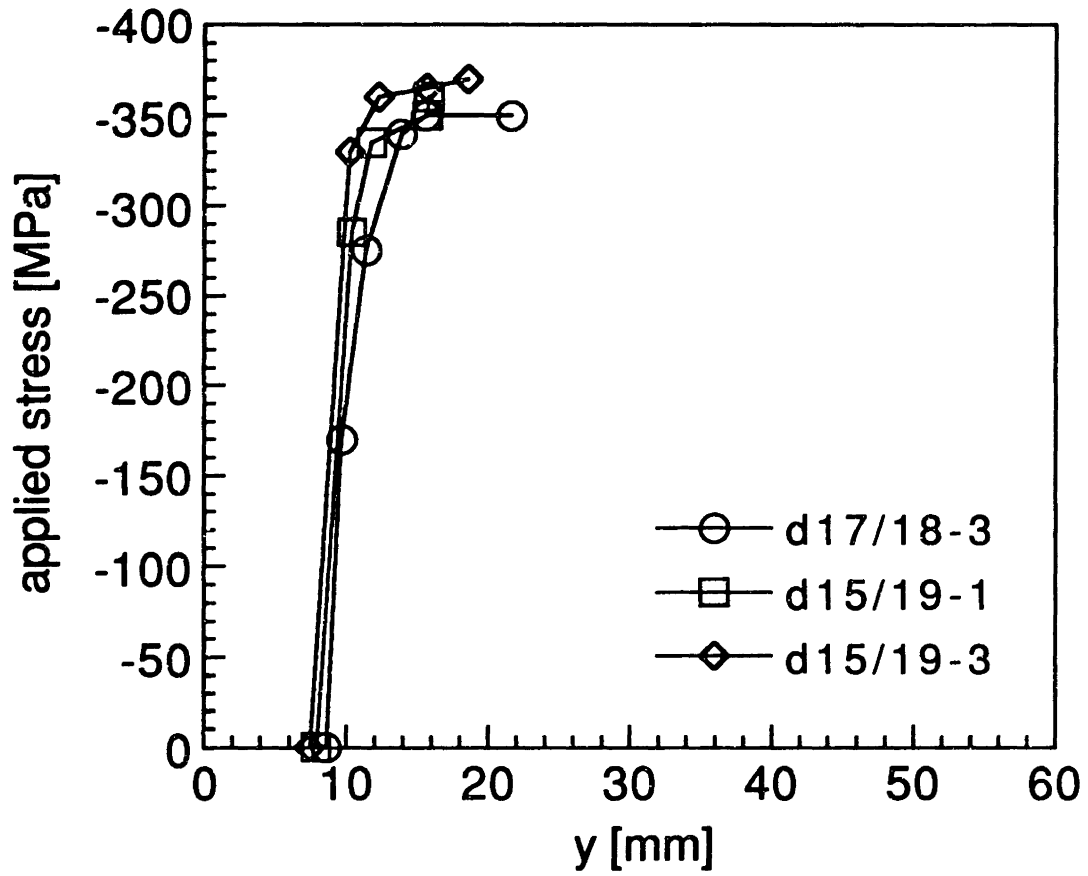


Figure D.4 Measured dimension of dimple along centerline perpendicular to loading at various applied stress levels for specimens with (0/90) facesheets and level 1 simulated core damage.

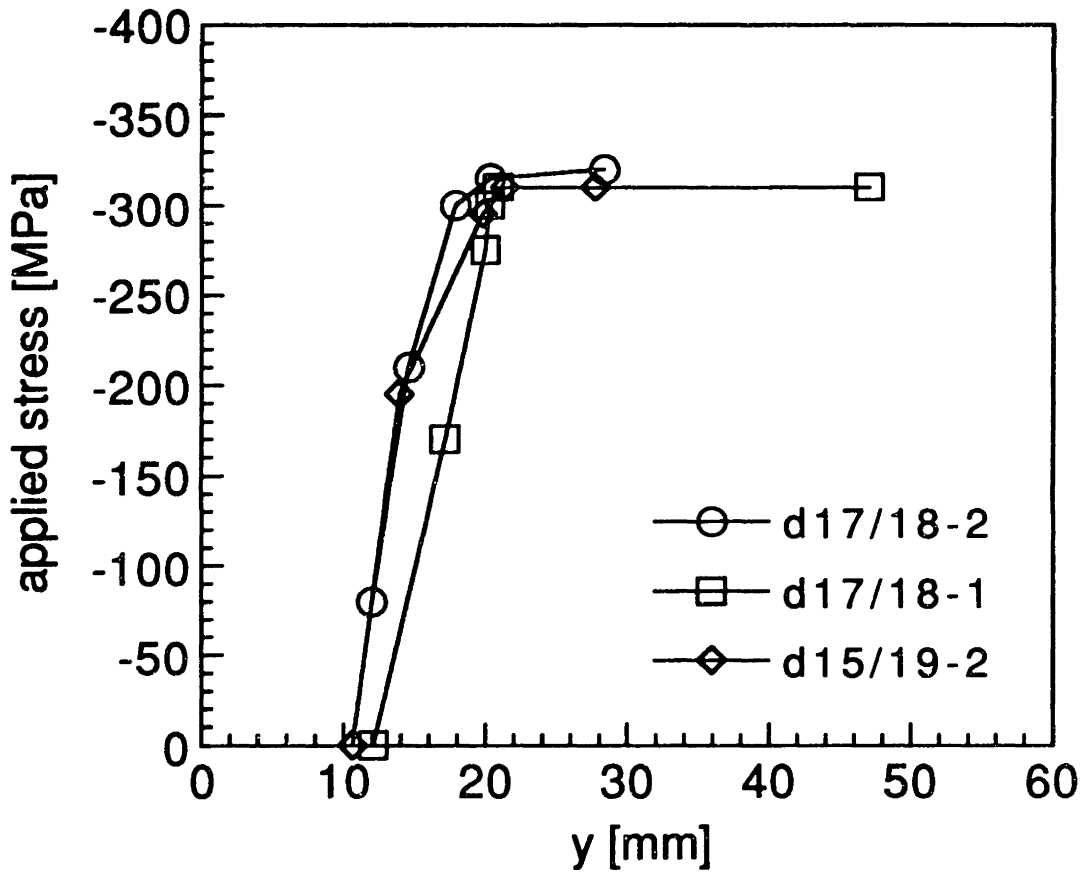


Figure D.5 Measured dimension of dimple along centerline perpendicular to loading at various applied stress levels for specimens with (0/90) facesheets and level 2 simulated core damage.

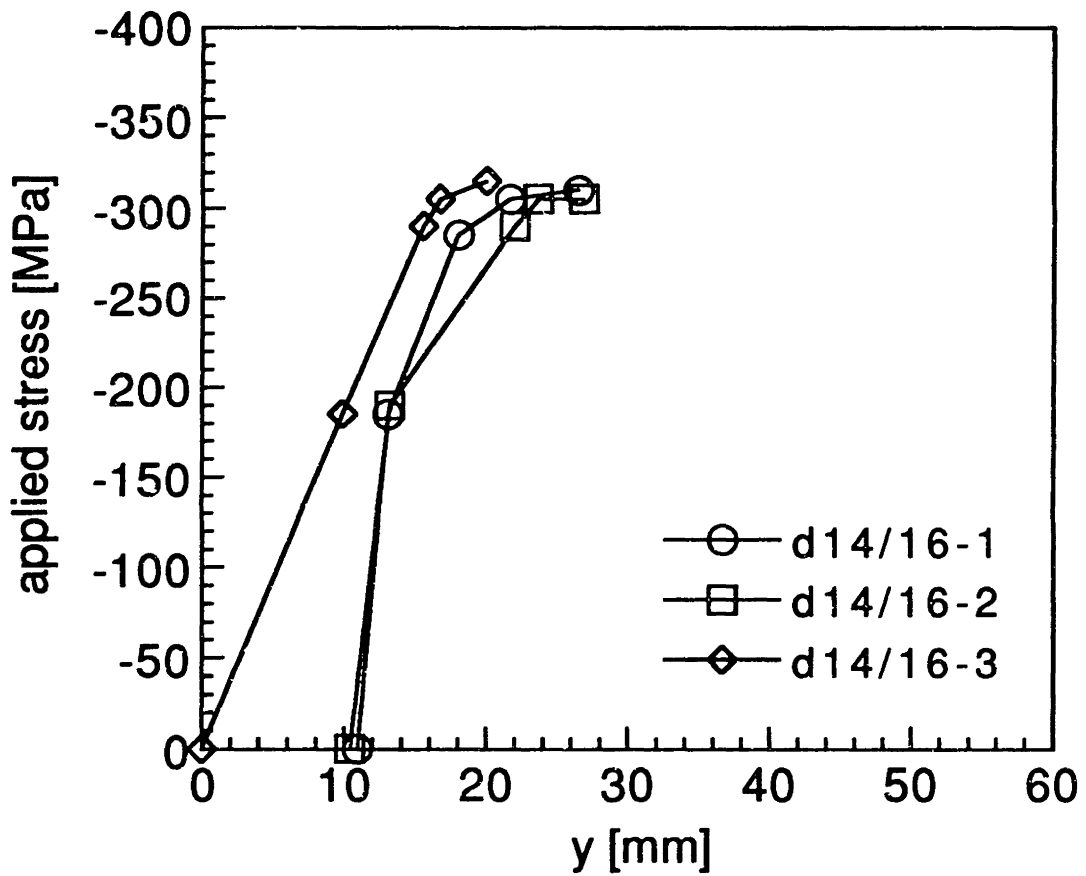


Figure D.6 Measured dimension of dimple along centerline perpendicular to loading at various applied stress levels for specimens with (0/90) facesheets and level 3 simulated core damage.

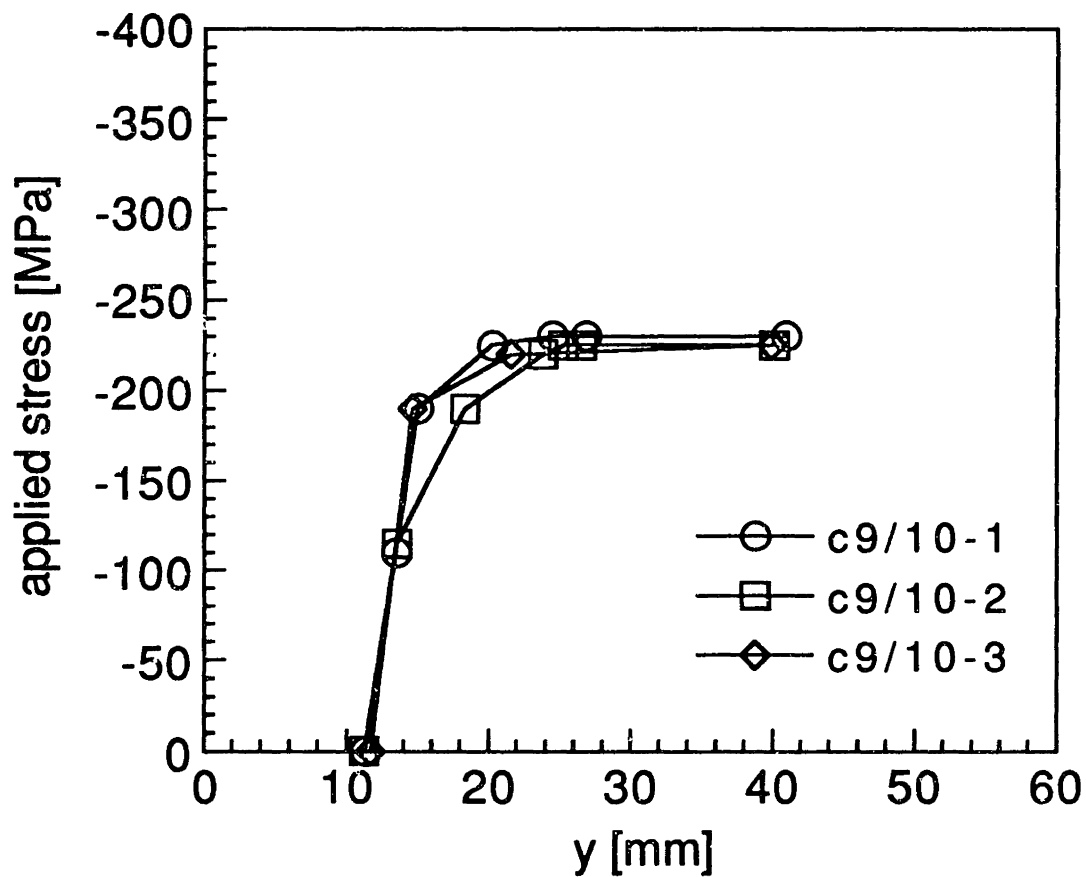


Figure D.7 Measured dimension of dimple along centerline perpendicular to loading at various applied stress levels for specimens with (± 45) facesheets and level 1 static indentation damage.

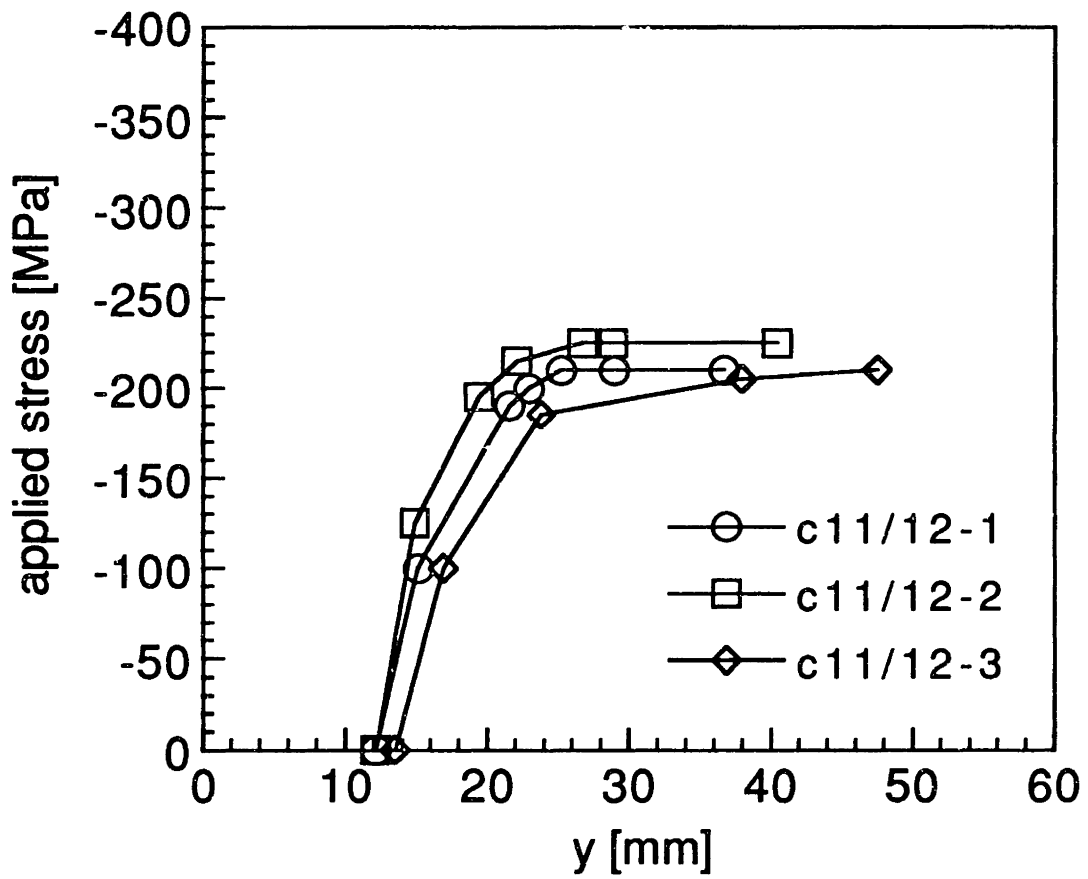


Figure D.8 Measured dimension of dimple along centerline perpendicular to loading at various applied stress levels for specimens with (± 45) facesheets and level 2 static indentation damage.

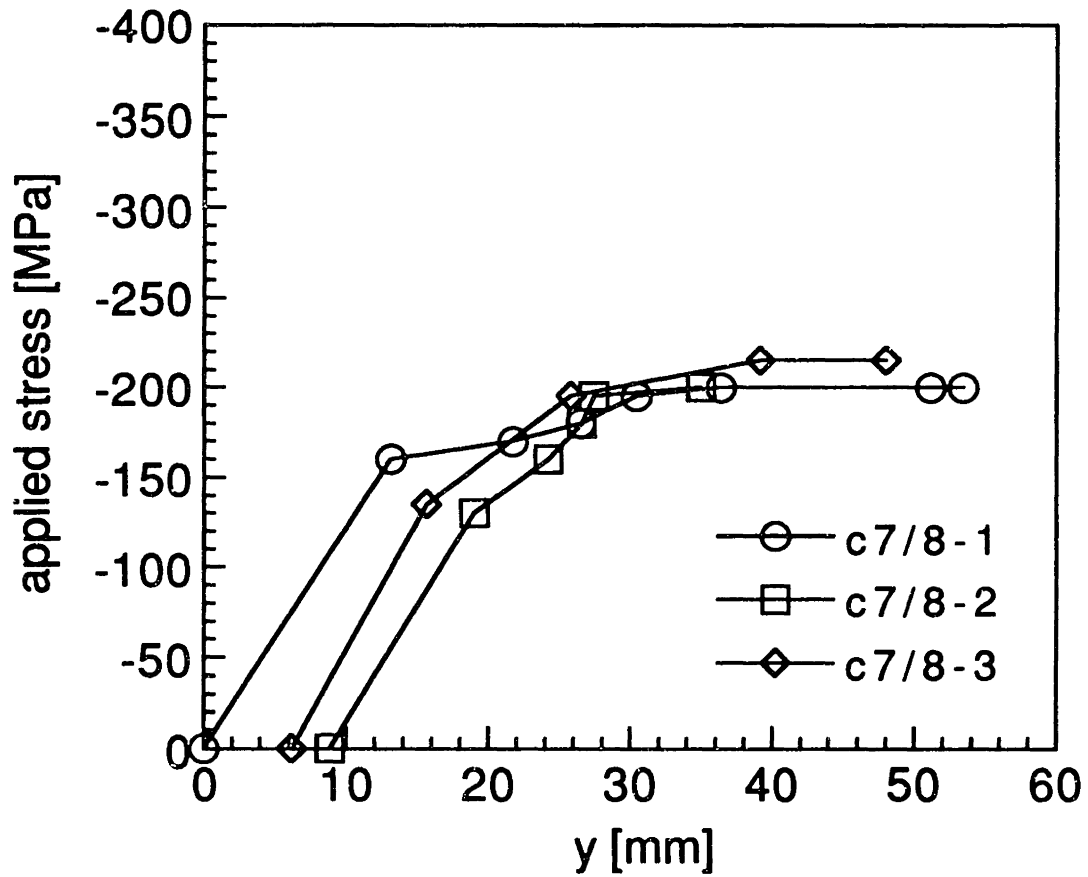


Figure D.9 Measured dimension of dimple along centerline perpendicular to loading at various applied stress levels for specimens with (± 45) facesheets and level 3 static indentation damage.

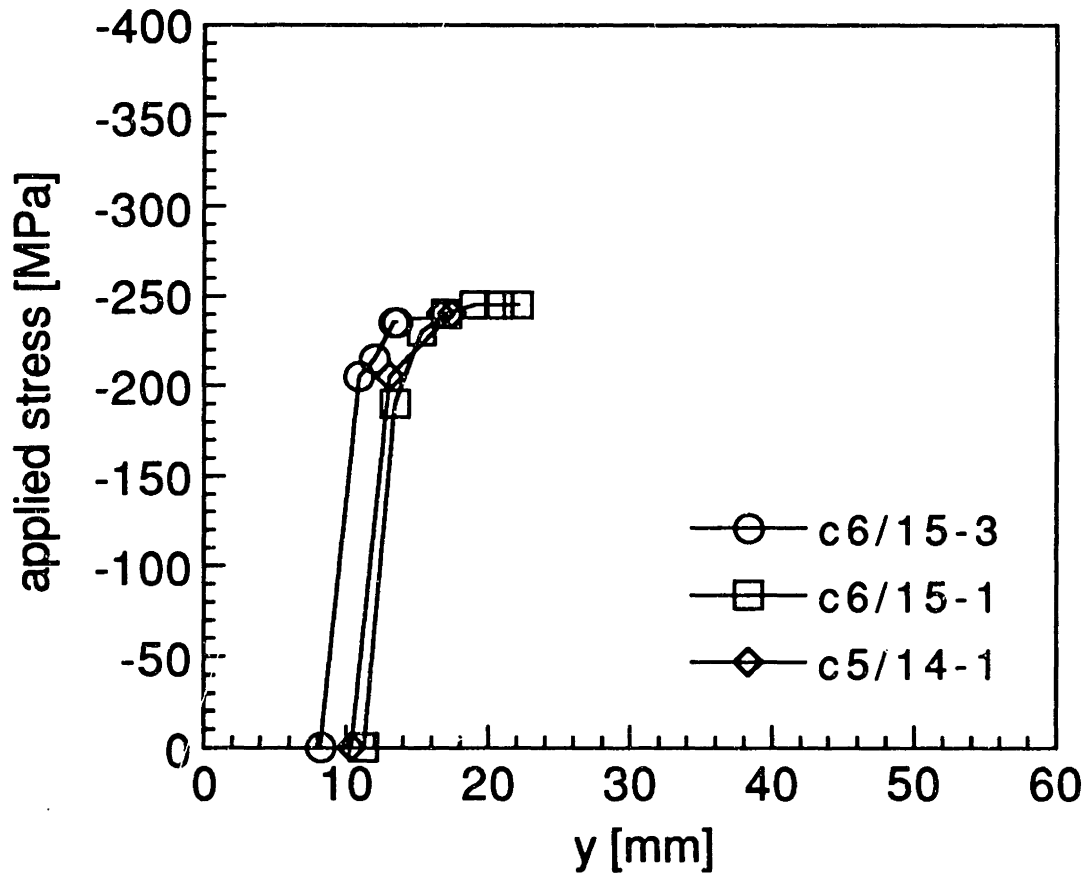


Figure D.10 Measured dimension of dimple along centerline perpendicular to loading at various applied stress levels for specimens with (± 45) facesheets and level 1 simulated core damage.

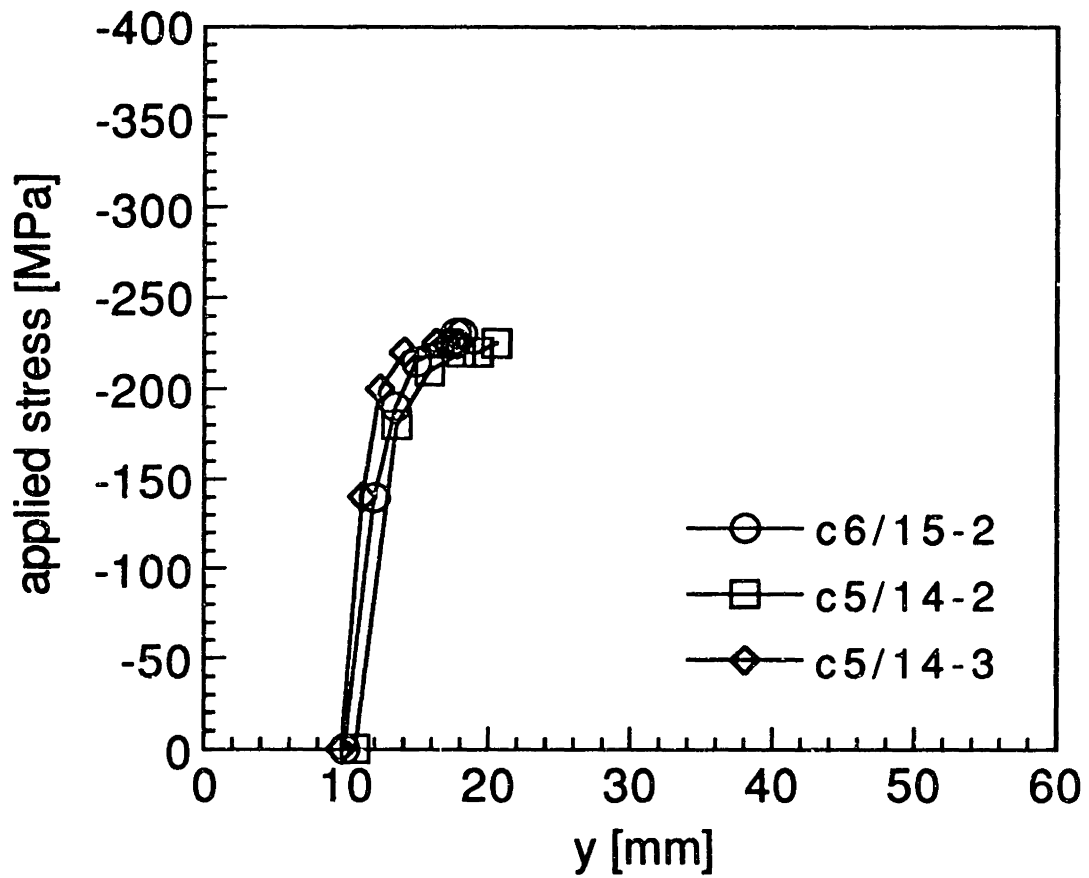


Figure D.11 Measured dimension of dimple along centerline perpendicular to loading at various applied stress levels for specimens with (± 45) facesheets and level 2 simulated core damage.